EPFL

Thèse n° 8700

The Role of the Composite Floor System and Framing Action in the Seismic Performance of Composite Steel Moment-Resisting Frames

Présentée le 3 mars 2022

Faculté de l'environnement naturel, architectural et construit
Laboratoire des structures métalliques résilientes
Programme doctoral en génie civil et environnement

pour l'obtention du grade de Docteur ès Sciences

par

Hammad EL JISR

Acceptée sur proposition du jury

Prof. A. Muttoni, président du jury
Prof. D. Lignos, directeur de thèse
Prof. R. Leon, rapporteur
Prof. A. Plumier, rapporteur
Prof. K. Beyer, rapporteuse

École polytechnique fédérale de Lausanne

2022

Acknowledgements

First, I would like to thank my supervisor Prof. Dimitrios Lignos for providing me with the opportunity to pursue a PhD at RESSLab and for his valuable supervision during the course of my doctoral studies. I would also like to thank the members of my jury, Prof. Aurelio Muttoni, Prof. André Plumier, Prof. Roberto Leon and Prof. Katrin Beyer for their insightful comments and suggestions. Additionally, I would like to express my sincere gratitude to Dr. Ahmed Elkady for his help and guidance during his time at RESSLab.

My gratitude extends to EPFL and the Swiss National Science Foundation (Project No. 200021_169248) for supporting my research. I would like to thank the staff at GIS, Gilles Guignet, Gerald Rouge, Serge Despont, Armin Krkic, Frédérique Dubugnon and Jonathan Martin, for their assistance with the experimental program. I am especially grateful to Elias Merhi for his tremendous help in constructing the test specimen. Thanks as well to Nathan Kempter, Kusum Shrestha, Raphaël Guby and Meriton Beqiraj for their help. Without the precious support of everyone involved in the experiment, I would not have been able to conduct it successfully. I also thank Dr. Albano de Castro e Sousa for his involvement in the fabrication of the test specimen and during the experimental program.

Thank you to my friends and colleagues, Andy, Martina, Hiro, Dinos, Alex, Gabriele, Selim, Athina, Nenad, Tatsuya and Diego for a cherished time spent together in the lab. A particular thanks to Prof. Nussbaumer for the stimulating discussions and to Karin for her gracious help with many matters.

Lastly, I would like to thank my parents, brother and sisters for their unconditional love. You mean the world to me.

Hammad El Jisr

Lausanne, January 2022

Abstract

With the advent of performance-based earthquake engineering (PBEE), the need for reliable prediction of earthquake-induced collapse of structures is essential. Despite the significant progress that has been made towards this goal, there are several hurdles that still need to be overcome. Deterioration models, which are currently used for simulating structural collapse, are largely based on available test data that featured subassemblies with overly simplified boundary conditions. These experiments did not account for the force redistribution occurring within structural systems after the onset of nonlinear geometric instabilities under cyclic loading. For the case of composite steel moment resisting frames (MRFs), which is the primary focus of this thesis, the influence of the axial restraint provided by the slab continuity and framing action on the seismic behavior of composite steel MRFs has been recognized in prior work. Nevertheless, these effects have neither been thoroughly investigated nor quantified at lateral drift demands associated with dynamic instability of composite steel MRFs under seismic loading.

In this doctoral thesis, a unique experimental program of a two-bay composite steel MRF subsystem was conducted at full-scale. The experimental program, which was corroborated by continuum finite element analyses, aimed at comprehending the role of the underlying physical mechanisms, associated with the slab continuity and framing action, on the hysteretic behavior of composite steel MRFs with a particular emphasis at large deformations associated with collapse. The research findings suggest that the slab continuity limits the extent of local buckling and beam shortening within the dissipative zones of composite steel MRFs. While nonlinear geometric instabilities attributable to local buckling and concrete crushing are pronounced in composite steel beams at large inelastic deformations, the framing action and slab continuity preserve the overall stability of the structural system even in cases that ductile cracks form within a dissipative zone. The test results suggest that the presence of the transverse beams within the floor system should be factored in capacity design principles of composite steel MRFs. The experimental findings also suggest that methods for computing the effective slab width in composite steel MRFs should be reassessed.

The available data along with information from prior experiments informed the development of practice-oriented engineering models for the seismic assessment of composite steel MRFs. Moreover, a macro-model was proposed for simulating the hysteretic behavior of composite steel beams under cyclic loading. The model, which was validated thoroughly with available experimental data, simulates explicitly the cyclic deterioration in strength and stiffness of composite steel beams and their respective beam-slab connections. The proposed macro-model was employed to benchmark the seismic collapse risk of prototype buildings with composite steel MRFs, as well as the repairability of beam-slab connections within the framework of PBEE.

Keywords

Composite steel moment-resisting frames, Collapse behavior, Slab restraint, Framing action, Full-scale experiments, Nonlinear simulations, Slab repairability, Deterioration models

Résumé

Avec l'avènement de l'ingénierie parasismique basée sur le dimensionnement en capacité (PBEE), une prédiction fiable de l'effondrement des structures induit par les séismes est impérative. Malgré les progrès significatifs qui ont été réalisés dans ce sens, plusieurs obstacles doivent être encore surmontés. Les modèles de détérioration, qui sont actuellement utilisés pour simuler l'effondrement des structures, se basent en grande partie sur données d'essai obtenus pour sous-ensembles ayant des conditions d'appuis très simplifiées. Par conséquent, ces essais ne tiennent pas compte de la redistribution des forces qui se produit au sein des systèmes structurels suite à l'apparition d'instabilités géométriques non linéaires sous charge cyclique. Pour ce qui concerne les cadres rigides (MRF) avec poutres mixtes acier-béton, qui est l'objet principal de cette thèse, l'influence de la contrainte axiale induite par la continuité de la dalle et l'effet cadre sur la réponse sismique des MRFs avec poutres mixtes acier-béton a été reconnue dans des travaux antérieurs. Cependant, ces effets n'ont été ni étudiés en profondeur ni quantifiés.

Dans cette thèse de doctorat, un programme expérimental unique à grande échelle a été conduit sur un sous-système MRF à deux portées avec poutres mixtes acier-béton. Le programme expérimental, qui a été corroboré par des analyses par éléments finis de continuum, visait à comprendre le rôle des mécanismes physiques liés à la continuité de la dalle et à l'effet cadre sur le comportement hystérétique des MRF avec poutres mixtes acier-béton, et plus particulièrement sur les grandes déformations lors de l'effondrement des structures. Les résultats de la recherche suggèrent que la continuité de la dalle limite le flambage local et le raccourcissement des poutres dans les zones dissipatives des MRF avec poutres mixtes acier-béton. Alors que les instabilités géométriques non linéaires attribuables au flambage local et à l'écrasement du béton sont prononcées dans les poutres mixtes lors de grandes déformations inélastiques, l'effet cadre et la continuité de la dalle préservent la stabilité globale du système structurel même dans les cas où des fissures se forment dans une zone dissipative. Les résultats des essais suggèrent que la présence de poutres transversales dans le système de plancher devrait être prise en compte lors du dimensionnement en capacité des MRF avec poutres mixtes acier-béton Les résultats expérimentaux suggèrent également que les méthodes de calcul proposées pour estiment la largeur effective de la dalle des MRF avec poutres mixtes acier-béton devraient être réévaluées.

Les données acquis ainsi que les informations provenant d'essais antérieures ont permis de développer des modèles pragmatiques pour l'évaluation sismique des MRF avec poutres mixtes acier-béton. En outre, un macro-modèle a été proposé pour simuler le comportement hystérétique des poutres mixtes acier-béton sous charge cyclique. Le modèle, qui a été validé de manière approfondie avec les données expérimentales disponibles, simule explicitement la détérioration cyclique de la résistance et de la rigidité des poutres mixtes acier-béton et de leurs connexions poutre-dalle. Le macro-modèle proposé a été utilisé pour évaluer le risque d'effondrement sismique de prototypes composés de MRF avec poutres mixtes acier-béton et la facilité de réparation des connexions poutre-dalle dans le cadre du PBEE.

Mots-clés

Cadres rigides avec poutres mixtes acier-béton, Effondrement structural, Dalle mixte, Effet cadre, Essais à grande échelle, Simulations non linéaires, Réparation de la dalle mixte, Modelés de détérioration

Contents

List of Figures

List of Tables

Chapter 1 Introduction

1.1 Research background

The principal objective of Performance-Based Design is to protect life safety by preventing structural collapse under natural hazards. In the case of earthquakes, uncertainties associated with regional construction practices, the seismic hazard, and the dynamic response of structures impose the acceptance of a "tolerable" probability of structural collapse. In recent years, several steps have been made towards understanding and predicting structural collapse within the framework of Performance-based Earthquake Engineering (PBEE), which has developed from a conceptual endeavor (Cornell and Krawinkler 2000) to a formal methodology for the seismic risk and loss assessment of structures (FEMA 2012). However, several challenges still remain to be addressed. A major challenge has been our (in)ability to physically simulate complex deterioration characteristics observed in key structural components within structural systems while experiencing large deformations prior to structural collapse. Another challenge has been the availability of comprehensive experiments that sufficiently characterize the behavior and interaction of structural components prior to collapse. In the case of composite steel moment resisting frames (MRFs), which form the primary focus of this thesis, the presence of the slab strongly influences the hysteretic behavior of composite steel beams, which becomes highly asymmetric under cyclic loading. Besides, the need for complementary testing of structural systems at large deformations to elucidate and quantitatively document the interaction of complex deteriorating mechanisms that could compromise the dynamic stability of structural systems has been recognized (Malley et al. 2011).

Prior experimental programs in Europe (Bursi and Gramola 2000; Plumier and Doneux 2001), the US (Civjan et al. 2001; Engelhardt et al. 2000; FEMA 2000a; Leon et al. 1998; Ricles et al. 2004; Uang et al. 2000) and Japan (Kishiki et al. 2010; Nakashima et al. 2007; Yamada et al. 2009) provided insight on the role of the slab on the seismic response of composite steel MRFs. However, these experiments were mostly conducted with overly simplified boundary conditions (e.g., T- or cruciform subassemblies), as shown in Figure 1.1a to d. These configurations assume fixed locations for the inflection points along the member length of typical MRFs. Referring to Figure 1.1a, the assumption that inflection points within beams and columns remain constant throughout the loading history is not true when members attain their nonlinear post-buckling regime due to force redistributions occuring in the actual system. Furthemore, in subassemblies, the composite steel beams had roller supports at their ends and were free to move axially as illustrated in Figure 1.1b and c. These boundary conditions

were not representative of the actual behavior in buildings where the slab continuity and adjacent columns, restrain movement of the composite steel beams along their axes. Accordingly, the influence of slab continuity and framing action on the global stability of composite steel MRFs was diminished. Prior work on earthquake-induced collapse (Lignos et al. 2011) suggests that the moment gradient could vary considerably within MRF members when experiencing cyclic deterioration in flexural strength and stiffness. Moreover, steel beams as part of subassembly tests with simplified boundary conditions, tend to experience a high degree of axial shortening (Civjan et al. 2001; MacRae et al. 2013) due to the accumulation of local buckling within the anticipated dissipative zone (see Figure 1.1e). This compromises the available plastic rotation capacity of composite steel beams under cyclic loading.

The above findings have a profound effect on seismic assessment criteria (ASCE 2017; CEN 2005a) and subsequent repair actions (FEMA 2012) of composite steel frame buildings in the aftermath of earthquakes. On the other hand, reconnaissance reports from previous major earthquakes (e.g., Clifton et al. 2011; Okazaki et al. 2013) suggest that beam axial shortening is typically not pronounced due to the presence of the concrete slab and the framing action. While this is also qualitatively discussed in prior work on the cyclic performance of beam-to-column connections after the 1994 Northridge and 1995 Kobe earthquakes (FEMA 2000a), there have not been studies that have systematically quantified these effects and their influence on the seismic stability of composite steel MRFs.

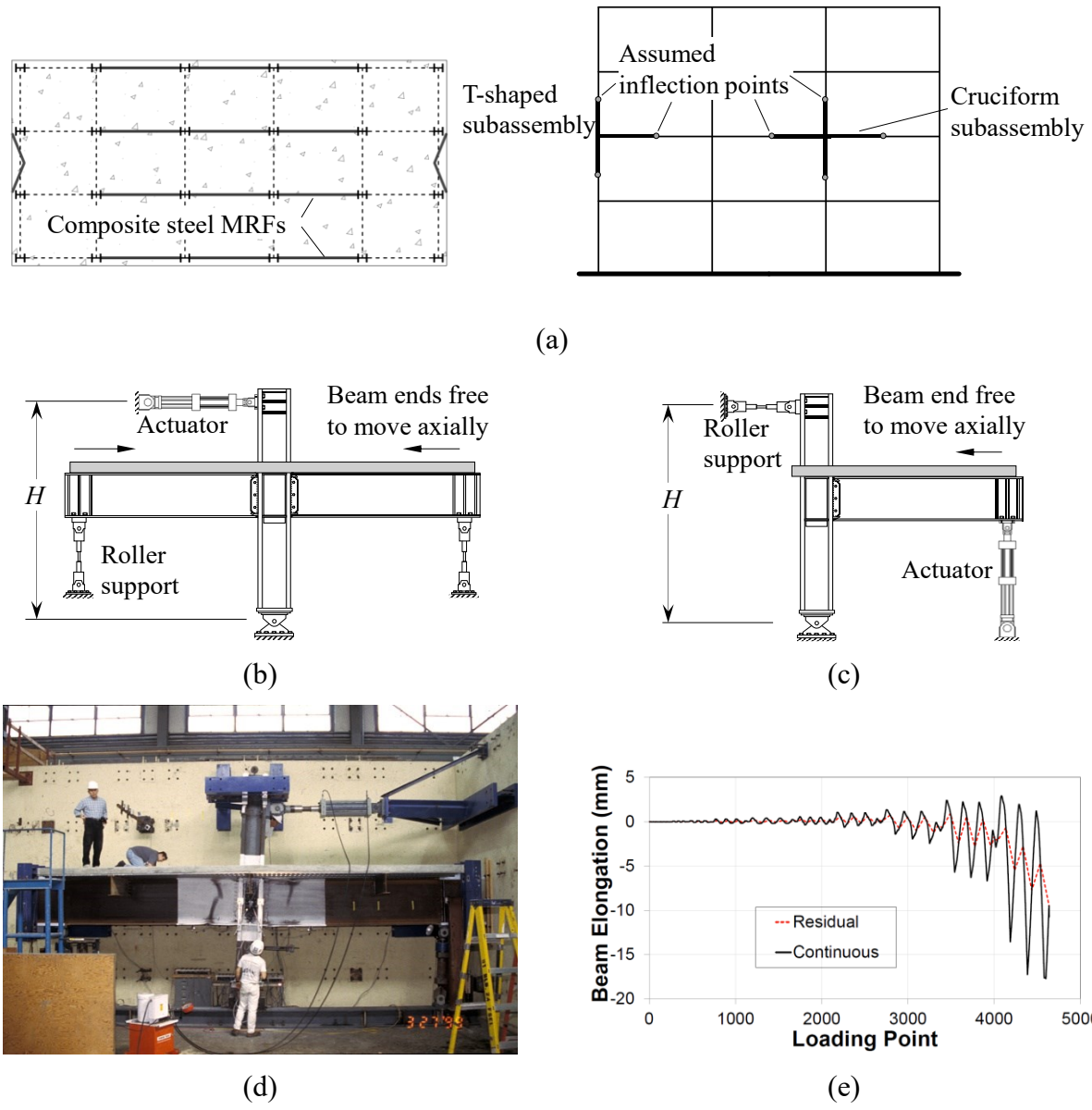

Figure 1.1 Simplified boundary conditions in subassembly tests, (a) assumed position of inflection points; (b) typical T-shaped subassembly; (c) typical cruciform subassembly; (d) testing of a cruciform subassembly with composite steel beams (image courtesy of Prof. Michael Engelhardt); (e) beam axial shortening versus loading history (image adopted from MacRae et al. (2013))

A handful of system-level tests (Cordova and Deierlein 2005; Del Carpio et al. 2014) have demonstrated that the behavior of composite steel beams is fairly different from what has been observed in subassembly experiments. For instance, Cordova and Deierlein (2005) reported only minor local buckling in the bottom flange of the steel beams that was fully straightened upon load reversals as illustrated in Figure 1.2a. A similar response was observed in Herrera (2005). However, in this case, the concrete slab was not explicitly considered (see Figure 1.2b). In recent work, Del Carpio et al. (2014) found that the rate of cyclic deterioration in the flexural strength of partially composite steel beams within a subsystem is lower than that anticipated from the current state-of-the-art deterioration

models (Lignos and Krawinkler 2011). These models, which are capable of predicting the cyclic deterioration of composite steel beams with emphasis on their post-buckling hysteretic response, have been mostly based on prior experiments on simplified subassembly tests (Lignos and Krawinkler 2013). Figure 1.3 shows indicative comparisons of the moment-rotation hysteretic response of partially composite beams under hogging and sagging bending from the testing program by Del Carpio et al. (2014). It is noteworthy that under hogging bending, the post-peak softening slope of the composite steel beam is considerably smoother than the numerical counterpart. Under sagging bending, no degradation in the flexural strength of composite steel beams was observed. This suggests that the reserve capacity of the composite steel beam within an MRF is considerably higher than what is expected. Ibarra and Krawinkler (2005) found that the earthquake-induced collapse risk of structural systems is most sensitive to the softening slope of structural members, which corroborates with more recent findings on predictive efforts of sidesway collapse of steel MRFs (Lignos et al. 2011, 2013). Therefore, from a collapse safety standpoint, the need of comprehensive experimental data that highlight the primary deteriorating mechanisms within a structural system is imperative for the further advancement of computational modeling approaches with emphasis at estimating the collapse capacity of structures under earthquake loading.

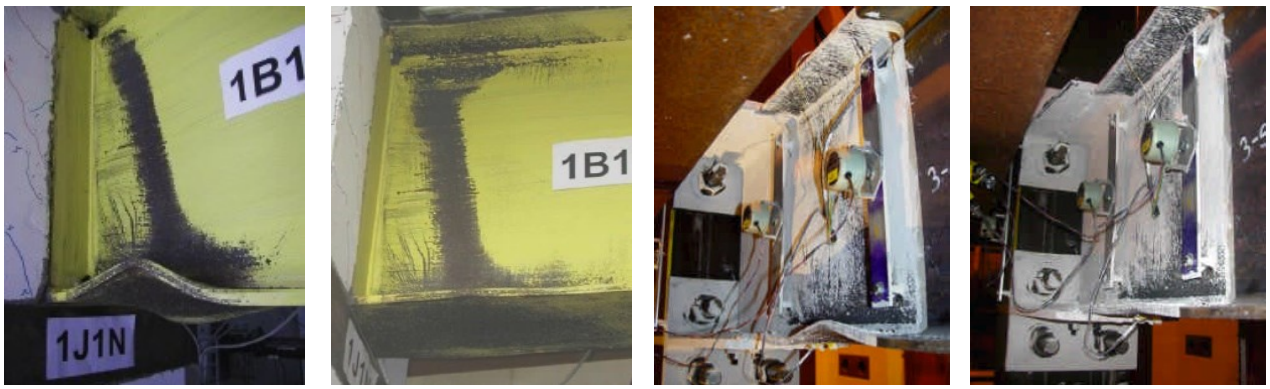

(a) (b)

Figure 1.2 Straightening of the local buckles in steel beams as part of system-level experiments, (a) images adopted from Cordova and Deierlein (2005), (b) images adopted from Herrera (2005)

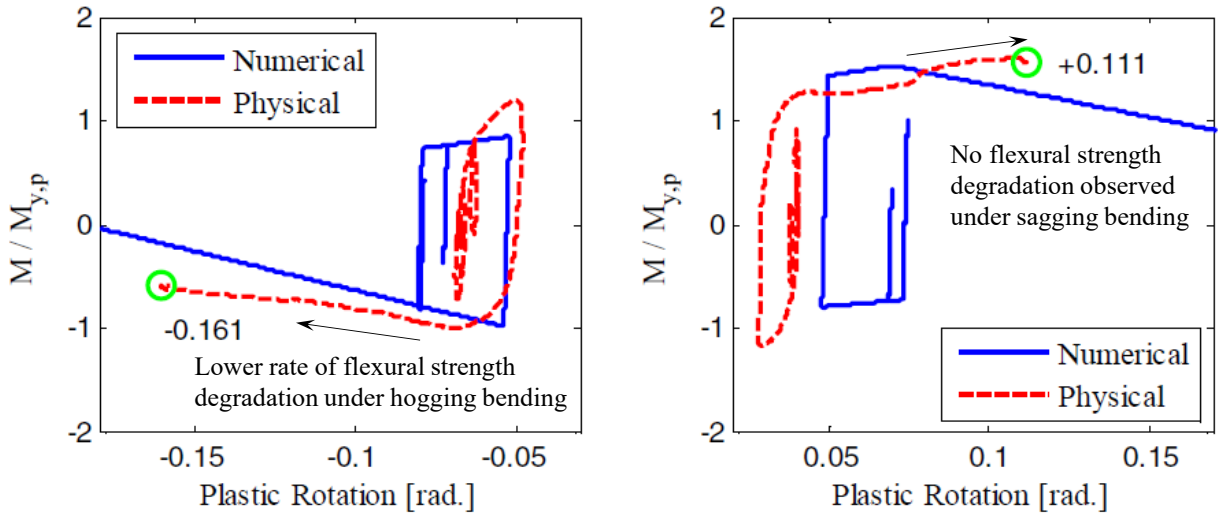

(a) (b)

Figure 1.3 Comparison of the predicted and measured hysteretic response of composite steel beams in a subsystem (a) behavior of composite steel beam under hogging bending; (b) behavior of composite steel beam under sagging bending (images adopted from Del Carpio et al. (2014))

The presence of the slab in composite steel MRFs strongly influences the flexural resistance of composite steel beams (e.g., Engelhardt et al. 2000; Leon et al. 1998; Ricles et al. 2002, 2004; Sumner and Murray 2002; Uang et al. 2000). In turn, this has a profound effect on the strong-column/weak-beam ratio that is adopted in current standards (AISC 2016a; CEN 2004a) for the capacity design of composite steel MRFs. Prior work on the topic in Europe (Bursi et al. 2009; Bursi and Gramola 2000; Plumier and Doneux 2001) and Japan (Nakashima et al. 2007; Yamada et al. 2009) has shown that the presence of the slab can amplify the flexural strength of composite steel beams by up to 50% when they feature shallow steel beams with depths less than 500 mm.

Prior tests on reinforced concrete structures (e.g., Leon 1983; Joglekar et al. 1984; Joglekar 1984; Leon and Jirsa 1986; Mahin and Bertero 1975) suggest that 3-dimensional effects, along with the presence of the transverse beams within the floor system, could significantly increase the flexural strength of the beam-to-column joints relative to what would have been expected based on standard flexural strength calculations using the effective slab widths according to current design standards. However, the above important issues have been overlooked in composite steel frame buildings. Figure 1.4a shows a full-scale 4-story building that featured composite steel MRFs designed according to the Japanese provisions (AIJ 2006). The building, which was tested at the E-Defense shake table facility in Japan (Suita et al. 2008), was subjected to the unscaled JR Takatori record from the 1995 Kobe earthquake. The building was prone to a soft story collapse mechanism (see Figure 1.4) despite the fact that capacity design was considered. The development of the soft story mechanism was

attributed to the 3-dimensional effects (i.e., role of the floor system, presence of the slab and 3-dimensional movement, inherent column base flexibility) along with the fact that the formation of local buckling at the column base of the steel MRFs caused moment redistribution within the first story columns, thereby increasing the moment demand at their top ends. System-level studies (Elkady and Lignos 2014) showed that capacity-designed steel MRFs in highly seismic regions may be prone to a soft story due to the presence of the slab when the strong-column/weak-beam ratio is less than 1.5. This issue deserves particular attention when benchmarking the collapse risk of structures (FEMA 2009) or when selecting building seismic performance factors (e.g., system overstrength, strength reduction factors (so-called behavior factors in Europe), displacement amplification factors) within the context of seismic design standards (ASCE 2016; CEN 2019).

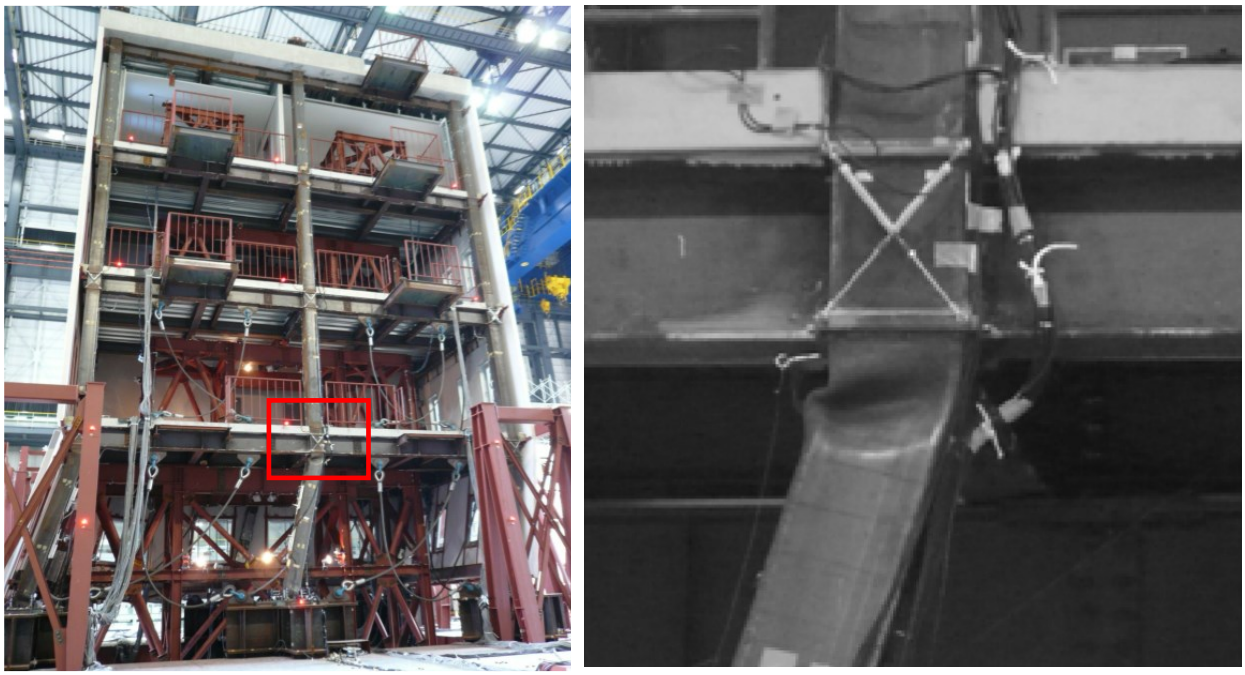

(a) (b)

Figure 1.4 E-defense test on a 4-story building: (a) formation of a first story mechanism (image adopted from Lignos et al. (2013)); (b) local buckling in the top of the columns adjacent to the composite steel beams (image adopted from Suita et al. (2008))

In the US, where perimeter steel MRFs with deep beams (i.e., depths larger than 600 mm) are promoted (Nakashima et al. 2000), the slab effects on the flexural strength of the composite steel beams are usually ignored. However, prequalification requirements on beam-to-column connections for seismic applications (AISC 2016a) dictate that, for certain connection typologies and geometric conditions, the slab should be isolated from the column face in order to minimize uncertainties that could change the capacity design hierarchy of beam-to-column connections. On the other hand, in Europe,

where space frames (Mele 2002) are commonly employed, MRFs usually feature shallow beams (i.e., depths less than 600 mm) and the role of slab on the seismic behavior of composite steel beams is significant, if the composite action is mobilized. In the current version of EN 1998-1 (CEN 2004a), the effective width of the slab under seismic loading is dependent on the configuration of the composite steel MRFs as well as the detailing of the slab reinforcement in the vicinity of the column. The sensitivity of the flexural resistance of composite steel beams to the effective widths has been questioned. Furthermore, a number of design requirements are stipulated in EN 1998-1 (CEN 2004a) in order to ensure that concrete crushing in dissipative composite steel beams is delayed. While the basis of these requirements relies on prior experimental and numerical studies (e.g., Plumier et al. 1998; Plumier and Doneux 2001), it does not account for the effects of slab confinement.

An important component that governs the behavior of composite steel beams is the connection between the slab and the beams. The beam-slab connection transfers the seismic loads from the slab to the beams of the composite steel MRF. Therefore, a loss in the composite action implies a potential loss in the load transfer mechanism. This can lead to unanticipated failures as the slab attempts to drag the force into the composite steel MRF (Cordova and Deierlein 2005). As a result, prior work (Civjan et al. 2001; Cordova and Deierlein 2005) has pointed out the necessity of maintaining the integrity of the beam-slab connections. In order to limit the slip demands on the beam-slab connection and the corresponding shear strength degradation, the current seismic provisions (AISC 2016a; CEN 2004a) impose a 25% reduction on the shear resistance of headed studs regardless of the respective beam depth. This requirement is based on a purely subjective decision. Standard cyclic pushout tests (e.g., Bursi and Gramola 1999; Civjan and Singh 2003; Zandonini and Bursi 2000) despite being informative, impose a large cumulative slip demand on the shear connectors. Moreover, they neither replicate the boundary conditions in a composite steel MRF nor do they account for force redistribution between the shear connectors along the length of the primary steel girders. Recent work on the topic (Suzuki and Kimura 2019) suggests that when the stress state of the slab is taken into consideration, the behavior of shear connectors is superior compared to that from standard cyclic push-out tests. The general consensus from the previous discussion is that the integrity of beam-slab connections in composite steel MRFs should be carefully assessed. In that respect, the slab repairability in the aftermath of earthquakes should also be considered within the context of PBEE. The above necessitate quantitative data from comprehensive physical system-level physical tests along with the development of nonlinear models that explicitly account for the slip demands and the shear strength degradation of beam-slab connections.

1.2 Problem statement and objectives

The previous section suggests that there is a lack of experiments that have investigated the behavior of composite steel MRFs at lateral drift levels associated with collapse, with the aim of comprehending the effects of slab restraint and framing action on the overall seismic stability at the system level. Moreover, the development of efficient, yet practical, numerical models that are able to simulate the primary deteriorating mechanisms observed in composite steel beams is imperative to benchmark the collapse risk of composite steel MRFs and to further refine seismic design criteria that control the extent of damage in beam-slab connections. In view of the above, the primary research objectives of this thesis are summarized as follows,

- to conduct and carefully document a comprehensive full-scale collapse experiment of a 2-bay composite steel MRF subsystem in order to comprehend the role of slab continuity and framing action on the overall seismic stability of composite steel MRFs. A side objective is to properly quantify the effects of transverse beams on the flexural resistance of composite beam-to-column connections,
- to propose refined seismic design requirements with emphasis on the required shear resistance of connectors and the effective slab width by means of available experiments and corroborating continuum finite element analyses,
- to provide practice-oriented models for seismic assessment of new or existing buildings featuring composite steel MRFs as their primary lateral load resisting system,
- to develop a computationally efficient macro-model for simulating the hysteretic behavior of composite steel beams while exhibiting nonlinear geometric instabilities under inelastic cyclic loading,
- to conduct system-level simulation studies of composite steel MRF buildings in order to benchmark their seismic collapse risk and develop novel risk-based metrics for assessing the repairability of beam-slab connections within the framework of performance-based earthquake engineering.

1.3 Thesis outline

The PhD thesis consists of five main chapters, in addition to the introductory chapter and the conclusions. Four of the five chapters are composed of peer-reviewed journal articles (three already

published and one is currently under review) and one chapter is planned to be submitted as a peer-reviewed journal paper. At the beginning of the chapters that were reproduced from journal articles, information on the authors, the contribution of the doctoral candidate to the chapter and the full bibliographic details of the article are presented. The thesis also includes a set of Appendices that provide supplementary information to the experimental program described in Chapter 5.

Chapter 2 discusses the development of a database of composite steel beams under cyclic loading. The database is utilized to assess current seismic provisions for composite steel beams and develop practice-oriented component models for the seismic performance assessment of composite steel MRFs. This chapter is reproduced from the journal article by El Jisr et al. (2019).

Chapter 3 investigates the influence of slab continuity and framing action on the hysteretic behavior of composite steel MRFs through continuum finite element analysis (CFE). The CFE model specifics are described and a parametric study of two-bay subsystems with various beam depths is conducted. The hysteretic behavior of the two-bay subsystems is compared with that of the corresponding cruciform subassemblies. The physical mechanisms influencing hysteretic behavior of the composite steel beam joints are thoroughly investigated. This chapter is reproduced from the journal article by El Jisr et al. (2020).

In Chapter 4, slip-based fragility functions for beam-slab connections are developed. To that end, a dataset of 42 cyclic push-out tests is assembled. The fragility functions, which include four damage states, constitute a valuable tool for assessing earthquake-induced damage in the beam-slab connection of composite steel MRFs. Specimen-to-specimen, as well as epistemic uncertainty, are incorporated into the fragility functions. An application of the proposed fragility functions is presented at the end of the chapter for a six-story building with composite steel MRFs designed according to European seismic provisions (CEN 2004a). This chapter is reproduced from the journal article by El Jisr and Lignos (2021)

Chapter 5 presents a full-scale collapse experiment of a 2-bay composite steel MRF subsystem under lateral cyclic loading. The testing program investigates, in a quantitative manner, the role of the slab on the seismic stability of composite steel MRFs. The considered loading protocols examine the response of the 2-bay composite steel MRF subsystem from the onset of damage through structural collapse. The employed loading protocol considers aspects related to prequalification of beam-to-column connections. The loading protocol also mimics the asymmetric loading (i.e., ratcheting) that MRFs experience at large deformations prior to structural collapse. Implications of the testing program on prospective seismic design provisions of composite steel MRFs are highlighted.

In Chapter 6, a computationally efficient, nonlinear macro-model is proposed for simulating the cyclic behavior of composite steel beams. The macro-model explicitly accounts for the observed slab-column force transfer mechanisms and is capable of simulating the asymmetric deteriorating response of the composite steel beams. The modeling approach, which is thoroughly validated with available experiments, is incorporated in nonlinear models of prototype buildings with composite steel MRFs. The buildings are designed at three European sites. The seismic collapse risk of the examined buildings is benchmarked. The composite steel MRFs are designed with various degrees of composite action. Novel slip hazard curves for the beam-slab connections are used to assess the integrity of the beam-slab connections and evaluate the beam-slab connection requirements in current seismic provisions (AISC 2016a; CEN 2004a). This chapter is reproduced from the submitted peer-reviewed manuscript by El Jisr et al. (2021b).

Chapter 7 summarizes the primary conclusions of the PhD thesis. Suggestions for future work are also discussed.

Appendix A summarizes the design of the composite steel MRF from which the 2-bay test frame subsystem, presented in Chapter 5, was extracted. Appendix B includes all the detailed drawings of the test frame subsystem. Appendix C includes all the mill certificates of the structural steel material, the welding procedure specifications and the welding procedure qualification records. Appendix D presents a detailed instrumentation plan and summary of all the sensors that were employed in the experiment. The procedure for deriving the forces and deformations in Chapters 5 and Appendix E is also described. Appendix E provides supplementary results from the experimental program that were not included in Chapter 5.

Chapter 2 Composite steel beam database for seismic design and performance assessment of composite-steel moment-resisting frame systems

Bibilograpic details

This chapter presents the post-print version of the article with the following full bibliographic details: El Jisr, H., Elkady, A., and Lignos, D. G. (2019). "Composite steel beam database for seismic design and performance assessment of composite-steel moment-resisting frame systems." *Bulletin of Earthquake Engineering*, Springer, 17(6), 3015–3039. DOI: https://doi.org/10.1007/s10518-019-00564-w

Authors' contribution

Hammad El Jisr assembled the composite steel beam database, analyzed the data, created the figures, wrote the manuscript draft and revised the manuscript. The co-authors contributed in developing the methodology presented in this chapter, supervising the work conducted by Hammad El Jisr, funding acquisition, and reviewing and editing the original and final manuscript drafts.

2.1 Abstract

This chapter discusses the development of a publicly available database of composite steel beam-to-column connections under cyclic loading. The database is utilized to develop recommendations for the seismic design and nonlinear performance assessment of steel and composite-steel moment-resisting frames (MRFs). In particular, the sagging/hogging plastic flexural resistance as well as the effective slab width are assessed through a comparison of the European, American and Japanese design provisions. The database is also used to quantify the plastic rotation capacity of composite steel beams under sagging/hogging bending. It is found that the Eurocode 8-Part 3 provisions overestimate the plastic rotation capacities of composite beams by 50% regardless of their web slenderness ratio. Empirical relationships are developed to predict the plastic rotation capacity of composite steel beams as a function of their geometric and material properties. These relationships can facilitate the seismic performance assessment of new and existing steel and composite-steel MRFs through nonlinear static analysis. The collected data underscores that the beam-to-column web panel zone in composite steel beam-to-column connections experience higher shear demands than their non-composite counterparts. A relative panel zone-to-beam resistance ratio is proposed that allows for controlled panel zone inelastic deformation of up to 10 times the panel zone's shear yield distortion angle. Notably, when this criterion was imposed, there was no fracture in all the examined beam-to-column connections.

2.2 Introduction

Modern seismic design provisions adopt capacity design principles that allow for controlled inelastic deformations within a lateral-load resisting system (Fardis 2018). In the case of steel and composite-steel moment-resisting frame (MRF) systems, steel beams act as the primary structural fuse to dissipate the seismic energy. Prior studies (Elkady and Lignos 2014, 2015a; Lignos et al. 2013) suggest that the amplified flexural resistance of composite steel beams could shift the plastic hinge formation to the MRF columns despite the fact that a strong-column/weak-beam (SCWB) criterion was imposed. Subassembly tests on deep beams (depth, h = 913 mm) with partial composite action (Jones et al. 2002; Uang et al. 2000), showed that their sagging flexural resistance (i.e. slab in compression) amplified by about 10% to 20% relative to the bare beam plastic bending resistance. Similarly, beams with a depth of 753 mm tested by Civjan et al. (2001) developed a sagging flexural resistance amplification of 10% to 30%. Elkady and Lignos (2014) assessed the hysteretic behavior of composite steel beams with reduced beam section (RBS) with depths varying between 533 mm and 911 mm. These sizes are typically used in perimeter steel MRFs in North America. They found that the composite

slab amplifies the sagging flexural resistance, on average, by 35%. In Japan and Europe, the use of space steel MRFs is promoted. This typically leads to the selection of shallow beams (h = 300 to 500 mm) even in tall buildings (Mele 2002; Nakashima et al. 2000). The amplification of the sagging flexural resistance in such beams is even more pronounced. In particular, Nakashima et al. (2007) showed that the composite action amplifies the sagging flexural resistance of 400 mm deep beams by up to 50%. This agrees with pior experimental studies (Bursi et al. 2009; Bursi and Gramola 2000).

The potential deficiencies associated with disregarding the composite action in seismic design can be alleviated by (a) totally disconnecting the slab from the column face (Tremblay et al. 1997); (b) by employing a larger SCWB ratio (Elkady and Lignos 2014); or (c) by explicitly considering the expected composite beam flexural resistance in the SCWB check. The European (CEN 2004a), American (AISC 2016a) and Japanese (AIJ 2010a) seismic design provisions compute the flexural resistance of composite steel beams differently. The main two reasons are the variations in the assumed effective width of the slab and the shear strength of the studs. The sensitivity of the flexural resistance of composite steel beams to the above assumptions has not been consistently quantified through direct comparisons with available experimental data.

Nonlinear modeling recommendations (e.g. ASCE/SEI 41-17 and Eurocode 8-Part 3) for the seismic assessment of new and existing structures (ASCE 2017; CEN 2005a) compute a beam's elastic flexural stiffness and plastic rotation capacity by ignoring the composite action. Nam and Kasai (2012) analyzed data from full-scale shake table experiments (Lignos et al. 2013; Suita et al. 2008) and showed that the presence of the slab may increase the beam stiffness by two to three times. Similarly, system-level tests (Nakashima et al. 2007) indicated that the composite steel beam stiffness was twice as high compared to that of a non-composite beam. Prior subassembly tests (Engelhardt et al. 2000; FEMA 2000a; Ricles et al. 2004) suggest that, depending on the slab arrangement and the associated degree of composite action, the plastic rotation capacity of a composite steel beam under sagging bending could be up to 80% larger than that of a non-composite beam. In a more recent study, Elkady and (Lignos 2014) assessed the plastic rotation capacity of composite deep beams with RBS. Those experienced an 80% and 35% increase in their pre- and post-capping plastic rotations, respectively, compared to non-composite steel beams (capping refers here to the onset of local and/or member geometrical instabilities). However, the above data-set did not cover shallow beams commonly seen in the European and Japanese design practice. This is particularly important for seismic performance assessment methodologies consistent with Eurocode 8-Part 3 (CEN 2005a).

A side issue related to the composite action effect is the increase in the shear demand on the beam-to-column web panel zone (Elkady and Lignos 2014; Leon et al. 1998). This could augment the panel zone inelastic deformations. It is desirable to allow for controlled panel zone inelastic deformation (Krawinkler 1978; Shin and Engelhardt 2013). While moderate levels of inelastic deformation are usually permitted within the various seismic design provisions in Europe, North America and Asia, there is no consensus on what an acceptable panel zone inelastic deformation range should be.

This chapter presents the development of a comprehensive experimental database for composite steel beams that addresses all the aforementioned issues. The database is used to assess several performance parameters that influence the cyclic behavior of composite steel beams in fully restrained beam-to-column connections. These parameters include (i) the flexural resistance, (ii) the effective stiffness, and (iii) the pre- and post-capping plastic rotation capacities. The gathered experimental data is also used to assess the shear resistance of the beam-to-column web panel in composite beam-to-column connections. Three design provisions are considered including the European (Eurocode 3, 4 and 8 (CEN 2004a; b, 2005a; b; c); the US (ANSI/AISC 360-16 (AISC 2016b) and ANSI/AISC 341-16 (AISC 2016a)); and the Japanese (AIJ 2010a; b) provisions. The chapter proposes a set of seismic design recommendations for composite-steel MRFs that could be adopted in future design provisions. Finally, nonlinear modeling recommendations are also proposed for estimating the flexural resistance, stiffness and plastic rotation capacity of composite steel beams. These recommendations can facilitate the seismic performance assessment of existing steel frame buildings as well as prospective designs.

2.3 Description of the assembled composite steel beam database

The assembled composite steel beam database comprises 24 experimental programs, which are summarized in Table 2.1. A total of 97 composite steel beams are gathered including 87 from subassembly tests and 10 from system-level experiments. The beam depths, h, range from 300 to 912 mm; shear span-to-depth ratios, L_o/h (L_o is the distance from the column face to the inflection point) range from 3.4 to 11.6; and web slenderness ratios, c/t_w, range from 36.1 to 53.8. Both partially- and fully-composite steel beam data were gathered. The main types of beam-to-column connections include:

- Bolted extended end-plate connections (BEEP) (see Figure 2.1a)
- Welded unreinforced flange welded web connections (WUF-W) (see Figure 2.1b)

- Reduced beam section connections (RBS) (see Figure 2.1c)
- Through diaphragm connections (TD) (see Figure 2.1d)
- Retrofitted connections (bottom flange RBS, top and/or bottom welded or bolted haunches, bottom flange horizontal stiffeners, bottom flange cover plate)
- Reinforced concrete column with steel beams (RCS) and concrete filled steel tube (CFT) steel beam-to-column connections

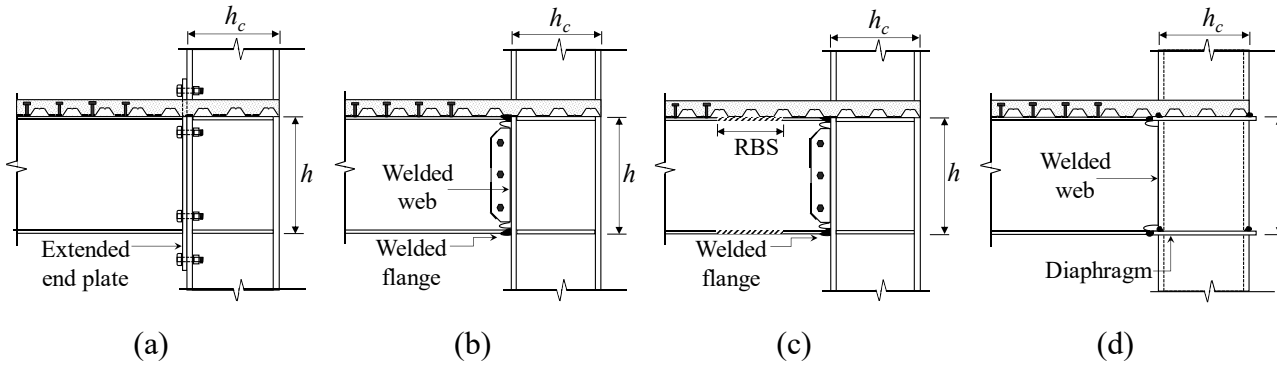

Figure 2.1 Typical fully restrained beam-to-column connection types included in the composite steel beam database: (a) BEEP; (b) WUF-W; (c) RBS; (d) TD connection

The collected steel beams are made of 10 steel material types. The measured-to-nominal yield stress ratio ($f_{y,m}/f_{y,n}$) for each steel type is plotted in Figure 2.2, which also summarizes the nominal yield stress values. This ratio varies from an average minimum of 1.1 for US A572 Gr.50 steel to an average maximum of 1.4 for Japanese SS400 steel. The values are consistent with the material overstrength values reported in ANSI/AISC 341-16 (AISC 2016a) for US steel grades, the OPUS[1] program (Braconi et al. 2013) for European steel grades, and in Fujisawa et al. (2013) for Japanese steel grades. The measured 28-day concrete compressive strength of the concrete slabs varies between 15 to 40 MPa. In summary, the composite steel beam database is publicly available online at http://resslab-tools.epfl.ch/steel.

[1] Optimizing the seismic performance of steel and steel-concrete structures by standardizing material quality control

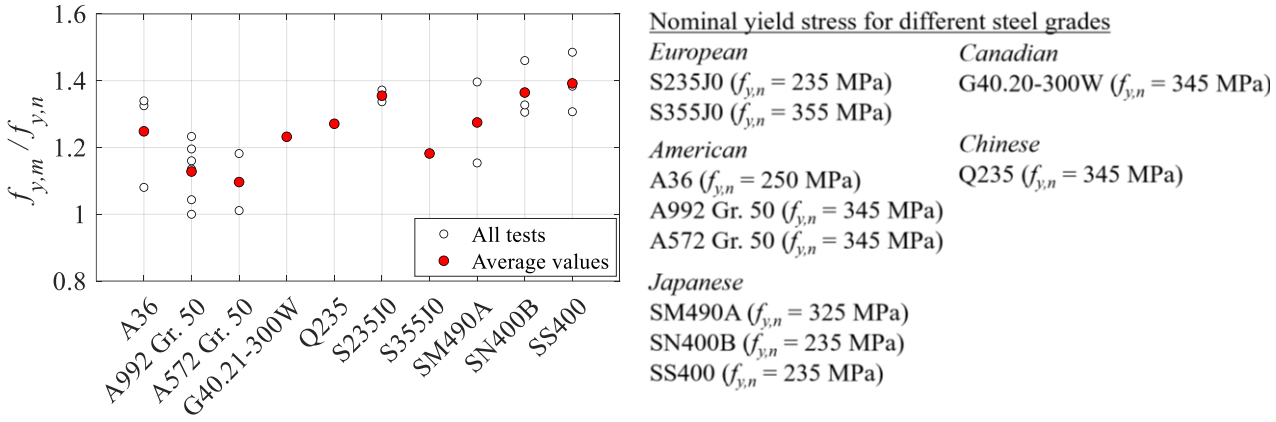

Figure 2.2 Ratio of measured-to-nominal yield stress of the various steel types in the assembled database

Table 2.1 Summary of the composite steel beam testing programs in the assembled database

Reference	Connection Type	h [mm]	Floor Slab*	Steel Grade	$\frac{L_o}{h}$	$\frac{c}{t_w}$
Ricles et al. (2004)	RBS	760/911	NWC - ||	A572/A992 Gr. 50	4.4/5.5	51.9/47.6
Chen and Chao (2001)	RBS	600	NWC - ||	A36	4.4	44.2
Civjan et al. (2001)	Retrofit	755	LWC - ⊥	A36	4.6	51.5
Leon et al. (1998)	WUF-W	683	NWC - ||	A36	4.9	48.6
Engelhardt et al. (2000)	RBS	911	NWC - ||	A572 Gr. 50	3.9	51.9
Tremblay et al. (1997)	RBS	535	NWC - ⊥	G40.21-300W	6.8	45.7
Ricles et al. (2002)	WUF-W	911	NWC - ||	A572 Gr. 50	4.7	51.9
Cheng et al. (2007)	CFT	450	NWC - ||	not reported	6.3	44.0
Cheng and Chen (2005)	RCS	596	NWC - ||	not reported	4.5	53.8
Uang et al. (2000)	Retrofit	911	LWC - ⊥	A36	3.4	51.9
Kim et al. (2004)	TD	612	NWC - SS	SM490	5.4	41.5
Yamada et al. (2009)	TD	400	NWC - ||	SN400B	5.9	43.5
Nakashima et al. (2006)	TD	400	NWC - ||	A572 Gr. 50	7.1	38.0
Nakashima et al. (2007)	TD	400	NWC - ||	SN400B	5.8	38.0
Cordova and Deierlein (2005)	RCS	600	NWC - NR	A572 Gr. 50	5.3	47.8
Bursi et al. (2009)	RCS	400	NWC - ||	S355	5.9	38.5
Kishiki et al. (2010)	TD	300	NWC - SS, ||, ⊥	SM490A/SN400B	5.4	39.4
Sumner and Murray (2002)	BEEP	600	NWC - ||	A572 Gr. 50	5.2	50.6
Bursi and Gramola (2000)	WUF-W	330	NWC - ||	S235	11.6	36.1
Kim and Lee (2017)	Retrofit	500	NWC - ⊥	SS400	7.6	44.2
Lee et al. (2016)	WUF-W/RBS	350	NWC - ⊥	SS400	6.0	51.3
Lu et al. (2017)	RBS	350	NWC - SS	Q235	4.3	43.1
Asada et al. (2015)	TD	400	NWC - ⊥	SS400	10.6	43.5
Del Caprio et al. (2014)	RBS	350	NWC - ||	A572 Gr. 50	6.0	48.1

*NWC: Normal-weight concrete
LWC: Light-weight concrete
\|\|: Deck with ribs parallel to the beam
⊥: Deck with ribs perpendicular to the beam

SS: Solid slab with no steel deck

2.4 Deduced performance parameters of composite steel beams under cyclic loading

A number of performance parameters are deduced from manually digitized and processed moment-rotation relations of the collected data-set. An example is illustrated in Figure 2.3. In this figure, the moment corresponds to that at the idealized center of the beam's plastic hinge region. The rotation represents the beam's rotation over its length (chord rotation). These definitions are consistent with those found in ASCE/SEI 41-17 (ASCE 2017). Referring to Figure 2.3a, a first-cycle envelope curve is first fitted to the moment-rotation relation data in both the positive (i.e., sagging bending) and negative (i.e., hogging bending) loading directions. These curves are then used to deduce a number of parameters that characterize the stiffness, flexural strength and plastic deformation capacity of a composite beam. The deduced parameters include the effective stiffness ($K^{+/-}$), the effective plastic flexural resistance ($M_y^{*,+/-}$), the ultimate flexural resistance ($M_u^{+/-}$), and the pre- and post-capping plastic rotation capacities ($\theta_p^{*,+/-}$ and $\theta_{pc}^{*,+/-}$, respectively). The star (*) superscrpit denotes that these parameters are based on the first-cycle envelope curve. Therefore, they are distinguished from those that define a monotonic backbone of a steel beam. The effective stiffness is systematically derived from the unloading stiffness of the first inelastic cycle excursion, which by definition includes both flexural and shear deformations; thus, the term "effective" is adopted. The flexural resistance and rotation parameters are deduced from a tri-linear idealized curve (see dashed lines in Figure 2.3b) fitted to the first-cycle envelope. The idealized curve is fitted such that the total energy dissipated up to the peak response ($M_u^{+/-}$) is the same as that in the tri-linear approximation. Albeit the extracted plastic rotation values are loading-history dependent (Krawinkler 2009), they are consistent with prior related studies (Panagiotakos and Fardis 2001) that are already adopted in Eurocode 8-Part 3 (CEN 2005a) and ASCE (2017). The subsequent sections provide a comprehensive assessment of the deduced performance parameters in comparison with relevant seismic code design provisions and performance assessment guidelines for nonlinear static analysis procedures.

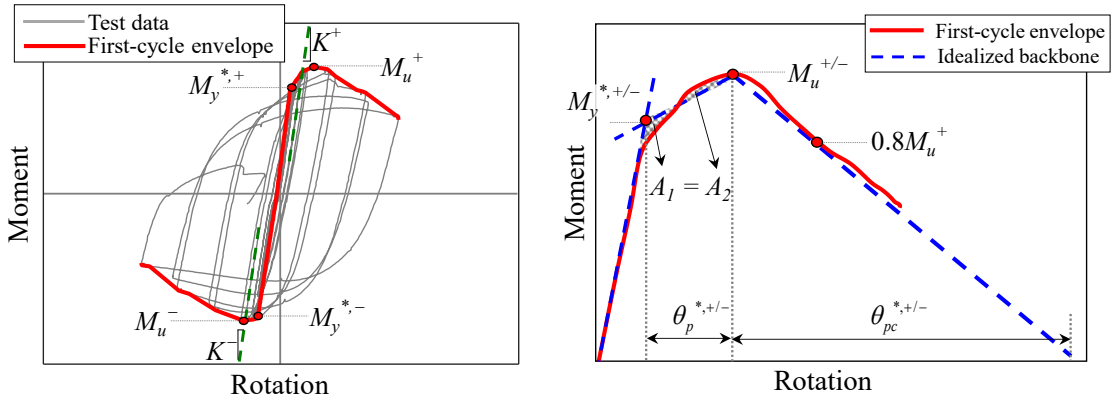

Figure 2.3 Definition of performance parameters for composite steel beams under cyclic loading

2.4.1 Sagging resistance

The deduced effective plastic flexural resistance of composite steel beams under sagging bending (simply noted as sagging resistance hereafter) is assessed based on 46 data points. These represent beams that reached their ultimate flexural resistance. Beams that experienced premature fracture were excluded from the data-set. The test data suggests that the sagging resistance amplification due to the composite action is mainly dependent on the beam depth, the shear span-to-depth ratio and the degree of composite action, η, which is defined in Eq. (2.1) In particular, η is the ratio of the actual number of used shear studs to that required ones to achieve full composite action.

$$\eta = \frac{\sum F_v}{\min\{F_c, N_{pl}\}} \leq 1 \tag{2.1}$$

in which $\sum F_v$ is the shear strength of the headed shear studs between the point of maximum positive moment and the point of zero moment based on the respective code, F_c is the compressive strength of the slab at the crushing limit state, and N_{pl} is the tensile plastic resistance of the steel section based on measured material properties.

The aforementioned dependencies are assessed by plotting the sagging resistance with respect to the aforementioned parameters. The sagging resistance is normalized with respect to the bare steel beam's expected plastic flexural resistance, $M_{p,e}$ ($M_{p,e}$ is the product of the plastic section modulus of the respective beam about the strong axis and the expected yield stress of the beam steel material, $f_{y,e}$). The $f_{y,e}$ is deduced based on the material's expected-to-nominal yield stress ratio, R_y, which is obtained from ANSI/AISC 341-16 (AISC 2016a) for North American steel grades and from available

literature (Aoki and Masuda 1985; Braconi et al. 2013; Fujisawa et al. 2013) for the rest of the steel grades.

Figure 2.4a shows that the sagging resistance is amplified by 13%, on average, for deep beams ($h >$ 500 mm). On the other hand, the sagging resistance of shallow composite steel beams ($h \leq 500$ mm) is amplified somewhere between 60% to 80%. This should be carefully considered in the SCWB criterion. Vis-à-vis the above discussions, system-level tests (Suita et al. 2008) and supplemental system-level simulations (Lignos et al. 2013) suggest that when the slab contribution is disregarded, the prediction of soft-story collapse mechanisms due to potential drift concentation may be missed.

Referring to Figure 2.4b, the sagging resistance of a beam increases when the degree of composite action, η increases. Due to brevity, the η values in Figure 2.4b are only computed based on the European provisions (CEN 2004a; b). Note that η varies between codes due to differences in the recommended stud's shear resistance and slab's effective width. This issue is discussed later on in great detail. It is worth noting that deep steel MRF beams may require a large number of shear studs to develop full composite action. However, a lesser number of shear studs is typically used in the actual design phase. In the context of the U.S. seismic provisions, a lower degree of composite action is actually desirable, considering that the AISC provisions (AISC 2016a) recommend that the SCWB ratio shall be just larger than 1.0.

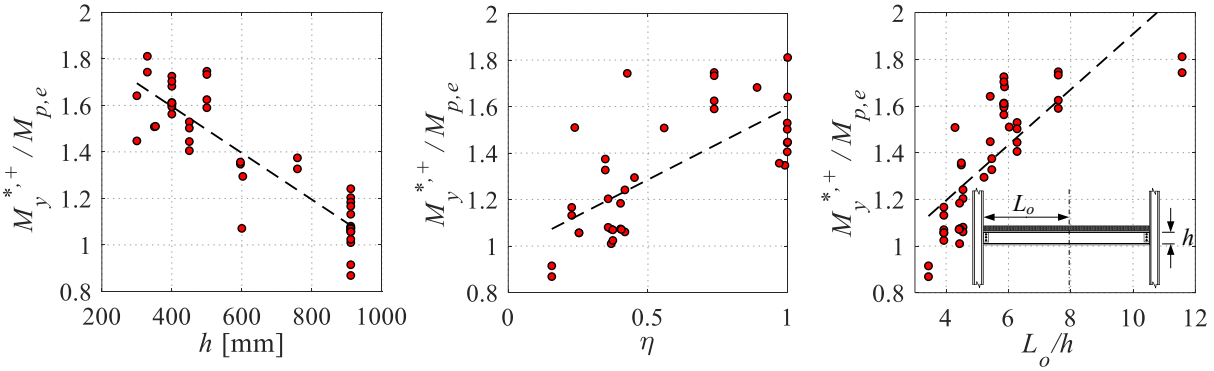

(a) (b) (c)

Figure 2.4 Dependence of the sagging resistance on the beam's (a) depth, (b) the degree of composite action based on Eurocode provisions (CEN 2004a, b) and (c) span-to-depth ratio

Figure 2.4c shows that composite steel beams with low L_o/h ratio (mainly deep beams) have a higher moment-shear interaction, which in turn decreases the beam's attained sagging resistance. The observed high dependence relates to the fact that the beam length in the subassembly tests is limited.

Hence, the higher the beam depth, the lower the span-to-depth ratio and the ratio $M_y^{*,+}/M_{p,e}$ ratio. Notably, although a number of composite steel beams had a $L_o/h < 5$, only two specimens did not develop their bare steel plastic resistance $M_{p,e}$. This suggests that the $L_o/h > 5$ limit specified by ANSI/AISC 358-16 (AISC 2016c) for prequalified beam-to-column connections is rational. Figure 2.5 shows the maximum shear demand on the beam, V_u, with respect to L_o/h. The shear demand, V_u, is normalized with respect to the plastic shear resistance, $V_{p,m}$, of the bare steel beam, based on the measured yield stress. Albeit the shear demand on the beam under sagging becomes maximum, V_u values are plotted for both sagging and hogging bending (i.e., V_u^+ and V_u^-, respectively). All but one specimen experienced a $V_u/V_{p,m}$ ratio less than 0.5. This implies that the moment-shear interaction was not relevant in most cases, which complies with the Eurocode seismic provisions. Ten beams experienced a $V_u/V_{p,m}$ ratio larger than 0.4. These beams do not comply with the L_o/h prequalification limits of ANSI/ASCI 358-16 (AISC 2016c).

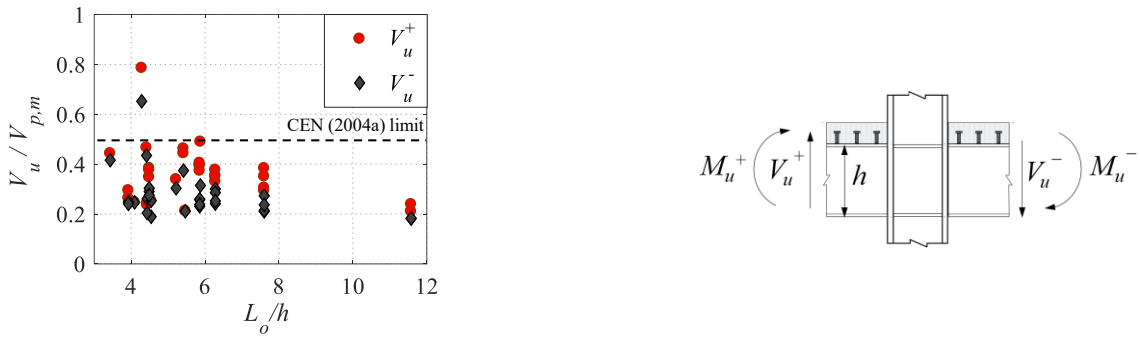

Figure 2.5 Dependence of maximum shear demand-to-shear resistance ratio on the beam's span-to-depth ratio

2.4.1.1 Assessment of the code-based sagging resistance of composite steel beams

With respect to the design sagging resistance, discrepancies between the design codes are limited to (i) the assumed effective width and compressive stress of the slab and (ii) the assumed shear stud resistance. In this context, a brief discussion of these differences is provided below.

Slab's Effective Width and Compressive Stress

An illustration of the basic dimensions used for effective width calculations by the three codes as well as a tabulated comparison of the formulas used for these calculations are shown in Figure 2.6a and b, respectively. The general consensus is that the effective width calculation as per the U.S. and Japanese provisions is simpler than that of the European provisions. For instance, the effective width according

to the Eurocode provisions differs depending on (i) the loading condition (gravity/seismic), (ii) the joint configuration (exterior/interior column), and (iii) the presence of transverse beams or anchored rebar in the slab. The Japanese provisions simply recommend an effective width equal to the column flange width. This agrees with past findings from Du Plessis and Daniels (1972) but it is a conservative (i.e., it underestimates the flexural strength) assumption in most cases.

For the concrete slab's design compressive stress, both the European (CEN 2004b) and American (AISC 2016b) provisions consider 85% of the concrete specified/characteristic compressive strength. This value is rational for partially-composite steel beams (Civjan et al. 2001; Cordova and Deierlein 2005). On the other hand, the Japanese provisions consider twice the compressive strength for fully composite steel beams, in which the effective stress can reach up to $1.8f'_c$. This is consistent with observations from past studies (Du Plessis and Daniels 1972; Tagawa et al. 1989).

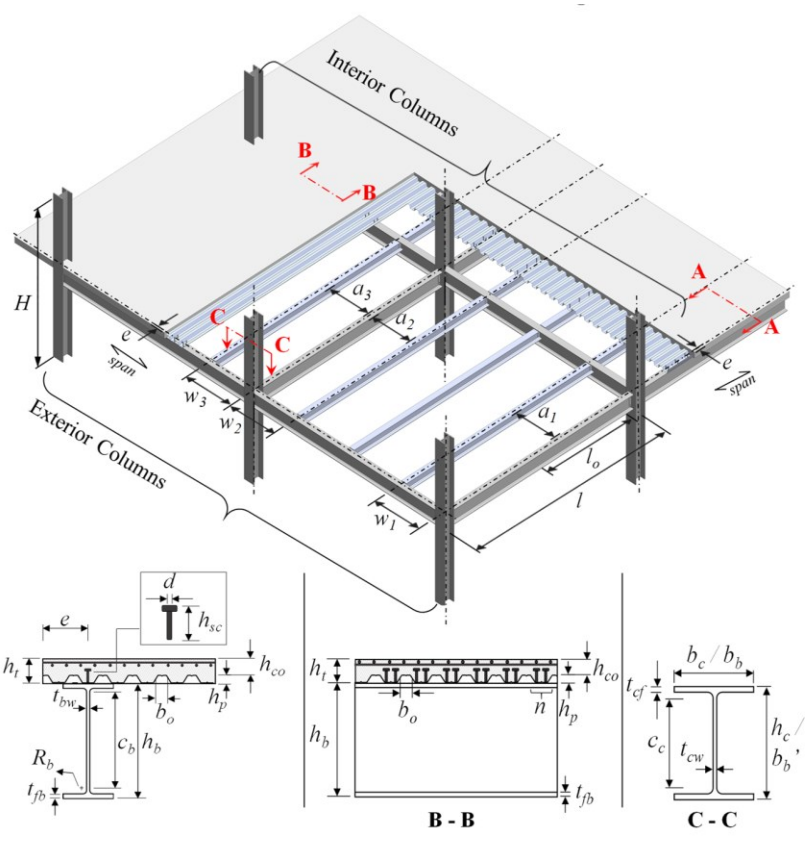

Code	Effective width*	
	Interior column	Exterior column
CEN (2004a)	$\min\begin{cases}0.075l\\e\end{cases}$	$^{(1)}\min\begin{cases}0.075l\\e\end{cases}$ $^{(2)}\min\begin{cases}0.5(b_b+0.7h_c)\\e\end{cases}$ $^{(3)}\min\begin{cases}0.5(b_b+0.7h_c)\\0.05l\\e\end{cases}$
AISC (2016a)	$\min\begin{cases}0.0125l\\w\\e\end{cases}$	
AIJ (2010a)	b_b	

* Effective width on each side of the beam web centerline
(1) Transverse beams with stud connectors and column strong axis oriented in loading direction. Concrete slab up to exterior face of column or beyond
(2) Same as (1) but without steel transverse beams or steel transverse beams without stud connectors
(3) All other layouts

(a) (b)

Figure 2.6 (a) Illustration of frame and composite steel beam dimensions for effective width computations; and (b) comparison of code-based effective width for plastic analysis

Shear Resistance of Headed Studs

Both Eurocode 4-Part 1 (CEN 2004b) and ANSI/AISC 360-16 (AISC 2016b) reduce the stud's shear resistance in the presence of a steel deck, regardless of its orientation. The Japanese provisions (AIJ 2010b) only consider this reduction if the steel deck ribs are oriented perpendicular to the steel beam. In general, the reduction factor is a function of the deck and stud dimensions. If the steel deck is oriented perpendicular to the beam, this factor becomes also dependent on the number of studs per rib. The U.S. (AISC 2016a) and European (CEN 2004a) provisions require an additional 25% reduction on the shear resistance of headed studs in seismic load resistant systems.

Comparison of Code-based and Test-based Sagging Resistances

The design sagging resistance, M_d^+, is calculated here using plastic analysis as adopted in the three considered design provisions. Figure 2.7a shows the ratios of test- to code-based sagging resistance, $M_y^{*,+}/M_d^+$, versus the beam depth. The trend lines suggest that the Eurocode tends to overestimate the sagging resistance of deep beams ($h \approx 900$ mm). This is due to the assumed constant material overstrength factor of 1.25, regardless of the steel material type. The collected deep beams are mainly made of A992 Gr.50 steel. This has a lower material overstrength (R_y = 1.1). This issue as well as the observed variability in the M_d^+ values diminish between the three codes when the measured yield stress is used to calculate the design sagging resistance, $M_{d,m}^+$ (see Figure 2.7b). Thus, the material overstrength shall be related to the steel grade (refer to Figure 2.2) as adopted in ANSI/AISC 341-16 (AISC 2016a). In a similar manner, the proposed material overstrength values from the OPUS program (Braconi et al. 2013) can be adopted in future editions of Eurocode 8. It is also worth noting that the Japanese steel industry addressed this issue by developing new steel grades with specified upper and lower limits on the yield stresss (Kanno 2016; Nakashima et al. 2000).

The findings also suggest that the sagging resistance is not sensitive to the rest of the aforementioned differences between design codes. Therefore, the ANSI/AISC approach (AISC 2016b; a) is recommended for the computation of the stud's shear resistance given its simpler formulation. Since the sensitivity of the results to variations in the slab's effective width is also negligible, the detailed approach of Eurocode 8-Part 1 (CEN 2004a) is not justifiable. Alternatively, either the AISC (2016b; a) or the (AIJ 2010b) approaches are recommended for future revisions of Eurocode 8-Part 1.

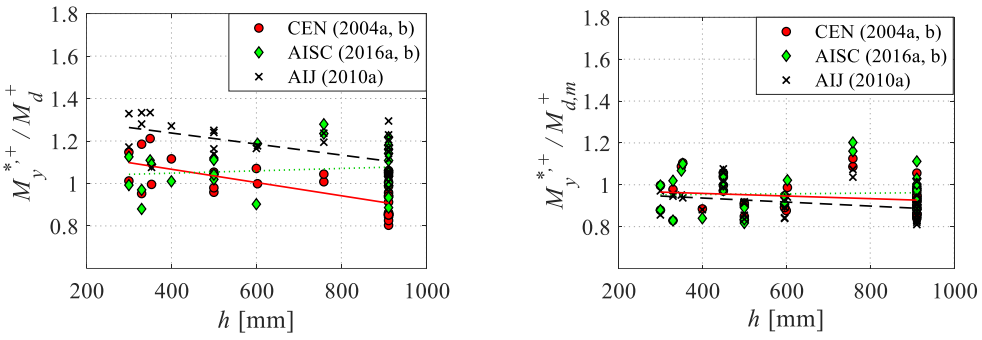

Figure 2.7 Test- to code-based sagging resistance ratio versus beam depth based on (a) expected material properties according to respective code; and (b) measured material properties

2.4.2 Hogging resistance

Figure 2.8 shows the ratio of the test-based hogging resistance to the expected bare steel beam plastic resistance ($M_p^{*,+}/M_{p,e}$) versus the beam depth. The test-based hogging resistance is, on average, 10% higher than $M_{p,e}$. This is consistent with prior observations by Elkady and Lignos (2014). This amplification is attributed to contributions from the slab longitudinal reinforcement and the metal deck. This becomes more evident in shallow beams. Note that the majority of the collected tests includes reinforced slabs with a steel wire mesh (reinforcement area less than 5 mm^2/cm slab width). Interestingly, shallow beams (h = 300 ~ 330 mm) with relatively high deck reinforcement (8~13 mm^2/cm), that were tested by Bursi and Gramola (2000) and Kishiki et al. (2010), developed the largest amplification factors of 1.4 to 1.5 as highlighted in Figure 2.8.

Most of the collected reports did not indicate the exact location of the slab reinforcement including their measured yield stress. Therefore, it was possible to calculate the design hogging resistance, $M_{d,m}^-$ for only eight of the collected specimens. The ANSI/AISC 360-16 (AISC 2016b) allows for the consideration of the slab reinforcement within the sagging plastic effective width (see Figure 2.4b) while the Eurocode 8 (CEN 2004a) distinguishes between the effective width under sagging and hogging bending. However, the average ratio, $M_y^{*,-}/M_{d,m}^-$, is found to be 0.97 and 0.96 for the (AISC 2016a; b) and Eurocode (CEN 2004a; b), respectively. This implies that the sensitivity of the hogging resistance to the slab effective width variation is negligible. Therefore, it is rational to adopt the simpler ANSI/AISC 360-16 (AISC 2016b) approach for the effective width computations in future editions of Eurocode 8-Part 1.

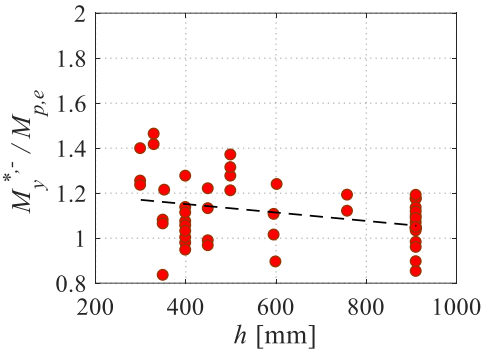

Figure 2.8 Normalized test-based hogging resistance versus beam depth

2.4.3 Effective stiffness

The effective stiffness under sagging (K^+) and hogging (K^-) bending is plotted versus the beam depth in Figure 2.9a and b, respectively. In this figure, the test-based stiffness is normalized by the theoretical stiffness of the non-composite steel beam, K_{nc}, considering both flexural and shear deformations. The test-based effective stiffness could only be obtained for 29 specimens; those are the ones where the beam's moment-rotation relation could be deduced from the reported test data.

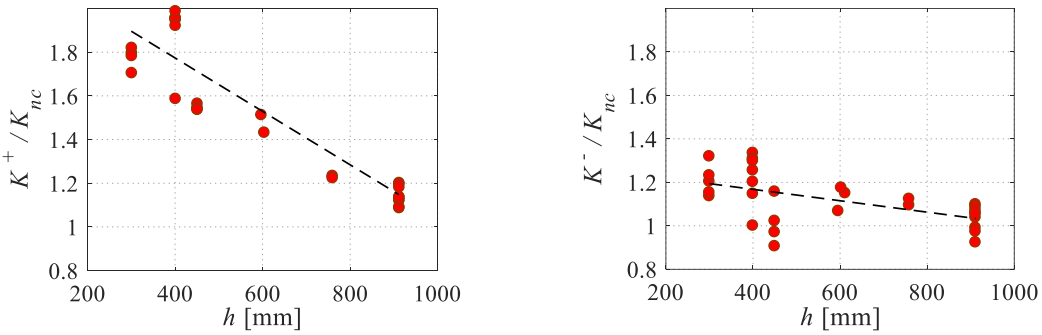

Figure 2.9 Dependence of the composite steel beam's effective stiffness on its depth for (a) sagging bending; and (b) hogging bending

Figure 2.9a shows that the composite action amplifies the effective stiffness of shallow beams ($h \leq$ 500 mm) under sagging bending by up to 100%. This agrees with findings from system-level experiments (Nakashima et al. 2007; Nam and Kasai 2012). For deep beams ($h >$ 500 mm), the effective stiffness increases, on average, by 30%. Referring to Figure 2.9b, the effective stiffness under hogging bending is amplified by up to 35% depending on the beam depth and the amount of slab reinforcement as discussed earlier. For few specimens, the K^-/K_{nc} values are slightly less than 1.0, which

is attributed to the sensitivity of K^- deduction from the test data. The effective stiffness is also dependent on the degree of composite action as discussed in the subsequent section.

2.4.3.1 Assessment of the code-based effective stiffness under sagging bending

The three codes calculate the effective stiffness under sagging bending, based on the effective moment of inertia of the un-cracked fully-composite cross section. The level of accuracy of these code estimates, that generally involve design-related reduction factors depending on a target limit state, is assessed here based on the deduced (i.e., actual) stiffness measurements of the collected test data (see Figure 2.3). Section C-13 commentary of the ANSI/AISC 360-16 (AISC 2016b) as well as the Japanese (AIJ 2010a) provisions employ Eq. (2.2) to estimate the moment of inertia for partially-composite steel beams, I_{pc}, in which, I_{nc}, and I_c are the moments of inertia of the non-composite and fully composite steel beams, respectively.

$$I_{pc} = I_{nc} + \sqrt{\eta} \cdot (I_c - I_{nc}) \tag{2.2}$$

The ANSI/AISC 360-16 (AISC 2016b) recommends an additional 25% reduction in the composite beam's moment of inertia for realistic deflection calculations (Leon and Alsamsam 1993; Leon 1990a). For the same purpose, the Japanese provisions (AIJ 2010b) use a larger modular ratio, n = 15 (defined as the ratio of the steel-to-concrete elastic modulus). Based on Eq. (2.2), the effective moment of inertia depends on the assumed slab effective width, which in turn differs in the elastic and plastic ranges. In the former, the effective width is related to the shear lag phenomenon (Castro et al. 2007). In the latter, stress redistribution in the slab occurs due to material nonlinearity, which increases the corresponding slab effective width. Accordingly, different effective widths shall be assumed for the plastic flexural resistance and the serviceability calculations (stiffness and deflection checks). Table 2.2 summarizes a comparison of the effective widths proposed by the three design codes for elastic analysis. In summary, Eurocode 8 considers a smaller slab effective width for elastic analysis than for plastic flexural resistance calculations. The effective width, as per Eurocode 8, is also dependent on the column configuration as well as the presence of transverse beams and anchored rebar in the slab (CEN 2004a). The ANSI/AISC 360-16 (AISC 2016b) provisions do not distinguish between elastic and inelastic analysis. The Japanese design recommendations propose a different effective width for elastic analysis that depends on the beam span. Both Eurocode 8 and Japanese provisions propose a fixed value for the modular ratio, n.

Figure 2.10 shows the ratio of the test- to code-based effective stiffness under sagging bending, K^+/K_d^+ versus the beam depth and degree of composite action. It appears that the 25% reduction imposed on I_{pc} by (AISC 2016a; b) for realistic deflection calculations results in a conservative estimate of the effective stiffness. However, long term effects, may actually reduce the effective stiffness of composite steel beams over a building's life-cycle. This effect cannot be assessed here since, in most cases, the collected tests were conducted within one month after concrete casting.

Table 2.2 Summary comparison of code-based effective width computation for elastic analysis

Code	Effective width*		Modular ratio, n
	Interior column	Exterior column	
CEN (2004a)	$\min\begin{cases}0.0375l\\ e\end{cases}$	$^{(1)}\min\begin{cases}0.0375l\\ e\end{cases}$ $^{(2)}\min\begin{cases}0.025l\\ e\end{cases}$	7
AISC (2016b)	$\min\begin{cases}0.0125l\\ w\\ e\end{cases}$		E_s/E_c
AIJ (2010b)	$\min\begin{cases}b+(0.5-0.6a/l)\cdot a & \text{if } a<0.5l\\ b+0.1l & \text{if } a\geq 0.5l\end{cases}$		15

* Effective width on each side of the beam web centerline
b = Flange width/2 for symmetric slab configuration.
= Flange width for asymmetric slab configuration.
(1) With transverse beams and anchored rebars
(2) Without transverse beams or rebars not anchored

In brief, the Eurocode and Japanese provisions provide close estimates of the effective stiffness with an average K^+/K_d^+ values of 0.96 and 0.91, respectively. The associated coefficient of variation (COV) is 0.12 and 0.06 for the Eurocode and Japanese data points, respectively. The higher dispersion based on the Eurocode is attributed to the fact that it always assumes a fully composite cross section; thus the Eurocode is conservative for beams with lower degree of composite action ($K^+/K_d^+ < 0.85$, see Figure 2.10b) as well as for fully-composite shallow beams ($K^+/K_d^+ > 1$).

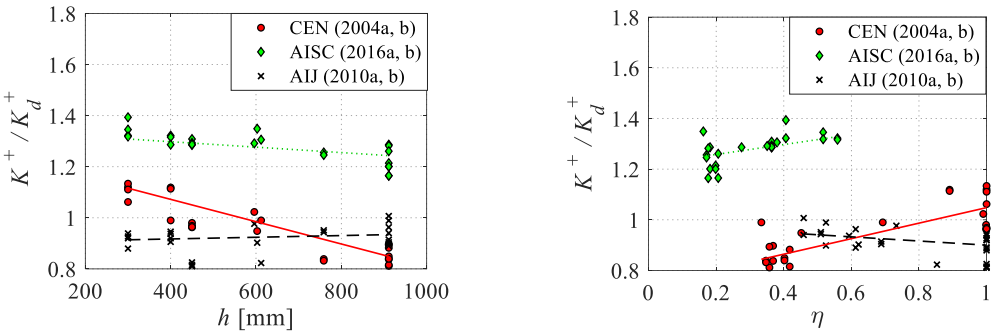

(a) (b)

Figure 2.10 Ratio of test- to code-based sagging effective stiffness; dependence on (a) beam depth; and (b) degree of composite action

2.4.4 Plastic rotation capacity of composite steel beams

The assembled database is used to quantify the pre- and post-capping plastic rotation capacities of composite steel beams, under sagging and hogging bending and to propose empirical equations for predicting these quantities. These equations can be used in the context of seismic assessment guidelines for new and existing steel frame buildings.

Eurocode 8-Part 3 (CEN 2005a) simply predicts a plastic rotation ($\theta_{p,pred}$) equal to $8\theta_y$ and $3\theta_y$ for Class 1 and 2 cross sections, respectively (where θ_y is the chord rotation at yielding) for non-composite steel beams. These values are anchored to the near-collapse limit state (Panagiotakos and Fardis 2001), which corresponds to the plastic rotation capacity at 20% drop in the beam's peak flexural resistance.

Using experimental data collected by Lignos and Krawinkler (2011, 2013), Hartloper and Lignos (2017) developed empirical equations to predict the pre- and post-capping plastic rotation of non-composite beams based on their first cycle envelope curve as defined in Figure 2.3b. These equations are further refined here by supplementing the collected experiments with data from non-composite steel beams that were conducted mostly in Europe. The equations are developed through standard multiple regression analysis (Chatterjee and Hadi 2015). The refined expressions are provided for θ_p^* and θ_{pc}^* as defined in Figure 2.3b. In particular, for standard non-composite steel non-RBS beams,

$$\theta_p^* = 0.25 \cdot \left(\frac{c}{t_w}\right)^{-0.9} \cdot \left(\frac{b}{2t_f}\right)^{-1.1} \cdot \left(\frac{L_b}{i_z}\right)^{-0.2} \cdot \left(\frac{L_o}{h}\right)^{1.1} \cdot \left(\frac{E}{f_{y,e}}\right)^{0.2} \qquad (COV = 0.38) \qquad (2.3)$$

$$\theta_{pc}^{*} = 12.67 \cdot \left(\frac{c}{t_w}\right)^{-0.9} \cdot \left(\frac{b}{2t_f}\right)^{-0.9} \cdot \left(\frac{L_b}{i_z}\right)^{-0.5} \cdot \left(\frac{E}{f_{y,e}}\right)^{0.1} \quad (COV = 0.44) \quad (2.4)$$

and for non-composite steel beams with RBS,

$$\theta_{p}^{*} = 0.12 \cdot \left(\frac{c}{t_w}\right)^{-0.5} \cdot \left(\frac{b}{2t_f}\right)^{-0.7} \cdot \left(\frac{L_b}{i_z}\right)^{-0.5} \cdot \left(\frac{L_o}{h}\right)^{0.8} \cdot \left(\frac{E}{f_{y,e}}\right)^{0.23} \quad (COV = 0.42) \quad (2.5)$$

$$\theta_{pc}^{*} = 4.91 \cdot \left(\frac{c}{t_w}\right)^{-1.1} \cdot \left(\frac{b}{2t_f}\right)^{-0.1} \cdot \left(\frac{L_b}{i_z}\right)^{-0.1} \cdot \left(\frac{E}{f_{y,e}}\right)^{0.09} \quad (COV = 0.47) \quad (2.6)$$

In which, L_b is the unbraced length of the beam, i_z is the weak-axis' radius of gyration, E and $f_{y,e}$ are the steel's modulus of elasticity and expected yield stress, respectively. The above equations are valid within the following ranges: $35 \leq c/t_w \leq 55$, $3 \leq b/2t_f \leq 8$, $20 \leq L_b/i_z \leq 80$ (RBS: $20 \leq L_b/i_z \leq 60$), $3 \leq L_o/h \leq 8$ (RBS: $5 \leq L_o/h \leq 8$), $440 \leq E/f_{y,e} \leq 830$.

To assess the predicted plastic rotation capacities based on the proposed Eqs. (2.3) to (2.6) as well as the Eurocode 8 approach, the pre- and post-capping plastic rotations under sagging and hogging bending are deduced from the gathered experimental data. To be consistent with the Eurocode 8 definition, the plastic rotation at 20% drop in peak flexural resistance, $\theta_{p,80\%M_u}^{*,+/-}$, is deduced from the test data. The same is done to deduce the predicted plastic rotation capacities corresponding to 80% $M_u^{+,-}$ based on Eqs. (2.3) to (2.6). In particular, $\theta_{p,pred} = \theta_p^{*,+/-} + 0.2\theta_{pc}^{*,+/-}$. The ratio of test-based to predicted plastic rotation, $\theta_{p,80\%M_u}^{*,+/-}/\theta_{p,pred}$, ratio versus the beam's web slenderness ratio (c/t_w) is plotted in Figure 2.11. The web slenderness ratio is used here since steel beams in fully restrained beam-to-column connections are mainly prone to web local buckling followed by flange buckling (Lignos and Krawinkler 2011). Also note that data points in this figure exclude tests where beams experienced premature fracture or those terminated prior to reaching 80% M_u.

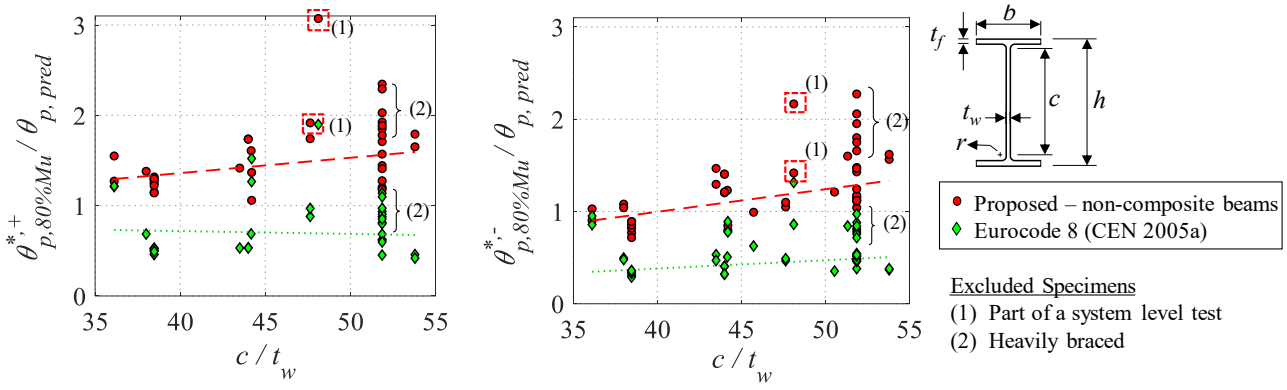

(a) (b)

Figure 2.11 Ratio of test-based to predicted plastic rotation at 20% flexural strength loss with respect to beam's web slenderness for (a) sagging bending; and (b) hogging bending

Referring to Figure 2.11a and b, the plastic rotation capacity under sagging bending is generally larger than that under hogging bending. This is due to the lateral restraint provided by the slab to the steel beam's top flange and top portion of the web, thereby delaying the top flange local buckling. Moreover, Eurocode 8-Part 3 consistently overestimates the plastic rotation capacity under both sagging and hogging bending by about 50%, regardless of the c/t_w and degree of composite action, η. This agrees with prior related studies (Araújo et al. 2017). The main reason is that this approach ignores the influence of geometric and material properties of a steel beam on its plastic rotation capacity. Referring to Figure 2.11b, for hogging bending, the plastic rotation predicted based on Eqs. (2.3) to (2.6) matches the measured one relatively well. Under sagging bending, the refined equations underestimate $\theta^{*,+}_{p,80\%M_u}$ by almost a constant value of 1.5. This is expected since these equations are meant for non-composite beams. The larger scatter around the predicted plastic rotation values at $c/t_w \approx 52$ is attributed to differences in lateral stability bracing between the collected tests. In fact, several of the collected specimens were heavily braced such that the predominant instability would be cross-sectional local buckling. Based on these observations, for composite steel beams under sagging bending, $\theta^{*,+}_{p,80\%M_u} = 1.5\theta_{p,pred}$ as per Eqs. (2.3) to (2.6) depending on the beam-to-column connection type. Similarly, under hogging bending, $\theta^{*,-}_{p,80\%M_u} = \theta_{p,pred}$.

Interestingly, one test specimen (highlighted in Figure 2.11) achieved a much larger $\theta^{*,+/-}_{p,80\%M_u}$ of 7.8% and 5.5% rad under sagging and hogging bending, respectively. This corresponds to an interior beam as part of a system-level test (Del Carpio et al. 2014). Cordova and Deierlein (2005) found that the axial restraint provided by the slab continuity in composite steel concrete MRFs increases the plastic rotation capacity of interior joint beams. This is not captured in the majority of the available

experimental data due to their simplified boundary conditions (FEMA 2000a). The authors are currently investigating this issue more thoroughly in a separate study.

The post-capping plastic rotation is deduced from 13 and 25 tests under sagging and hogging bending, respectively. The deduced $\theta_{pc}^{*,+/-}$ values are normalized with respect to the post-caping rotation predicted by Eqs. (2.4) and (2.6) and plotted versus c/t_w in Figure 2.12. Note that Eurocode 8-Part 3 does not provide estimates for this quantity. The data trends suggest that the influence of the concrete slab on the post-capping plastic rotation is not as pronounced as on $\theta_{p,80\%M_u}^{*,+/-}$. This agrees with prior findings by Elkady and Lignos (2014). Under sagging bending, the post-capping plastic rotation is about 20% larger than that predicted for the non-composite beam (see Figure 2.12a). Under hogging bending (see Figure 2.12b), $\theta_{pc}^{*,-}$ is, on average, 10% lower than that predicted by the regression equations for non-composite steel beams. Under hogging bending, a bigger portion of the steel cross section is under compression, which increases the potential for local and/or lateral torsional buckling (PEER/ATC 2010). In conclusion, it is recommended that for composite steel beams under sagging bending, the post-capping plastic rotation shall be taken as 1.2 times θ_{pc}^{*} of non-composite beams as per Eqs. (2.4) and (2.6). Under hogging bending, the post-capping plastic rotation shall be computed directly from Eqs. (2.4) and (2.6).

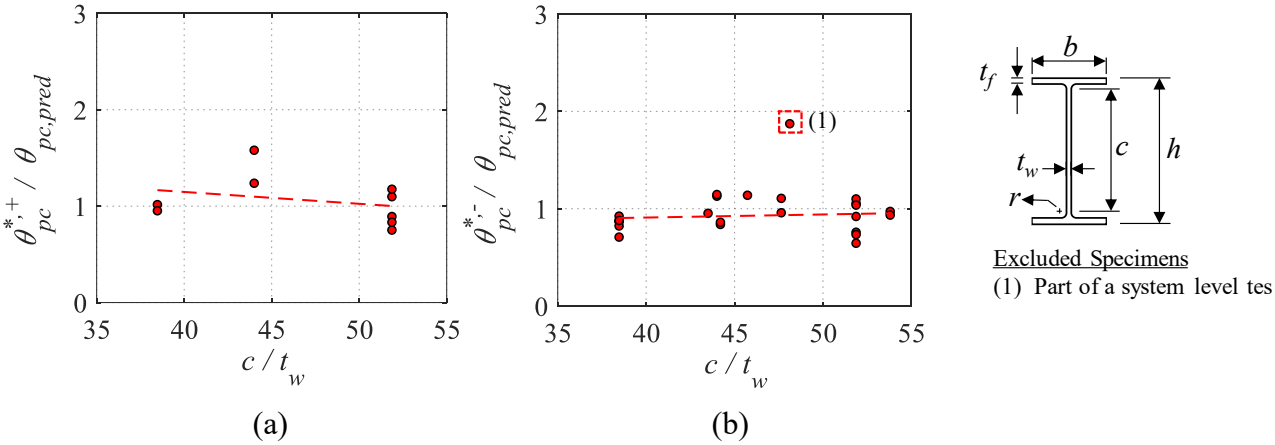

Figure 2.12 Ratio of test-based to predicted post-capping plastic rotation with respect to the beam's web slenderness for (a) sagging bending; and (b) hogging bending

2.5 Influence of composite action on beam-to-column web panel zone

The shear demand on the beam-to-column web panel zone of 45 composite steel beams is deduced and assessed with respect to the web panel shear resistance computed by the American, European and

Japanese steel design specifications (AIJ 2010a; AISC 2016b; CEN 2005c). Referring to Figure 2.13, based on the equilibrium of the external forces at a given joint, the maximum shear demand on the panel zone, $V_{PZ,demand}$, is deduced from the tests as follows,

$$V_{PZ,demand} = \frac{M_u^+}{d_{eff}^+} + \frac{M_u^-}{d_{eff}^-} - V_{col} = \frac{M_u^+}{d_{eff}^+} + \frac{M_u^-}{d_{eff}^-} - \frac{M_u^+ + M_u^-}{H} \cdot \frac{l}{l - h_c} \tag{2.7}$$

in which, M_u^+ and M_u^- are the peak sagging and hogging bending demands at the column face, respectively, d_{eff}^+ and d_{eff}^- are the effective panel zone depths for sagging and hogging bending, V_{col} is the shear force in the column, l and H are defined in Figure 2.6a. Note that M^- is zero for exterior joints. Under hogging bending, the effective depth d_{eff}^- is equal to the bare steel beam depth, h. Under sagging bending, the top flange resultant force shifts towards the slab and the resulting d_{eff}^+ is deduced by Eq. (2.8) that considers the concrete slab geometry (Elkady and Lignos 2014; Kim and Engelhardt 2002),

$$d_{eff}^+ = h + h_t - 0.5h_c - 0.5t_{bf} \tag{2.8}$$

Generally, the yield shear resistance of the panel zone, V_y, is expressed by Eq. (2.9), in which A_v is the shear area of the panel zone, f_{yv} is the shear yield stress (taken as $0.58 \sim 0.6f_{y,n}$), and α is a reduction factor that accounts for the axial load-shear interaction. In the American and Japanese provisions, α depends on the column axial load demand. The axial force-shear interaction is ignored in Eurocode 3 (CEN 2005c). Instead, a flat reduction factor equal to 0.9 is considered. Ciutina and Dubina (2003) stated that this factor accounts for the reduction due to axial load-shear interaction.

$$V_y = \alpha A_v f_{yv} \tag{2.9}$$

Eurocode 8 allows up to 30% contribution of the panel zone to the joint's total inelastic deformation. The panel zone plastic shear resistance is expressed by Eq. (2.10) as per ANSI/AISC 360-16 (AISC 2016b) and Eq. (2.11) as per Eurocode 3, in which, b_c and t_{cf} are the width and thickness of the column flange, respectively; h_b and t_{bf} are the beam's depth and flange thickness, respectively (see Figure 2.13). The Japanese code reduces the shear demand by 25%. The joint is then designed for V_y (Nakashima et al. 2000).

$$V_p = V_y \left(1 + 3\frac{b_c t_{cf}^2}{h_b h_c t_p}\right) \tag{2.10}$$

$$V_p = V_y + \left(\frac{b_c t_{cf}^2}{h_b - 2t_{bf}}\right) f_{y,n} \tag{2.11}$$

None of the three design provisions suggests how the composite slab shall be considered in the panel zone shear demand and resistance computations. The panel zone's yield and plastic shear resistances are calculated based on the three code provisions based on nominal material properties.

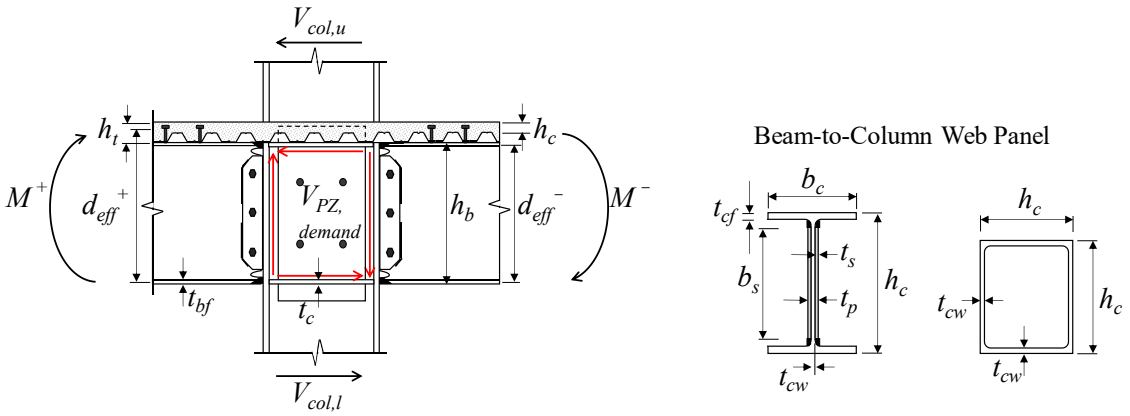

Figure 2.13 Panel zone dimensions and definition of the effective depth under sagging and hogging bending

Figure 2.14a and b show the panel zone shear resistance, $V_{PZ,d}$, versus the panel zone shear demand, $V_{PZ,demand}$, for wide-flange and hollow structural section (HSS) columns, respectively. For reference, three dashed lines are superimposed in Figure 2.14 that represent a $V_{PZ,d}$ to $V_{PZ,demand}$ ratio of 0.6, 1.0 and 1.67. Also in Figure 2.14a, the labeled specimens were intentionally designed for a very strong ('S') or very weak ('W') panel zone. The figure shows that the estimated yield shear resistance based on AISC (2016b) and AIJ (2010a) is between 0.70 to 1.25 times the panel zone shear demand. In total, 14 out of 23 wide-flange specimens experienced a shear demand greater than the yield resistance because the amplified sagging flexural resistance of the composite beam was neglected in design; hence underestimating the shear demand.

The estimated panel zone shear resistance according to Eurocode 3 varied between 0.6 to 1.1 times the corresponding shear demand. The Eurocode approach is particularly conservative for panel zones with doubler plates. This is because i) the Eurocode only considers a single doubler plate thickness even if two plates exist and ii) the panel zone shear resistance includes a 0.9 reduction factor regardless of the imposed axial load demand. All but two specimens experienced a shear demand greater than the Eurocode-based panel zone shear resistance. This conservatism is due to the associated

uncertainty in estimating the panel zone contribution to the plastic rotation demands of the beam-to-column joint (Castro et al. 2008).

Referring to Figure 2.14b, about half of the specimens with HSS and built-up box sections experienced a lower demand than the panel zone shear resistance, regardless of the respective code provision. Specimens in which the demand was higher than the code-based yield shear resistance experienced panel zone shear yielding (see Table 2.3). According to Nakashima et al. (2000), while Japanese limit state design principles encourage panel zone yielding, Japanese buildings are less commonly controlled by panel zone yielding.

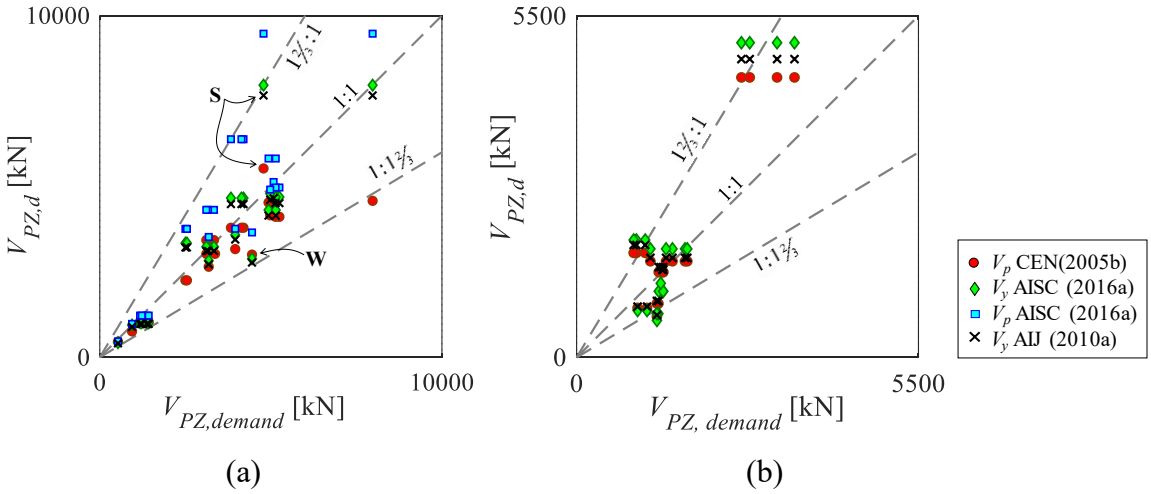

Figure 2.14 Code-based panel zone shear resistance versus maximum panel zone shear demand for (a) wide-flange columns; and (b) HSS and built-up columns

The gathered experimental data suggest that story drift demands exceeding 5% can be sustained even if the panel zone develops a total shear distortion up to $10\gamma_y$ (≈ 0.023 rad). This can be achieved with a $V_{PZ,d}/V_{pl,b}$ ratio of 0.8. The limit, which is applicable to all three design provisions, is based on the panel zone's yield shear resistance and the plastic flexural resistance of composite steel beams. Because this finding is based on subassembly test data, system-level studies shall be conducted in order to evaluate the influence of controlled inelastic behavior of panel zones on the dynamic response of steel MRFs relative to "strong" panel zone designs. However, this is outside the scope of the present work.

2.5.1 Recommendations for Panel Zone Shear Resistance

While design provisions allow for controlled inelastic panel zone yielding, there is no clear guidance on the relative panel zone-to-beam shear resistance. For this purpose, specimens for which the panel zone yield deformation was reported are analyzed separately. The collected specimens are summarized in Table 2.3 along with their reported failure mode. Specimens that fractured prior to a peak story-drift ratio of 5% and those that do not reflect the current design practice according to modern design provisions, are listed in Table 2.3 but are excluded from the subsequent assessment.

Figure 2.15 shows the panel zone shear resistance, $V_{PZ,d}$, normalized by $V_{pl,b}$ versus the panel zone total rotation (expressed as multiples of the nominal yield rotation in shear, γ_y). The $V_{pl,b}$ is the shear demand on the panel zone due to the development of the composite beam's plastic flexural resistance. This is calculated according to the respective design provision using the measured material properties to eliminate the material uncertaintly (i.e., $M_{d,m}^{+}$ and $M_{d,m}^{-}$ as defined earlier). This measure of the beam's relative shear resistance has been adopted in prior related studies (Lee et al. 2005; Roeder 2002). Note that the calculated beam plastic shear resistance accounts for the presence of the slab and neglects cyclic hardening.

Referring to Figure 2.15a, composite connections with wide-flange columns and a $V_{PZ,d}$-to-$V_{pl,b}$ ratio larger than 0.8, attained a shear distortion angle of up to $10\gamma_y$ ($\gamma_y = 0.023$ rad) without experiencing premature fracture. Lee et al. (2005) found that a $V_{PZ,d}$-to-$V_{pl,b}$ ratio between 1.10 and 1.42 is sufficient for the panel zone to develop a plastic rotation of 0.01 rad. However, the influence of the composite slab was disregarded in this case. When the $V_{PZ,d}$-to-$V_{pl,b}$ ratio is between 1.10 to 1.42, the panel zone develops a rotation of $8.5\gamma_y$ i.e., the plastic rotation is equal to 0.019 rad, which still exceeds 0.01 rad.

Referring to Figure 2.15b, for HSS columns, only three data points were collected (Kishiki et al. 2010; Yamada et al. 2009). Although inconclusive, two of these specimens experienced a panel zone shear distrortion more than $15\gamma_y$. Those were through-diaphragm connections with fully-composite shallow beams. The specimen tested (Kishiki et al. 2010) had a fully composite beam with a solid slab. Consequently, the composite beam remained elastic due to the large amplification in the plastic bending resistance and the plastic deformations of the subassembly were mainly concentrated in the panel zone.

Table 2.3 Composite steel beam specimens with reported panel zone shear distortion

Reference	Specimen ID	Column section	$\frac{\gamma}{\gamma_y}$	Failure Mode	SDR_{max} [%]
Ricles et al. (2004)	SPEC-1	W36x230	4.91	Fracture in RBS bottom flange	5.0
	SPEC-2	W27x194	8.28	Fracture in RBS top flange	5.0
	SPEC-3	W27x194	4.64	Fracture in RBS	5.0
	SPEC-4	W36x150	5.78	Low cycle fatigue cracks	5.0
	SPEC-5	W27x146	7.93	Low cycle fatigue cracks	5.0
Ricles et al. (2002)	C5[(a)]	W14x398	6.67	Fracture in top flange at shear stud in plastic hinge region	2.6 [(b)]
Engelhardt et al. (2000)	DBBWC	W14x398	7.8	Fracture at beam groove weld	6.0
	DBWWC	W14x398	8.40	Ductile tearing through top beam flange	7.0
	DBBWSPZC	W14x398	1.10	No fracture; test terminated	7.0
	DBWWPZC[(a)]	W14x283	23.23	Fracture in beam flange weld and shear-tab-to-column weld	7.0
Uang et al. (2000)	NIST-2C[(a)]	W14x426	2.58	No fracture; test terminated	4.0
Yamada et al. (2009)	Beam 1	HSS300x300x9	18.15	No fracture; test terminated	9.0
	Beam 2[(a)]	HSS300x300x9	3.60	Beam fracture at scallop location	2.5
Kishiki et al. (2010)	F_Full	HSS250x250x9	22.07	No fracture; test terminated	5.0
	D_LS	HSS250x250x12	5.19	No fracture; test terminated	5.0
	D_SS[(a)]	HSS250x250x12	4.84	Beam fracture	3.5
Sumner and Murray (2002)	4E-1.25-1.375-24	W14x257	1.83	Bolt tension rupture	5.0
Kim and Lee (2017)	PN500-C[(a)]	H400x400x13x21	15.17	Fatigue fracture in bottom flange weld	4.0[(b)]
	PN500C-HST[(a)]	H400x400x13x21	28.56	Low cycle fatigue beam fracture	7.0[(b)]
	PN500C-SH	H400x400x13x21	5.42	No fracture	>5.0[(b)]
	PN500C-TH	H400x400x13x21	9.07	No fracture	>5.0[(b)]
Del Caprio et al. (2014)	RBS-A	W12x30	3.81	No fracture; test terminated	16.4

[(a)] Specimens that are excluded from subsequent discussion
[(b)] Total plastic rotation reported instead of story drift ratio

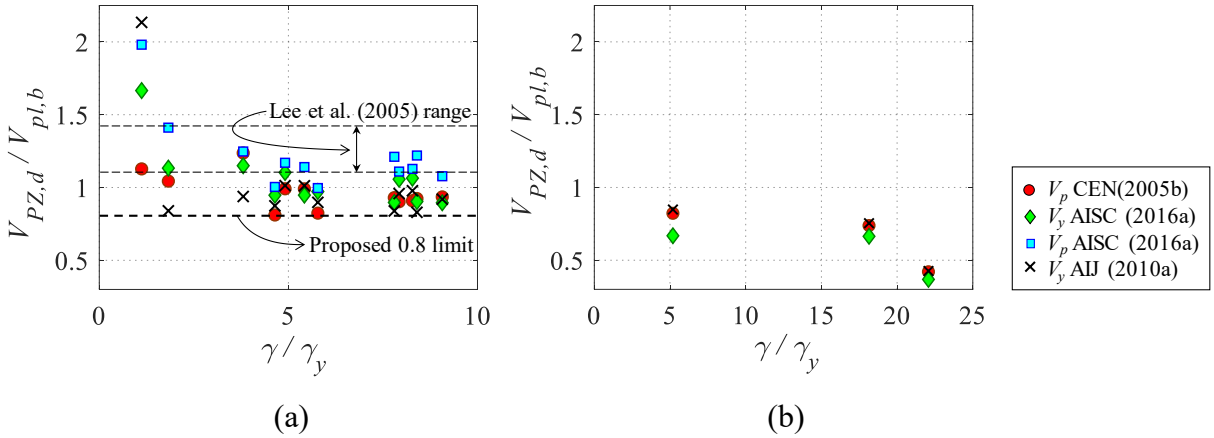

(a) (b)

Figure 2.15 Relative panel-zone-to-beam shear resistance against the normalized panel zone's distortion angle for (a) wide-flange columns; and (b) HSS columns

2.6 Conclusions

This chapter investigates the composite steel beam effects on the seismic design and performance assessment of composite-steel moment resisting frames (MRFs). For this purpose, a publicly available database of 97 composite steel beams was assembled. Several parameters were investigated including the sagging and hogging flexural resistances, the effective stiffness and the plastic rotation capacity of composite steel beams. The influence of the slab on the beam-to-column web panel shear resistance was also investigated. A comparison between the European, American and Japanese provisions was conducted; the aim of which is to provide design recommendations on how to properly consider the composite action in future design code revisions. Empirical formulations were also developed that capture the asymmetric behavior of composite steel beams under cyclic loading. Such relationships can be used in seismic assessment of new and existing steel frame buildings based on nonlinear static (pushover) analysis. The main findings are as follows:

- The sensitivity of the results to discrepancies between the three evaluated design provisions with regards to the computation of the sagging flexural resistance, $M_y^{*,+}$, is not significant. Therefore, the detailed approach presented in Eurocode 8-Part 1 (CEN 2004a) for calculating the slab effective width is not justified. Instead, this approach should be replaced with a simpler one (e.g., ANSI/AISC 360-16 (AISC 2016b)).

- The ratio of composite-to-bare sagging flexural resistance, $M_y^{*,+}/M_{p,e}$, of shallow composite steel beams (h < 500 mm) is at least 1.4 times larger than that of deep beams. This value may vary considerably depending on the corresponding degree of composite action. In low rise steel frame

buildings and/or steel buildings with space steel MRFs in which the degree of composite action is at least 0.4, the strong-column/weak-beam ratio shall be based on a beam's sagging flexural resistance.

- The hogging flexural resistance, $M_y^{*,-}$, of a composite steel beam is, on average, 10% larger than the corresponding one of the bare steel beam. This is attributed to the slab longitudinal reinforcement and the metal deck. The hogging plastic flexural resistance of a composite steel beam is sensitive to the steel material overstrength. This is traced well based on the ANSI/AISC 341-16 (AISC 2016a) seismic provisions because expected material properties are employed depending on the corresponding steel material grade. It is recommended that the material overstrength factors developed within the OPUS program (Braconi et al. 2013) are adopted in future editions of Eurocode 8-Part 1.

- Shallow composite steel beams ($h \leq 500$ mm) under sagging bending have an equivalent flexural stiffness of at least 1.6 times the effective flexural stiffness of the bare steel beam. This value decreases by up to 20% for deep composite steel beams ($h > 500$ mm). As such, the Eurocode (CEN 2004a; b) stiffness formulation exhibits higher dispersion because its estimation is not based on partially composite steel beams. Hence, the approaches discussed in the AISC and Japanese provisions are recommended for calculating the effective beam stiffness under sagging bending.

- The pre-capping plastic rotation capacity of composite steel beams is, on average, 50% higher than that of bare steel beams under sagging moment. When the beam is under hogging bending, the observed differences between composite and bare steel beams diminish. The Eurocode 8-Part 3 (CEN 2005a) formulations overestimate the measured plastic rotation capacities of steel beams in all the examined cases. This is attributed to the fact that the Eurocode approach does not consider the influence of the geometric and material properties of a steel beam on its plastic rotation capacity.

- The post-capping plastic rotation of composite steel beams is less sensitive to the presence of the slab. This is attributed to the fact that in the post-peak response, the slab is typically cracked, thereby becoming less effective in delaying local buckling-induced softening under cyclic loading.

- Empirical expressions are developed to reliably compute the plastic rotation capacity of composite steel beams. These expressions can be directly used for the seismic assessment of new and

existing steel MRF systems based on nonlinear static analysis within the framework of Eurocode 8-Part 3 (CEN 2005a) and ASCE/SEI 41-17 (ASCE 2017). These expressions effectively capture the dependencies of pre- and post-capping plastic rotation capacities of composite steel beams with respect to the beam's geometric and steel material properties.

- System-level tests suggest that the plastic rotation capacity of interior beam-to-column connections is at least 50% larger than that of exterior joints due to the slab continuity that is not properly traced in typical beam-to-column subassembly experiments. This deserves more attention in future studies and requires system-level physical testing.

- The panel zone shear yield resistance is nearly the same in the three design provisions that were evaluated. However, Eurocode 3-Part 1-8 (CEN 2005c) is conservative if doubler plates exist on both sides of the column web. The reason is that one of the two doubler plates is disregarded from the computation of the panel zone shear resistance.

- The panel zone in wide-flange steel columns may be designed such that the relative panel zone-to-beam shear resistance, $V_{PZ,d}/V_{pl,b} = 0.8$. This value is based on composite steel beam test data for which at least a 5% peak story drift ratio was attained. In these tests, the panel zones developed a total shear distortion up to about $10\gamma_y$ without experiencing pre-mature fracture within the corresponding beam-to-column connection.

Chapter 3 Hysteretic behavior of moment-resisting frames considering slab restraint and framing action

Bibilograpic details

This chapter presents the post-print version of the article with the following full bibliographic details: El Jisr, H., Elkady, A., and Lignos, D. G. (2020). "Hysteretic behavior of moment-resisting frames considering slab restraint and framing action." *Journal of Structural Engineering*, American Society of Civil Engineers, 146(8), 04020145. DOI: https://doi.org/10.1061/(ASCE)ST.1943-541X.0002696

Authors' contribution

Hammad El Jisr developed the continuum finite element (CFE) models, carried out the CFE simulations, analyzed the simulations results, created the figures, wrote the manuscript draft and revised the manuscript. The co-authors contributed in developing the methodology presented in this chapter, supervising the work conducted by Hammad El Jisr, funding acquisition, and reviewing and editing the original and final manuscript drafts.

3.1 Abstract

This chapter examines the influence of framing action and slab continuity on the hysteretic behavior of composite steel momentresisting frames (MRFs) by means of high-fidelity continuum finite-element (CFE) analyses of two-bay subsystems and typical cruciform subassemblies. The CFE model, which is made publicly available, was thoroughly validated with available full-scale experiments and considers variations in the beam depth and the imposed loading history. The simulation results suggest that beams in subsystems may experience up to 25% less flexural strength degradation than those in typical subassemblies. This is because of local buckling straightening from the slab continuity and framing action evident in subsystems. For the same reason, beam axial shortening attributable to local buckling progression is up to five times lower in subsystems than in subassemblies, which is consistent with field observations. While the hysteretic behavior of interior panel zone joints is symmetric, exterior joint panel zones in subsystems experience large asymmetric shear distortions regardless of the employed lateral loading history. From a design standpoint, it is found that the probable maximum moment in deep and slender beams ($d_b \geq 700$ mm) may be up to 25% higher than that predicted by current design provisions with direct implications to capacity design of steel MRFs. The 25% reduction in the shear stud capacity as proposed by current seismic provisions is not imperative for MRFs comprising intermediate to shallow beams and/or featuring a high degree of composite action ($\eta > 80\%$) as long as ductile shear connectors are employed.

3.2 Introduction

The 1994 Northridge and 1995 Kobe earthquakes led to a paradigm shift in the seismic design of steel moment resisting frames (MRFs). As part of the SAC[2] project (Mahin 1998), multiple testing programs were conducted on beam-to-column subassemblies (Engelhardt et al. 2000; FEMA 2000a; Ricles et al. 2002, 2004; Sumner and Murray 2002; Tremblay et al. 1997; Uang et al. 2000). These tests formed the basis for the development of today's pre-qualified beam-to-column connections for seismic applications in the US (AISC 2016a). A concerted effort is currently underway in Europe (Landolfo et al. 2018) regarding the same matter.

[2] SAC is a joint venture of the Structural Engineers Association of California (SEAOC), the Applied Technology Council (ATC) and California Universities for Research in Earthquake Engineering (CUREe)

The significant majority of the tests conducted as part of the SAC project involved subassemblies with T- or cruciform-shaped configurations. While these subassemblies may be convenient for physical testing due to their overly simplified boundary conditions, they do not represent reality at damage states associated with large inelastic deformations (Cordova and Deierlein 2005; Zerbe and Durrani 1989). Beams in cruciform subassemblies are free to shorten axially (Civjan et al. 2001; MacRae et al. 2013) after the formation of local buckling within the anticipated dissipative zone of a steel beam. This is not evident in system-level tests (Cordova and Deierlein 2005; Del Carpio et al. 2014) and field observations (Clifton et al. 2011; Okazaki et al. 2013), where beam local buckling is delayed due to the axial restraint provided by the slab continuity (Cordova and Deierlein 2005; Donahue et al. 2017; FEMA 2000a; Herrera et al. 2008). Moreover, the floor slab and adjacent columns in buildings provide restraint to the beam and inhibit axial shortening (PEER/ATC 2010). This may result in an appreciable increase in the plastic rotation capacity of the steel beam (FEMA 2000a; Kwasniewski et al. 2002). Although inconclusive, El Jisr et al. (2019) highlighted that the plastic rotation capacity of composite steel beams directly deduced from system-level or subsystem tests may be at least two times larger than that deduced from beams in cruciform configurations.

The effect of the slab axial restraint may have significant implications on nonlinear modeling of steel MRF beams. Common numerical modeling approaches include point plastic hinge models as well as distributed finite-element approaches (Deierlein et al. 2010). While point hinge (Elkady and Lignos 2014; Ibarra et al. 2005; Lignos and Krawinkler 2011; Rassati et al. 2004) and resultant section models (El-Tawil and Deierlein 2001; Mehanny and Deierlein 2000) for composite steel beams are available in the literature, they have been established on the basis of subassembly tests. Hence, potential differences, due to the framing action, in the hysteretic behavior of beams between interior and exterior joints of a steel MRF are ignored. Furthermore, these models typically neglect the interface slip between the steel beam and the concrete slab. These effects may be captured with fiber models (Amadio and Fragiacomo 1993; Ayoub 2005; Ayoub and Filippou 2000; Bursi et al. 2005; Bursi and Ballerini 1996; Gattesco 1999; Salari and Spacone 2001). Albeit these models are computationally efficient, they require effective stress-strain formulations with softening to trace strength and stiffness deterioration (Kolwankar et al. 2018; Suzuki and Lignos 2018). In the absence of comprehensive experimental data, continuum finite element (CFE) models offer a rational alternative to quantify the aforementioned effects. Past studies involving CFE models (Alashker et al. 2010; Elkady and Lignos 2015a, 2018a; Ricles et al. 2004; Zhou et al. 2007) focused mostly on the dependence of strength and stiffness deterioration of steel members on nonlinear geometric instabilities (e.g., local and/or lateral torsional buckling). To the best of the authors' knowledge, there are no comprehensive studies to

elucidate the physical mechanisms associated with the slab axial restraint at interior and exterior beam-to-column joints within a subsystem (entire story) and/or structural system.

From a seismic design standpoint, headed shear studs transfer seismic inertia forces through the slab into the MRF steel beams. Early degradation in the shear stud strength results in the loss of this load-transfer mechanism, thereby triggering loss of composite action (Cheng and Chen 2005; Civjan et al. 2001; Leon et al. 1998). As a precaution against severe shear strength degradation of the studs, current seismic provisions (AISC 2016a; CEN 2004a) propose a 25% reduction in the stud design shear resistance. This requirement is based on a purely subjective decision. Albeit this reduction may be rational in steel MRFs comprising deep beams (depths larger than 400 mm), it is not justifiable in prospective steel MRF designs comprising shallow composite beams with a high degree of composite action, $\eta \geq 80\%$ (η is the ratio of the actual number of shear studs to that required to achieve full composite action). Moreover, cyclic push-out tests (Bursi and Gramola 1999; Civjan and Singh 2003; Zandonini and Bursi 2000), although informative, do not replicate the actual stress state and boundary conditions in the slab due to bending, nor do they account for the force redistribution between the studs (Schafer et al. 2019; Sjaarda et al. 2018; Suzuki and Kimura 2019).

This chapter addresses all the aforementioned issues by means of CFE analyses. The proposed CFE modeling approach, which is validated on the basis of composite subassembly tests, explicitly accounts for the synergy between the composite slab and the steel beams. The modeling approach is extended to two-bay subsystems to comprehend the influence of the slab axial restraint and framing action on the hysteretic behavior of beams and panel zones in interior/exterior beam-to-column joints. These subsystems comprise beams with depths representative of both the North American and European seismic design practice. Aspects associated with the shear stud resistance in contemporary designs of composite steel MRFs are discussed.

3.3 Proposed continuum finite element modeling approach

This section discusses the CFE modeling specifics of a typical beam-to-column subassembly with a composite floor slab as illustrated in Figure 3.1a. The modeling approach is validated with data from a full-scale subassembly test (Ricles et al. 2004) featuring fully restrained beam-to-column connections with reduced beam sections (RBS). The commercial finite element software Abaqus 6.14 (Abaqus 2014) is used for this purpose. Referring to Figure 3.1, column and beam regions within contact zones are meshed with first-order brick elements with incompatible modes, *C3D8I*. These

elements are suitable for nonlinear analysis involving contact (Selamet and Garlock 2010). They are fully integrated with additional internal degrees of freedom to eliminate shear locking and they capture bending with an accuracy similar to that of quadratic elements. A structured mesh is implemented in the beam's anticipated plastic hinge location to produce elements with reasonable aspect ratios. Three elements per flange thickness are considered as recommended by Bursi and Jaspart (1998) for flexure-dominated problems. The remaining beam and column regions are modeled using four-node double-curved *S4R* shell elements with five integration points along the element thickness based on the recommendations by (Elkady and Lignos 2018a). A shell-to-solid coupling constraint is used to connect the shell edge regions of the beam to the column flange. The concrete slab is modeled using eight-node first-order brick elements with reduced integration, *C3D8R*. Five elements across the slab thickness are considered to provide satisfactory performance against hourglassing (Genikomsou and Polak 2015). Slab rebar and wire mesh reinforcement are modeled using two-node linear truss elements, *T3D2*. The steel deck is modeled using four-node membrane elements, *M3D4R*.

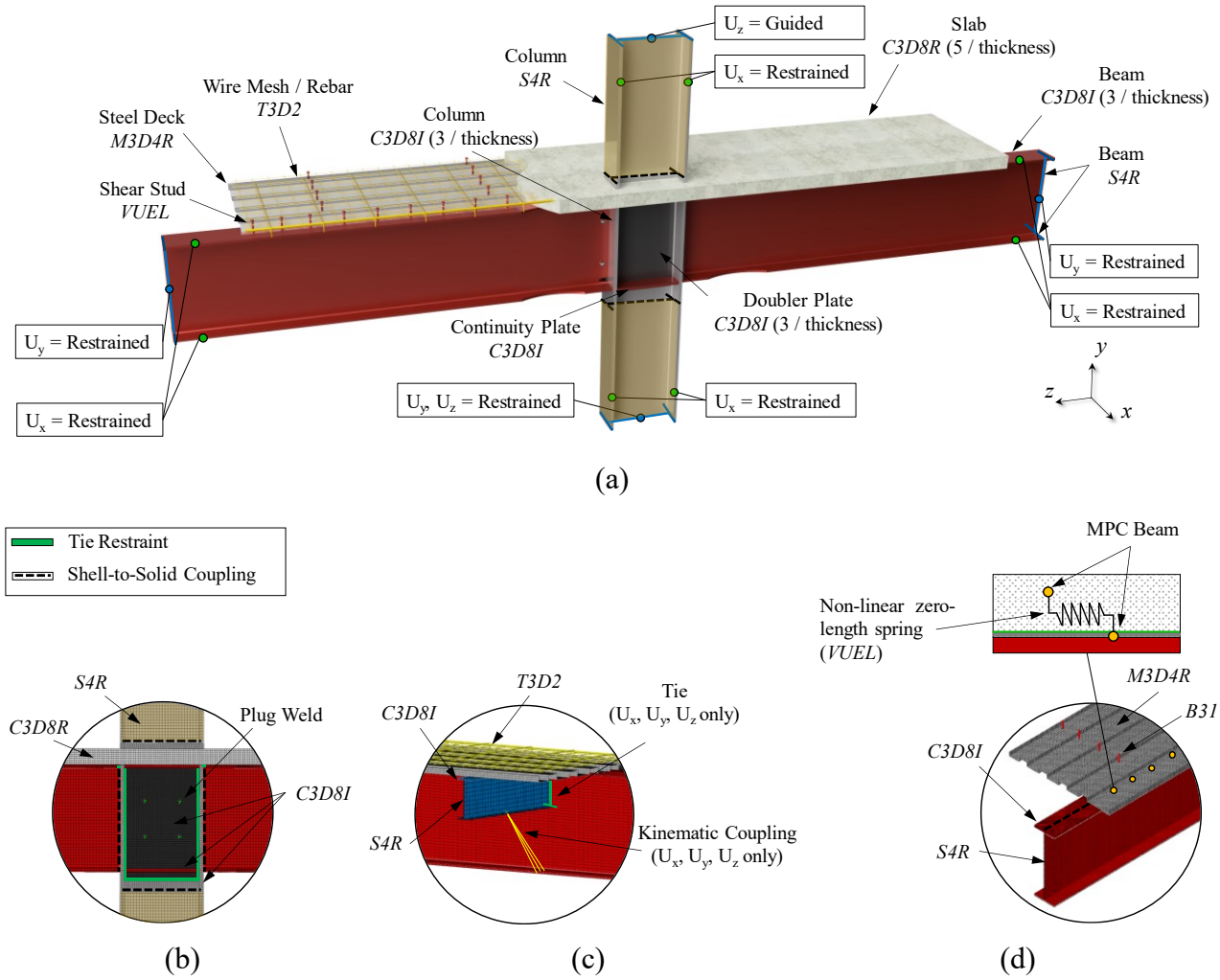

Figure 3.1 (a) Continuum finite element model specifics for a typical subassembly configuration with composite floor slab (b) column web panel detail; (c) transverse beams detail; (d) shear studs detail

Shear studs connecting the slab to the transverse beams are modeled with two-node linear beam elements, *B31*. The cross-sectional area of these elements is modified to make it equivalent to the actual shear stud strength and stiffness (Baskar et al. 2002; Liang et al. 2005). The shear studs between the main beams and the slab may exhibit a pinched hysteretic degrading response. To capture this response, the interface slip should be modeled using a nonlinear load-slip behavior (Ayoub and Filippou 2000; Bursi et al. 2005). For this purpose, a user-defined element (VUEL) is developed by the authors and implemented as shown in Figure 3.1d. This VUEL, which is publicly available from https://github.com/eljisr/IMK_Pinching_VUEL, employs the modified Ibarra-Medina-Krawinkler (IMK) deterioration model (Ibarra et al. 2005; Lignos and Krawinkler 2011). The model assumes a pinched hysteretic behavior that explicitly simulates the effects of stiffness, strength, post-capping strength and accelerated reloading stiffness deterioration (Ibarra et al. 2005). It is loading-history independent and assumes a reference inherent hysteretic energy dissipation capacity regardless of the

applied protocol. The set of parameters that define the deterioration model are calibrated with cyclic push-out tests available in literature. Past conventional cyclic push-out tests have demonstrated severe degradation in the shear studs (Bursi and Gramola 1999; Civjan and Singh 2003; Zandonini and Bursi 2000). However, they do not accurately replicate the mechanical behavior of the shear stud connectors under fully reversed cyclic loading. More importantly, they do not consider the force redistribution occurring in the studs once they experience cyclic deterioration. For this reason, the shear studs are calibrated with recently conducted cyclic-push out tests that account for the stress state in the slab under reversed cyclic loading (Suzuki and Kimura 2019). These tests were subjected to symmetric loading protocols, which impose far higher inelastic demands to studs than non-symmetric loading protocols. In that respect, the calibration is on the conservative side. Figure 3.2 shows a calibration of the hysteretic behavior of a cluster of four 19 mm shear studs. Based on this calibration, the following parameters are obtained for a single stud (positive and negative superscripts refer to the stud parameters when the slab is under compression and tension, respectively): the ultimate shear strengths $Q_u^+ = 82$ kN and $Q_u^- = 36$ kN, the effective yield strengths $Q_y = 90\%$, the pre-capping slip capacities $s_p^+ = 6$ mm and $s_p^- = 10$ mm, the post-capping slip capacities $s_{pc}^+ = 11$ mm and $s_{pc}^- = 5$ mm, the ultimate slip capacities $s_u^\pm = 15$ mm, the strength and stiffness deterioration parameters $\lambda_s = 40$ and $\lambda_k = 15$, the deterioration rate parameters $D^\pm = 1.0$, and the parameters that define the break point of the pinching model $\kappa_d = 0.4$ and $\kappa_f = 0.2$.

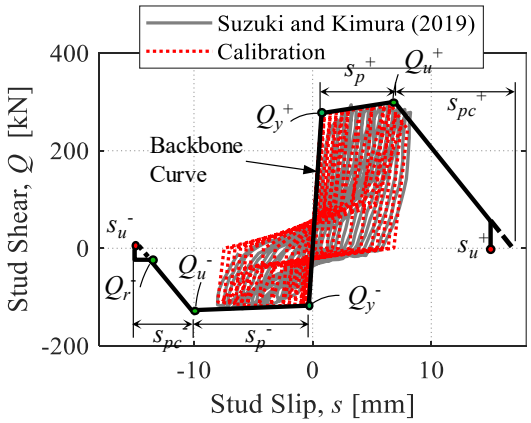

Figure 3.2 Calibration example of a cluster of four 19 mm cyclically-loaded shear studs (data values were reproduced from Suzuki and Kimura (2019))

The steel material multi-axial constitutive relationship for beams and columns is based on the well-established Voce-Chaboche multiaxial plasticity model (Lemaitre and Chaboche 1990; Voce 1948). The input model parameters are adopted based on studies by Sousa and Lignos (2018) for A992 Gr.

50 steel (ASTM 2015). An elastic perfectly plastic material model is assigned to the steel deck and slab reinforcement.

The concrete behavior under cyclic loading is simulated through the concrete damaged plasticity (CDP) model, available in Abaqus 6.14 (Abaqus 2014). The yield function of this model under multiaxial stress state accounts for damage in the concrete (Lee and Fenves 1998; Lubliner et al. 1989). The plastic flow potential is defined using the Drucker-Prager hyperbolic function. The parameters recommended by Goto et al. (2010) are implemented in the developed CFE model. The stress-strain relation of concrete under compression is defined according to Carreira and Chu (1985) and Baskar et al. (2002). The concrete compressive strength is $f_c' = 32$ MPa. Under tension, a linear elastic behavior is assumed up to the concrete tensile strength, $f_t = 10\% f_c'$ (Matsumura and Mizuno 2007). A tension stiffening strain of 0.1 is employed (Baskar et al. 2002; Rex and Easterling 2000). Stiffness degradation mechanisms are incorporated in the CDP model through compressive and tensile damage variables (Goto et al. 2010).

Referring to Figure 3.1a, the pinned boundary conditions assumed at the main beams and column ends correspond to those expected at the inflection point locations in a typical MRF under lateral loading. Out-of-plane movement and twisting are restrained at the main beams and column ends at the indicated points shown in Figure 3.1a. The transverse floor beams supporting the floor slab are connected to the main beams via a conventional shear tab connection (see Figure 3.1c). A tie constraint is used to idealize this connection for the translational degrees of freedom. Therefore, the connection can resist moment under strong-axis bending only. This assumption is based on the fact that the shear-tab connection is not an ideal pin and has a non-negligible strong-axis rotational strength and stiffness (Liu and Astaneh-Asl 2004). Furthermore, the strong-axis flexural demand on the connection (due to twisting) is low and is mainly resisted by the diagonal brace and the slab. On the other hand, under weak axis bending, the rotational stiffness and flexural strength of the shear tab connection is negligible. The out-of-plane movement of the main beam's bottom flanges is prevented with diagonal braces connected to the transverse beams. Modeling of these braces is simplified by employing a kinematic coupling constraint as shown Figure 3.1c.

The steel beams are rigidly connected to the column through a surface-based tie constraint. Continuity plates are fully tied to the column web and flanges, while doubler plates are tied to the column web at their edges. Plug welds are modeled using connector elements with an influence radius equal to that of the plug weld radius, and fully-constrained degrees of freedom (see Figure 3.1b). The shear studs are connected to the beam and slab through multi-point beam constraints. A perfect bond is

assumed between the concrete slab, and the rebar reinforcement. The inner surface of the steel deck is fully tied to the concrete slab.

Both the restraint provided by the slab to the top beam flanges, and the bearing of the slab on the column flanges are simulated using a general contact interaction. The interface action between the slab and the steel components consists of a hard contact relationship with balanced master-slave weighing and allowed separation. The friction behavior is expressed using a Coulomb model with a steel-to-concrete friction coefficient, $\mu = 0.2$ (Johansson and Gylltoft 2002).

Local and global imperfections are introduced in the dissipative zones (i.e., RBS region) to properly trigger nonlinear geometric instabilities based on the modeling procedures proposed by Elkady and Lignos (2018a). Residual stresses are also modeled using the distribution proposed by Young (1972).

3.4 Validation of the modeling approach

The proposed CFE modeling approach is validated with the subassembly specimen, SPEC3 from Ricles et al. (2004). The specimen features W36x150 main girders, a W27x194 column, W14x22 transverse beams and a 133 mm (5.25”) slab. The floor slab is 1219 mm (4’) wide, with a 305 mm (12”) overhang. It consists of an 83 mm (3.25”) concrete fill (32 MPa) on top of a 51 mm (2”) deep Vulcraft 2VLI steel deck, oriented such that the ribs are parallel to the main girders. The slab reinforcement includes a W4xW4 welded wire mesh, as well as No. 3 (9.5 mm) and No. 4 (12.7 mm) bars. Nine 19 mm (0.75”) shear studs connect each main girder to the slab. A single 12.7 mm (0.5”) doubler plate is welded to the column web. The specimen was subjected to a cyclic symmetric loading history (SAC Joint Venture 1997) at the column tip.

The nonlinear quasi-static analysis is run at EPFL’s high performance computing center (Fidis Cluster) using a Message Passing Interface-based domain decomposition parallel implementation. The Abaqus/Explicit dynamic analysis procedure is employed. This procedure has a robust contact functionality to solve very complex contact problems (Prior 1994). This is critical for simulating the slab restraint to the top beam flange and the slab bearing on the column. In particular, the loading rate is assumed to be sufficiently small to ensure that the inertial force is nearly zero (i.e., equivalent to static loading). The main drawback of the explicit solution technique is that the time step is limited by the size of the stable time-increment, $t_{stable} \leq 2/\omega_{max}$, where ω_{max} is the highest element eigenfrequency in the model. To overcome this shortcoming, the stable time-increment is increased through mass-scaling. Quasi-static response is verified through the equilibrium of static forces and the energy

balance in the model. Referring to Figure 3.3, the ratio of the kinetic and viscous energies to the internal energy is less than 5% and the total energy in the model is nearly zero (Chung et al. 1998; Prior 1994). Artificial strain energy due to hourglassing control as well as distortion control dissipation energy are examined and found to be negligible.

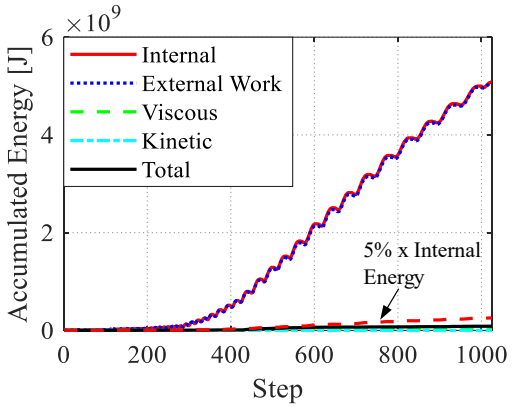

Figure 3.3 Model energies accumulated throughout the explicit continuum finite element analysis

Figure 3.4a and b shows a comparison between the measured and simulated hysteretic response of the composite steel beam. In this figure, M_b is the beam moment at the column face; V_{PZ} is the panel zone shear force; SDR_b, SDR_{PZ}, and SDR_c are the beam, panel zone and column contributions to the story drift ratio, respectively. Referring to Figure 3.4a, the CFE model predicts the onset of local buckling fairly well under sagging (slab in compression) and hogging (slab in tension) bending excursions. The predicted flexural strength and stiffness of the beam possesses an outstanding agreement with the measured one up to 6% story drift ratio. Deviation from the test results occurs in the last sagging excursion as ductile tearing initiated in the bottom flange of the beam during the test. Figure 3.4b shows that the model marginally over-predicts the panel zone deformations by about 10%. This is due to the slightly higher predicted beam moment. However, the panel zone contribution to the story drift, in both the CFE model and test, does not exceed 1%. Consequently, the slight deviation in the panel zone response does not practically influence the energy dissipation capacity of the beam-to-column connection as shown in Figure 3.4d.

Figure 3.4c demonstrates a noteworthy agreement between the predicted and measured decomposed deformation contributions to the story drift. Referring to Figure 3.4d, the same observations hold true with regards to the accumulated energy dissipated by each component. Note that the peak deformation in the panel zone, in both the CFE and the test, occurs at 3% SDR. At 6% SDR, the demand on the panel zone drops substantially as the beams experience flexural strength degradation. Accordingly,

the panel zone contribution at 6% SDR is negligible in both the CFE and the test (0.03% and 0.15% respectively).

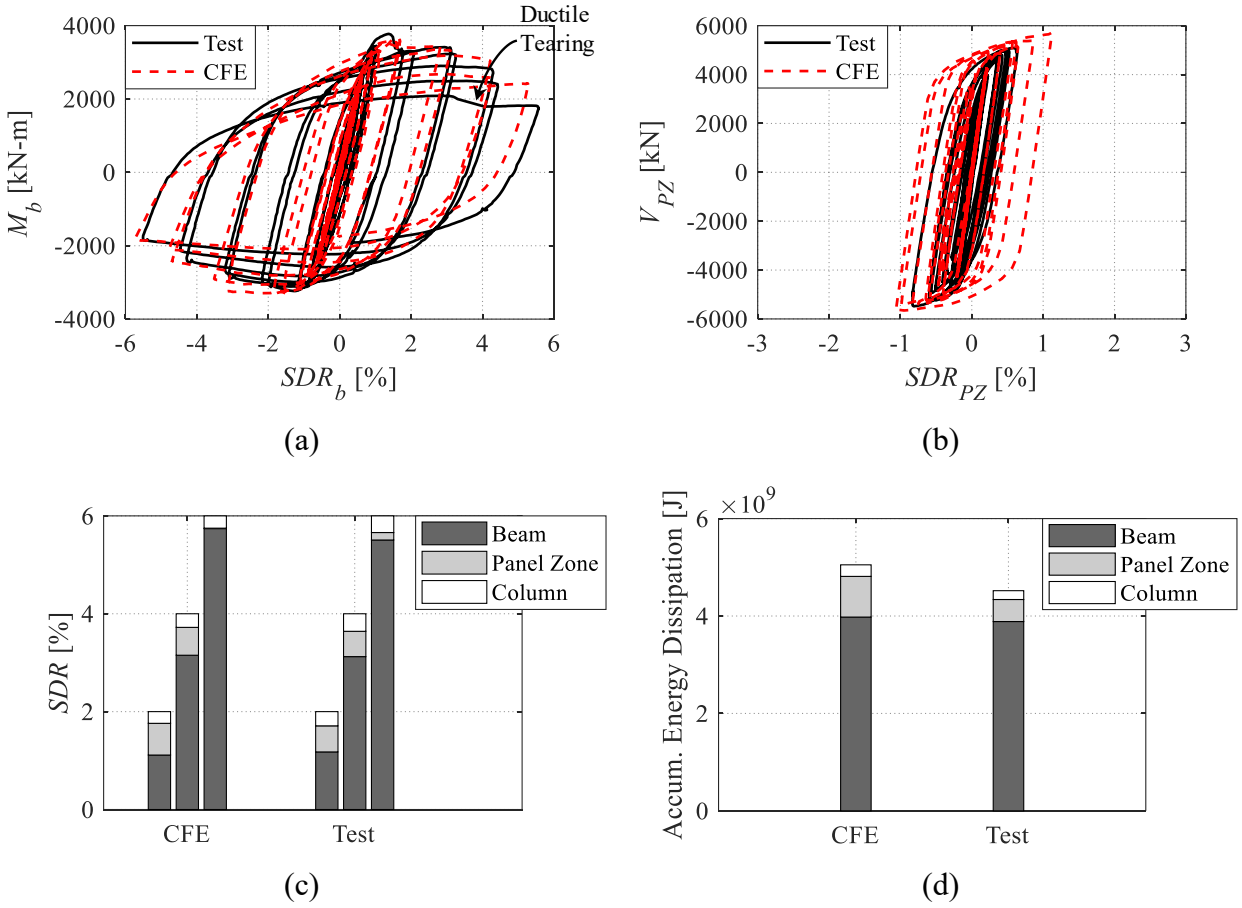

Figure 3.4 Comparison between simulated and experimental results (experimental data are reproduced from Ricles et al. (2004)) (a) beam hysteretic behavior; (b) panel zone hysteretic behavior; (c) component contribution to the story drift at the first cycle of 2%, 4% and 6% amplitudes; (d) accumulative energy dissipation in each component

3.5 Parametric study with two-bay subsystem models

Having established confidence in the CFE modeling approach, the effects of the floor slab continuity and framing action on the seismic performance of steel MRFs is assessed. The presence of neighboring gravity frames is also expected to provide some degree of additional restraint on the steel MRF (Donahue et al. 2017), thereby enhancing these effects. However, the influence of gravity framing is not considered in this chapter. Three two-bay subsystems, summarized in Table 3.1, are considered herein: S_D with deep beams, S_I with beams of intermediate depth, and S_S with shallow beams. The subsystems cover a range of beam sizes employed in typical low to mid-rise steel MRF buildings (Elkady and Lignos 2014, 2015b; Tartaglia et al. 2018; Tsitos et al. 2018). The centerline span length,

$L = 8992$ mm (29-1/2'), column height, $H = 3962$ mm (13'), maximum unbraced length, $L_b = 1676$ mm (5-1/2''), and the slab dimensions correspond to those of subassembly specimen SPEC3 (Ricles et al. 2004). In all three subsystems, the member slenderness ratio L_b/r_y, summarized in Table 3.1, is compliant with ANSI/AISC 341-16 (AISC 2016a) for special moment frames. The shear span-to-depth ratio L_o/d_b of specimen S_D does not quite satisfy the ductility requirements of ANSI/AISC 341-16 (AISC 2016a). Nonetheless, the moment-shear interaction was found to be insignificant, especially in the absence of gravity load. This is consistent with available test data on composite connections (El Jisr et al. 2019). Since the maximum shear force that can be transferred through the shear studs is governed by the capacity of the concrete slab, the degree of composite action, as defined by ANSI/AISC 360-16 (AISC 2016b), is the same for all three subsystems ($\eta \sim 20\%$). The columns are sized to remain elastic (see strong-column-weak-beam (SCWB) ratio in Table 3.1), whereas the web panel zones are sized to comply with ANSI/AISC 341-16 (AISC 2016a). Equal displacement was imposed at the top of the columns. This loading technique assumes a rigid diaphragm for the floor slab above the considered subsystem. The subsystems are subjected to a cyclic symmetric lateral loading history up to an SDR of 6% (SAC Joint Venture 1997). Sub-system S_D is also subjected to a collapse-consistent protocol (Suzuki and Lignos 2019) to investigate the influence of loading history on the subsystem cyclic performance. For each subsystem, the seismic behavior is compared with that of the corresponding interior joint subassembly featuring simplified boundary conditions. Particular emphasis is placed on the hysteretic behavior of the composite beams, panel zones, and shear studs, the accumulated beam axial shortening and beam axial force demands.

Table 3.1 CFE virtual testing matrix

	Beam						Column		R_v/V_d		SCWB	
	Section	d_b [mm]	$\frac{h_b}{t_w}$	$\frac{b_f}{2t_f}$	$\frac{L_o}{d_b}$	$\frac{L_b}{r_y}$	Section	t_d [mm]	Int.	Ext.	Int.	Ext.
S_D[a,b]	W36x150	911	51.9	6.4	4.5	26.7	W27x194	12.7	1.1	1.2	1.5	2.81
S_I[a]	W21x122	551	31.3	6.5	7.6	22.6	W24x162	22.2	1.2	1.2	2.1	3.81
S_S[a]	W16x45	409	41.1	6.2	10.5	42.0	W14x132	6.4	1.2	1.9	3.4	5.98

a = Cyclic symmetric loading history up to 6% story drift (SAC Joint Venture 1997)
b = Collapse consistent loading protocol with two phases (Suzuki and Lignos 2019)
R_v = Panel zone inelastic shear strength (AISC 2016b)
V_d= Panel zone shear demand (AISC 2016a)
SCWB = Strong-column-weak-beam ratio (AISC 2016a)

3.5.1 Lateral drift demand contributions

The deformation demands at the interior and exterior joints of the subsystems are examined. Figure 3.5 depicts the decomposed deflection contributions to the story drift ratios of specimens S_D and S_S at selected SDRs. In particular, the columns remain elastic, as intended, with minimal contribution to the SDR. At the interior joint of S_D and at 4% lateral drift demand (Figure 3.5a and b), the panel zone contribution to the story drift is around 35%. This is considerably higher than the panel zone contribution in the corresponding interior joint subassembly (see Figure 3.4c). The axial restraint in the subsystem delays the flexural strength degradation in the beams, thereby increasing the panel zone shear demand. At 6% drift amplitude, when beam local buckling becomes more evident and the inelastic deformations concentrate in the beam, the panel zone contribution to the story drift decreases to about 10%. While a similar behavior is observed in S_S (Figure 3.5c and d), the panel zone contribution to the story drift remains appreciable (~25%) at 6% drift amplitude. Flexural strength degradation in shallow beams is minimal as discussed in the following section. Notably, exterior joints exhibit a distinct asymmetric behavior. Therefore, the panel zone contribution to the story drift is dependent on the direction of lateral loading. Particularly, the demand on the panel zone is higher when the framing beam is subjected to sagging (Figure 3.5a and c) compared to hogging bending (Figure 3.5b and d). The reasons behind this asymmetric demand are investigated more thoroughly in the subsequent sections. Referring to Figure 3.5c, the exterior joint panel zone contribution to the 6% story drift is nearly 40% despite being designed with a resistance-to-demand ratio, $R_v/V_d = 1.9$ (R_v and V_d are defined in Table 3.1). Moreover, at large lateral drift demands (SDR $\geq$ 4%), the exterior joint panel zones deform in one loading direction although the lateral drift demand is symmetric as shown in Figure 3.5b and d. In order to offset this negative contribution of the panel zone, the beam contribution to the story drift at the exterior joints exceeds the imposed drift demand. The behavior is nearly identical at both exterior joints of the subsystems.

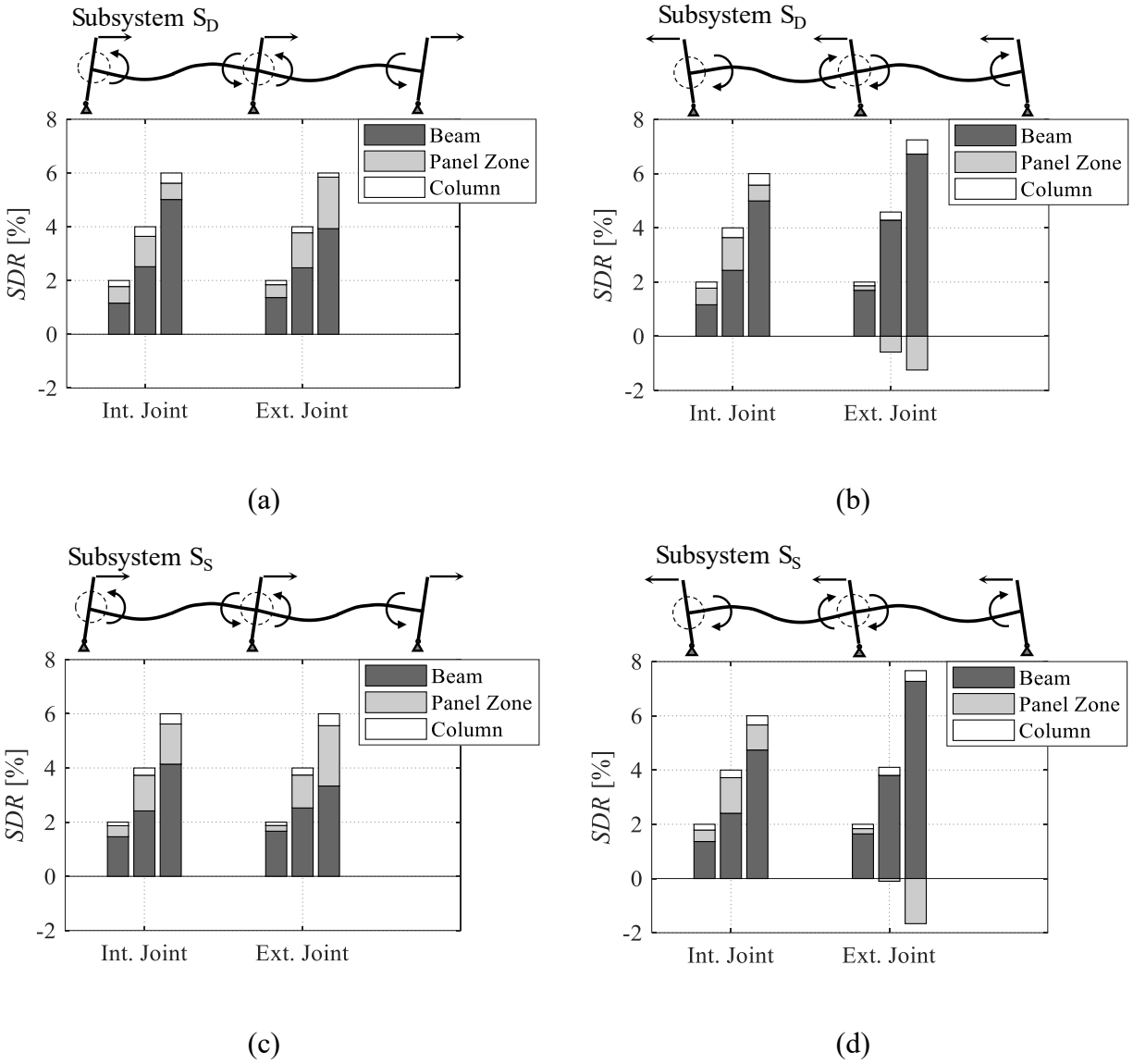

Figure 3.5 Component contribution to the story drift at the 2%, 4% and 6% cycles; (a) subsystem S_D loading in the east direction; (b) subsystem S_D loading in the west direction; (c) subsystem S_S loading in the east direction; (d) subsystem S_S loading in the west direction

3.5.2 Beam hysteretic response

Referring to Figure 3.6, the hysteretic response of the west beam is obtained for all three configurations and compared to that of the corresponding interior joint subassembly. For reference, $M_{b,West,C1}$ and $M_{b,West,C2}$ are the west beam moments at the face of columns C1, and C2, respectively. Referring to Figure 3.6a, the beam flexural strength degradation under sagging bending occurs at a fairly slow rate, even at 6% lateral drift demand, in the interior joint of subsystem S_D when compared to that of the corresponding subassembly. Table 3.2 shows that beams in the two-bay subsystems may experience up to 25% less flexural strength degradation, than those in subassemblies under symmetric-

cyclic lateral loading. This particularly applies to deep and slender beams that are prone to local buckling (Lignos and Krawinkler 2011). This behavior is attributed to the restraint provided by the floor slab and adjacent columns against the beam axial shortening, which results in the straightening of the beam local buckles. The straightening effect is more evident under sagging than hogging bending. Figure 3.6a shows that under hogging bending, the strength degradation is only slightly lower in the subsystem than in the subassembly. The beam hysteretic response at the interior joint of subsystems S_I and S_S shows minimal flexural strength degradation, similar to that of the corresponding subassemblies. The former has a low web slenderness ratio, $h_b/t_w = 31.3$, which delays the formation of web and flange local buckling at large inelastic cycles (Lignos and Krawinkler 2011). On the other hand, subsystem S_S consists of a shallow steel beam; as such, the slab contribution to the flexural resistance of the composite beam is higher than that in S_D and S_I. This results in a lower compressive stress in the top beam flange, thereby limiting local buckling under sagging bending.

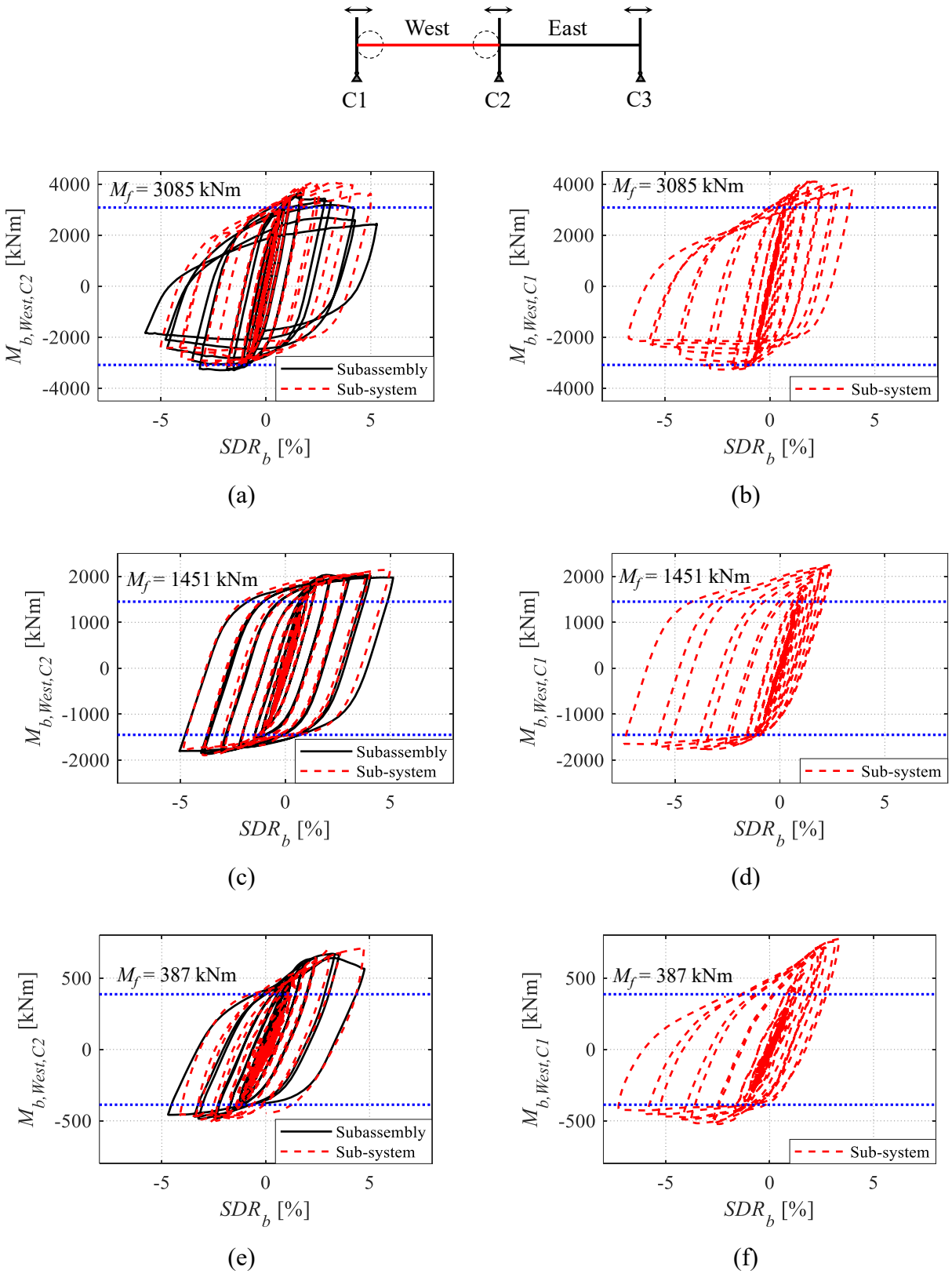

Figure 3.6 West beam hysteretic response - comparisons between subsystem and subassembly response: (a) W36x150, S_D interior joint; (b) W36x150, S_D exterior joint; (c) W21x122, S_I interior joint; (d) W21x22, S_I exterior joint; (e) W16x45, S_S interior Joint; and (f) W16x45, S_S exterior Joint

Table 3.2 Maximum west beam moment degradation at 6% SDR

		Sagging Bending		Hogging Bending	
		WI	WE	WI	WE
S_D	Subassembly	34%	NA	44%	NA
	Sub-system	12%	4%	23%	38%
S_I	Subassembly	3%	NA	6%	NA
	Sub-system	0%	0%	6%	6%
S_S	Subassembly	16%	NA	9%	NA
	Sub-system	0%	0%	10%	19%

Beam flexural strength degradation under hogging bending occurs as a result of the formation of large buckles in the bottom flange of the beam. In a subsystem, these buckles are straightened out during the sagging bending excursions due to the slab restraint against axial shortening. This agrees with earlier observations from physical testing of composite-steel MRFs (Cordova and Deierlein 2005). Furthermore, the beam and slab continuity at the interior joint augments this restraint (Cordova and Deierlein 2005; Herrera et al. 2008). Referring to Figure 3.7a and b, the buckled portions of the beam web and flanges experience notable straightening upon load reversal. As a result, pinching behavior, caused by an increase in the rotational stiffness of the composite beams, is observed in their hysteretic response (see Figure 3.6). The axial restraint induces additional tensile axial forces ($F_{a,W}^{\pm}$ and $F_{a,E}^{\pm}$) and moments ($M_{a,W}^{\pm}$ and $M_{a,E}^{\pm}$) in the beams. The latter are caused by non-uniform buckling along the beam depth. On the other hand, beams in cruciform subassemblies are free to shorten at their ends due to the simplified boundary conditions, resulting in an "accordion" effect due to the build-up of local buckles. Figure 3.7c and d suggest that, in a subassembly, beam flanges that buckled experience minor straightening upon load reversal. A comparison between Figure 3.7a and b and Figure 3.7c and d reveals that the extent of bottom flange local buckling is closely akin in subassemblies and subsystems. Hence, the rate of strength degradation under hogging bending is also expected to be cognate. This is not the case for sagging bending. First, the net tensile axial force acting on the beam is larger under sagging than hogging bending ($|F_{a,E/W}^{+} + F_{b,E/W}^{+}| > |F_{a,E/W}^{-} + F_{b,E/W}^{-}|$). Second, the additional moment induced by non-uniform buckling along the beam depth is lower under sagging than hogging bending ($|M_{a,E/W}^{+}| < |M_{a,E/W}^{-}|$) due to the restraint provided by the slab to the top flange of the beam. Third, the rate of stud degradation is lower in subsystems when compared to that of subassemblies. The composite action is maintained even at large lateral drift demands (SDR ≥ 4%), which alleviates the compressive force near the top flange and enhances it near the bottom flange.

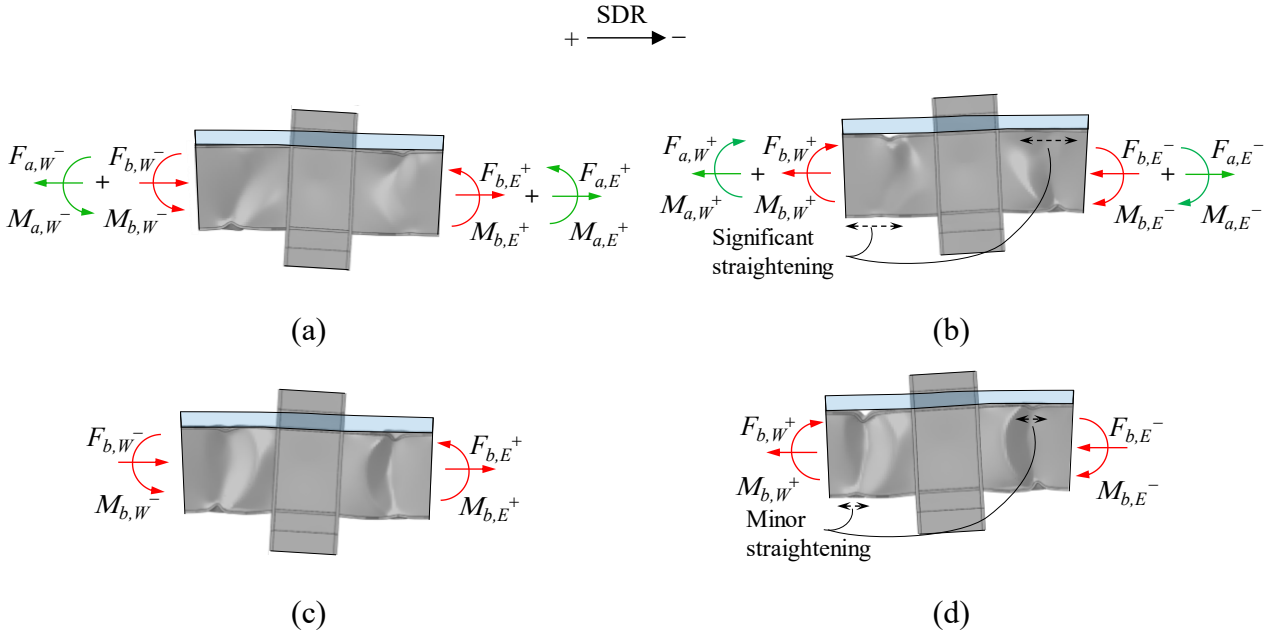

Figure 3.7 Straightening mechanism of the buckles in the steel beam upon load reversal: (a) subsystem, negative SDR; (b) subsystem, positive SDR; (c) subassembly, negative SDR; and (d) subassembly, positive SDR

Referring to Figure 3.6b, d and f, the beam hysteretic response at the exterior joint of subsystems is fully asymmetric despite the fact that the imposed loading history is symmetric. Particularly, the exterior joint beams experience flexural strength deterioration only under hogging bending. This behavior is a consequence of the asymmetric demand on the exterior column web panel zone. The mechanistic reason behind the observation above is explained in the next section.

Another consequence of the beam local buckling extenuation due to the slab restraint, is the underestimation of the probable maximum moment in the beam, M_f, calculated as per ANSI/AISC 358-16 (AISC 2016c). Figure 3.6 suggests that although M_f is predicted fairly well for the subassembly featuring deep beams, it is underestimated by about 25% in subsystem S_D. The delay in local buckling in the beams results in additional cyclic hardening that does not occur in the subassembly. Additionally, since the North American design practice typically employs deep beams with a low degree of composite action, the slab contribution to M_f is ignored according to ANSI/AISC 358-16 (AISC 2016c). Hence, the underestimation of M_f is larger in subsystems with shallower beams (S_I and S_S), where composite action is more pronounced. This issue is critical (a) for sizing columns to remain elastic based on the SCWB ratio; and (b) for estimating the panel zone shear demands. The implications of the latter are discussed in the next section.

3.5.3 Panel zone hysteretic response

The hysteretic response of the beam-to-column web panel zones is shown in Figure 3.8 for both the interior and exterior joints. Referring to Figure 3.8a, c and e, the interior joint panel zones of the subsystems experience more shear yielding than their subassembly counterparts. This is particularly true for specimens S_D and S_S in which higher moments are attained in the beams framing the joint. At 4% SDR, the shear distortion reaches $6\gamma_y$, $3.6\gamma_y$ and $5.7\gamma_y$ for specimens S_D, S_I and S_S, respectively (γ_y is the shear distortion at initial yielding as defined according to ANSI/AISC 341-16 (AISC 2016a)). At exterior joints, the column web panel zone hysteresis shows a distinct asymmetric response (see Figure 3.8b, d and f). The shear distortion in the exterior joint panel zones at 4% SDR reaches $7.3\gamma_y$, $8.5\gamma_y$ and $5.2\gamma_y$ for specimens S_D, S_I and S_S, respectively. Despite being designed for a maximum distortion of $4\gamma_y$ as per ANSI/AISC 341-16 (AISC 2016a), the composite action and axial restraint provided by the floor slab cause additional inelastic shear distortion. This is not expected to cause premature fracture in view of recent experimental findings (Shin and Engelhardt 2013). Interestingly, El Jisr et al. (2019) found that in composite beam-to-column connections, panel zones can develop a total shear distortion of $10\gamma_y$ without experiencing premature fracture within the beam-to-column connection at a 5% lateral drift demand. However, for tall buildings, the excessive distortion in the panel zones may become a concern when considering second-order effects. The panel zone shear resistance at a given inelastic shear distortion should be compared with the respective shear demand from the intersecting beams and columns to avoid the formation of soft story mechanisms that could increase the collapse risk due to P-delta effects.

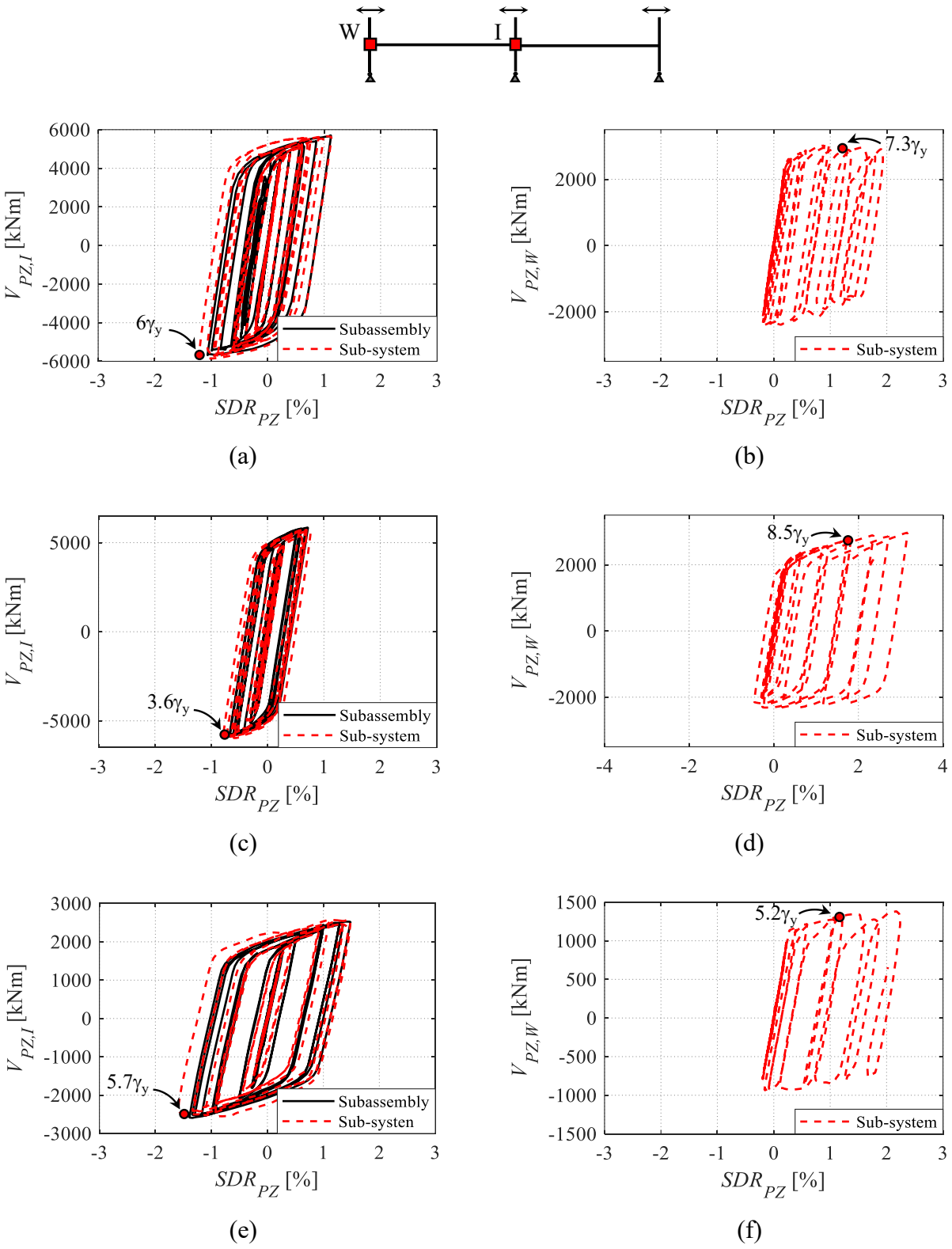

Figure 3.8 Panel zone hysteretic response - comparisons between subsystem and subassembly response: (a) S_D interior joint; (b) S_D exterior joint; (c) S_I interior joint; (d) S_I exterior joint; (e) S_S interior Joint; and (f) S_S exterior Joint

The asymmetry observed in the hysteretic response of the exterior column web panel zones is explained through the development of three mechanisms. The first two are related to the asymmetric

flexural demand in the beam framing the exterior joint. That is, the flexural demand in the beam is higher under sagging than under hogging bending.

Mechanism 1 is a direct consequence of the composite action in the beam. The sagging flexural resistance of the beam is enhanced (up to 80%) due to the composite action, while the hogging flexural resistance is also enhanced, but to a lesser degree (up to 40%) depending on the slab reinforcement (El Jisr et al. 2019). The factor α_1, shown in Figure 3.9, accounts for this enhancement: $\alpha_1^{\pm} = W_{pl,c}^{\pm}/W_{pl}$ and $\alpha_1^{+} > \alpha_1^{-} > 1.0$ ($W_{pl,c}^{\pm}$ is the plastic modulus of the composite section under sagging ($W_{pl,c}^{+}$) or hogging ($W_{pl,c}^{-}$) bending, and W_{pl} is the plastic modulus of the bare steel cross section with respect to its strong axis). Furthermore, the presence of the slab increases the depth of the region in the steel cross section subjected to compressive stresses under hogging bending and decreases it under sagging bending. Hence, flexural strength degradation is hastened under hogging excursions, and delayed under sagging excursions. The factor $\beta_1^{\pm}$ shown in Figure 3.9, accounts for the phenomenon associated with the delay of local buckling under sagging bending (β_1^{+}), and the progression of local buckling under hogging bending (β_1^{-}) in the composite beam: $\beta_1^{+} > 1.0 > \beta_1^{-} > 0$. Mechanism 1 is more prominent in shallow beams ($d_b \leq 500$ mm) where the effects of composite action are more pronounced compared to deep beams ($d_b \geq 700$ mm).

Mechanism 2 involves the restraint that the slab provides to the top flange of the beam. The slab restraint delays the formation of local buckles, and hence the flexural strength degradation of the beam under sagging loading excursions. The flexural strength of the beam increases due to strain-hardening. The factor α_2, shown in Figure 3.9a, accounts for the additional strain hardening in the beam due to the restraint provided by the slab on the top beam flange: $\alpha_2 > 1.0$ regardless of the beam depth. The extent of the slab restraint to the top flange is dependent on the orientation of the steel deck. Cordova and Deierlein (2005) reported a higher restraint when the steel deck is oriented parallel to the beam. However, this issue is outside the scope of the present chapter.

Mechanism 3 is caused by the axial restraint provided by the slab and the adjacent columns. This restraint induces a moment, as well as a net tensile force in the composite beam. The tensile force is non-uniform across the beam depth. That is, the axial force is comprised of a tensile force in the beam and a compressive force in the slab. Figure 3.9a and b show an idealization of the panel zone shear demand induced by the axial force in the composite beam. A force couple is assumed to act on the top and bottom locations of the panel zone. The factor $\gamma^{\pm} > 0$ represents the fraction of the composite beam axial force, N_b, acting in compression on the top beam flange under sagging (γ^{+}) and hogging (γ^{-}) bending respectively. Accordingly, the axial force increases the shear demand on the panel zone

for sagging excursions by $\gamma^+ N_b^+$ (see Eq. (3.1) and decreases it for hogging excursions by $\gamma^- N_b^-$ (see Eq. (3.2)). The shear demand on the panel zone under hogging bending is further reduced as the bottom flange buckles and the moment $M_{b,max}^-$ (see Figure 3.9b) decreases. Note that the $d_{eff}^{\pm}$ defined in Figure 3.9, is the effective depth of the panel zone as per the recommendations of Kim and Engelhardt (2002). Under hogging bending, d_{eff}^- is equal to the distance between the centroid of the beam flanges, whereas under sagging bending, d_{eff}^+ is equal to the distance between the centroid of the concrete section and that of the beam bottom flange. Mechanism 3 is prevalent in beams that develop a large axial force due to the axial restraint. Typically, these are deep beams ($d_b \geq 700$ mm) with a low degree of composite action ($\eta < 50\%$) as will be explained in the following sections.

$$V_{PZ}^+ = M_{b,max}^+ / d_{eff}^+ - V_T^+ + \gamma^+ N_b^+ \tag{3.1}$$

$$V_{PZ}^- = M_{b,max}^- / d_{eff}^- - V_T^- - \gamma^- N_b^- \tag{3.2}$$

Mechanisms 1 and 2 appear to be the most dominant. This is based on findings from past experiments on T-section subassemblies with composite floor slabs (Kim and Lee 2017; Yamada et al. 2009). The tests showed a distinct ratcheting response in the web panel zones despite the absence of axial restraint on the beam end. However, further studies should be conducted to quantify the relative importance of each mechanism on the panel zone demand.

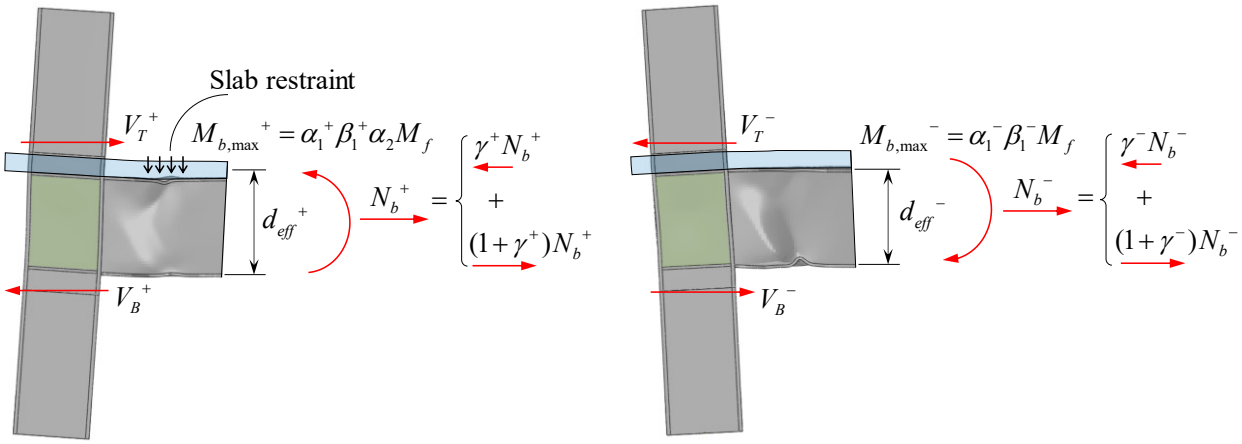

(a) (b)

Figure 3.9 Shear demand on the exterior column web panel zone under (a) sagging; (b) hogging excursions

3.5.4 Beam axial shortening

The phenomenon of beam axial shortening has been observed in subassembly tests in which the steel beams are free to move axially at their ends (Civjan et al. 2001; FEMA 2000a; MacRae et al. 2013; Qi et al. 2018). Axial shortening occurs as local buckling builds up in the plastic hinge region (Cordova and Deierlein 2005). However, in an actual building, the axial restraint provided by the composite slab and adjacent columns is likely to limit this shortening. This is particularly true at interior joints where the slab is continuous, and for composite slabs with the deck ribs placed parallel to the steel girder (Civjan et al. 2001; Cordova and Deierlein 2005). Accordingly, the over-simplified subassembly boundary conditions may lead to overestimation of the extent of a beam's local buckling and subsequent axial shortening.

Figure 3.10a shows the definition of beam axial shortening, δ_x, within a steel MRF bay. Referring to Figure 3.10b, subassembly S_D beam experiences an excessive axial shortening of 50 mm at 6% SDR. Top and bottom flange buckling mostly accumulate after 3% SDR, which leads to a rapid progression of axial shortening. Figure 3.10c and d shows that subassembly S_I and S_S beams do not shorten as much (6 mm and 3 mm at 6% SDR respectively). The former comprises a W21x122 beam with a fairly low $h_b/t_w = 31.3$; the latter consists of a shallow beam ($d_b = 409$ mm) in which composite action is pronounced. In both specimens, the growth of local buckling across the beam depth is insignificant. Hence, axial shortening is minimal. Beams in subsystems shorten much less compared to their subassembly counterparts. For instance, subsystem S_D beam shortens by 7 mm at 6% SDR while subsystems S_I and S_S beams do not practically experience shortening. The axial restraint provided by the composite slab and the adjacent columns alleviates the local buckling in the anticipated dissipative zone of the steel beam.

Beams in subsystems S_D and S_I experience fairly minor elongation (up to 4 mm). MacRae et al. (2013) attributed this elongation to the difference in the positions of the neutral axes at the beam ends. Under sagging bending, the neutral axis moves upward toward the slab, whereas under hogging bending the neutral axis remains close to the beam centerline. This difference in neutral axis positions is particularly noticeable in shallow beams. As a result, net centerline elongation results from tension yielding at the beam center near the sagging end and compression yielding near the hogging end. Furthermore, the asymmetric shear distortion in the exterior joint panel zone exaggerates this net centerline elongation.

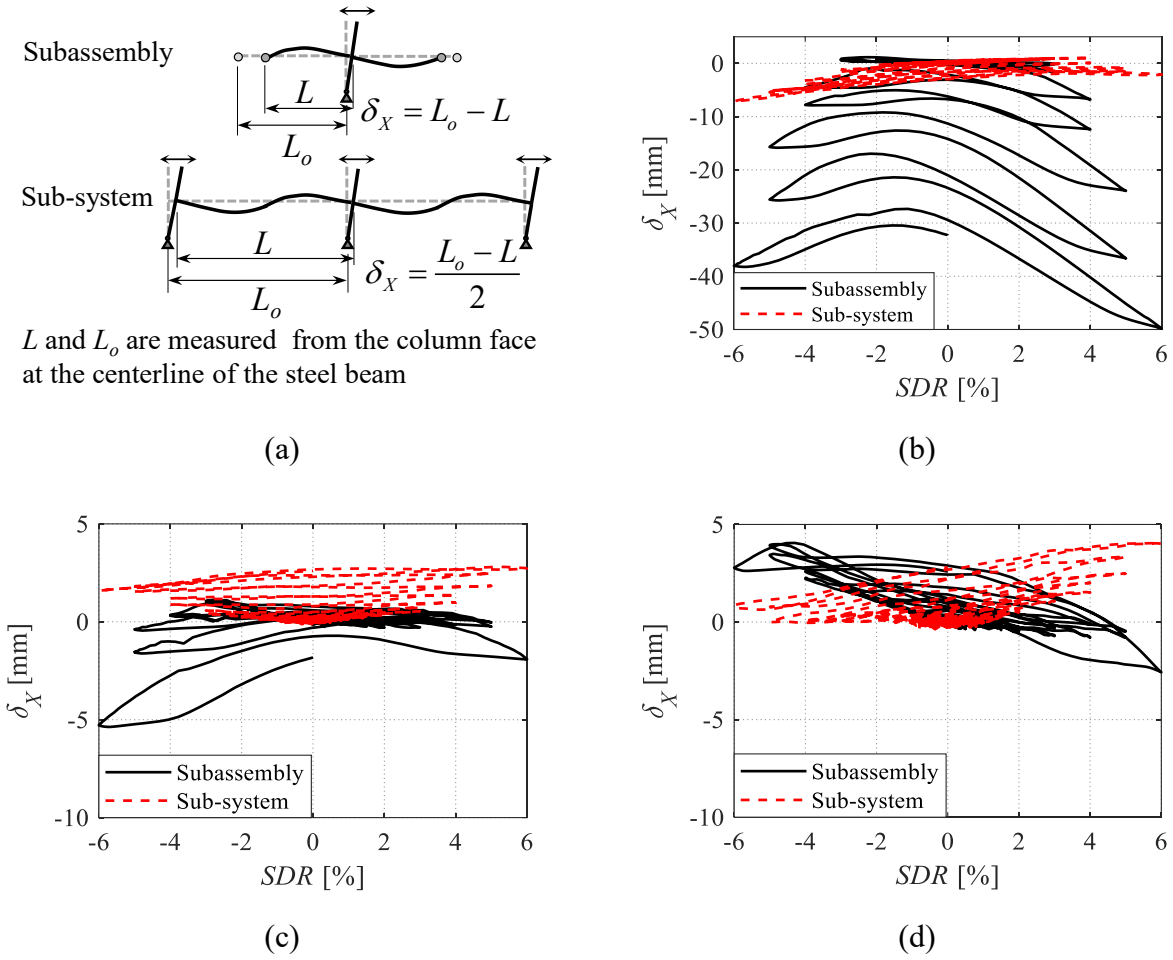

Figure 3.10 West beam axial shortening – comparisons between subsystem and subassembly response: (a) definition; (b) W36x150, S_D; (c) W21x122, S_I; and (d) W16x45, S_S

3.5.5 Beam axial force

Lateral loads are transferred to the column through the floor slab via two load paths (Cordova and Deierlein 2005; MacRae and Clifton 2015). The first one consists of direct bearing of the slab on the column face and a direct compression strut to the back of the column flange. The second load path involves the transfer of shear forces from the slab to the beam through friction and the shear studs. The resulting axial force in the beam is transferred to the column through the beam-to-column connection. In subassemblies, the beam axial force at the location of the assumed inflection points is zero, increasing to its maximum value at the column face. In subsystems, the axial restraint provided by the floor slab and columns causes an additional axial force in the beam. The magnitude of the beam axial force is not constant along the length of the beam and depends on the extent of the axial restraint. The beam axial force is higher near interior joints, where the axial restraint is higher, than near exterior joints. In subsystems, unlike subassemblies, the axial force at the beam inflection point location is not zero. Accordingly, the additional axial force resulting from the axial restraint in

subsystems is quantified at the inflection point. Since the subsystems were subjected to quasi-static loading, the axial force in the beams due to the inertia forces are not quantified herein.

Figure 3.11 shows the axial forces developed in the three subsystems at the west beam inflection point. At 4% SDR, the peak normalized tensile force ratio in the steel beam at the location of the inflection point N_s/N_{pl} ($N_{pl} = R_y F_{yb} A_g$ as defined in Figure 3.11a is 8%, 2% and 5% for subsystems S_D, S_I and S_S respectively. The tensile force ratio at 6% SDR is 16%, 8% and 9% for subsystems S_D, S_I and S_S respectively. These values are expected to be higher near the interior joint. EN 1998-1 (CEN 2004a) states that the bending-axial force interaction in the steel beams may be disregarded as long as $N_s/N_{pl} < 15\%$. The floor slab is restrained by the shear studs, friction at the beam-slab interface and the columns. As the steel beam attempts to shorten due to the spread of local buckling across its depth, a compressive force, N_c, is generated in the slab in conjunction with the tensile force in the steel beam. The compressive force is transferred through shear in the studs, friction, bearing of the slab on the column face and a direct compression strut. At large lateral drift demands (SDR $\geq$ 4%), the studs lose their shear capacity, and the last two load paths transfer the compressive force to the slab. This is particularly true for deep beams ($d_b \geq 700$ mm) with low degree of composite action ($\eta < 50\%$) as discussed in the next section.

The axial forces in the steel beam and slab are dependent on several parameters. These relate to the extent of beam axial shortening experienced in the absence of axial restraint, as well as the level of axial restraint. First and foremost, the magnitude of the tensile force in the steel beam is dependent on the susceptibility of the steel beam to local buckling across its depth. Since all three configurations studied herein are adequately braced laterally (see Table 3.1) and have nominally identical material properties, the difference in local buckling initiation in the beams is mostly governed by the beam's cross section geometry. Lignos and Krawinkler (2011) found that h_b/t_w, in particular, largely influences local buckling initiation in intermediate to deep steel beams. The maximum N_s/N_{pl} ratio increases with increasing h_b/t_w (see Table 3.1). This is observed in Figure 3.11 where specimen S_D experiences the highest axial tensile force ratio.

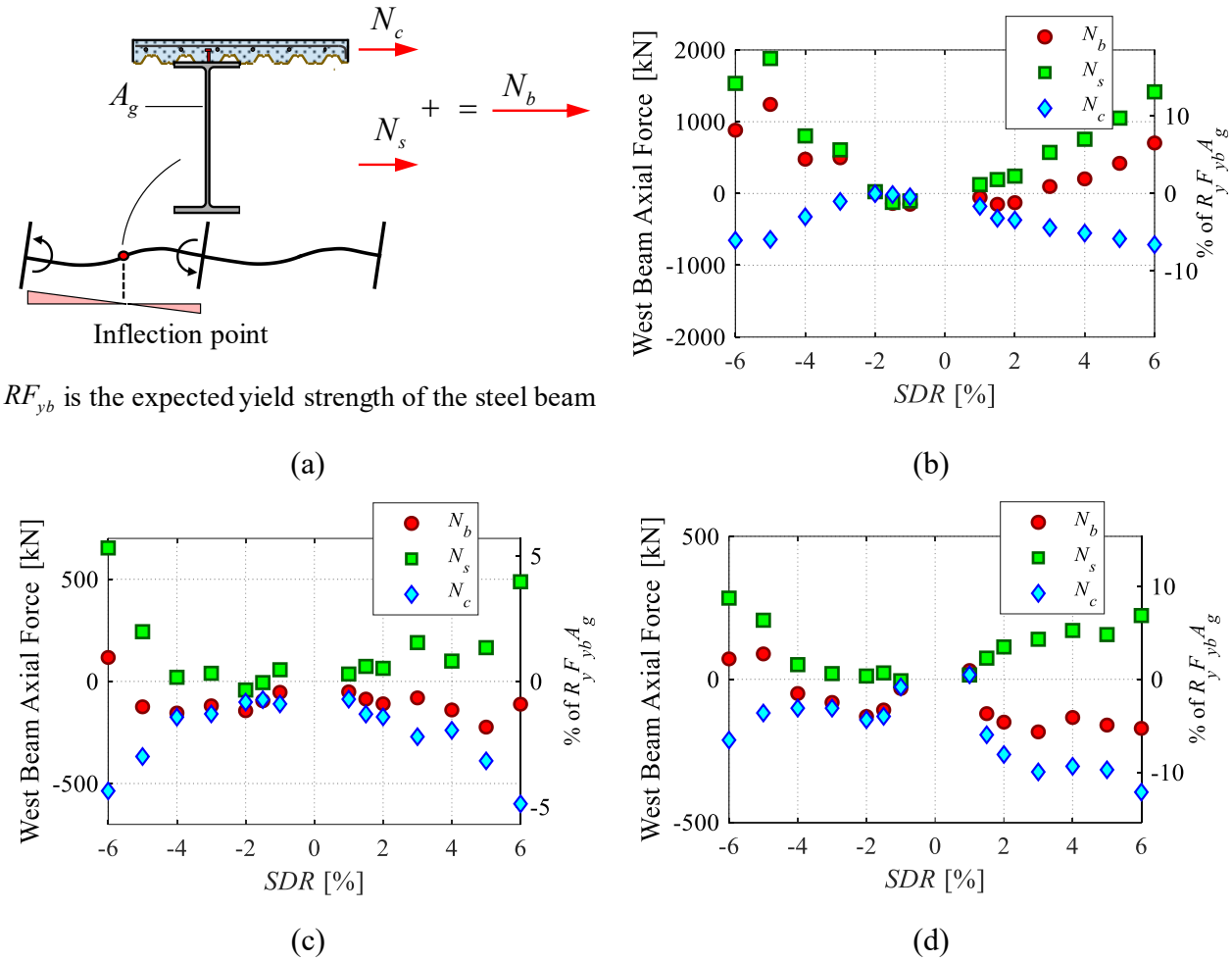

Figure 3.11 Slab restraint-induced axial forces in the west beam of the subsystems at peak story drifts: (a) definition; (b) W36x150, S_D; (c) W21x122, S_I; and (d) W16x45, S_S

Local buckling in shallow beams ($d_b \leq 500$ mm) is localized in the lower portion of the beam due to the slab restraint on the top flange of the beam. This is also true for beams with high degree of composite action ($\eta > 80\%$). Moreover, in the above cases, a compatibility compressive force occurs when the beam ends are pushed apart (see previous section). The compressive force alleviates the tensile force in the beam. Axial restraint is provided by the slab and the columns. In shallow beams, the axial restraint provided by the slab is relatively higher than that in deep beams. This is because the relative slab in-plane stiffness-to-beam axial stiffness is higher in shallow beams than in deep beams. On the other hand, the axial restraint provided by the columns is dependent on their flexural stiffness. Since columns sizes are strongly influenced by the SCWB ratio, the flexural stiffness of the columns normally increases with the beam depth. Therefore, the axial restraint provided by the columns is expected to be high in deep beams. As mentioned earlier, the level of axial restraint is higher at the interior joint than at the exterior joint due to (i) slab continuity and (ii) potentially stiffer columns at the interior joints. In the configurations considered in this chapter, the same column cross

sections are used at the interior and exterior joints. Thus, we postulate that the difference in the axial restraint should not be substantial. The magnitude of the axial force in the beam also depends on its axial stiffness. However, for equal depth beams, a larger axial stiffness implies a stockier section with a lower susceptibility to local buckling. Based on the above, the major factor that determines the magnitude of N_s/N_{pl} is the susceptibility of the beam to local buckling across its depth. The main controlling parameters in the examined cases are the beam depth, d_b and the web local slenderness ratio, h_b/t_w.

3.5.6 Shear stud hysteretic response

Seismic loads are transferred from the slab into the beam through shear in the stud connectors and friction at the beam-slab interface. In composite beams with shear studs as the weak link, early loss of composite action is likely to occur as a result of shear stud failure (Cordova and Deierlein 2005). Consequently, seismic loads are predominantly transferred to the column by bearing of the slab on the column face and a direct compression strut. This can lead to severe damage in the slab due to concrete spalling. Damage in the slab can be reduced if the integrity of the shear studs is maintained. From a design perspective, the shear studs at the slab-beam interface should sustain their load-carrying capacity. To this end, both ANSI/AISC 341-16 (AISC 2016a) and EN 1998-1 (CEN 2004a) recommend a 25% reduction in the design shear resistance of the studs. However, past studies have shown that the performance of shear studs in composite steel MRFs is better than anticipated (Cordova and Deierlein 2005). An assessment of the stud degradation behavior is performed by obtaining the hysteretic stud shear-stud slip response in each of the composite beam specimens subjected to cyclic loading.

Figure 3.12 shows the hysteretic response of the west beam shear stud nearest to the interior joint. The shear studs in subassemblies S_D, S_I and S_S, lose their load carrying capacity in sagging bending at 4%, 5% and 6% SDR respectively. At 4% lateral drift demands, the studs belonging to subassemblies S_I and S_S exhibit satisfactory behavior with little or no degradation, whereas that of specimen S_D fails. This is despite the fact that all three specimens have the same slab configuration, and degree of composite action; hence, the same number of shear studs according to EN 1994-1-1 (CEN 2004b). The deeper the beam is, the higher the shear demand; hence, the more degradation in the shear studs connecting the beam to the slab. In subsystems, the stud shear force degradation is lower than that in the corresponding subassembly. Referring to Figure 3.12b, the shear stud in subsystem S_D loses its capacity at 5% SDR compared to 4% in the subassembly. Similarly, Figure 3.12c and d depict that

the shear studs of subsystem S_I and S_S remain intact at the end of the analysis. In subassemblies, noticeable axial shortening in the beams tends to pry the beam away from the slab. Consequently, the shear studs that restrain the beam against axial shortening are subjected to an additional shear demand. The additional demand increases the stud shear force in the sagging bending regions and reduces it in the hogging bending regions. A higher rate of strength degradation is observed in studs belonging to subassemblies when compared to those in subsystems. Initially, the hysteretic behavior of the shear studs coincides as shown in Figure 3.12. Once beam axial shortening initiates, a discrepancy in the behavior of the shear studs is observed.

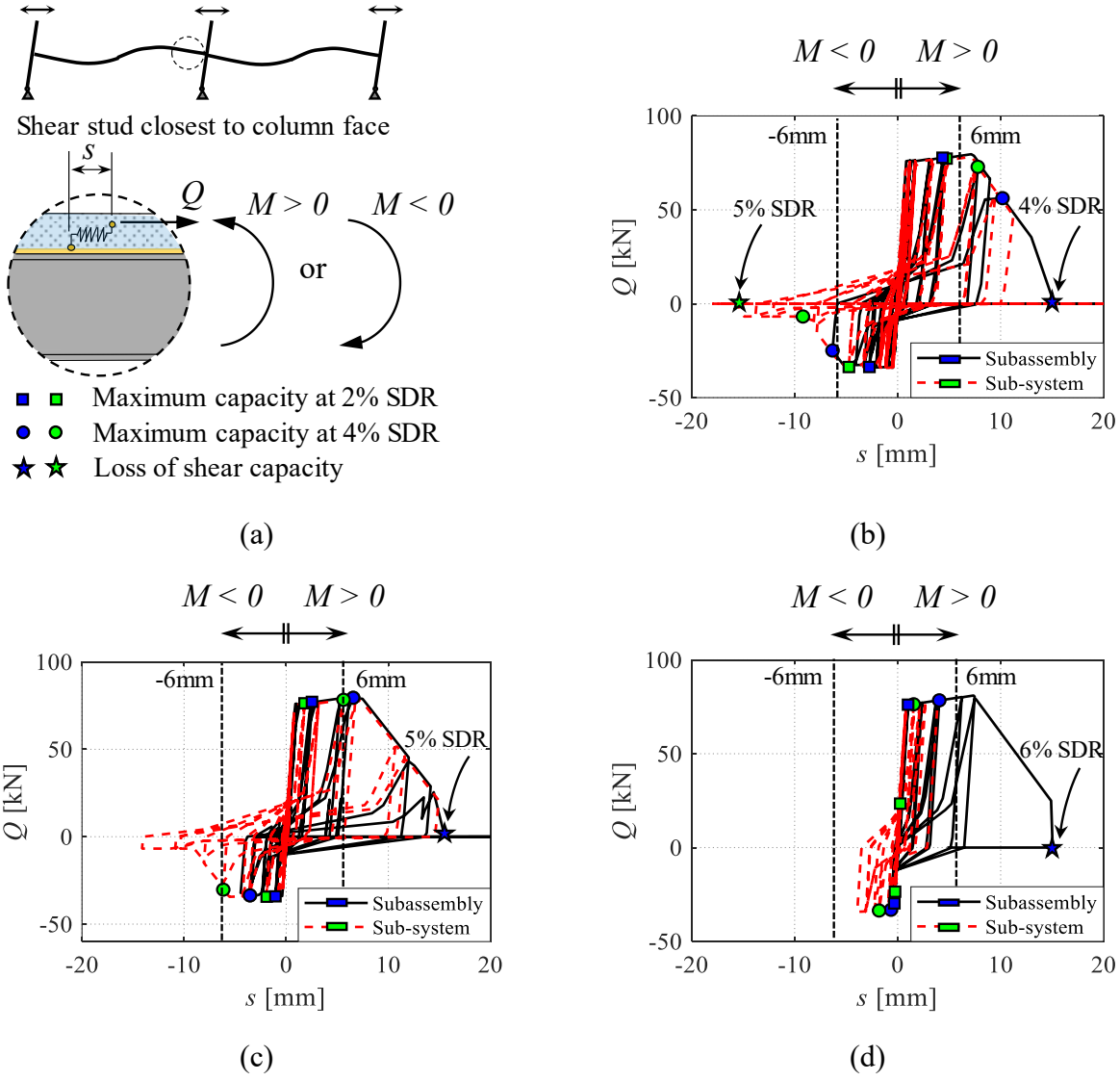

Figure 3.12 West beam shear stud hysteretic response – comparisons between subsystem and subassembly response: (a) definition; (b) W36x150, S_D; (c) W21x122, S_I; and (d) W16x45, S_S

In EN 1994-1-1 (CEN 2004b), ductile shear connectors are defined as the ones with a characteristic deformation capacity, $\delta_{uk} = 6$ mm at 90% of the ultimate shear resistance (Bärtschi 2005). Hence,

the headed shear studs, with which the non-linear springs are calibrated, are ductile as per EN 1994-1-1 (CEN 2004b). The maximum stud slip demands at 4% SDR are 1 mm, 8 mm and 2 mm for subsystems S_D, S_I and S_S respectively. Out of the three subsystems, only the stud slip demand in S_S, does not exceed the characteristic deformation capacity of ductile shear connectors. However, the stud slip in all cases is within 6 mm (4 mm, 2 mm at 1 mm for S_D, S_I and S_S respectively) at modest lateral drift demands (i.e., 2%) characteristic of a design-basis earthquake corresponding to a probability of exceedance of 10% in 50 years. Additionally, a higher degree of composite action would decrease the shear demand on the studs. Vis-à-vis the above discussion, the general consensus is that for shallow to intermediate composite beams ($d_b \leq 500$ mm) no reduction in the shear resistance of studs is imperative as long as ductile shear studs are used. For deeper beams, a reduction in the shear resistance of studs is deemed reasonable.

3.5.7 Influence of loading protocol

In the previous sections, the hysteretic behavior of the 2-bay subsystems was examined under a symmetric cyclic lateral-loading protocol. However, this protocol overestimates the seismic demand in the frame and subsequently the cyclic deterioration of the beams (FEMA 2009), if limit states associated with structural collapse are of interest. In that respect, collapse-consistent protocols (Krawinkler 2009; Maison and Speicher 2016; Suzuki and Lignos 2019) are more realistic for estimating seismic demands in structural components at limit states associated with earthquake-induced collapse (Lignos et al. 2011). In order to further comprehend the differences in the hysteretic behavior of subsystems subjected to symmetric cyclic and collapse-consistent protocols, subsystem S_D is subjected to a collapse consistent-loading protocol derived according to Suzuki and Lignos (2019) (see Figure 3.13). The protocol consists of three phases and represents a near-fault ground motion with a low probability of occurrence. Each phase includes a few inelastic cycles followed by a large monotonic push. The asymmetric drift demand replicates the characteristic "ratcheting" behavior of frame structures prior to collapse (Lignos et al. 2011).

Referring to Figure 3.14a, at 5% SDR, the west beam hogging moment ($M_{b,West,C2}$ at the face of column C2) degrades by less than 5% under the collapse-consistent protocol. On the other hand, the beam's flexural strength degradation is more than 20% under the symmetric cyclic loading protocol. Due to ratcheting of the frame, no degradation in the sagging moment occurs. Local buckling is minor and is localized in the lower portion of the steel beam. This explains the marginally lesser amount of axial shortening (4 mm) experienced in the west beam under the collapse-consistent protocol

compared to the symmetric cyclic protocol (7 mm) as depicted in Figure 3.14c. The beam experiences greater cyclic degradation under the symmetric cyclic loading protocol than the collapse-consistent loading protocol due to the larger number of inelastic cycles in the former. This agrees with prior observations from large- and full-scale physical testing (Elkady and Lignos 2018b; Suzuki and Lignos 2015). Figure 3.14b shows that the peak panel zone shear distortion is higher under the collapse-consistent protocol ($10\gamma_y$) than that observed under the symmetric cyclic protocol ($6\gamma_y$). The ratcheting response is mostly attributed to the asymmetric drift demand. Finally, the hysteretic behavior of the west shear stud nearest to the interior joint is compared in Figure 3.14d. The stud loss of shear resistance occurs at 5% SDR, regardless of the employed lateral loading protocol. Prior to 5% SDR, the seismic shear demand in the studs is similar under both loading conditions. Furthermore, since the shear strength degradation due to cyclic loading is not significant (see Figure 3.2), the rate of degradation is nearly the same in both cases.

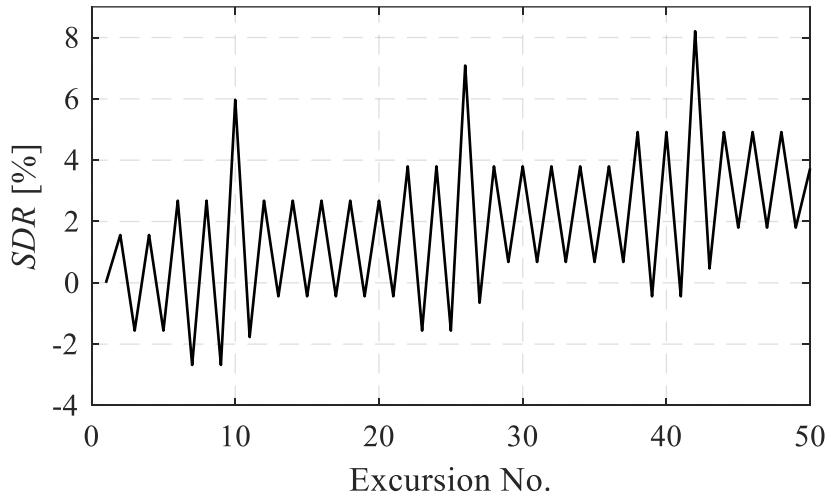

Figure 3.13 Collapse-consistent loading protocol (Suzuki and Lignos 2019)

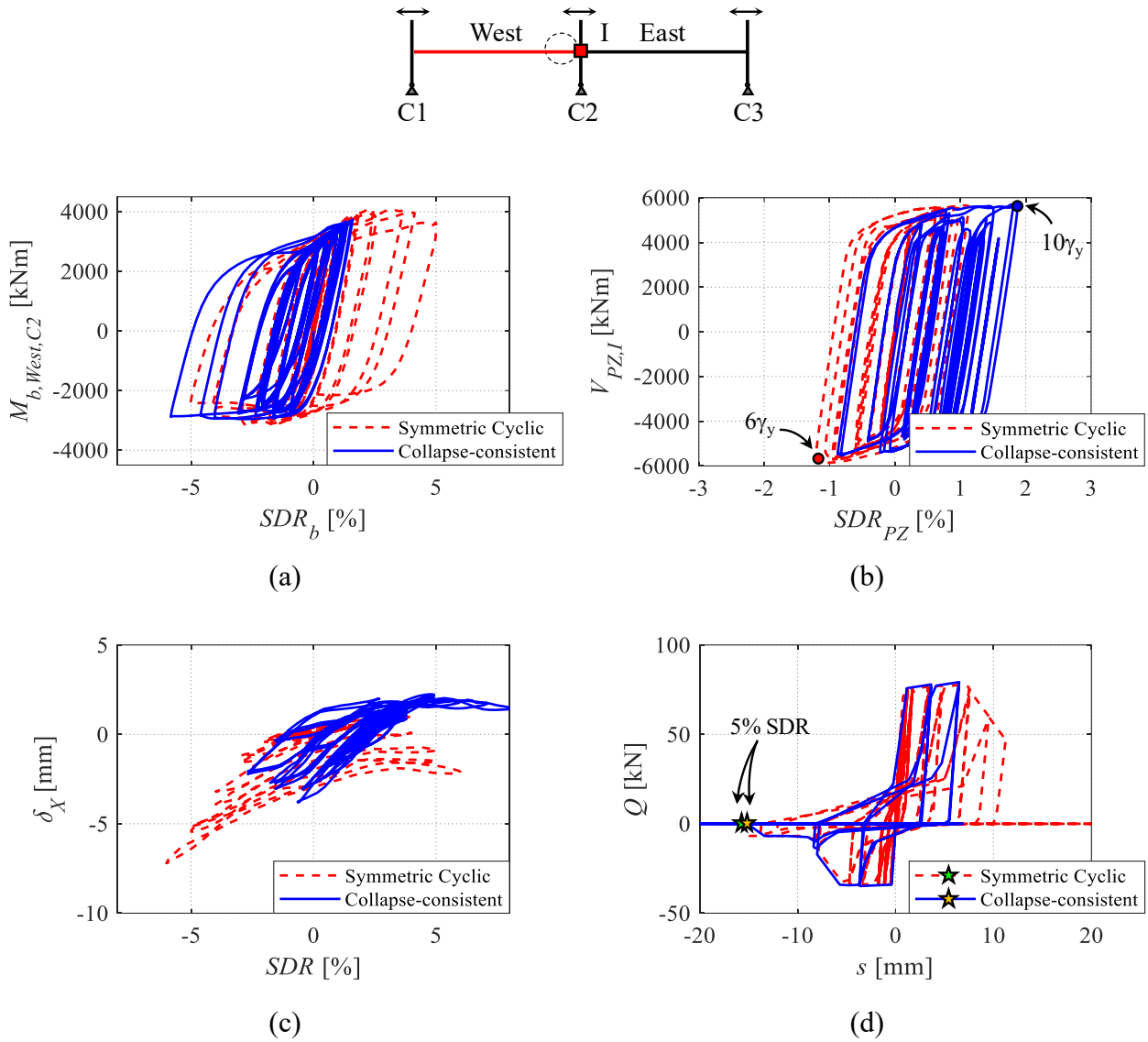

Figure 3.14 Sub-system S_D hysteretic response: comparisons between symmetric cyclic and collapse-consistent loading protocols: (a) west beam hysteretic response; (b) panel zone hysteretic response; (c) west beam axial shortening; and (d) shear stud hysteretic response

3.6 Limitations and assumptions

Considering the modeling assumptions and simplifications discussed herein, it is worth highlighting the following limitations: (i) the CFE model is not capable of capturing fracture in the beam-to-column connection and ductile tearing due to extensive local buckling; (ii) bond slip between the reinforcement and concrete is not modeled explicitly; (iii) no separation is allowed between the concrete slab and the steel deck; and (iv) concrete spalling due to crushing is not explicitly considered. Despite these shortcomings, the modeling approach is deemed capable of simulating the physical mechanisms associated with the slab restraint and the overall cyclic behavior of connections in subsystems and subassemblies.

3.7 Conclusions

This chapter investigates the effects of the axial restraint provided by the slab and the columns (frame continuity) on the hysteretic behavior of typical beam-to-column connections with a composite floor slab. First, a detailed continuum finite element (CFE) model is proposed and validated with available experimental data. The CFE model explicitly captures the interaction between the slab and the beam, as well as the cyclic degradation of the shear stud connectors. Next, the CFE approach is extended to model two-bay subsystems with three different beam depths representative of both North American and European design practice. The effects of the axial restraint and framing action are examined by comparing the behavior of subsystems with that of the corresponding subassemblies. The major findings are summarized below:

- Qualitatively, the panel zone contribution to the story drift is higher in the subsystem interior joints than in the corresponding cruciform subassembly joints. This is attributed to the lower rate of the beams' flexural strength degradation. In the subsystem exterior joints, the panel zone contribution to the story drift is dependent on the direction of loading: under sagging excursions, the panel zone contribution to the story drift may reach up to 40%, despite the panel zone design compliance to the ANSI/AISC-341-16 seismic provisions (AISC 2016a). On the other hand, under hogging bending, the beam deformation dominates the lateral drift demand.

- Under symmetric-cyclic lateral loading, beams in two-bay subsystems may experience up to 25% less flexural strength degradation than their subassembly counterparts. This is particularly evident in deep and slender beams. In subsystems, the local buckles in the beams are straightened due to the axial restraint provided by the floor slab and the columns. It is observed that the straightening is more prominent under sagging bending than hogging bending. This leads to the underestimation of the probable maximum moment M_f (by up to 25%), even in deep beams where the flexural strength amplification due to composite action is fairly small. This issue may be compelling for sizing columns and estimating the shear demand in panel zones of capacity-designed steel MRFs.

- The interior joint panel zones in subsystems experience up to 15% higher shear distortion than their subassembly counterparts. Their hysteretic behavior is symmetric. On the other hand, exterior joint panel zones in subsystems exhibit a distinct asymmetric response due to the different shear demands under sagging and hogging bending. The difference in shear demands is attributed to three underlying mechanisms namely: (i) composite action, (ii) the slab restraint against top flange local buckling; and (iii) the axial restraint provided by the slab and the columns. The CFE

analysis reveals that panel zones in subsystems may experience a shear distortion higher than the anticipated value for which they were designed (i.e., $4\gamma_y$). Nonetheless, premature fracture due to panel zone shear distortion is not expected as the maximum shear distortion is lower than $10\gamma_y$.

- Subassembly beams may experience severe axial shortening (up to 50 mm at 6% SDR). The degree of axial shortening is higher in deep beams with high web slenderness ratios close to the current compactness limits of highly ductile members according to the ANSI/AISC 341-16 seismic provisions (AISC 2016a). On the other hand, beam axial shortening observed in subsystems is considerably less (up to 7 mm at 6% SDR) than that observed in subassemblies (up to 50 mm at 6% SDR). It is inferred that axial shortening is overestimated in subassembly experiments commonly used in experimental earthquake engineering. In real buildings, beam axial shortening is much lower, akin to that in subsystems.

- Axial forces develop in composite beams as a consequence of the axial restraint. At the inflection point, the axial tensile force in the steel beam's cross section may reach slightly higher than 15%N_{pl} at 6% SDR. The tensile force magnitude is dependent on the susceptibility of the beam to local buckling across its depth, as well as on the level of axial restraint. The former is particularly high in deep and slender beams ($d_b \geq 700$ mm) with low degree of composite action ($\eta < 50\%$). The latter depends on the relative in-plane slab-to-beam axial stiffness (higher in shallow beams) and the flexural stiffness of the columns (higher in deep beam subsystems). This issue should be examined in conjunction with the catenary action imposed to the steel girders of a beam-to-column connection due to column axial shortening (Elkady and Lignos 2018b; Suzuki and Lignos 2015).

- Comparisons between the hysteretic behavior of shear studs in subsystems and subassemblies suggest that the shear force degradation in the latter is higher than that of the former. This is due to axial shortening in the beam that tends to pry the beam away from the slab. The CFE models indicate that higher stud shear force degradation occurs in subsystems with deep beams than in those with intermediate to shallow beams. However, at 2% lateral drift demands associated with a design-basis earthquake, the stud slip demand remains within the characteristic deformation capacity of ductile shear connectors (6 mm) according to EN 1994-1-1 (CEN 2004b). At 4% lateral drift demand, the slip demand exceeded 6 mm in all but the subsystem with shallow beams. For shallow beams or beams with high degree of composite action (i.e., above 80%), it seems reasonable to omit the 25% reduction in shear strength of the studs required in both ANSI/AISC 341-16 (AISC 2016a) and EN 1998-1 (CEN 2004a).

- The response of subsystems under collapse-consistent lateral load protocols suggests that beam flexural strength deterioration and axial shortening is inconsequential compared to that under a symmetric loading history. Conversely, the panel zone shear distortion may reach $10\gamma_y$ in exterior joints. The shear stud hysteretic behavior does not seem to be influenced by the employed loading history.

3.8 Notation

The following symbols are used in this chapter:

A_g	=	cross-sectional area of the steel beam
D^-	=	rate of cyclic deterioration of the shear stud when the slab is under tension
D^+	=	rate of cyclic deterioration of the shear stud when the slab is under compression
d_b	=	depth of the steel beam
d_{eff}^-	=	effective depth of the column web panel zone for framing beam under hogging bending
d_{eff}^+	=	effective depth of the column web panel zone for framing beam under sagging bending
$F_{a,E}^-$	=	tensile force in the steel beam east of the interior column due to axial restraint (hogging bending)
$F_{a,E}^+$	=	tensile force in the steel beam east of the interior column due to axial restraint (sagging bending)
$F_{a,W}^-$	=	tensile force in the steel beam west of the interior column due to axial restraint (hogging bending)
$F_{a,W}^+$	=	tensile force in the steel beam west of the interior column due to axial restraint (sagging bending)
$F_{b,E}^-$	=	tensile force in the steel beam east of the interior column due to composite action (hogging bending)
$F_{b,E}^+$	=	tensile force in the steel beam east of the interior column due to composite action (sagging bending)
$F_{b,W}^-$	=	tensile force in the steel beam west of the interior column due to composite action (hogging bending)
$F_{b,W}^+$	=	tensile force in the steel beam west of the interior column due to composite action (sagging bending)

F_{yb} = specified minimum yield stress of steel

f_c' = compressive strength of concrete

f_t = tensile strength of concrete

H = height of the column

h_b = fillet-to-fillet web depth of the beam

L = span length of the beam

L_b = maximum laterally unbraced length of the beam

L_o = shear span of the beam

$M_{a.E}^-$ = moment in the steel beam east of the interior column due to axial restraint (hogging bending)

$M_{a.E}^+$ = moment in the steel beam east of the interior column due to axial restraint (sagging bending)

$M_{a.W}^-$ = moment in the steel beam west of the interior column due to axial restraint (hogging bending)

$M_{a.W}^+$ = moment in the steel beam west of the interior column due to axial restraint (sagging bending)

M_b = beam moment at the column face

$M_{b,E}^-$ = moment in the steel beam east of the interior column due to composite action (hogging bending)

$M_{b,E}^+$ = moment in the steel beam east of the interior column due to composite action (sagging bending)

$M_{b,max}^-$ = maximum beam moment at the column face (hogging bending)

$M_{b,max}^+$ = maximum beam moment at the column face (sagging bending)

$M_{b,W}^-$ = moment in the steel beam west of the interior column due to composite action (hogging bending)

$M_{b,W}^+$ = moment in the steel beam west of the interior column due to composite action (sagging bending)

$M_{b,west,C1}$ = west moment in the composite beam at column C1 face

$M_{b,west,C2}$ = west moment in the composite beam at column C2 face

M_f = probable maximum beam moment at the column face as per ANSI/AISC 358-16 (AISC 2016c)

N_b^- = axial force in the composite beam due to axial restraint (hogging bending)

N_b^+ = axial force in the composite beam due to axial restraint (sagging bending)

N_c = compressive force in the slab due to axial restraint

N_{pl} = axial yield strength of the beam

N_s = tensile force in the steel beam due to axial restraint

Q = stud shear force

Q_u^- = ultimate strength of the shear stud when the slab is under tension

Q_u^+ = ultimate strength of the shear stud when the slab is under compression

Q_y^- = effective yield strength of the shear stud when the slab is under tension

Q_y^+ = effective yield strength of the shear stud when the slab is under compression

R_v = column web panel zone inelastic shear strength as per ANSI/AISC 360-16 (AISC 2016b)

R_y = ratio of the expected to the specified minimum yield stress of steel beam

r_y = radius of gyration of the beam about its weak axis (y-axis)

S_D = specimen with deep beams

SDR_b = beam contribution to story drift ratio

SDR_c = column contribution to story drift ratio

SDR_{PZ} = panel zone contribution to story drift ratio

S_I = specimen with beams of intermediate depth

S_S = specimen with shallow beams

s = stud slip

s_p^- = pre-capping slip capacity of shear stud when slab is under tension

s_p^+ = pre-capping slip capacity of shear stud when slab is under compression

s_{pc}^- = post-capping slip capacity of shear stud when slab is under tension

s_{pc}^+ = post-capping slip capacity of shear stud when slab is under compression

s_u^- = ultimate slip capacity of shear stud when slab is under tension

s_u^+ = ultimate slip capacity of shear stud when slab is under compression

t_d = thickness of doubler plate

t_{stable} = size of the stable time increment in explicit dynamic analysis

t_w = thickness of beam web

U_x = displacement degree of freedom in x-direction

U_y = displacement degree of freedom in y-direction

U_z = displacement degree of freedom in z-direction

V_B^- = shear force in the column below web panel zone (hogging bending)

V_B^+ = shear force in the column below web panel zone (sagging bending)

V_d = column web panel zone shear demand as per ANSI/AISC 341-16 (AISC 2016a)

V_{PZ} = column web panel zone shear demand

$V_{PZ,I}$ = interior column web panel zone shear demand

$V_{PZ,W}$ = west column web panel zone shear demand

V_T^- = shear force in the column above web panel zone (hogging bending)

V_T^+ = shear force in the column above web panel zone (sagging bending)

W_{pl} = plastic section modulus of the bare steel section about its strong axis

$W_{pl,c}^-$ = plastic section modulus of the composite beam section about its strong axis (hogging bending)

$W_{pl,c}^+$ = plastic section modulus of the composite beam section about its strong axis (sagging bending)

α_1^- = factor that accounts for the enhancement of beam flexural resistance due to composite action (hogging bending)

α_1^+ = factor that accounts for the enhancement of beam flexural resistance due to composite action (sagging bending)

α_2 = factor that accounts for the additional strain hardening due to slab restraint on the top beam flange (sagging bending)

β_1^- = factor that accounts for the progression of beam local buckling under hogging bending

β_1^+ = factor that accounts for the delay of beam local buckling under sagging bending

γ^- = factor that represents the fraction of N_b^- acting on the top flange of the beam

γ^+ = factor that represents the fraction of N_b^+ acting on the top flange of the beam

γ_y = shear distortion of the column web panel zone at initial yielding as per ANSI/AISC 341-16 (AISC 2016a)

δ_{uk} = characteristic deformation capacity of ductile shear studs as per EN 1994-1-1 (CEN 2004b)

δ_X = centerline axial shortening of the beam

η = degree of composite action as per ANSI/AISC 360-16 (AISC 2016b)

κ_d = parameter for the break point displacement due to pinching behavior in the stud

κ_f = parameter for the break point force due to pinching behavior in the stud

λ_k = parameter for stiffness deterioration of the shear stud under cyclic loading

λ_s = parameter for strength deterioration of the shear stud under cyclic loading

μ = steel-to-concrete coefficient of friction

ω_{max} = highest element eigenfrequency in the CFE model

Chapter 4 Fragility assessment of beam-slab connections for informing earthquake-induced repairs in composite-steel moment resisting frames

Bibilograpic details

This chapter presents the post-print version of the article with the following full bibliographic details: El Jisr, H., and Lignos, D. (2021). "Fragility assessment of beam-slab connections for informing earthquake-induced repairs in composite-steel moment resisting Frames." *Frontiers in Built Environment*, 7(1), DOI: https://doi.org/10.3389/fbuil.2021.691553

Authors' contribution

Hammad El Jisr derived the fragility functions, conducted the performance-based assessment of the composite-steel moment-resisting frame, created the figures, wrote the manuscript draft and revised the manuscript. Dimitrios Lignos contributed in developing the methodology presented in this chapter, supervising the work conducted by Hammad El Jisr, funding acquisition, and reviewing and editing the original and final manuscript drafts.

4.1 Abstract

Earthquake loss estimation in composite-steel moment resisting frames (MRFs) necessitates a proper estimation of the level of damage in steel beam-to-slab connections. These usually feature welded headed shear studs to ensure the composite action between the concrete slab and the steel beam. In partially composite steel beams, earthquake-induced damage in the shear studs and the surrounding concrete occurs due to shear stud slip demands. Within such a context, this chapter proposes shear slip-based fragility functions to estimate the probability of being or exceeding four damage states in steel beam-slab connections. These damage states include cracking and crushing of the concrete slab in the vicinity of the shear studs, as well as damage in the shear studs themselves. The developed fragility functions are obtained from a gathered dataset of 42 cyclic push-out tests. They incorporate uncertainty associated with specimen-to-specimen variability, along with epistemic uncertainty arising from the finite number of available experimental results. An application of the proposed fragility functions is conducted on a six-story building with composite-steel MRFs. It is shown that steel beam-slab connections along the building height only exhibit light cracking (i.e., crack sizes of 0.3 mm or less) at design basis seismic events. At seismic intensities associated with a low probability of occurrence seismic event (i.e., return period of 2475 years) the nonlinear building simulations suggest that the 25% reduction of the shear stud resistance in steel beam-slab connections with beam depths of 500 mm or less is not imperative to maintain the integrity of the shear stud connectors.

4.2 Introduction

In composite-steel moment-resisting frames (MRFs) seismic loads are transmitted to the MRF through bearing on the column flanges, friction and the shear stud connectors between steel beams and the concrete slab. Past experimental studies (e.g., Civjan et al., 2001; Ricles et al., 2004; Cheng and Chen, 2005) have demonstrated that structural damage in the steel beam-slab connection could lead to extensive cracking and crushing of concrete and even complete loss of composite action. Severe concrete spalling may also occur (Cordova and Deierlein 2005). Accordingly, in full and partial-composite steel MRFs it is essential to ensure that the integrity of the shear stud connectors is maintained during an earthquake. Current seismic provisions (AISC 2016a; CEN 2004a) impose a 25% reduction in the shear capacity of stud connectors in order to diminish the consequences associated with uncertainty in shear stud hysteretic behavior during earthquake shaking. While this reduction aims at preventing loss of composite action, there is no quantitative information regarding the

extent of potential earthquake-induced damage in the steel beam-slab connection to inform post-earthquake repair actions.

Advancements in performance-based seismic design within the framework established in the Pacific Earthquake Engineering Research Center (Cornell and Krawinkler 2000; FEMA 2012) necessitates the use of fragility functions to express damage in a probabilistic manner (Porter et al. 2007). For this purpose, several researchers have developed fragility functions for non-structural elements (Retamales et al. 2013; Ruiz-García and Negrete 2009; Taghavi and Miranda 2003) as well as steel and reinforced concrete members and their connections (Aslani and Miranda 2005; Elkady et al. 2018; Gardoni et al. 2002; Gulec et al. 2011; Lignos et al. 2010; Lignos and Karamanci 2013; Roeder et al. 2012). Similar efforts have been conducted for masonry infill walls (e.g., Cardone and Perrone 2015). As yet, no means for the estimation of damage in steel beam-slab connections exists. However, this would entail the consideration of local engineering demand parameter (EDP) indicators to relate with various damage states of the steel beam-slab connection. Recent advancements in building-specific loss estimation (Elkady et al. 2020) suggests that local EDPs may be key for reliable post-earthquake decisions regarding repairs of a building. However, the significant majority of available fragility functions in the literature (e.g., FEMA 2012) are usually expressed as a function of a story-based EDP, such as the story drift ratio (SDR).

The objective of this chapter is to develop fragility functions that permit the estimation of the level of damage in steel beam-slab connections in composite floor systems as a function of the imposed local slip demands on the headed shear stud connectors. This is achieved by assembling an experimental dataset of 42 cyclic push-out tests. Four sets of fragility functions for four different damage states seen in steel beam-slab connections are developed. The first set consists of all the assembled cyclic push-out tests, whereas the remaining ones account for the stress state (i.e. tension or compression) in the slab (Suzuki and Kimura 2019) as well as the slab type. Finally, the use of the proposed fragility functions to facilitate performance-based seismic design of buildings is demonstrated through an application to a six-story prototype building with composite-steel MRFs.

4.3 Definition of damage states

Beam-slab connections in composite-steel MRFs constitute welded headed shear stud connectors as well as the surrounding concrete in which the studs are embedded. Since damage at specific shear stud slip demands occurs in both components of the steel beam-slab connection, thereafter, these are

not separated in seismic assessment of steel beam-slab connections. Four discrete damage states (DS) of steel beam-slab connections are defined. Figure 4.1a depicts a schematic representation of a composite-steel beam-to-column connection along with the geometric characteristics of the shear stud and the concrete slab. The definition of damage states is based on a typical hysteretic response of steel beam-slab connections as shown in Figure 4.1b in terms of shear force, Q versus slip, Δ_s. Figure 4.1c to f depict schematically the observed state of a steel beam-slab connection at each DS. While in a typical cyclic push-out test, damage occurs at both sides of the headed stud connectors, for illustration purposes damage states are only shown for one loading direction.

4.3.1 DS1 light cracking

Light cracking corresponds to crack widths less than 0.3 mm (An and Cederwall 1996; Aslani and Miranda 2005) that initiate in highly stressed areas near the shear stud head and may propagate to the surface of the slab. Steel beam-slab connections with higher concrete strength can sustain larger slip values before light cracking becomes visible. These cracks do not affect the structural integrity of concrete and typically require either no or cosmetic repairs as shown in Figure 4.1c. Hence, the shear capacity of the steel beam-slab connection is maintained.

A decrease in the initial stiffness of the steel beam-slab connection occurs at DS1. Nevertheless, the change in initial stiffness cannot be accurately determined. Saari et al. (1999) found that appreciable deviation from the initial stiffness occurs at 50% of the ultimate shear strength of the studs. Accordingly, DS1 is deduced from the cyclic envelope at 50% of the ultimate shear strength of the steel beam-slab connection as shown in Figure 4.1b.

4.3.2 DS2 extended cracking / stud yielding and concrete crushing near the base of the shear studs

This damage state involves visible cracks with widths between 0.3 mm and 2 mm (Aslani and Miranda 2005) as well as stud yielding and crushing of concrete at the base of the shear studs. Both flexural (Bursi and Gramola 1999; Suzuki and Kimura 2019) and shear yielding of the studs (Zandonini and Bursi 2000) have been reported in past push-out tests. Civjan and Singh (2003) employed finite element analysis and found that the main contributors to the Von Mises stresses at the base of shear studs are normal stresses due to bending followed by shear stresses. Past monotonic push-out tests have shown that extended cracking is observed in the slab once the peak shear, Q_{max}, is reached

(e.g., Ollgaard et al., 1971; An and Cederwall, 1996). Herein, it is assumed that this behavior applies to cyclic push-out tests as well. Within such a context, DS2 corresponds to the slip demand at the peak shear capacity of the studs (see Figure 4.1b). Figures 4.1d and 4.2a illustrate the slab state at DS2. The latter shows the crack pattern, obtained using digital image correlation (DIC), from a recently conducted cyclic push-out test (El Jisr et al. 2021a). The measured crack widths were found to be greater than 0.3 mm.

The extent of steel beam-slab connection damage is influenced by the material properties of the shear stud connectors and the surrounding concrete. Depending on the concrete compressive strength and the ultimate tensile strength of the shear studs, their ultimate shear capacity may be governed by either (i) stud yielding; and/or (ii) concrete crushing at the stud base (Lam and El-Lobody 2005). The current design provisions (AISC 2016b; CEN 2004b) acknowledge this difference in the equations used to calculate the ultimate shear strength of a steel beam-slab connection. Generally speaking, for concrete compressive strength values of 20 to 40 MPa, stud yielding is dominant but a high compressive stress concentration at the base of the shear studs may result in some concrete crushing (Zandonini and Bursi 2000). Additionally, about 90% of the collected cyclic push-out tests were governed by stud yielding as per EN 1994-1-1 (CEN 2004b).

4.3.3 DS3 low-cycle fatigue microcracking in the shear studs / extensive cracking

This damage state corresponds to microcracking in the shear studs due to ultra-low-cycle fatigue (Civjan and Singh 2003; Zandonini and Bursi 2000). Unlike monotonic push-out tests in which the reduction in the shear strength of the steel beam-slab connection is mainly attributed to concrete crushing, ultra-low-cycle fatigue cracking in cyclic push-out tests results in rapid cyclic degradation of the connection's shear strength and stiffness. The quality of shear stud welds on the steel beam's top flange strongly influences DS3. Weld defects and/or out-of-straightness in the shear studs may result in early crack initiation at the tension side of the shear studs (Civjan and Singh 2003) as shown in Figure 4.1e. This is usually accompanied by extensive slab cracking as shown in Figure 4.2b.

Referring to Figure 4.1b, the slip at DS3 is derived from the first cycle envelope at 10% drop in peak shear capacity of the shear studs. This corresponds to the permissible characteristic slip capacity as per EN 1994-1-1 (CEN 2004b).

4.3.4 DS4 loss of shear load carrying capacity

The last damage state is associated with the loss of shear load carrying capacity of the steel beam-slab connection. According to Cordova and Deierlein (2005), loss of force transfer in the steel beam-slab connection is detrimental and could lead to other types of failure as the slab attempts to drag the inertia forces into the MRF. Damage state DS4 is characterized by shank failure and/or fracture at the weld-collar/shank interface (Zandonini and Bursi 2000) as schematically depicted in Figure 4.1f. Moreover, Figure 4.2c and d show typical examples of fracture at the weld-collar/shank interface in the steel beam-slab connection. Concrete cracking and crushing around the base of the shear studs are also prevalent (Civjan et al. 2001; Civjan and Singh 2003; Zandonini and Bursi 2000).

Zandonini and Bursi (2000) reported shear failures of the studs when their shear resistance reached 20% of their peak shear strength; hence, DS4 is deduced from the cyclic envelope curve at this shear strength level as shown in Figure 4.1b.

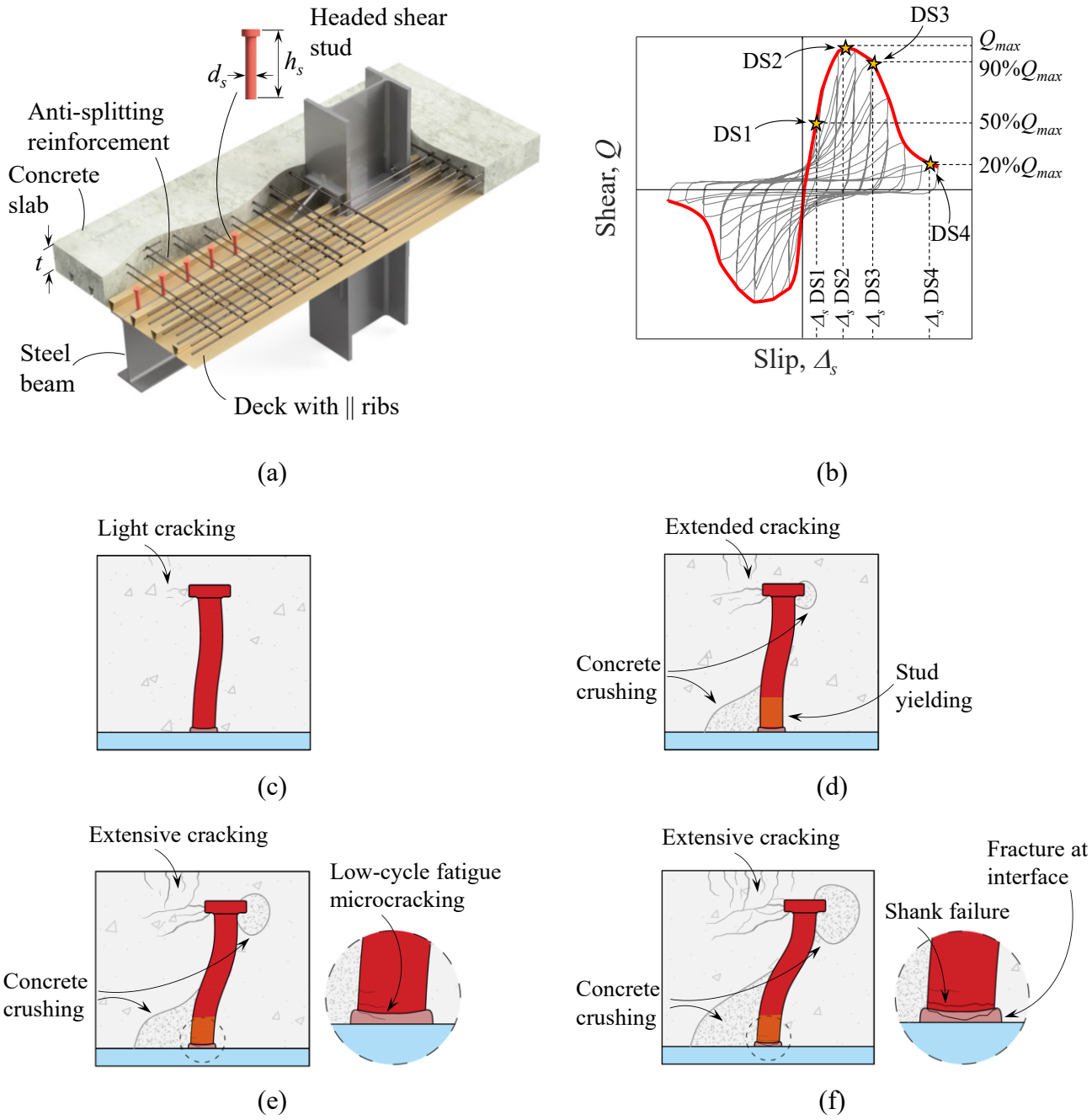

Figure 4.1 (a) Typical beam-slab connection in a composite steel MRF; (b) definition of damage states from a cyclic push-out test; schematic view of the four damage states considered for steel beam-slab connections: (c) DS1; (d) DS2; (e) DS3; and (f) DS4

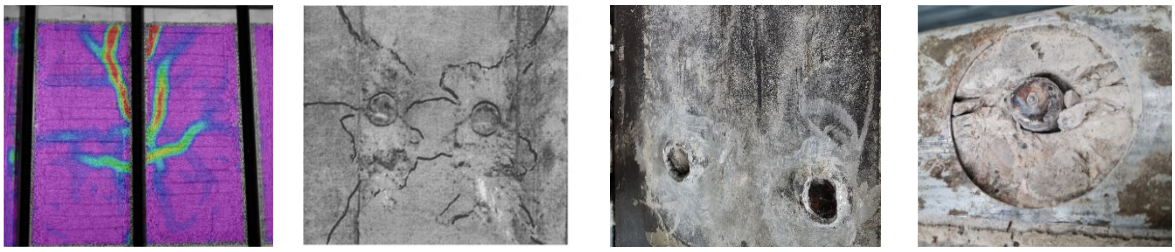

(a) (b) (c) (d)

Figure 4.2 Observed damage in cyclic push-out tests (a) DS2: Extended cracking in the slab measured using digital image correlation (DIC) (El Jisr et al. 2021a) (b) DS3: Extensive cracking in the slab (image from Zandonini and Bursi, (2000)); (c) DS4: Loss of shear load carrying capacity / fracture of weld collar (El Jisr et al. 2021a); and (d) DS4: Loss of shear load carrying capacity / shearing of headed studs (El Jisr et al. 2021a)

4.4 Description of dataset of cyclic push-out experiments

Data from past cyclic push-out tests are used to establish different sets of slip demands at which DS1 to DS4 occur. For this purpose, a dataset consisting of 42 symmetric cyclic push-out tests from 11 prior test programs (Aribert and Lachal 2000; Ciutina and Stratan 2008; Civjan and Singh 2003; Fan and Liu 2014; Hawkins and Mitchell 1984; Nakajima et al. 2003; Saari et al. 2004; Sun et al. 2019; Suzuki and Kimura 2019; Zandonini and Bursi 2000; Zhai et al. 2018) is assembled. Tests in which brittle failures of the shear studs occurred (e.g., rib shear or concrete pull-out failure) are not included as these are not deemed to be representative in capacity-designed composite steel MRFs. Unlike conventional push-out tests, thirteen specimens (Suzuki and Kimura 2019) accounted for the stress state (tensile or compressive) depending on the direction of the loading excursion. This was achieved with a customized test setup that featured two steel beams sandwiched between the slabs. The slip demand was applied by either pulling the two beams away from each other or by pushing them towards each other. This setup has the advantage of alternating the stress state in the slab between tension and compression depending on the loading direction. Accordingly, test specimens from Suzuki and Kimura (2019) provide a more realistic representation of the shear stud behavior in composite steel beams.

The assembled dataset features test specimens with various geometric and material properties. In brief, the dataset covers shear stud diameters between 13 mm and 22 mm, floor slab thicknesses between 102 mm and 300 mm, as well three different floor slab configurations. Particularly, (i) 29 tests with a solid slab (SS) with no steel deck; (ii) 12 tests with a slab with steel deck featuring ribs parallel (||) to the loading direction; and (iii) one test with a slab with steel deck ribs perpendicular

(⊥) to the loading direction. While the nominal ultimate tensile strength of shear studs was 450 MPa in all cases, their reported ultimate tensile strength ranges between 414 MPa and 535 MPa. The reported concrete compressive strength ranges between 21 MPa and 53 MPa. These correspond to a characteristic normal strength (C25/30 to C40/50) concrete. Specimen-to-specimen variability also includes the type of shear stud welds (stud gun welding vs. shield metal arc welding) as well the degree of imperfections in the welds. Figure 4.3 demonstrates the corresponding slip demand, on the steel beam-slab connections per damage state. The results indicate that the specimen-to-specimen variability necessitates the development of fragility functions that can estimate the probability of reaching or exceeding DS1 to DS4 in steel beam-slab connections. Note that the associated variability in slip demands increases considerably for DS2 to DS4 compared to DS1. The slip demands at each of the four damage states are summarized in Table 4.1. Slip demand values that are available but not reported in the respective experimental program are labeled as "NR", whereas those not available due to early termination of the tests are labeled as not applicable, "NA".

Table 4.1. Dataset of cyclic push-out tests

		Geometric Properties[a]				Material Properties[b]		Damage States			
Reference	Specimen ID	d_s [mm]	h_s [mm]	t [mm]	Deck	$f_{u,s}$ [MPa]	f_c [MPa]	DS1 [mm]	DS2 [mm]	DS3 [mm]	DS4 [mm]
Hawkins and Mitchell (1984)	1R	19	76	102	SS	514	23	NR	1.7	2.7	3.0
	3R	19	114	140	SS	514	25	0.2	1.0	2.7	3.9
	5R	19	114	140	SS	514	34	NR	1.8	2.6	3.7
	7R	19	114	140	||	514	35	NR	0.3	3.9	7.7
Zandonini and Bursi (2000)	NPC-01	16	102	120	||	528	33	0.3	1.1	1.4	3.6
	NPC-02	16	102	120	||	528	33	0.6	1.1	2.9	6.9
	NPC-04	16	102	120	||	528	33	0.3	0.6	1.0	5.5
	NPC-05	16	102	120	||	528	33	0.6	0.9	2.4	4.0
	RPC-01	22	126	150	||	457	42	0.4	2.5	4.8	7.2
	RPC-02	22	126	150	||	457	42	0.3	3.1	NA	NA
	RPC-03	22	126	150	||	457	42	0.2	3.4	NA	NA
	RPC-04	22	126	150	||	457	42	0.3	4.5	NA	5.3
	RPC-05	22	126	150	||	457	42	0.6	5.4	NA	NA
Civjan and Singh (2003)	S2C	13	102	155	SS	NR	24	NR	NR	NR	5.1
	S4C	13	102	155	SS	NR	41	NR	NR	NR	2.9
	S5C	13	102	155	SS	NR	25	NR	NR	NR	7.3
	S6C	13	102	155	SS	NR	24	NR	NR	NR	4.7
	S10C	13	102	155	SS	NR	21	NR	NR	NR	6.2

Aribert and Lachal (2000)	Group 3	19	NR	120	||	NR	NR	NR	1.0	1.7	3.5
Suzuki and Kimura (2019)	No. 1	22	130	175	SS	464	29	1.0	5.5	NA	NA
	No. 2	22	130	175	SS	464	29	0.6	4.1	6.5	NA
	No. 3	16	130	175	SS	473	29	0.2	5.0	6.0	NA
	No. 4	19	130	175	SS	486	29	0.4	5.1	NA	NA
	No. 5	22	80	175	SS	461	29	0.7	3.4	5.0	4.4
	No. 6	22	100	175	SS	446	29	0.8	2.9	4.4	8.1
	No. 7	22	130	175	SS	464	29	0.7	2.9	4.5	7.5
	No. 8	22	130	175	SS	464	29	0.3	4.5	6.6	NA
	No. 9	22	130	175	SS	464	29	0.5	1.7	3.1	6.0
	No. 10	22	130	175	SS	464	29	0.4	2.6	4.3	NA
	No. 11	22	130	175	SS	464	29	0.4	0.9	1.5	7.6
	No. 12	22	130	175	SS	464	29	0.7	2.6	6.0	NA
	No. 13	22	130	175	SS	464	39	0.5	4.4	5.8	NA
Nakajima et al. (2003)	B (Alt.)	13	100	150	SS	NR	40	0.4	3.4	NA	5.5
Ciutina and Stratan (2008)	PT-16/I-C	16	120	120	SS	NR	NR	0.3	1.4	2.3	3.3
	PT-22-C	22	120	120	SS	NR	NR	0.3	1.3	1.9	5.2
Zhai et al. (2018)	P-S-13-C	13	NR	300	SS	525	53	0.4	1.3	NA	2.5
	P-S-16-C	16	NR	300	SS	455	53	0.3	1.8	2.1	2.7
	P-S-19-C	19	NR	300	SS	535	53	0.6	2.5	3.8	5.4
Fan and Liu (2014)	C2	19	100	150	||	NR	NR	NR	1.1	3.1	8.2
Sun et al. (2019)	C3	19	100	150	⊥	497	NR	0.2	1.8	3.8	6.2
	C5	19	100	150	SS	497	26	0.3	1.8	2.6	4.9
Saari et al. (2004)	4	19	127	NA	SS	414	32	0.1	0.9	2.4	3.2

[a] d_s: stud diameter; h_s: stud height; t: slab thickness; SS: solid slab (i.e. without steel deck); ||: steel deck with ribs parallel to the beam; ⊥ steel deck deck with ribs perpendicular to the beam

[b] $f_{u,s}$: stud tensile strength; f_c: concrete compressive strength

NA: not available; NR: not reported

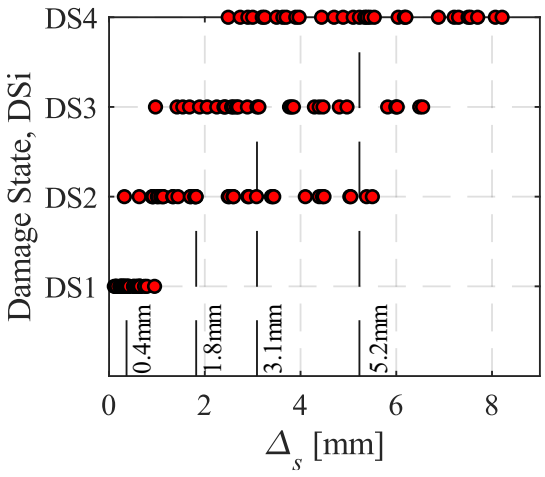

Figure 4.3 Distribution of slip demands, Δ_s, corresponding to the four damage states

4.5 Slip-based fragility functions

In order to estimate the likelihood of damage in steel beam-slab connections, slip-based fragility functions are developed based on the assembled dataset of Table 4.1. These provide the probability of reaching or exceeding a damage state as a function of the peak slip demands on headed shear stud connectors.

The employed methodology to derive the fragility functions has already been successfully implemented in prior related work (Aslani and Miranda 2005; Elkady et al. 2018; Gulec et al. 2011; Lignos et al. 2010; Ramirez et al. 2012; Ruiz-García and Negrete 2009). In brief, the slip values at each damage state are sorted in ascending order. The empirical cumulative probability is then calculated as $p_i = i/n$, in which n is the total number of data points for each damage state (see Table 4.2), and i is the position of the slip value within the sorted data. If needed, outlier data points are excluded as per Chauvenet's criterion (Taylor 1997). For a given damage state, the calculated p_i is plotted at its corresponding slip value in order to obtain the empirically derived cumulative distribution function (CDF). Four different CDFs (lognormal, gamma, Weibull, and Gumbel) are fitted to the empirically derived CDFs using the maximum likelihood approach (Venables and Ripley 2013). The Kolmogorov-Smirnov (K-S) goodness-of-fit test (Benjamin and Cornell 1970) is conducted at a 5% significance level in order to assess which of the four CDFs provides the best fit to the empirical CDF. A goodness-of-fit is assumed if the K-S test fails to reject the null hypothesis at 5% significance level; that is, the K-S statistic defined as the largest absolute difference between the theoretical and empirical CDF is less than the critical value at 5% significance level, $D_{crit,5\%}$. The K-S test is shown in Figure 4.4 for DS1. The hypothesis that the lognormal CDF fits the empirically derived CDF holds

true if all data points lie between the upper and lower bounds represented by the dashed lines. It is found that both the lognormal (see Figure 4.4a) and the gamma (see Figure 4.4b) CDFs provide a relatively good fit for the empirical CDF because they yielded the highest p-value of K-S test.

Table 4.2 Statistical parameters of the lognormal distributions for each damage state

	Dam-age State	μ_{Δ_s} [mm]	$\sigma_{\ln\Delta_s}$	Number of Specimens (n)	μ_{Δ_s} [mm] | 90% CI		$\sigma_{\ln\Delta_s}$ | 90% CI	
					Lower	Up-per	Lower	Up-per
Full Dataset	DS1	0.37	0.53	34	0.31	0.42	0.44	0.66
	DS2	1.82	0.68	37	1.51	2.19	0.57	0.85
	DS3	3.09	0.50	29	2.65	3.60	0.41	0.64
	DS4	5.23	0.35	31	4.71	5.81	0.29	0.45
Suzuki and Kimura (2019)	DS1	0.52	0.41	13	0.43	0.63	0.31	0.61
	DS2	3.42	0.51	13	2.71	4.31	0.38	0.77
	DS3	4.97	0.42	11	4.02	6.14	0.32	0.68
	DS4	7.50	0.24	5	6.26	8.99	0.16	0.58
Solid Slab (SS)	DS1	0.40	0.42	20	0.34	0.47	0.34	0.58
	DS2	2.60	0.54	22	2.14	3.14	0.43	0.73
	DS3	4.05	0.46	18	3.38	4.85	0.36	0.65
	DS4	5.10	0.37	19	4.43	5.87	0.29	0.51
Parallel Steel Deck (‖)	DS1	0.34	0.39	9	0.27	0.42	0.28	0.67
	DS2	1.13	0.86	12	0.75	1.70	0.64	1.33
	DS3	2.65	0.54	8	1.93	3.62	0.38	0.97
	DS4	5.54	0.33	9	4.61	6.65	0.24	0.57

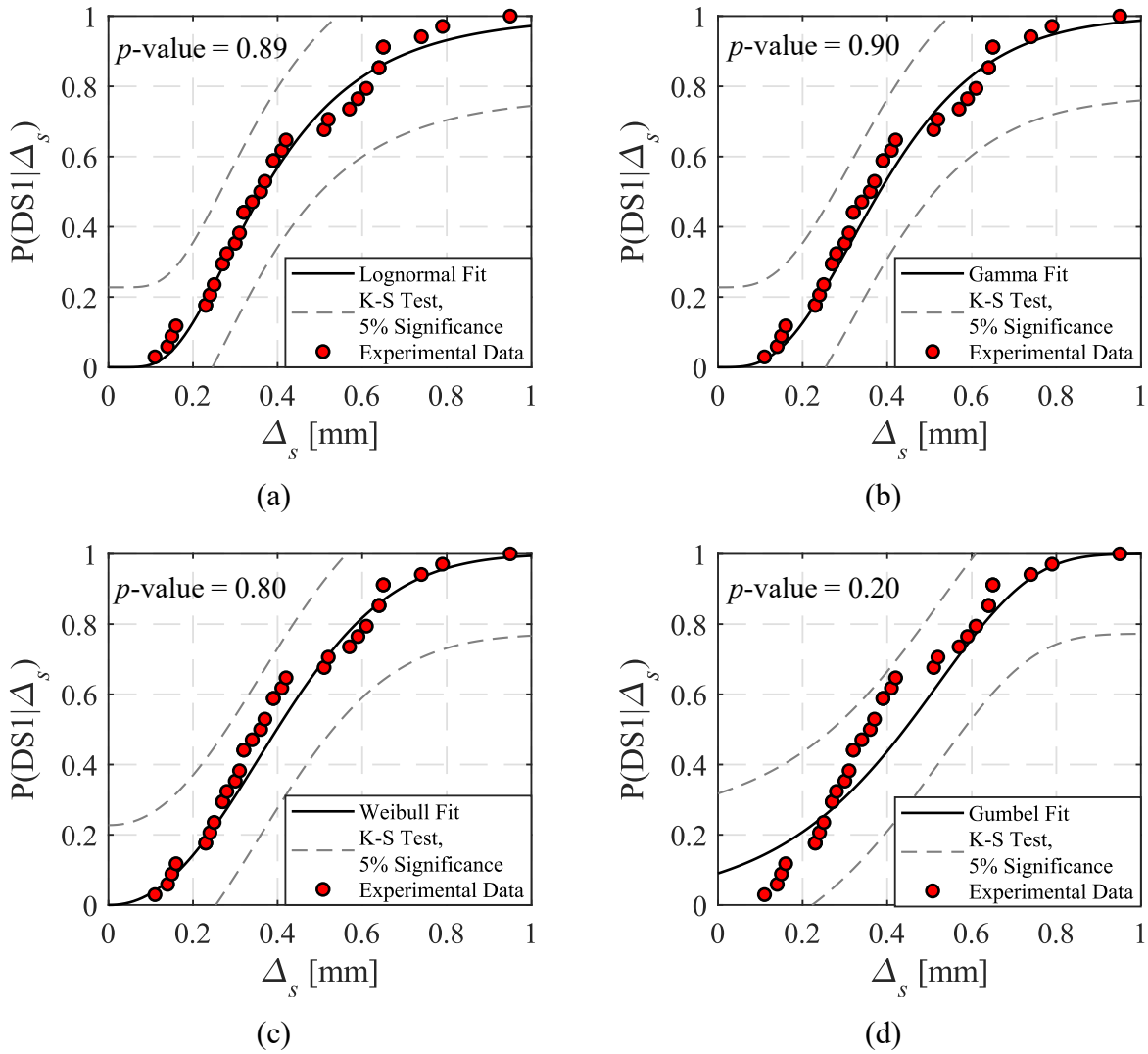

Figure 4.4 Comparison of four theoretical CDFs fitted to the empirically derived CDF for damage state DS1: (a) lognormal; (b) gamma; (c) Weibull; and (d) Gumbel

The lognormal distribution is selected hereinafter due to its ease of implementation and for consistency with available fragility functions defined in FEMA P-58-1 (FEMA 2012) as well as other related studies. The lognormal CDF is defined as follows:

$$\mathrm{P}(\mathrm{DS} \geq \mathrm{ds}_i | \Delta_s = \delta_s) = \Phi\left[\frac{\ln \Delta_s - \ln \mu_{\Delta_s}}{\sigma_{\ln \Delta_s}}\right] \tag{4.1}$$

in which $\mathrm{P}(\mathrm{DS} \geq \mathrm{ds}_i | \Delta_s = \delta_s)$ is the conditional probability of reaching or exceeding damage state i in the steel beam-slab connection at a specified slip value δ_s; μ_{Δ_s} is the counted median of slip values at damage state i; $\sigma_{\ln \Delta_s}$ is the standard deviation of the natural logarithm of the slip values at damage state i; and Φ is the cumulative standard normal distribution. Figure 4.5 shows that the lognormal CDF fits the empirically derived CDF fairly well for all four damage states.

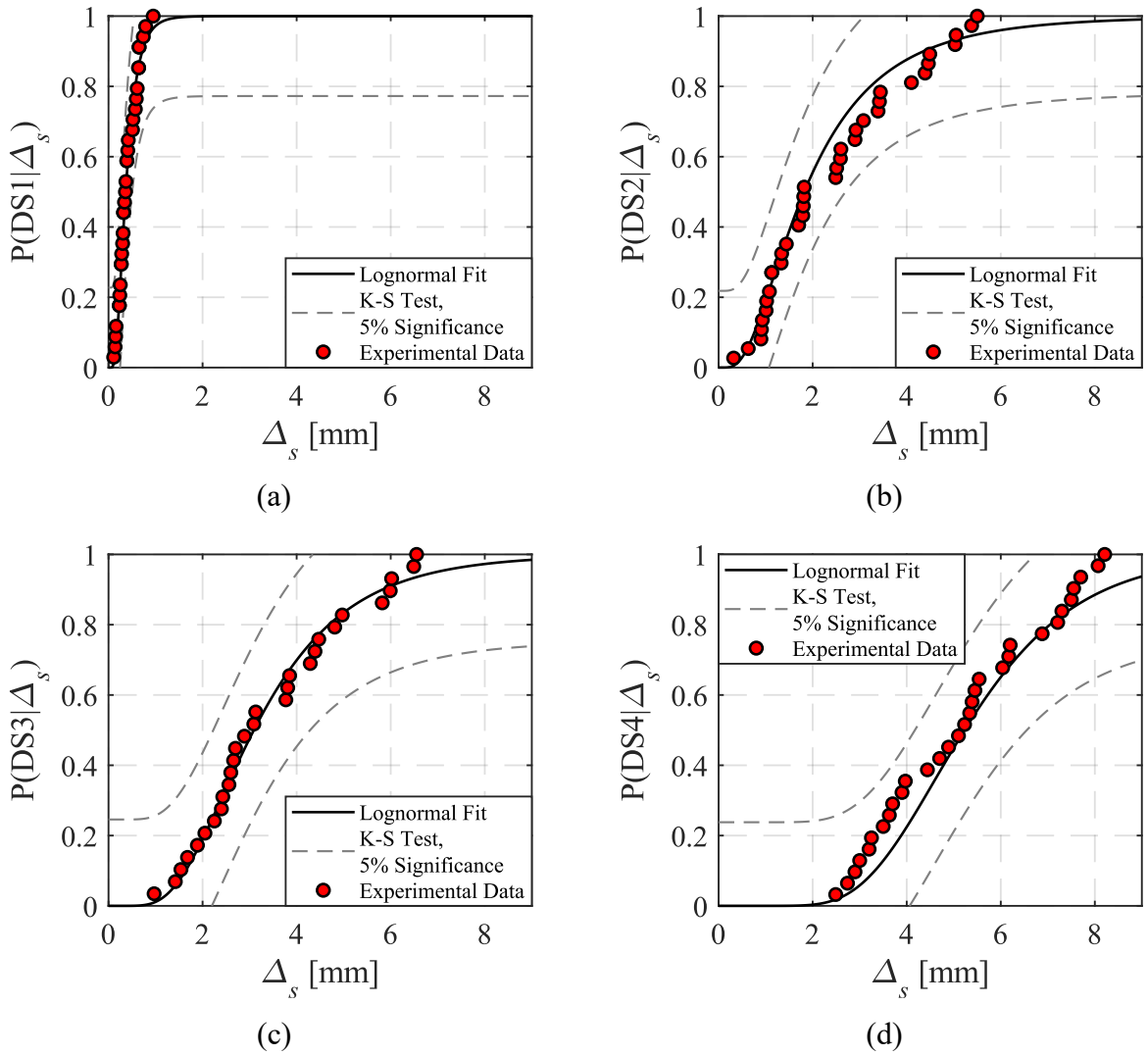

Figure 4.5 Slip-based fragility functions corresponding to the four damage states in steel beam-slab connections: (a) damage state DS1; (b) damage state DS2; (c) damage state DS3; and (d) damage state DS4

4.6 Influence of epistemic uncertainty

The developed fragility functions incorporate the specimen-to-specimen uncertainty as discussed earlier. Nevertheless, the epistemic uncertainty arising from the finiteness of the dataset is not accounted for. This finite sample uncertainty can be considered by estimating confidence intervals (CI) of the peak slip demands for each damage state (Benjamin and Cornell 1970; Crow et al. 1960). The confidence intervals of the median and logarithmic standard deviation of a lognormal CDF is computed using Eqs. (4.2) and (4.3) respectively (Crow et al. 1960):

$$\mu_{\Delta_s} \cdot \exp\left[\pm z_{a/2} \cdot \frac{\sigma_{ln\,\Delta_s}}{\sqrt{n}}\right] \tag{4.2}$$

$$\sqrt{\frac{n-1}{\chi^2_{a/2,n-1}}} \cdot \sigma_{\ln \Delta_s} \text{ and } \sqrt{\frac{n-1}{\chi^2_{1-a/2,n-1}}} \cdot \sigma_{\ln \Delta_s} \tag{4.3}$$

in which, $z_{a/2}$ is the value of the standard normal deviation such that the probability of a random deviation numerically greater than $z_{a/2}$ is a; $\chi^2_{a/2,n-1}$ and $\chi^2_{1-a/2,n-1}$ are the inverse of the distribution with $n-1$ degrees of freedom and a probability of occurrence $a/2$ and $1-a/2$, respectively. Table 4.2 summarizes the 10% and 90% confidence intervals of the median, μ_{Δ_s}, and the logarithmic standard deviation, $\sigma_{ln\,\Delta_s}$, for each damage state. The effects of the epistemic uncertainty are depicted through the uncertainty envelopes in Figure 4.6. This provides the upper- and lower-bound probability of reaching or exceeding each damage state from local slip demands. For instance, according to EN 1994-1-1 (CEN 2004b), the characteristic slip capacity, δ_{uk}, shall be greater than or equal to 6 mm at DS3. Figure 4.6c shows that the probability of reaching or exceeding DS3 at a slip demand of 6 mm varies between 80% and 95%; that is, the probability that the shear stud connectors in the steel beam-slab connection are ductile (CEN 2004b) is low (5% to 20%). While it is true that shear studs subjected to cyclic loading may have a lower characteristic slip capacity than that recommended by EN 1994-1-1, continuum finite element analyses (El Jisr et al. 2020) and system-level nonlinear response history analysis conducted hereinafter on composite-steel MRFs with shallow beams (depth of 500 mm or less), have shown that the shear stud demands are considerably lower than δ_{uk}. In fact, at design basis earthquake events, the probability of DS2 at slip demands of 0.5 mm (see section 4.9) varies between 1 to 10%. Even if the slip demands were to be twice as high (i.e., 1 mm), the upper bound probability of DS2 remains below 30% and repairs due to extended cracking in the slab are highly unlikely.

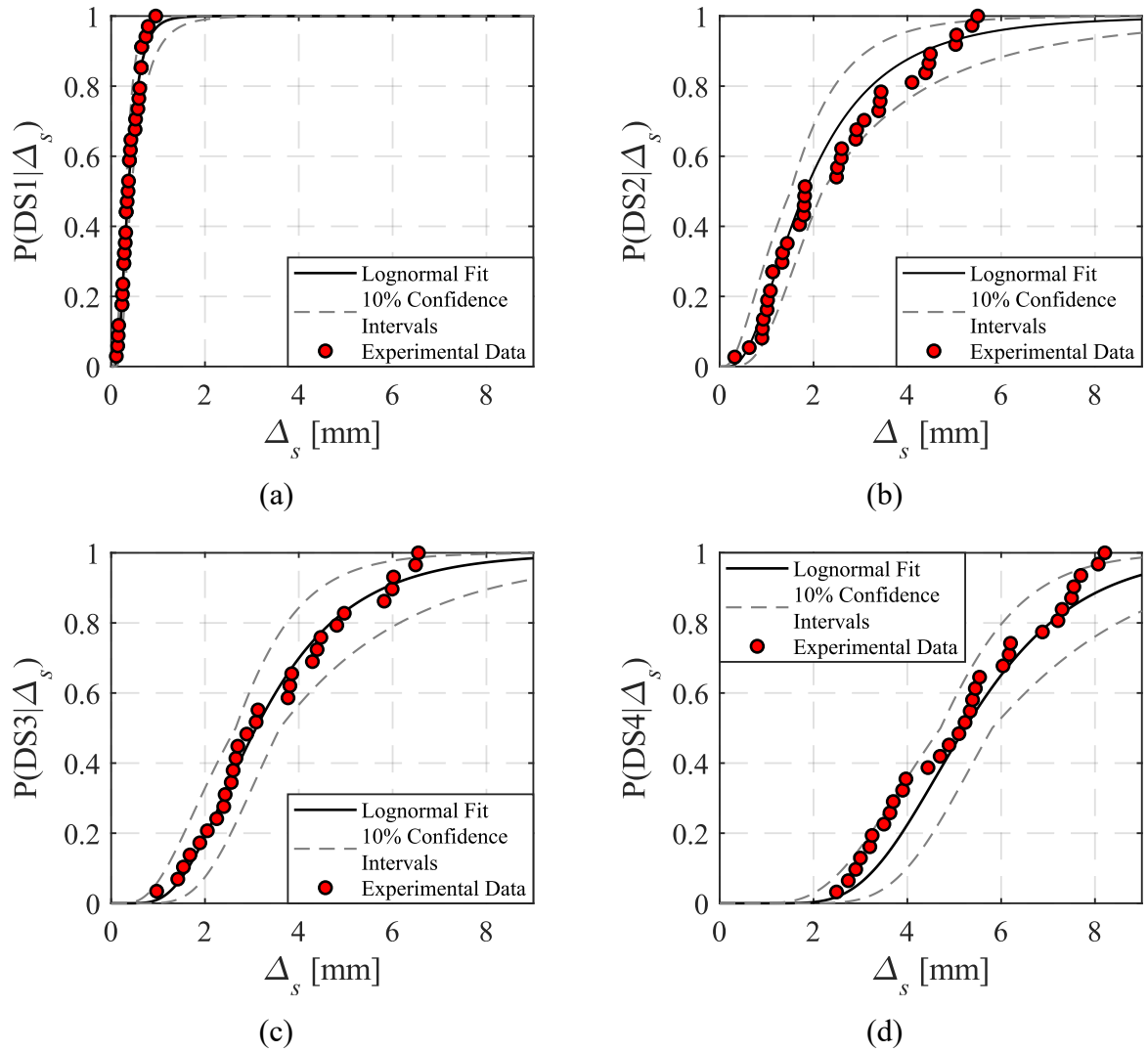

Figure 4.6 Envelope of epistemic uncertainties on fragility functions of steel beam-slab connections derived from the full dataset: (a) damage state DS1; (b) damage state DS2; (c) damage state DS3; and (d) damage state DS4

4.7 Effect of the stress state in the slab

The effect of the slab stress state on the steel beam-slab connection behavior has been investigated in a recent experimental program conducted by Suzuki and Kimura (2019). In composite steel MRFs, the slab is subjected to compressive stresses under sagging bending and tensile stresses under hogging bending depending on the direction of lateral loading. These tests better emulate the steel beam-slab connection in composite steel MRFs since the stress state in the floor slab is taken into consideration. Table 4.1 suggests that the dataset of Suzuki and Kimura (2019) achieves appreciably higher slip demands than those from conventional push-out tests prior to reaching DS2 to DS4.

Albeit the limited available data at this point, a separate subset consisting of 13 cyclic push-out tests from Suzuki and Kimura (2019) is used to derive four complementary fragility functions at each damage state to comprehend the differences at the achieved slip demands between the two datasets. The statistical parameters of the fitted lognormal CDFs, derived with the same methodology discussed earlier, are summarized in Table 4.2. The reported logarithmic standard deviations from the smaller subset demonstrate a lower variability in slip demands compared to those from the full dataset, regardless of the DS under consideration. Figure 4.7a suggests that the effect of the slab stress state on the slip demands at DS1 (light cracking) is minimal. Conversely, DS2 to DS4 are significantly influenced by the stress state in the slab as shown in Figure 4.7b to d, respectively.

A possible explanation of the observed discrepancy is the fact that the shear studs in conventional push-out tests are subjected to fairly similar demands in both loading directions, while those in Suzuki and Kimura (2019) are asymmetric. The cyclic push-out tests showed that normal strains due to bending at the base of the shear studs are more than 10 times lower when the slab is in tension than when it is in compression. On the other hand, in conventional cyclic push-out tests, the strain demands at the base of the shear studs are nearly the same in both loading directions, thereby leading to crack initiation due to low-cycle fatigue. This often causes fracture as depicted in Figure 4.7d. Particularly, the probability of being or exceeding DS4 (i.e., loss of shear load carrying capacity) at 6 mm slip is more than 65% based on the full dataset, whereas when the effect of stress state in the slab is considered, the probability of being or exceeding DS4 is less than 20%. In prior work (El Jisr et al. 2020), the influence of loading history on the shear stud demands has been stressed. While physical data is not available to examine this issue, the fragility functions presented herein are considered to be a conservative estimate of the observed damage seen in beam-slab connections of composite steel MRFs under earthquake loading

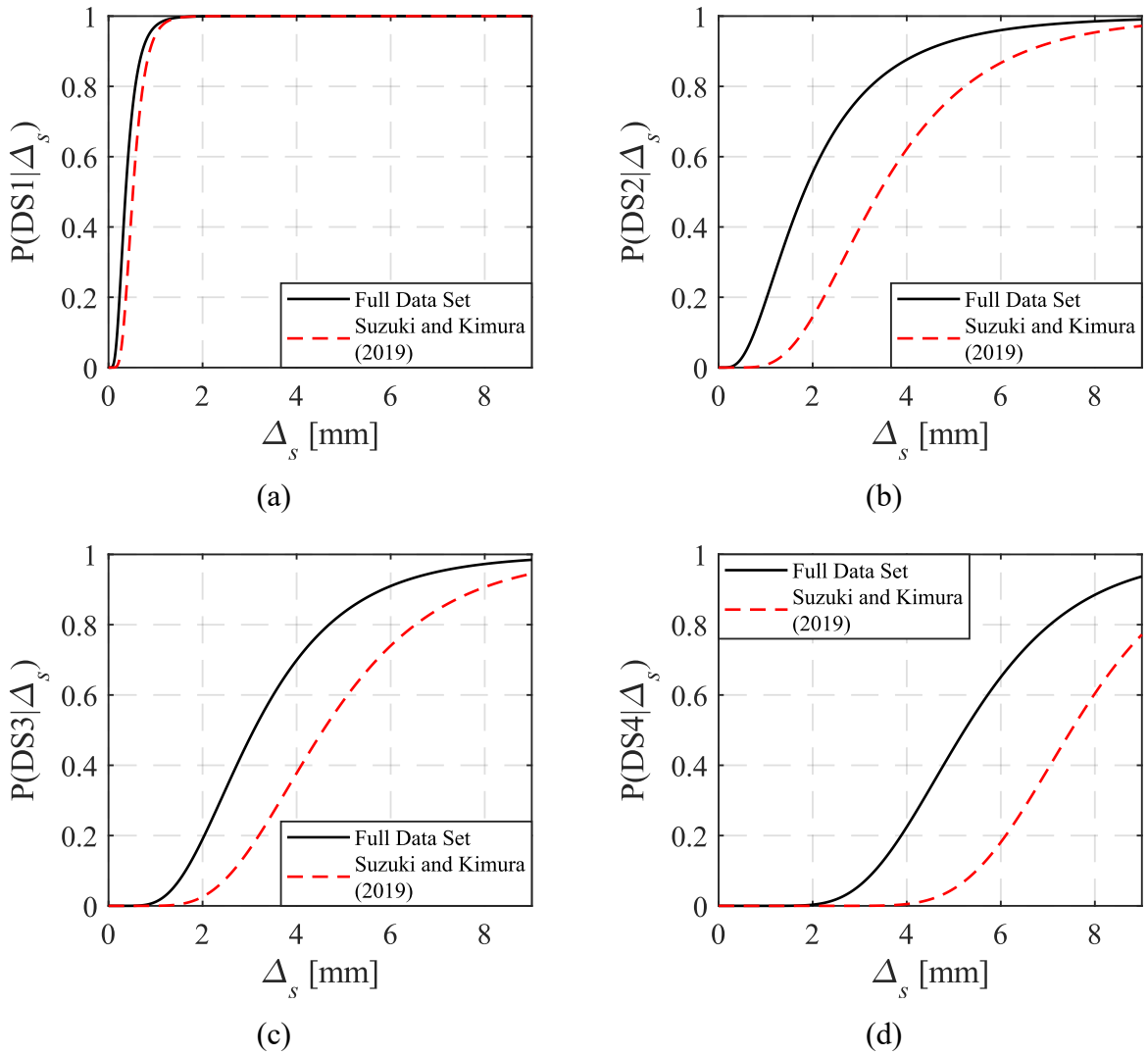

Figure 4.7 Comparison between fragility functions of steel beam-slab connections derived from the full dataset and those derived from Suzuki and Kimura (2019) subset: (a) damage state DS1; (b) damage state DS2; (c) damage state DS3; and (d) damage state DS4

4.8 Effect of slab type

In composite construction practice, a steel deck is typically present as part of the composite floor system. Nevertheless, a large portion (about 70%) of the cyclic push-out tests available in the literature consist of a solid slab with no steel deck. Referring to Table 4.2, the dispersion measured by the logarithmic standard deviation, $\sigma_{\ln \Delta_s}$, is fairly high in the full dataset for DS1 to DS3. This dispersion is due to specimen-to-specimen variability, which comprises differences in geometry, material properties as well as the loading protocol. In order to examine how the aleatoric uncertainty is influenced by the presence of a steel deck, the full dataset is divided into two additional subsets with: (i) solid slab test specimens (29) and (ii) test specimens that consist of a steel deck with ribs parallel to the

beam (12). Subsequently, fragility functions at DS1 to DS4 are derived for each subset. Referring to Figure 4.8, it is evident that specimens with a solid slab have a higher slip capacity at DS2 and DS3 damage states. At DS1, the difference between the two types of fragility functions is negligible because damage is mostly associated with fairly light slab cracking. Moreover, at DS4, loss of shear load carrying capacity due to fracture of the shear stud is not practically influenced by the slab type.

Table 4.2 shows that $\sigma_{\ln \Delta_s}$ in the solid slab subset is lower at DS2 (21%) and DS3 (8%) than that in the full dataset. In contrast, for the subset with the steel deck, $\sigma_{\ln \Delta_s}$ is 26% higher at DS2 and 9% higher at DS3. The reason for the higher dispersion in the subset with the steel deck is the fact that damage in these specimens is also dependent on the deck geometry (i.e., rib height and width). Additionally, the number of data points is relatively small (12) and most of the data points are obtained from Zandonini and Bursi (2000) in which the stud dimensions, concrete compressive strength, and loading protocol were varied. In solid slabs, the studs are fully confined with the surrounding concrete, whereas in slabs consisting of a steel deck, the level of confinement is dependent on the rib dimensions. Since the slip values at DS2 and DS3 are influenced by concrete crushing, the effect of concrete compressive strength on Δ_s is more evident in slabs with a steel deck where less confinement is present. In the assembled dataset, the slip at DS2 and DS3, in test specimens with a steel deck present, exhibits an increasing trend with respect to the concrete compressive strength (see Table 4.1). Nevertheless, this dependency is inconclusive because of the limited data available. In the collected test specimens with a solid slab, the slip demand is not found to be statistically significant with respect to the concrete compressive strength.

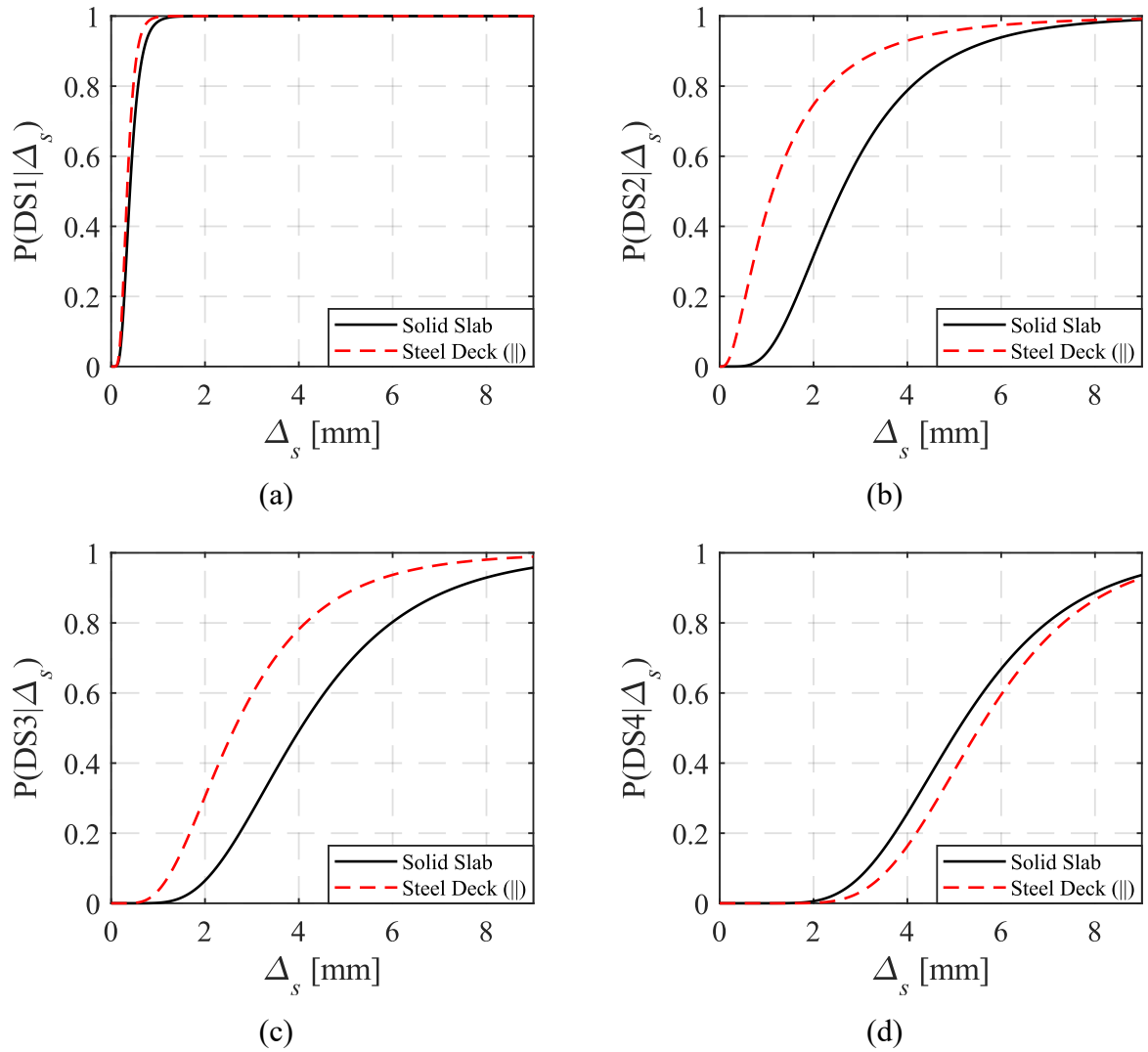

Figure 4.8 Comparison between fragility functions of steel beam-slab connections derived for solid slabs and those derived for slabs consisting of a steel deck with ribs parallel to the steel beam: (a) damage state DS1; (b) damage state DS2; (c) damage state DS3; and (d) damage state DS4

4.9 Performance-based assessment of a composite steel MRF

In this section, an application of the proposed fragility functions is demonstrated for a six-story prototype building designed according to current European design provisions (CEN 2004a; b, 2005b; c) for a site in Sion, Switzerland. The aim is to assess the integrity of beam-slab connections in composite-steel MRFs with shallow steel beams (depth of 500 mm or less) and partial degree composite action. The latter can be used in the design of composite-steel MRFs to effectively target a lower number of shear stud connectors, thereby leading to appreciable cost savings in composite construction.

The main seismic design parameters of the prototype building are: (i) building importance class II; (ii) reference peak ground acceleration, $a_{gR} = 0.22$ g; (iii) a behavior factor, $q = 3$ [i.e., strength reduction factor, R according to the US provisions (AISC 2016a)] and (iv) soil Type D. Referring to Figure 4.9a, the building consists of space composite-steel MRFs in the E-W loading direction. The elevation view of the building is shown in Figure 4.9b. Headed shear studs ($h_s = 100$ mm, $d_s = 16$ mm) connect the MRF girders to a 125 mm thick floor slab with a 56 mm steel deck. The ribs of the deck are parallel to the girders. An 80% degree of composite action (defined as the ratio of the actual number of shear studs to that required for full composite action) is achieved in the seismic design. This corresponds to the minimum value permitted by EN-1998-1 (CEN 2004a). However, the 25% reduction in shear stud capacity is intentionally waived. Recent findings (El Jisr et al. 2020) have shown that slip demands in composite-steel beams with depths of less than 500 mm are fairly minimal and they should not affect the integrity of the steel beam-slab connection.

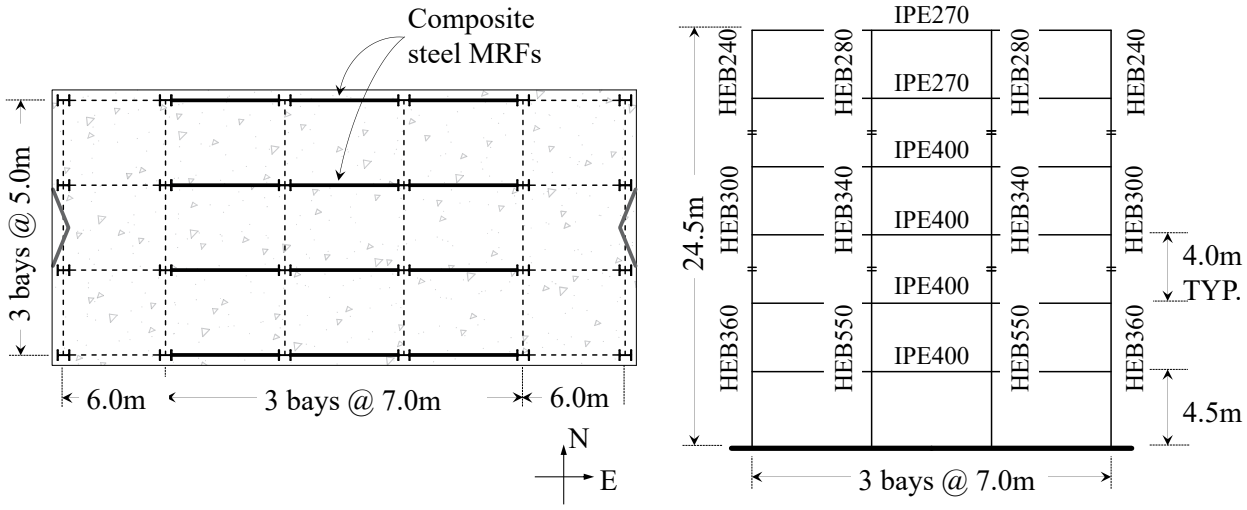

Figure 4.9 Typical (a) plan and (b) elevation view of the six-story building with composite steel MRFs

Half of the prototype building is modelled in 2-dimensions (2-D) in the open-source simulation platform OpenSEES (McKenna 1997). Particularly, two of the composite steel MRFs are modelled in series including a leaning column to properly represent (i) the lateral strength and stiffness of the building in the E-W direction; and (ii) de-stabilizing effects due to gravity loading (i.e., P-Delta). The composite beam-to-column joints are modeled by using a validated macro-model that features several nonlinear zero length elements as shown in Figure 4.10a. More details regarding this model are presented in Chapter 6 of this thesis. The macro-model can explicitly simulate slab-column interaction

through the two force transfer mechanisms in EN-1998-1 (CEN 2004a). The first mechanism consists of slab bearing on the column flange (noted as mechanism 1), whereas the second one is a strut-and-tie mechanism (noted mechanism 2). Slip demands on the steel beam-slab connection are captured by lumping the shear studs into a single translational zero length element. A similar approach has been implemented in past studies for partial-strength beam-to-column connections (Amadio et al. 2008; Braconi et al. 2007; Rassati et al. 2004). Flexural strength and stiffness deterioration of composite-steel beams as well as composite beam-to-column web panel zone joints are simulated according to the procedures discussed in Elkady and Lignos (2014) and El Jisr et al. (2019). Figure 4.10b illustrates a comparison between the simulated and experimentally obtained moment-rotation relation of a fully-composite steel beam of 400 mm (Yamada et al. 2009). Moreover, as expected, the shear force, Q, versus slip demand, Δ_s, relation in the steel beam-slab connection is elastic as shown in Figure 4.10c. The modeling approach is deemed to be rational as it represents the hysteretic response of the composite steel beam reasonably well and can also capture slip demands on the steel beam-slab connection.

Nonlinear response history analysis is conducted on the composite steel MRF at two different seismic intensities: the design basis earthquake (DBE) with a return period T_R =475 years and the maximum considered earthquake (MCE) with a return period T_R =2475 years. The earthquake records at each seismic intensity are selected to target the conditional mean spectrum (CMS) obtained from the mean magnitude and distance from rupture for each T_R (Baker 2011; Kohrangi et al. 2017; Lin et al. 2013). Figure 4.11 shows the two sets of 40 ground motions that were obtained by conducting probabilistic seismic hazard analysis for Sion for average spectral acceleration values, Sa, over a period range of 0.4 to 4.4s.

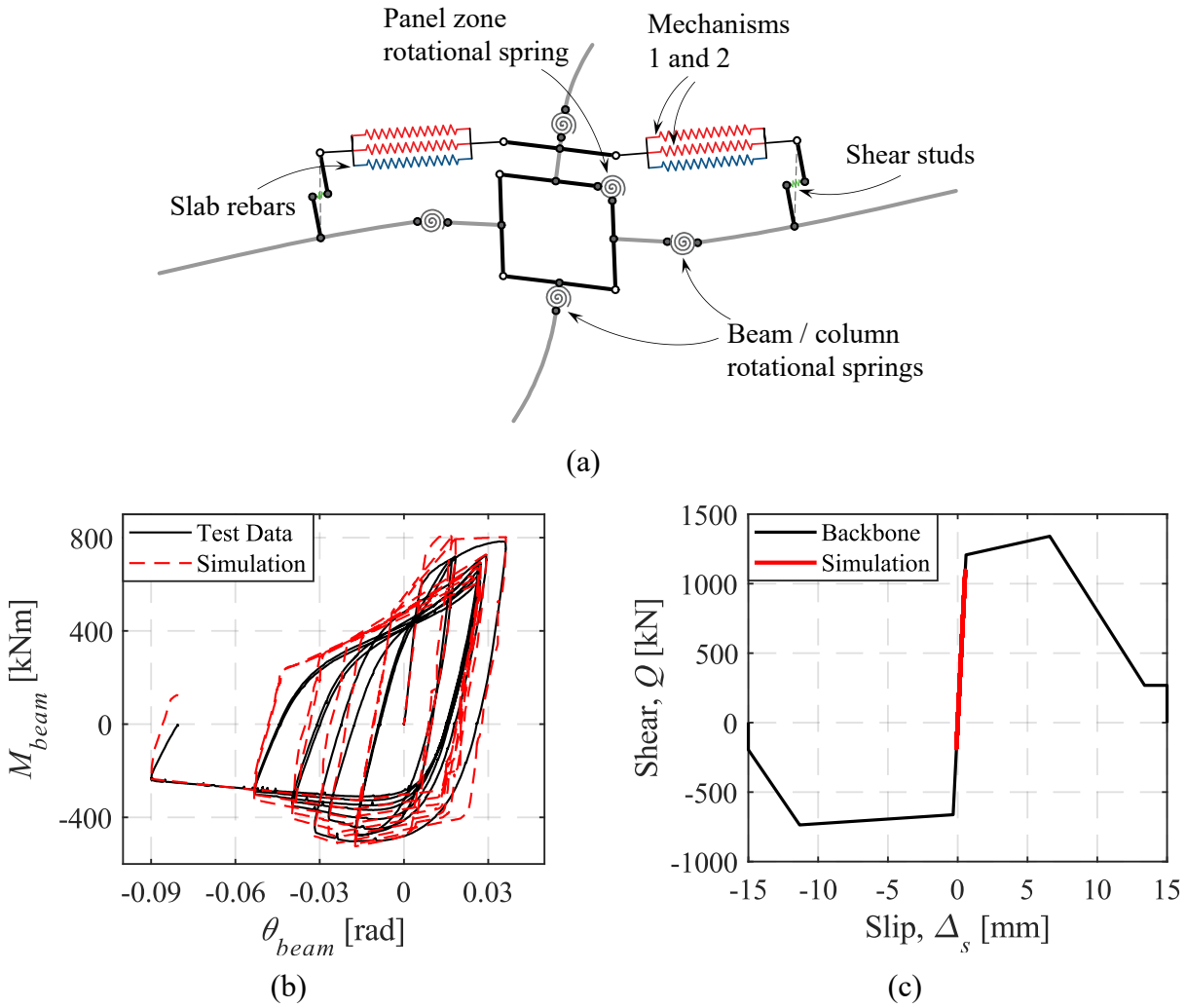

Figure 4.10 Modeling approach implemented for the system-level response history analysis of the 6-story composite steel building: (a) macro-model; (b) model validation with Yamada et al. (2009); (c) shear-slip response of the beam-slab connection

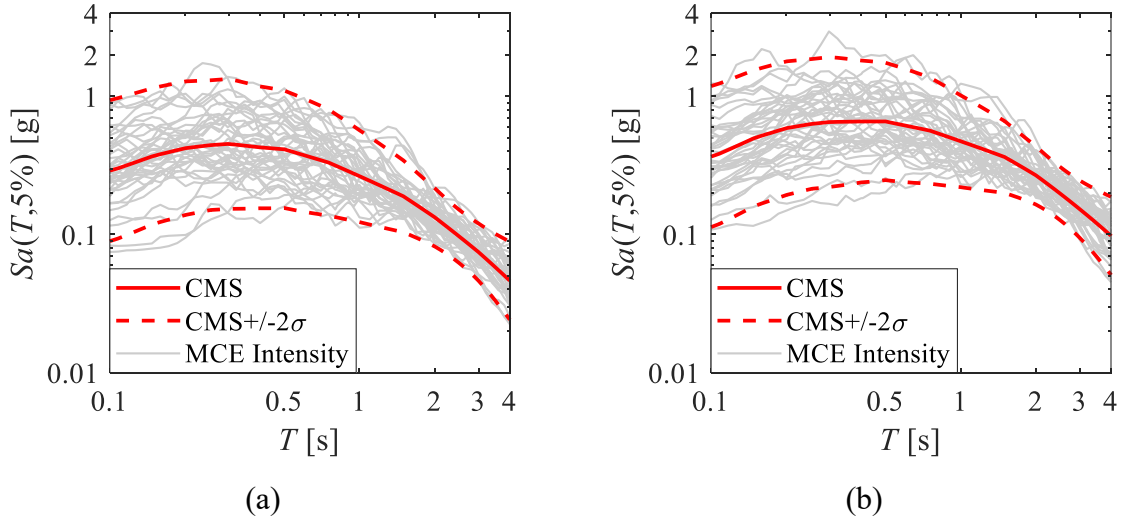

Figure 4.11 Selected ground motion records for Sion in Switzerland for two different return periods; (a) 475 years; (b) 2475 years

The peak slip demands on the steel beam-slab connections are obtained along the height of the building through nonlinear response history analyses and plotted together with the median, 16th and 84th percentiles. Referring to Figure 4.12, the median peak slip demand values at DBE and MCE are 0.5 mm and 1.8 mm, respectively. Based on these values, the potential damage in the steel beam-slab connection is captured by using the developed fragility functions.

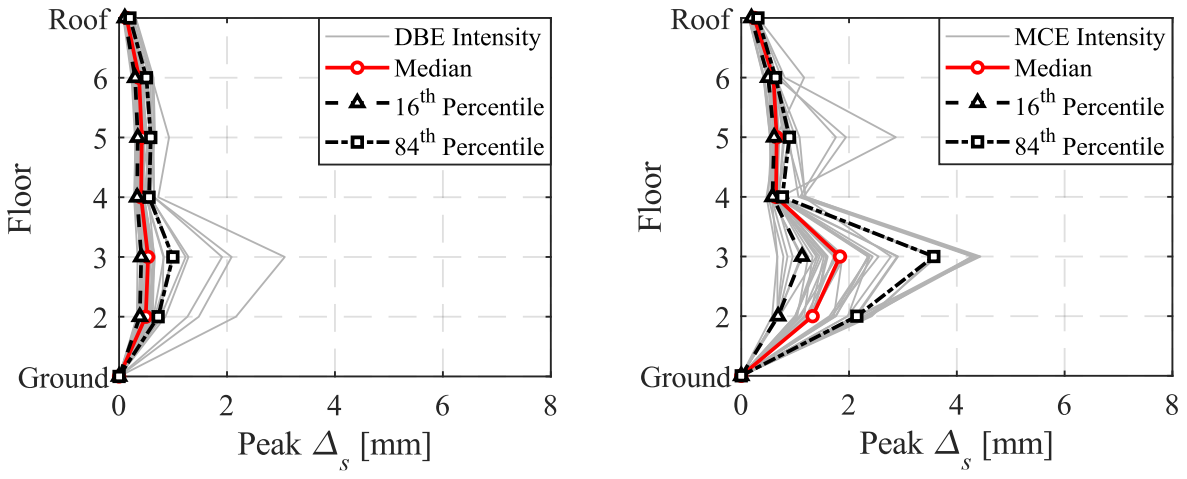

Figure 4.12 Peak Δ_s profile for the prototype composite steel MRF at (a) DBE seismic intensity and (b) MCE seismic intensity

Figure 4.13a shows the likelihood of occurrence of each damage state based on the fragility functions that were derived from the full dataset. The largest damage in the steel beam-slab connections occurs at the third floor where the demand on the composite steel beams is the highest. At DBE, the probability of attaining or exceeding DS2 (i.e., extended cracking / shear stud yielding and crushing of concrete) is less than 5%. Hence, most of the damage in the slab is attributed to light cracking, which corresponds to DS1. The probability of reaching DS1 varies between 3% at the roof to 73% at the third floor. Waiving the 25% reduction in the capacity of the shear stud connectors does not practically affect the integrity of steel beam-slab connections at seismic intensities associated with DBE. At seismic events with a low probability of occurrence, i.e., MCE, there is a 50% chance that DS2 is attained. Nevertheless, the probability of low-cycle fatigue microcracking (DS3) and therefore severe degradation in the steel beam-slab connection strength is less than 15%. Furthermore, the probability of complete loss of composite action (DS4) is negligible. Noteworthy stating that the aforementioned values are fairly conservative as they do not account for the stress state in the slab. Within such a context, the simulation results demonstrate that the 25% reduction in the shear resistance of the stud connectors may be potentially waived in seismic designs with beam depths less than 500 mm.

Particularly, Figure 4.13b depicts the probability of being or exceeding in DS1 to DS4 according to the fragility functions that were derived based on the Suzuki and Kimura (2019) subset. Interestingly, the probability of being or exceeding DS1 at DBE becomes negligible and that of attaining DS2 at MCE drops to nearly 10%. The results convey the importance of the developed fragility functions for performance-based seismic design of frame buildings with composite-steel MRFs.

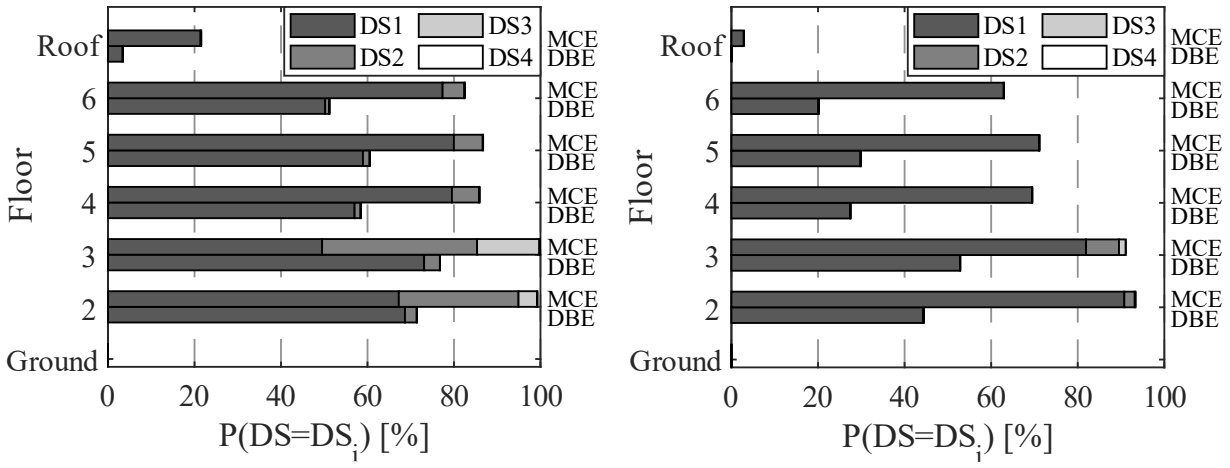

Figure 4.13 Probability of attaining each damage state along the height of the composite steel MRF at DBE and MCE seismic intensities using (a) full dataset; and (b) Suzuki and Kimura (2019) subset

4.10 Summary and conclusions

This chapter proposes slip-based fragility functions that permit the estimation of damage in steel beam-slab connections as part of composite-steel MRFs. The proposed fragility functions provide the probability of reaching or exceeding four discrete damage states as a function of the local slip demands on the steel beam-slab connections. To this end, an experimental dataset of 42 cyclic push-out tests is assembled. The four damage states include light to extensive cracking and crushing of the concrete slab, shear stud connector yielding, low-cycle fatigue microcracking in the shear studs and ultimately fracture of the steel beam-slab connection.

The fragility functions incorporate uncertainty due to specimen-to-specimen variability as well as epistemic uncertainty associated with the finite number of the collected tests. The latter is accounted for through confidence band intervals. Moreover, the dependency of the steel beam-slab connection damage on the slab stress state (tension or compression) is acknowledged through four

complementary fragility functions that are derived from a subset of 13 cyclic tests (Suzuki and Kimura 2019). These complementary fragility functions are considered more representative to describe, in a probabilistic manner, the damage of steel beam-slab connections in composite-steel MRFs. It is shown that the fragility functions derived from the full dataset provide conservative estimates of the anticipated damage in the steel beam-slab connections. Separate fragility functions are also derived for the two predominant slab types in the dataset: (i) solid slab and (ii) slab consisting of a steel deck with ribs parallel to the beam. The results suggest that higher damage is experienced at DS2 and DS3 if a steel deck is present. Furthermore, damage states DS2 and DS3 in specimens with a steel deck parallel to the beam are more dependent on the compressive strength of concrete than those with a solid slab.

A six-story prototype building with composite-steel MRFs is used to illustrate the potential benefits of the proposed fragility functions. The building is located in Sion, Switzerland and it is designed according to the current European seismic provisions with 80% degree of composite action. Nevertheless, the code-required 25% reduction in the shear capacity of the stud connectors is intentionally neglected. Nonlinear response history analysis is conducted at two seismic intensities, namely DBE and MCE. It is found that, at DBE, there is at least 50% to 70% chance for the slab to exhibit only minor cracking depending on the employed fragility function type. At seismic intensities associated with a low probability of exceedance, i.e., MCE, the probability of shear studs in steel beam-slab connections to exhibit low-cycle fatigue drops from about 35% to less than 10% when considering the stress state of the steel beam-slab connection in the seismic performance assessment of the building. Interestingly, the loss of the shear capacity of the steel beam-slab connections is negligible, at the same seismic intensity, regardless of the employed fragility function type. In that sense, disregarding the 25% reduction in the shear strength of the stud connectors of the examined composite steel MRF seems rational.

Chapter 5 Full-scale collapse test of a 2-bay composite steel moment-resisting frame subsystem under cyclic loading

5.1 Introduction

The hysteretic behavior of steel beam-to-column connections with a floor slab has been traditionally investigated by testing subassemblies with cruciform (e.g., Engelhardt et al. 2000; Leon et al. 1998; MacRae et al. 2013; Ricles et al. 2002, 2004; Sumner and Murray 2002; Uang et al. 2000) or T-shaped configurations (e.g., Bursi and Gramola 2000; Kim and Lee 2017; Yamada et al. 2009). In this case, the location of the inflection points within the structural members is assumed to remain constant throughout the imposed loading history. It has been recognized (FEMA 2000a) that while these subassemblies provide valuable information on the role of the slab on the nonlinear cyclic response of composite steel beams, the overly simplified boundary conditions do not allow for a realistic consideration of the slab restraint and framing action on the seismic stability of composite steel moment-resisting frames (MRFs). This aspect is particularly important at large lateral drift demands associated with structural collapse. Accordingly, prior subassembly tests (e.g., Civjan et al. 2001; MacRae et al. 2013) suggest that local buckling within the anticipated dissipative zone of the composite steel beams induces axial shortening. Unlike reinforced concrete (RC) MRFs where beam elongation has been investigated (Fenwick and Megget 1993) and observed in prior earthquakes (e.g., Henry et al. 2017), beam shortening is fairly unlikely in composite steel MRFs under cyclic loading.

Detailed continuum finite element studies have demonstrated that partially composite steel beams (i.e., degree of composite action, $\eta < 100\%$) in subsystems experience up to 25% less flexural strength degradation than their subassembly counterparts (El Jisr et al. 2020). Restraint against beam axial shortening creates tensile forces in the beams that may alter the seismic behavior of composite steel beams (El Jisr et al. 2020; Herrera et al. 2008; Leon and Deierlein 1996). This behavior has been observed in a handful of system-level experiments (Cordova and Deierlein 2005; Del Carpio et al. 2014) where local buckling in composite steel beams was fairly mild compared to what was observed in subassembly tests. Force redistributions occuring within the aforementioned tests were neither quantified nor comprehended.

System-level shake table collapse experiments (Suita et al. 2008) demonstrated that the presence of the slab could trigger a soft story collapse mechanism due to the increase of the flexural resistance of the respective beam relative to that of the adjoining column even in cases that capacity design has been considered (Lignos et al. 2013). However, inelastic deformations in this case were mostly concentrated in columns. Nakashima et al. (2007) tested a 2-story building with composite steel MRFs that featured welded beam-to-column connections with shallow beams. The presence of the slab in this case caused fractures at the welds of the bottom beam flanges within the beam-to-column connections at a lateral drift demand of 4% rads. This was due to shifting of the neutral axis of the composite cross section towards the upper flange under sagging bending that increased the tensile strain demands at the bottom flanges. Although the experiment was continued to a lateral drift demand of 12% rads, the imposed loading was symmetric cyclic, which did not reflect the lateral drift demands prior to collapse where ratcheting is dominant (Lignos et al. 2011). Other researchers in Europe (Bouwkamp et al. 1998; Plumier and Doneux 2001) and the US have conducted system-level experimental programs on composite steel MRFs. However, the tested frames featured either semi-rigid beam-to-column connections (Ammerman 1988; Leon 1990b), and therefore were not intended for use in zones of high seismicity or aimed to investigate the behavior of the composite beam-to-column connections at modest lateral drift demands associated with a design basis earthquake.

Prior work on RC MRF buildings (e.g., Leon 1983; Joglekar 1984; Mahin and Bertero 1975) has shown that the transverse beams of the floor system could have a significant effect on the flexural resistance of RC beam-to-column joints. On the other hand, the 3-dimensional effects due to the floor system have only been investigated in the seismic response of steel frame gravity systems (Donahue 2019). Detailed measurements on the floor slab and the beam-slab connections within a floor system could effectively benchmark (a) the cross-sectional classification of composite steel beams; (b) the effective width in composite steel cross sections; and (c) the lateral stiffness of composite steel beams relative to their bare beam counterparts.

Current standards (AISC 2016a; CEN 2004a) with emphasis on the seismic design of composite steel MRFs, impose a 25% reduction on the shear resistance of stud connectors when the steel girders of the primary seismic resistant system are designed as composite. While the basis of this design rule is not clear in the literature, it is assumed that it is mostly based on results from conventional push-out tests (Bursi and Gramola 1999; Civjan and Singh 2003; Zandonini and Bursi 2000) that do not account for force redistributions while the composite steel MRF experiences damage during an earthquake. Moreover, the stress state and actual boundary conditions in the slab are not preserved. El Jisr et al. (2020) found that the above design rule may not be imperative for seismic designs of composite

steel MRFs that feature shallow steel beams (i.e., depths less than 500 mm). On the other hand, there has not been a comprehensive experiment that carefully documents the slip demands of the floor system with a particular emphasis on the repairability of composite floors in the aftermath of earthquakes.

In order to advance the state-of-knowledge in the seismic stability of composite steel MRF buildings, this chapter presents the results from a full-scale experiment of a 2-bay composite steel MRF subsystem under lateral cyclic loading. The primary objectives of the testing program were (a) to comprehend the effects of the slab continuity and framing action on the seismic performance of composite steel MRFs with emphasis at lateral drift demands associated with structural collapse; (b) to quantify the effects of transverse beams and slab confinement on the flexural resistance of composite beam-to-column connections; (c) to comprehend the effects of inelastic behavior of shear connectors on the seismic behavior of composite steel MRFs; and (d) to provide unique experimental data that could serve for the validation of multi-fidelity finite element models for benchmarking the earthquake-induced collapse risk and repairability requirements of composite steel MRFs designed in seismic regions.

5.2 Description of the test program

5.2.1 Test frame

Figures 5.1 and 5.2 show key design aspects of the test frame along with selected images during its construction sequence. The test frame corresponds to a subsystem of a six-story, two-bay composite steel MRF, which is shown in Figure 5.1a. The composite steel MRF was designed according to current European provisions (CEN 2004a; b, 2005b; c) for an importance class II, a reference peak ground acceleration, $a_{gR} = 0.22$ g and ground type D. A behavior factor of $q = 3$ was utilized. A summary of the design of the prototype composite steel MRF is presented in Appendix A. The overall dimensions of the test frame are illustrated in Figure 5.1b. Note that the prototype composite steel MRF was intentionally designed with a centerline span length of 5000 mm due to the space limitation in the available laboratory facilities at EPFL. The span length is somewhat smaller than commonly employed values, which range between 6000 and 8000 mm (Nakashima et al. 2007). However, the geometry can be assumed representative of small construction steel frame buildings. Because the emphasis was on the role of the floor system on the seismic stability of the composite steel MRF, the length of the columns (HEM320), which were designed to remain elastic throughout the loading

history, represent the distance from the mid-height of the first to the second story of the composite steel MRF (i.e. at the location of the inflection points).

The transverse beams featured an IPE270 (i.e., $h_s/t_w = 30$, $b/2t_f = 6.2$ based on nominal geometric properties of the steel cross section) and were connected to the primary girders that featured an IPE360 (i.e., $h_s/t_w = 40.5$, $b/2t_f = 6.7$ based on nominal dimensions) with partial depth extended shear tab connections according to Motallebi et al. (2019). Conventional shear tab connections were used to connect the transverse beams to the beam-to-column web panel zone joints at both the exterior and interior steel columns. The transverse beams to column web panel zone connections were not full restrained. As such, the shear stud connectors on the transverse beams were not designed to transmit horizontal forces to the slab, i.e., mechanism 3 according to EN 1998-1 (CEN 2004a) was not activated. The aim herein was to investigate the slab confinement due to the presence of transverse beams and the corresponding enhancement in the flexural strength of the composite steel beams. The maximum unbraced length in the primary girders was $L_{br} = 1660$ mm; hence, the corresponding member slenderness ratio was $L_{br}/i_z = 43.5$, where i_z is the radius of gyration of the steel beam about its weak axis. Detailed shop drawings of the test frame are shown in Appendix B.

The beam-to-column connections of the composite steel MRF featured four-bolt stiffened end-plate connections. The structural bolts were M30x120 mm Grade 12.9. The bolts were pretensioned to 70% of their minimum specified yield strength (1100 MPa). Figure 5.1c shows the final design of the exterior beam-to-column connection. The extended end-plate connections were sized according to AISC 358-16 (AISC 2016c) because similar procedures at this time were not available in Europe for the seismic design of prequalified stiffened end plate connections. Nevertheless, AISC (2016c) does not allow the use of extended end-plate connections in composite-steel MRFs when these feature beams with nominal depth less than 600 mm. Moreover, according to AISC-358-16 (AISC 2016c), the slab shall be isolated from the columns. Accordingly, the maximum probable moment of the composite cross section was employed instead of that of the bare section in AISC 358-16 (AISC 2016c). Moreover, a steel material overstrength of 1.25 (equivalent to the R_y value according to (AISC 2016a) and an amplification of 1.2 due to cyclic hardening within the anticipated dissipative zones were considered. The center of compression under sagging bending was conservatively assumed to act at the center of the top flange of the steel beam. The presence of the fin stiffener alters the center of compression towards the bottom bolt row under sagging bending. The shear demand on the panel zone from composite steel beams is calculated using the effective depths as proposed by Kim and Engelhardt (2002). A 15 mm doubler plate was welded through partial joint penetration welds per column web side (i.e., two plates in total) of the interior column panel zone to ensure that

this will remain elastic. All members of the test frame were fabricated by S355J2+M steel (except for the doubler plates which were fabricated by S355J2+N). This is a thermomechanically rolled structural steel with a minimum Charpy V-Notch toughness of 27 Joules at -20ºC. Table 5.1 summarizes the chemical composition of the employed structural steels per structural component along with the yield and tensile stresses based on the mill certificate. Moreover, the Carbon equivalent per structural steel (CEV) was calculated based on the respective chemical composition. The Carbon equivalent is 0.36 to 0.43, which ensures a good weldability of the base metal.

Table 5.1 Material properties of the steel components based on the mill certficates

			Chemical Analysis (weight %)																Tensile Test			Impact Test at -20°C
	Steel Grade	Heat No.	C	Si	Mn	P	S	N	Al	Nb	V	Cr	Cu	Ni	Mo	Ti	B	CEV	f_y [MPa]	f_u [MPa]	ε_u [%]	*IE* [J]
HEM320	S355J2+M	85951	0.09	0.24	1.38	0.018	0.021	NA	0.011	0.008	0.041	0.1	0.23	0.14	0.04	NA	NA	0.38	408	526	26.8	151
IPE360	S355J2+M	28525	0.08	0.19	1.39	0.016	0.021	0.008	0.015	0.037	0.007	0.09	0.29	0.14	0.03	0.022	NA	0.36	451	530	30	142
IPE270	S355J2+M	64821	0.11	0.21	1.15	0.012	0.019	0.01	0.027	0.0011	0.05	0.11	0.43	0.15	0.03	0.001	0.0003	0.38	386	524	29	114
		64893	0.12	0.25	1.17	0.012	0.008	0.0109	0.033	0.001	0.05	0.06	0.35	0.0109	0.02	0.001	0.0003	0.37	392	520	28	111
		64894	0.11	0.23	1.16	0.011	0.006	0.0089	0.027	0.0009	0.05	0.07	0.32	0.1	0.02	0.001	0.0003	0.36	392	533	29	107
		64895	0.11	0.22	1.2	0.012	0.006	0.0116	0.03	0.0011	0.05	0.08	0.32	0.11	0.02	0.001	0.0003	0.37	404	534	29	115
Doubler Plate	S355J2+N	00275	0.16	0.19	1.55	0.01	0.002	0.005	0.042	0.001	0.003	0.04	0.06	0.05	0.002	0.002	NA	0.43	408	557	28	163

CEV	Equivalent carbon content
f_y	Yield strength
f_u	Ultimate tensile strength
ε_u	Elongation
IE	Average absorbed impact energy
NA	Not available

All welds between the beams to the end plates were placed using 1.2 mm FILARC/PZ61-2 welding electrodes. The measured average material yield strength of the steel filler was 488 MPa. Ultrasonic testing (UT) revealed that the weld defects conformed to the acceptance level for execution class 2 (EXC2) and quality level C as per EN 1090-2 (CEN 2018). Moreover, the welds had a Charpy-V Notch toughness of 69 J at -20 °C. Therefore, they were compliant with the toughness requirements according to AISC 358-16 (AISC 2016c). Figure 5.2a and b show one exterior and the interior beam-to-column connection after installation of the primary girders and the transverse beams. The mill test certificates of the structural steel materials as well as the welding procedure specifications are found in Appendix C.

The floor slab had a total thickness of 140 mm and comprised a 56 mm deep profiled steel deck (Cofrastra 56). The ribs of the steel deck were oriented parallel to the IPE360 girders as shown in Figure 5.2c and d; hence, the rib shape efficient factor was, $k_r = 1.0$. The width of the slab was 1700 mm and was intentionally chosen to be larger than the effective width of the slab under sagging (744 mm) and hogging (992 mm) bending as per EN 1998-1 (CEN 2004a). The slab was reinforced in the longitudinal and transverse directions with grade B500B rebars (i.e., nominal yield stress, $f_y = 500$ MPa). Two layers of $\phi 10$ longitudinal rebars were spaced at 150 mm across the slab width. Transverse reinforcement comprised five $\phi 10$ seismic rebars that were placed within a column depth from the face of the columns (CEN 2004a), as well as $\phi 8$ rebars spaced at 150 mm over the entire length of the slab. Figure 5.2e shows a snapshot of the slab reinforcement after the completion of installation.

Two rows of headed shear studs (diameter $d_{sc} = 16$ mm, and height $h_{sc} = 125$ mm) were welded to the top flange of the primary girders to achieve full composite action. The shear studs were considered to be ductile with $h_{sc}/d > 4.0$ and did not require a reduction in their shear resistance ($k_t = 1.0$) due to the presence of a profiled steel deck according to CEN (2004b). No studs were placed in the vicinity of the columns over 540 mm, which was equal to 1.5 times the beam depth, d_b, to prevent premature fracture within the anticipated dissipative zones due to strain localization (AISC 2016c; Cordova and Deierlein 2005; FEMA 2000b). Note that the distance $1.5d_b$ is less than $2b_{eff}^{+}$ required by EN 1998-1 (CEN 2004a) to disregard composite action. Furthermore, the slab was in contact with the column flanges. Therefore, the transmission of the composite steel beam moments was allowed at the beam-to-column connections. Furthermore, the 25% reduction in the resistance of the shear studs according to EN 1998-1 (CEN 2004a) provisions was intentionally waived based on supplemental continuum finite element analyses prior to the testing program (El Jisr et al. 2020).

The employed concrete type was grade C25/30 (i.e., characteristic cylinder compressive strength, $f_{ck} = 25$ MPa). It is noteworthy stating that the ductility of the composite steel beam under sagging bending, which is characterized by the ratio x_{pl}^{+}/h (x_{pl}^{+} is the position of the plastic neutral from the top of the slab and h is the total depth of the composite cross section including the slab) is 0.31. This value is higher than the maximum limit in EN 1998-1 (CEN 2004a) of 0.27, which assumes a concrete crushing strain of $\varepsilon_{cu} = 0.0025$ and a nominal yield strain $\varepsilon_y = 0.0017$ (Elghazouli 2015). However, the latter has been put in place based on past experimental studies that do not account for the effect of slab confinement on the crushing strain (Doneux 2002; Plumier and Doneux 2001). According to Plumier and Doneux (2001), slab confinement can increase ε_{cu} by about two times; hence, ε_{cu} was assumed to be 0.0048 and the maximum limit was assumed to be 0.48 to design the test frame. Details of the composite cross section are shown in Figure 5.1d and e. The concrete slab was casted within two hours after receiving the concrete mix. Figure 5.2f and g show snapshots of the concrete casting and finishing of the concrete surface. A professional contruction company was hired for casting to ensure analogous conditions with standard practice. After the completion of casting, the slab was wrapped with nylon as shown in Figure 5.2h for the curing process.

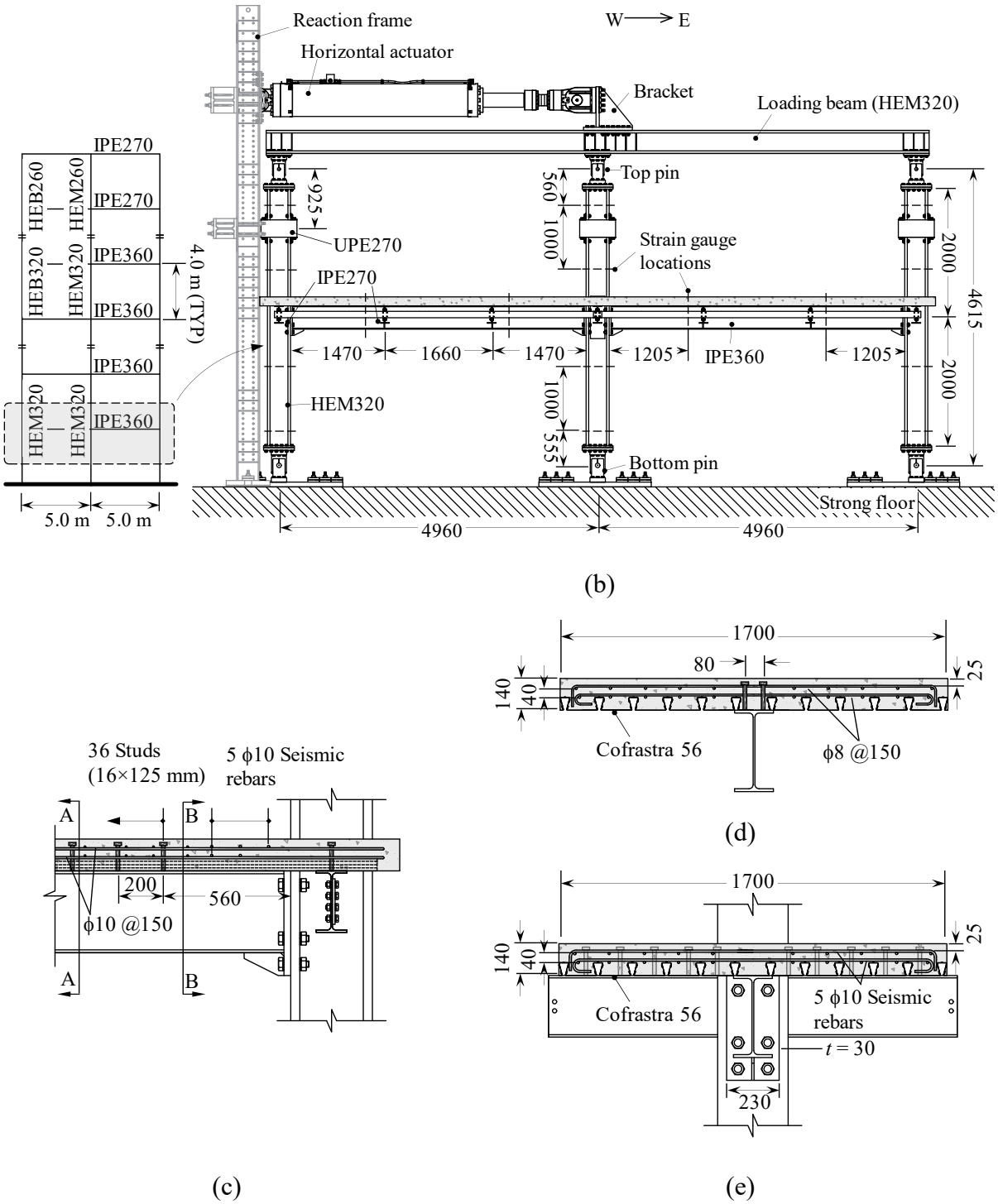

Figure 5.1 Test frame: (a) prototype composite steel MRF; (b) south elevation view; (c) composite steel beam-to-column connection; (d) Section A-A; (e) Section B-B (dimensions in mm)

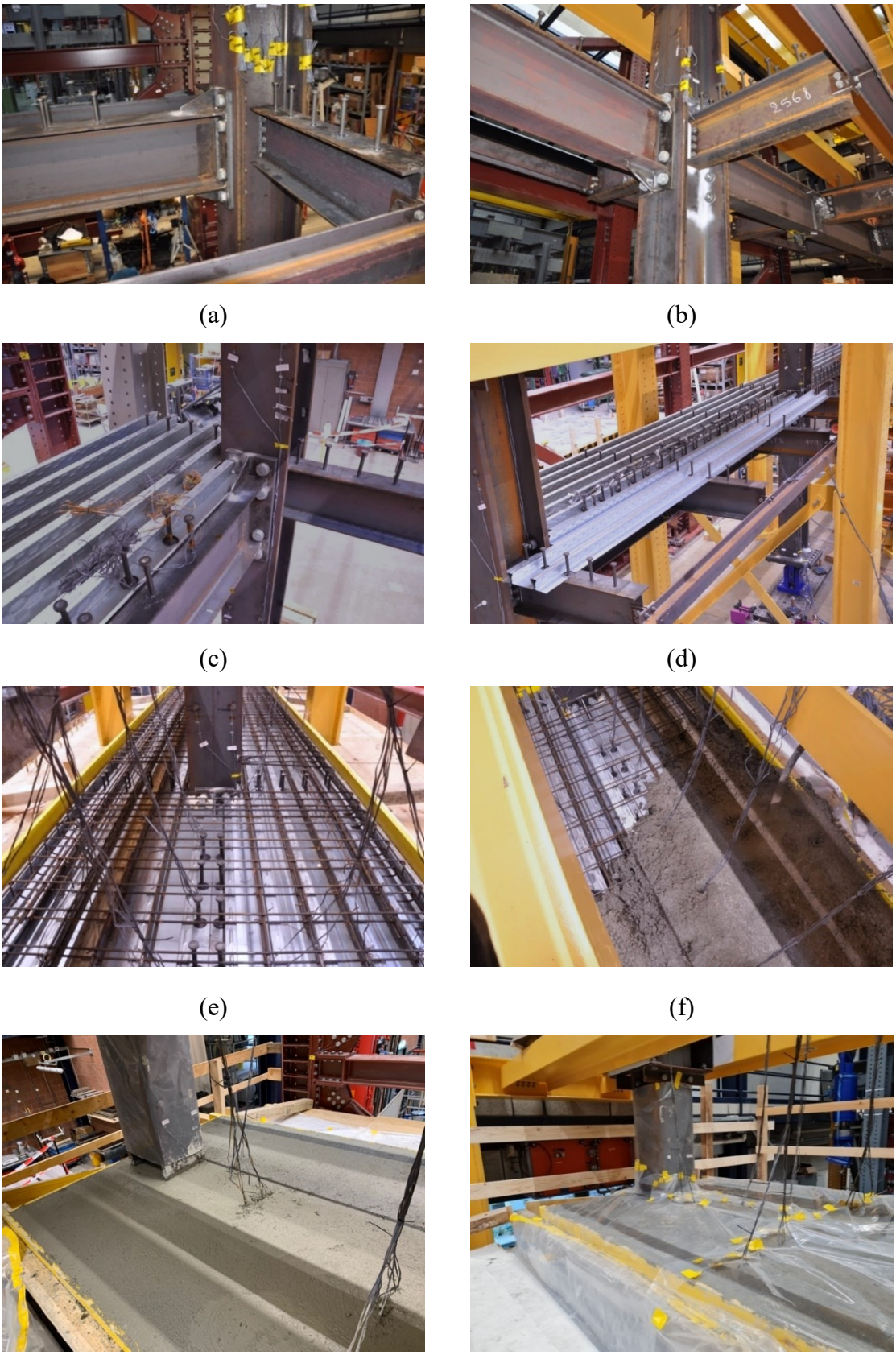

(a) (b)

(c) (d)

(e) (f)

(g) (h)

Figure 5.2 Test frame under construction

5.2.2 Test apparatus

The test program was conducted at the Structural Engineering Group (GIS) Laboratory at École Polytechnique Fédérale de Lausanne (EPFL). Figure 5.3 shows the global view of the test apparatus. Structural pins were bolted at the column ends through adapter steel plates to idealize the inflection points of the steel columns. In this case, the force redistribution within the columns is not accurately represented throughout loading. Nevertheless, since the aim of this experimental program was to investigate the role of the floor system on the seismic stability of composite steel MRFs, the assumption is deemed reasonable. The structural pins allowed only the imposition of planar loading. The effects of bidirectional loading on the behavior of the joints were not addressed in this experimental program. Moreover, no gravity loads were applied to the slab and columns. However, the use of short construction implies that the effective width of the slab and demand on the shear stud connectors is not strongly influenced by the presence of gravity loads on the slab as opposed to long construction. This is not the case for longer constructions where the gravity load in the composite steel beams is likely to have a strong influence in the shear stud performance.

The bottom pins were mounted on the strong floor via 75 mm thick base plates while the top pins were connected to an axially 'rigid' loading beam. The axial stiffness of the loading beam was chosen to be four orders of magnitude higher than that of the primary girders of the test frame in order to achieve rigid diaphragm action in the loading plate. This ensured that the horizontal actuator, which was connected to the loading beam through a bracket, imposed the same lateral story drift ratio (SDR) at each column. It is important to note that the choice of the stiffness of the loading beam affects the level of axial forces that are developed in composite steel beams (Leon and Deierlein 1996). Herein, the aim was to simulate rigid diaphragm action akin to Nakashima et al. (2006, 2007) and Zerbe and Durrani (1989). This configuration is suitable for investigating the effect of axial restraint on beam axial shortening. In reality, the floor diaphragm is not axially rigid, and the bottom columns can potentially move relative to each other. The effect of axial restraint may be exaggerated. However, the authors believe that this configuration is deemed reasonable, especially in first stories where the foundations cannot expand (Zerbe and Durrani 1989). The loading beam was connected to a 2500 kN +/- 2400 mm stroke servo hydraulic actuator, which was in turn connected to a 'stiff' reaction frame to transfer the horizontal load safely to the strong floor (see Figure 5.3).

A lateral support system was designed to laterally brace the columns near their top end by means of a customized UPE270 bracket as shown in Figures 5.1b and 5.3. The IPE270 transverse beams (see Figure 5.1b), on the North and South side of the test frame were bolted to HEA100 beams at their free ends. The aim was to replicate the continuity of transverse beams in an actual composite steel

MRF and ensure that out-of-plane displacement was prevented at their ends. The HEA100 beams were laterally braced by the columns of the lateral support system. Teflon sheets were glued to the surfaces in contact in order to minimize friction between all the sliding surfaces discussed above.

The test frame was whitewashed with hydrated lime to qualitatively detect any sign of yielding during testing. Moreover, the slab was painted with a thin layer of white water-based latex paint to provide the contrast required for tracking the surface strains using digital image correlation (DIC).

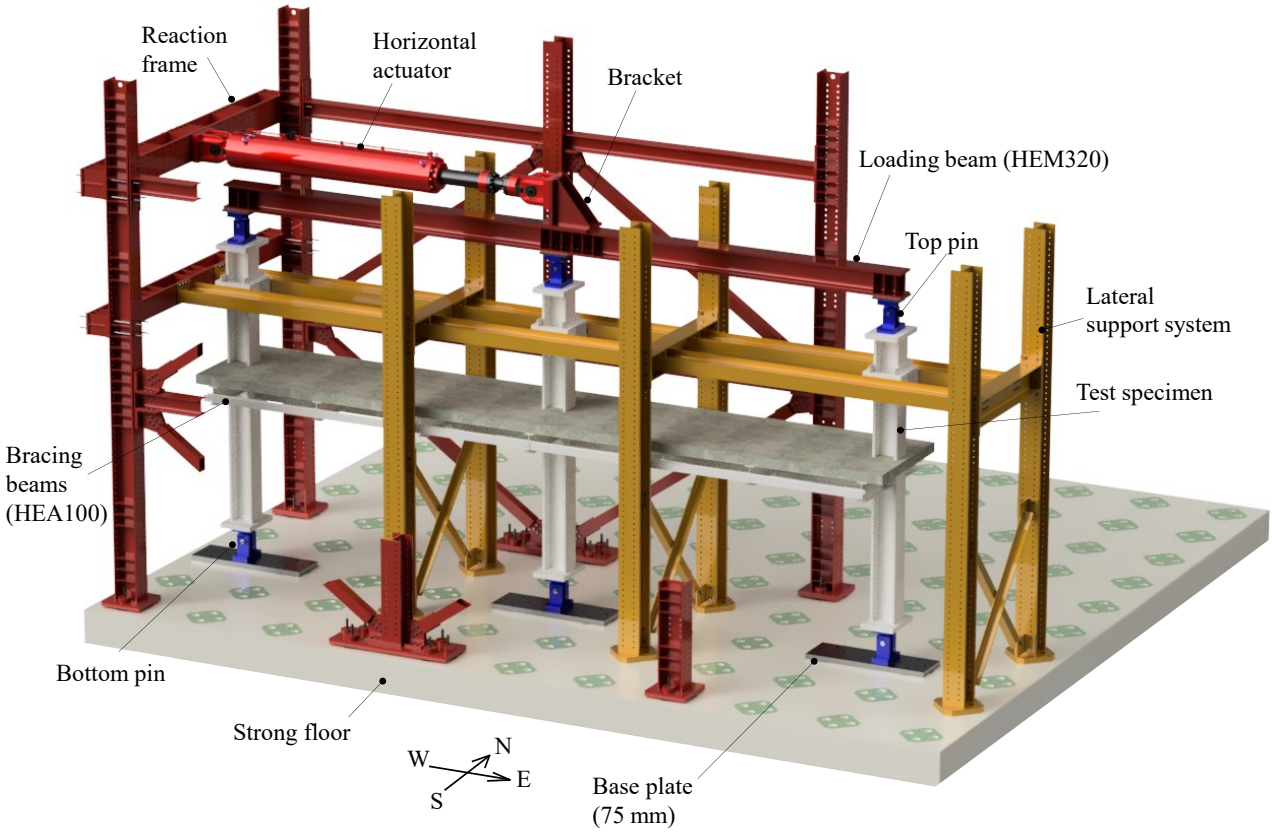

Figure 5.3 Global view of the test apparatus

5.2.3 Instrumentation

A unique feature of the experimental program is that it employed dense instrumentation to measure both the local and global force/deformation demands among others. In total, the test frame carried 338 sensors (including the actuator load cell and displacement transducer), most of which were strain gauges. A detailed instrumentation plan of all the sensors along with detailed procedures on how various quantities reported herein after were deduced based on the acquired data can be found in Appendix D.

The structural steel members were instrumented with seven uniaxial strain gauges at selected cross sections along their length as shown in Figure 5.4a and b in order to deduce the member forces (i.e., axial load, shear and bending). Figure 5.1b indicates the precise locations of the strain gauges along the length of the respective members. The flexural demands in the composite steel beams were deduced by assuming that the slab force acts on the centerline of the concrete above the steel deck. This is analogous to the approach presented in Nakashima et al. (2007). The column shear forces were derived from the deduced moments by assuming a linear bending moment diagram along the column length. Similarly, the beam shear forces were computed by assuming that the bending moment in the composite steel beams varies linearly between the two instrumented cross sections (see Figure 5.1b).

The beam and column rotations were derived from a set of three inclinometers that were installed at each beam-to-column connection. The inclinometers were attached to customized steel plates that were fabricated in GIS of EPFL. These plates were mounted on the beam-to-column connections as shown in Figure 5.4c. At each beam end, two string potentiometers were placed to measure the beam axial shortening and rotation over a theoretical distance of 1000 mm away from the face of the end plates (see Appendix D for the exact locations). Furthermore, a pair of linear variable displacement transducers (LVDTs) installed in a V-shaped configuration, was used to measure the panel zone shear distortions. Out-of-plane displacements of the end plates were also tracked using LVDTs that were placed near the bottom stiffeners of the end plate connections. Moreover, a total of 46 light-emitting diodes (LED bulbs) were attached to the interior joint region and tracked using an LED Coordinate Tracking System as illustrated in Figure 5.4d. The measurements from this system were also employed to verify those deduced by the string potentiometer and LVDT measurements.

The slip demands in the beam-slab connections were measured along each beam using three LVDTs placed at a theoretical distance of 760 mm from the face of all the columns, and 2160 mm from the face of the West exterior and East interior columns (see Appendix D for the measured locations). Figure 5.4d shows indicatively two of these LVDTs installed on each side of the interior joint. Six shear studs in the West span (at 840 mm and 3240 mm from the face of the columns) were instrumented with four pressure gauges along the height of their shank. Furthermore, 10 shear studs in the East span (at 840 mm, 1440 mm, 2040 mm, 2640 mm and 3240 mm from the face of the columns) were instrumented with six uniaxial strain gauges along the height of their shank. The slab-column interaction at the interior and exterior beam-to-column connections was traced using a total of four pairs of high-speed digital image correlation (DIC) cameras. The cameras measured the strain demands at the surface of the slab and tracked the evolution and propagation of cracks. Information regarding the resolution of the DIC system and the associated level of noise is presented in Appendix

D. Tie action in the seismic rebars was measured with uniaxial strain gauges that were glued at the center of each seismic rebar. In the West span, the axial strain was measured continuously over 3600 mm of 10 longitudinal rebars on the South side of the test frame using a fiber optic measurement (FOM) system (see Figure 5.4e).

Finally, seven LVDTs were deployed to critical locations of the test apparatus to ensure that there was no slip in any of the assembled connections during loading, which was confirmed by the measurements during the loading stage.

During the tests, data was lost in some sensors. The lost data corresponds to sensors that were damaged, detached or, in the case of LED bulbs, hidden. The sensors are presented in detail in Appendix D.

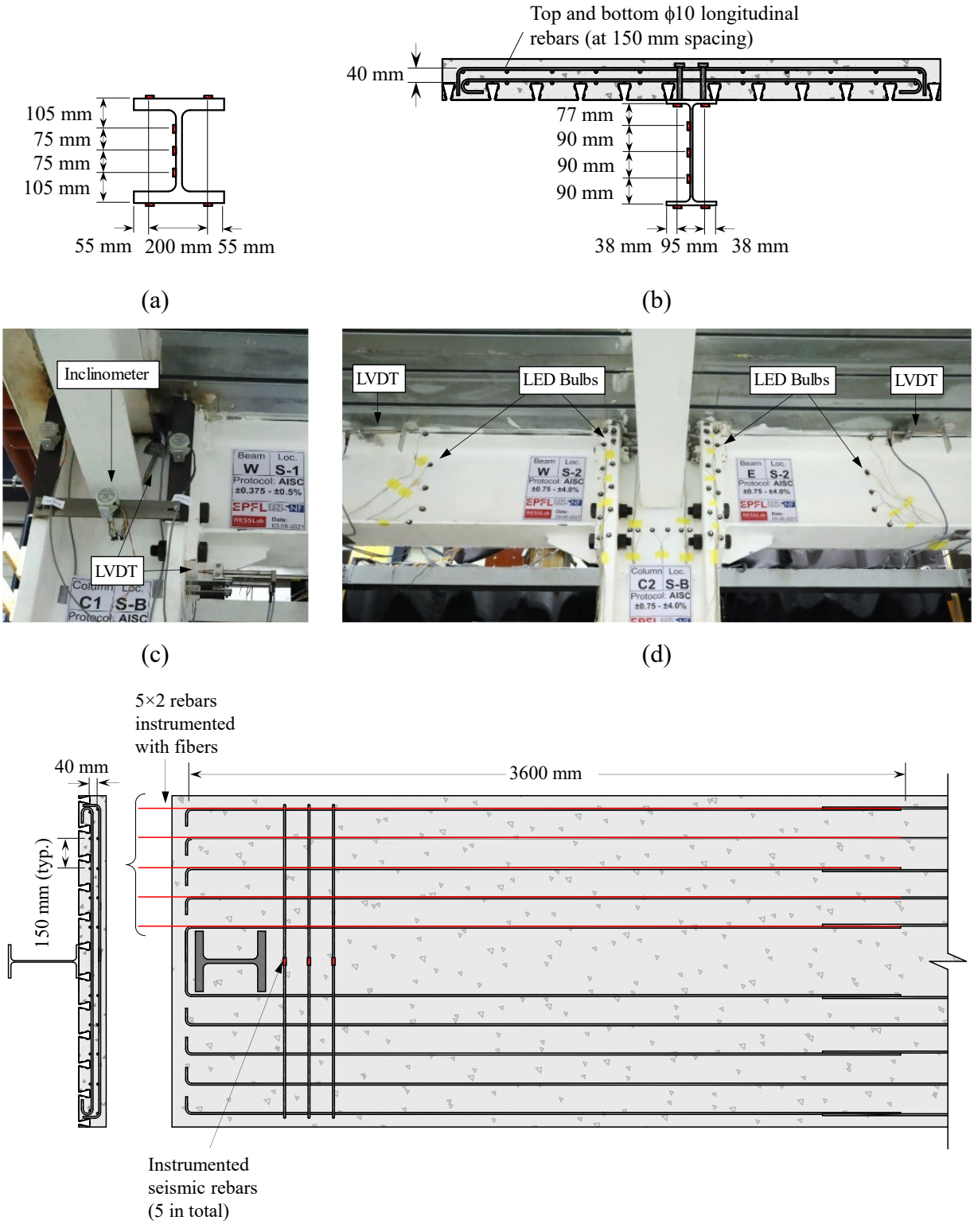

Figure 5.4 Test frame instrumentation: (a) column section strain gauge distribution; (b) composite steel beam cross section strain gauge distribution; (c) inclinometers installed in the exterior joint; (d) indicative instrumentation installed in the interior joint; (e) instrumented slab reinforcement in the West exterior joint

5.2.4 Ancillary tests

Ancillary tests were conducted in order to measure the actual material properties of all the structural components of the test frame. The yield and ultimate stresses of the IPE360 beams, the HEM320 columns, the interior column web panel zone doubler plates and the slab longitudinal reinforcement were obtained by standard tensile coupon tests according to ASTM (2016). Each value reported in Table 5.2 is obtained by averaging the measured values from five tensile coupons. Table 5.2 shows that the measured yield and ultimate stresses are higher than the nominal values for the beams, columns, and doubler plates. Moreover, the test results suggest that the measured values are somewhat smaller than those from the mill certificates, which are summarized in Table 5.1.

For S355J2 steel, the $f_{y,m}/f_y$ ratios are slightly less than 1.17, which is reported in Braconi et al. (2013) for nominally identical European structural steels. These values are somewhat consistent with the R_y values for A992 Gr. 50 steel according to Table A3.1 in AISC 341-16 (AISC 2016a). For the steel reinforcement, the yield overstrength is within 5% of the specified nominal yield stress. Moreover, the measured ultimate-to-yield stress ratio of the rebars ($f_{u,m}/f_{y,m}$) exceeds the minimum ratio (1.08) specified in EN 1992-1-1 (CEN 2004c) for grade B500B rebars.

Moreover, uniaxial cyclic tests were conducted on round coupons that were extracted from the steel beams and column to infer representative material properties under inelastic cyclic straining. The experimental procedures discussed in de Castro e Sousa et al. (2020) were employed for this purpose. Figure 5.5 illustrates the true stress - true strain cyclic behavior of round coupons extracted from the IPE360 beam flange for four representative uniaxial inelastic cyclic loading protocols. The test results confirmed that the cyclic hardening of the steel material within the dissipative zones of the steel beams was analogous with those reported in prior studies (de Castro e Sousa et al. 2020).

The ultimate tensile stress of the M30 Grade 12.9 bolts was obtained by testing four structural bolts. The value of the ultimate tensile stress and bolt elongation at fracture are reported in Table 5.3. All structural bolts attained an ultimate tensile stress that exceeded the minimum specified nominal value (1220 MPa).

Table 5.2 Measured and specified material properties of the steel profiles, rebars and concrete

Component		Grade	Measured material properties			Specified nominal material properties		$\frac{f_{y,m}}{f_y}$	$\frac{f_{u,m}}{f_u}$
			E_m [GPa]	$f_{y,m}$ [MPa]	$f_{u,m}$ [MPa]	f_y [MPa]	f_u [MPa]		
IPE360 (Beam)	Flange	S355J2+M	204	375	528	355	510	1.06	1.04
	Web		203	419	563			1.18	1.10
HEM320 (Column)	Flange	S355J2+M	200	382	500			1.08	0.98
	Web		203	391	499			1.10	0.98
Double Plate (15 mm)		S355J2+N	203	393	527			1.11	1.03
ϕ10 Rebars		B500B	193	520	600	500	540	1.04	1.11
Concrete*		C25/30							

*Material properties derived from cylinder compression tests:
14 day compressive strength, $f_{c,14}$ = 39 MPa
28 day compressive strength, $f_{c,28}$ = 41 MPa; Elastic modulus $E_{c,28}$ = 35 GPa
Day of third loading stage, $f_{c,m}$ = 49 MPa, Elastic modulus $E_{c,m}$ = 39 GPa

Table 5.3 Measured material properties for the M30 Grade 12.9 bolts

Nb.	#1	#2	#3	#4	μ	σ
d_{bo} [mm]	29.6	29.8	30.0	29.8	29.8	0.16
L_o [mm]	119.9	120.8	120.8	120.0	120.4	0.49
L_f [mm]	123.1	125.3	126.4	124.2	124.8	1.42
$\varepsilon_{u,b}$ [%]	2.7%	3.7%	4.6%	3.5%	3.6%	0.8%
F_u [kN]	733	753	732	745	741	10
$f_{u,b}$ [MPa]	1307	1342	1304	1329	1321	18

d_{bo}	Full bolt diameter
L_o	Initial length of the bolt measured from the bottom of the head to the tip of the shank
L_f	Final length of the bolt measured from the bottom of the head to the tip of the shank
$\varepsilon_{u,b}$	Bolt elongation at fracture
$F_{u,b}$	Bolt ultimate load
$f_{u,b}$	Bolt ultimate tensile stress assuming the threaded area to be $A_s = 561$ mm^2
μ	Mean
σ	Standard deviation

To deduce the measured material properties for concrete, standard compression tests were conducted using 16×32 cm cylinders at 14, 28 days and at the last day of testing. The cylinders were equipped with three extensometers to measure the stress-strain behavior according to ASTM C469 (ASTM 2014). Figure 5.6 shows the measured stress-strain response at 28 days and at the last day of testing. The average compressive strengths at characteristic days after concrete casting are shown in Table

5.2 along with the elastic moduli derived according to ASTM C469 (ASTM 2014). Referring to Figure 5.6, the concrete compressive strain at the peak stress is, on average, equal to 0.2% at 28 days and 0.22% at the last day of testing. This value is consistent with the value in EN 1992-1-1 (CEN 2004c) for C25/30 concrete (i.e., 0.21%). However, the measured compressive strength of concrete is around twice as high as the characteristic cylinder compressive strength of C25/30 ($f_{ck} = 25$ MPa).

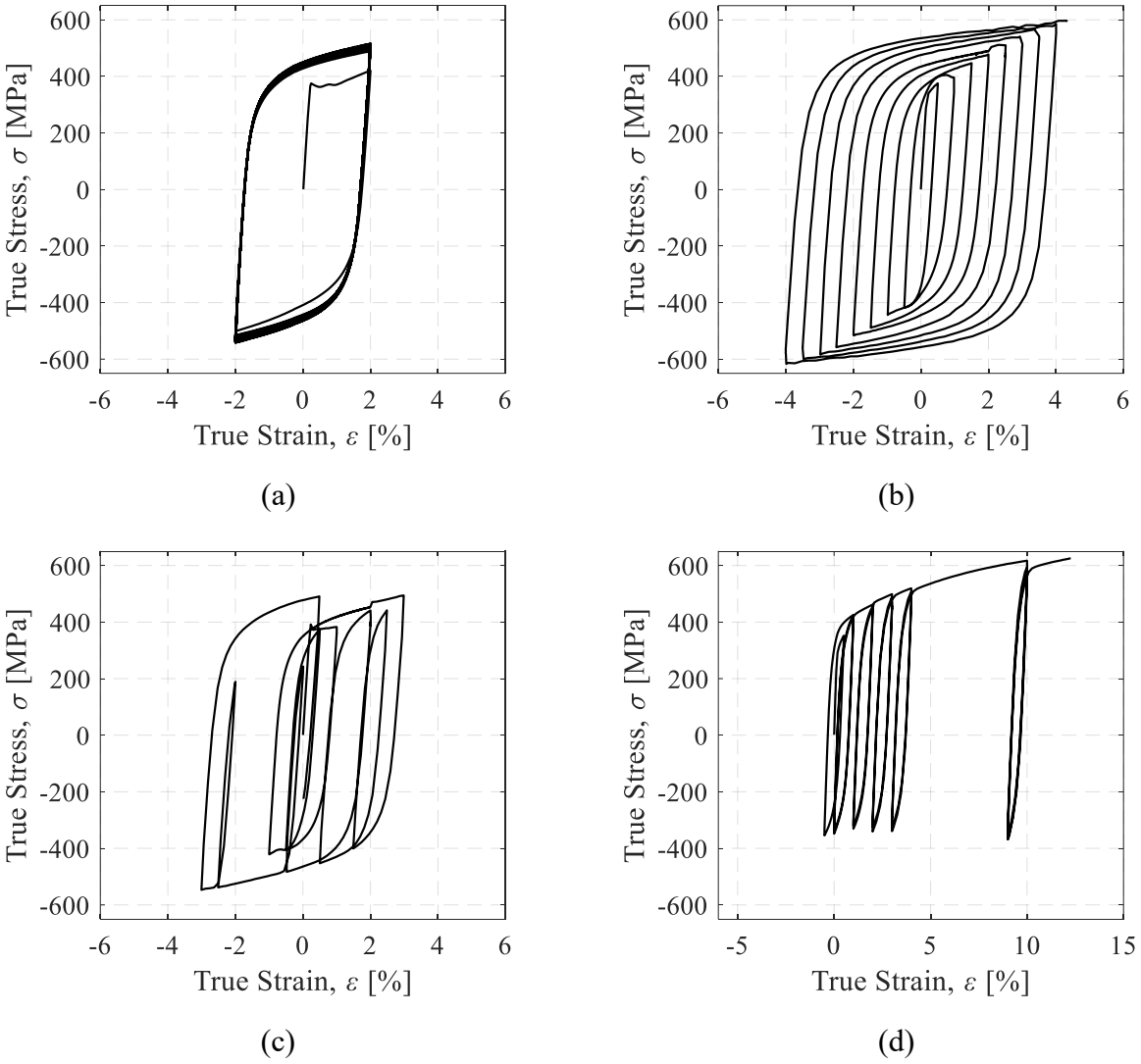

Figure 5.5 Cyclic true stress-strain behavior of the IPE360 beam flange coupons for four representative uniaxial strain-based loading protocols: (a) load protocol 5; (b) load protocol 6; (c) load protocol 9; (d) load protocol 10

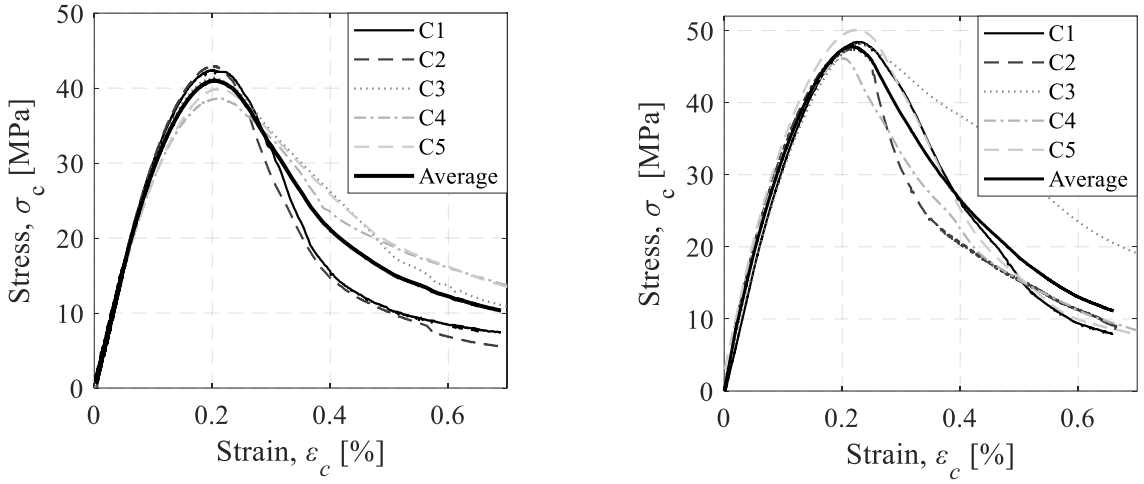

Figure 5.6 Stress-strain behavior of the slab concrete, (a) at 28 days after casting; (b) at the last day of testing

Standard monotonic and cyclic push-out tests were also conducted to deduce the shear-slip behavior of the beam-slab connections. The monotonic push-out test was conducted according to EN 1994-1-1 (CEN 2004b). For the cyclic push-out test, the top of the slabs was restrained with a 20 mm thick steel plate that was anchored to the supporting beam with ϕ24 Grade 10.9 threaded rods as shown in Figure 5.7a. The European Convention for Constructional Steelwork (EECS) loading protocol (EECS 1986) was employed. Referring to Figure 5.7b, the monotonic push-out test showed that the characteristic slip capacity defined according to EN 1994-1-1 (CEN 2004b) exceeds 6 mm; hence, the behavior of the headed studs is considered to be ductile. In the cyclic push-out test, the shear resistance of the beam-slab connection degraded quickly. Shear stud fracture due to ultra-low cycle fatigue was the ultimate failure mode. The specimen lost its shear carrying capacity at 6.6 mm. Nevertheless, it is important to note that the EECS protocol imposes large cumulative slip demands, which are not representative of the actual demands seen in beam-slab connections as part of actual composite steel MRFs. The behavior of the beam-slab connection from the cyclic push-out test is contrasted with that of the test frame later on.

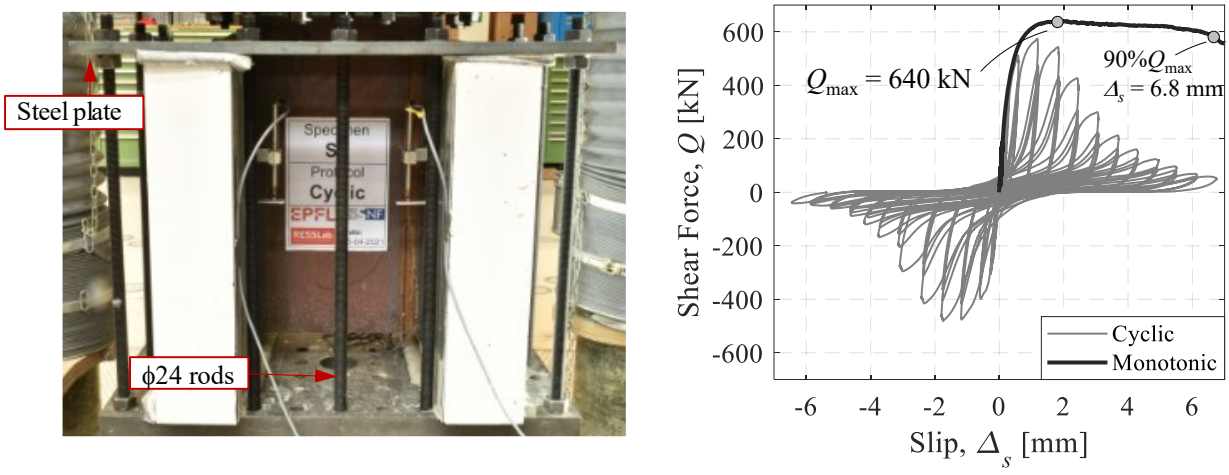

(a) (b)

Figure 5.7 Beam-slab connection push-out tests: (a) cyclic push-out test apparatus; (b) comparison of the monotonic and cyclic behavior

5.2.5 Imposed loading histories

The test frame was subjected to quasi-static cyclic loading that comprised three lateral loading protocols, which were subjected to the test frame one after the other as shown in Figure 5.8a. The first one was the AISC symmetric cyclic loading protocol (AISC 2016a) up to a lateral drift demand of 4% rads. This protocol aims at assessing if connection prequalification requirements are met. Moreover, the test results would provide a basis of comparisons with prior subassembly tests on composite beam-to-column connections standard cruciform subassemblies.

The second lateral loading history that was employed as part of the testing program, was the SAC near-fault protocol (Krawinkler et al. 2000). In this case, the cyclic performance of the test frame was evaluated under asymmetric lateral loading, which is characteristic of near-fault ground motions. This is particularly important for the considered test frame and overall testing program because the selected design location is prone to near-fault ground motions based on rigorous probabilistic seismic hazard analysis that was conducted for the design site El Jisr et al. (2021b).

Finally, during the third loading stage, the collapse behavior of the test frame was assessed by employing a collapse-consistent protocol that mimics the ratcheting behavior of MRFs prior to incipient collapse (Lignos et al. 2011, 2013; Suzuki and Lignos 2021). The test frame was pushed up to a lateral drift demand of 15% rads at which two of the test frame's connections lost their lateral load carrying capacity. The three selected loading histories are suitable for providing quantitative data for the validation of numerical models from the onset of structural damage through collapse.

5.3 Experimental results and discussion

This section presents the results of the experimental program. The experimental data are publicly available in the Zenodo public repository (doi: https://www.doi.org/10.5281/zenodo.5884983) and at resslab-hub.epfl.ch. First, the global hysteretic behavior of the test frame is described in a quantitative manner. The main events that occurred during the loading history are highlighted in Figure 5.8a. The hysteretic response of the composite steel beams is then discussed in detail along with the primary damage mechanisms that influence the flexural resistance from the onset of damage till incipient collapse. Emphasis is put on the effects of slab confinement and transverse beams on the flexural demands of the composite steel beams. Furthermore, the influence of the slab restraint and framing action on the behavior of the composite steel beams is described and quantified. Finally, the crack patterns in the slab are depicted along with the load transfer mechanisms between the slab and the test frame columns. Supplementary results of the experimental program are presented in Appendix E.

5.3.1 Global response

Figure 5.8a highlights the main sequence of events that occurred throughout the entire loading history leading to incipient collapse. Figure 5.8b shows the base shear of the test frame versus the SDR up to 15% rads. The discussion is also facilitated by Figure 5.9, which shows the deduced moment versus chord rotation response at both ends of the composite steel beams. In this figure, all moments were calculated at the face of the end plates.

Referring to Figure 5.8b, the elastic stiffness of the test frame was 45475 kN/rad. This value was found to be more than 45% higher than that of the corresponding bare frame (i.e., prior to casting of the slab). The lateral stiffness of the bare frame was obtained by preliminary elastic tests that were conducted prior to concrete casting. The observed difference corroborates with findings from prior experimental work (El Jisr et al. 2019).

During the 1% drift amplitude of the AISC symmetric loading protocol, flaking of the whitewash was observed in the bottom flange of the beams at the face of the stiffeners, thereby indicating flexural yielding at the same location. The flaking occurred under hogging bending and propagated to the beam web from the bottom flange. Upon further loading, only light flexural cracks were observed in the slab under hogging bending. These were only evident at the exterior beam-to-column connections. Moreover, no crushing of concrete occurred. Slab confinement due to the presence of transverse

reinforcement in the vicinity of the column prevented the concrete from crushing as intended (Braconi et al. 2007; Plumier and Doneux 2001). Interestingly, it is hypothesized that the transverse beams framing the joints and the primary girders, also contributed to the flexural resistance of the joints up to a lateral drift ratio of about 2% to 3% rads. While this phenomenon is elaborated in section 5.3.5, quantification of the extent of the contribution to the flexural resistance requires further experimental investigation.

The bottom row of structural bolts of the end plate connections was deemed critical to fracture because of the above contributions to the flexural resistance of the beam-to-column connections along with the considerable overstrength in the concrete compressive strength (see Table 5.2) relative to the nominal value of 25 MPa. Accordingly, for safety reasons, it was decided to install a customized assembly to ensure that the bolts would have been caught in case of bolt fracture following the 2% loading cycles of the AISC symmetric cyclic loading protocol. These are shown in Figure 5.10a and b at 2% and 4% rads, respectively.

Referring to Figure 5.8b and Figure 5.9, the base shear and moment demands at the composite steel beams were capped at the 3% lateral drift amplitude of the symmetric cyclic loading protocol. Particularly, the shear demands on the headed shear studs were capped. The peak base shear, $V_{max} = 643$ kN, was attained at the same drift amplitude (see Figure 5.8b). Moreover, local buckling occurred at the bottom flange of the composite steel beams that initiated during the 3% loading cycle and became evident at a lateral drift ratio of 4% rads (see Figure 5.10b). Light spalling of concrete at the column face also occurred during the same drift amplitude. Base shear strength deterioration occurred in a symmetric manner (see Figure 5.8b). The composite steel beams experienced asymmetric flexural strength deterioration due to concrete spalling under sagging bending and local buckling of the bottom flanges of the steel cross section under hogging bending, as depicted in Figure 5.9. After the completion of the symmetric cyclic loading protocol, the customized assemblies that were placed around the bolts were removed because of the localization of the inelastic deformations within the dissipative zone of the composite steel beams.

Referring to the SAC near-fault loading protocol, the hysteretic behavior of the test frame was stable even when the lateral drift amplitude was widened to 6% rads (see Figure 5.8b). The subsequent lateral drift reversals demonstrated that local buckles in the bottom flanges/web of composite steel beams fully straightened (see Figure 5.10c and d). Moreover, during this loading protocol, the rate of cyclic deterioration in flexural strength at the beam ends was fairly slow as shown in Figure 5.9. The above were mainly attributed to the axial restraint provided by the slab and framing action as

discussed later on. At the end of the SAC near-fault loading protocol, the test frame was able to maintain at least 80% of its peak base shear resistance. Figures 5.8b and 5.9 suggest that cyclic deterioration in story shear and flexural strength was less evident under loading sequences representing the anticipated seismic demands from near-fault ground motions. The above observations corroborate well with prior related experimental findings that examined the influence of the loading protocol on the hysteretic behavior of structural steel members, beam-to-column connections and steel MRFs (Elkady and Lignos 2018b; Krawinkler 2009; Lignos et al. 2011; Suzuki and Lignos 2021; Uang et al. 2000).

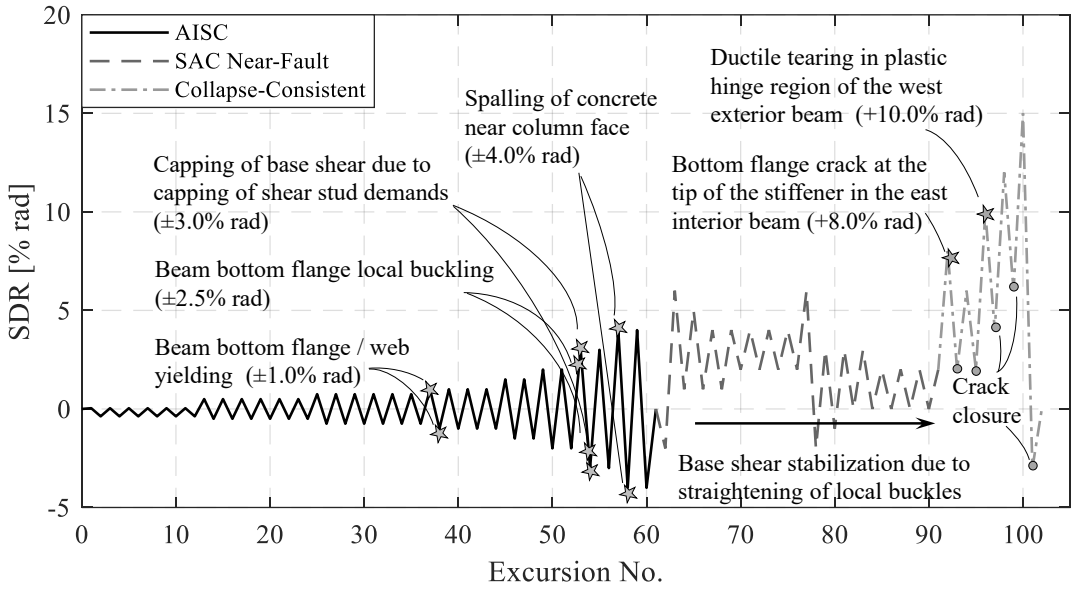

(a)

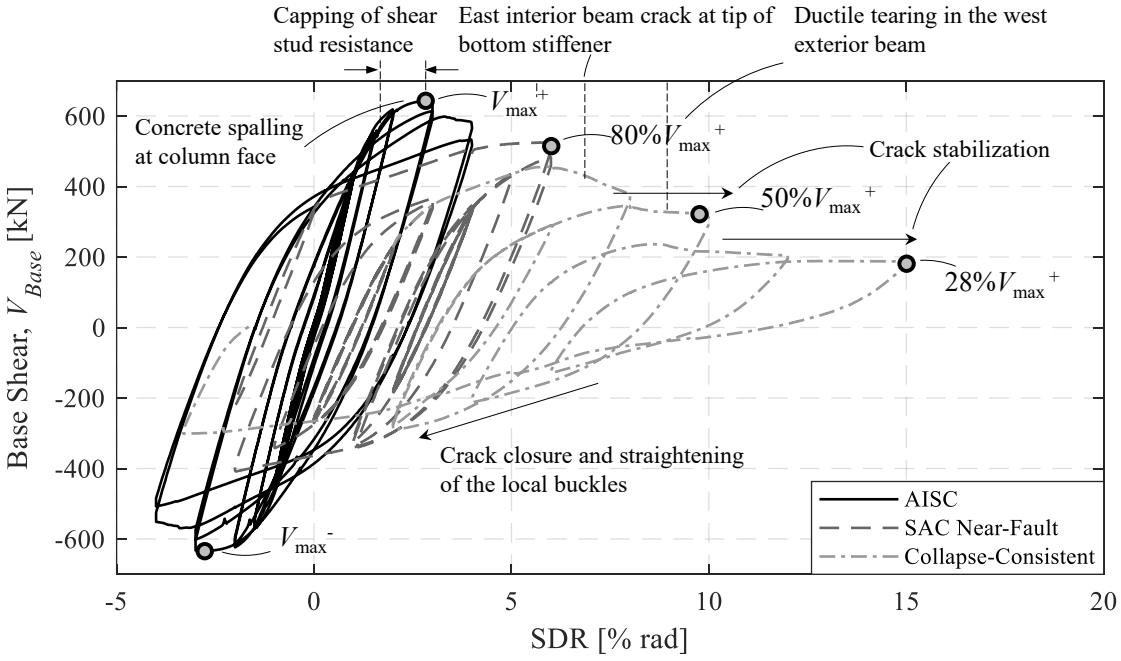

(b)

Figure 5.8 Employed loading protocol and base shear versus story drift ratio of the test frame

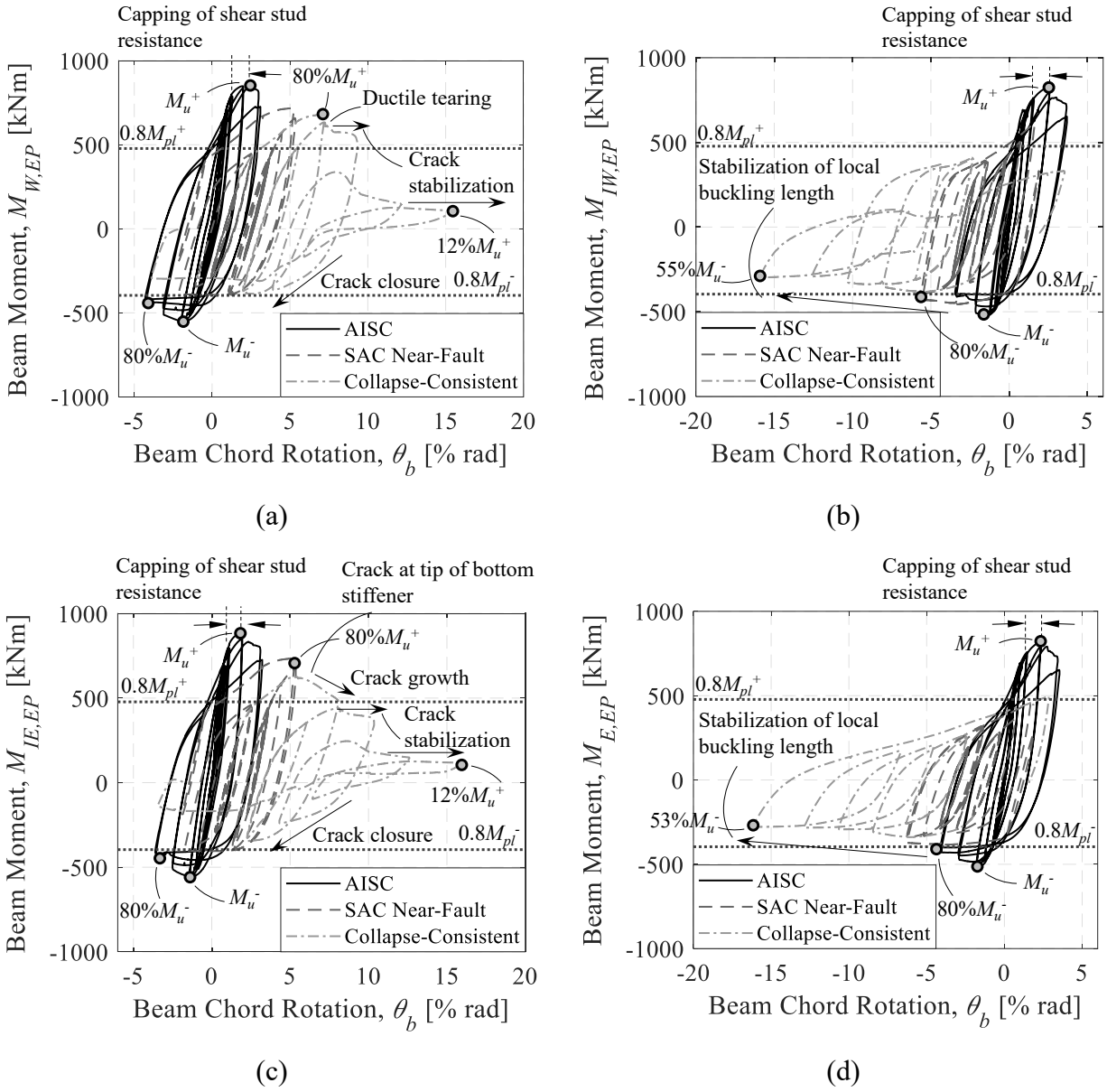

Figure 5.9 Hysteretic behavior of the composite steel beams throughout the loading history; (a) West exterior joint; (b) West interior joint; (c) East interior joint; (d) East exterior joint

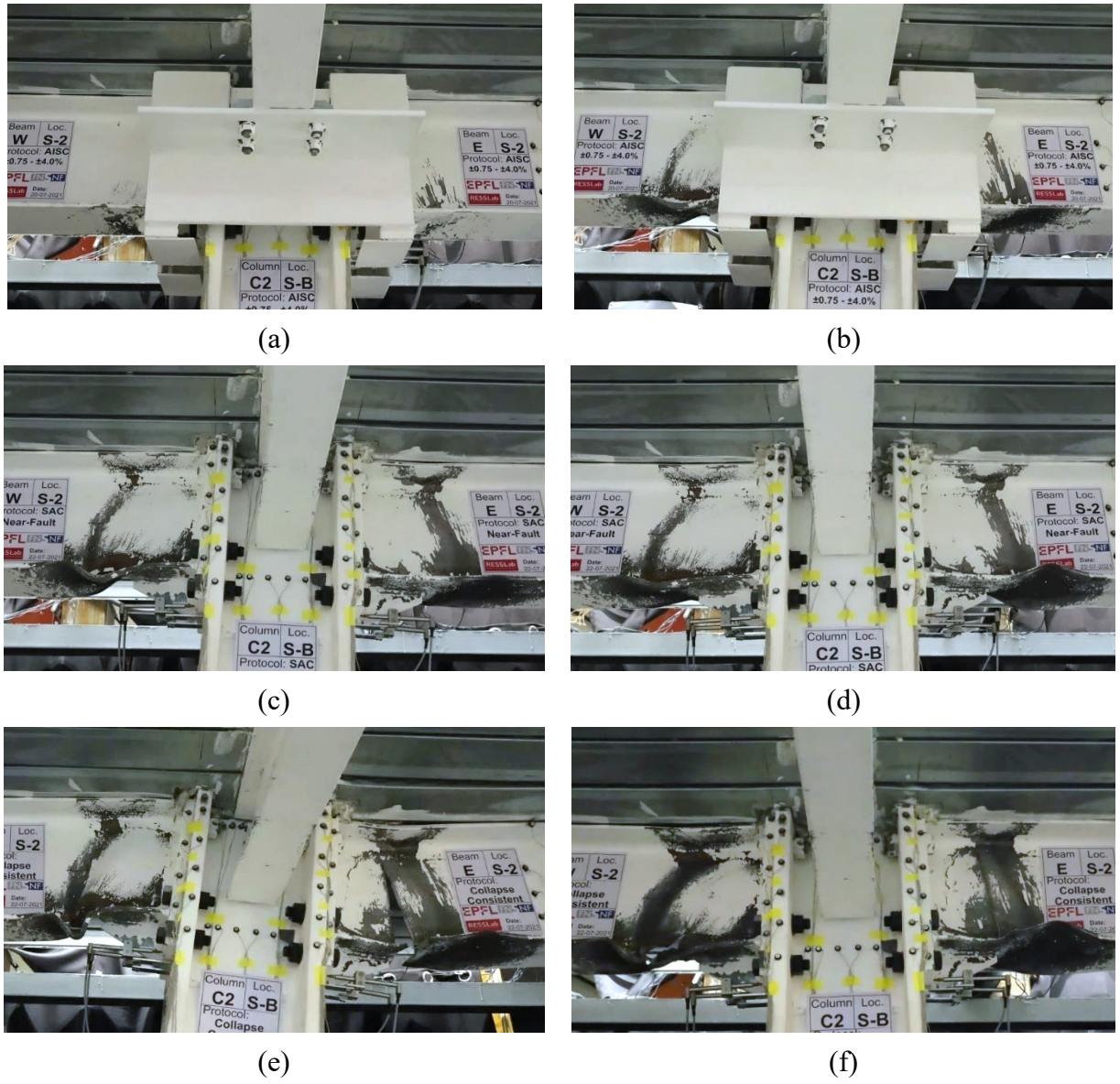

Figure 5.10 Main test events at the interior joint at selected lateral drift demands: (a) bottom flange and web yielding (+2.0% rads, AISC symmetric loading protocol); (b) bottom flange local buckling (+4.0% rads, AISC symmetric loading protocol); (c) bottom flange local buckling (+6.0% rads, near-fault protocol); (d) partial straightening of local buckles at load reversal (-2% rads, SAC near-fault protocol); (e) crack propagation in the East interior beam (+15% rads, collapse-consistent protocol); (f) crack closure in the East interior beam (-3% rads, collapse-consistent protocol)

In the subsequent loading stages, the collapse-consistent loading history began with a wider lateral drift excursion to 8% rads where a crack initiated at the tip of the end plate stiffener in the East beam near the interior beam-to-column connection (called East interior beam hereinafter) (see Figure 5.11a). This crack was attributed to a sharp geometric notch (see Figure 5.11b) that formed on the side of the root of the weld of end plate stiffener. While there was some partial loss of shear strength (see Figure 5.8b) the crack was deemed to be fairly stable and in the subsequent load reversal it fully closed. The test frame was able to maintain at least 60% of its peak shear resistance at this lateral drift

amplitude. To explicitly characterize the response of the test frame at large deformations with emphasis on redistributions occuring due to the primary two deteriorating modes (i.e., nonlinear geometric and material instabilities), the test frame was subjected to progressively increasing lateral drift amplitudes of 10, 12 and 15% rads as shown in Figure 5.8a. The in-between lateral loading reversals aimed at characterizing the unloading stiffness of the test frame and its ability to redistribute loads while experiencing cyclic deterioration in its story shear strength and stiffness. At a lateral drift of 10% rads, the crack in the East interior beam slightly progressed (see Figure 5.11c) to the beam web but overall was stable. Referring to Figure 5.9a, the West beam end near the exterior beam-to-column connection (called West exterior beam hereinafter) experienced ductile tearing due to ultra low cycle fatigue at the bottom beam flange (see Figure 5.11d).

The primary loss of the lateral load carrying capacity of the test frame at this point forward was mostly attributed to the further development of the two aforementioned cracks since local buckling stabilization had occurred in prior loading cycles. The composite steel beam ends that were under hogging bending near the West interior and East exterior beam-to-column connections, attained a residual path due to local buckling length stabilization (see Figure 5.9b and d, respectively). An axial load that mainly passed through the slab held the cracks to remain stable. This is why the hysteretic response of the test frame did not attain a negative lateral stiffness while widening the lateral drift demand, as shown in Figure 5.8b. In the subsequent lateral drift reversal, the test frame experienced unloading stiffness deterioration. However, the framing action caused crack closure and partial straightening of the local buckles. This resulted in a considerable regain of lateral story shear resistance in the test frame (see Figure 5.8b). When the test frame was subjected to a lateral drift ratio of 12% rads, both cracks propagated to the beam web and the flexural strength of the West exterior (see Figures 5.9a and 5.11f) and East interior (see Figures 5.9c and 5.11e) beam ends attained about 15% of the peak sagging flexural resistance. However, the test frame was able to maintain about 30% of the peak story shear resistance (See Figure 5.8b). Upon further loading at 15% rads, the cracks in the West exterior and East interior beam ends reached to about ½ and ¾ of the respective beam depths (see Figure 5.11g and h), respectively. On the other hand, the test frame was able to practically maintain about 30% of its peak story shear resistance. At this stage, the test ended due to safety considerations. Particularly, due to the crack developments in the West exterior and East interior beam ends, these would reach the point where they would lose their ability to carry the gravity load from the floor system. Figure 5.12 depicts the deformed shape of the test frame at characteristic lateral drift demands during the collapse-consistent loading protocol.

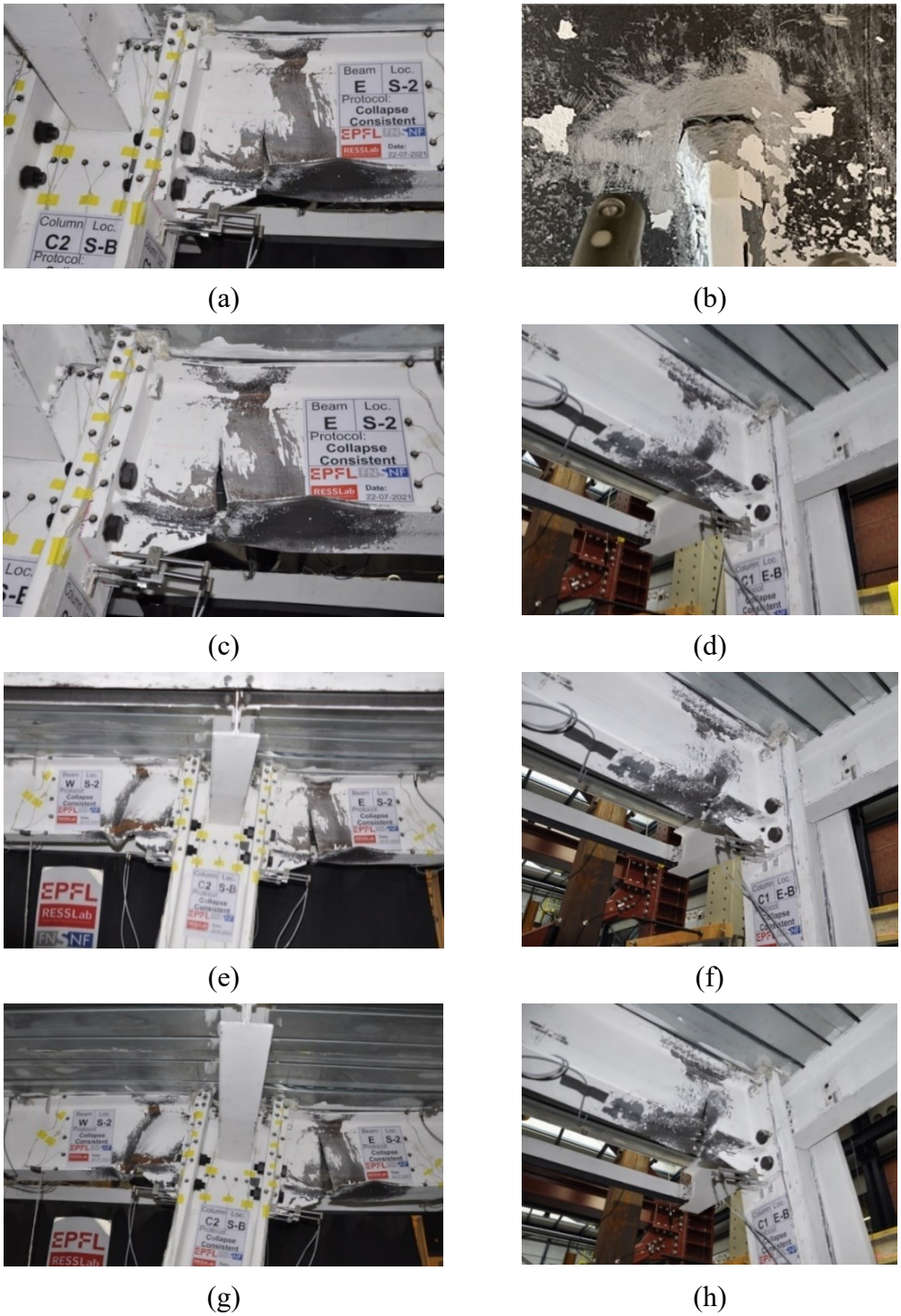

Figure 5.11 Crack initiation and propagation in the East and West beams at interior and exterior beam-to-column connection: (a) crack development at East interior beam end at 8% rads; (b) notch at the tip of the bottom rib stiffener of the East interior beam end; (c) crack propagation at East interior beam end at 10% rads; (d) crack initiation due to ultra-low cycle fatigue at West exterior beam at 10% rads; (e) crack propagation at East interior beam end at 12% rads; (f) crack propagation at West exterior beam end at 12% rads; (g) crack propagation at East interior beam end at 15% rads; (h) crack propagation at West exterior beam end at 15% rads

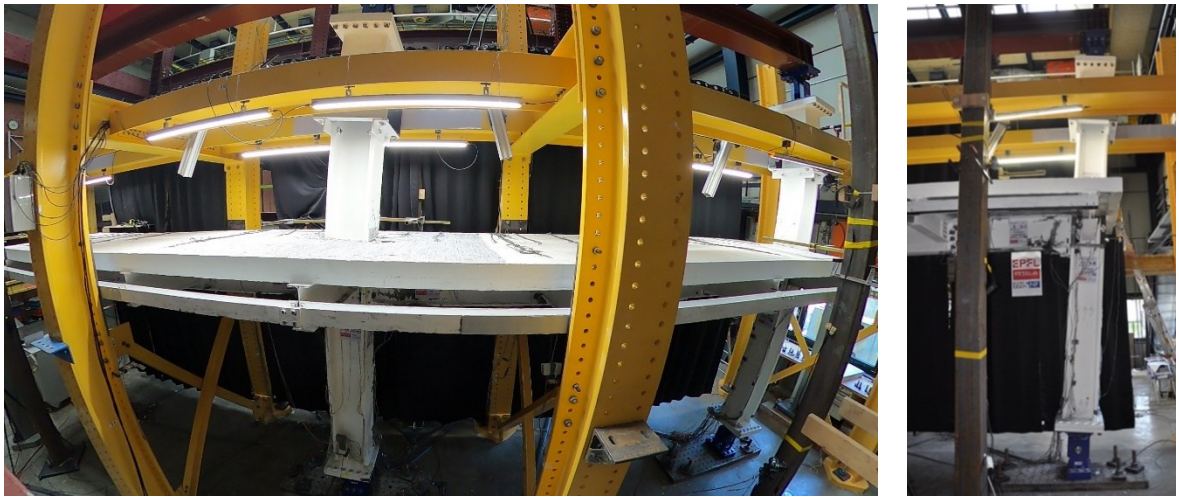

(a)

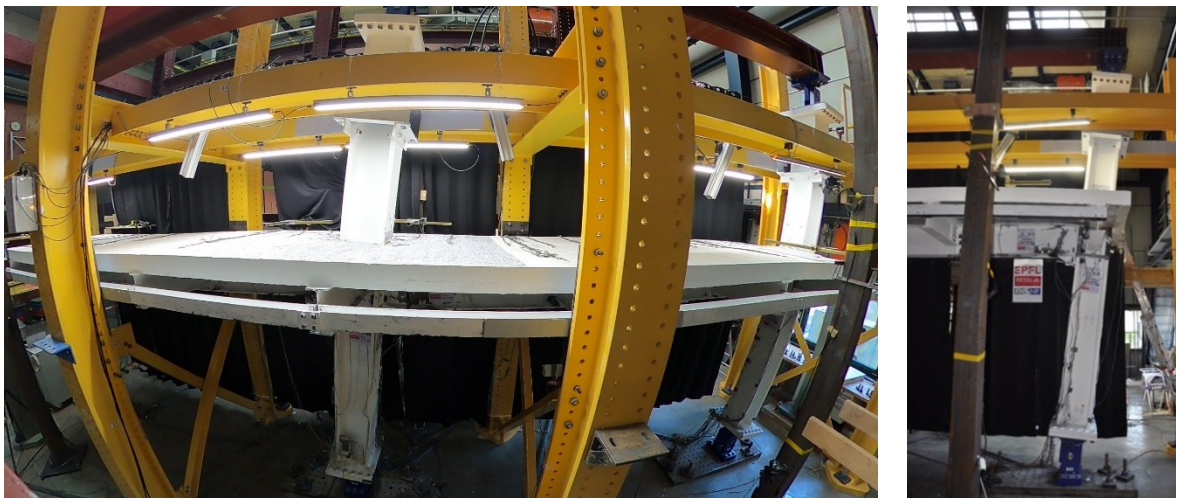

(b)

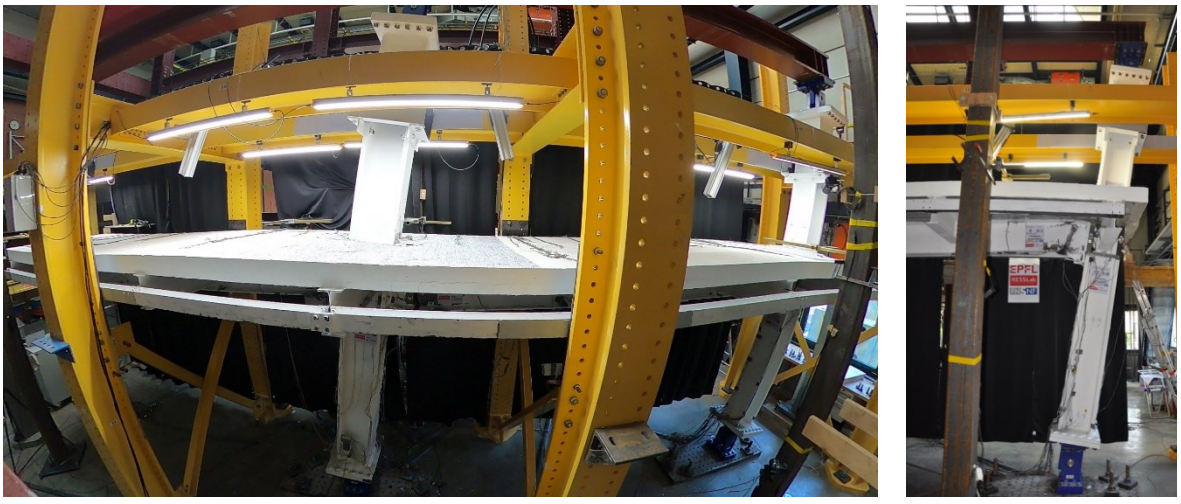

(c)

Figure 5.12 Deformed shape of the test frame during the collapse-consistent protocol: (a) 8% rads; (b) 12% rads; and (c) 15% rads

While the effects of gravity on the overall stability of the test frame were not explicitly considered, cyclic deterioration in flexural strength of the composite steel beam ends ramped the transient component of the axial load demand at both exterior columns as shown in Figure 5.13. On the other hand, the axial load in the interior column remained fairly constant throughout the loading history, as expected. The procedure to deduce the axial load in the columns is summarized in Appendix D.

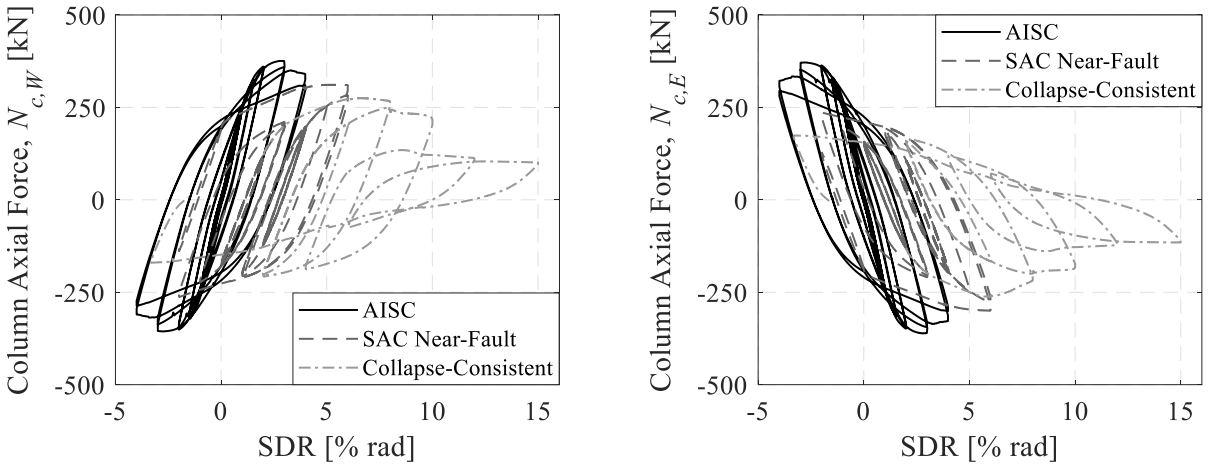

(a) (b)

Figure 5.13 Column axial force versus story drift ratio throughout the loading history; (a) West column; and (b) East column

5.3.2 Hysteretic response of composite steel beams

Referring to Figure 5.9, during the AISC symmetric cyclic loading protocol, flexural yielding initiated at the bottom flange of the composite steel beams under hogging bending and propagated to the web as shown in Figure 5.10a. Table 5.4 summarizes the SDRs and chord rotations, θ_b, at the peak flexural strength and at 80% of the peak flexural strength of the composite steel beam ends. Their flexural strength capped at $\theta_b = 2$ to 2.5% rads under sagging bending and $\theta_b = 1.5$ to 2% rads under hogging bending. Figure 5.9 and Table 5.4 suggest that each composite beam end was able to sustain at least $0.8M_{pl}^{\pm}$ ($M_{pl}^{\pm}$ is the flexural resistance of the composite steel beam calculated using nominal material properties, under sagging and hogging bending, respectively (see Table 5.4)) at a story drift ratio of 4% rads. Accordingly, all four beam-to-column connections conformed to the performance requirements for pre-qualified connections as per AISC 341-16 (AISC 2016a) in the US and Europe (Landolfo et al. 2018). Moreover, the composite steel beam-to-column connections conform to the acceptance criteria for composite steel MRFs designed according to a seismic design category DC3

according to the new Eurocode 8 Part 1-2 (CEN 2019), i.e., the joint plastic rotation at $0.8M_{pl}^{\pm}$ exceeds 3.5% rads.

Table 5.4 Performance summary of the composite steel beams

			Sagging Bending				Hogging Bending		
		M_{pl}^{+} [kNm]	M_b [kNm]	SDR [% rad]	θ_b [% rad]	M_{pl}^{-} [kNm]	M_b [kNm]	SDR [% rad]	θ_b [% rad]
West Exterior	Peak	599(1) / 559(2)	855	3.5	2.5	497(1) / 494(2)	-552	-1.9	-1.8
	80% Peak		684	8.1	7.0		-441	-3.9	-4.1
West Interior	Peak		824	-3.0	2.5		-516	2.5	-1.6
	80% Peak		NA	NA	NA		-413	5.1	-5.6
East Interior	Peak		883	2.9	1.9		-559	-2.0	-1.4
	80% Peak		707	6.0	5.3		447	-3.8	-3.4
East Exterior	Peak		823	-3.0	2.3		-513	2.0	-1.7
	80% Peak		NA	NA	NA		-410	4.3	-4.4

NA: Not applicable

(1) Plastic flexural resistance at the face of the end plate for seismic loading (CEN 2004a; b)

(2) Plastic flexural resistance at the face of the end plate for seismic loading (AISC 2016a; b)

Under hogging bending, the primary instability mode that caused flexural strength deterioration in the composite steel beams was local buckling in their bottom flanges. This occurred at modest lateral drift demands (i.e., 2.5% rads). On the other hand, under sagging bending, the flexural strength of the composite steel beams reached their peak at about 3% rads once the shear connectors in the beam-slab connections capped after which concrete crushing occured. This issue will be further elaborated later on. The neutral axis within the composite steel cross section under sagging bending moved only slightly towards the centroid of the bare cross section, thereby resulting in minimal local buckling in the top flange of the steel beams (see Figure 5.10c to f).

To put the hysteretic behavior of the composite steel beams into perspective, it is compared with that of a bare IPE360 beam that was tested by D'Aniello et al. (2018) as part of the EQUALJOINTS project. The beam was part of a T-shaped subassembly and was subjected to the AISC symmetric loading protocol up to 7% rads. Once local buckling occurred at 5% rads, the beam experienced flexural strength degradation due to the progression of local buckling followed by ultra-low cycle fatigue fracture in the plastic hinge region. The flexural strength of the bare IPE360 beam attained at 7% rads was 20% of the peak flexural strength. The absence of the axial restraint due to the framing action resulted in a rapid progression of local buckling as opposed to what was observed in the composite steel beams of the test frame.

From a collapse assessment standpoint, Figure 5.9 suggests that cyclic deterioration in flexural strength (often called in-cycle deterioration) of composite beams was minor during asymmetric lateral loading (i.e., SAC near-fault and collapse-consistent loading protocols). The composite steel beam ends that were mostly under hogging bending at progressively increasing lateral drift demands (see Figure 5.9b and d) attained a flexural strength stabilization path from about 6% to 15% rads. This is attributed to the fact that within the dissipative zone of each beam the respective local buckling wave stabilized. This corroborates with seminal work by Krawinkler et al. (1983). Similarly, flexural strength deterioration at the ends of the West exterior (see Figure 5.9a) and East interior (see Figure 5.9c) composite steel beams was mostly attributed to the development of the two types of cracks that were discussed earlier. Because of the framing action and the slab continuity, the steel beam cracks were deemed to be stable. An interesting observation is that at lateral drift reversals from 12% and 15% rads, both beam ends experienced pinching (see Figure 5.9a and c) in an analogous manner with RC members when experiencing crack development under cyclic loading.

Moment redistribution in the composite steel beams caused a shift in the location of the inflection points within the individual beam spans. Figure 5.14 depicts the location of the inflection points within the composite steel beams at representative lateral drift amplitudes. The locations were derived by interpolating the point of zero moment from the moment profile along the beams (i.e., moments at the face of the end plates and at the two instrumented cross sections). Note that during the collapse-consistent protocol, an axial force developed in the composite steel beam; hence the moment gradient became non-linear due to second-order effects. The figure suggests that the location of the inflection points varied within $0.15L_b$ and $0.25L_b$ from the mid-span of the composite steel beams during the AISC and SAC near-fault lateral loading protocols. Flexural strength deterioration attributable to bottom flange local buckling in composite steel beam ends under hogging bending shifted the location of the inflection point towards these ends. Similarly, during the collapse-consistent loading protocol, the formation of the two cracks near the West and East composite steel beam ends of the exterior and interior joints, respectively, shifted the inflection points of each beam near the same ends. Upon the load reversal, the moment gradient was altered due to crack closure in the beams under sagging bending and the straightening of local buckles in the beams under hogging bending.

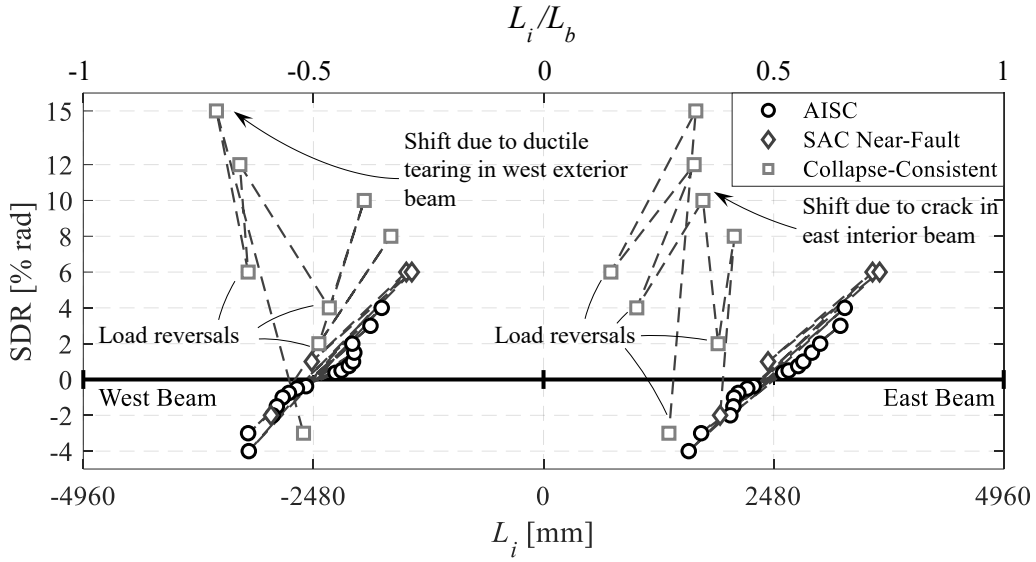

Figure 5.14 Inflection point locations in the composite steel beams throughout the loading history at representative lateral drift amplitudes

5.3.3 Crack patterns and slab load-transfer mechanisms

The crack pattern in the slab in the vicinity of the columns is derived from maximum principal tensile strain fields measured using DIC as shown in Figure 5.15. The same system enables the measurement of the crack widths throughout loading. Figure 5.16 shows the crack pattern evolution at selected peak lateral drift ratios of the AISC symmetric loading protocol, along with the marked crack widths (dimensions in millimeters). For the purpose of tracking the crack evolution and comparing the slab behavior at the interior and exterior beam-to-column connections of the test frame, the crack patterns are shown for the same loading direction. The above information is deemed useful for composite steel MRFs from a repairability standpoint in the aftermath of earthquakes.

At a lateral drift ratio of -0.5% rads, light cracking occurred (crack widths < 0.3 mm) in the slab near the columns as illustrated in Figure 5.16a. In the East exterior and West interior composite steel beams subjected to sagging bending, two types of cracks were observed: longitudinal cracks (< 0.1 mm) that initiated at the column face and diagonal cracks that extended to the back of the column flanges. The former occurred along the direct compression strut due to the bearing of the slab on the column face (i.e., mechanism 1 in EN 1998-1 (CEN 2004a)). The latter occurred along the inclined compression struts that formed on the sides of the column (i.e., mechanism 2 in EN 1998-1 (CEN 2004a)). The crack pattern revealed that at this drift level, both mechanisms were activated at the interior joint. Conversely, at the exterior joint only mechanism 1 was activated. In the West exterior and East interior composite steel beams under hogging bending, horizontal flexural cracks appeared. The flexural

cracks developed at the face of the columns and were spaced at around 200 to 300 mm. Notice that in the West exterior composite steel beams, flexural cracking was more prominent than in the East interior composite steel beam. Furthermore, the maximum crack width at the exterior joints was around 0.25 mm compared to 0.15 mm at the interior joint. This is attributed to the higher level of confinement in the slab in the interior joint due to the slab continuity and the presence of the transverse beams equipped with two rows of shear studs, as discussed later on.

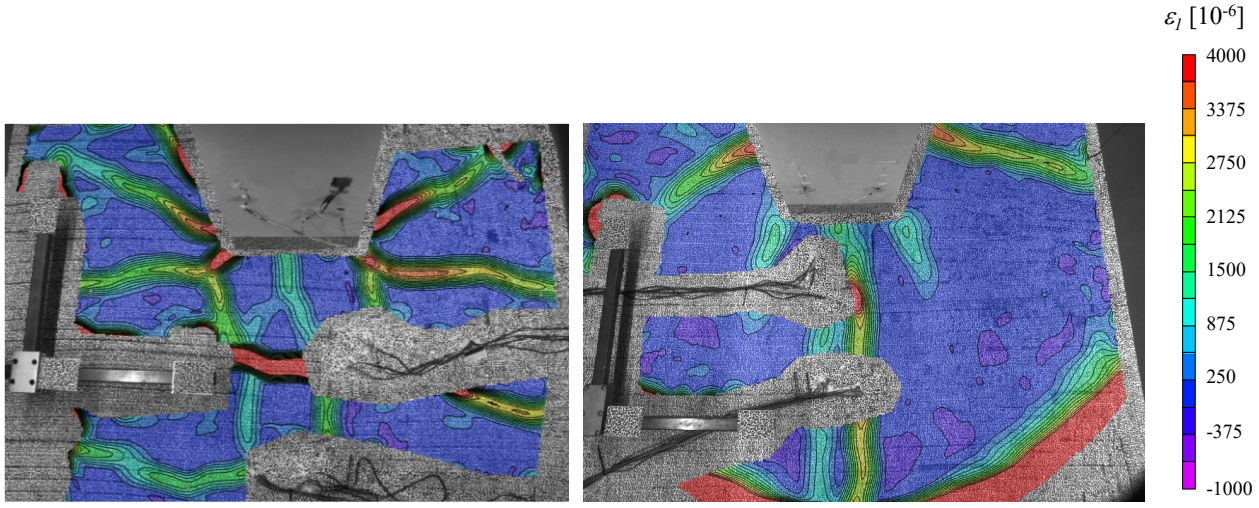

Figure 5.15 Maximum principal strains at the surface of the slab at -1% rads: (a) West exterior and; (b) West interior joints

Referring to Figure 5.16b, the inclined struts were at an angle of around 40º at the exterior joint, and 50º to 65º at the interior joint. Current Eurocode seismic provisions (CEN 2004a) assume a strut angle of 45º for the computation of the force transferred to the slab through mechanism 2. Plumier and Doneux (2001) have shown that the choice of the strut angle can significantly alter the required area of seismic rebars. For instance, the area of seismic rebars required to develop mechanism 2 for struts inclined 60º is 50% higher than currently required in EN 1998-1. At a lateral drift ratio of -1% rads, light cracking was still dominant (crack widths < 0.3 mm), with a higher degree of flexural cracking observed near the exterior joint than near the interior joint. The flexural cracks extended across the slab width. Furthermore, at this drift amplitude, mechanism 2 was activated in the East exterior composite steel beam.

At a lateral drift ratio of -2% rads, the cracks developed as shown in Figure 5.16c. Under sagging bending, the cracks in the slab along the inclined struts extended and grew up to 0.6 mm near the East interior composite steel beam. Under hogging bending, the horizontal flexural cracks extended and

expanded up to 0.9 mm near the West exterior column and 0.4 mm near the East interior column. The difference between the crack widths at the exterior and interior joints is attributed to the higher degree of slab confinement in the latter.

Figure 5.16d depicts concrete crushing and spalling, which only occurred at the face of the columns at -4% rads. This was also noticeable by visual inspection as shown in Figure 5.17a at the end of the AISC symmetric loading protocol. Therefore, during the subsequent loading, minimal development of the crack widths occurred along with a continuation of spalling at the column face. In fact, crack closure occurred in the inclined struts. Furthermore, wide flexural cracks up to 1.4 mm were observed at the exterior joint under hogging bending.

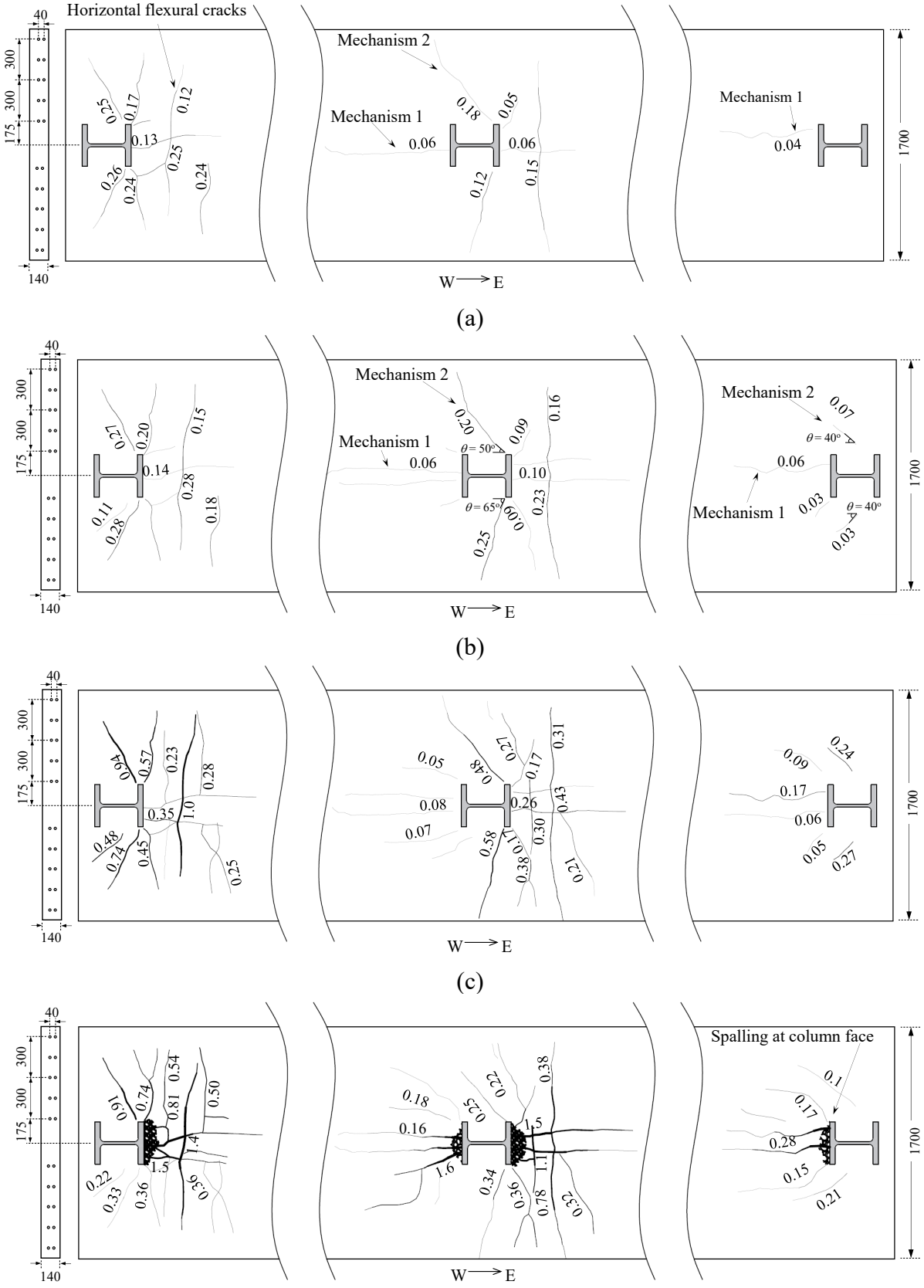

(a)

(b)

(c)

(d)

Figure 5.16 Crack pattern/crack width (mm) evolution in the slab around each column at selected peak lateral drift demands of the AISC symmetric loading protocol; (a) -0.5% rads; (b) -1% rads; (c) -2% rads; (d) -4% rads

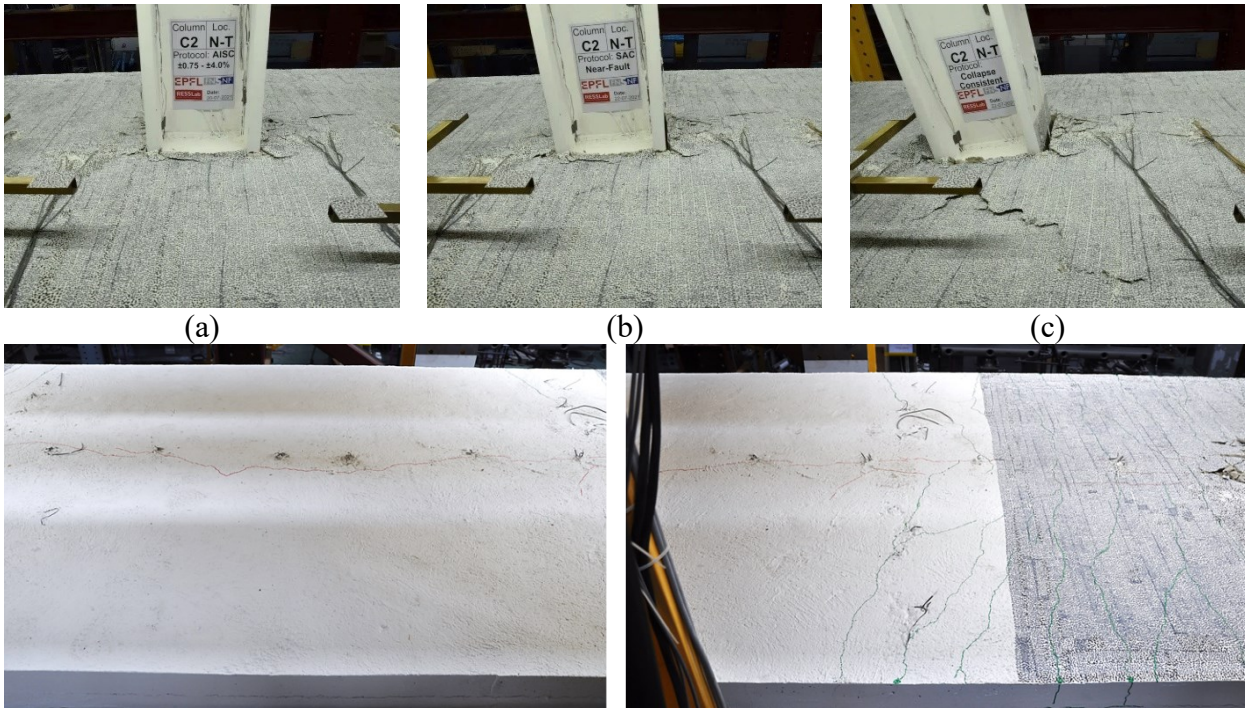

Figure 5.17 Slab state during loading: (a) interior joint at the end of the AISC symmetric loading protocol; (b) interior joint at 6% rads during the SAC near-fault protocol; (c) interior joint at 15% rads during the collapse-consistent protocol; (d) longitudinal crack, marked in red, along the line of the shear studs at the West beam

At the peak lateral drift demands of the SAC near-fault and collapse-consistent loading protocols, uplift of the concrete around the columns was observed. This is also evident in Figure 5.17b and c, respectively. Moreover, inspection of the slab at the end of the test revealed the presence of a longitudinal crack along the line of the studs as shown in Figure 5.17d after marking the cracks on the concrete slab.

5.3.4 Characterization and quantification of slab restraint and framing action

The experimental data offer the opportunity to explicitly quantify the effects of the framing action and slab continuity on the hysteretic response of the test frame from the onset of damage through collapse.

Referring to Figure 5.18a, axial shortening in the steel beam, δ_b, was calculated by assuming that it mostly occurs within the dissipative zones of the beam; hence, $\delta_b = 0.5 \cdot (\delta_{e,t} + \delta_{e,b} + \delta_{i,t} + \delta_{i,b})$. Figure 5.18b and c show the deduced amount of axial shortening in the West and East steel beams. Under the AISC and SAC near-fault loading histories, axial shortening in the East and West steel beams was less than 4 mm despite the large cumulative inelastic rotational demands at the composite

steel beams' ends. To put these results into perspective, prior subassembly tests with shallow composite steel beams (d_b = 300 mm) have shown that axial shortening may exceed 15 mm at 5% rads (MacRae et al. 2013).

During the collapse-consistent protocol, axial shortening increased to around 5 mm in the West beam and decreased in both beams after the crack formation near the exterior and interior beam-to-column connections (see Figure 5.11). At a lateral drift ratio of 15% rads, the West beam elongated by around 2 mm (see Figure 5.18a). This elongation is attributed to the crack opening near the West exterior beam-to-column connection (see Figure 5.11e to h). Nevertheless, the slab restrained this elongation.

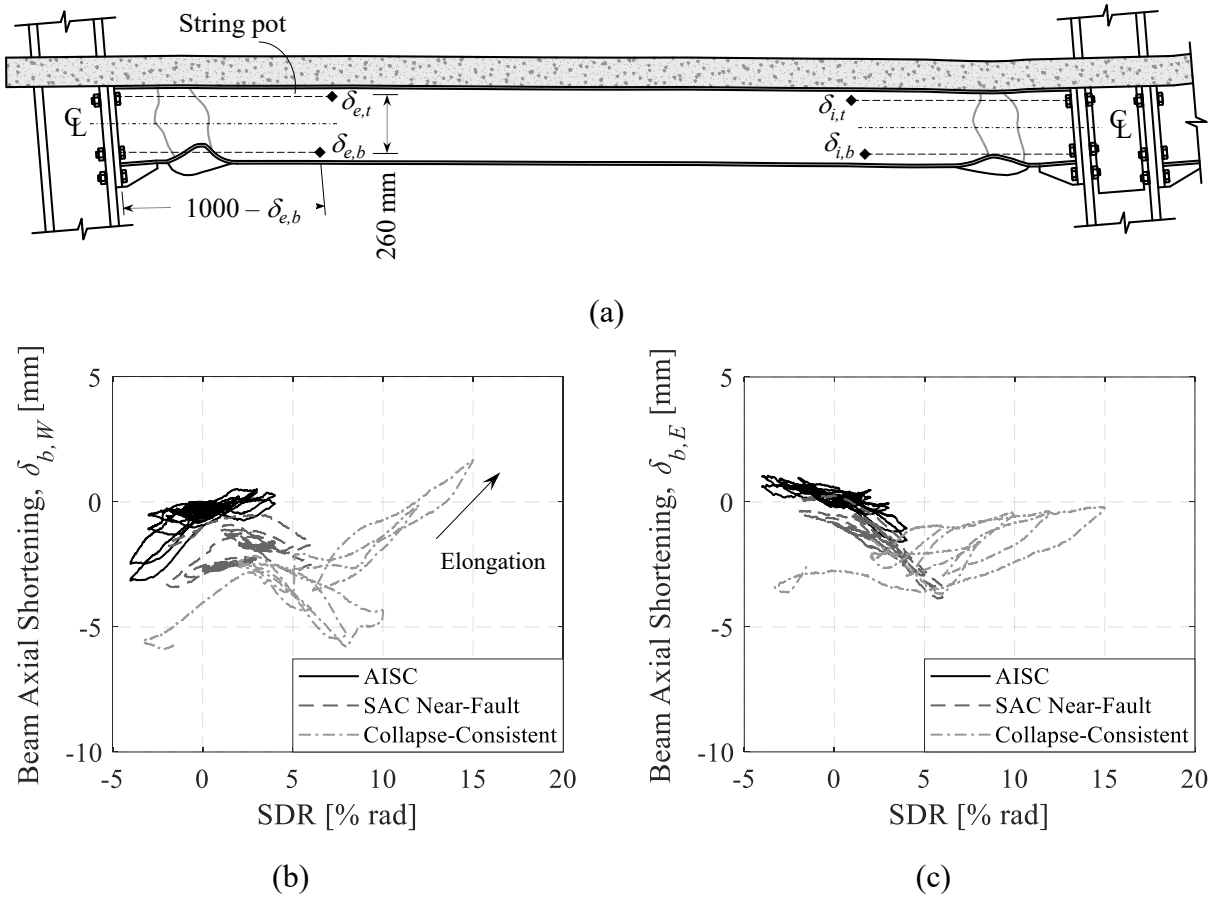

Figure 5.18 Beam axial shortening versus story drift ratio, (a) derivation from the string pot measurements; (b) West beam axial shortening; (c) East beam axial shortening

Past experimental studies have shown that the slab contributes to the lateral stability of steel beams (Nakashima et al. 2007; Ricles et al. 2004). However, the onset of local buckling results in the out-of-plane displacement of the bottom flange, which usually induces torsional demands on the columns (Chi and Uang 2002; Ricles et al. 2004). Nevertheless, the axial restraint, which hindered the local buckling progression, reduced the out-of-plane displacement of the bottom flange of the composite

steel beams. Figure 5.19 depicts the out-of-plane displacements of the West and East beams near the interior joint right outside their respective dissipative zones. Referring to Figure 5.19a, the West interior composite beam bottom flange experienced only minor out-of-plane deformations up to a lateral drift demand of 4% rads. During asymmetric loading, the bottom flange of the same beam reached a maximum out-of-plane displacement of 12 mm at 15% rads. Prior to the collapse-consistent protocol, the bottom flange of the East beam near the interior beam-to-column connection experienced similar out-of-plane displacement at the instrumented location (see Figure 5.19b). However, the LED bulbs on the East beam were placed slightly closer to the plastic hinge region than those on the West beam. Furthermore, the crack initiation at the tip of the stiffener (see Figure 5.11a) led to an increase in the out-of-plane displacement to about 25 mm at a lateral drift demand of 15% rads. Figure 5.19 suggests that the top flange of both composite steel beams experienced minimal out-of-plane displacement (about 2 mm) throughout the loading history.

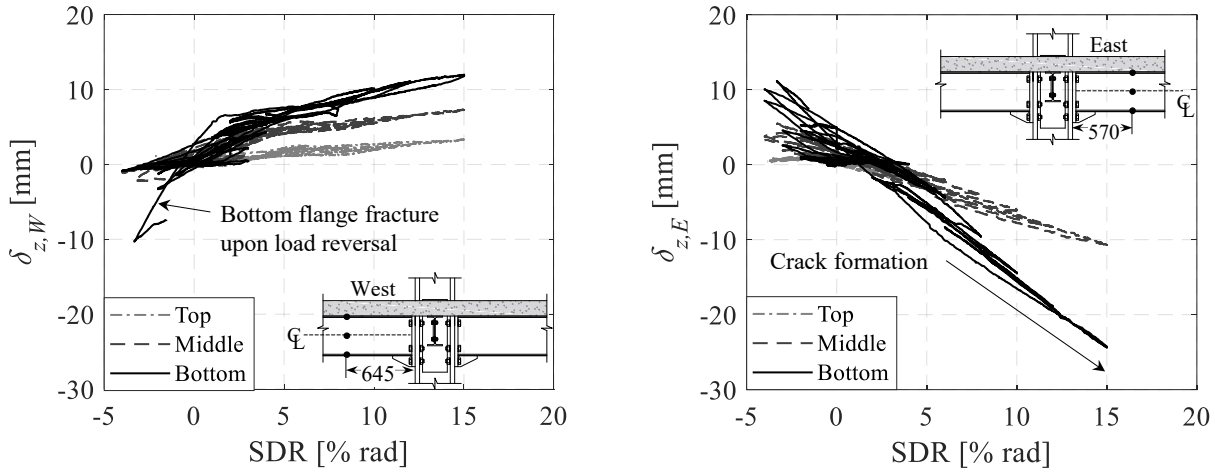

(a) (b)

Figure 5.19 Beam out-of-plane displacements in the vicinity of the (a) West beam; and (b) East beam interior joints

The longitudinal strain profiles were examined at characteristic cross sections located at a distance of 1205 mm away from the three column faces in order to quantify the slab restraint and framing action. Figure 5.20 depicts the longitudinal strain demands throughout loading for the west beam at representative lateral drift demands throughout the loading history. The location of the neutral axis (i.e., zero strain) was derived by linear interpolation of the longitudinal strain demands along the height of the cross section as shown in Figure 5.20 for the West beam at the exterior beam-to-column connection.

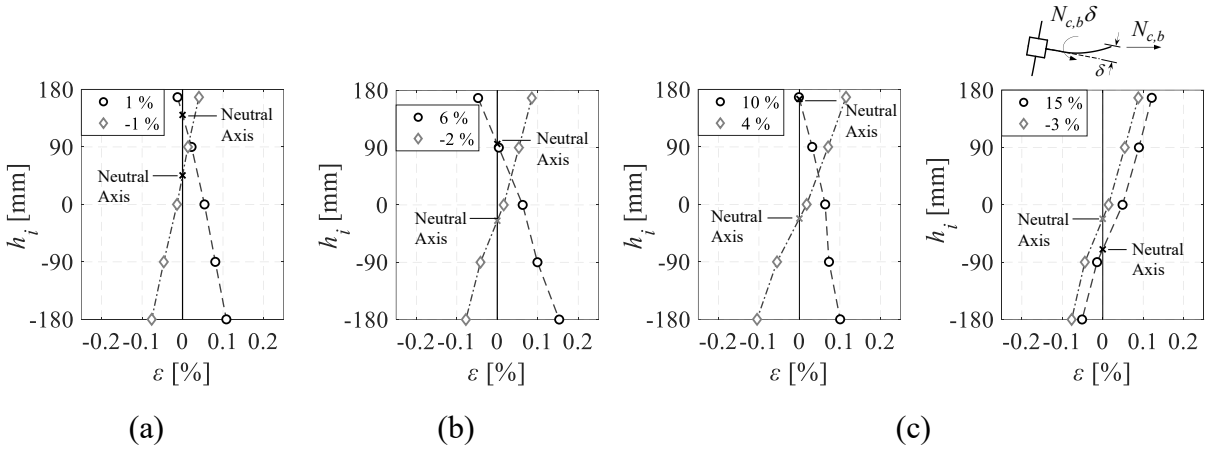

Figure 5.20 Longitudinal strain profile at 1205 mm from the column face of the West beam at the exterior joint: (a) AISC symmetric loading protocol; (b) SAC near-fault protocol; (c) collapse-consistent protocol

Figure 5.21 depicts the locations of the neutral axis for the West beam at the interior and exterior beam-to-column connections. Prior to concrete crushing, due to bearing of the slab to the column face (i.e., 3% rads), the cross-sectional neutral axis of the composite steel beam under sagging bending remained near the top flange of the steel beam (see Figure 5.21a). From the same figure, under hogging bending and at modest lateral drift demands (i.e., 1% rads), the neutral axis of the West beam at its both ends remained at about 45 mm above the centroid of the bare steel beam due to the presence of the longitudinal reinforcement of the concrete slab. This increased the compressive stress demand at the bottom flange of the steel beams, thereby accelerating the onset of local buckling at the same locations under hogging bending. At lateral drift demands larger than 2% and up to 4% rads, the position of the neutral axis in the composite steel beam under sagging and hogging bending shifted progressively towards the bottom flange due to concrete crushing and decreased in the longitudinal strain demands on the rebars, respectively. A close look at the longitudinal strain distribution on the top rebars (see Figure 5.22), 1205 mm from the West exterior column face, reveals that the strain demands generally decreased at lateral drift demands higher than 1% rads. This was due to the onset of light flexural cracking and debonding between the longitudinal rebars and the surrounding concrete, which corroborates with earlier findings by Nakashima et al. (2007). The above became more evident during the SAC near-fault loading protocol (see Figures 5.20b, 5.21b and c).

During the collapse-consistent protocol, the neutral axis of the cross section of the West beam at the exterior joint (see Figures 5.20c and 5.21b) shifted upwards under sagging bending due to the presence of a tensile force acting through the steel cross section to restrain the axial shortening in the beam. At a lateral drift demand of 10% rads, the same cross section was subjected to longitudinal tensile strain demands (see Figure 5.20c) as the tensile force through the steel cross section increased.

During the loading reversal to 4% rads, the neutral axis position shifted near the steel beam centerline as the tensile force decreased because of crack closure and straightening of local buckles. At 15% rads, the bending moment changed signs (hogging rather than sagging) due to the presence of a tensile axial force acting on the composite steel beam (see Figure 5.20c). Member P-delta effects induced a hogging moment in the composite steel beam as illustrated in Figure 5.20c. Due to the crack development in the steel beam, the sagging moment was fairly small. The compressive load that was passing through the slab progressively decreased after the crack initiation in the West beam, thereby stabilizing the crack in the subsequent loading cycles. Upon further loading and till 15% rads, the neutral axis location of the West beam's cross section at the exterior joint remained at 140 mm away from the bottom flange of the steel beam due to the presence of the tensile load.

Referring to Figure 5.21c, at the West interior cross section, the neutral axis shifted by about 90 mm below the centroid of the bare steel beam during the peak excursions of the SAC near-fault and collapse-consistent protocols. At the subsequent load reversals, the same cross section was subjected to sagging bending, which shifted the neutral axis above the centerline. However, in this case, the position of the neutral axis remained lower than that of the West exterior beam cross section. This is because the tensile force due to the axial restraint decreased once the local buckles at the bottom flange of the steel beam were straightened under the subsequent load reversals.

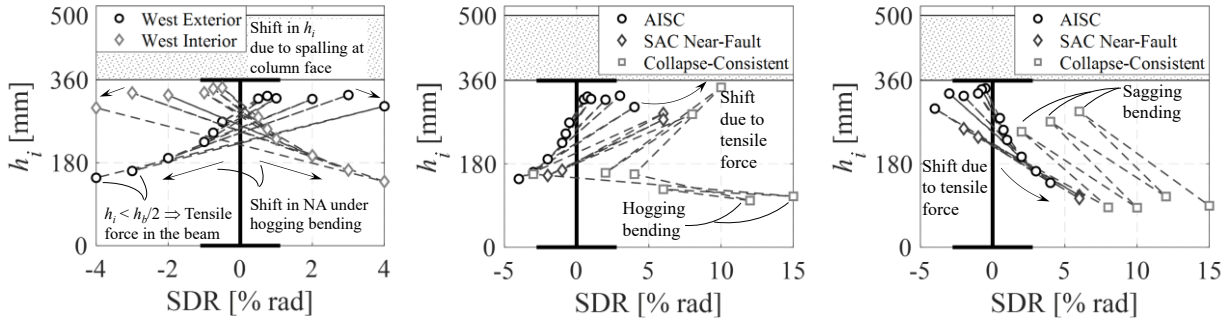

Figure 5.21 Neutral axis positions of West beam at exterior and interior joints: (a) AISC symmetric loading protocol; (b) West beam at exterior joint; (c) West beam at interior joint

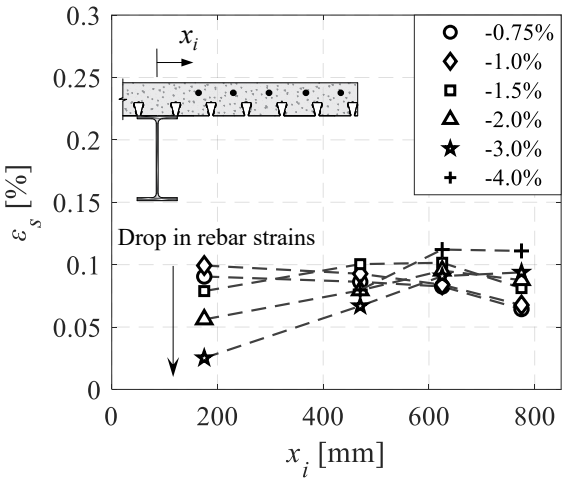

Figure 5.22 Longitudinal strain distribution on the top slab rebars, 1205 mm from the face of the west exterior column at selected lateral drift demands during the AISC symmetric cyclic loading protocol

The effects of the slab restraint and framing action were quantified by calculating the axial force in the composite steel beam. The net axial force acting on the composite composite cross section was derived by computing the difference in the column shear forces below ($V_{c,b}$) and above ($V_{c,t}$) the floor level as shown in Figure 5.23a (i.e., $N_{cb} = V_{c,b} - V_{c,t}$). Figure 5.23b illustrates the maximum axial force in the West beam at selected peak drift ratios of the imposed loading history. Under the AISC symmetric protocol, the axial force was compressive and became highest (115 kN) at -3% rads. This force was transferred to the composite steel beam due to the in-plane flexibility of the slab and the beam-slab connection; the slab did not act as a perfectly rigid diaphragm; therefore, the columns transferred compressive axial load demands to the composite steel beams. However, the maximum compressive axial force was around 4%$N_{pl,Rm}$ ($N_{pl,Rm}$ is the plastic resistance of the bare steel beam cross section that is calculated using the measured yield stress, $f_{y,m}$ for the respective flange and web of the cross section that is summarized in Table 5.2).

During the SAC near-fault and collapse-consistent loading protocols, the compressive force was counteracted by the tensile force that developed due to the restraint against beam axial shortening. The developed tensile force may be calculated as the difference between the maximum compressive force and tensile as shown in Figure 5.23b. At a lateral drift demand of 10% rads, the maximum tensile force in the composite steel beam was around 220 kN (i.e., 8%$N_{pl,Rm}$). The tensile force dropped by about 25% following ductile tearing near the West exterior joint as the axial stiffness of the beam was reduced. However, the tensile force recovered afterwards as the crack stabilized. Furthermore, the tensile force in the composite steel beams decreased upon load reversal as the local buckles in the bottom flange of the beam were straightened.

The axial force passing through the slab, N_s, was derived at the instrumented locations in the West beam through section equilibrium (see Figure 5.23a). Referring to Figure 5.23c and d, the peak compressive force in the slab at the exterior and interior joints was capped during the 3% rads lateral drift amplitude of the AISC symmetric loading protocol, as the shear resistance of the beam-slab connection was attained. For reference, the shear resistance of the beam-slab connection is superimposed in Figure 5.23c and d. It was calculated as $n_s P_{Rk}$, in which: $n_s = 16$ is the number of shear studs between the location of the measured axial force and the point of zero moment at 3% rads; and $P_{Rk} = 72$ kN is the characteristic shear resistance of one shear stud, and corresponds to 90% the peak shear capacity obtained through the monotonic pushout test as per Eurocode 1994-1-1 (CEN 2004b).

Upon further loading, the compressive force in the slab slightly decreased. However, N_s increased again during the collapse-consistent protocol as shown in Figure 5.23c. The slab restrained the beam from axial shortening, which induced a compressive force in the slab. At the West exterior cross section, the compressive force reached around 1000 kN, which indicates that the shear studs in the beam-slab connection were mobilized. Following ductile tearing in the West beam at the exterior joint, the compressive force in the slab dropped by around 50%. The slab helped stabilize the crack by restraining the beam against axial elongation as the crack propagated through the beam web (see Figure 5.11), thereby resulting in a drop in the slab compressive axial force. It is noteworthy stating that a compressive force was maintained in the slab during the load reversal when the West exterior cross section was under hogging bending. In fact, after the AISC symmetric loading protocol, the axial force in the slab was compressive at the West interior cross section despite the latter being under hogging bending (see Figure 5.23d). The above findings substantiate quantitatively the axial restraint provided by the slab. To the best of our knowledge, this is considered to be a unique feature of the testing program.

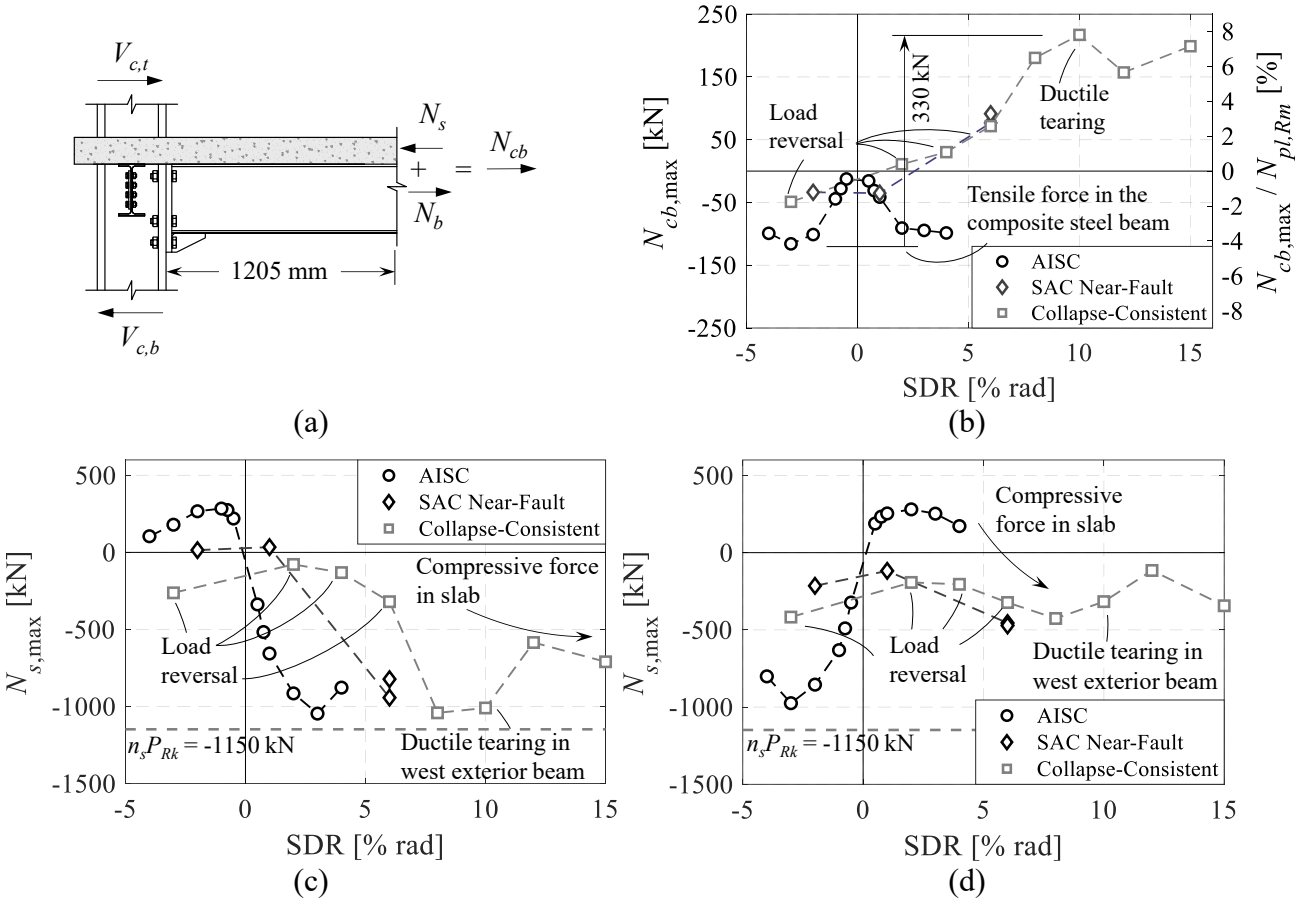

Figure 5.23 Axial force in the West composite steel beam (N_{cb}) and slab (N_s), 1205 mm from the face of the exterior and interior columns (i.e., at the instrumented cross sections) at selected peak lateral drift demands: (a) derivation; (b) maximum axial force in the composite steel beam; (c) maximum axial force in the slab at the exterior cross section; (d) maximum axial force in the slab at the interior cross section

5.3.5 Effect of transverse steel beams

The test results revealed one additional source of overstrength, which relates to the presence of the transverse beams framing into the beam-to-column connections. Current Eurocode seismic provisions account for the influence of the transverse beams on the flexural resistance of the composite steel beams under sagging bending; however, the transverse beams in that case are assumed to be fully restrained and therefore capable of transmitting the horizontal forces acting on the shear studs. Often, the horizontal forces transmitted are limited by the low torsional stiffness of the transverse beams (Plumier and Doneux 2002). On the other hand, in this experimental program, the transverse beams were not fully restrained. This allows for the assessment of the influence of the transverse beams on the confinement on the concrete in the vicinity of the joints. Figure 5.24 depicts the transverse compressive strains up to a lateral drift demand of 3% rads during the AISC lateral loading protocol with the DIC system. The presence of compressive transverse strains (i.e., transverse to the primary

IPE360 girder) is indicative of confinement in the slab. From this figure, the compressive transverse strain demands were negligible at -1% rads (see Figure 5.24a and d) under sagging bending near the West interior and East exterior joints, respectively. However, the compressive strains in the transverse direction became more prominent at a lateral drift demand of -2% rads particularly at the interior joint (see Figure 5.24b). At -3% rads, the maximum transverse strains were around 0.0025 at the West interior joint (Figure 5.24c) and 0.001 at the East exterior joint (see Figure 5.24f). The higher compressive transverse strain demands that were observed at the interior joint are attributed to the higher degree of confinement due to the slab continuity. The transverse beams at the interior joint were equipped with two rows of shear connectors, whereas those at the exterior joints had only one row of shear studs.

The presence of compressive transverse strains in the slab, due to the transverse beams of the floor system, demonstrates that this additional source of overstrength may have implications on capacity design of composite steel MRFs. Particularly, this effect should be properly quantified and factored as part of the strong column/weak beam ratio in current standards (AISC 2016a; CEN 2004a).

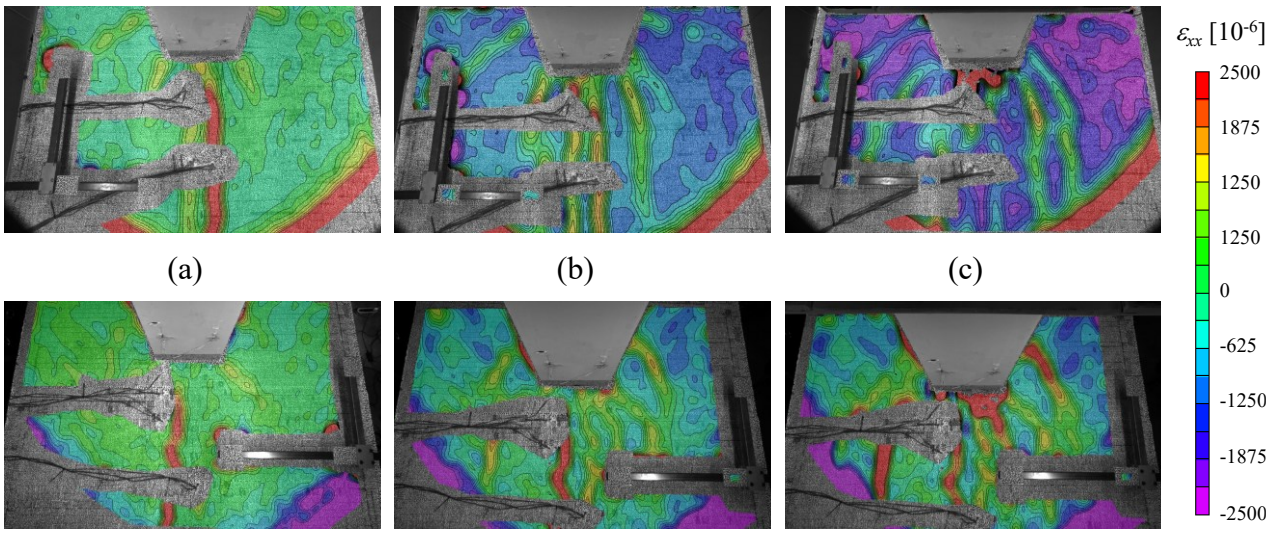

Figure 5.24 Transverse strains at the surface of the slab at selected peak lateral drift demands up to -3% rads under sagging bending; Top: West interior joint at (a) -1% rads; (b) -2% rads; (c) -3% rads; Bottom: East exterior joint at (d) -1% rads; (e) -2% rads; (f) -3% rads

5.4 Seismic design implications

In this section, results from the experimental program are used to highlight several aspects related to the seismic design of composite steel MRFs. In particular, the moment of inertia and effective width

of the composite steel beams are computed and compared with those from current EN 1998-1 provisions (CEN 2004a). The ductility requirements to control concrete crushing within a dissipative zone are also assessed. Moreover, the hysteretic response of the beam-slab connection is assessed in line with current seismic design requirements.

5.4.1 Moment of inertia of composite steel beams

Past studies have shown that the rotational stiffness of shallow composite steel beams is at least 60% higher than that of their bare counterparts (El Jisr et al. 2019; Nakashima et al. 2007; Nam and Kasai 2012), which can significantly influence the lateral stiffness of a composite steel MRF. The procedure outlined below is used to derive the equivalent moment of inertia of the composite steel beams under sagging (I_c^+) and hogging bending (I_c^-).

First, the elastic rotational stiffness is obtained from the initial loading cycles of the deduced moment rotation diagrams shown in Figure 5.9 for sagging (K_{el}^+) and hogging bending (K_{el}^+). The flexural component of the rotational stiffness of the composite steel beams is then deduced by assuming that only the steel cross section contributes to the shear stiffness of the composite steel beam. Hence, the equivalent moment of inertia of the composite steel beams is computed as follows,

$$K_{el,f}^{\pm} = \frac{K_s - K_{el}^{\pm}}{K_s \cdot K_{el}^{\pm}} \tag{5.1}$$

$$I_c^{\pm} = K_{el,f}^{\pm} \cdot \frac{L_c^{\pm}}{3E} \tag{5.2}$$

In which, $K_{el,f}^{\pm}$ is the elastic flexural stiffness of the composite steel beam under sagging ($K_{el,f}^+$) and hogging ($K_{el,f}^-$) bending; K_s is the shear rotational stiffness of the IPE360 girder calculated according to Cowper (1966) and Charney et al. (2005); $L_c^{\pm}$ is the shear span under sagging ($L_c^{\pm}$) and hogging bending ($L_c^{\pm}$) and $E = 199$ GPa is the measured elastic modulus of the steel beam (see Table 5.2).

Figure 5.25 shows the values of the equivalent moment of inertia of the composite steel beams near each joint. A comparison with the values calculated according to current Eurocode provisions (CEN 2004a; b) is also shown. At the exterior joints, the moment of inertia of the composite steel beam is estimated well for both sagging and hogging bending according to current standards. The ratio $I_c^{\pm}/I_{bare}$ (I_{bare} is the moment of inertia of the bare IPE360 steel beam) ranges between 1.0 and 1.2 under hogging bending, and between 2.3 and 2.4 under sagging bending. The slab contribution to the

flexural stiffness of the composite steel beams is quite pronounced under sagging bending, as expected. However, under hogging bending, flexural cracking implies that the stiffness contribution from the slab is mainly due to the longitudinal steel reinforcement bars and the presence of the transverse beams. The assumption of cracked section analysis (i.e. concrete in tension is neglected) in EN 1994-1-1 (CEN 2004b) for composite steel beams under hogging bending, seems reasonable at the exterior joints. Interestingly, at the interior joint, the moment of inertias of the West and East composite steel beams are underestimated by 25% for sagging bending and 35% for hogging bending. The higher moment of inertia of the composite steel beams at the interior joint is attributed to the continuity of the slab and reinforcement at the interior joint, as well as the transverse beams supporting the slab. Furthermore, unlike in the exterior joints where flexural cracking was more pronounced in the early loading stage, the EN 1994-1-1 (CEN 2004b) assumption that the composite cross section is fully cracked under hogging bending leads to an underestimation of the equivalent moment of inertia of the composite steel beams. It should be noted that long-term effects on concrete as well as the presence of gravity loads on the floor slab have been neglected as part of the above assessment.

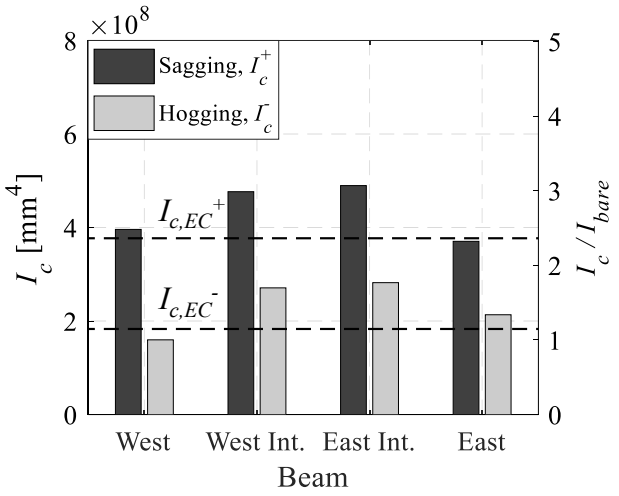

Figure 5.25 Comparison of the derived moment of inertia of the composite steel beams at each beam-to-column connection with that computed using EN 1998-1 provisions (CEN 2004a), (i.e., $I_{c,EC}^+$ and $I_{c,EC}^-$)

5.4.2 Ductility requirements for controlling concrete crushing within a dissipative zone

The slab confinement is beneficial in that it increases the crushing strain of concrete at the slab-column interface. Current EN 1998-1 (CEN 2004a) provisions provide a strict ductility requirement to ensure that concrete crushing within a dissipative zone of a composite steel beam is delayed. This requirement limits the ratio x_{pl}^+/h as follows,

$$\frac{x_{pl}^{+}}{h} \leq \frac{\varepsilon_{cu}}{\varepsilon_{cu} + q \cdot \varepsilon_{y}} \tag{5.3}$$

This limit was derived by assuming a uniform strain profile (slip in the composite steel beam was ignored) acting on the composite cross section as shown in Figure 5.26. Moreover, the limit is quite restrictive in seismic designs requiring higher strength reduction factors (q-factor in Europe, R-factor in the US), thereby limiting the applicability of composite construction in seismic applications. As mentioned earlier, the above limit was intentionally violated during the seismic design of the test frame. Nevertheless, the hysteretic behavior of the composite steel beam was very ductile. Concrete crushing only occurred after the 3% lateral loading drift amplitude near the column face. According to Plumier and Doneux (2001), the assumed ε_{cu} of 0.0025 does not consider the effects of slab confinement due to the presence of transverse reinforcement in the vicinity of the column. The DIC system offers the opportunity to quantify the longitudinal strain demands at the surface of the slab to provide insight on the above requirements.

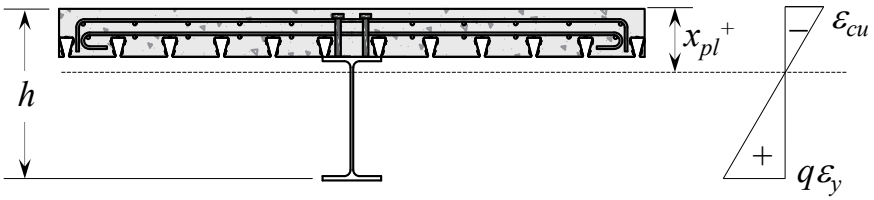

Figure 5.26 Strain profile in the composite steel cross section at the ductility limit specified in EN 1998-1 (CEN 2004a)

Figure 5.27 shows the longitudinal strain demands at the surface of the slab at the West interior (see Figure 5.27a to c) and East exterior (see Figure 5.27d to f) joints. At a lateral drift demand of about -1% rads (i.e., onset of flexural yielding at the bottom flange of the respective steel beam), the longitudinal strain demands at the slab surface were fairly low due to the upward shift of the neutral axis at the respective cross sections near the interior and exterior joints as discussed earlier. Upon further loading, relatively high longitudinal strain demands (0.005 to 0.006) were measured by the DIC system at the slab surface near the column face (see Figure 5.27b, c, e and f). Nevertheless, the integrity of the concrete near the column was maintained. The concrete at the slab-column interface sustained longitudinal compressive strains of up to 0.006 prior to crushing only at the same location. The ability of the concrete to withstand high compressive strains is attributed to confinement of the concrete in the joint area. This is due to (i) the presence of transverse beams framing the joint as discuss earlier, (ii) the excellent anchorage detailing of the transverse rebars and, (iii) the configuration of the profiled

steel deck. For the latter, a large rib angle [> 80° as per EN 1998-1 (CEN 2004a)] provides appreciable confinement to the concrete inside the rib. Conversely, a small rib angle (< 80° i.e., trapezoidal deck) provides less confinement to the concrete. It is also important to note that the additional confinement due to the continuity at the edges of the slab was not considered in the test. Based on the above discussion, the current EN 1998-1 (CEN 2004a) ductility requirements are stringent and require modification in future versions of the same standard.

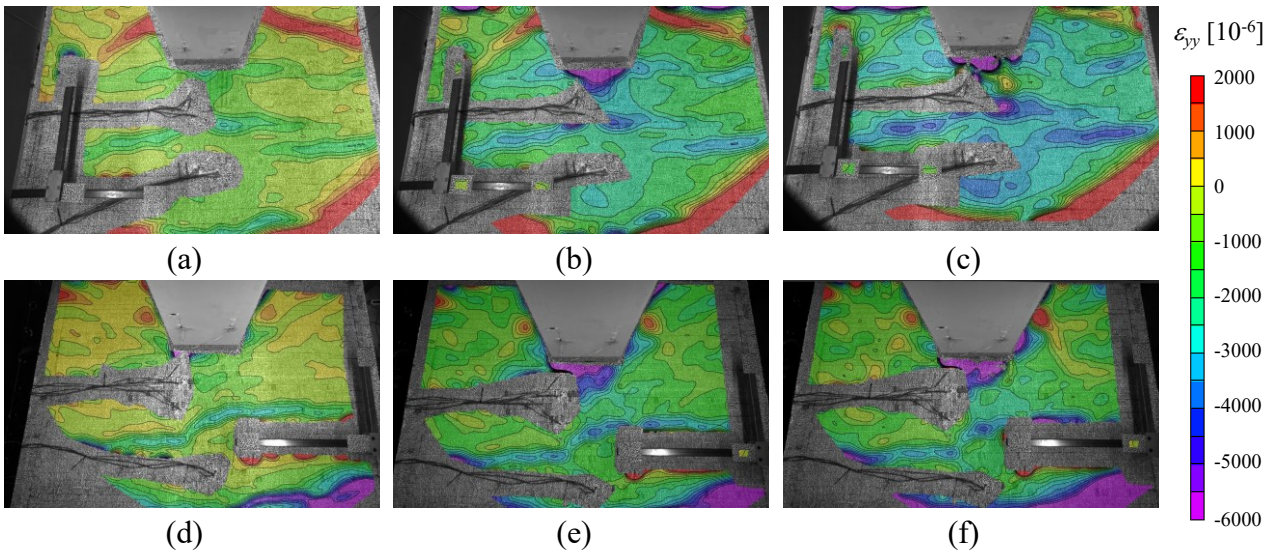

Figure 5.27 Longitudinal strains at the surface of the slab at selected peak lateral drift ratios up to -3% rads under sagging bending; Top: West interior joint at (a) -1% rads; (b) -2% rads; (c) -3% rads; Bottom: East exterior joint at (d) -1% rads; (e) -2% rads; (f) -3% rads

5.4.3 Beam-slab connection performance

The beam-slab connections of the test frame were originally designed to provide full composite action while waiving the 25% reduction in the shear resistance of headed studs according to the current EN 1998-1 (CEN 2004a). Nevertheless, due to the high overstrength in the concrete, as well as the additional sources of overstrength that were previously discussed, the actual degree of composite action was less than what was originally calculated. Herein, the degree of composite action is re-calculated as per EN 1994-1-1 (CEN 2004b) by using the measured compressive strength of the concrete at the day of testing ($f_{c,m} = 49$ MPa) and the characteristic shear resistance of the shear connectors obtained from the monotonic push-out test ($P_{Rk} = 72$ kN). It was found to be 55% rather than 100%. Accordingly, the shear studs are the weakest elements in the composite steel beams. This could, in principle, lead to high slips demands and failure of the beam-slab connection at modest lateral drift demands, thereby leading to a loss of the seismic load transfer mechanism between the slab and the steel beams

(Cheng and Chen 2005; Civjan et al. 2001; Cordova and Deierlein 2005). However, the composite steel beams conformed to the prequalification requirements as discussed earlier. Having said that, a detailed assessment of the slip demands, and shear resistance of the beam-slab connections was conducted hereinafter.

The slip demands in the beam-slab connection were traced along the West and East composite steel beams at characteristic peak lateral drift demands of the AISC lateral loading protocol (see Figure 5.28a) and the SAC near-fault and collapse consistent loading protocols (see Figure 5.28b). During the AISC symmetric loading protocol, the maximum slip demands were around 0.5 mm at the 1% lateral drift amplitude and increased until they reached a maximum value of 2 mm at the 3% lateral drift amplitude of the same protocol. Moreover, Figure 5.28a illustrates that the slip demands were slightly higher near the mid-span of the composite steel beams than near the columns because the slip is restrained near the beam-to-column connections (Zona et al. 2008). At the 4% drift amplitude of the AISC symmetric loading protocol, the slip demands decreased to around 1.5 mm. The beam-slab connection unloaded following the spalling of concrete at the slab-column interface and the loss of the bearing mechanism between the slab and the face of the column (i.e., mechanism 1).

Referring to Figure 5.28b, the slip demands continued to decrease upon further lateral loading at lateral drift demands associated with structural collapse. In the East beam at the interior joint, the slip demands increased while the lateral drift amplitude exceeded 8% rads, to a maximum of around 2.5 mm at 15% rads. The crack formation and propagation within the steel beam at the same location imposed additional slip demands on the beam-slab connection near the interior joint.

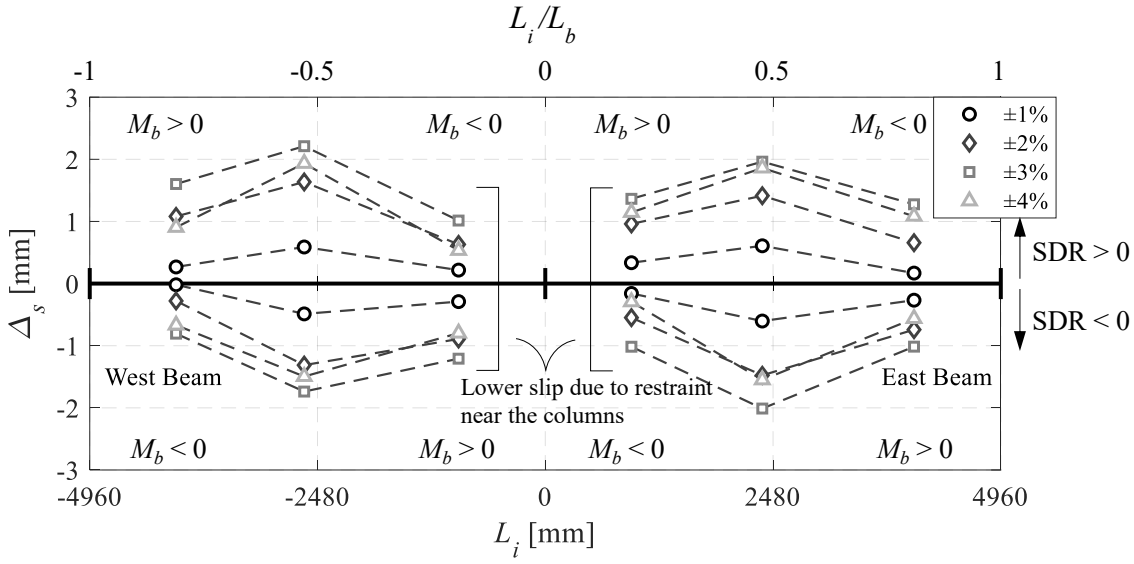

(a)

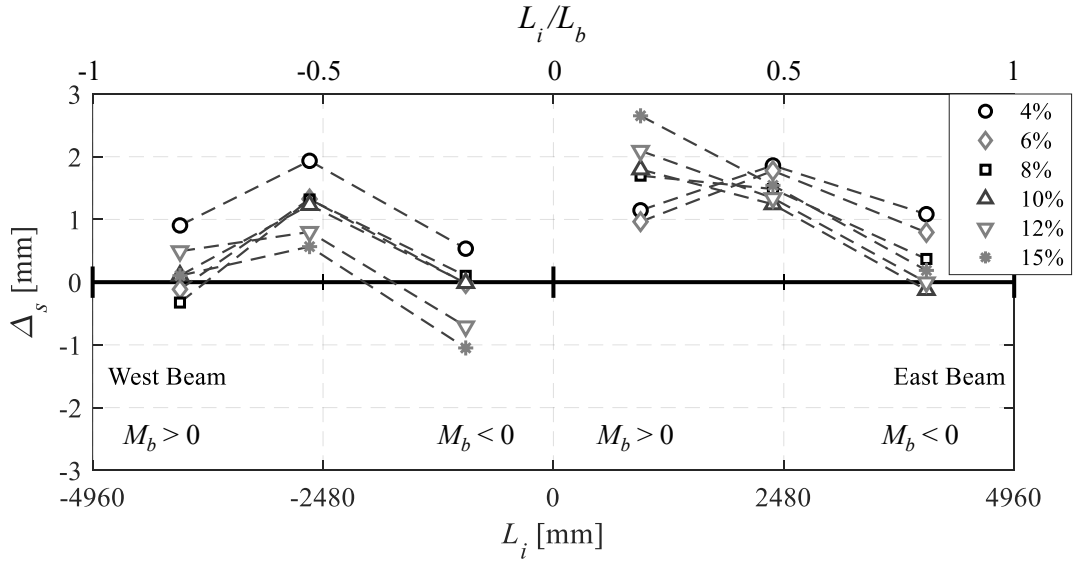

(b)

Figure 5.28 Maximum slip in the beam-slab connection along the length of the West and East beams at selected peak lateral drift demands: (a) AISC protocol; (b) SAC near-fault and collapse-consistent protocols

The focus in this section is on the behavior of the beam slab connection at lateral drift demands associated with a design basis earthquake (i.e., 10% probability of exceedance over 50 years) and a maximum considered earthquake with a 2% probability of exceedance over 50 years building life expectancy. Therefore, the integrity of the beam-slab connections under the AISC symmetric loading protocol is examined. Referring to Figure 5.29a, the shear force demand, Q, on the beam-slab connection at the locations instrumented with strain gauges is equal to the force in the slab (N_s). The slip demand at this location is obtained through linear interpolation of the measured slip demands on

either side of the cross section. Figure 5.29b illustrates the hysteretic behavior of the beam-slab connection at the cross section that was situated near the West exterior joint. The behavior is characterized by an increasing shear demand under sagging bending ($Q_W > 0$) and a decreasing shear demand under hogging bending ($Q_W < 0$) especially during the 2% to 4% lateral drift amplitudes of the AISC symmetric loading protocol. This is attributed to the variation in the number of engaged shear studs throughout the loading, under both sagging and hogging bending. To elucidate this phenomenon, the shear studs engaged up to the instrumented location are shown in Figure 5.29a. The number of engaged shear studs, n_e, is dependent on the location of the inflection point in the composite steel beam. A change in the moment gradient due to moment redistribution in the composite steel beams leads to either an increase or decrease in n_e. For instance, referring to Figure 5.29b, during the lateral drift loading cycles of 3% and 4% rads, following the initiation of bottom flange local buckling, the number of engaged shear studs increased under sagging bending and decreased under hogging bending. This phenomenon has a profound influence on the integrity of the beam-slab connection especially in shallow composite steel beams in which the hysteretic behavior is fairly asymmetric under flexural demands (see Figure 5.9). Furthermore, this phenomenon cannot be captured in subassembly beam-to-column tests where no moment redistribution occurs in the composite steel beams and the number of engaged shear studs remains the same regardless of the flexural demands at the beam ends.

Figure 5.29c depicts the average shear force per engaged shear stud, which is calculated as Q/n_e versus the corresponding peak lateral drift amplitudes of the AISC symmetric loading protocol for the West exterior and West interior cross sections. Under sagging bending, ($Q/n_e > 0$) the average shear force per engaged stud capped at 2% and 3% rads. This led to capping of the force in the slab as explained earlier. The average shear force per engaged stud decreased following concrete spalling at the column face. Figure 5.29d shows that the slip demand also decreased at this lateral drift ratio. Under hogging bending ($Q/n_e < 0$), the average shear force per engaged stud capped at the 2% lateral drift amplitude and decreased thereafter as the force in the rebars decreased at the cross section (see Figure 5.22). As with sagging bending, the slip demands on the beam-slab connection decreased as the shear force decreased. Figure 5.29c also illustrates that the capping average shear force per engaged stud was around 10 to 15% lower than the characteristic strength of the shear studs P_{Rk} defined earlier.

The above findings demonstrate that beam-slab connections maintained their integrity during the AISC symmetric loading protocol despite waiving the required 25% reduction in the shear stud resistance (CEN 2004a) and the additional sources of overstrength that were highlighted earlier. While the actual degree of composite action was 55%, which is less than the minimum required by EN 1998-

1 (CEN 2004a), the slip demands at the West beam cross sections instrumented with strain gauges, were less than 2 mm (see Figure 5.29d) . Unlike in conventional cyclic push-out tests, which tend to be overly conservative, the beam-slab connections in the test frame account for realistic boundary conditions and the associated force redistribution that is occuring within a composite steel MRF while it experiences structural damage within its dissipative zones. In fact, the cumulative slip demands on the beam-slab connections were much higher in the cyclic push-out test (around five times) than in the test frame. Figure 5.29d shows that the cumulative slip demand at which Q_{max} obtained from the cyclic push-out test (see Figure 5.7b) degraded by 50%, is 20% higher than the total cumulative slip demand on the west exterior beam-slab connection throughout the three loading stages. Therefore, it seems reasonable to waive the 25% reduction in the shear stud resistance in EN 1998-1 (CEN 2004a) in shallow composite steel beams (i.e., depths less than 500 mm). The test suggests that allowing some degree of slip in the beam-slab connection could be beneficial as it could be engineered by following a capacity design hierarchy to control the additional overstrength that may arise due to the uncertainty of the concrete material and the slab confinement. The uncertainty in shear resistance of ductile headed shear studs is much less than that in the compressive strength of concrete. Accordingly, allowing for a controlled slip response in the beam-slab connection of shallow composite steel beams is a design approach that deserves more attention in future studies.

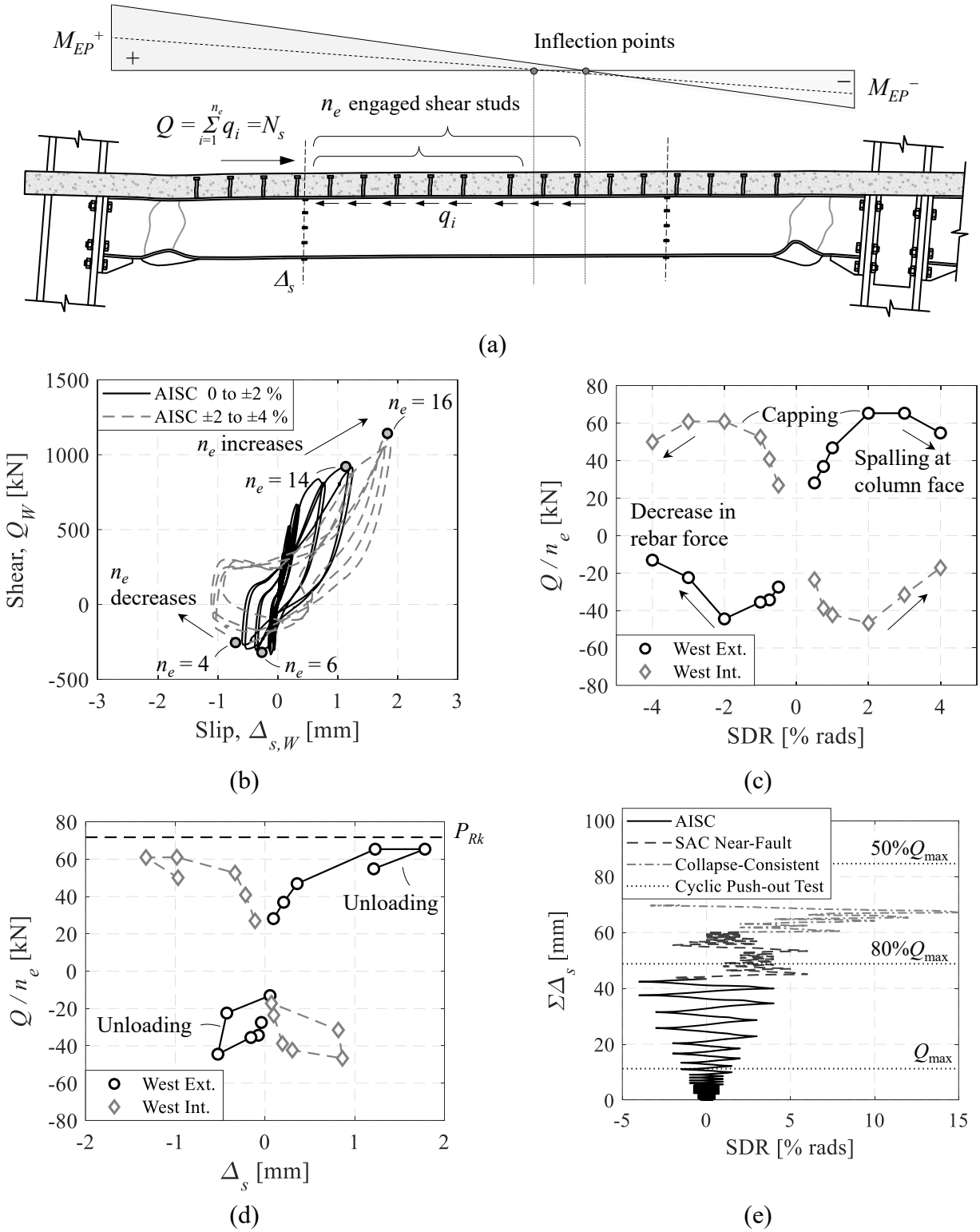

Figure 5.29 Beam-slab connection response: (a) derivation of shear demand on beam-slab connection in the West composite steel beam; (b) hysteretic behavior of the beam-slab connection at the instrumented West exterior cross section under the AISC protocol; (c) average shear force per engaged studs at characteristic peak lateral drift demands (last excursions); (d) average shear force per engaged studs and the corresponding slip demands at characteristic peak lateral drift demands (last excursions); (e) cumulative slip demands in the beam-slab connection at the West exterior cross section

5.4.4 Slab effective width

This section assesses the slab effective width in the test frame under seismic loading. Under sagging bending, the composite steel beams were partially composite due to the overstrength in the slab. Therefore, the effective width in this case was not fully mobilized and cannot be deduced based on the approach discussed herein after the shear force in the studs capped. Nevertheless, the effective widths under sagging bending, b_{eff}^{+} (up to +2% rads), and hogging bending, b_{eff}^{-}, can be derived from the longitudinal strain demands that were extracted from the longitudinal steel reinforcement in the slab at the West exterior joint using the high resolution FOM system (see Figure 5.4e).

A number of simplifying assumptions were made in order to deduce b_{eff}^{+} up to a lateral drift of +2% rads: (i) the slab concrete remained elastic; (ii) no debonding occurred between the longitudinal steel rebars and surrounding concrete when the slab was in compression (i.e, the strain in the rebars coincides with that in the concrete); (iii) the effective depth of the concrete above the profile steel deck only was active; and (iv) the strain profile was linear along the width of the slab and symmetric on each side of the main girder. Based on these assumptions, the strain profile along the centerline of the effective depth of the slab was derived through linear interpolation between the FOM measurements, and extrapolation along the width of the slab. Referring to Figure 5.30b, the effective width, b_{eff}^{+}, was derived as follows,

$$b_e^{+} = \frac{\sum_{i=1}^{6} 0.5(\varepsilon_{cl,i} + \varepsilon_{cl,i+1}) \cdot \delta_{x,i} \cdot E_{c,m}}{f_{c,m}} \tag{5.4}$$

$$b_{eff}^{+} = 2b_e^{+} \tag{5.5}$$

In which, b_e^{+} is the half the effective width of the slab under sagging bending (i.e., on one side of the steel beam as defined in EN 1998-1 (CEN 2004a)); $\varepsilon_{cl,i}$ is the normal strain along the centerline of the effective slab depth (i.e., at $0.5t_c$ from the top of the slab); $\delta_{x,i}$ is defined in Figure 5.30b; $E_{c,m}$ is the modulus of elasticity of concrete; and $f_{c,m}$ is the compressive strength of concrete (see Table 5.2).

The variation of the effective width under sagging bending was traced along the West beam at +1%, +1.5% and +2% rads as shown in Figure 5.30a. It is observed that a higher effective width was mobilized as the lateral drift demand increases. Moreover, the effective width at the face of the column was comparable to the width of the column flange regardless of the lateral drift demand. The effective width at the face of the rib stiffener at +2% rads is around 40% lower than that proposed by EN 1998-1 (CEN 2004a). This behavior is expected since the composite steel beam was partially composite ($\eta = 55\%$) and the full effective width in the slab cannot be mobilized. Further away from the column

face, the effective width in the slab increased to reach its maximum value at 500 mm away from the rib stiffener (see Figure 5.30d).

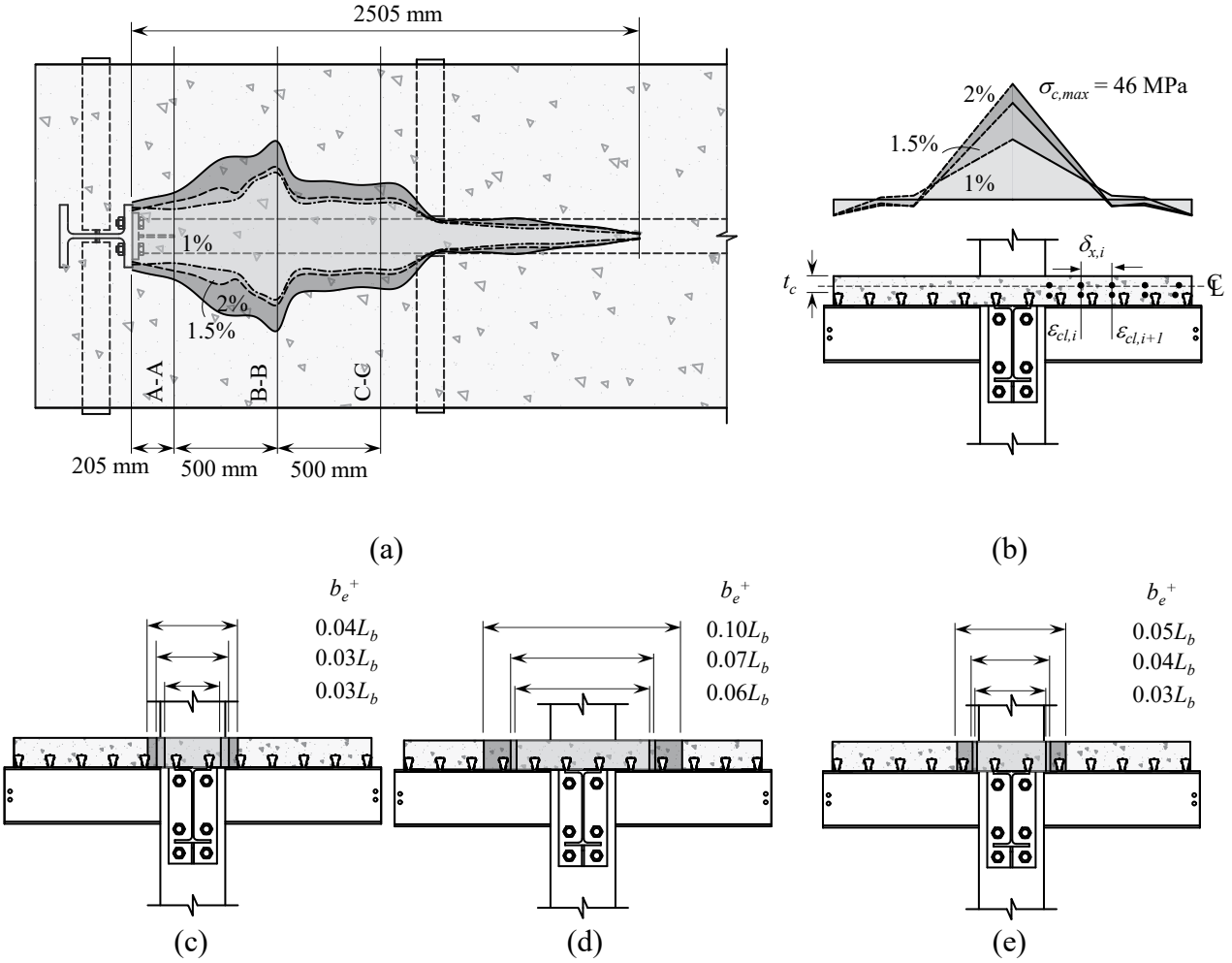

Figure 5.30 Slab effective width under sagging bending: (a) slab effective width profile along the West beam at +1%, +1.5% and +2% rads; (b) normal stress distribution along the slab width at cross section A-A; (c) slab effective width variation at cross section A-A; (d) B-B and; (e) C-C at the target lateral drift demands

The derivation of b_{eff}^{-} at the face of the rib stiffener of the West exterior beam (i.e., in the plastic hinge region) is presented herein. First, the stresses in the rebars should be computed. This is achieved by providing the uniaxial cyclic strain demands that were directly measured from the steel reinforcement to a calibrated constitutive material model that describes the hysteretic response of the B500 steel rebars under inelastic cyclic straining. Characteristic strain demands extracted from the FOM system are shown in Figure 5.31a for three selected rebars. The Voce-Chaboche (VC) constitutive material model (Lemaitre and Chaboche 1990; Voce 1948) was employed for this purpose. The constrained optimization approach proposed by de Castro e Sousa et al. (2021) was implemented in order

to infer consistent input model parameters from the available monotonic tensile tests on B500B steel rebars. Figure 5.31b shows a comparison between the simulated and measured true stress-true strain behavior of one of the steel rebars. For each rebar, the strain history is obtained from the FOM, and the hysteretic stress-strain response throughout loading is derived based on the VC constitutive model as illustrated in Figure 5.31c for three indicative rebars. The stress profile at peak lateral drift demands of the AISC symmetric loading protocol is shown in Figure 5.31d. Finally, b_{eff}^{-} may be calculated as follows,

$$b_e^- = \left(\frac{\Sigma\sigma_{s,i}}{2f_{y,n}} - 1\right) \cdot s + s_o \tag{5.6}$$

$$b_{eff}^- = 2b_e^- \tag{5.7}$$

In which, b_e^- is the half the effective width of the slab under hogging bending (i.e., on one side of the steel beam as defined in EN 1998-1 (CEN 2004a)); $\sigma_{s,i}$ is the normal stress in each rebar at the desired peak lateral drift demands; $f_{y,n}$ is the nominal yield stress of the rebars (500 MPa); s is the average spacing between the slab rebars; and s_o is the distance between the beam centerline and the nearest longitudinal rebar.

Referring to Figure 5.31e, the effective width under hogging bending increased with increasing lateral drift demands. Also shown in Figure 5.31e are the values corresponding to half the effective width, b_e^-, which is equal to $0.1L_b$ according to EN 1998-1 (CEN 2004a). During elastic loading (-0.75% rads), the effective width was around a third of that proposed by EN 1998-1, $b_{eff,EC}^-$ (CEN 2004a). The effective width increased at -2% rads to 90%$b_{eff,EC}^-$. However, following the -2% lateral drift amplitude, yielding in the slab rebars closest to the column resulted in the redistribution of stresses to the rebars further away from the column as shown in Figure 5.31d. A 20% higher effective width than that proposed by EN 1998-1 (CEN 2004a), was mobilized as the rebars near the column experienced axial yielding. Referring to Figure 5.31a, the strain demand in the top rebar further away from the beam centerline (rebar C) is considerably lower, initially, than in the rebars closer to the beam centerline (rebars A and B). However, upon further loading axial yielding in rebars A and B (see Figure 5.31c) resulted in stress redistribution along the width and an increase in the strain demands in the rebars away from the beam centerline. Note that the effective width could not be determined at -4% rads because the fibers on the rebars closest to the column failed.

Figure 5.32 shows the variation of the effective width under hogging bending along the West beam at -1%, -2% and -3% rads. At -3% lateral drift demand, the effective width was highest at the face of

the column and decreased to around 60% and 25% of its maximum value at a distance of 500 mm and 1000 mm, respectively, from the face of the rib (see Figure 5.32d and e).

The above findings demonstrate that the EN 1998-1 formulation for b_{eff}^{-} is satisfactory for modest lateral drift demands associated with a design-basis earthquake (i.e., 10% probability of exceedance over a 50 year building life expectancy). Nevertheless, at higher lateral drift demands, the stress re-distribution, following the axial yielding of the rebars, mobilizes a larger effective width. This may have an impact on the strong-column/weak-beam ratio that is employed by current seismic design standards for collapse prevention of composite steel MRFs. Accordingly, the slab contribution to the flexural resistance of the composite steel beam under hogging bending increases. This issue requires further investigation as part of future studies.

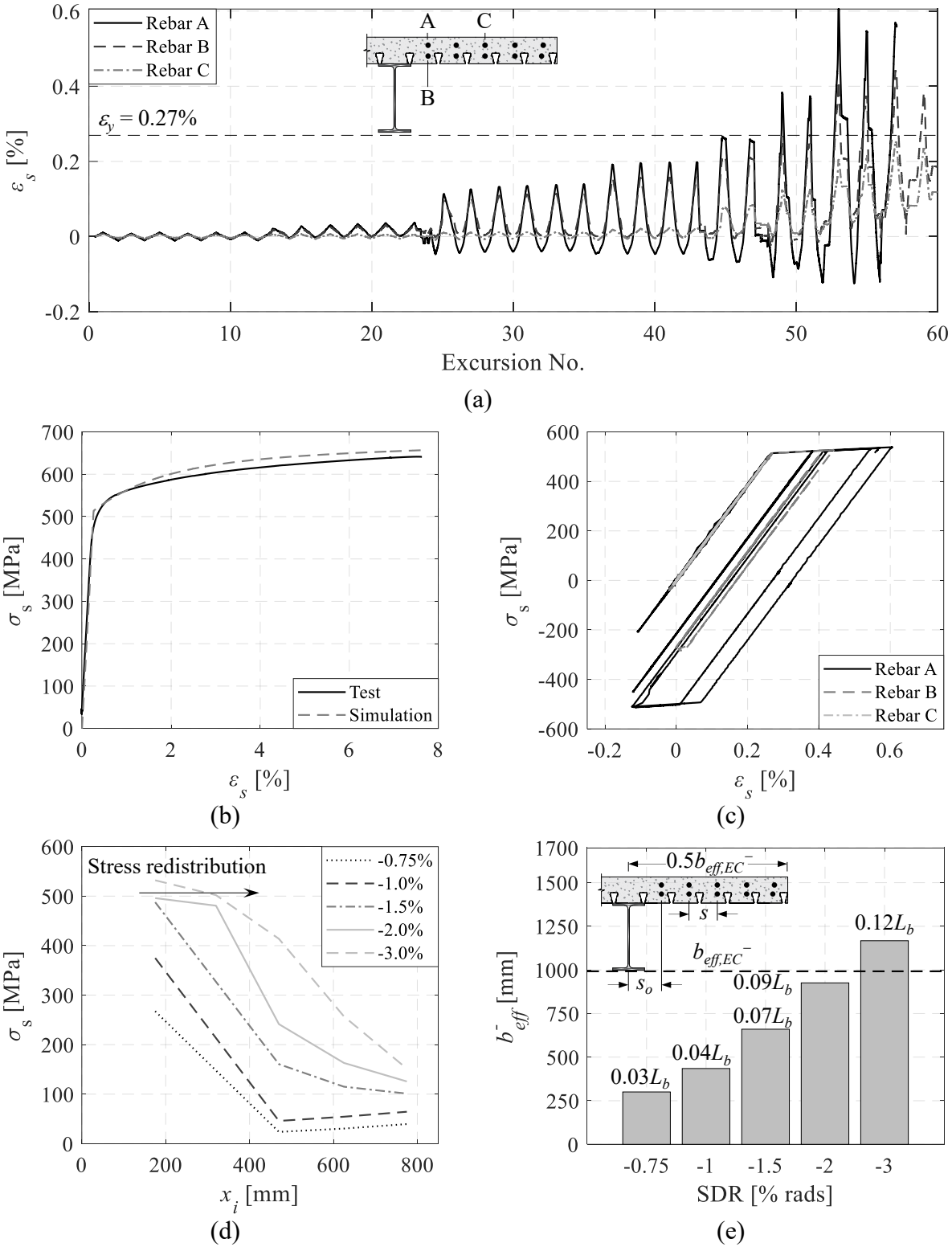

Figure 5.31 Derivation of the slab effective width under hogging bending: (a) uniaxial strain history at selected rebars; (b) comparison between the monotonic tensile test of the rebars and the simulated behavior with optimized Voce-Chaboche parameters; (c) stress-strain behavior of the three selected rebars obtained from the uniaxial strain history; (d) stress distribution in the top rebars at x_i from the beam centerline; (e) derived effective widths at selected peak lateral drift demands of the AISC symmetric protocol and comparison with EN 1998-1 (CEN 2004a)

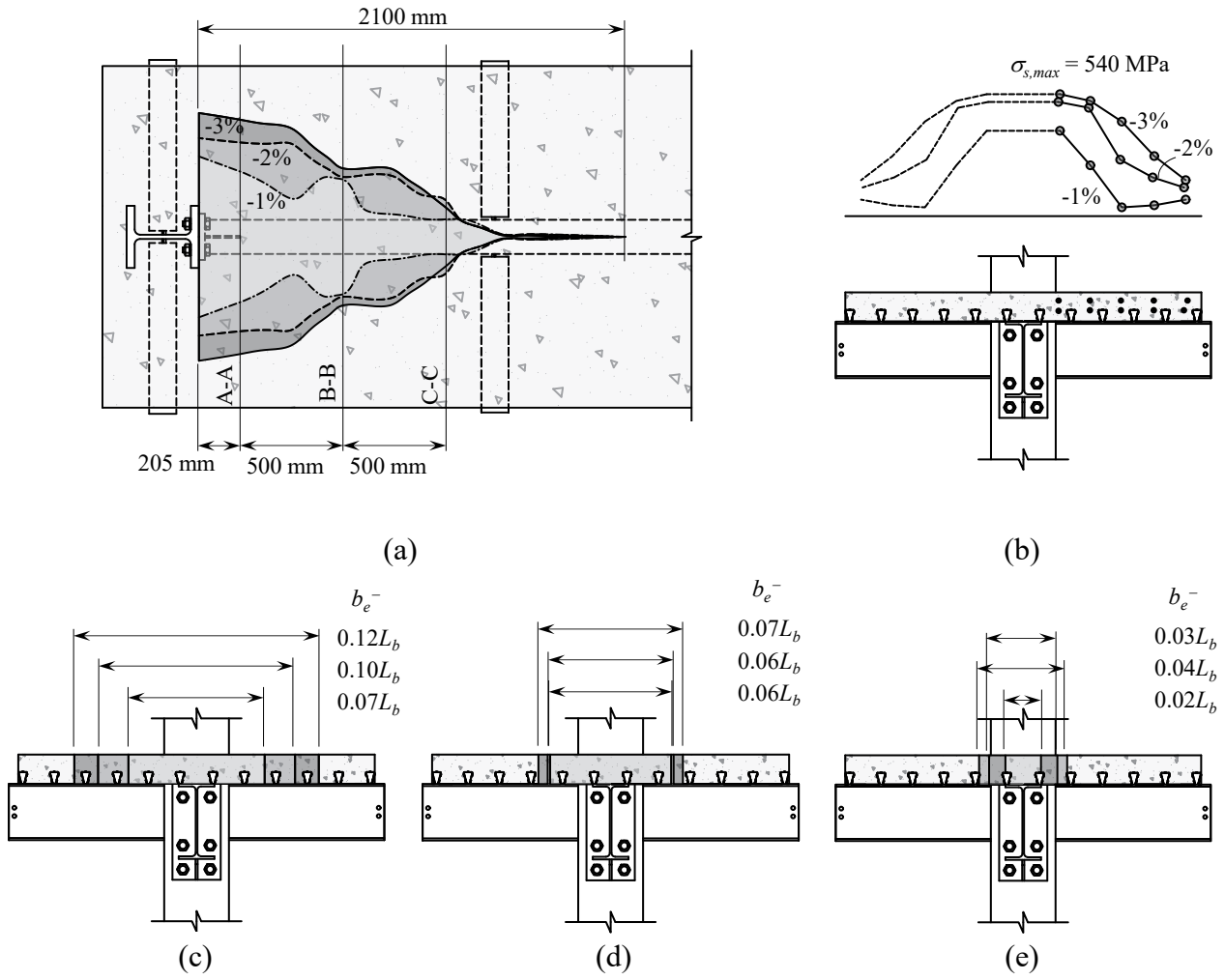

Figure 5.32 Slab effective width under hogging bending: (a) slab effective width profile along the West beam at -1%, -2% and -3% rads; (b) normal stress distribution in the top rebars at cross section A-A; (c) slab effective width variation at cross section A-A; (d) B-B and; (e) C-C at the target lateral drift demands

5.5 Conclusions

This chapter presents findings from a full-scale experimental program of a two-bay composite steel MRF subsystem from a prototype composite steel MRF designed according to current Eurocode provisions (CEN 2004a; b, 2005b; c). The test frame was subjected to three loading histories (AISC symmetric, SAC near-fault and collapse-consistent protocols) up to a lateral drift demand of 15% rads. Extensive instrumentation was employed (350 sensors in total) to capture the hysteretic response at the global and local level. The test data are unique since unlike prior experiments, the effects of slab restraint and framing action were assessed on the system behavior and quantified from the onset of damage through structural collapse. Moreover, the influence of transverse beams and slab confinement on the flexural resistance of composite steel beams were investigated. Finally, implications on

the design of composite steel beams and beam-slab connections in composite steel MRFs were highlighted. The main findings are summarized below:

- Composite action augmented the elastic stiffness of the composite steel MRF by around 50% compared to that of the corresponding bare frame which is consistent with findings from prior experimental work (El Jisr et al. 2019).
- The composite steel beams experienced yielding in the bottom flange at a lateral drift demand of 1% rads followed by local buckling initiation during the 3% loading cycles. This was due to the presence of longitudinal reinforcement in the slab, which increased the compressive strain demand on the bottom flange. Moreover, composite action resulted in minimal local buckling in the top flange of the composite steel beams. The base shear and flexural resistance of the beams under sagging bending capped at 3% lateral drift demand due to the capping of the shear resistance of the heads shear studs. Upon further loading, crushing and spalling of the slab at the column face resulted in a drop in the flexural resistance of the composite steel beams. Nevertheless, all beam-to-column connections conform to the acceptance criteria for prequalification in AISC 341-16 (AISC 2016a), and seismic design category DC3 in the new Eurocode 8 provisions (CEN 2019).
- The hysteretic behavior of the test frame showed cyclic deterioration in story shear resistance at large lateral drift demands (up to 8% rads) due to local buckling at the bottom flanges of the composite steel beams as well as concrete crushing. Additional instabitlies that caused cyclic deterioration in story shear resistance was the crack initiation and ductile tearing that occurred in the West and East composite steel beams, respectively. Nevertheless, the axial restraint provided by the slab and framing action stabilized the cracks, hindering crack propagation along the beam depth, and caused partial straightening of the local buckles. The test frame was able to maintain about 30% of its peak resistance at a lateral drift demand of 15% rads.
- Minimal axial shortening was observed (5 mm) in the composite steel beams throughout the loading history. The straightening of local buckles that occurred due to the axial restraint provided by the slab and framing action had a profound effect on the rate of flexural strength degradation of the composite steel beams under hogging bending. The composite steel beams were able to sustain about 50% of their peak flexural strengths under hogging bending.

- Quantification of the effects of slab continuity and framing action showed that a tensile force equal to 8% of the axial plastic resistance of the bare steel beam was induced at lateral drift demand of 10% rads. Moreover, the axial restraint induced a compressive force in the slab, which reached around 35% of the axial plastic resistance of the bare steel beam during the collapse consistent protocol and decreased following crack propagation, thereby stabilizing the crack. The developed axial forces have a significant effect on the stabilization of the local buckles and crack propagation in composite steel beams.

- The presence of transverse beams, framing the column web panel zones and primary girders, influenced the flexural resistance of the composite beam-to-column connections. Transverse compressive strains, due to slab confinement, were observed at the surface of the slab in the vicinity of the columns at both the interior and the exterior joints. Moreover, higher compressive strains (0.0025 compared to 0.001) were observed at the interior joints due to the slab continuity and the transverse beams being equipped with two rows of headed shear studs. This source of overstrength in the composite steel beams should be accounted for in capacity design and requires further attention.

- The crack patterns, that were derived from DIC measurements, revealed the presence of two load transfer mechanisms under sagging bending: (a) bearing of the slab on column face, and (b) inclined compression struts on the sides of the column (CEN 2004a; Plumier et al. 1998). Under hogging bending, horizontal flexural cracks were observed at the surface of the slab. The horizontal cracks grew to a maximum of 0.9 mm at a lateral drift demand of 2% rads. At the same drift amplitude, the observed cracks were wider at the exterior joint than the interior joint (0.4 mm) due to higher degree of confinement at the interior joints.

- The equivalent moment of inertia of the composite steel beams is estimated well at the exterior joints for both sagging and hogging bending. However, at the interior joint the equivalent moment of inertia is underestimated by 25% and 35% for sagging and hogging bending respectively. The difference is attributed to the continuity of the slab and reinforcement in the vicinity of the column, as well as the presence of transverse beams with two rows of shear connectors.

- Prior to crushing of the concrete at the slab-column interface, the longitudinal compressive strain demands at the surface of the slab reached 0.005 to 0.006 when the composite steel beams were subjected to sagging bending due to the slab confinement. These findings suggest

that the ductility requirements for composite steel beams in EN 1998-1 (CEN 2004a), that limit position of plastic neutral axis to avoid premature crushing, should be revised.

- Modest slip demands (< 2 mm) were observed in the beam-slab connection of the test frame during the AISC symmetric protocol. The low slip demands were due to force redistribution between the studs and the shift in the location of the inflection points, which allowed more studs to be engaged under sagging bending. Moreover, the integrity of the beam-slab connection was maintained despite the degree of composite action being 55% based on the measured material properties. In that respect, it seems rational to waive the 25% reduction in shear resistance of headed studs required by current seismic design provisions (AISC 2016a; CEN 2004a), at least for shallow composite steel beams (depth less than 500 mm).

- The shear demands of the headed shear studs capped at a lateral drift demand of 3% rads, thereby limiting the force in the slab under sagging bending. These findings show that allowing some degree of slip in the ductile shear studs in shallow composite steel beams could be beneficial to control the overstrength that may arise due to concrete overstrength and slab confinement.

- The slab effective width under hogging bending, which is derived by using the EN 1998-1 (CEN 2004a) formulation, estimates the effective width fairly well at 2% rads. However, at higher lateral drift demands, stress redistribution occurs in the longitudinal reinforcement, thereby leading to a larger mobilized effective width. This issue may impact the capacity design hierarchy in composite steel beams under hogging bending and requires further attention.

5.6 Notation

a_{gR} = reference peak ground acceleration

b = flange width of the steel member

b_e^+ = half the slab effective width under sagging bending

b_e^- = half the slab effective width under hogging bending

b_{eff}^+ = slab effective width under sagging bending

b_{eff}^- = slab effective width under hogging bending

$b^{-}_{eff,EC}$ = slab effective width under hogging bending according to CEN (2004a)

d_b = depth of the primary steel girder

d_{bo} = full bolt diameter

d_{sc} = diameter of the headed shear studs

$f_{c,14}$ = compressive strength of concrete at 14 days after casting

$f_{c,28}$ = compressive strength of concrete at 28 days after casting

$f_{c,m}$ = compressive strength of concrete at the day of the third loading stage

f_{ck} = characteristic cylinder compressive strength of concrete

f_y = yield strength of the steel material based on the mill certificates

$f_{y,m}$ = measured yield strength of the steel material

$f_{y,n}$ = nominal yield stress of the steel reinforcement

f_u = ultimate strength of the steel material based on the mill certificates

$f_{u,b}$ = bolt ultimate tensile stress assuming the threaded area to be $A_s = 561$ mm^2

$f_{u,m}$ = measured ultimate strength of the steel material

h = depth of the composite cross section (including the slab)

h_i = distance along the depth of the steel beam measured from the bottom flange

h_s = depth of the steel member

h_{sc} = height of the headed shear studs

i_z = radius of gyration of the primary girder about its weak axis

k_r = rib shape efficiency factor according to CEN (2004a)

k_t = factor for reduction in the shear resistance of headed studs (CEN 2004a)

n_e = number of engaged shear studs

n_s = number of shear studs between the point of zero moment and the cross section instrumented with strain gauges

q = behavior factor

s = average spacing between the slab rebars

s_o = distance between the beam centerline and the nearest longitudinal rebar

t_c = effective depth of the slab

t_f = flange thickness of the steel member

t_w = web thickness of the steel member

x_i = distance from the beam centerline

x_{pl}^+ = position of the plastic neutral axis in the composite cross section from the top of the slab

E = measured elastic modulus of the steel beam

$E_{c,14}$ = measured elastic modulus of concrete at 14 days after casting

$E_{c,28}$ = measured elastic modulus of concrete at 28 days after casting

$E_{c,m}$ = measured elastic modulus of concrete at the day of the third loading stage

$F_{u,b}$ = bolt ultimate load

I_{bare} = moment of inertia of the bare IPE360 girder

I_c^+ = equivalent moment of inertia of the composite steel beam under sagging bending

I_c^- = equivalent moment of inertia of the composite steel beam under hogging bending

$I_{c,EC}^+$ = equivalent moment of inertia of the composite steel beam under sagging bending according to CEN (2004a)

$I_{c,EC}^-$ = equivalent moment of inertia of the composite steel beam under hogging bending according to CEN (2004a)

K_{el}^+ = elastic flexural stiffness of the composite steel beam under sagging bending

K_{el}^- = elastic flexural stiffness of the composite steel beam under hogging bending

K_s = shear rotational stiffness of the IPE360 girder

L_b = beam length measured from the centerline of the columns

L_{br} = maximum unbraced length in the primary girders

L_c^+ = shear span in the composite steel beam under sagging bending

L_c^- = shear span in the composite steel beam under hogging bending

L_f = final length of the bolt measured from the bottom of the head to the tip of the shank

L_o = initial length of the bolt measured from the bottom of the head to the tip of the shank

L_i = distance along the beams measured from the centerline of the interior column

M_{pl}^+ = plastic flexural resistance of the composite steel beam under sagging bending calculated at the face of the end plate

M_{pl}^{-} = plastic flexural resistance of the composite steel beam under hogging bending calculated at the face of the end plate

M_{u}^{+} = peak moment in the composite steel beams under sagging bending

M_{u}^{-} = peak moment in the composite steel beams under hogging bending

M_{EP}^{+} = sagging moment in the composite steel beam at the face of the end plate

M_{EP}^{-} = hogging moment in the composite steel beam at the face of the end plate

$M_{E,EP}$ = moment in the East composite steel beam at the face of the East exterior joint end plate

$M_{IE,EP}$ = moment in the East composite steel beam at the face of the interior joint end plate

$M_{IW,EP}$ = moment in the West composite steel beam at the face of the interior joint end plate

$M_{W,EP}$ = moment in the West composite steel beam at the face of the West exterior joint end plate

N_{cb} = axial force in the composite steel beam

$N_{cb,\max}$ = maximum axial force in the composite steel beam

$N_{c,E}$ = axial force in the bottom region of the East exterior column

$N_{c,W}$ = axial force in the bottom region of the West exterior column

$N_{pl,Rm}$ = plastic resistance of the bare steel beam cross section that is calculated using the measured yield stress

N_{s} = axial force in the slab

$N_{s,\max}$ = maximum axial force in the slab

P_{Rk} = characteristic shear resistance of one shear stud (CEN 2004b)

Q = shear force in the beam-slab connection

Q_{max} = maximum shear force in the beam-slab connection

Q_{W} = shear demand in the beam-slab connection at the instrumented cross section near the West exterior joint

R_{y} = material overstrength factor according to AISC (2016a)

SDR = story drift ratio

$V_{c,b}$ = column shear force below the floor level

$V_{c,t}$ = column shear force above the floor level

V_{max} = peak base shear in the test frame

δ_b = axial shortening in the steel beam measured along the centerline

$\delta_{b,E}$ = axial shortening in the East steel beam

$\delta_{b,W}$ = axial shortening in the West steel beam

$\delta_{e,b}$ = measurement of the bottom string pot in the beam located at the exterior joint

$\delta_{e,t}$ = measurement of the top string pot in the beam located at the exterior joint

$\delta_{i,b}$ = measurement of the bottom string pot in the beam located at the interior joint

$\delta_{i,t}$ = measurement of the top string pot in the beam located at the interior joint

$\delta_{x,i}$ = distance between two normal compressive strain values along the centerline of the effective slab depth

$\delta_{z,W}$ = out-of-plane displacements in the West steel beam in the vicinity of the interior joint

$\delta_{z,E}$ = out-of-plane displacements in the East steel beam in the vicinity of the interior joint

ε = true axial strain in the steel coupons

ε_c = concrete compressive strain

$\varepsilon_{cl,i}$ = normal strain along the centerline of the effective depth of the slab

ε_{cu} = concrete crushing strain

ε_s = axial strain in the rebars

ε_u = ultimate tensile elongation of the steel material

$\varepsilon_{u,b}$ = bolt elongation at fracture

ε_y = yield strain in the bottom flange of the steel beam

θ_b = beam chord rotation

σ = true axial stress in the steel coupons

σ_c = concrete compressive stress

$\sigma_{c,max}$ = maximum compressive stress along the centerline of the slab effective depth

$\sigma_{s,i}$ = axial stress in the rebar instrumented with FOM

$\sigma_{s,max}$ = maximum axial stress in the rebars

Δ_s = slip in the beam-slab connection

Chapter 6 Proposed nonlinear macro-model for seismic risk assessment of composite-steel moment resisting frames

Bibliographic details

This chapter presents the pre-print (submitted) version of the article with the following full bibliographic details: El Jisr, H., Kohrangi, M., and Lignos, D. G. (2021). "Proposed nonlinear macro-model for seismic risk assessment of composite-steel moment resisting frame." *Earthquake Engineering & Structural Dynamics*, Wiley, (Under review).

Authors' contribution

Hammad El Jisr developed the proposed nonlinear micromodel, carried out the nonlinear system level simulations, analyzed the simulations results, conducted the seismic risk assessment of composite steel moment resisting frames, created the figures, wrote the manuscript draft and revised the manuscript. Mohsen Kohrangi conducted the site-specific probabilistic seismic hazard analysis. Dimitrios Lignos contributed in developing the methodology presented in this chapter, supervising the work conducted by Hammad El Jisr, funding acquisition, and reviewing and editing the original and final manuscript drafts.

6.1 Abstract

This chapter proposes a macro-model for simulating the hysteretic behavior of composite steel beams as part of fully restrained beam-to-column connections in composite steel moment-resisting frames (MRFs). Comparisons with experimental data suggest that the proposed model captures the asymmetric hysteretic response of composite steel beams including the cyclic deterioration in strength and stiffness. Moreover, the proposed model captures the primary slab-column force transfer mechanisms and predicts the slip demands in beam-slab connections under inelastic cyclic loading. The modeling approach is employed in a system-level study to benchmark the seismic collapse risk of composite steel MRF buildings across Europe. Moreover, the beam-slab slip demands are quantified through the development of beam-slab slip hazard curves. The simulation studies suggest that the examined composite steel MRFs exhibit a system overstrength of about 4. This is attributed to the drift requirements in the current European seismic provisions. The annualized probability of collapse of the prototype buildings is well below 1% over a 50-year building life expectancy regardless of the design site and the degree of composite action. Beam-slab connections with a partial degree of composite action experience minimal damage for frequently occurring seismic events (i.e., 50% probability of exceedance over 50 years); and light cracking in the slab for a design basis earthquake. The above are important from a seismic repairability standpoint. Accordingly, it is recommended that the 25% reduction in the shear resistance of stud connectors is not imperative for seismic designs that feature steel beams with depths less than 500 mm.

6.2 Introduction

Performance-based seismic evaluation of frame buildings has gained attention over the past two decades (Cornell and Krawinkler 2000; FEMA 2012). While capacity design rules have been benchmarked to establish a tolerable risk for collapse safety of modern steel (Elkady and Lignos 2014, 2015b; Gupta and Krawinkler 1999; Macedo et al. 2019; Sanchez-Ricart and Plumier 2008; Tsitos et al. 2018; Zareian and Kanvinde 2013) and reinforced concrete (RC) moment-resisting frames (MRFs) (Dooley and Bracci 2001; FEMA 2009; Galanis and Moehle 2015; Haselton et al. 2011; Leon 1990a), there is a lack of similar studies for composite steel MRFs, that constitute the main focus of this chapter. (Denavit et al. 2016) proposed seismic performance factors for moment frames with steel-concrete composite columns and steel beams by employing the FEMA P695 methodology (FEMA 2009). However, the role of slab was disregarded in this case.

Prior modeling approaches to consider the role of slab in full- and/or partially-composite steel MRFs disregarded important aspects of the composite beam behavior. Mehanny and Deierlein (2000) examined the seismic behavior of composite MRFs. However, the resultant section models ignored the effects of shear stud degradation. Others (Bursi et al. 2005; Elghazouli et al. 2008; Zona et al. 2008) employed fiber-based models to simulate the hysteretic behavior of composite-steel members, with the same limitations as those discussed in Mehanny and Deierlein (2000). Furthermore, these models disregarded the influence of cyclic deterioration due to cross-sectional local buckling. Elkady and Lignos (2014) proposed a holistic approach to consider the effects of the composite action on the hysteretic behavior of composite steel beams exhibiting cyclic deterioration in flexural strength and stiffness. However, they only focused on deep beams (i.e., depths larger than 500 mm), which are typical in the US seismic design practice, with a relatively low degree of composite action (i.e., 10%). Moreover, the deteriorating behavior of the shear stud connectors was disregarded. Other modeling approaches include the component method (Tschemmernegg and Queiroz 1995) which is suitable for system-level nonlinear simulations of MRFs with composite floor slabs. However, this method has been mainly used to simulate the behavior of partially-restrained beam-to-column connections (Amadio et al. 2008; Braconi et al. 2007; Rassati et al. 2004). In particular, the degrading hysteretic behavior of the shear studs as well as that of steel beams has been neglected.

Bursi et al. (2005) and Zona et al. (2008) studied the nonlinear dynamic response of composite steel MRFs with a variable degree of composite action. Composite steel beams with a partial degree of composite connection (i.e., < 80%) may result in cost savings through the reduction in the number of shear studs and the transverse reinforcement of the slab. Moreover, partially composite beams impose lower demands on the columns and the beam-to-column web panel zone joint than their fully composite counterparts (Bursi et al. 2005). On the other hand, the loss of composite action due to cyclic deterioration in the shear resistance of beam-slab connectors is undesirable since it leads to the loss of the load transfer mechanism between the beam-slab connections (Cordova and Deierlein 2005).

The current seismic provisions (AISC 2016a; CEN 2004a) propose a 25% reduction in the design shear resistance of the beam-slab connectors in order to decrease the inelastic slip demand on the shear studs and maintain their integrity. According to EN 1998-1 (CEN 2004a), the beneficial aspects of the composite action may only be considered in seismic design when the degree of composite action is at least 80%. Moreover, conventional push-out (Bursi and Gramola 1999; Civjan and Singh 2003; Zandonini and Bursi 2000) and subassembly tests (Cheng and Chen 2005; Civjan et al. 2001) have shown that shear studs experience severe shear degradation under cyclic loading. Nevertheless, Suzuki and Kimura (2019) found that in composite steel MRFs, the shear stud hysteretic performance

is far different from that deduced by conventional cyclic push-out tests because of the stress state in the slab (i.e., concrete slab subjected to tensile or compressive stresses upon load reversals). This is acknowledged in recent beam-slab connection tests with more realistic boundary conditions (Suzuki and Kimura 2019). El Jisr et al. (2020) showed that the slip demands in beam-slab connections of capacity-designed composite-steel MRFs is not large enough to endanger the integrity of partially composite beams with shallow cross sections (depth less than 500 mm). To the best of our knowledge, the shear connector slip demands have never been benchmarked by means of system-level nonlinear response history analyses. These are essential in establishing failure rate criteria for beam-slab connections in capacity-designed composite steel MRFs in a consistent manner with performance-based design. Such an endeavor requires a nonlinear model that explicitly simulates the slip demands within beam-slab connections.

In this chapter, we propose a nonlinear macro-model for simulating the deteriorating cyclic behavior of fully restrained beam-to-column connections in composite steel MRFs. The proposed model, which is computationally efficient, captures the deteriorating response of the shear connectors and the composite steel beam under monotonic and reversed cyclic loading. The proposed macro-model is thoroughly validated with available experimental data from prior testing programs. The model is then incorporated in nonlinear models of prototype composite steel MRF buildings designed according to EN 1998-1 (CEN 2004a) at three different European sites. The degree of composite action in the composite beam is varied and its influence on the seismic behavior of the composite steel MRFs is evaluated by means of nonlinear building simulations. Particularly, we quantify the site-specific collapse risk dependence on the assumed degree of composite action. Finally, we quantify the integrity of the beam-slab connection in the prototype composite steel MRFs through novel beam-slab connection slip hazard curves, which may constitute a valuable tool for more effective designs of composite steel MRFs in prospective revisions of current seismic design standards (AISC 2016a; CEN 2004a).

6.3 Behavioral insights on composite beam-to-column connections

Experimental studies on subassemblies (Bursi and Gramola 2000; Civjan et al. 2001; Engelhardt et al. 2000; Ricles et al. 2004) and frames (Del Carpio et al. 2018; Nakashima et al. 2006, 2007) with a composite slab have demonstrated that the behavior of composite connections differs from their bare steel counterparts. The differences are primarily manifested in (i) the flexural stiffness and strength of composite steel beams under sagging and hogging bending; (ii) the pre- and post-peak plastic

rotation under sagging and hogging and (iii) the inelastic behavior of the beam-to-column web panel zones.

The presence of the slab augments the flexural stiffness of beams under sagging bending by up to two times (El Jisr et al. 2019). Moreover, a flexural strength enhancement (up to 80%) is particularly evident under sagging bending and is dependent on the beam depth, the slab properties and the degree of composite action (El Jisr et al. 2019). Figure 6.1a illustrates the axial forces ($F_s^{\pm}$, $F_b^{\pm}$) and bending moments ($M_s^{\pm}$, $M_b^{\pm}$) in the floor slab (noted with subscript *s*) and steel beam (noted with subscript *b*) under sagging and hogging bending, respectively. During an earthquake, the inertia forces are transferred to the steel beams through the shear connectors and friction between the beam-slab interface. Moreover, the inertia forces pass to the column through two primary mechanisms, i.e., column face bearing and the strut-and-tie mechanism (CEN 2004a; Doneux 2002; Plumier et al. 1998) as shown in Figure 6.1b.

The characterization of the hysteretic behavior of the shear connectors is imperative for capturing the flexural resistance of composite steel beams. Cyclic push-out tests that accounted for the slab stress state (Suzuki and Kimura 2019) demonstrated that the hysteretic behavior of the shear studs becomes asymmetric under reversed cyclic loading. Moreover, shear strength degradation of the studs is not as pronounced as that inferred by conventional cyclic push-out tests (Bursi and Gramola 1999; Civjan and Singh 2003; Zandonini and Bursi 2000).

The presence of the slab restraints the top beam flange against local buckling (Ricles et al. 2004). As a consequence, the rate of flexural strength deterioration under sagging bending decreases relative to that of the bare steel beam (Engelhardt et al. 2000; FEMA 2000a; Ricles et al. 2004). On the other hand, the plastic rotation capacity under hogging bending decreases relative to that of the bare steel beam. This is cause by the upward shift of the neutral axis of the composite beam cross section due to the presence of reinforcing rebars in the slab. Figure 6.1c shows schematically the influence of the floor slab on the backbone monotonic curve of a composite steel beam under sagging and hogging bending.

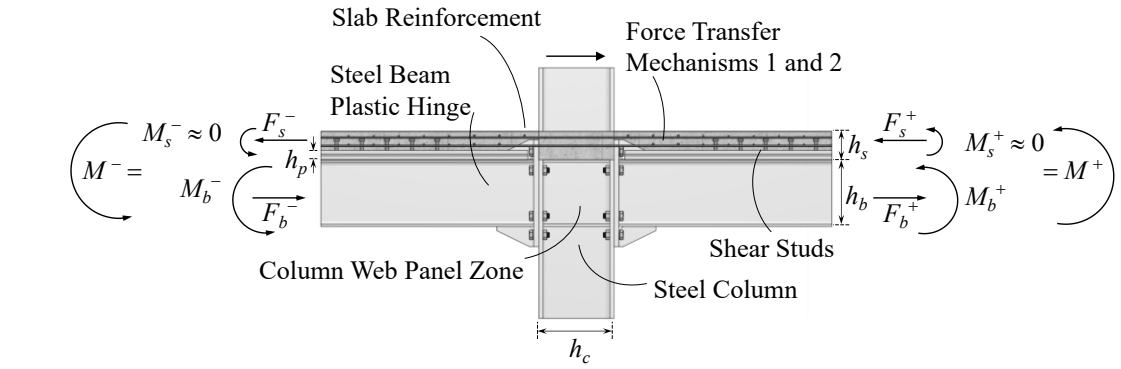

(a)

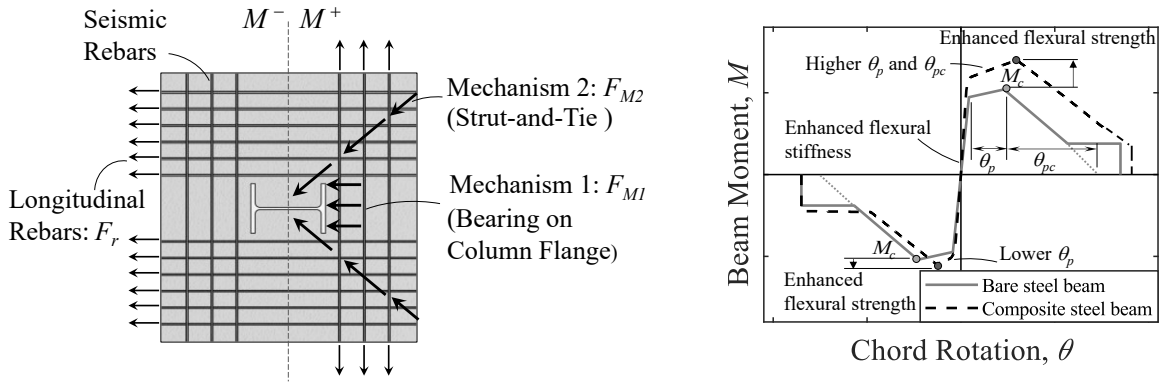

(b) (c)

Figure 6.1 Typical fully-restrained composite beam-to-column connection (a) internal forces in the composite steel beams; (b) slab-column force transfer mechanisms; (c) comparison between the moment rotation response of a bare and a composite steel beam

The presence of the slab may influence the behavior of the beam-to-column web panel zone. This is attributed to the increased moment demand at the center of the panel zone, and the increased effective depth of the panel zone under sagging bending (Kim and Engelhardt 2002). Collectively, the above important findings are confirmed through experimental evidence (El Jisr et al. 2019) as well as high-fidelity continuum finite element analyses (El Jisr et al. 2020). The aforementioned behavioral insights should be incorporated in the proposed macro-model of composite steel beams.

6.4 Proposed model for composite steel beams

Figure 6.2 shows schematically the proposed macro-model for simulating the response of composite steel beams. The model consists of an elastic beam-column element and seven nonlinear elements. These elements simulate both the bearing and strut-and-tie force transfer mechanisms of the slab-column. Moreover, the slab rebars and beam-slab interaction are considered.

The flexural stiffness of the elastic beam-column element is adjusted by using an equivalent moment of inertia, which may be calculated as follows,

$$I_{eq} = 0.6I^{+} + 0.4I^{-} \tag{6.1}$$

$$I^{+} = I_{bare} + \sqrt{\eta} \cdot (I_{c,f} - I_{bare}) \tag{6.2}$$

$$I^{-} = I_{bare} \tag{6.3}$$

$$I_{eq} = I_{bare} + 0.6\sqrt{\eta} \cdot (I_{cf} - I_{bare}) \tag{6.4}$$

in which, I^{+} and I^{-} are the moments of inertia of the composite steel beam under sagging and hogging bending, respectively; they are calculated as per EN 1998-1 (CEN 2004a) or ANSI/AISC 360-16 (AISC 2016b); I_{bare} is the second moment of area of the bare steel beam; $I_{c,f}$ is the moment of inertia of the uncracked fully composite steel beam under sagging bending. It may be calculated either by EN 1998-1 (CEN 2004a) or by ANSI/AISC 360-16 (AISC 2016b); and η is the degree of composite action under sagging bending. This is defined as the ratio of the actual number of shear studs to that required to achieve full composite action.

Referring to Figure 6.2, the three axial nonlinear elements represent the two mechanisms of the slab-to-column force transfer under sagging bending, in addition to the longitudinal rebars under hogging bending. These elements are assumed to act at the mid-depth portion of the slab above the profiled steel deck. Their length is assumed to be equal to 1.5 times the column depth, h_c (Menapace 1997; Rassati et al. 2004). The dissipative zones of the bare steel beams are idealized by zero-length rotational elements. Furthermore, the beam-slab connection is modeled using axial zero-length elements that lump together the shear force – slip relationship of all the shear studs per shear span. Referring to Figure 6.2, the parallelogram model (Gupta and Krawinkler 1999) may be adopted to simulate the hysteretic behavior of the beam-to-column web panel zone.

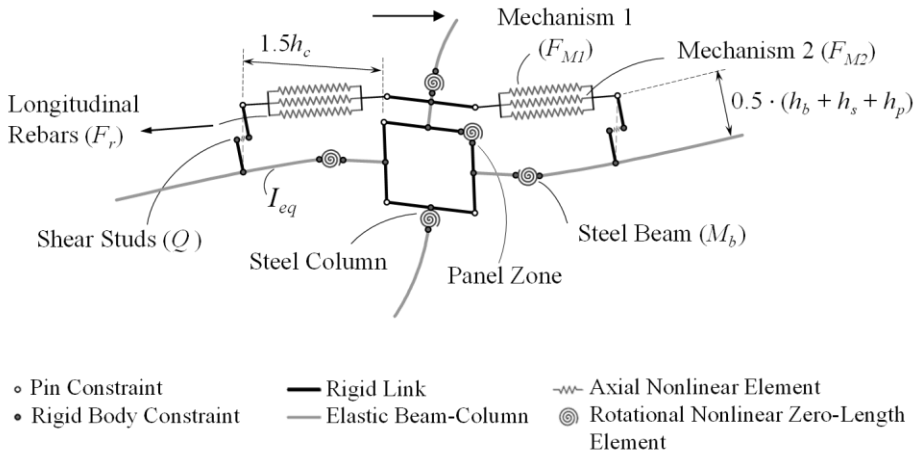

Figure 6.2 Nonlinear macro-model schematic representation

The sagging and hogging flexural demands on the composite steel beam may be calculated as follows (see Figure 6.1),

$$M^{\pm} = M_b^{\pm} - 0.5F_s^{\pm} \cdot (h_b + h_s + h_p) \tag{6.5}$$

in which, $M_b^{\pm}$ is the bending moment in the steel beam that considers the interaction of bending and axial load due to the presence of the slab as discussed later on; $F_s^{\pm}$ is the axial force in the slab due to the composite action. Referring to Figure 6.1a, this force is assumed to act at the centerline of the concrete above the profiled steel deck; h_b is the depth of the steel beam; h_s is the thickness of the floor slab; and h_p is the height of the profiled steel deck (see Figure 6.1a).

Figure 6.3a shows mechanism 1 i.e., bearing of the slab on the column flange. The force transferred by direct compression spreads through the effective width of the slab under sagging bending, b_{eff}^{+}, as per EN-1998-1 (CEN 2004a). The length of the compression strut along the direction of loading, is assumed to be $L_{M1} = 0.5b_{eff}^{+}$ (Doneux 2002). The force-displacement relationship of the axial nonlinear element is shown in Figure 6.3b. The peak force, F_{R1}, transferred to the column through mechanism 1 is calculated as follows,

$$F_{R1} = f_c' b_c (h_s - h_p) \tag{6.6}$$

in which, f_c' is the concrete compressive strength and b_c is the width of the column flange.

Referring to Figure 6.3b, the adopted constitutive relationship is a tri-linear backbone under monotonic loading. A peak-oriented hysteretic response represents the cyclic behavior of the connection. In the first segment of the backbone, the concrete strut is elastic up to a force of $0.6F_{R1}$. The corresponding displacement at $0.6F_{R1}$ is $\delta_{el,1} = 0.6(f_c'/E_c) \cdot L_{M1}$ (E_c is the modulus of elasticity of

concrete). In the second segment, F_{R1} is attained at a displacement of $\delta_{p,1} = 0.2\% \cdot L_{M1}$. The post-peak capping behavior assumes that the concrete is confined and therefore crushing is delayed. If the slab is properly detailed according to EN-1998-1 (CEN 2004a) the degradation in F_{M1} may be disregarded (Amadio et al. 2008; Rassati et al. 2004). On the other hand, Braconi et al. (2007) distinguished between confined and unconfined concrete below and above the reinforcing steel, respectively. The former exhibits elastic-perfectly plastic behavior while the latter exhibits degrading behavior. In the proposed model, the post-peak portion is linear and is characterized by a 15% strength drop at $\delta_{u,1} = 2\% \cdot L_{M1}$ as shown in Figure 6.3b. Validation studies with subassembly tests of composite beam-to-column connections featuring slab detailing that conforms to EN-1998-1 (CEN 2004a) showed that the assumed modeling assumptions result in a relatively good agreement with the experimental findings as discussed in the next section.

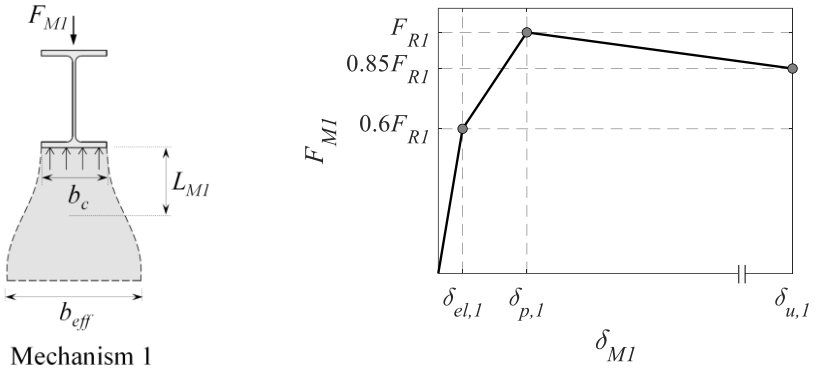

(a) (b)

Figure 6.3 Compression force transfer mechanism 1: (a) schematic representation; (b) axial nonlinear constitutive relationship assigned to the axial nonlinear element

Referring to Figure 6.4a, mechanism 2 (strut-and-tie) is composed of two compressive concrete struts and one steel tie in tension. Mechanism 2 can be considered as a combination of the compressive struts in series with the tension tie in the direction of force F_{M2}. The strut inclination, θ, is assumed to be 45° and the strut crushing resistance factor, $\nu = 0.6$ (Plumier and Doneux 2001). The length of the concrete struts, along the direction of loading, $L_{M2} = 2h_c$, while the length of the steel tie $L_{Tie} = 2L_{M2} + b_c$. The peak compressive force in the concrete struts, along the direction of loading, is shown below for $\theta = 45°$ and $\nu = 0.6$,

$$F_{R2} = 0.6 f_c' h_c (h_s - h_p) \tag{6.7}$$

a bi-linear elastic perfectly plastic behavior is assigned to the steel tie. The yield tensile force in the tie, F_{Tie} may be calculated as follows,

$$F_{Tie} = 2A_t f_{ys} \tag{6.8}$$

in which, A_t is the area of the seismic rebars within h_c from the column face (CEN 2004a); and f_{ys} is the expected yield stress of the seismic rebars.

Referring to Figure 6.4b, the yield displacement, along the direction of loading is $\delta_{ys} = 0.5(f_{ys}/E_s) \cdot L_{Tie}$ (E_s is the modulus of elasticity of steel). Furthermore, Figure 6.4b shows that the constitutive law of the concrete struts in mechanism 2 is akin to that of the concrete strut in mechanism 1. The difference lies in the peak resistance, F_{R2}, and the length along the direction of loading, L_{M2} of the struts. Accordingly, $\delta_{el,2} = 0.6(f_c'/E_c) \cdot L_{M2}$, $\delta_{p2} = 0.2\% \cdot L_{M2}$ and $\delta_{u,2} = 2\% \cdot L_{M2}$. Referring to Figure 6.4b, mechanism 2 is controlled by yielding of the ties prior to crushing of the struts. Noteworthy stating that mechanism 2 is not activated in perimeter composite steel MRFs. The lack of slab continuity at the edge implies that the width of the floor slab is insufficient for the development of the strut-and-tie mechanism (CEN 2004a; Doneux 2002; Plumier et al. 1998).

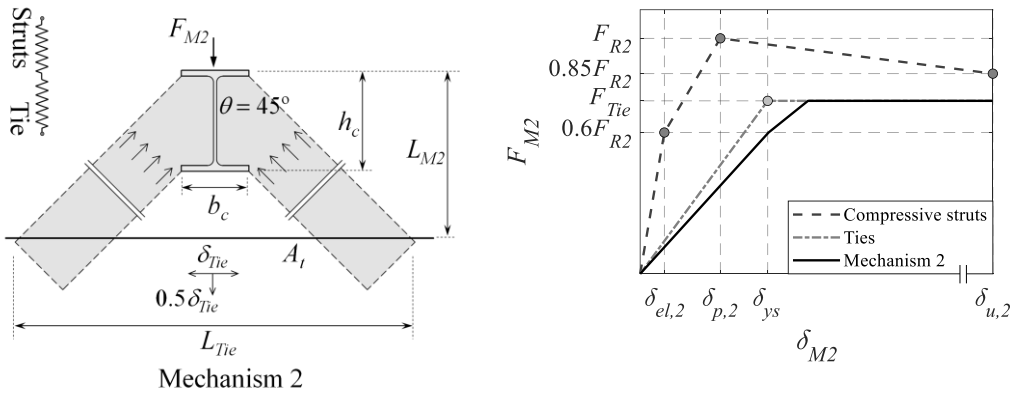

(a) (b)

Figure 6.4 Compression force transfer mechanism 2: (a) schematic representation; (b) nonlinear constitutive relationship assigned to the axial nonlinear element

The nonlinear element corresponding to the slab longitudinal reinforcement is characterized by an elastic perfectly plastic axial force-displacement relationship. The yield force in the element is equal to $A_{sr}f_{yr}$; where A_{sr} is the area of slab reinforcement within the effective width, b_{eff}^{-}, under hogging bending (CEN 2004a); and f_{yr} is the expected yield stress of the slab reinforcement. The elastic stiffness of the nonlinear element is evaluated according to (Menapace 1997; Rassati et al. 2004).

The degrading response of the bare steel beam is simulated by the modified Ibarra-Medina-Krawinkler (IMK) deterioration model (Ibarra et al. 2005; Lignos and Krawinkler 2011). The monotonic backbone and cyclic degradation parameters of the rotational zero-length element of the bare steel beam are based on those developed by Lignos and Krawinkler (2011) and the modeling guidelines by Elkady and Lignos (2014). The parameters are adjusted for the physical phenomena discussed earlier. The effective yield moments of the bare steel beam hinge, $M_{y,b}^{\pm}$, may be calculated as follows,

$$M_{y,b}^{\pm} = 1.1 \cdot (1 - \alpha) W_{pl,y} f_y \tag{6.9}$$

in which, $W_{pl,y}$ is the bare beam plastic section modulus and f_y is the expected material yield strength; α is a strength reduction factor to account for the moment-axial force interaction in the steel beam due to composite action. The strength reduction factor may be computed as per ANSI/AISC 360-16 (AISC 2016b) (see Eq. (6.13)). To that end, the axial load ratios in the steel beam under sagging (P^+/P_y) and hogging (P^-/P_y) bending are considered. Note that if the axial load ratios were to be calculated assuming the maximum force under sagging and hogging bending, $M_{y,b}^{\pm}$ would be overly conservative. The axial load ratio varies during the earthquake and the peak axial force is only transmitted once the peak force in the slab is attained. The axial load decreases as the concrete and/or shear stud strength degrades. Accordingly, an average axial force corresponding to half the maximum axial force is considered; P^+ is the average axial force that is transferred from the slab to the steel beam under sagging bending (see Eq. (6.10)); P^- is the average axial force that is transferred from the slab to the steel beam under hogging bending (see Eq. (6.11)); and $P_y = A_b f_y$ is the plastic axial resistance of the steel beam with a cross-sectional area A_b, and an expected yield stress, f_y.

$$P^+ = 0.5 \cdot (F_{R1} + F_{R2}) \leq 0.5 n_o Q_u \tag{6.10}$$

$$P^- = 0.5 A_{s,r} f_{yr} \leq 0.5 n_o Q_u \tag{6.11}$$

in which, n_o is the number of shear studs in the shear span of the composite beam; and Q_u is the resistance of the shear studs according to EN-1998-1 (CEN 2004a).

The proposed strength reduction factor, α, is calculated as the average reduction under sagging (α^+) and hogging (α^-) bending as follows,

$$\alpha = (\alpha^+ + \alpha^-)/2 \tag{6.12}$$

$$\alpha^{+} = \begin{cases} 1/8 \cdot (9P^{\pm}/P_y - 1), & P^{\pm}/P_y \geq 0.2 \\ P^{\pm}/2P_y, & \text{otherwise} \end{cases} \tag{6.13}$$

On the other hand, the peak effective flexural resistance of the bare steel beam differs under sagging, $M_{c,b}^{+}$, and hogging, $M_{c,b}^{-}$, bending. The slab restrains the top flange of the beam against local buckling, thereby resulting in a higher peak flexural resistance of the bare steel beam under sagging bending than under hogging bending. Particularly,

$$M_{c,b}^{+} = 1.4M_{y,b}^{+} \tag{6.14}$$

$$M_{c,b}^{-} = 1.1M_{y,b}^{-} \tag{6.15}$$

The pre- and post-peak rotations of the bare steel beam are modified to account for the slab effects according to Elkady and Lignos (2014). As discussed earlier, under hogging bending, the upward shift in the neutral axis expedites local buckling in the bottom flange of the beam. Accordingly, the pre- and post-peak rotations are reduced. This reduction is dependent on several factors such as the beam depth, the slab reinforcement ratio, and the degree of composite action under hogging bending, η^{-}. Due to the lack of measured data, only the latter is considered herein; thus,

$$\eta^{-} = n_o Q_u/(A_{sr} f_{yr}) \tag{6.16}$$

Composite steel beams compliant with EN-1998-1 (CEN 2004a), shall have $\eta \geq 1.0$. For beams with low η^{-}, the compressive force transferred from the rebars to the steel beam is minor; therefore, the behavior, under hogging bending, is akin to that of the bare cross section. The following modifications are applied to the pre- (θ_p) and post-peak (θ_{pc}) rotations calculated as per Lignos and Krawinkler (2011),

$$\theta_p^{-} = \begin{cases} 0.5\theta_p, & \eta^{-} \geq 50\% \\ 0.9\theta_p, & \text{otherwise} \end{cases} \tag{6.17}$$

$$\theta_{pc}^{-} = \begin{cases} 0.8\theta_{pc}, & \eta^{-} \geq 50\% \\ \theta_p, & \text{otherwise} \end{cases} \tag{6.18}$$

Under sagging bending, the slab augments the pre- and post- peak rotations. The modified θ_p^{+} and θ_{pc}^{+} equations are adopted from Elkady and Lignos (2014),

$$\theta_p^{+} = 1.8\theta_p \tag{6.19}$$

$$\theta_{pc}^{+} = 1.35\theta_{pc} \tag{6.20}$$

The rates of cyclic deterioration are modified to account for the differences in flexural strength degradation under sagging ($D^{+} = 0.75$) and hogging bending ($D^{-} = 1.0$).

The beam-slab connection is modeled using a single zero-length element that is assigned a peak-oriented hysteretic response of the modified IMK deterioration model (Ibarra et al. 2005). Shear studs in a shear span are all lumped to a single zero length element; hence redistribution of forces within the studs is not taken into consideration. Moreover, friction at the interface of the beam flange and the slab is disregarded. The force-slip displacement of the shear studs is obtained through calibration with available cyclic push-out tests on shear stud connectors that account for the stress state in the slab (Suzuki and Kimura 2019). The ultimate resistance of the beam-slab connection when the slab is in compression, Q_u^{+}, and tension Q_u^{-}, is calculated according to Suzuki and Kimura (Suzuki and Kimura 2019). Figure 6.5 demonstrates a comparison between the simulated and measured shear resistance versus slip displacement of typical headed studs under cyclic loading. The comparisons indicate a relatively good match. Referring to Figure 6.5a, the following parameters are used for 16 mm headed shear studs: the effective yield strengths $Q_y^{\pm} = 90\%Q_u^{\pm}$, the pre-capping slip capacities $\Delta_{s,p}^{\pm} = 8$ mm, the post-capping slip capacities $\Delta_{s,pc}^{+} = 13$ mm and $\Delta_{s,pc}^{-} = 8$ mm, the ultimate slip capacities $\Delta_{s,u} = 15$ mm, the strength and stiffness deterioration parameters, $\lambda_s = 80$ and $\lambda_k = 30$ and the deterioration rate parameters $D^{\pm} = 1.0$. The parameters for 19 mm headed shear studs in Figure 6.5b are obtained from El Jisr et al. (2020). Note that the all shear studs considered herein are ductile with $h_{sc}/d > 4.0$ (h_{sc} and d are the height and diameter of the shear studs, respectively).

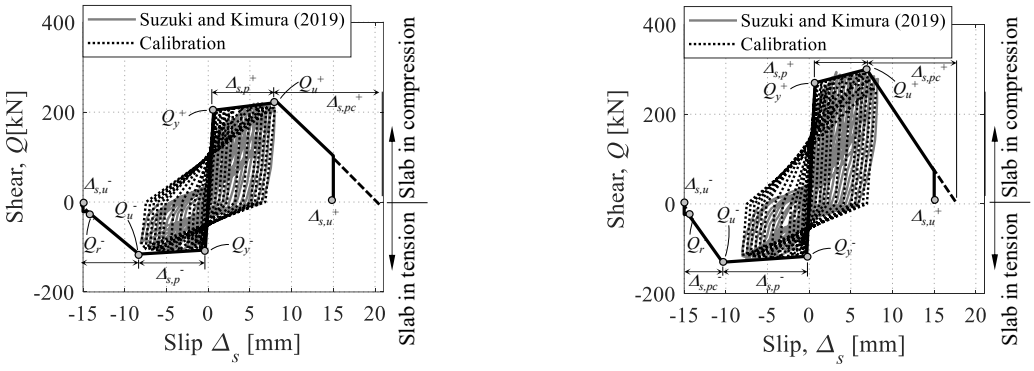

(a) (b)

Figure 6.5 Calibration of a cluster of four (a) 16 mm and (b) 19 mm shear studs subjected to cyclic loading (Data from Suzuki and Kimura (2019))

6.4.1 Validation studies

The proposed macro-modeling approach for composite steel beams is validated with available physical experiments. These include both interior (MacRae et al. 2013; Ricles et al. 2004) and exterior (Kim and Lee 2017; Yamada et al. 2009; Zandonini and Bursi 2000) subassemblies. The slab configurations are either symmetric (Bursi and Gramola 2000; Kim and Lee 2017; MacRae et al. 2013; Yamada et al. 2009) or asymmetric (Ricles et al. 2004). Moreover, the tests comprise profiled sheeting that is either parallel (Bursi and Gramola 2000; Ricles et al. 2004; Yamada et al. 2009) or perpendicular (Kim and Lee 2017; MacRae et al. 2013) to the primary steel girder. Finally, full, and partially composite steel beams are considered. The reported measured material properties are used for the validations. Figure 6.6a shows the configurations of the employed specimens along with the relevant force-deformation parameters used to obtain the hysteretic response per test.

Referring to Figure 6.6, the proposed modeling approach predicts well the flexural stiffness of the composite steel beams. For fully composite beams, the effective flexural strength is within 10% of that achieved in the tests regardless of the orientation of the deck. While cyclic deterioration in flexural strength of composite steel beams is generally predicted well, in cases where the orientation of the deck is transverse to the primary girder (see Figure 6.6f), the proposed model underestimates the cyclic deterioration in flexural strength. This is due to extensive spalling that often occurs at the slab-column interface (MacRae et al. 2013).

The proposed model tends to slightly overestimate the slip demands in the composite slab as it does not account for the redistribution of the shear force between the studs. Referring to Figure 6.7, in subassembly L.P.C (Bursi and Gramola 2000) the maximum reported slip is 10% (14 mm versus about 13 mm) lower than that obtained by the macro-model under sagging bending and about 25% lower under hogging bending (8 mm versus 6 mm). Considering the simplified assumptions of the proposed model, it captures the shear stud slip reasonably well.

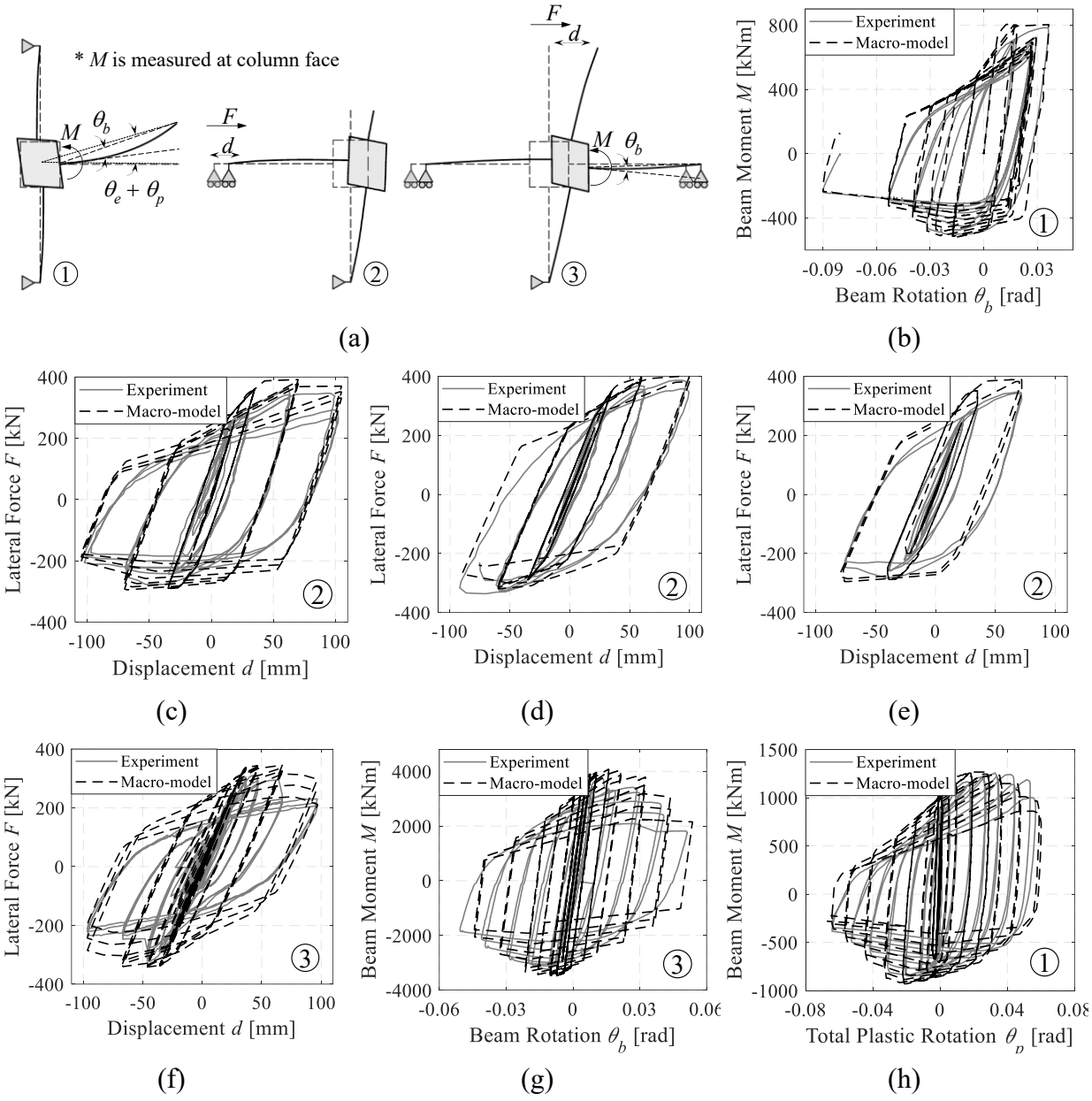

Figure 6.6 Validation of the proposed modeling approach with subassembly specimens; (a) Sub-assembly configurations (b) Composite Beam 1 (Yamada et al. 2009); (c) F.C. (Bursi and Gramola 2000); (d) L.P.C (Bursi and Gramola 2000); (e) I.P.C (Bursi and Gramola 2000); (f) Transverse deck unit (MacRae et al. 2013); (g) SPEC3 (Ricles et al. 2004); (h) PN500C–TH (Kim and Lee 2017)

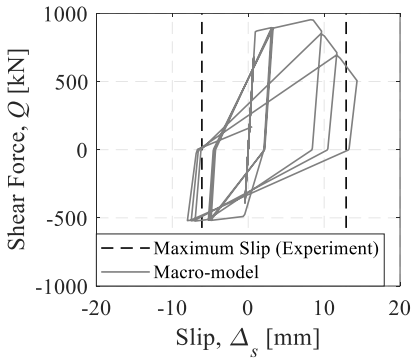

Figure 6.7 Modeled hysteretic response of the beam-slab connection for specimen L.P.C (Bursi and Gramola 2000)

6.5 Prototype composite steel frame buildings

A 6-story prototype building of importance class II is designed according to the European seismic provisions (CEN 2004a; b, 2005b; c). The building consists of 3-bay space composite steel MRFs in the East-West (EW) direction, and two perimeter CBFs in the North-South (NS) direction (Figure 6.8a). A typical elevation view of the composite steel MRF is shown in Figure 6.8b. The composite steel MRFs are designed with full-strength rigid stiffened end plate beam-to-column connections. The beam-to-column web panel zones are designed to remain elastic. Columns are spliced at stories 3 and 5 (see Figure 6.8b). The prototype building is designed for a reference peak ground acceleration, a_{gR}, of 0.22 g. This value is identical for different European sites: Sion in Switzerland, Aikaterini in Greece and Braila in Romania (Giardini et al. 2013). As per EN-1998-1 (CEN 2004a), all three sites have the same Type 1 design spectrum (behavior factor $q = 3$, ground Type D and viscous damping ratio, $\xi = 2\%$). The prototype building is designed with response spectrum analysis. All members are fabricated by S355J2 steel (i.e., nominal yield stress of $f_{yn} = 355$ MPa).

The floor slab has a total thickness of 125 mm and consists of a 56 mm profiled sheeting (Cofrastra 56) with ribs oriented parallel to the MRF girders. The characteristic compressive strength of concrete is 30 MPa. The slab reinforcement ($f_{yr} = 500$ MPa) includes two layers of longitudinal 8 rebars at 150 mm spacing, as well as $5\phi10$ seismic rebars placed within h_c from the face of the column. Details of the composite cross section near the interior MRF column are shown in Figure 6.8c. Three different designs with full ($\eta = 100\%$) and partial ($\eta = 80\%$ and 50%) composite action are considered. For the designs with partially composite steel beams, the 25% reduction in the shear stud capacity required by EN 1998-1 (CEN 2004a) is intentionally waived. Moreover, a lower degree of composite action results in lower flexural demand on the columns as well as the panel zones. Nevertheless, the difference between the column sizes is negligible because their design is mostly governed by the

interaction of bending with the axial force. As such, the same member sizes are employed in the three designs.

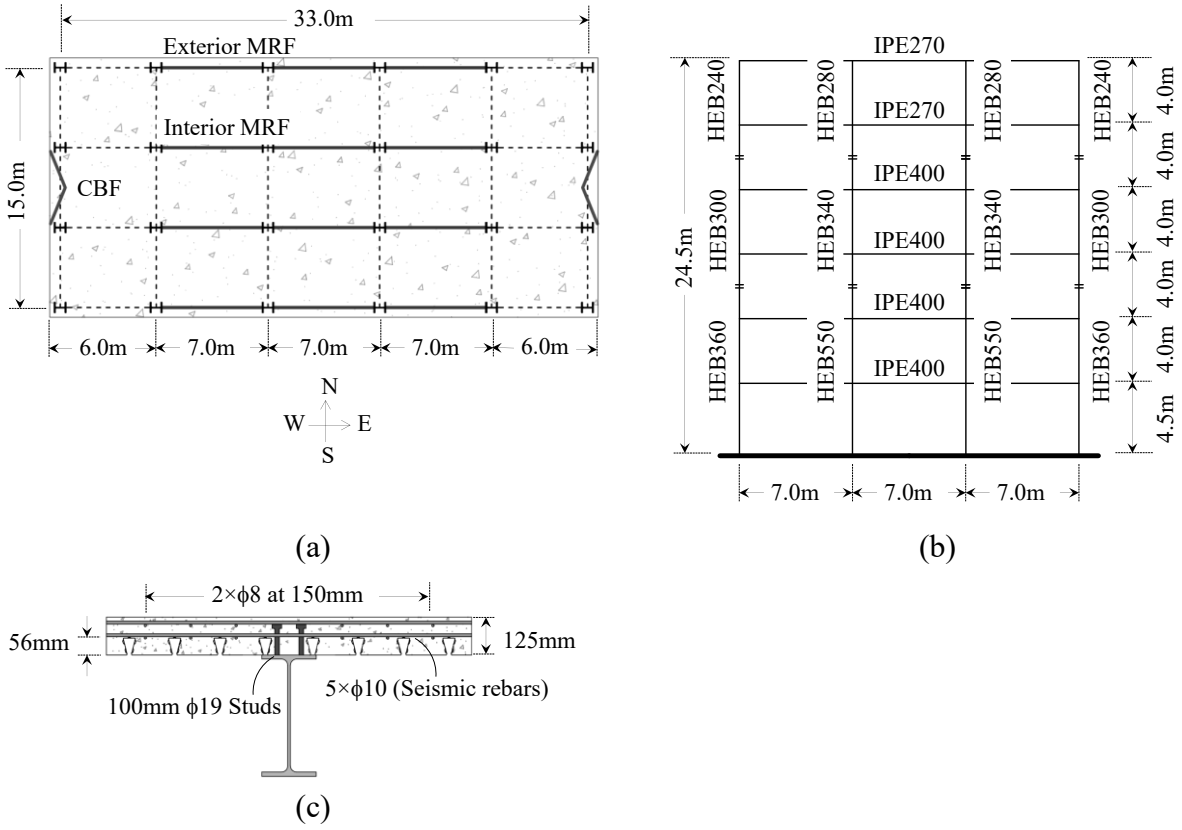

Figure 6.8 (a) Typical plan view of the prototype buildings; (b) elevation view of the six-story composite MRF; (c) detail of the composite cross section at interior MRF columns

6.6 Nonlinear building models

The three prototype buildings are modeled using two-dimensional (2D) nonlinear models in the EW loading direction. The models are developed in the open-source simulation platform OpenSEES (McKenna 1997). Half of each prototype building is modeled. The interior and exterior composite steel MRFs (see Figure 6.8a) are linked in series via axially rigid truss elements as shown in Figure 6.9. Both frames should be considered in the model to properly simulate the destabilizing effects due to gravity on the overall building response. For the steel members, the expected yield strength is obtained by multiplying the nominal yield strength f_{yn} by a material overstrength factor of 1.17 for S355J2 steel (Braconi et al. 2013). Inelastic deformations in the steel columns are modeled as proposed in Lignos et al. (2019). The panel zone rotational springs are modeled by assuming an asymmetric behavior to account for different effective depths of the panel zone due to the presence of the slab under sagging and hogging bending (Elkady and Lignos 2014). Composite steel beams are

modeled with the proposed modeling approach discussed earlier. The flexural stiffness of the exterior composite steel MRF composite beams is lower than that in the interior composite steel MRF beams owing to the larger effective width in the latter. Gravity loads are assigned to the composite steel MRF columns based on the respective tributary area around the columns.

A fictitious leaning column is added to properly consider the effect of gravity loading, P', from the 6m edge spans of the prototype building that are not part of the tributary areas around the columns. The leaning column is connected with axially rigid truss elements to the two composite steel MRFs as shown in Figure 6.9 and a vertical load of $P'/2$ is applied to the leaning column at each story.

Rayleigh damping is incorporated in the model according to the approach summarized in Zareian and Medina (2010). A 2% critical damping ratio is applied at the first and third modes of the building model as recommended by PEER/ATC (2010).

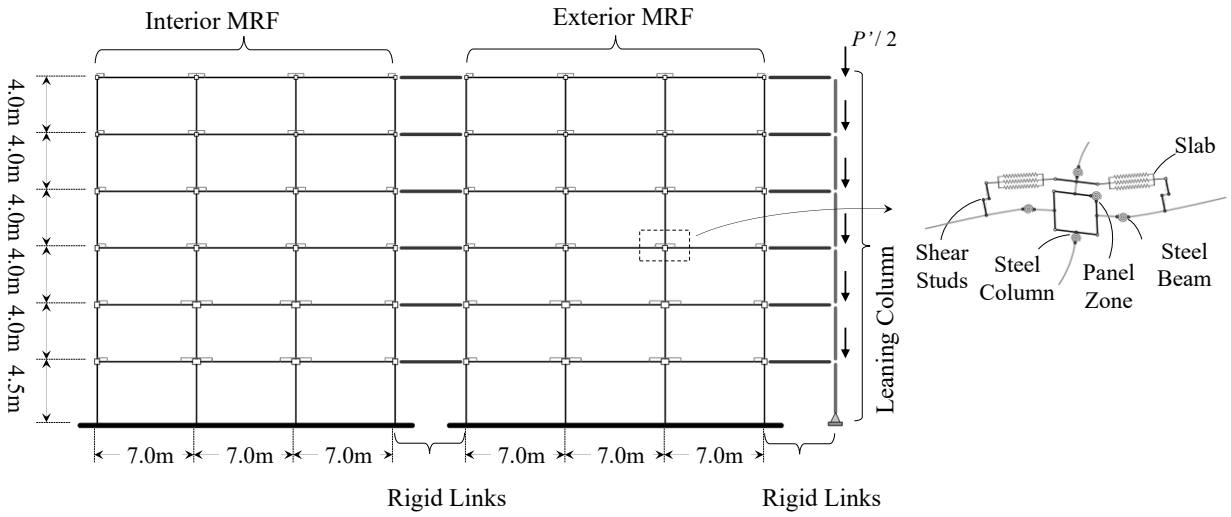

Figure 6.9 OpenSEES nonlinear model of the prototype building

6.7 Site-specific probabilistic seismic hazard analysis and ground motion selection

Site-specific ground motion records are selected for nonlinear response history analysis (NRHA) that is discussed later on. For this reason, probabilistic seismic hazard analysis is performed for the three design sites. In brief, the ground motion prediction equation (GMPE) of Boore and Atkinson (Boore and Atkinson 2008) is employed. The area source model of SHARE (Giardini et al. 2013) is adopted and all sources within 200 km from the specific site are accounted for. The average shear wave velocity (150 m/s) corresponds to ground type D. Seismic hazard and disaggregation analyses are performed using OpenQuake (Monelli et al. 2012).

Seismic hazard analysis is performed for each site for the average spectral acceleration, Sa_{avg}. This intensity measure (IM) is computed as the geometric mean of spectral acceleration ordinates over a period range of 0.4 to 4.4s with an increment size of 0.1s (Eads et al. 2015). Figure 6.10 shows the seismic hazard curves for the three considered sites. While a_{gR} is the same at all three sites, the seismic hazard is quite different. Particularly, the design site at Braila is mostly controlled by more frequent earthquakes, whereas the one in Sion is strongly influenced by seismic events with a low probability of occurrence. At Aikaterini, the seismic hazard is higher than the other two design sites. The annual rate of exceedance is close to that in Braila for $Sa_{avg} < 0.15$ g and slightly higher than that in Sion for $Sa_{avg} > 0.4$ g.

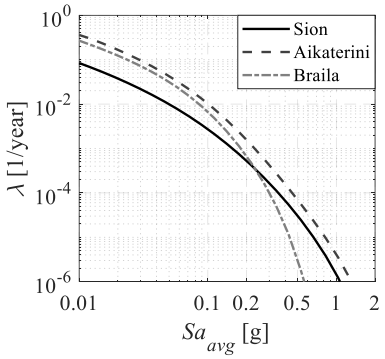

Figure 6.10 Seismic hazard curves at the three design locations

Two earthquake record sets corresponding to Sa_{avg} levels at two return periods ($T_R = 475$ years and 2475 years) are selected at each design site. The record selection utilizes the conditional spectrum (CS) with mean magnitude ($\bar{M}$) and distance from rupture ($\bar{R}$) as the target spectrum (Baker 2011; Kohrangi et al. 2017; Lin et al. 2013). The values of $\bar{M}$ and $\bar{R}$ for record selection are listed in Table 6.1 along with the Sa_{avg} values at 475 and 2475 years return periods. No limitations on parameters $\bar{M}$, $\bar{R}$ and v_{s30} of the selected records are considered; it is assumed that the spectral shape can define all the characteristics of the hazard at each site (Tarbali and Bradley 2016). Each ground motion set consists of 40 records and was assembled from the NGA-West database. Figure 6.11 shows the ground motion sets per design location for a return period of 2475 years. Both pulse-like and non-pulse-like records are chosen and the scaling factor for record selection is limited to a maximum of 10.

Table 6.1 Average spectral acceleration, mean magnitude and distance obtained from disaggregation analysis for the three sites at 475 and 2475 years return periods

T_R [years]	Sion (Switzerland)			Aikaterini (Greece)			Braila (Romania)		
	Sa_{avg} [g]	$\bar{M}$	$\bar{R}$ [km]	Sa_{avg} [g]	$\bar{M}$	$\bar{R}$ [km]	Sa_{avg} [g]	$\bar{M}$	$\bar{R}$ [km]
475	0.11	6.4	26.9	0.18	7.1	55.2	0.15	7.1	99.2
2475	0.22	6.5	15.5	0.30	7.2	32.0	0.23	7.2	89.1

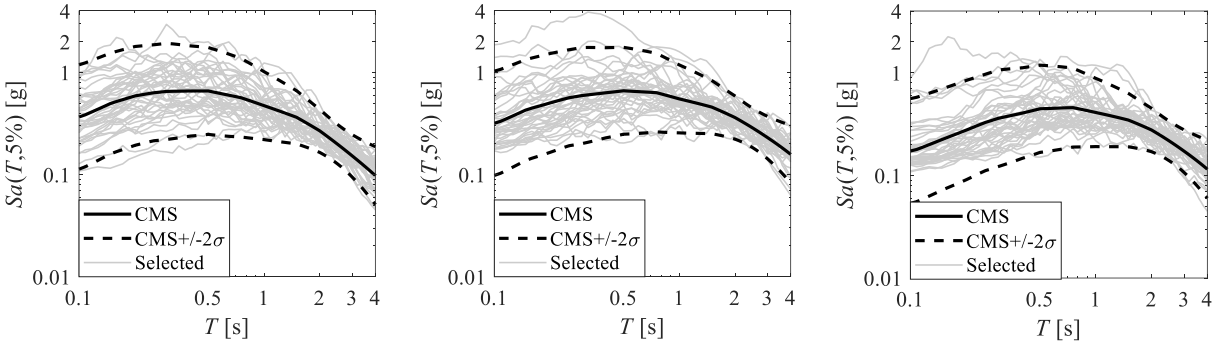

Figure 6.11 Selected records for T_R = 2475 years; (a) Sion; (b) Aikaterini; (c) Braila

6.8 Nonlinear static analysis

Nonlinear static analysis based on a first mode lateral load pattern is conducted for the prototype buildings. Figure 6.12a shows the pushover curve of the three nonlinear building models in terms of first story base shear versus roof displacement. The base shear, V_{base}, is normalized with respect to the seismic weight of the modeled frames (i.e. seismic weight of half the prototype building), W_s = 10869 kN. The roof drift ratio, θ_r, is calculated as δ_r/H, where δ_r is the roof displacement and H is the total height of the prototype building. Figure 6.12a suggests that the nonlinear static response of the prototype buildings is not significantly influenced by the degree of composite action.

The static overstrength factor, Ω, and period-based ductility factor, μ_T (FEMA 2009) are obtained from the pushover curves as shown in Figure 6.12b. The system level parameters are summarized in Table 6.2. The same table includes the first mode periods of each nonlinear building model based on standard eigenvalue analyses. Note that the first mode period increases with decreasing degree of composite action due to the decrease in the flexural stiffness of the composite steel beams. Nevertheless, the difference between periods is less than 5%.

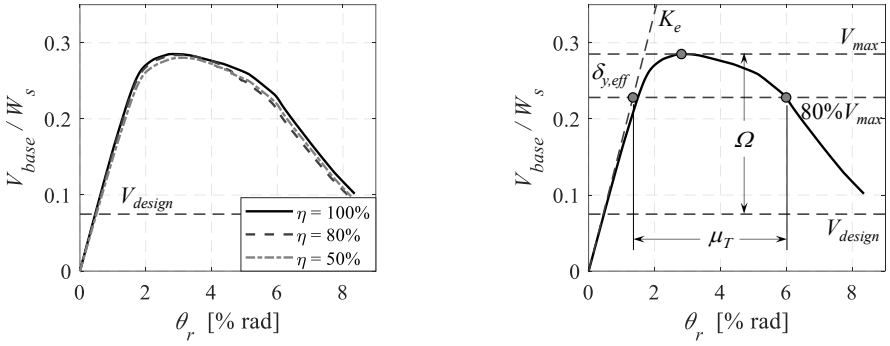

(a) (b)

Figure 6.12 Comparison of pushover curves for the three prototype composite steel frames; (b) derivation of performance parameters

Referring to Table 6.2, the high values of the global yield drift are commonly observed in buildings featuring space MRFs. Unlike in buildings with only perimeter MRFs (Elkady and Lignos 2014; NIST 2010), beams that are part of space-frame systems tend to be of shallower depths (i.e., beam depths less than 500 mm) and have larger span-to-depth ratios (> 8.0). For the prototype composite steel MRF, the shear span-to-depth ratio varies between 8 in the bottom stories and 12.5 in the top stories.

Table 6.2 Prototype composite steel MRFs first mode periods and performance parameters obtained from nonlinear static analysis

	η = 100%	η = 80%	η = 50%
T_1 [s]	1.70	1.66	1.62
$\theta_{y,eff}$ [% rad]	1.3	1.4	1.4
Ω	3.8	3.8	3.7
μ_T	4.5	4.2	4.2

Referring to Figure 6.12b, the static overstrength factor, Ω, is computed as the ratio between the maximum base shear, V_{max}, and the design base shear obtained through modal response spectrum analysis, V_{design}.

Table 6.2 shows that is close to 4.0 regardless of the employed degree of composite action. The high Ω values are attributed to (i) the steel material overstrength; (ii) the discrete choice of beam and column cross sections; (iii) oversizing the beams and columns to resist gravity loads; and most importantly (iv) the drift control requirements. The above matters are elaborated in Osteraas and Krawinkler (1989) based on field reconnaissance and corroborating structural analyses of actual buildings after the 1985 earthquake in Mexico city. According to Elghazouli (2010), a typical MRF

designed according to EN 1998-1 (CEN 2004a) can have considerable overstrength. European drift requirements (CEN 2004a) are more stringent than those in the US (ASCE 2016). Moreover, the stability coefficient is fairly conservative, which leads to considerable overstrength (Elghazouli 2010; Macedo et al. 2019; Tsitos et al. 2018). Haselton et al. (2011) noted that beams in space MRFs are designed for higher gravity loads than those in perimeter MRFs, which generally results in higher overstrength. In general, further research is required to refine the EN 1998-1 provisions (CEN 2004a) through the benchmarking of the seismic performance of composite steel MRFs.

Table 6.2 summarizes the period-based ductility, μ_T, defined as the ratio between the roof drift at 20% drop in base shear and the roof drift ratio at yield (see Figure 6.12b). Figure 6.13 shows the progression of the collapse mechanism of the prototype composite steel MRF ($\eta = 100\%$) along its height. The three-story collapse mechanism, evident at a roof drift ratio of 8% rad, is attributed to the high strong-column-weak-beam (SCWB > 2) ratio in the first two stories. The column section sizes in these stories are governed by the moment and axial force demands. Despite the intrinsic value and simplicity of nonlinear static analysis, it cannot be used for the earthquake-induced collapse risk assessment of the composite steel MRFs due to the associated limitations of the simplified analysis technique (Krawinkler and Seneviratna 1998). For the above reasons, nonlinear response history analyses are conducted as discussed in the subsequent sections.

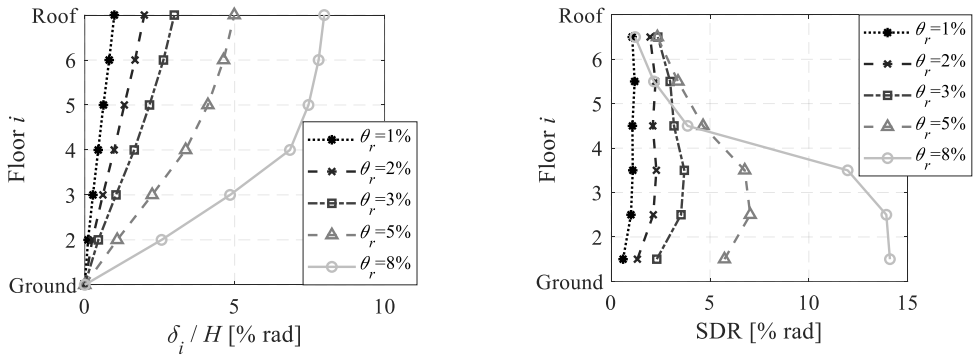

(a) (b)

Figure 6.13 (a) Normalized displacement profile of the prototype composite steel frame ($\eta = 100\%$) at different roof drift levels based on pushover analysis; (b) Peak SDR at targeted roof drift levels

6.9 Collapse risk assessment

This section investigates the collapse risk of the prototype buildings. The dependence on the design site and the degree of composite action of the composite steel beams is examined. To this end, incremental dynamic analysis (IDA) is conducted (Vamvatsikos and Cornell 2002). The ground motion

records discussed earlier are scaled incrementally with respect to the 5%-damped average spectral acceleration, Sa_{avg} until dynamic instability occurs; that is, until a story, or a number of a stories, deforms laterally and the story shear resistance becomes zero due to second order effects accelerated by structural component deterioration. This definition of structural collapse is consistent with prior shake table experiments of steel MRFs (Lignos et al. 2013). This definition of structural collapse is consistent with prior shake table experiments in steel MRF Herein, the adopted IM is the average spectral acceleration because of its sufficiency and efficiency relative to other commonly used IMs (Eads et al. 2015).

Figure 6.14a shows the IDA curves for the prototype building ($\eta = 100\%$) in Sion. The Sa_{avg} is plotted versus the absolute maximum story drift ratio (SDR_{max}). The median,16th and the 84th percentiles are also superimposed in the figure. Referring to Figure 6.14b, the peak floor acceleration (PFA) caps as the building response becomes inelastic. Nevertheless, the median PFA is high (~ 2.0 g) due to the high system overstrength (see Table 6.2).

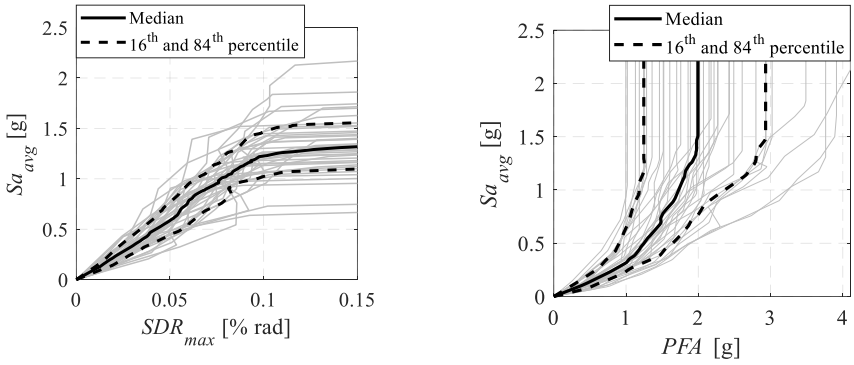

(a) (b)

Figure 6.14 IDA curves for the prototype fully composite steel frame ($\eta = 100\%$) in Sion; (a) peak story drift ratios; (b) peak floor absolute accelerations

The collapse fragility curves are obtained by fitting the cumulative probabilities of collapse corresponding to the 40 collapse intensities with a lognormal cumulative distribution. Figure 6.15 shows the dependence of the collapse fragility curves on the degree of composite action of the composite steel beams and the design site. The median collapse intensities, $\mu_{Sa_{avg,c}}$, and lognormal standard deviations, $\sigma_{\ln Sa_{avg,c}}$, of the collapse intensities are summarized in Table 6.3 for the analyzed buildings. Referring to Figure 6.15a, the collapse capacity of the prototype buildings is somewhat influenced by the degree of composite action of the composite steel beams. The collapse capacity decreases with decreasing degree of composite action. This decrease is explained by the lower lateral

stiffness of the composite steel MRFs with lower degree of composite action. Consequently, global P-Delta effects are more prominent for lower degrees of composite action. However, the difference in the median collapse capacity is minor (within 15%) as shown in Table 6.3.

Figure 6.15b depicts the dependence of the collapse capacity of the prototype buildings on the design site. The choice of the ground motion record set influences their collapse capacity. Nevertheless, the use of Sa_{avg} ensures that the record-to-record variability is not significant and hence the difference in median collapse capacity is around 15%. This is also reflected in the low $\sigma_{\ln Sa_{avg,c}}$ values, which are summarized in Table 6.3.

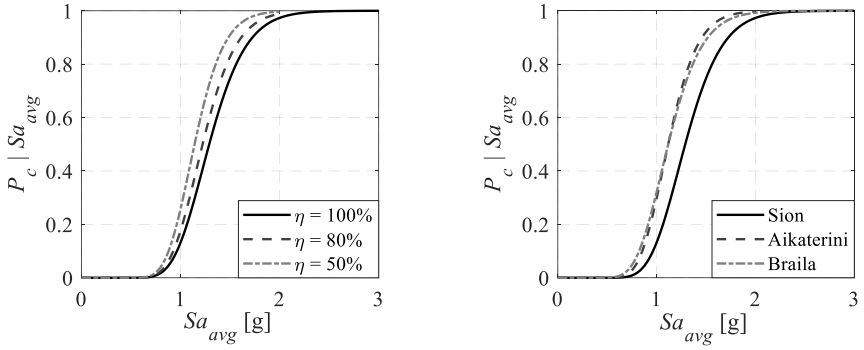

(a) (b)

Figure 6.15 Comparison of collapse fragility curves for (a) the three prototype composite steel frames in Sion; and (b) the fully composite steel frame at the three design sites

Table 6.3 Median collapse intensity and standard deviation of the collapse fragility curves for the three prototype composite steel MRFs at three design sites

	Sion (Switzerland)			Aikaterini (Greece)			Braila (Romania)		
η[%]	100	80	50	100	80	50	100	80	50
$\mu_{Sa_{avg,c}}$ [g]	1.29	1.22	1.14	1.12	1.05	1.00	1.12	1.06	1.03
$\sigma_{\ln Sa_{avg,c}}$	0.23	0.22	0.20	0.21	0.19	0.19	0.24	0.23	0.23

The collapse risk of the prototype buildings is evaluated through the mean annual frequency of collapse, λ_c. This is computed by integrating the collapse fragility curves over the corresponding hazard curves for a given design site,

$$\lambda_c = \int_0^\infty \left(P_c \middle| Sa_{avg} = x\right) \cdot \left| d\lambda_{Sa_{avg}}(x) \right| \tag{6.21}$$

In which, $\left(P_c \middle| Sa_{avg} = x\right)$ is the probability of collapse given Sa_{avg} equals to a seismic intensity x, obtained from the collapse fragility curve; and $\lambda_{Sa_{avg}}(x)$ is the mean annual rate of Sa_{avg} exceeding x obtained from the seismic hazard curve. The integral is solved numerically according to Eads et al.

(2013). The corresponding probability of collapse, P_c(50 years), of the prototype buildings is calculated over a period of a 50-year building life expectancy, by assuming that earthquakes follow a Poisson distribution over time. Table 6.4 summarizes the values for all the examined cases. The P_c(50 years) is considerably lower than the 1% limit specified in ASCE/SEI 7-16 (ASCE 2016) regardless of the design site. This is because the annual rate of seismic hazards associated with the median collapse intensities is practically insignificant ($\lambda < 10^{-6}$) compared to other design sites from around the world, such as southern California. Other reasons for the relatively low annualized probabilities of structural collapse relate to the stringent EN 1998-1 (CEN 2004a) lateral drift requirements that also contribute to appreciable system-level overstrength (see Table 6.2) as well as the stability requirements with regard to global P-Delta effects. Of interest from a repairability standpoint are potential repair actions in designs featuring beams with partial degrees of composite action, given that the 25% reduction in the shear stud resistance has been waived.

Table 6.4 Mean annual frequency of collapse and the probability of collapse in 50 years for the three prototype composite steel MRFs at the three design sites

	Sion (Switzerland)			Aikaterini (Greece)			Braila (Romania)		
η [%]	100	80	50	100	80	50	100	80	50
λ_c [1/year]	5.9e-07	7.5e-07	1.0e-06	4.1e-06	5.0e-06	6.6e-06	2.2e-08	3.0e-08	3.9e-08
P_c(50 years) [%]	0.0029	0.0037	0.0053	0.021	0.025	0.033	0.0001	0.0002	0.0002

6.10 Peak slip hazard curves for beam-slab connections and damage assessment

The proposed macro-model approach allows for the explicit quantification of the peak slip demands of beam-slab connections along the building height, Δ_{sp}. Figure 6.16 shows Δ_{sp} along the building height based on single-stripe analysis at a design-basis earthquake (DBE) for Aikaterini. The slip demands are generally higher in the lower stories. The slip demands can be quantified in the context of the performance-based earthquake engineering framework through the development of Δ_{sp} hazard curves. Potential cyclic deterioration in the shear resistance of beam-slab connections may result in high slip demands. Therefore, the Δ_{sp} hazard curves provide an effective means of quantifying the peak slip demands within the framework of performance-based earthquake engineering, and hence the damage in the beam-slab connections at return periods of interest to the engineering community. This is achieved by computing a mean annual rate of exceeding a slip value, $\lambda_{\Delta_{sp}}$, for any given return period that is associated with a seismic event (e.g., design basis and/or serviceability earthquakes). This relates to the concept of EDP hazard curves as described in prior-related work (Krawinkler and

Miranda 2004). For simplicity, Δ_{sp} is taken as the maximum slip demand on all beam-slab connections in the prototype buildings.

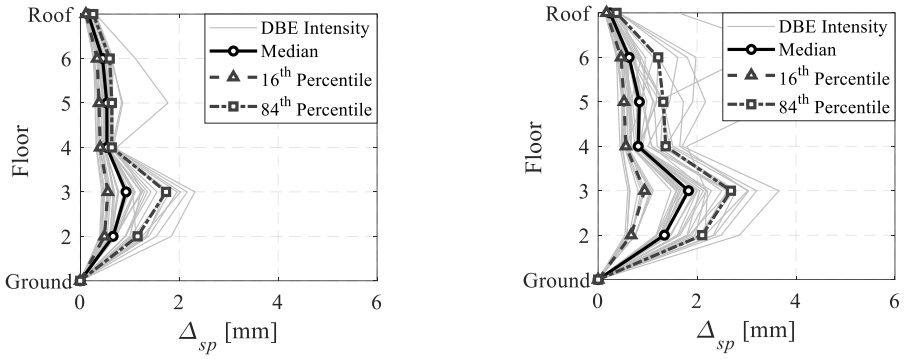

Figure 6.16 Peak slip, Δ_{sp}, profile along the height of the prototype building in Aikaterini at DBE seismic intensity, (a) $\eta = 80\%$ and; (b) $\eta = 50\%$

The beam-slab connection slip hazard curves are developed according to Krawinkler and Miranda (2004). The slip demands obtained directly by the proposed model (see Figure 6.17a for a single simulation) are used for this purpose. The mean annual rate of Δ_{sp} exceeding y is computed as follows,

$$\lambda_{\Delta_{sp}}(y) = \int P[\Delta_{sp} > y | Sa_{avg} = x] \cdot |d\lambda_{Sa_{avg}}(x)| \tag{6.22}$$

in which, $P[\Delta_{sp} > y | Sa_{avg} = x]$ is the probability of Δ_{sp} exceeding y given Sa_{avg} equals to a seismic intensity x; and $\lambda_{Sa_{avg}}(x)$ is the mean annual rate of Sa_{avg} exceeding x obtained from the corresponding seismic hazard curve. The probability $P[\Delta_{sp} > y | Sa_{avg} = x]$ is computed according to Eq. (6.23). It is assumed that at the collapse intensities, $P(\Delta_{sp} > y) = 1$.

$$P\left[\Delta_{sp} > y \middle| Sa_{avg} = x\right] = \left(P_c \middle| Sa_{avg} = x\right) + \left[1 - \left(P_c \middle| Sa_{avg} = x\right)\right] \cdot \left(1 - \Phi\left(\frac{\ln y - \ln \mu_{\Delta_{sp}}}{\sigma_{\ln \Delta_{sp}}}\right)\right) \tag{6.23}$$

In which, $\left(P_c \middle| Sa_{avg} = x\right)$ is the probability of collapse given $Sa_{avg} = x$, and is obtained by the collapse fragility curves; Φ is the lognormal cumulative distribution function; $\ln \mu_{\Delta_{sp}}$ is the natural logarithm of the median of Δ_{sp} for the non-collapse cases; and $\sigma_{ln\Delta_s}$ is the standard deviation of the natural logarithm of Δ_{sp} for the non-collapse cases. Referring to Figure 6.17b, the Δ_{sp} values at Sa_{avg} obtained from the IDA curves are fitted with a lognormal distribution. The mean annual rate of exceedance, $\lambda_{\Delta_{sp}}(y)$ is then obtained by numerical integration. Figure 6.17c shows the Δ_{sp} hazard

curves for two of the analyzed buildings with partially composite beams at the three design sites. The Δ_{sp} values are generally higher in composite steel MRFs in Braila and Aikaterini than in Sion for annual rates $\lambda_{\Delta_{sp}} < 10^{-4}$. This is because the seismic hazard in the first two design sites is characterized by more frequently occurring seismic events. Conversely, Sion is characterized by seismic events with low probability of occurrence; hence, slip demands of beam-slab connections are lower than those determined in Braila.

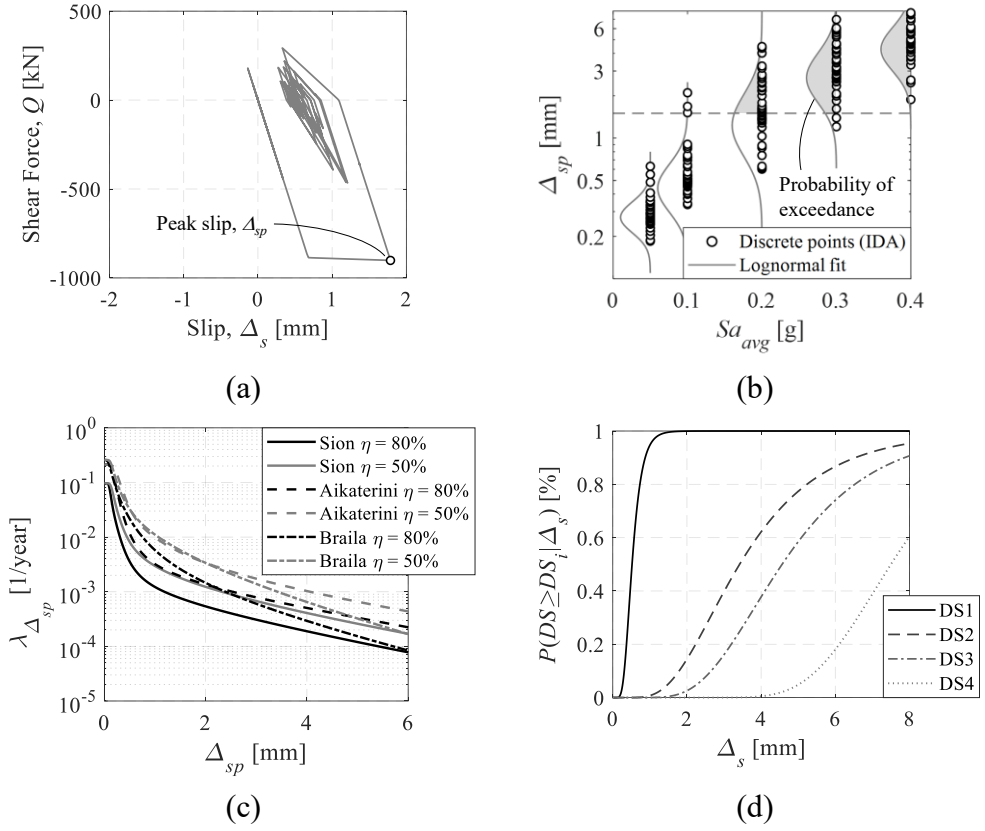

Figure 6.17 (a) Peak slip demands, Δ_{sp}, shown for the most critical beam-slab connection along the building height (Sion, $\eta = 80\%$); (b) distribution of Δ_{sp}, for selected Sa_{avg} values (Sion, $\eta = 80\%$); (c) developed Δ_{sp}, hazard curves for the two prototype buildings with partially composite steel beams at the three design sites; (d) typical fragility functions for the beam-slab connections (El Jisr and Lignos 2021)

The median Δ_{sp} values at three representative return periods ($T_R = 72$, 475 and 2475 years) are summarized in Table 6.5. At a return period of 72 years (i.e., service level earthquake), the median Δ_{sp} values are less than 1 mm regardless of the design location, and the degree of composite action. At return periods associated with a design-basis earthquake (DBE), the median Δ_{sp} values are within 2 mm for $\eta = 80\%$ and 3 mm for $\eta = 50\%$. On the other hand, at return periods associated with a maximum considered earthquake (MCE), the median Δ_{sp} values vary between the three sites and

range between 2.5 and 4.5 mm for $\eta = 80\%$, and 4.0 to about 6.0 mm for $\eta = 50\%$. In order to better comprehend the significance of the above values, these are correlated with slip-based fragility functions that estimate the likelihood of reaching or exceeding discrete damage states in beam-slab connections as defined in (El Jisr and Lignos 2021). The employed fragility functions in Figure 6.17d were derived from cyclic push-out tests (Suzuki and Kimura 2019) that account for the stress state in the slab. Four damage states are considered: (i) DS1, light cracking in the concrete; (ii) DS2, extended cracking in the concrete accompanied with stud yielding and/or crushing near the base of the shear studs; (iii) DS3, low-cycle fatigue microcracking in the shear studs and extensive cracking in the concrete; and (iv) DS4, loss of shear load carrying capacity of the beam-slab connection.

Table 6.5 Comparison between the median Δ_{sp} [mm] values of the prototype composite steel MRFs at three representative return periods

	Sion (Switzerland)		Aikaterini (Greece)		Braila (Romania)	
η [%]	80	50	80	50	80	50
$T_R = 72$ years	0.3	0.4	0.5	0.8	0.6	0.9
$T_R = 475$ years	0.7	1.3	1.4	2.7	1.7	2.5
$T_R = 2475$ years	2.5	4.0	4.5	6.2	3.5	4.7

Figure 6.18 illustrates the probability of occurrence of each damage state in the beam-slab connections. Referring to Figure 6.18a, for $\eta = 80\%$, beam-slab connections are very likely to experience light cracking in the slab (DS1) or no damage (30% to 95%), for seismic events with a 72-year return period (i.e. 50% probability in 50 years). For a 475-year return period associated with a DBE (i.e., 10% probability in 50 years), the probability of extended cracking in the slab and stud yielding or concrete crushing near the base of the studs (DS2), is negligible for Sion and less than 10% for Aikaterini and Braila. Figure 6.18b shows the damage in beam-slab connections at the three design sites for $\eta = 50\%$. For a 72-year return period, the damage is minimal as in the design with $\eta = 80\%$. For a 475-year return period, the probability of extended cracking in the slab and stud yielding or concrete crushing near the base of the studs is up to 20% for Aikaterini and Braila. On the other hand, extensive damage in the slab and low-cycle fatigue microcracking (DS3) are unlikely to occur ($<$10% probability). The probability of the loss of shear load carrying capacity in the beam-slab connections is negligible for all three design sites regardless of the degree of composite action. The above findings demonstrate that the integrity of the beam-slab connections in shallow partially composite steel beams ($d_b < 500$ mm) is maintained for a DBE event ($T_R = 475$ years) even though the 25% reduction in capacity of shear studs was disregarded in the design.

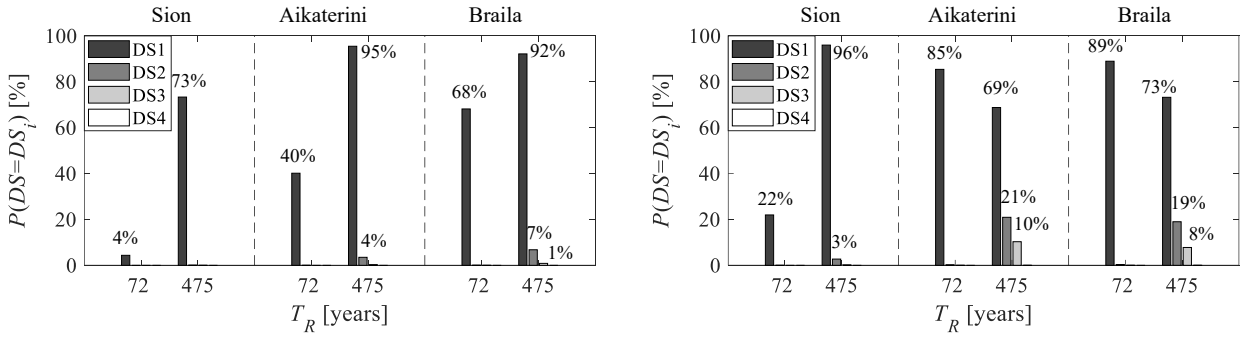

(a) (b)

Figure 6.18 Probability of damage in the beam-slab connection for the prototype composite steel frames with partially composite beams; (a) $\eta = 80\%$; and (b) $\eta = 50\%$

6.11 Limitations

It is worth mentioning that although the proposed macro-modeling approach can simulate the global frame and local component behaviors, it comes with several limitations. The present model cannot capture the following phenomena: (i) the redistribution of the demands on the shear studs; (ii) the slip profile in the beam-slab connections along the length of the beams; (iii) uplift of the shear studs; (iv) the effects of framing action, which has been shown to increase the plastic rotation capacity of the beams (Donahue et al. 2017; FEMA 2000a); (v) fracture of the beam-to-column connection; and (vi) concrete spalling at the beam-column interface. Spalling of concrete leads to a loss of the bearing mechanism, which in turn decreases the shear demands on beam-slab connections at lateral drift demands higher than 3% rads. Furthermore, since the employed slip-based fragility functions were derived from a database of cyclic push-out tests, they tend to overestimate the expected damage in the beam-slab connections (Cordova and Deierlein 2005; El Jisr et al. 2020). Hence, the probabilities of damage presented in this paper are upper-bound probabilities. The proposed modeling approach is valid for 2D nonlinear response history analysis. Further enhancements, that account for three-dimensional effects and the influence of transverse beams on the global frame and local component seismic behavior, should be carefully considered.

6.12 Conclusions

This chapter proposes a nonlinear, computationally efficient, macro-model for simulating the deteriorating behavior of fully restrained beam-to-column connections with composite steel beams. The model incorporates the effects of the floor slab on the flexural strength through mechanics-based

constitutive laws that account for damage in the slab. Furthermore, the model can capture the asymmetric hysteretic response and flexural strength deterioration that occurs in composite steel beams. The model can explicitly predict the slip demands in beam-slab connections. Test data from available subassembly tests were used to carefully validate the proposed model.

System-level nonlinear static analysis as well as incremental dynamic analysis (IDA) through collapse are conducted to benchmark the seismic risk of a set of prototype buildings that feature composite steel MRFs as their primary lateral load resisting system. These are designed in accordance with EN 1998-1 (CEN 2004a) for three different European sites. Additionally, the code requirements for the number of shear stud connectors are waived for the MRFs with partially composite beams. The collapse risk of the prototype MRFs is computed and its dependence on the degree of composite action and design sites is explicitly quantified. The results from nonlinear building simulations are also employed to develop novel peak slip hazard curves for beam-slab connections that enable the assessment of their integrity at characteristic return periods of interest to the engineering profession. While benchmarking the collapse risk relates to life safety in rare seismic events, the proper quantification of peak slip demands in beam-slab connections relates to structural repair actions in the aftermath of more frequently occurring earthquakes. The main findings are summarized as follows:

- Results from nonlinear static analysis suggest that the static overstrength factor, Ω, is close to 4 and the period-based ductility, μ_T, ranges between 4.2 and 4.5. The high value of Ω is due to the lateral drift requirements in the current EN 1998-1 (CEN 2004a).

- The collapse assessment of the examined buildings indicates that their median collapse intensity is somewhat sensitive to the degree of composite action. While the design sites have the same design spectrum according to the current EN 1998-1 seismic provisions (CEN 2004a), the median collapse capacity between the examined cases is site dependent due to differences associated with the seismic hazard curves of each design location.

- The collapse risk of the three prototype buildings at all design sites in terms of annualized probabilities of collapse over a 50-year building life expectancy is considerably lower than the 1% limit specified in ASCE/SEI 7-16 (ASCE 2016). The highest values are noted in Aikaterini/Greece, $\eta = 50\%$ and are equal to 0.03%. The relatively low annualized probabilities of collapse are mostly attributed to the strict lateral drift limits according to EN 1998-1(CEN 2004a).

- The peak slip demands in beam-slab connections are strongly influenced by seismic events with a high probability of occurrence. The developed beam-slab connection peak slip hazard curves

suggest that for $\eta = 80\%$, the slip demands at a return period associated with a DBE event ($T_R = 475$ years) are up to 2 mm. On the other hand, for $\eta = 50\%$, the slip demands can reach up to 3 mm.

- In prototype buildings with partially composite steel beams ($\eta = 80\%$ and $\eta = 50\%$), the beam-slab connections experience minimal or no damage for frequently occurring seismic events (i.e., $T_R = 72$ years). For DBE events, the probability of damage in beam-slab connections is mainly characterized by light cracking in the slab (>70%) for $\eta = 80\%$. For the same degree of composite action, no extensive damage or loss of shear-load carrying capacity of the beam-slab connections is expected. On the other hand, for $\eta = 50\%$, the likelihood of shear stud yielding and/or crushing may reach up to 20% for seismic events with a return period of 475 years. Moreover, the probability of extensive damage in the slab and low-cycle fatigue microcracking is less than 10% regardless of the design site.

The findings suggest that for composite steel MRF designs with shallow composite steel beams (d_b < 500 mm), the 25% reduction in the capacity of shear connectors, which is recommended by current seismic provisions (AISC 2016a; CEN 2004a) is not substantiated. However, additional experimental and system-level studies with various slab configurations should be conducted to further support this finding.

This chapter provides methodological developments for modeling composite steel MRFs that can be utilized to refine current and future seismic design standards (e.g., EN 1998-1 (CEN 2004a)). Further system-level nonlinear simulations can be used to benchmark the seismic performance of composite steel concrete buildings from the onset of earthquake damage to structural collapse, thereby leading to more effective seismic designs.

Chapter 7 Conclusions and future work

7.1 Summary

This doctoral thesis advanced the state-of-knowledge regarding the role of slab continuity and framing action on the seismic stability of composite steel moment resisting frames (MRFs) with emphasis on earthquake-induced collapse. This was achieved through a comprehensive full-scale collapse experiment of a 2-bay composite steel MRF subsystem and corroborating continuum finite element (CFE) analyses. The test data from the experimental program were made publicly available. A computationally efficient macro-model that captures the asymmetric cyclic deterioration in composite steel beams, the nonlinear geometric instabilities and the hysteretic behavior of the beam-slab connections was also developed as part of this thesis. The macro-model, which was validated with physical testing, was employed in nonlinear system-level simulations to benchmark the collapse risk of composite steel MRFs designed according to Eurocode seismic provisions (CEN 2004a). Novel risk-based metrics were used in conjunction with a set of newly proposed fragility functions to assess the repairability of beam-slab connections within the framework of performance-based earthquake engineering. Other practice-oriented contributions of the thesis involve the refinement of seismic design requirements for composite steel MRFs (CEN 2004a) and the development of nonlinear models for seismic assessment within the framework of Eurocode 8 (CEN 2005a).

7.2 Conclusions

7.2.1 Role of slab continuity and framing action on the collapse behavior of composite steel MRFs

The full-scale experimental program of a 2-bay composite steel MRF subsystem showed that the slab continuity and framing action have a profound effect on the seismic stability of composite steel MRFs. Findings from the experimental program corroborated with high-fidelity continuum finite element analyses that featured a comparison between the hysteretic behavior of composite steel beams in 2-bay subsystems and typical cruciform subassemblies with overly simplified boundary conditions that are commonly used in experimental earthquake engineering.

The experimental results revealed that the base shear resistance of the test frame experienced cyclic deterioration due to local buckling in the bottom flanges of the composite steel beams and concrete crushing due to bearing of the slab to the column faces. While softening (i.e., negative stiffness) in the base shear occurred following concrete crushing and the formation of cracks in the steel beams,

the hysteretic response stabilized after these incidents. This behavior was attributed to two phenomena that are characteristic of subsystems in which axial restraint is present: straightening of local buckles of bottom beam flanges upon load reversals, and stabilization of the developed cracks within the dissipative zones of the respective composite steel beams. At a lateral drift ratio of 15% rads, the composite steel beams under hogging bending sustained 50% of their maximum flexural resistance. The test frame itself sustained about 30% of its maximum base shear at the same lateral drift ratio, which is an important finding for collapse safety evaluation of structures under earthquake loading. In that respect, the experimental data are considered unique in the sense that composite steel beams of the test frame attained a complete loss of their lateral load carrying capacity. Therefore, the data constitute an important source for the further development and validation of deterioration models for simulating ultimate limit states in composite steel concrete structures.

Complementary CFE analyses demonstrated a lower degree (25% less) of flexural strength degradation in partially composite steel beams in subsystems, than those in typical cruciform subassemblies with simplified boundary conditions. Moreover, the axial restraint provided by the slab and framing action was shown to augment the maximum probable moment in composite steel beams by up to 25%, even in cases where deep beams (i.e., depths larger than 700 mm) were featured. In this case the effect of composite action on the flexural resistance of the composite steel beam is usually not as pronounced.

The presence of the axial restraint in composite steel MRFs impedes beam axial shortening, that is generally observed in subassemblies, due to the accumulation of local buckling in the dissipative zones of composite steel beams. Both the experimental program and corroborating CFE analyses revealed that axial shortening in subsystems is minimal (i.e., less than 10 mm) at lateral drift demands higher than 4% rads. Conversely, in subassemblies, beam axial shortening is significantly more pronounced and could reach up to five times that in subassemblies especially for deep beams (i.e., depth greater than 700 mm) with a low degree of composite action ($\eta < 50\%$). These findings concur with field observations (Clifton et al. 2011; Okazaki et al. 2013) from past earthquakes.

Moment redistribution in the composite steel beams was observed in the subsystems. This is more evident when nonlinear geometric and material instabilities occur, thereby shifting the inflection points within the composite steel beams. The shift in moment gradient due to moment redistribution was found to particularly influence the behavior of the beam-slab connection. An increase in the shear span under sagging bending leads to the engagement of a higher number of shear stud connectors under cyclic loading. Furthermore, a comparison between the hysteretic behavior of shear studs in

subsystems and subassemblies suggested that the latter experience higher slip demands. This is attributed to axial shortening in the composite steel beams of subassemblies. In view of the above, the shear stud connectors in composite steel beams that are part of subsystems experienced lower shear strength degradation than those in the corresponding subassemblies.

The CFE analysis showed that the exterior joint panel zones in subsystems exhibited a distinct asymmetric response under sagging and hogging bending. The column web panel zones were designed to experience a shear distortion four times as high as their yield shear distortion. Nevertheless, they experienced higher distortions due to their asymmetric response. The difference in shear demands was attributed to three underlying mechanisms, namely, composite action, the slab restraint against top flange local buckling, and the axial restraint provided by the slab and framing action.

7.2.2 Implications on the seismic design and assessment provisions for composite steel MRFs

The seismic design requirements of composite steel MRFs were refined. These refinements were based on the full-scale experimental program, an assembled database of 97 composite steel beams and both the CFE and system-level simulation studies. New recommendations for performance assessment of new and existing composite-steel MRFs through nonlinear static analysis are also proposed. The main design and assessment implications and/or recommendations are summarized in this section.

The sensitivity of the sagging plastic flexural resistance of composite steel beams to the slab effective width was evaluated based on the assembled composite steel beams database. It was revealed that the sensitivity is not significant and the detailed approach, for estimating the effective width under sagging bending, in the current version of EN 1998-1 (CEN 2004a) is not justified. A simpler formulation based on AISC (2016b) or AIJ (2010b) is recommended.

The effective width of the slab under hogging bending, which was explicitly derived from uniaxial strain measurements on the rebars, is estimated fairly well using EN 1998-1 (CEN 2004a) up to a lateral drift demand of 2% rads. Nevertheless, at higher lateral drift demands ($\geq$ 3% rads), stress redistribution in the reinforcement along the slab width mobilizes a larger effective width, which can change the capacity design hierarchy in composite steel beams. This finding is important for collapse safety evaluation of composite steel MRFs under seismic loading.

The transverse beams framing the columns and primary girders in composite steel MRFs have a considerable influence on the flexural resistance and equivalent moment of inertia of composite steel beam-to-column connections. This influence is particularly evident at interior beam-to-column joints where the equivalent moment of inertia in composite steel beams was underestimated by 25% for sagging bending and 35% for hogging bending in the current EN 1998-1 provisions (CEN 2004a). A higher level of slab confinement was also present in this case. The source of overstrength due to the transverse beams is important and should be factored in the capacity design of composite steel MRFs in prospective seismic design provisions.

The ductility requirements for composite steel beams under sagging bending that limit the position of the plastic neutral axis, are quite stringent in the current Eurocode seismic provisions (CEN 2004a). Digital image correlation (DIC) measurements revealed that the longitudinal compressive strains (i.e. along the main girder) in the vicinity of the columns reached up to 0.005 and 0.006 prior to crushing of the concrete, which is much higher than 0.0025 upon which the CEN (2004a) limits were set. It is recommended that the ductility limits are refined by assuming a higher crushing strain that accounts for the slab confinement effects due to the slab reinforcement and the presence of the transverse beams. This issue deserves further investigation.

The integrity of beam-slab connections in shallow partially composite steel beams (i.e., beam depth less than 500 mm) is maintained even for a low degree of composite action (= 50%). The 25% reduction in the shear resistance of headed stud connectors that is required by current seismic provisions (AISC 2016a; CEN 2004a) is not substantiated for composite steel MRFs with shallow beam designs. These findings were put in place based on the experimental program, CFE analysis of subsystems with shallow partially composite steel beams, and performance-based assessment of beam-slab connections through nonlinear system-level simulations. Accordingly, it is recommended to waive 25% reduction in the shear resistance of headed stud connectors, if ductile stud connectors are employed as part of the seismic design process.

Allowing some degree of slip in ductile shear stud connectors could be beneficial to control the sources of overstrength in the concrete slab. These include the overstrength in the compressive strength of concrete due to the associated material variability, as well as the overstrength due to the slab confinement and the presence of the transverse beams in the floor system. However, it is necessary to ensure that the integrity of the beam-slab connection is maintained. Mobilizing the ductility of the shear stud connectors to control the compressive force in the slab warrants further investigation.

The column web panel zones in composite steel MRFs may be designed with a relative panel zone-to-beam shear resistance ratio of 0.8. This allows for a controlled panel zone inelastic deformation of up to 10 times the panel zone shear yield distortion angle. The proposed value is based on composite steel beam test data for which a lateral drift demand of at least 5% rads was attained without the occurrence of premature fracture in the composite steel beam-to-column connections.

Empirical expressions were developed to predict the plastic rotation capacity of composite steel beams in terms of their geometric and material properties that could be readily adopted in future versions of seismic assessment standards, such as EN 1998-3 (CEN 2005a), ASCE/SEI 41-17 (ASCE 2017), AISC-342-22 (AISC 2022) and SIA 269/3 (SIA 2011).

7.2.3 Performance-based evaluation of composite steel MRFs through a computationally efficient macro-model for system-level simulation

A computationally efficient nonlinear macro-model was proposed to simulate the asymmetric hysteretic response of fully restrained beam-to-column connections with composite steel beams. The model explicitly accounts for the two slab-column load transfer mechanisms that were detected by the digital image correlation (DIC) measurements from the experimental program (i.e., slab bearing on the face of the column and strut-and-tie mechanisms). Moreover, the macro-model can capture the cyclic deterioration in flexural strength of composite steel beams due to nonlinear geometric instabilities, as well as the anticipated slip demands on the beam-slab connections. The macro-model, which was thoroughly validated with available experimental data on characteristic configurations of composite steel beams, does not simulate the crack initiation and propagation within a dissipative zone of a composite steel beam under cyclic loading.

The macro-model was employed in system-level nonlinear response history simulations of composite steel MRFs designed at three European sites with varying degree of composite action. These simulations were used to benchmark the collapse risk of composite steel MRFs designed according to European provisions. Novel risk-based metrics were also used in conjunction with a set of proposed fragility functions for informing earthquake-induced repair actions in the beam-slab connections of composite steel MRFs at characteristic earthquake return periods of interest to the engineering profession.

Nonlinear static analysis of the composite steel MRFs showed that their static system overstrength is around 4.0. Because the seismic designs were all drift-controlled, the large system level overstrength

values are attributed to the lateral drift requirements in the current Eurocode seismic provisions CEN (2004a). For the same reason, the annualized probability of collapse over a 50-year building life expectancy was found to be considerably small (i.e., less than 0.01%). While in Europe there are no established limits for benchmarking the earthquake-induced collapse risk of frame structures in a probabilistic manner, the annualized probability of collapse over the lifecycle of the analyzed structure is considerably smaller than the 1% limit specified ASCE/SEI 7-16 (ASCE 2016) regardless of the design site and the employed degree of composite action of the composite steel beams. In that respect, the design requirements regarding P-Delta effects and the lateral drift lmits in the current EN 1998-1 (CEN 2004a) provisions appear to be conservative.

From a repairability standpoint, it was demonstrated that for frequently occurring seismic events (i.e., 50% probability of exceedance over 50 years) minimal or no damage is expected in the beam-slab connection with the current seismic design requirements and composite slab reinforcement details. The median slip demands in the beam-slab connections at a return period associated with a design basis event (i.e., 10% probability of exceedance over 50 years) were less than 2 and 3 mm for an employed degree of composite action of 80% and 50% respectively. The probability that the integrity of the beam-slab connection is maintained exceeds 90% for design basis seismic events; only light cracking is expected in the slab even though the 25% reduction in the shear resistance of the stud connectors was waived. The above findings suggest that this seismic design requirement may be waived in cases where shallow steel beams (i.e., beam depths less than 600 mm) are employed in composite construction.

7.3 Recommendations for future research

A set of potential research topics is proposed for further investigation based on the contributions of this doctoral thesis:

- The further development of new frame analysis nonlinear models for simulating (a) the axial tensile force induced in composite steel beams due to slab axial restraint and framing action, and (b) the effects of force redistribution within the beam-slab connection by means of a distributed approach for modeling shear stud connectors.
- The development of new models for simulating crack initiation and propagation due to ultra-low-cycle fatigue within dissipative zones of composite steel beams at ultimate limit states in composite steel concrete structures under earthquake shaking.

- The collapse risk evaluation of mid- to high-rise buildings with composite steel MRFs by means of nonlinear response history simulations that can capture three dimensional effects due to three dimensional shaking.

- The doctoral thesis focused on composite steel beams with their profiled steel deck ribs oriented parallel to the main girder. Experimental and simulation studies should be conducted to investigate the influence of various slab configurations (i.e., solid slab and slab with profiled steel deck oriented perpendicular to the main girders) on the mechanisms of load transfer between the slab and the columns, as well as the shear strength degradation behavior of the stud connectors in the beam-slab connection. Moreover, the role of transverse beams should be further comprehended by additional experimental studies.

- The experimental program showed that allowing controlled slip in the beam slab connections is beneficial to control the overstrength in the flexural resistance of composite steel beams and control the additional overstrength within a system that could potentially alter the seismic design hierarchy. Further investigation of this design concept should be conducted through experimental and CFE studies in order to propose a rational design process for partially composite steel MRFs.

Appendix A Design summary of the composite steel moment-resisting frame (MRF)

Description

This appendix provides a summary of the design of the composite steel MRF from which the 2-bay test frame subsystem was extracted.

A.1 Design standards

The following design standards are used in the design of the prototype building:

- EN 1990: Eurocode 0 (CEN 2002a) for the combination of actions at serviceability and ultimate limit state
- EN 1991: Eurocode 1 for the value of the dead permanent and variable actions on the building. These include EN 1991-1-1: Eurocode 1 – Part 1-1 (CEN 2002b) for general actions, EN 1991-1-3: Eurocode 1 – Part 1-3 (CEN 2003) for snow loads and EN 1991-1-4: Eurocode 1 – Part 1-4 (CEN 2010) for wind loads
- EN 1992-1-1: Eurocode 2 – Part 1-1 (CEN 2004c) for the design of the reinforced concrete slab
- EN 1993: Eurocode 3 for the design of the structural steel components. These include EN 1993-1-1: Eurocode 3 – Part 1-1 (CEN 2005b) for the design of the design of the beam, columns and braces and EN 1993-1-8: Eurocode 3 – Part 1-8 (CEN 2005c) for the design of the beam-column web panel zone
- EN 1994-1-1: Eurocode 4 – Part 1-1 (CEN 2004b) for the design of the composite steel beams
- EN 1998-1: Eurocode 8 – Part 1 (CEN 2004a) for the capacity design and detailing of the building components under the seismic load combination

A.2 Structural type and layout

The prototype building is a 6-story office building with a total height of 24 m. The building is located in Sion, Switzerland. The building is designed for a medium ductility class (DCM) according to EN 1998-1 (CEN 2004a). The height of each story 4.0 m. The building is composed of two bays in the E-W direction and three bays in the N-S direction. The width of each bay is 5 m. Two lateral-load resisting systems are employed in the design: Four steel moment-resisting frames (MRFs) in the E-W direction and two perimeter concentrically braced frames (CBFs) in the N-S direction with an X configuration. The columns are oriented with their strong axis in the direction of the MRFs (E-W direction). Additionally, the base of the first story column is fixed in the E-W direction and pinned in the N-S direction. The primary beams in the E-W direction are connected to the columns with stiffened extended end-plate connections, while those in the N-S direction are pinned at their ends. Secondary beams, located at one-thirds of the bay width, span in both directions. The secondary beams are pinned at their ends. A 140 mm reinforced concrete slab is connected to the beams through ductile headed shear stud connectors to achieve full composite action.

Figure A.1 shows the building plan and elevation view of both the interior and exterior composite steel MRFs as well as the CBFs. Detailed drawings of the first story beams, columns, and connection detailing, corresponding to the test frame, are shown in Appendix B.1. The same drawings were used for fabrication of the test frame discussed in Chapter 5. Tables A.1 and A.2 summarize the final members of the lateral load resisting systems.

Table A.1 Summary of the members for the MRFs (E-W direction)

Story	Beams	Columns Interior MRF		Columns Exterior MRF	
		Interior	Exterior	Interior	Exterior
6 5	IPE270	HEM260	HEB260	HEM260	HEB260
4 3	IPE360	HEM320	HEB320	HEM320	HEB260
2 1	IPE360	HEM320	HEM320	HEM320	HEB260
Column splices in the 3rd and 5th stories					

Table A.2 Summary of the members for the CBFs (N-S direction)

Story	Brace	Columns	Beams
6	RRW 60·60·3	HEB260	IPE270
5	RRK 80·80·4		
4	RRK 80·80·6	HEM320	IPE270
3	RRK 80·80·8		
2		HEM320	IPE270
1	RRK 90·90·8		
Column splices in the 3rd and 5th stories			

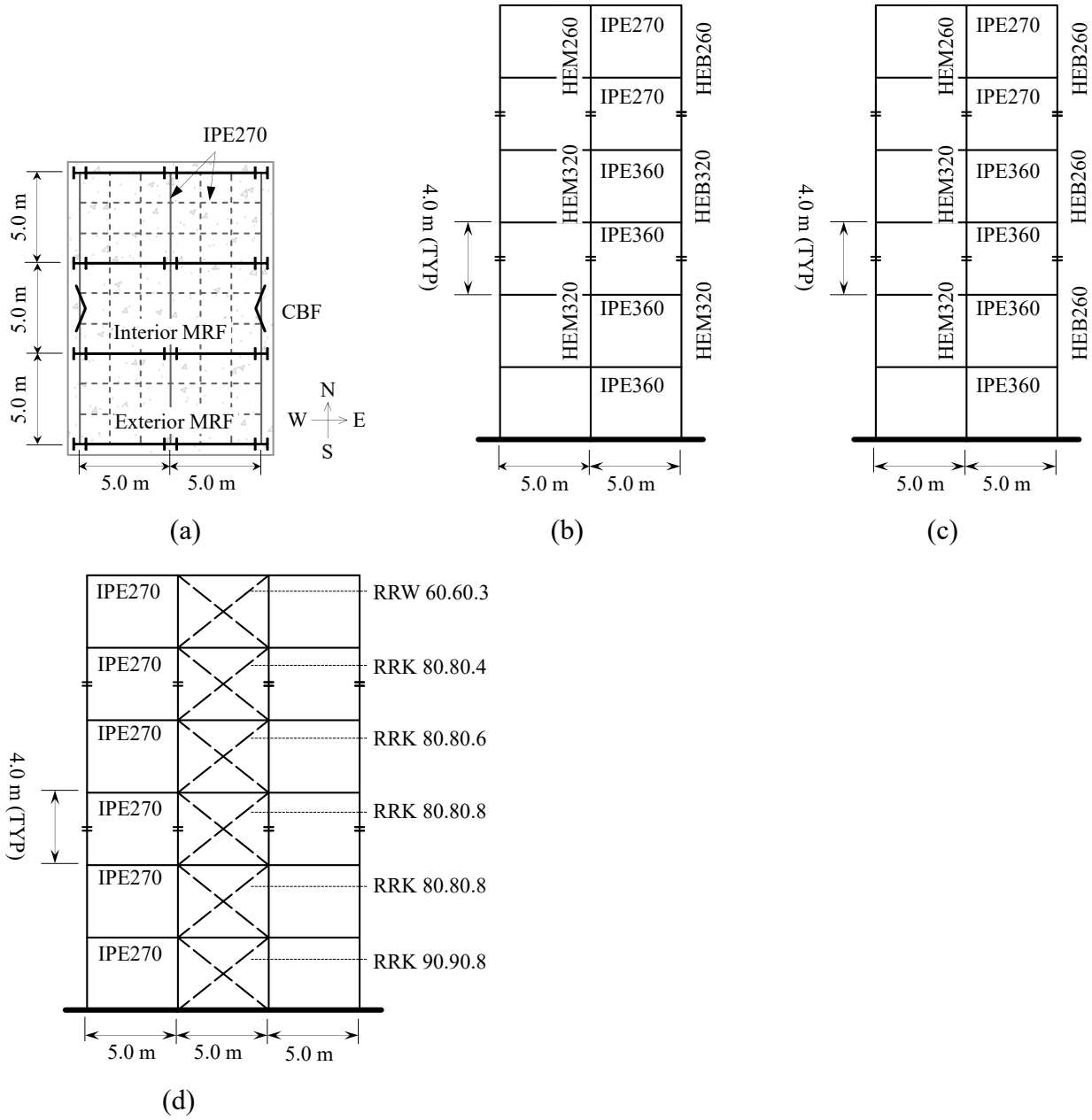

Figure A.1 Prototype building: (a) plan view; (b) elevation view of the interior composite steel MRF; (c) elevation view of the exterior composite steel MRF; (d) elevation view of the CBF

The slab consists of a 56 mm deep profiled steel deck, Cofrastra 56 steel deck with its ribs oriented parallel to the main girders. A total of 36 16 mm headed shear stud connectors spaced at 120 mm are used to achieve full composite action in each composite steel beam. The 25% reduction in the shear resistance of the headed studs according to Clause 7.6.2 in EN 1998-1 (CEN 2004a) is internationally waived. The headed shear studs are ductile with $h_{sc}/d_{sc} > 4.0$ as per EN 1994-1 (CEN 2004b). Details of the slab, reinforcing rebars and beam-slab connection, corresponding to the test frame, are shown in Appendix B.2.

A.3 Design material properties

The nominal material properties of the primary structural components are summarized in Table A.3. In compliance with Clause 5.4.1.1 in EN 1998-1 (CEN 2004a), only ribbed reinforcing steel can be used in the critical regions of the primary seismic elements (i.e., the dissipative zones of the composite steel beams). Additionally, the reinforcing steel shall be either grade B or C. For this design, B500B rebars were employed.

Table A.3 Design material properties of the building components

Structural Steel			Slab Reinforcement			Concrete		
Beam Grade	S355J2+M		Grade	B500B		Type	NWC*	-
$f_{y,b}$	355	MPa	f_{sk}	500	MPa	Grade	C25/30	-
$f_{u,b}$	510	MPa	E_{sk}	210,000	MPa	f_{ck}	25	MPa
Column Grade	S355J2+M		Steel Deck			f_{cm}	33	MPa
$f_{y,c}$	355	MPa	Grade	S350GD	-	f_{ctm}	2.6	MPa
$f_{u,c}$	510	MPa	$f_{y,pk}$	350	MPa	ρ_c	2,450	kg/m^3
Doubler Plate Grade	S355J2+N		$\rho_{A,ps}$	8.53	kg/m^2	E_{cm}	31,475	MPa
$f_{y,d}$	355	MPa	Shear Studs					
$f_{u,d}$	510	MPa	$f_{u,sc}$	450	MPa			
Brace Grade	S355J2H		End Plate Connection Bolts					
$f_{y,br}$	355	MPa	Grade	12.9	-			
$f_{u,br}$	510	MPa	$f_{y,bo}$	1100	MPa			
E_s	210,000	MPa	$f_{u,bo}$	1220	MPa			
G_s	80,769	MPa	$f_{uv,bo}$	730	MPa			

* Normal weight concrete

f_{cm}, f_{ctm} and E_{cm} are calculated as per Table 3.1 of EN 1992-1-1 (CEN 2004c).

$$f_{cm} = f_{ck} + 8 \ (f_{cm} \text{ and } f_{ck} \text{ in MPa}) \tag{A.1}$$

$$f_{ctm} = 0.3 \cdot (f_{ck})^{\frac{2}{3}} \ (f_{ctm} \text{ and } f_{ck} \text{ in MPa}) \tag{A.2}$$

$$E_{cm} = 22 \cdot \left(\frac{f_{cm}}{10}\right)^{0.3} (E_{cm} \text{ in GPa and } f_{ck} \text{ in MPa}) \tag{A.3}$$

The structural steel in the dissipative zones (i.e., MRF primary composite steel beams and CBF braces), shall have an upper value of the yield strength $f_{y,max} \leq 1.1\gamma_{OV} f_y$ as per Clause 6.3 in EN 1998-1 (CEN 2004a). The recommended material overstrength factor $\gamma_{OV} = 1.25$. Hence, for the MRF beams and braces, $f_{y,max} \leq 488$ MPa.

A.4 Actions

A.4.1 Dead and imposed loads

The variable actions include the imposed (live) loads, the snow load, in addition to the wind load. The imposed loads are calculated according to Table 6.2 in Eurocode 1-1-1 (CEN 2002b) for Category B buildings. The snow load on the roof is determined for the persistent/transient design situations only and not for accidental design situations where exceptional snow load is the accidental action. The snow load is calculated according to Clause 5.2 in Eurocode 1-1-3 (CEN 2003). A summary of the permanent and variable loads is presented in Table A.4.

Table A.4 Summary of permanent and variable loads

Load Description		Load	
Dead	Columns (avg.)	1.60	kN/m
	Primary Beams (avg.)	0.42	kN/m
	Secondary Beams (avg.)	0.26	kN/m
	Slab	3.15	kN/m^2
Super-Imposed Dead Load (SDL)	Finishing	1.00	kN/m^2
	Partitions	1.20	kN/m^2
	Windows	0.50	kN/m^2
	Heating + Ventilation	0.50	kN/m^2
Imposed	Floors	3.00	kN/m^2
	Roof	1.00	kN/m^2
Snow		1.63	kN/m^2
Wind		0.95	kN/m^2

A.4.2 Notional horizontal loads

The notional horizontal loads are applied at each story in order to account for the global sway imperfections of the MRFs and CBFs according to Clause 5.3.2 in EN 1993-1-1 (CEN 2005b). Table A.5 shows the values of the notional horizontal load at each story in the E-W direction (MRF), $H_{Ed,EW}$ and N-S direction (CBF), $H_{Ed,NS}$. V_{Ed} is the design value of the vertical load at each story for the persistent/transient design situations.

Table A.5 Notional horizontal loads at each story in the E-W (MRF) and N-S (CBF) directions

Story	P_{Ed} [kN]	$H_{Ed,EW}$ [kN]	$H_{Ed,NS}$ [kN]
6	1,724	5	5
5	4,010	11	12
4	6,343	17	18
3	8,683	24	25
2	11,042	30	32
1	13,438	37	39

A.4.3 Seismic action

The reference horizontal peak ground acceleration, $a_{gR} = 0.22$g for return period, $T_R = 475$ years (Giardini et al. 2013). The design ground acceleration $a_g = \gamma_I \cdot a_{gR}$, where γ_I is the importance factor $= 1.0$ for a building of importance class II, as per Table 4.3 in EN 1998-1 (CEN 2004a); hence, $a_g =$ 0.22g.

The behavior factors for DCM are chosen in accordance with the limits provided in Table 6.2 in EN 1998-1 (CEN 2004a). Both the MRFs and CBFs are designed for $q = 3$. The horizontal design spectrum, $S_d(T)$, is the same for the E-W and N-S directions. $S_d(T)$ is defined using Clause 3.2.2.5 in EN 1998-1 (CEN 2004a). The lower bound factor for the horizontal design spectra, $\beta = 0.2$, based on the recommended value in Clause 3.2.2.5 in EN 1998-1 (CEN 2004a). Figure A.2 shows the horizontal design spectrum in the E-W and N-S directions.

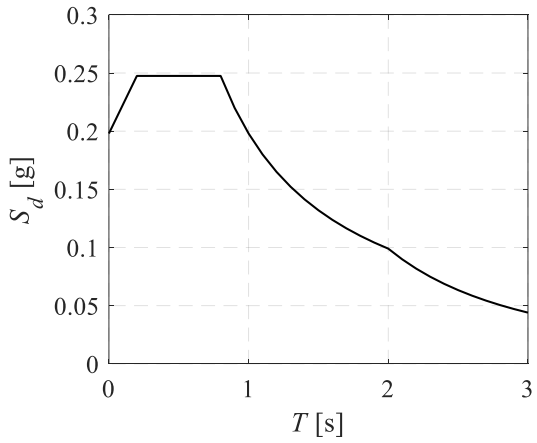

Figure A.2 Horizontal design response spectrum in E-W and N-S directions

A.5 Seismic mass

The inertia effects of the design seismic action are considered by considering the presence of a seismic mass at each floor. The seismic mass is calculated using the gravity loads combination in Clause 3.2.4 in EN 1998-1 (CEN 2004a) for category B buildings. The seismic mass at each floor is shown in Table A.6.

Table A.6 Seismic mass at each floor

Floor	Seismic Mass [kg]
Roof	91,921
6	128,878
5	132,478
4	132,952
3	134,388
2	137,208

A.6 Load combinations

A.6.1 Combination of actions for ultimate limit state (ULS) design

The combinations of actions at ULS are obtained from Table A1.2B in EN 1990 (CEN 2002a):

$$\gamma_{Gj,sup}G_{kj,sup} + \gamma_{Gj,inf}G_{kj,inf} + \gamma_{Q,1}Q_{k,1} + \gamma_{Q,i}\psi_{0,i}Q_{k,i}$$

The combination for the seismic design situation is obtained from Table A1.3 in EN 1990 (CEN 2002a):

$$G_{kj,sup} + G_{kj,inf} + \psi_{2,i}Q_{k,i} + A_{Ed}$$

in which, $G_{kj,sup}$ is the unfavorable permanent action, $\gamma_{Gj,sup} = 1.35$; $G_{kj,inf}$ is the favorable permanent action, $\gamma_{Gj,inf} = 1.0$; $Q_{k,1}$ is the leading variable action, $Q_{k,i}$ is the accompanying variable action, $\gamma_{Qi} = 1.5$ if the variable action is favorable and 0 if the variable action is unfavorable and A_{Ed} is the leading accidental or seismic action. The ψ factors are obtained from Table A1.1 in EN 1990 (CEN 2002a):

For an office building of category B, $\psi_0 = 0.7$, $\psi_1 = 0.5$ and $\psi_2 = 0.3$.

For snow loads on buildings, $\psi_{0,s} = 0.5$, $\psi_{1,s} = 0.2$ and $\psi_{2,s} = 0$.

For wind loads, $\psi_{0,w} = 0.6$, $\psi_{1,w} = 0.2$ and $\psi_{2,w} = 0$.

The seismic action in both directions should be combined as $E_{EW} + 0.3E_{NS}$ and $E_{NS} + 0.3E_{EW}$ as per Clause 4.3.3.5.1 in EN 1998-1 (CEN 2004a). Accordingly, the ULS combinations are:

- $1.35G + 1.5Q + 1.5\psi_{0,s}S + 1.5\psi_{0,w}W = 1.35G + 1.5Q + 0.75S + 0.9W$
- $1.35G + 1.5S + 1.5\psi_{0}Q + 1.5\psi_{0,w}W = 1.35G + 1.5S + 1.05Q + 0.9W$
- $1.35G + 1.5W + 1.5\psi_{0}Q + 1.5\psi_{0,s}S = 1.35G + 1.5W + 1.05Q + 0.75S$
- $G + \psi_{2}Q + \psi_{2,w}W + \psi_{2,s}S + E_{EW} + 0.3E_{NS} = G + 0.3Q + E_{EW} + 0.3E_{NS}$
- $G + \psi_{2}Q + \psi_{2,w}W + \psi_{2,s}S + E_{NS} + 0.3E_{EW} = G + 0.3Q + E_{NS} + 0.3E_{EW}$

A.6.2 Combination of actions for serviceability limit state (SLS) design

The characteristic combinations at SLS are obtained from Table A1.4 in EN 1990 (CEN 2002a):

$G_{kj,sup} + G_{kj,inf} + Q_{k,1} + \psi_{0,i}Q_{k,i}$

The SLS combinations are:

- $G + Q + \psi_{0,s}S + \psi_{0,w}W = G + Q + 0.5S + 0.6W$
- $G + S + \psi_{0}Q + \psi_{0,w}W = G + S + 0.7Q + 0.6W$
- $G + W + \psi_{0}Q + \psi_{0,s}S = G + S + 0.7Q + 0.5S$

A.7 Structural model

A.7.1 Description of the model

The structural analysis package, SAP 2000 v20.1.0 (CSI 2019), is used to model and analyze the building. As per Clause 6.7.2 in EN 1998-1 (CEN 2004a), for the CBFs with X-bracing, the structural model under seismic combinations shall include the tension only braces unless non-linear analysis is carried out. The energy dissipation capacity of the compression brace is neglected. Therefore, two models must be developed one with braces titled in one direction and the other with braces tilted in the other direction. Under the persistent/transient design combinations, both the compression and tension braces are considered.

In order to account for the increase in the stiffness of the beams due to composite action, an equivalent moment of inertia of the beams, I_{eq}, is considered according to Clause 7.7.2 in EN 1998-1 (CEN 2004a). The floor loads are applied as "uniform area to frame" loads on each floor to ensure a proper distribution of the loads on the floor beams. Diaphragm constraints are applied at each floor to simulate the diaphragm action of the slab.

Modal spectrum analysis is used to obtain the member forces due to the seismic action in the E-W and N-S directions (E_{EW} and E_{NS}). Moreover, accidental torsional effects are accounted for by assuming an eccentricity at each floor of $\pm 5\%$ of the floor dimension perpendicular to the seismic action, according to Clause 4.3.2 in EN 1998-1 (CEN 2004a). Hence,

$e_{EW} = 0.75$ m for seismic loading in the E-W direction (E_{EW})

$e_{NS} = 0.5$ m for seismic loading in the N-S direction (E_{NS}).

A.7.2 Modal response spectrum analysis

The periods of vibration of the building in the direction of the applied seismic loading are obtained from modal analysis using SAP 2000. Table A.7 shows the period of the first five modes and the corresponding effective modal mass participation ratios for each loading direction.

Table A.7 Periods of vibration and modal participating mass ratio in each direction

Mode i	T_i [s]	$\Sigma M_{i,EW} / M_T$	$\Sigma M_{i,NS} / M_T$
1	1.25	0.81	0.00
2	1.04	0.81	0.79
3	0.82	0.81	0.79
4	0.44	0.92	0.79
5	0.39	0.92	0.93

According to Clause 4.3.3.1 in EN 1998-1 (CEN 2004a), the sum of the effective modal masses must be $\geq 90\%$ of the total seismic mass (M_T). This criterion is satisfied in both directions as shown in Table A.7. Additionally, all modes with an effective mass $\geq 5\%$ should be considered. For higher modes, the effective mass was found to be less than 5%. For the combination of modes, square-root-of-sum-of-squares (SRSS) is allowed only if the period of vibrations are independent. According to Clause 4.3.3.2 in EN 1998-1 (CEN 2004a), this condition is satisfied if $T_i \leq 0.9T_j$, (T_i and T_j are two

periods vibrations corresponding to different modes). This condition applies in this case for the first five considered modes. Hence, SRSS combination method is used.

A.8 Interior composite steel MRFs verifictions for seismic action

In this section, the verifications for the design of the interior composite steel MRF are summarized. Summary tables for the design of the composite steel beams, the columns and the column web panel zones are also included.

A.8.1 Damage limitation verification

The story drift, δ, is obtained from the SAP2000 model at each story, in the E-W under the seismic combinations. These drifts are due to elastic loads. Accordingly, the design story drift $\delta_r = q\delta$ according to Clause 4.3.4 in EN 1998-1 (CEN 2004a).

For damage limitation verification, Clause 4.4.3.2 in EN 1998-1 (CEN 2004a) states the story drift δ_r should be multiplied by a ν factor = 0.5 for buildings of Class II importance. It is assumed that the building has ductile non-structural elements. Therefore, the limit on the story drift ratio is 0.75% as per Clause 4.4.3.2 in EN 1998-1 (CEN 2004a). Table A.8 shows a summary of the damage limitation verification at each story. Figure A.3 shows the maximum normalized floor displacement along the height of the composite steel MRF and the maximum story drift ratios.

Table A.8 Damage limitation verification for the interior composite steel MRF

Story	h [m]	δ_r [m]	$\nu\delta_r$ [m]	0.75% h [m]	
6	4.00	0.027	0.014	0.030	OK
5	4.00	0.036	0.018	0.030	OK
4	4.00	0.045	0.023	0.030	OK
3	4.00	0.045	0.023	0.030	OK
2	4.00	0.047	0.024	0.030	OK
1	4.00	0.036	0.018	0.034	OK

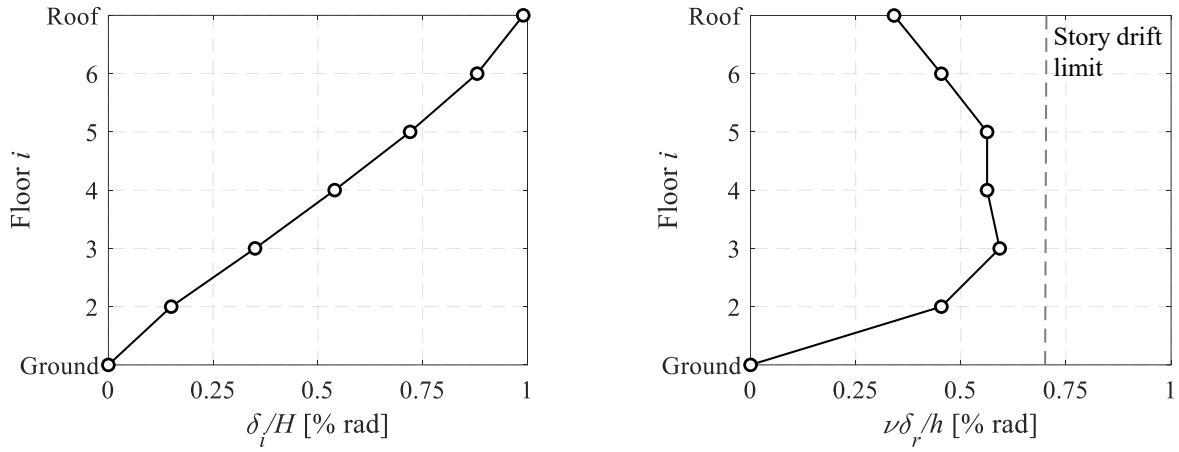

(a)

Figure A.3 (a) Normalized displacement profile of the interior composite steel MRF; (b) peak story drift ratio and damage limitation verification

A.8.2 Second-order effects

In order to account for the second order effects on the frame stability, the design actions due to lateral loading are amplified by the Merchant-Rankine multiplier for the seismic combinations.

Shown below are the second-order effects calculated for the seismic combinations at ULS as per Clause 4.4.2.2 in EN 1998-1 (CEN 2004a). Table A.9 show the stability coefficient (θ) at each story per loading direction in addition to the Merchant-Rankine multiplier α_{EW}.

Table A.9 Second-order effects in the E-W direction (MRF) under the seismic combinations

Story	h [m]	δ_r [m]	$V_{tot,EW}$ [kN]	P_{tot} [kN]	θ_i	α_{EW}
6	4.000	0.027	151	714	0.032	
5	4.000	0.036	307	1,792	0.053	
4	4.000	0.045	426	4,222	0.111	1.13
3	4.000	0.045	524	6,621	0.142	1.17
2	4.000	0.047	595	5,073	0.101	1.12
1	4.000	0.036	633	6,196	0.089	

A.8.3 Design of the composite steel beams

The slab is designed with minimum longitudinal reinforcement. The minimum reinforcement ratio $\rho_{s,min} = 1.2\%$, is obtained according to Clause 5.5.1 in EN 1994-1-1 (CEN 2004b). Two layers of $\phi 10$ longitudinal rebars at a spacing of 150 mm are employed.

The minimum slab transverse reinforcement ratio, $\rho_{w,min} = 0.1\%$ is obtained according to Clause 9.2.2 in Eurocode 2-1-1 (CEN 2004c). The slab transverse reinforcement is required to ensure that longitudinal shear is transferred in the concrete without failure of the concrete flange in accordance with Clause 6.6.6.4 in EN 1994-1-1 (CEN 2004c) and Clause 6.2.4 in EN 1992-1-1 (CEN 2004c). Two $\phi 8$ transverse rebars at a spacing of 150 mm are employed. Furthermore, transverse seismic rebars are employed in the vicinity of the columns to ensure the development of the compressed concrete struts according to Clauses C3.2 and C3.3 in EN 1998-1 (CEN 2004a). A total of five $\phi 10$ seismic rebars are placed within a distance h_c from the columns.

Cross section classification of the composite steel beams is conducted according to Table 5.2 of EN 1993-1-1 (CEN 2005b). All beam cross sections are Class 2. The ductility of the composite steel beams is checked according to Table 7.4 in EN 1998-1 (CEN 2004a). The values for x_{pl}^{+}/h_b exceed the upper limit in EN 1998-1 (CEN 2004a). Nevertheless, if the assumed crushing strain of concrete ε_{cu} = 0.0048, x_{pl}^{+}/h_b is within the limit and the check is satisfied. The rationale behind this assumption is elaborated in Chapter 5 of this thesis.

The plastic moment resistance of the composite steel beams under sagging (M_{Rd}^{+}) and hogging (M_{Rd}^{-}) bending was calculated according to Clause 6.2.1 in EN 1994-1-1 (CEN 2004b). The effective widths to calculate the plastic moment resistance of the composite steel beams under seismic loading were obtained from Table 7.5 II in EN 1998-1 (CEN 2004a). The resistance of the composite steel beams is checked according to Clauses 6.2 and 6.3 in EN 1993-1-1 (CEN 2005b). Table A.10 shows a summary of the design of the composite steel beam along with the overstrength ratio at each story.

Table A.10 Summary of the composite steel beam design and overstrength

Story	Beam	Class	M_{Ed}^{+}/M_{Rd}^{+}	M_{Ed}^{-}/M_{Rd}^{-}	$V_{Ed}/V_{pl,Rd}$	Ω_i
6	IPE270	2	0.14	0.17	0.30	5.77
5	IPE270	2	0.23	0.29	0.32	3.37
4	IPE360	2	0.25	0.31	0.36	3.19
3	IPE360	2	0.34	0.39	0.36	2.52
2	IPE360	2	0.36	0.45	0.36	2.23
1	IPE360	2	0.29	0.38	0.37	2.61

A.8.4 Design of the columns

The column demands are calculated based on Clauses 6.6.3 and 6.7.4 in EN 1998-1 (CEN 2004a). Moreover, the remaining columns are sized to satisfy the strong-column/weak-beam (SCWB)

criterion in Clause 4.4.2.3 in EN 1998-1 (CEN 2004a). The resistance of the columns is checked according to Clauses 6.2 and 6.3 in EN 1993-1-1 (CEN 2005b). Tables A.11 and A.12 shows a summary of the design of the exterior and interior columns of the composite steel MRFs.

Table A.11 Summary of interior columns design and SCWB ratios

Story	Section	Class	$\frac{M_{Ed}}{M_{Rd}}$	N_{Ed}/N_{Rd}	V_{Ed}/V_{Rd}	$\frac{N_{Ed}}{N_{b,y,Rd}}+k_{yy}\frac{M_{y,Ed}}{M_{b,Rd}}$	$\frac{N_{Ed}}{N_{b,z,Rd}}+k_{zy}\frac{M_{y,Ed}}{M_{b,Rd}}$	SCWB
6	HEM260	1	0.20	0.03	0.05	0.11	0.22	
5			0.36	0.07	0.10	0.22	0.41	3.12
4	HEM320	1	0.27	0.07	0.10	0.18	0.33	2.91
3			0.37	0.09	0.14	0.25	0.44	2.93
2	HEM320	1	0.39	0.12	0.15	0.29	0.48	2.95
1			0.55	0.14	0.13	0.36	0.65	2.85

Table A.12 Summary of exterior columns design and SCWB ratios

Story	Section	Class	$\frac{M_{Ed}}{M_{Rd}}$	N_{Ed}/N_{Rd}	V_{Ed}/V_{Rd}	$\frac{N_{Ed}}{N_{b,y,Rd}}+k_{yy}\frac{M_{y,Ed}}{M_{b,Rd}}$	$\frac{N_{Ed}}{N_{b,z,Rd}}+k_{zy}\frac{M_{y,Ed}}{M_{b,Rd}}$	SCWB
6	HEB260	1	0.23	0.09	0.05	0.19	0.30	
5			0.40	0.26	0.10	0.45	0.57	3.12
4	HEB320	1	0.33	0.29	0.10	0.42	0.54	2.56
3			0.50	0.51	0.14	0.71	0.75	2.38
2	HEM320	1	0.26	0.40	0.08	0.52	0.51	4.67
1			0.58	0.43	0.10	0.62	0.81	4.18

A.8.5 Design of the beam-to-column web panel zone

The beam-to-column web panel zones are designed to remain elastic. The shear demands on the panel zones are calculated as described in Chapter 5. The shear resistance is calculated according to Clause 6.2.6.1 in EN 1993-1-8 (CEN 2005c). However, the provisions consider the contribution of only one doubler plate to the shear resistance of the column web panel zone even if two doubler plates are used. Herein, the full contribution of two doubler plates is considered in the design, which corroborates with recent findings on the seismic design of panel zones (Skiadopoulos et al. 2021).

Tables A.13 and A.14 summarize the design of the column web panel zone for the interior and exterior columns respectively.

Table A.13 Panel zone design for the interior columns

Story	Column	Beam	Doubler Plates			Continuity Plates		$V_{wp,Ed}/V_{wp,Rd}$
			Nº	b_d [mm]	t_d [mm]	b_{ct} [mm]	t_c [mm]	
6	HEM260	IPE270	2	175	12	177	20	0.94
5			2	175	12	177	20	0.91
4	HEM320	IPE360	2	225	15			0.95
3			2	225	15			0.96
2	HEM320	IPE360	2	225	15			0.95
1			2	225	15			0.98

Table A.14 Panel zone design for the exterior columns

Story	Column	Beam	Doubler Plates			Continuity Plates		$V_{wp,Ed}/V_{wp,Rd}$
			Nº	b_d [mm]	t_d [mm]	b_{ct} [mm]	t_c [mm]	
6	HEB260	IPE270	1	175	15	177	25	0.84
5			1	175	15	177	25	0.81
4	HEB320	IPE360	1	225	15	225	25	0.94
3			1	225	15	225	25	0.91
2	HEM320	IPE360						0.90
1								0.93

A.9 Notation

a_g = design horizontal peak ground acceleration

a_{gR} = reference horizontal peak ground acceleration

b_{ct} = column web panel zone continuity plate length

b_d = column web panel zone doubler plate width

d_{sc} = diameter of the shear stud connectors

e_{EW} = seismic load eccentricity in the E-W direction of the floor plan

e_{NS} = seismic load eccentricity in the N-S direction of the floor plan

f_{ck} = characteristic compressive strength of the slab concrete

f_{cm} = mean compressive strength of the slab concrete

f_{ctm} = mean tensile strength of the slab concrete

f_{sk} = nominal yield strength of the slab rebars

$f_{u,b}$ = ultimate tensile strength of the beam structural steel

$f_{u,bo}$ = ultimate tensile strength of the bolts

$f_{u,br}$ = ultimate tensile strength of the brace structural steel

$f_{u,c}$ = ultimate tensile strength of the column structural steel

$f_{u,d}$ = ultimate tensile strength of the doubler plates structural steel

$f_{uv,bo}$ = ultimate shear strength of the bolts

$f_{y,b}$ = nominal yield strength of the beam structural steel

$f_{y,bo}$ = nominal yield strength of the bolts

$f_{y,br}$ = nominal yield strength of the brace structural steel

$f_{y,c}$ = nominal yield strength of the column structural steel

f_{yd} = nominal yield strength of the doubler plates structural steel

$f_{y,max}$ = upper value for the yield strength of the structural steel

$f_{y,pk}$ = nominal yield strength of the profiled steel deck

h = story height

h_b = total depth of the composite steel beam including the slab

h_c = column depth

h_{sc} = height of the shear stud connectors

k_{yy} = interaction factor (see Table B.1 in EN 1993-1-1)

k_{zy} = interaction factor (see Table B.1 in EN 1993-1-1)

q = behavior factor

t_c = column web panel zone continuity plate thickness

t_d = column web panel zone doubler plate thickness

x_{pl}^{+} = position of the plastic neutral axis (from the top of the slab) in the composite steel beam under sagging bending

E_{cm} = modulus of elasticity of the slab concrete

E_s = modulus of elasticity of the structural steel

E_{sk} = modulus of elasticity of the slab rebars

E_{EW} = seismic action in the E-W direction

E_{NS} = seismic action in the N-S direction

G = dead, super-imposed dead and notional loads

G_s = shear modulus of elasticity of the structural steel

H = total building height

$H_{ED,EW}$ = notional horizontal loads in the E-W direction

$H_{ED,NS}$ = notional horizontal loads in the N-S direction

I_{eq} = equivalent moment of inertia of the composite steel beam

$M_{b,Rd}$ = design lateral torsional buckling resistance of the column

$M_{i,EW}$ = effective modal mass in the E-W direction for mode *i*

$M_{i,NS}$ = effective modal mass in the N-S direction for mode *i*

M_{Ed} = moment demand on the column

M_{Ed}^{-} = maximum hogging bending moment demand in the composite steel beam

M_{Ed}^{+} = maximum sagging bending moment demand in the composite steel beam

M_{Rd} = plastic moment resistance of the column

M_{Rd}^{-} = plastic moment resistance of the composite steel beam under hogging bending

M_{Rd}^{+} = plastic moment resistance of the composite steel beam under sagging bending

M_T = total seismic mass of the building

$N_{b,y,Rd}$ = design strong-axis flexural buckling resistance of the column

$N_{b,z,Rd}$ = design weak-axis flexural buckling resistance of the column

N_{Ed} = axial force demand on the column

N_{Rd} = axial resistance of the column cross section

P_{tot} = total gravity load in each story under the seismic load combinations

P_{Ed} = design value of the vertical load at each story for the persistent/transient design situations

Q = imposed load on all floors

S_d = horizontal design spectrum

T_i = period for the i^{th} mode of vibration of the building

$V_{pl,Rd}$ = plastic shear resistance of the columns/composite steel beams

$V_{tot,EW}$ = total story shear in the E-W direction under the seismic load combinations

$V_{wp,Ed}$ = column web panel zone shear demand

$V_{wp,Rd}$ = column web panel zone shear resistance

V_{Ed} = shear demand on the columns/composite steel beams

W = wind load on the building

α_{EW} = Merchant-Rankine multiplier for the composite steel MRF

β = lower bound for the horizontal design spectrum

γ_I = building importance factor

γ_{OV} = material overstrength factor for structural steel

δ = story drift amplitude obtained from the SAP2000 model

δ_r = design story drift amplitude

ε_{cu} = concrete crushing strain

θ_i = stability coefficient at story, i

ν = factor used for damage limitation verification

ρ_c = density of the slab concrete

$\rho_{s,min}$ = minimum slab longitudinal reinforcement ratio

$\rho_{w,min}$ = minimum slab transverse reinforcement ratio

$\rho_{A,ps}$ = area density of the profiled steel deck

Ω_i = beam overstrength ratio at each story

Appendix B Design drawings of the 2-bay composite steel moment-resisting frame

Description

This appendix includes all the drawings of the 2-bay composite steel moment-resisting frame sub-sys-tem that was physically tested as part of this thesis (see Chapter 5). The seismic design of the test frame was briefly discussed in Appendix A.

B.1 Detailed drawings of the test frame

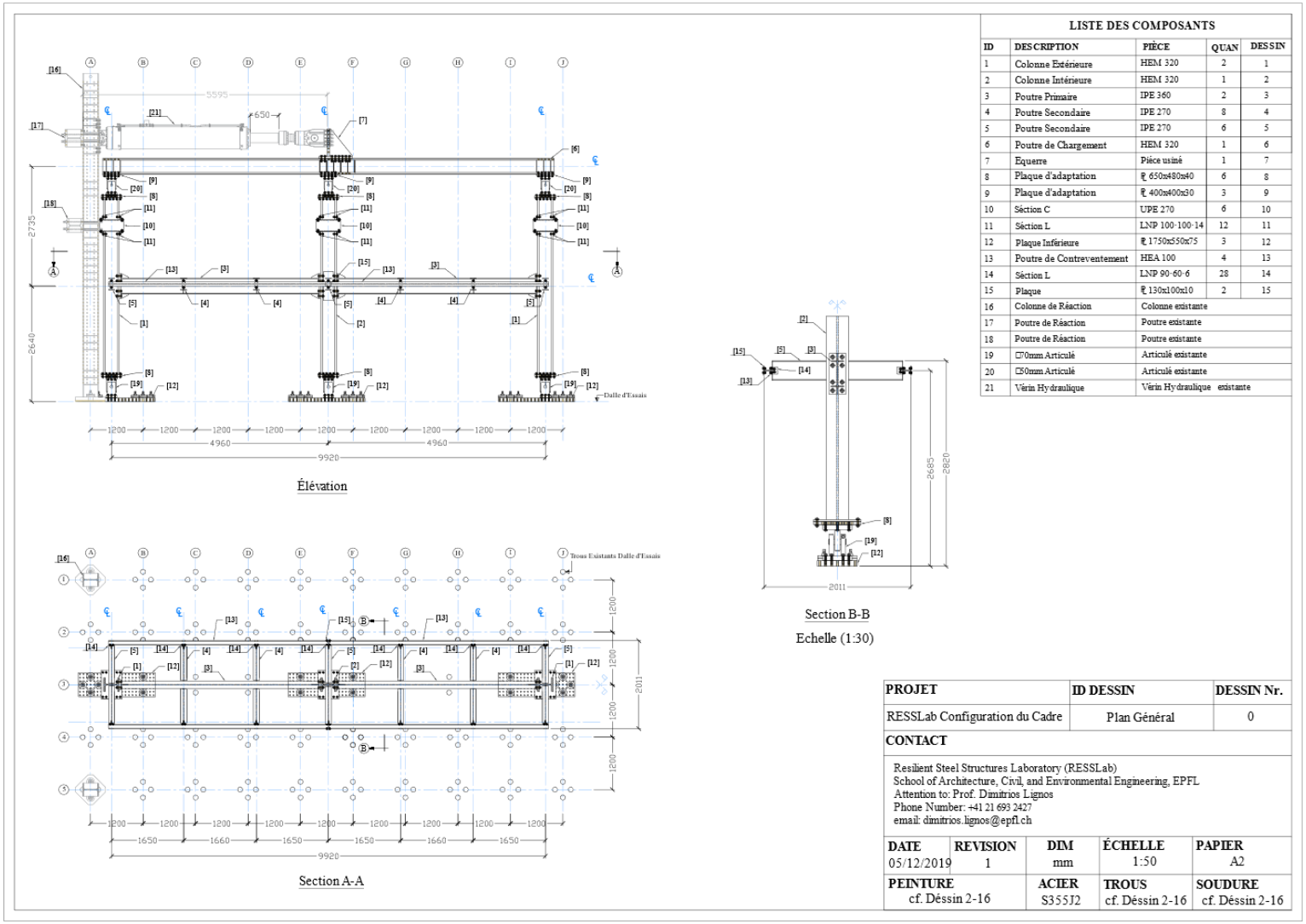

LISTE DES COMPOSANTS

ID	DESCRIPTION	PIÈCE	QUAN	DESSIN
1	Colonne Extérieure	HEM 320	2	1
2	Colonne Intérieure	HEM 320	1	2
3	Poutre Primaire	IPE 360	2	3
4	Poutre Secondaire	IPE 270	8	4
5	Poutre Secondaire	IPE 270	6	5
6	Poutre de Chargement	HEM 320	1	6
7	Equerre	Pièce usiné	1	7
8	Plaque d'adaptation	₹ 650x480x40	6	8
9	Plaque d'adaptation	₹ 400x400x30	3	9
10	Séction C	UPE 270	6	10
11	Séction L	LNP 100·100·14	12	11
12	Plaque Inférieure	₹ 1750x550x75	3	12
13	Poutre de Contreventement	HEA 100	4	13
14	Séction L	LNP 90·60·6	28	14
15	Plaque	₹ 130x100x10	2	15
16	Colonne de Réaction	Colonne existante		
17	Poutre de Réaction	Poutre existante		
18	Poutre de Réaction	Poutre existante		
19	□70mm Articulé	Articulé existante		
20	□50mm Articulé	Articulé existante		
21	Vérin Hydraulique	Vérin Hydraulique existante		

PROJET	ID DESSIN	DESSIN Nr.
RESSLab Configuration du Cadre	Plan Général	0

CONTACT

Resilient Steel Structures Laboratory (RESSLab)
School of Architecture, Civil, and Environmental Engineering, EPFL
Attention to: Prof. Dimitrios Lignos
Phone Number: +41 21 693 2427
email: dimitrios.lignos@epfl.ch

DATE	REVISION	DIM	ÉCHELLE	PAPIER
05/12/2019	1	mm	1:50	A2

PEINTURE	ACIER	TROUS	SOUDURE
cf. Déssin 2-16	S355J2	cf. Déssin 2-16	cf. Déssin 2-16

DIV	MARQUE	QUAN	DESCRIPTION	LONGUEUR	REMARQUES	POIDS [kg]	ITEM
	P1	2	HEM 320	4000	2x850mm longeur supplémentaire à partir du même couleé (cf Dessin 16)	1960	
	P2	4	PL 650x480x30			294	
	P3	4	PL 200x70x12			5	

ID Projet: PR	EXTRA No.	**Dessin Nr.**
RESSLab Configuration du Cadre		1

Colonne Extérieure [1]

Resilient Steel Structures Laboratory (RESSLab)
School of Architecture, Civil, and Environmental Engineering,
École Polytechnique Fédérale de Lausanne (EPFL)
Adresse: GC B3 485 (Bâtiment GC) Station 18 CH-1015 Lausanne
Attention to: Prof. Dimitrios Lignos, Hammad El Jisr
Phone Number: +41 21 693 2427
email: dimitrios.lignos@epfl.ch

DATE	REV.	DIM	ÉCHELLE	PAPIER
05/12/2019	1	mm	1:20	A3
PEINTURE		**ACIER**	**TROUS**	**SOUDURE**
SANS PEINTURE		S355J2	VAR	EN 1090-2

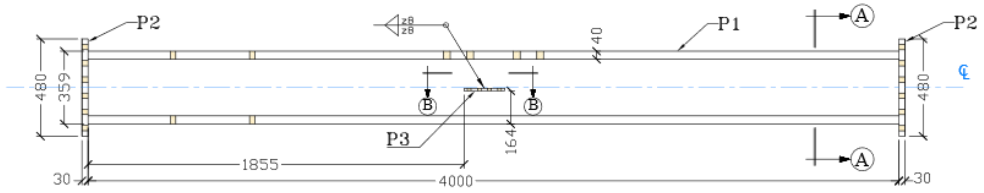

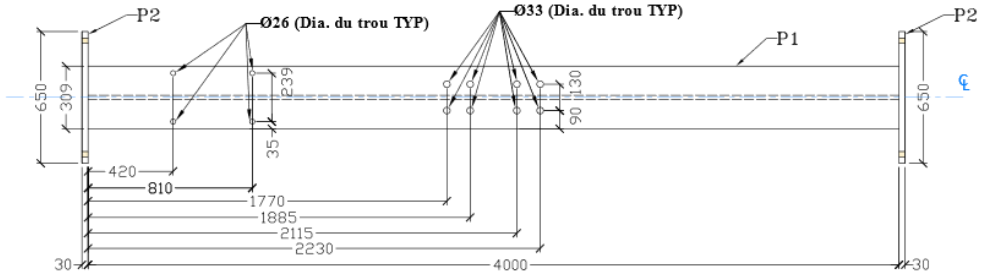

Élément (Colonne Extérieure)

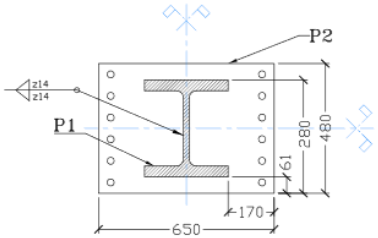

Section A-A

Echelle (1:15)

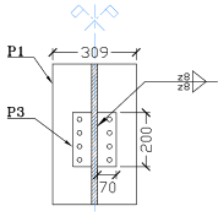

Section C-C

Echelle (1:15)

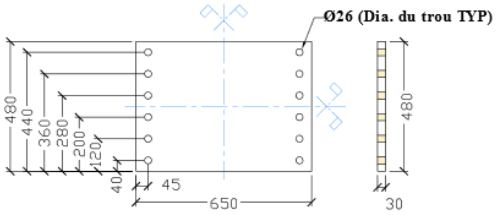

Piéce P2

Echelle (1:15)

(Plaque - Épaisseur: 30mm)

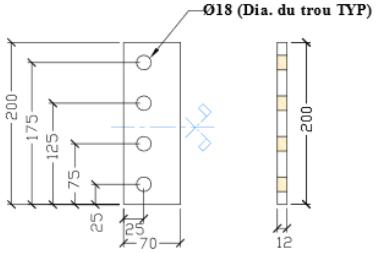

Piéce P3

Echelle (1:5)

(Plaque - Épaisseur: 12mm)

NOTES DE FABRICATION

- TOLERANCES SELON LES NORMES SIA 263, SIA 263-1, EN 1090 ET EN10034
- ORDRE DE SOUDAGE DES PLAQUES DOIT ETRE PENSÉ AVEC LE BUT DE MINIMISER LES DISTORSIONS DES AILES ET ASSURER LES TOLERANCES

DIV	MARQUE	QUAN	DESCRIPTION	LONGUEUR	REMARQUES	POIDS [kg]	ITEM
	P1	1	HEM 320	4000		980	
	P2	2	PL 650x480x30			147	
	P3	2	PL 200x70x12			3	
	P4	2	PL 660x225x15		2 plaques supplémentaires à partir du même couleé (cf Dessin 16)	35	

ID Projet: PR		EXTRA No.	**Dessin Nr.**
RESSLab Configuration du Cadre			2

Colonne Intérieure [2]

Resilient Steel Structures Laboratory (RESSLab)
School of Architecture, Civil, and Environmental Engineering,
École Polytechnique Fédérale de Lausanne (EPFL)
Adresse: GC B3 485 (Bâtiment GC) Station 18 CH-1015 Lausanne
Attention to: Prof. Dimitrios Lignos, Hammad El Jisr
Phone Number: +41 21 693 2427
email: dimitrios.lignos@epfl.ch

DATE	REV.	DIM	ÉCHELLE	PAPIER
05/12/2019	1	mm	1:20	A3
PEINTURE		**ACIER**	**TROUS**	**SOUDURE**
SANS PEINTURE		S355J2	VAR	EN 1090-2

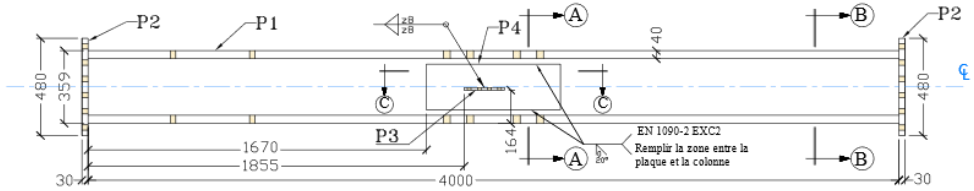

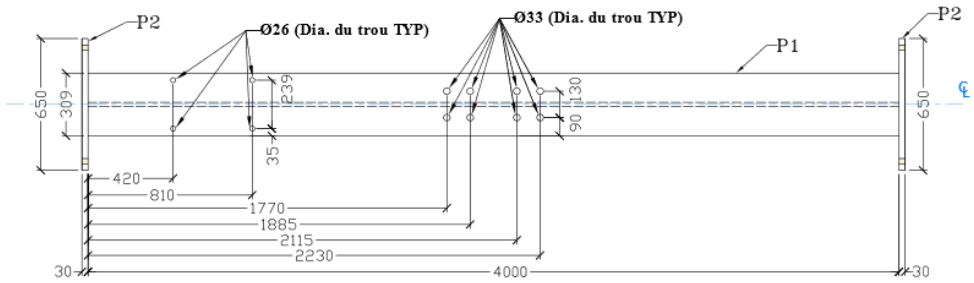

Élément (Colonne Intérieure)

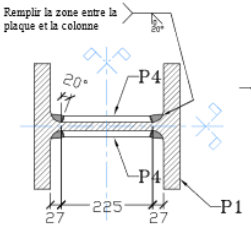

Section A-A
Echelle (1:10)

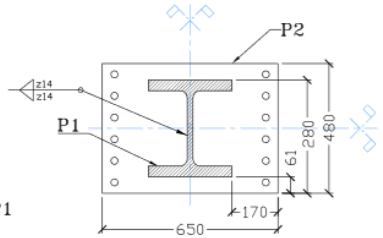

Section B-B
Echelle (1:15)

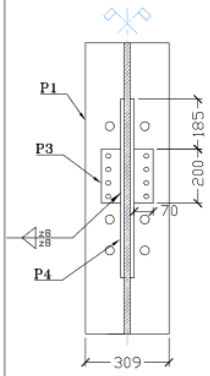

Section C-C
Echelle (1:15)

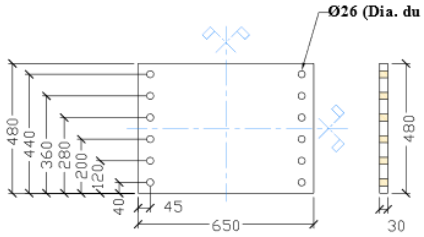

Piéce P2
Echelle (1:15)
(Plaque - Épaisseur: 30mm)

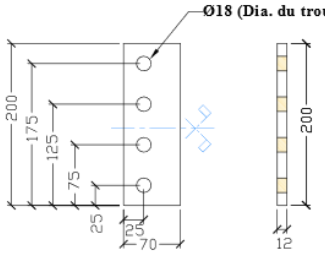

Piéce P3
Echelle (1:5)
(Plaque - Épaisseur: 12mm)

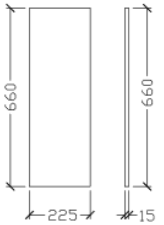

Piéce P4
Echelle (1:15)
(Plaque - Épaisseur: 15mm)

NOTES DE FABRICATION

- TOLERANCES SELON LES NORMES SIA 263, SIA 263-1, EN 1090 ET EN10034
- ORDRE DE SOUDAGE DES PLAQUES DOIT ETRE PENSÉ AVEC LE BUT DE MINIMISER LES DISTORSIONS DES AILES ET ASSURER LES TOLERANCES
- FOURNIR LE PROTOCOLE DE SOUDURE

DIV	MARQUE	QUAN	DESCRIPTION	LONGUEUR	REMARQUES	POIDS [kg]	ITEM
	P1	2	IPE 360	4541	3x850mm longeur supplémentaire à partir du même couleé (cf Dessin 16)	518	
	P2	4	PL 560x230x30			121	
	P3	8	PL 175x100x10			11	
	P4	8	PL 334x195x12			49	

ID Projet: PR		EXTRA No.	**Dessin Nr.**
RESSLab Configuration du Cadre			3

Poutre Primaire [3]

Resilient Steel Structures Laboratory (RESSLab)
School of Architecture, Civil, and Environmental Engineering,
École Polytechnique Fédérale de Lausanne (EPFL)
Adresse: GC B3 485 (Bâtiment GC) Station 18 CH-1015 Lausanne
Attention to: Prof. Dimitrios Lignos, Hammad El Jisr
Phone Number: +41 21 693 2427
email: dimitrios.lignos@epfl.ch

DATE	REV.	DIM	ÉCHELLE	PAPIER
05/12/2019	1	mm	1:15	A3
PEINTURE		**ACIER**	**TROUS**	**SOUDURE**
SANS PEINTURE		S355J2	VAR	EN 1090-2

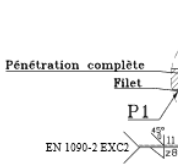

Détail A
(Échelle 1:2.5)

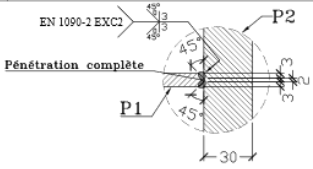

Détail B
(Échelle 1:2.5)

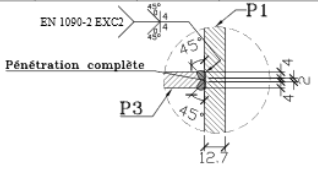

Détail C
(Échelle 1:2.5)

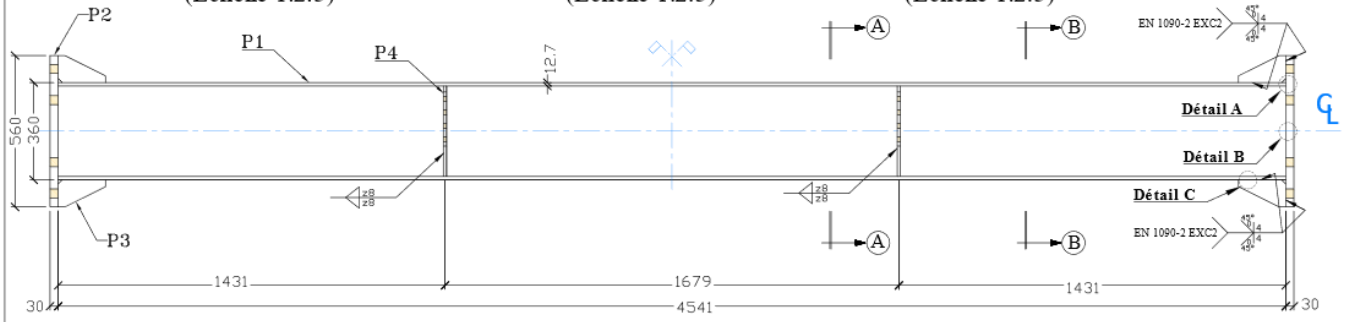

Élément (Poutre Primaire)

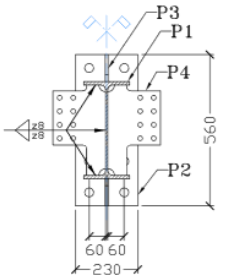

Section A-A

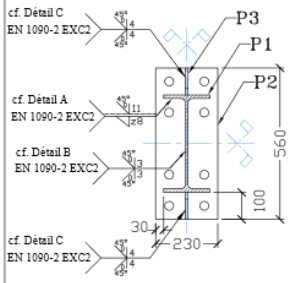

Section B-B

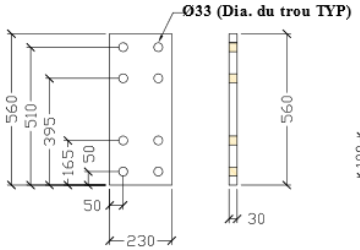

Piéce P2
(Plaque - Épaisseur: 30mm)

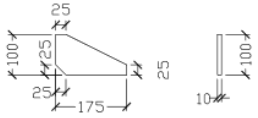

Piéce P3
Echelle (1:10)
(Raidisseur - Épaisseur: 10mm)

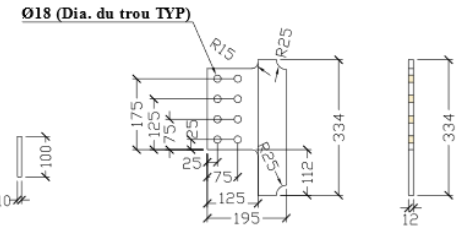

Piéce P4
Echelle (1:10)
(Plaque - Épaisseur: 12mm)

NOTES DE FABRICATION

- TOLERANCES SELON LES NORMES SIA 263, SIA 263-1, EN 1090 ET EN10034
- ORDRE DE SOUDAGE DES PLAQUES DOIT ETRE PENSÉ AVEC LE BUT DE MINIMISER LES DISTORSIONS DES AILES ET ASSURER LES TOLERANCES
- FOURNIR LE PROTOCOLE DE SOUDURE

DIV	MARQUE	QUAN	DESCRIPTION	LONGUEUR	REMARQUES	POIDS [kg]	ITEM	
	P1	8	IPE 270	775		224		

ID Projet: PR	EXTRA No.	**Dessin Nr.**
RESSLab Configuration du Cadre		4

Poutre Secondaire [4]

Resilient Steel Structures Laboratory (RESSLab)
School of Architecture, Civil, and Environmental Engineering,
École Polytechnique Fédérale de Lausanne (EPFL)
Adresse: GC B3 485 (Bâtiment GC) Station 18 CH-1015 Lausanne
Attention to: Prof. Dimitrios Lignos, Hammad El Jisr
Phone Number: +41 21 693 2427
email: dimitrios.lignos@epfl.ch

DATE	REV.	DIM	ÉCHELLE	PAPIER
05/12/2019	1	mm	1:10	A3

PEINTURE	ACIER	TROUS	SOUDURE
SANS PEINTURE	S355J2	Ø18 (TYP)	EN 1090-2

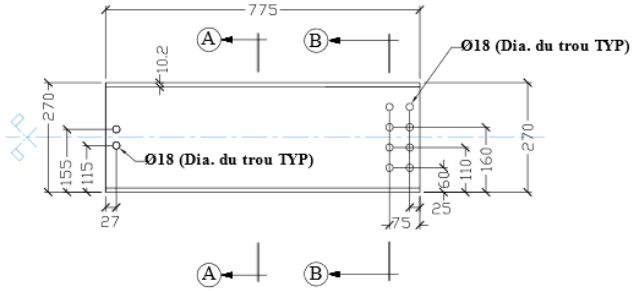

Piéce P1

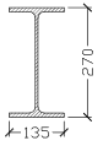

Section A-A

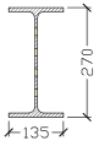

Section B-B

NOTES DE FABRICATION

- TOLERANCES SELON LES NORMES SIA 263, SIA 263-1, EN 1090 ET EN10034

DIV	MARQUE	QUAN	DESCRIPTION	LONGUEUR	REMARQUES	POIDS [kg]	ITEM	
	P1	6	IPE 270	850		184		

ID Projet: PR	EXTRA No.	**Dessin Nr.**
RESSLab Configuration du Cadre		5

Poutre Secondaire [5]

Resilient Steel Structures Laboratory (RESSLab)
School of Architecture, Civil, and Environmental Engineering,
École Polytechnique Fédérale de Lausanne (EPFL)
Adresse: GC B3 485 (Bâtiment GC) Station 18 CH-1015 Lausanne
Attention to: Prof. Dimitrios Lignos, Hammad El Jisr
Phone Number: +41 21 693 2427
email: dimitrios.lignos@epfl.ch

DATE	REV.	DIM	ÉCHELLE	PAPIER
05/12/2019	1	mm	1:10	A3

PEINTURE	ACIER	TROUS	SOUDURE
SANS PEINTURE	S355J2	Ø18 (TYP)	EN 1090-2

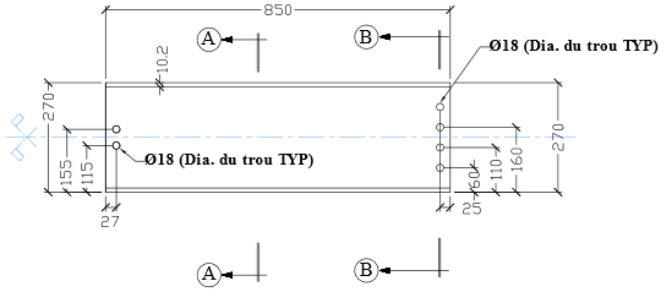

Piéce P1

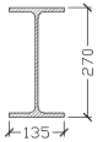

Section A-A

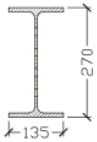

Section B-B

NOTES DE FABRICATION

- TOLERANCES SELON LES NORMES SIA 263, SIA 263-1, EN 1090 ET EN10034

DIV	MARQUE	QUAN	DESCRIPTION	LONGUEUR	REMARQUES	POIDS [kg]	ITEM	
	P1	1	HEM 320	10320		2528		
	P2	24	PL 279x144x10			76		

ID Projet: PR	EXTRA No.	**Dessin Nr.**
RESSLab Configuration du Cadre		6

Poutre de Chargement [6]

Resilient Steel Structures Laboratory (RESSLab)
School of Architecture, Civil, and Environmental Engineering,
École Polytechnique Fédérale de Lausanne (EPFL)
Adresse: GC B3 485 (Bâtiment GC) Station 18 CH-1015 Lausanne
Attention to: Prof. Dimitrios Lignos, Hammad El Jisr
Phone Number: +41 21 693 2427
email: dimitrios.lignos@epfl.ch

DATE	REV.	DIM	ÉCHELLE	PAPIER
05/12/2019	1	mm	1:30	A3
PEINTURE		**ACIER**	**TROUS**	**SOUDURE**
ZINGUÉ - ROUGE (RAL 8012)		S355J2	VAR	EN 1090-2

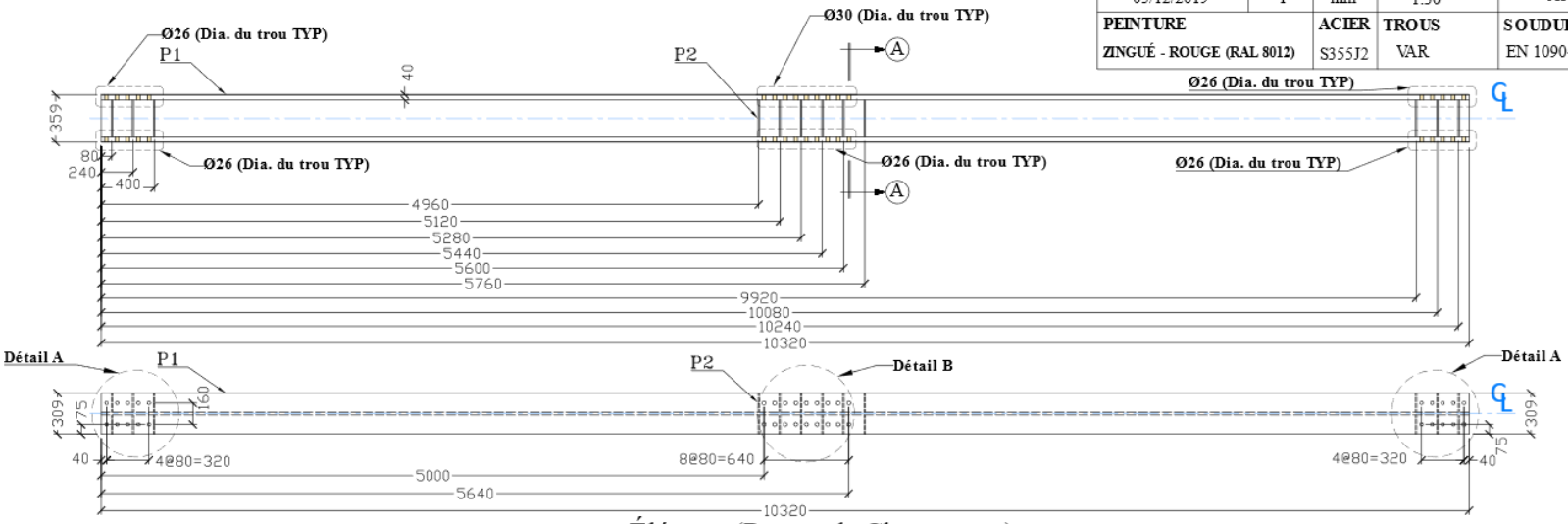

Élément (Poutre de Chargement)

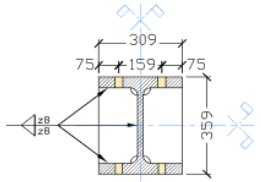

Section A-A
Echelle (1:15)

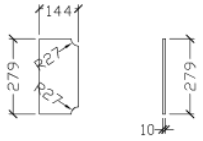

Piéce P2
Echelle (1:15)
(Raidisseur - Épaisseur: 10mm)

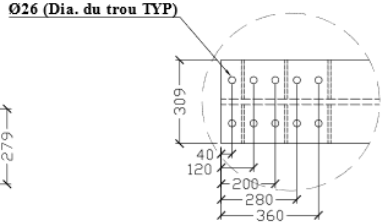

Détail A
(Échelle 1:15)

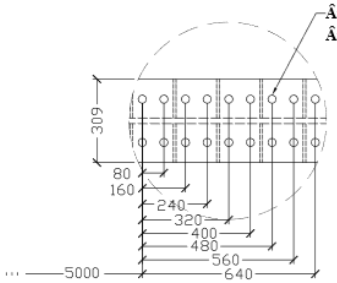

Détail B
(Échelle 1:15)

NOTES DE FABRICATION

- TOLERANCES SELON LES NORMES SIA 263, SIA 263-1, EN 1090 ET EN10034
- ORDRE DE SOUDAGE DES PLAQUES DOIT ETRE PENSÉ AVEC LE BUT DE MINIMISER LES DISTORSIONS DES AILES ET ASSURER LES TOLERANCES

DIV	MARQUE	QUAN	DESCRIPTION	LONGUEUR	REMARQUES	POIDS [kg]	ITEM	
	P1	1	PL 760x480x50			143		
	P2	1	PL 630x480x50			119		
	P3	2	PL 650x515x30			158		

ID Projet: PR		EXTRA No.	**Dessin Nr.**
RESSLab Configuration du Cadre			7

Equerre [7]

Resilient Steel Structures Laboratory (RESSLab)
School of Architecture, Civil, and Environmental Engineering,
École Polytechnique Fédérale de Lausanne (EPFL)
Adresse: GC B3 485 (Bâtiment GC) Station 18 CH-1015 Lausanne
Attention to: Prof. Dimitrios Lignos, Hammad El Jisr
Phone Number: +41 21 693 2427
email: dimitrios.lignos@epfl.ch

DATE	REV.	DIM	ÉCHELLE	PAPIER
05/12/2019	1	mm	1:15	A3
PEINTURE		**ACIER**	**TROUS**	**SOUDURE**
ZINGUÉ - ROUGE (RAL 8012)		S355J2	VAR	EN 1090-2

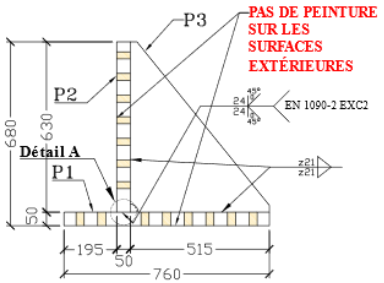

Équerre

Élévation

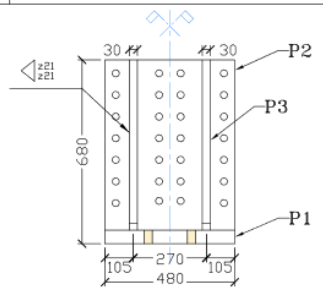

Équerre

Vue de côté

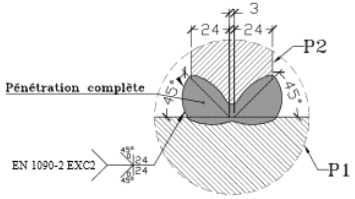

Détail A

(Échelle 1:2.5)

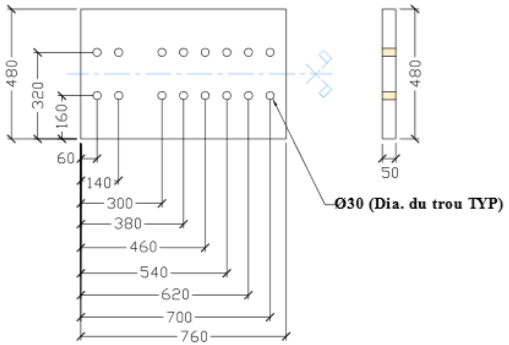

Piéce P1

(Plaque - Épaisseur: 50mm)

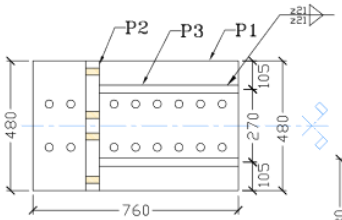

Équerre

Vue en plan

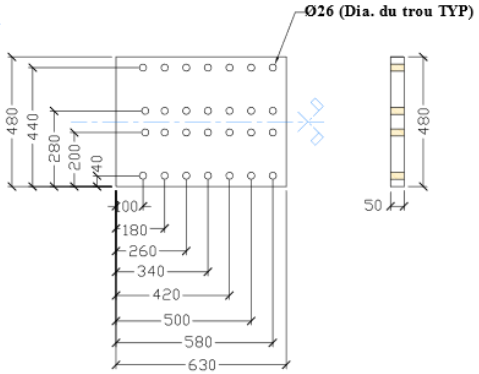

Piéce P2

(Plaque - Épaisseur: 50mm)

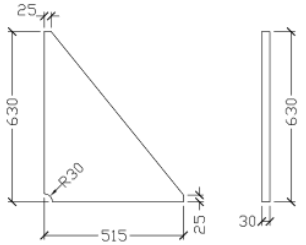

Piéce P3

(Raidisseur - Épaisseur: 30mm)

NOTES DE FABRICATION

- TOLERANCES SELON LES NORMES SIA 263, SIA 263-1, EN 1090 ET EN10034
- RECOUVRIR TOUS LES TROUS AVANT LA PROCEDURE DE PEINTURE
- ORDRE DE SOUDAGE DES PLAQUES DOIT ETRE PENSÉ AVEC LE BUT DE MINIMISER LES DISTORSIONS DES AILES ET ASSURER LES TOLERANCES
- PROCEDURES DE PEINTURE SELON SIA 263-1 ET SELON LES INDICATIONS DU FABRICANT
- FOURNIR LE PROTOCOLE DE SOUDURE

DIV	MARQUE	QUAN	DESCRIPTION	LONGUEUR	REMARQUES	POIDS [kg]	ITEM	
	P1	6	PL650x480x40			588		

ID Projet: PR	EXTRA No.	**Dessin Nr.**
RESSLab Configuration du Cadre		8

Plaque d'adaptation [8]

Resilient Steel Structures Laboratory (RESSLab)
School of Architecture, Civil, and Environmental Engineering,
École Polytechnique Fédérale de Lausanne (EPFL)
Adresse: GC B3 485 (Bâtiment GC) Station 18 CH-1015 Lausanne
Attention to: Prof. Dimitrios Lignos, Hammad El Jisr
Phone Number: +41 21 693 2427
email: dimitrios.lignos@epfl.ch

DATE	REV.	DIM	ÉCHELLE	PAPIER
05/12/2019	1	mm	1:8	A3
PEINTURE		**ACIER**	**TROUS**	**SOUDURE**
SANS PEINTURE		S355J2	Ø26 (TYP)	EN 1090-2

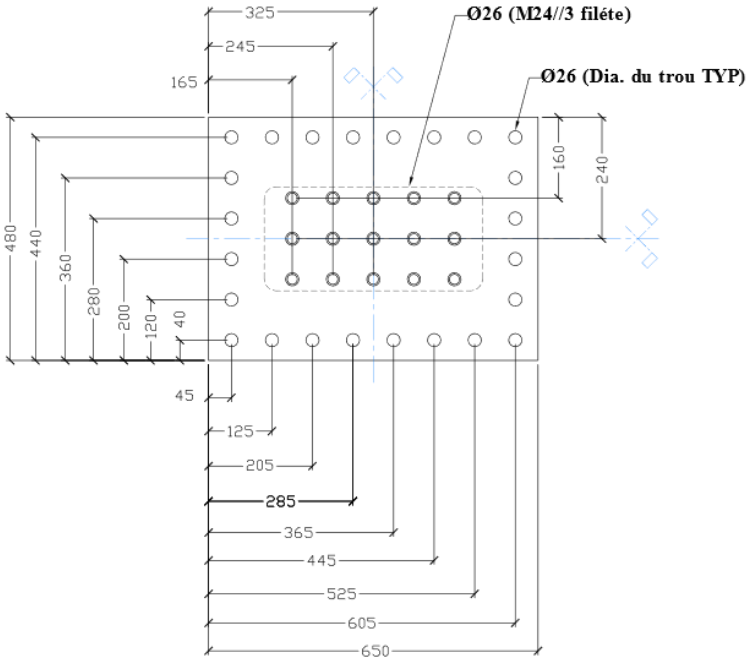

Piéce P1

(Plaque - Épaisseur: 40mm)

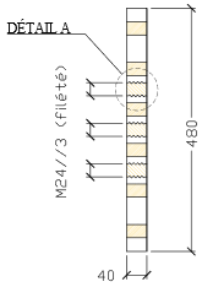

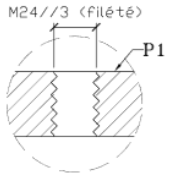

Détail A
Echelle (1:2.5)

NOTES DE FABRICATION

- TOLERANCES SELON LES NORMES SIA 263, SIA 263-1, EN 1090 ET EN10034

DIV	MARQUE	QUAN	DESCRIPTION	LONGUEUR	REMARQUES	POIDS [kg]	ITEM	
	P1	3	PL 400x400x30			113		

ID Projet: PR	EXTRA No.	**Dessin Nr.**
RESSLab Configuration du Cadre		9

Plaque d'adaptation [9]

Resilient Steel Structures Laboratory (RESSLab)
School of Architecture, Civil, and Environmental Engineering,
École Polytechnique Fédérale de Lausanne (EPFL)
Adresse: GC B3 485 (Bâtiment GC) Station 18 CH-1015 Lausanne
Attention to: Prof. Dimitrios Lignos, Hammad El Jisr
Phone Number: +41 21 693 2427
email: dimitrios.lignos@epfl.ch

DATE	REV.	DIM	ÉCHELLE	PAPIER
05/12/2019	1	mm	1:8	A3
PEINTURE		**ACIER**	**TROUS**	**SOUDURE**
SANS PEINTURE		S355J2	Ø26 (TYP)	EN 1090-2

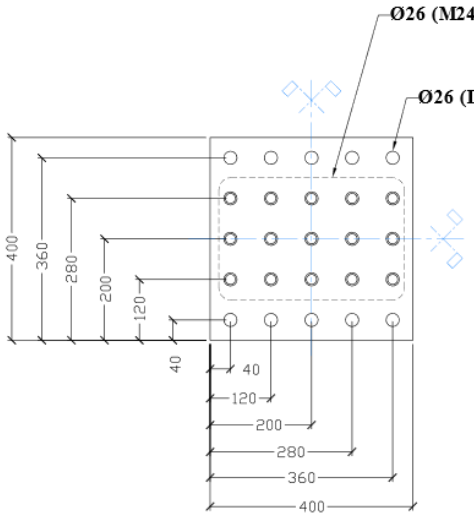

Piéce P1

(Plaque - Épaisseur: 30mm)

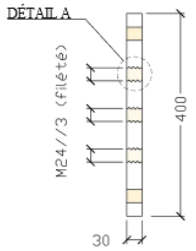

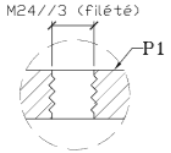

Détail A

Echelle (1:2.5)

NOTES DE FABRICATION

- TOLERANCES SELON LES NORMES SIA 263, SIA 263-1, EN 1090 ET EN10034

DIV	MARQUE	QUAN	DESCRIPTION	LONGUEUR	REMARQUES	POIDS [kg]	ITEM	
	P1	6	UPE 270	559		118		

ID Projet: PR				EXTRA No.	Dessin Nr.
RESSLab Configuration du Cadre					10
Séction C [10]					
Resilient Steel Structures Laboratory (RESSLab) School of Architecture, Civil, and Environmental Engineering, École Polytechnique Fédérale de Lausanne (EPFL) Adresse: GC B3 485 (Bâtiment GC) Station 18 CH-1015 Lausanne Attention to: Prof. Dimitrios Lignos, Hammad El Jisr Phone Number: +41 21 693 2427 email: dimitrios.lignos@epfl.ch					
DATE	**REV.**	**DIM**	**ÉCHELLE**	**PAPIER**	
05/12/2019	1	mm	1:8	A3	
PEINTURE		**ACIER**	**TROUS**	**SOUDURE**	
SANS PEINTURE		S355J2	Ø26 (TYP)	EN 1090-2	

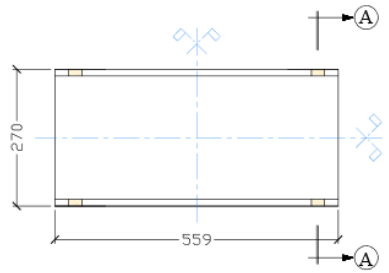

Piéce P1

Élévation

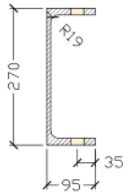

Section A-A

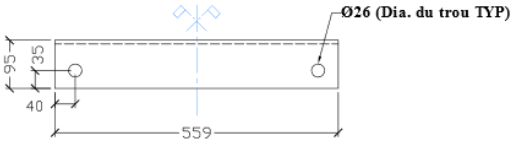

Piéce P1

Vue en plan

NOTES DE FABRICATION

- TOLERANCES SELON LES NORMES SIA 263, SIA 263-1, EN 1090 ET EN10034
- RECOUVRIR TOUS LES TROUS AVANT LA PROCEDURE DE PEINTURE
- PROCEDURES DE PEINTURE SELON SIA 263-1 ET SELON LES INDICATIONS DU FABRICANT

DIV	MARQUE	QUAN	DESCRIPTION	LONGUEUR	REMARQUES	POIDS [kg]	ITEM	
	P1	12	LNP 100·100·14	560		139		

ID Projet: PR	EXTRA No.	**Dessin Nr.**
RESSLab Configuration du Cadre		11

Séction L [11]

Resilient Steel Structures Laboratory (RESSLab)
School of Architecture, Civil, and Environmental Engineering,
École Polytechnique Fédérale de Lausanne (EPFL)
Adresse: GC B3 485 (Bâtiment GC) Station 18 CH-1015 Lausanne
Attention to: Prof. Dimitrios Lignos, Hammad El Jisr
Phone Number: +41 21 693 2427
email: dimitrios.lignos@epfl.ch

DATE	REV.	DIM	ÉCHELLE	PAPIER
05/12/2019	1	mm	1:8	A3
PEINTURE		**ACIER**	**TROUS**	**SOUDURE**
SANS PEINTURE		S355J2	Ø26 (TYP)	EN 1090-2

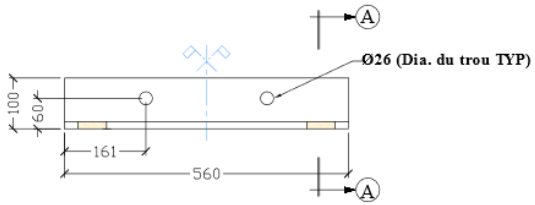

Piéce P1

Élévation

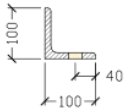

Section A-A

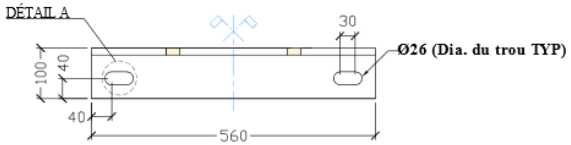

Piéce P1

Vue en plan

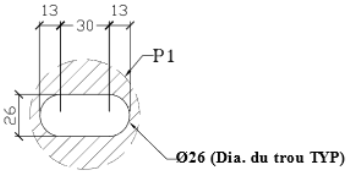

Détail A

Echelle (1:2.5)

NOTES DE FABRICATION

- TOLERANCES SELON LES NORMES SIA 263, SIA 263-1, EN 1090 ET EN10034
- RECOUVRIR TOUS LES TROUS AVANT LA PROCEDURE DE PEINTURE
- PROCEDURES DE PEINTURE SELON SIA 263-1 ET SELON LES INDICATIONS DU FABRICANT

DIV	MARQUE	QUAN	DESCRIPTION	LONGUEUR	REMARQUES	POIDS [kg]	ITEM	
	P1	3	PL1750x550x75			1700		

ID Projet: PR	EXTRA No.	Dessin Nr.
RESSLab Configuration du Cadre		12

Plaque Inférieure [12]

Resilient Steel Structures Laboratory (RESSLab)
School of Architecture, Civil, and Environmental Engineering,
École Polytechnique Fédérale de Lausanne (EPFL)
Adresse: GC B3 485 (Bâtiment GC) Station 18 CH-1015 Lausanne
Attention to: Prof. Dimitrios Lignos, Hammad El Jisr
Phone Number: +41 21 693 2427
email: dimitrios.lignos@epfl.ch

DATE	REV.	DIM	ÉCHELLE	PAPIER
05/12/2019	1	mm	1:10	A3
PEINTURE		**ACIER**	**TROUS**	**SOUDURE**
SANS PEINTURE		S355J2	VAR	EN 1090-2

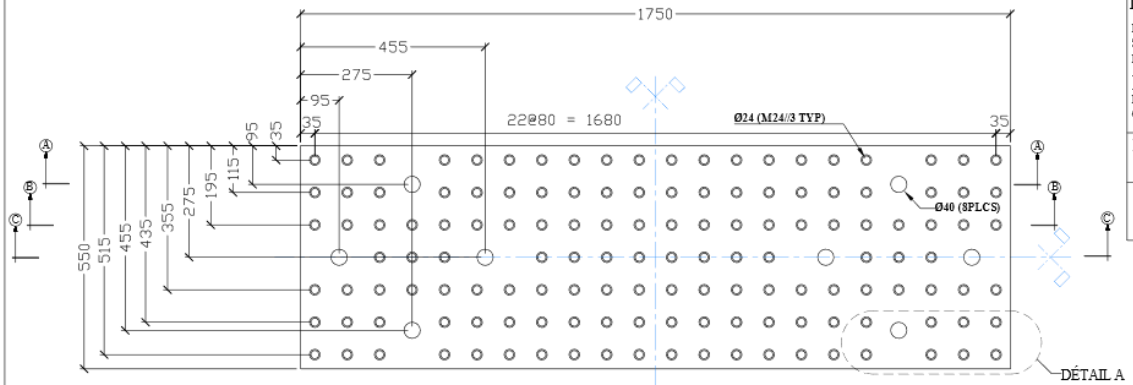

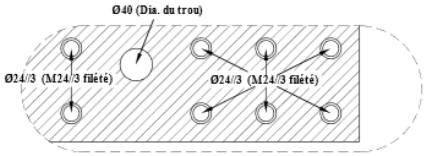

Détail A
Echelle (1:5)

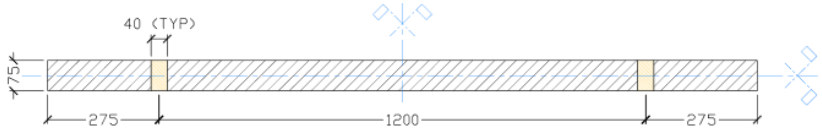

SEC A-A

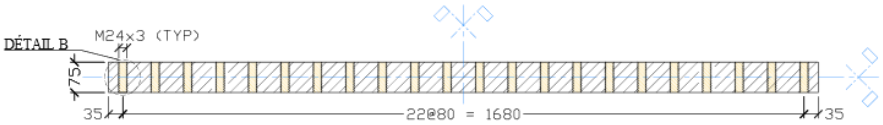

SEC B-B

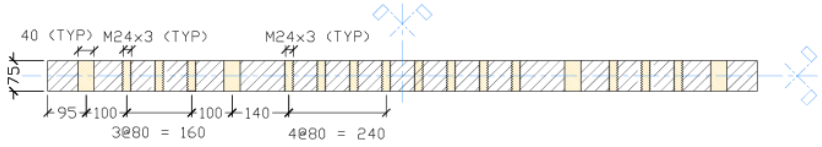

SEC C-C

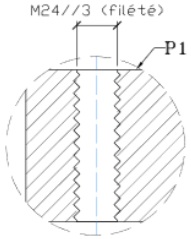

Détail B
Echelle (1:2.5)

Piéce P1
(Plaque - Épaisseur: 75mm)

NOTES DE FABRICATION

- TOLERANCES SELON LES NORMES SIA 263, SIA 263-1, EN 1090 ET EN10034

DIV	MARQUE	QUAN	DESCRIPTION	LONGUEUR	REMARQUES	POIDS [kg]	ITEM	
	P1	4	HEA 100	5020		335		

ID Projet: PR	EXTRA No.	**Dessin Nr.**
RESSLab Configuration du Cadre		13

Poutre de Contreventement [13]

Resilient Steel Structures Laboratory (RESSLab)
School of Architecture, Civil, and Environmental Engineering,
École Polytechnique Fédérale de Lausanne (EPFL)
Adresse: GC B3 485 (Bâtiment GC) Station 18 CH-1015 Lausanne
Attention to: Prof. Dimitrios Lignos, Hammad El Jisr
Phone Number: +41 21 693 2427
email: dimitrios.lignos@epfl.ch

DATE	REV.	DIM	ÉCHELLE	PAPIER
05/12/2019	1	mm	1:15	A3

PEINTURE	ACIER	TROUS	SOUDURE
SANS PEINTURE	S355J2	Ø14 (TYP)	EN 1090-2

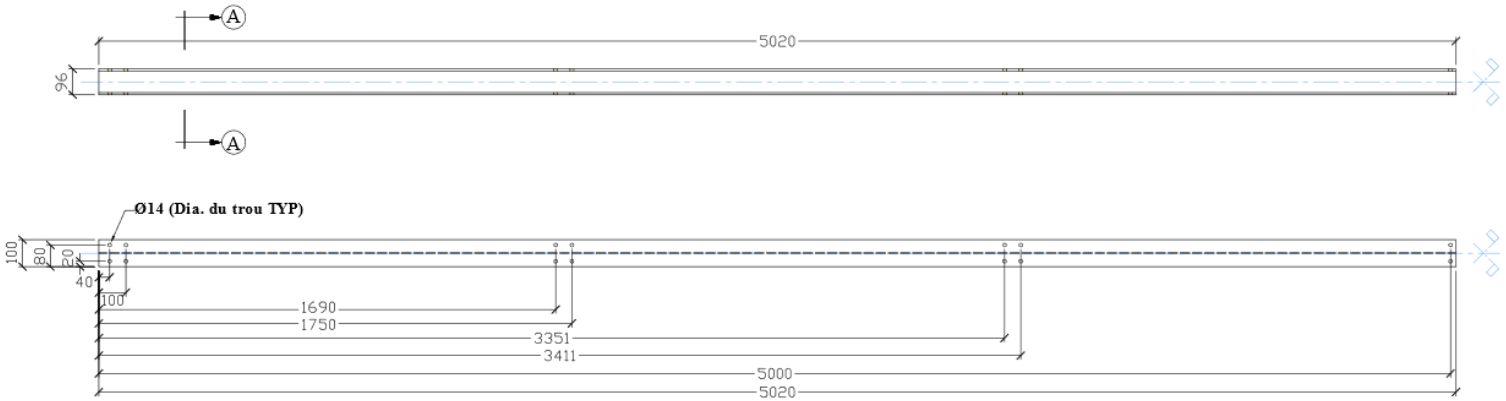

Piéce P1

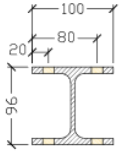

Section A-A

Echelle (1:5)

NOTES DE FABRICATION

- TOLERANCES SELON LES NORMES SIA 263, SIA 263-1, EN 1090 ET EN10034

DIV	MARQUE	QUAN	DESCRIPTION	LONGUEUR	REMARQUES	POIDS [kg]	ITEM	
	P1	28	LNP 90·60·6	100		19		

ID Projet: PR	EXTRA No.	Dessin Nr.
RESSLab Configuration du Cadre		14

Séction L [14]

Resilient Steel Structures Laboratory (RESSLab)
School of Architecture, Civil, and Environmental Engineering,
École Polytechnique Fédérale de Lausanne (EPFL)
Adresse: GC B3 485 (Bâtiment GC) Station 18 CH-1015 Lausanne
Attention to: Prof. Dimitrios Lignos, Hammad El Jisr
Phone Number: +41 21 693 2427
email: dimitrios.lignos@epfl.ch

DATE	REV.	DIM	ÉCHELLE	PAPIER
05/12/2019	1	mm	1:2.5	A3

PEINTURE	ACIER	TROUS	SOUDURE
SANS PEINTURE	S355J2	VAR	EN 1090-2

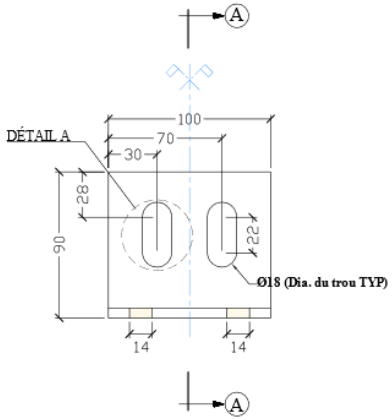

Piéce P1

Élévation

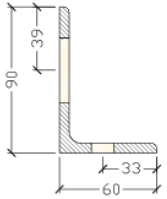

Section A-A

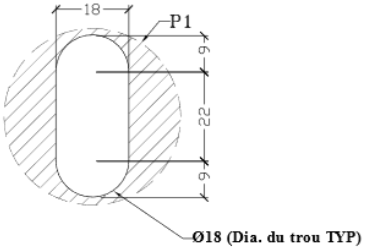

Détail A

Echelle (1:1)

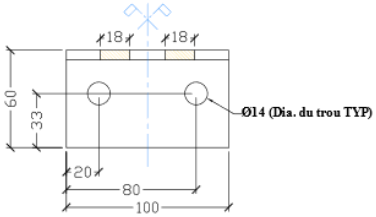

Piéce P1

Vue en plan

DIV	MARQUE	QUAN	DESCRIPTION	LONGUEUR	REMARQUES	POIDS [kg]	ITEM	
	P1	2	PL 130x100x10			2		

ID Projet: PR	EXTRA No.	**Dessin Nr.**
RESSLab Configuration du Cadre		15

Plaque [15]

Resilient Steel Structures Laboratory (RESSLab)
School of Architecture, Civil, and Environmental Engineering,
Ecole Polytechnique Fédérale de Lausanne (EPFL)
Adresse: GC B3 485 (Bâtiment GC) Station 18 CH-1015 Lausanne
Attention to: Prof. Dimitrios Lignos, Hammad El Jisr
Phone Number: +41 21 693 2427
email: dimitrios.lignos@epfl.ch

DATE	REV.	DIM	ÉCHELLE	PAPIER
05/12/2019	1	mm	1:2.5	A3

PEINTURE	ACIER	TROUS	SOUDURE
SANS PEINTURE	S355J2	Ø14 (TYP)	EN 1090-2

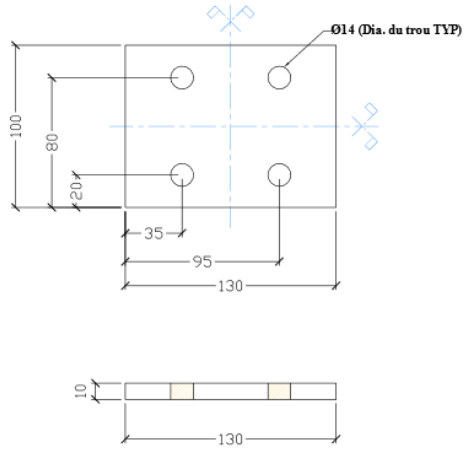

Piéce P1

(Plaque - Épaisseur: 10mm)

DIV	MARQUE	QUAN	DESCRIPTION	LONGUEUR	REMARQUES	POIDS [kg]	ITEM
	P1	2	HEM 320	850		417	
	P2	3	IPE 360	850		97	
	P3	2	PL 660x225x15			32	

ID Projet: PR			EXTRA No.	**Dessin Nr.**
RESSLab Configuration du Cadre				16

Composants Supplémentaires

Resilient Steel Structures Laboratory (RESSLab)
School of Architecture, Civil, and Environmental Engineering,
École Polytechnique Fédérale de Lausanne (EPFL)
Adresse: GC B3 485 (Bâtiment GC) Station 18 CH-1015 Lausanne
Attention to: Prof. Dimitrios Lignos, Hammad El Jisr
Phone Number: +41 21 693 2427
email: dimitrios.lignos@epfl.ch

DATE	**REV.**	**DIM**	**ÉCHELLE**	**PAPIER**
05/12/2019	1	mm	1:15	A3
PEINTURE		**ACIER**	**TROUS**	**SOUDURE**
SANS PEINTURE		S355J2	-	EN 1090-2

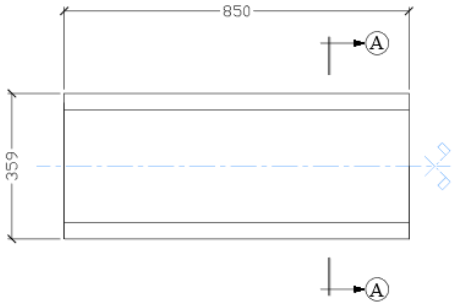

Piéce P1

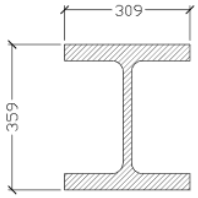

Section A-A

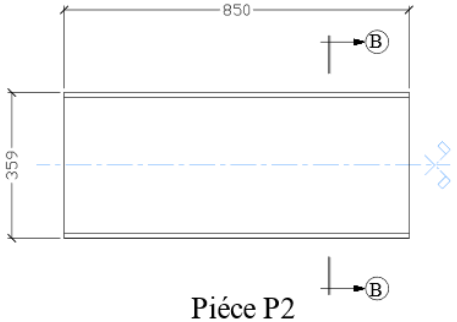

Piéce P2

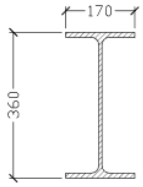

Section B-B

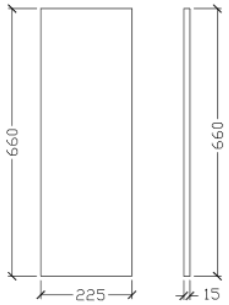

Piéce P3

(Plaque - Épaisseur: 15mm)

LISTE DES BOULONS

QUAN	TYPE x Longueur	Pas de vis (mm)	Longueur filetée (mm)	REMARQUES
62	M12-SHV x 35mm - Classe 10.9	1.5 TYP.	23 TYP.	1 Ecrous + 2 Rondelles par Boulon
9	M12-SHV x 40mm - Classe 10.9	1.5 TYP.	23 TYP.	1 Ecrous + 2 Rondelles par Boulon
128	M16-SHV x 45mm - Classe 10.9	2.0 TYP.	28 TYP.	1 Ecrous + 2 Rondelles par Boulon
27	M24-SHV x 65mm - Classe 10.9	3.0 TYP.	39 TYP.	1 Ecrous + 2 Rondelles par Boulon
27	M24-SHV x 90mm - Classe 10.9	3.0 TYP.	39 TYP.	1 Ecrous + 2 Rondelles par Boulon
9	M24-SHV x 100mm - Classe 10.9	3.0 TYP.	39 TYP.	1 Ecrous + 2 Rondelles par Boulon
30	M24-SHV x 100mm - Classe 10.9	3.0 TYP.	Fileté sur toute la longuer	1 Rondelle par Boulon
112	M24-SHV x 105mm - Classe 10.9	3.0 TYP.	39 TYP.	1 Ecrous + 2 Rondelles par Boulon
79	M24-SHV x 110mm - Classe 10.9	3.0 TYP.	Fileté sur toute la longuer	1 Rondelle par Boulon
40	M24-SHV x 125mm - Classe 10.9	3.0 TYP.	39 TYP.	1 Ecrous + 2 Rondelles par Boulon
30	M24-SHV x 125mm - Classe 10.9	3.0 TYP.	Fileté sur toute la longuer	1 Rondelle par Boulon
18	M27-SHV x 130mm - Classe 10.9	3.0 TYP.	41 TYP.	1 Ecrous + 2 Rondelles par Boulon
35	M30-SHV x 120mm - Classe 12.9	3.5 TYP.	44 TYP.	1 Ecrous + 2 Rondelles par Boulon

ID Projet: PR		EXTRA No.		**Dessin Nr.**
RESSLab Configuration du Cadre				17
Boulons				
Resilient Steel Structures Laboratory (RESSLab) School of Architecture, Civil, and Environmental Engineering, Ecole Polytechnique Fedérale de Lausanne (EPFL) Adresse: GC B3 485 (Bâtiment GC) Station 18 CH-1015 Lausanne Attention to: Prof. Dimitrios Lignos, Hammad El Jisr Phone Number: +41 21 693 2427 email: dimitrios.lignos@epfl.ch				
DATE 05/12/2019	**REV.** 1	**DIM**	**ÉCHELLE**	**PAPIER** A3
PEINTURE		**ACIER**	**TROUS**	**SOUDURE**

B.2 Detailed drawings of the slab and beam-slab connection

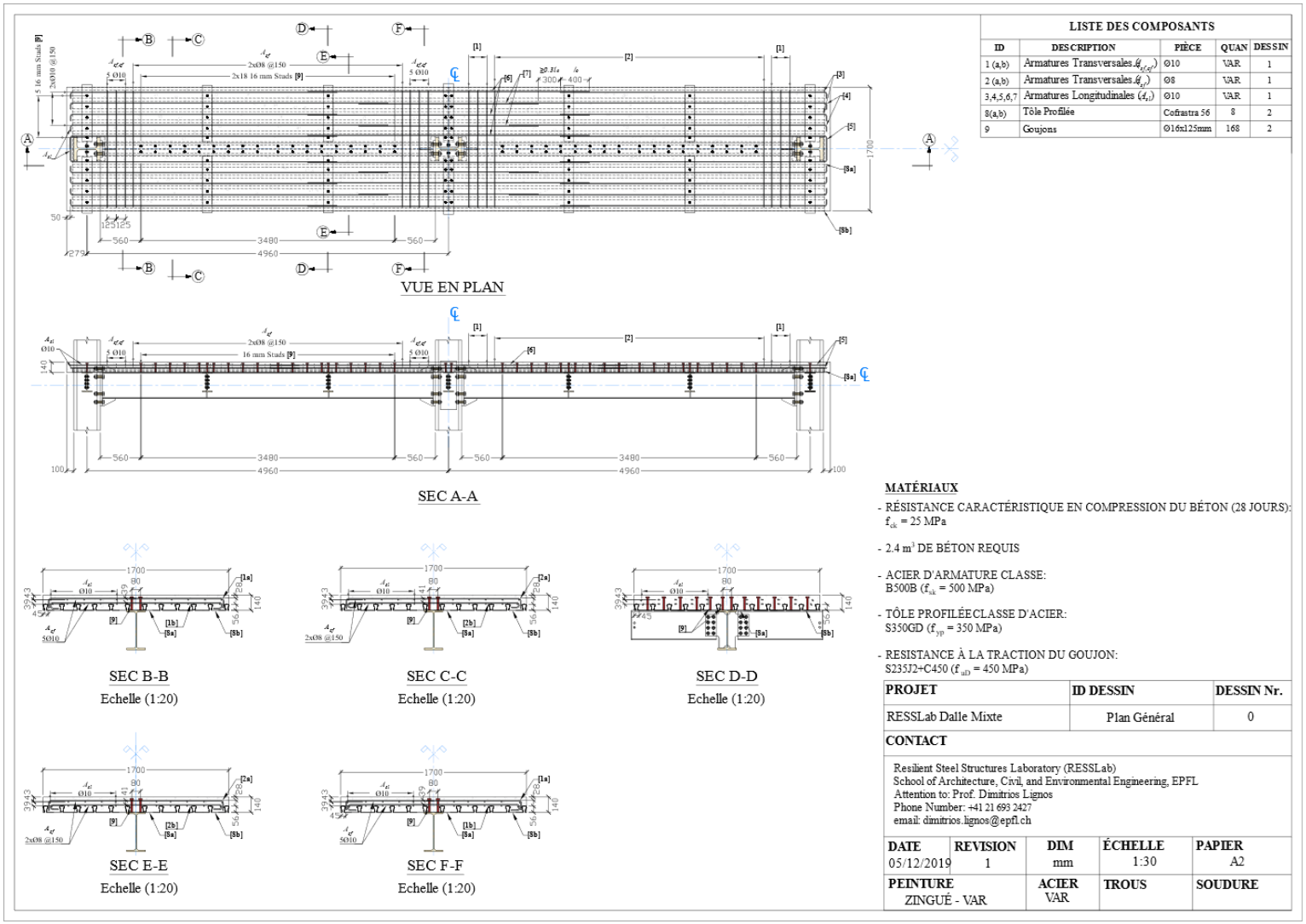

ARMATURES DE LA DALLE

ID	TYPE	DIAM	DIMENSIONS	QUAN
1a	Coude Normal (Armatures Transversales Supérieures)	Ø10	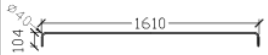	12
1b	Crochet Normal (Armatures Transversales Inférieures)	Ø10	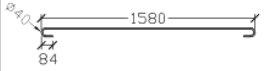	8
2a	Coude Normal (Armatures Transversales Supérieures)	Ø8	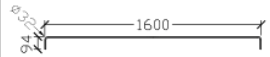	52
2b	Crochet Normal (Armatures Transversales Inférieures)	Ø8	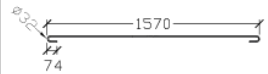	52
3	Coude Normal (Armatures Longitudinales)	Ø10	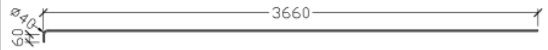	16
4	Coude Normal (Armatures Longitudinales)	Ø10	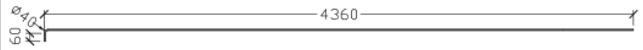	16
5	Barre en U (Armatures Longitudinales)	Ø10	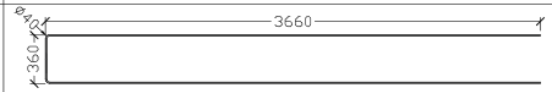	4
6	Barre Droite (Armatures Longitudinales)	Ø10		12
7	Barre Droite (Armatures Longitudinales)	Ø10		8
8	Barre Droite (Supplémentaires)	Ø10		5

ID Projet: PR	EXTRA No.	Dessin Nr.
RESSLab Dalle Mixte		1

Composant: Armatures de la Dalle

Resilient Steel Structures Laboratory (RESSLab)
School of Architecture, Civil, and Environmental Engineering,
École Polytechnique Fédérale de Lausanne (EPFL)
Adresse: GC B3 485 (Bâtiment GC) Station 18 CH-1015 Lausanne
Attention to: Prof. Dimitrios Lignos, Hammad El Jisr
Phone Number: +41 21 693 2427
email: dimitrios.lignos@epfl.ch

DATE	REV.	DIM	ÉCHELLE	PAPIER
29/01/2020	1	mm	1:30	A3
PEINTURE		**ACIER** B500B/C	**TROUS**	**SOUDURE**

MATÉRIAUX

- ACIER D'ARMATURE CLASSE: B500B ou B500C (f_{sk} = 500 MPa)

TÔLE PROFILÉE ET GOUJONS

ID	TYPE	LONGEUR (mm)	DIMENSIONS	QUAN
8a	Tôle Profilée Cofrastra 56	5160	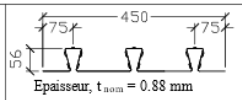 Epaisseur, t_{nom} = 0.88 mm	4
8b	Tôle Profilée Cofrastra 56	5160	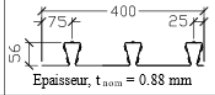 Epaisseur, t_{nom} = 0.88 mm	4
9	Goujons Ø16	125		168

ID Projet: PR	EXTRA No.	Dessin Nr.
RESSLab Dalle Mixte		2

Composant: Tôle Profilée et Goujons

Resilient Steel Structures Laboratory (RESSLab)
School of Architecture, Civil, and Environmental Engineering,
Ecole Polytechnique Fedérale de Lausanne (EPFL)
Adresse: GC B3 485 (Bâtiment GC) Station 18 CH-1015 Lausanne
Attention to: Prof. Dimitrios Lignos, Hammad El Jisr
Phone Number: +41 21 693 2427
email: dimitrios.lignos@epfl.ch

DATE	REV.	DIM	ÉCHELLE	PAPIER
05/12/2019	1		1:10	A3
PEINTURE		**ACIER** VAR	**TROUS**	**SOUDURE**

MATÉRIAUX

- TÔLE PROFILÉE CLASSE D'ACIER: S350GD (f_{yp} = 350 MPa)
- RESISTANCE À LA TRACTION DU GOUJON: S235J2+C450 (f_{uD} = 450 MPa)

Appendix C Material and welding procedure specifications

Description

This appendix includes all the mill certificates of the structural steel material for the primary IPE360 girders, the transverse IPE270 beams, the HEM320 columns and the doubler plates that were used in the construction of the test frame. The welding procedure specifications are also included in this appendix along with the welding procedure qualification records

C.1 IPE360 mill certificate

SWT
STAHLWERK THÜRINGEN

A01 Stahlwerk Thüringen GmbH
A05 Quality Assurance Department
Kronacher Straße 6
07333 Unterwellenborn
Germany

A08 Our Order No.: 0020002195
A07 Your Order No.: OSC1980362

B02 Quality: S355J2+M
according to: EN 10025-2/2004

A03 Certificate No. 171/9-2019 2 / 2
Advice No. A190901033

A02 Inspection Certificate 3.1

according to EN 10204:2004/3.1

SWT

A04
A06

MANNI SIPRE SPA
VIA A RIGHI 7
37135 Verona
ITALY

Impact test (ISO148-1)

Heat No.	Type	Temperature	L C02 1 [J]	2	3	M
B07	C40/C41	C03	C42	C42	C42	C43
min			19			27
28525	KV 450	-20°C	184	162	81	142

Z01

- electric arc melting
- surface condition according to DIN EN 10163-3, class C, subclass 1

Material number: 1.0577

General technical terms of delivery for hot rolled structural steel products: EN 10025-1
Intended uses: Welded, bolted and riveted structures
Expressed as indicated in the DoP:
Tolerances / Tensile strength / Yield strength / Elongation
Impact strength / Weldability / Durability

Tolerances on dimensions and shape:
HE / IPE / UB / UC / UBP / HP according to EN 10034
UPN / UPE / PFC according to EN 10279

The delivered products do not exceed the limit values of surface contamination according to the German Radiation Protection Ordinance.

We confirm herewith that the delivered material complies with the terms of the order.

Z03 Works inspector
René Merbach

Z02 Sep 2, 2019

Z04

CE
0769
18
032 CPR 2019-08-29 SWT

C.2 IPE270 mill certificate

MANNI SIPRE
STEEL ENGINEERING
UFFICIO CERTIFICATI - COPIA INFORMATICA CONFORME ORIGINALE
NS. CONFERMA: 0000092509
RIF. ORDINE: ORD. 2020535500
DDT: 0000402111
PLACCA/COLATA: 64894

ArcelorMittal Hunedoara S. A
DJ 687, nr. 4, Cod 331111, Hunedoara-Romania

ArcelorMittal

Certificat de Inspectie / Inspection Certificate
SR EN 10204:2005 (EN 10204:2004) 3,1

ArcelorMittal HUNEDOARA S.A:
Quality Inspection & Statistics
Hunedoara-Romania Cod 331111

Destinatar/ Destined to:	ARCELORMITTAL COMMERCIAL SECTIONS	Nr./No 1450047835	Data/ Date 11.04.2019
Adresa/Addre Tara/State:	66 RUE LUXEMBOURG ESCH ITALIA	Comanda nr./Order no.	1100560470
Vagon/Wagon Auto/Truck:	315335563963		
Conditii de livrare/ Condition of delivery:	SR EN 10025-2:2004		

Nr. Crt/ No. Item	Nr.Sarja /Heat No	Lot	Marca/ Quality	Produs/ Product	Buc./ Pieces	Lungime/Length [mm]	Lungime/Length toleranta/ tolerances	Incercari mecanice/Mechanical tests R_{P02} [N/mm²]	R_m [N/mm²]	A [%]	Tip epruveta /Type of sample	Incovoiere prin soc/Charpy impact test Temp [°C]	1 [J]	2 [J]	3 [J]
1	64821	1	S355J2+M	IPE270	4	18100	+100/-0	386	524	29	300/10	-20	114	110	118
2	64893	1	S355J2+M	IPE270	16	18100	+100/-0	392	520	28	300/10	-20	104	112	116
3	64894	1	S355J2+M	IPE270	44	18100	+100/-0	392	533	29	300/10	-20	90	114	116
4	64895	1	S355J2+M	IPE270	16	18100	+100/-0	404	534	29	300/10	-20	114	120	112

Nr.Crt / No Item	Nr. Sarja /Heat No	Compozitie chimica pe otel lichid/Chemical analysis of the liquid steel [%] C	Mn	Si	S	P	Cr	Ni	Cu	Mo	V	Al	N	Ti	B	Nb	CEV	Observatii/ Remarks
1	64821	0,110	1,15	0,21	0,019	0,012	0,11	0,15	0,43	0,03	0,050	0,027	0,0100	0,001	0,0003	0,0011	0,38	
2	64893	0,120	1,17	0,25	0,008	0,011	0,06	0,11	0,35	0,02	0,050	0,033	0,0109	0,001	0,0003	0,0010	0,37	
3	64894	0,110	1,16	0,23	0,006	0,011	0,07	0,10	0,32	0,02	0,050	0,027	0,0089	0,001	0,0003	0,0009	0,36	
4	64895	0,110	1,20	0,22	0,006	0,012	0,08	0,11	0,32	0,02	0,050	0,030	0,0116	0,001	0,0003	0,0011	0,37	

Utilizare preconizata/Intended uses: Structuri metalice si/sau structuri mixte otel-beton/Metalic structures and/or mixed structures steel-concrete
Durabilitate/Durability: Compozitie chimica / Chemical analysis
Sudabilitate/Weldability:CEV
Substanta reglementata/Regulated substance: Performanta nedeterminata/No performance determined
Marcaj/Marked: SR EN 10025-1:2005 (EN 10025-1:2004)
Suprafata/Surfa SR EN 10163-3:2005, clasa C, subcl.1 (EN 10163-3:2004)
Dimensiuni/Dimension: CONFORM COMANDA (ACC.TO SALES PROGR.)
Tolerante la dimensiuni si forma/ SR EN 10034:1995(EN 10034-1993)
Tolerances on dimension and shape :

The above mantioned material has not displayed any radiation
Materialul mai sus mentionat nu prezinta radiatii

ArcelorMittal Hunedoara Control Tehnic 10 HUNEDOARA

Inspectia Calitatii si Statistica / Quality Inspection & Statistics
Quality Manager Ileana Cristea Eng.

Intocmit/Elaborate:
BILTAC EUGEN

CE 12/1823
AMHU-2/09-CPR-13-1

Form.PC-12 rev.4

C.3 HEM320 mill certificate

A10 **Sales Agent:**
ArcelorMittal Commercial
Italy Srl
43, Str. Torino
I-10043 ORBASSANO TO

A01 **Plant:**
ArcelorMittal Belval & Differdange
Site de Differdange
L-4503 Differdange

ArcelorMittal Belval & Differdange
Service Gestion Qualité
66, rue de Luxembourg
L-4009 Esch/Alzette
A05

MANNI SIPRE STEEL ENGINEERING
UFFICIO CERTIFICATI - COPIA INFORMATICA CONFORME ORIGINALE
NS. CONFERMA: 0000092509
RIF. ORDINE: ORD. 2020030500
DDT: 0000402111
PLACCA/COLATA: 85951

Certificate Nr X 4084902
Delivery note number 4084902 from 23 October 2019 A03

A08 Our reference : 1100575264
A07 Your reference : OSC1980333
19.07.2019
MANNI SIPRE S.P.A.

MANNI SIPRE S.P.A.
VIA A. RIGHI 7
I-37135 VERONA VR
A06

S355J2+M ACCORDING TO EN 10025-2/2004 SUITABLE FOR GALVANIZING
B02

Inspection certificate according to EN 10204:2004 / 3.1
A02

Ord.item	B01 Product	Length	B13 Weight	B07 Heat nr	Weight	Bund.	B08 Bars
000023	HE 320 M	20.100 mm	4,860 to	85951	4,860 to		1

Heat nr B07		Heat analysis (%) C	Mn	P	S	Si	Al	Cu	Ni	Cr	V	Nb	Mo	CEV
	Min					0,14								
	Max	0,22	1,60	0,030	0,030	0,25		0,55				0,060		0,45
85951		0,09	1,38	0,018	0,021	0,24	0,011	0,23	0,14	0,10	0,041	0,008	0,040	0,38

Heat nr		Tensile test N/mm2 ReH C11	N/mm2 Rm C12	5,65VS A(%) C13	Charpy impact test C40 KV Position C01	C02	UNAGED mm C41	°C C03	J 1 C42	2	3	M C43
	Min	345	470	22,00	FL.1/3	L		-20		19		27
	Max		630									
85951		408	526	26,78	FL.1/3	L		-20	161	165	127	151

Z05
Hot rolled products of structural steels according to EN10025-1:2004
Intended uses : Building constructions or civil engineering
Durability : No performance determined
Regulated substance : No performance determined
Weldability : according to EN 1011-2
EAF-Steel
Dimension and Shape tolerances :
I- Profiles : EN 10365 and EN10034
H-Profiles: EN 10365 and EN10034
Angles I : EN10056 Part 1 and 2
U-Profiles : EN 10365 and EN 10279
UB-und UC-Profiles und UBP-support piles : EN 10365 and EN10034
Environmental product declaration:
https://sections.arcelormittal. com/documentation/Product_decla ration/EN

Klecker Roberto
Porteur de signature spéciale
Z03

Z04
CE
0769
06

Code of the product type: 1.0577 / DOP: AMDI-2/09-CPR-13-1

EN 10168:2004

Page : 1 / 2

A10 Sales Agent:
ArcelorMittal Commercial
Italy Srl
43, Str. Torino
I-10043 ORBASSANO TO

A01 Plant:
ArcelorMittal Belval & Differdange
Site de Differdange
L-4503 Differdange

A04
ArcelorMittal Belval & Differdange
Service Gestion Qualité
66, rue de Luxembourg
L-4009 Esch/Alzette

A05
Certificate Nr X 4084902
Delivery note number 4084902 from 23 October 2019
A03

A08 Our reference : 1100575264
A07 Your reference : OSC1980333
19.07.2019
MANNI SIPRE S.P.A.

MANNI SIPRE S.P.A.
VIA A. RIGHI 7
I-37135 VERONA VR
A06

S355J2+M ACCORDING TO EN 10025-2/2004 SUITABLE FOR GALVANIZING

B02
Inspection certificate according to EN 10204:2004 / 3.1
A02

Declaration of Performance
https://sections.arcelormittal. com/3444/3134/EN

Klecker Roberto
Porteur de signature spéciale
Z03

Z04
CE
0769
06

Code of the product type: 1.0577 / DOP: AMDI-2/09-CPR-13-1

EN 10168:2004

Page : 2 / 2

C.4 Doubler plates mill certificate

ILSENBURGER GROBBLECH
Ein Unternehmen der Salzgitter Gruppe

Abnahmeprüfzeugnis 3.1
Inspection certificate 3.1
Certificat de reception 3.1
DIN EN 10204
(A02)

Nr./No./N° (A03) **1190819**
Seite/Page/Page 1/5
Datum/Date/Date 08.10.2019

Nr. (A07) 0071235279 SHG5 13.08.2019
Besteller Salzgitter Mannesmann Stahlhandel
Purchaser GmbH NL Gladbeck
Acheteur 45955 Gladbeck
(A06)

Nr. (A07)
Empfänger Salzgitter Mannesmann Stahlhandel
Customer GmbH NL Gladbeck
Destinataire 45955 Gladbeck
(A06)

Erzeugnis Grobblech
Product Heavy plate
Produit Tôle forte
(B01)

Werkstoff und Lieferbedingung S355J2+N
Steel grade and terms of delivery DIN EN 10025-2 04/05
Nuance et conditions de livraison AD 2000 W1 05/2018
(B02-B03) DIN EN 10029 A 02/11
DIN EN 10163-2 Kl. B UG3 03/05

Werksauftrags-Nr. 0000100712
Works order No.
N° de commande
(A08)

Lieferschein-Nr. 0088492523
Dispatch note No. 07.10.2019
Avis d'expédition N°

Abnahme WS
Inspection
Reception
(A05)

Kennzeichnung des Materials / Marking of the product / Marquage du produit (B06)
Herstellerzeichen/Stahlsorte/Schmelzen-Nr/
Erzeugnis-Nr./Sachverständigenstempel
Trademark/Steelgrade/Heat-No/Product-No/
inspector's stamp
Sigle de l´usine/Nuance de l´acier/N° coulée/
N° produit/Poinçon de l' expert

Materialdaten / Material data / Données des matériaux (B01-B99)

Pos. Item Poste	Anzahl Quantity Nombre (B08)	Erzeugnis-Nr. Product No. N° produit (B07)	Schmelzen-Nr. Heat No. N° Coulée (B07)	Lieferzustand Cond. of delivery Etat de livraison (B04)	Dicke x Breite x Länge mm x mm x mm Thickness x Width x Length Epaisseur x Largeur x Longueur (B09-B11)
02	1	152904 1	732241	N	16,00 x 2500,0 x 12000
02	1	152904 2	732241	N	16,00 x 2500,0 x 12000
02	1	152905 1	732241	N	16,00 x 2500,0 x 12000
02	1	152905 2	732241	N	16,00 x 2500,0 x 12000
03	1	150830 1	00275	N	22,00 x 3000,0 x 12000
03	1	150830 2	00275	N	22,00 x 3000,0 x 12000

02	4	Gewicht	15.072	kg
03	2	Weight	12.434	kgs
		Poids		kgs
Σ	6	(B12)	27.506	

N: normalisiert / normalized / normalisé

Maßprüfung und Sichtkontrolle auf äußere Beschaffenheit: ohne Beanstandung
Dimensional check and visual examination of the surface condition:
without objection
Contrôle dimensionnel et examen visuel de l'état de surface: satisfaisants

Es wird bestätigt, daß die Lieferung den Anforderungen der Lieferbedingung entspricht.
We hereby certify that the delivered material complies with the terms of the order.
Nous certifions que la fourniture répond aux conditions de livraison.
(Z01)
QM-System: Certification as per ISO 9001 since 28 February 1990

Herstellerzeichen
Trademark
Sigle du producteur
(A04)

Ilsenburger Grobblech GmbH
Veckenstedter Weg 10
D-38871 Ilsenburg
(A01)

Abnahmestempel
Inspection Stamp
Poinçon de l'expert
(Z03)

CE

Abnahmebeauftragter
Inspection Representative
Représentant autorisé
(Z02)

Cyron

Diese durch ein geeignetes Datenverarbeitungssystem erstellte Bescheinigung ist gemäß EN 10 204, Abschnitt 5, ohne Unterschrift gültig.
This certificate was prepared by a suitable data processing system and is valid without signature according to EN 10 204, section 5.
Ce certificat a été établi par un système adéquat de traitement de données, il est valable sans signature selon EN 10 204, section 5.

SALZGITTER: 118342 33297286 2020051101 - Giulio Zanelli 06.05.2020 Z1361623.001 S. 1

ILSENBURGER GROBBLECH
Ein Unternehmen der Salzgitter Gruppe

Abnahmeprüfzeugnis 3.1
Inspection certificate 3.1
Certificat de reception 3.1
DIN EN 10204
(A02)

Nr./No./N° (A03) **1190819**
Seite/Page/Page 2/5
Datum/Date/Date 08.10.2019

Nr. (A07) 0071235279 SHG5 13.08.2019
Besteller Salzgitter Mannesmann Stahlhandel
Purchaser GmbH NL Gladbeck
Acheteur 45955 Gladbeck
(A06)

Nr. (A07)
Empfänger Salzgitter Mannesmann Stahlhandel
Customer GmbH NL Gladbeck
Destinataire 45955 Gladbeck
(A06)

Erzeugnis Grobblech
Product Heavy plate
Produit Tôle forte
(B01)

Werksauftrags-Nr. 0000100712
Works order No.
N° de commande
(A08)

Lieferschein-Nr. 0088492523
Dispatch note No. 07.10.2019
Avis d'expédition N°

Werkstoff und Lieferbedingung S355J2+N
Steel grade and terms of delivery DIN EN 10025-2 04/05
Nuance et conditions de livraison AD 2000 W1 05/2018
(B02-B03) DIN EN 10029 A 02/11
DIN EN 10163-2 Kl. B UG3 03/05

Abnahme WS
Inspection
Reception
(A05)

Schmelzenanalyse / Ladle analysis / Analyse de coulée (C70-C99)

Herstellerangaben / Manufacturer standard / Données du fabricant

Schmelzen-Nr. Heat No. N° Coulée (B07)	C % ≤ 0,20	Si % 0,14 – 0,25	Mn % ≤ 1,60	P % ≤ 0,025	S % ≤ 0,025	N %	Al %	Cu % ≤ 0,55	Cr %	Ni %
00275	0,16	0,19	1,55	0,01	0,002	0,005	0,042	0,06	0,04	0,05
732241	0,17	0,18	1,52	0,010	0,003	0,005	0,043	0,03	0,04	0,03

Schmelzen-Nr. Heat No. N° Coulée (B07)	Mo % ≤ 0,08	V %	Ti %	Nb %	EV1 1) % ≤ 0,45
00275	0,002	0,003	0,002	0,001	0,43
732241	0,01	0,001	0,003	0,001	0,44

1) EV1: CEV=C+Mn/6+Mo/5+Ni/15+Cr/5+V/5+Cu/15

Stahlherstellung: Sauerstoffaufblasverfahren
Steel making: Basic oxygen process
Fabrication d´acier: Procédé au convertisseur à l´oxygène
(C70)

Es wird bestätigt, daß die Lieferung den Anforderungen der Lieferbedingung entspricht.
We hereby certify that the delivered material complies with the terms of the order.
Nous certifions que la fourniture répond aux conditions de livraison.
(Z01)
QM-System: Certification as per ISO 9001 since 28 February 1990

Herstellerzeichen / Trademark / Sigle du producteur (A04)
Ilsenburger Grobblech GmbH
Veckenstedter Weg 10
D-38871 Ilsenburg
(A01)

Abnahmestempel / Inspection Stamp / Poinçon de l'expert (Z03)

CE

Abnahmebeauftragter / Inspection Representative / Représentant autorisé (Z02)
Cyron

Diese durch ein geeignetes Datenverarbeitungssystem erstellte Bescheinigung ist gemäß EN 10 204, Abschnitt 5, ohne Unterschrift gültig.
This certificate was prepared by a suitable data processing system and is valid without signature according to EN 10 204, section 5.
Ce certificat a été établi par un système adéquat de traitement de données, il est valable sans signature selon EN 10 204, section 5.

SALZGITTER: 118342 33297286 2020051101 - Giulio Zanelli 06.05.2020 Z1361623.002 S. 2

ILSENBURGER GROBBLECH
Ein Unternehmen der Salzgitter Gruppe

Abnahmeprüfzeugnis 3.1
Inspection certificate 3.1
Certificat de reception 3.1
DIN EN 10204
(A02)

Nr./No./N° (A03) **1190819**
Seite/Page/Page 3/5
Datum/Date/Date 08.10.2019

Nr. (A07) 0071235279 SHG5 13.08.2019
Besteller Salzgitter Mannesmann Stahlhandel
Purchaser GmbH NL Gladbeck
Acheteur 45955 Gladbeck
(A06)

Nr. (A07)
Empfänger Salzgitter Mannesmann Stahlhandel
Customer GmbH NL Gladbeck
Destinataire 45955 Gladbeck
(A06)

Erzeugnis Grobblech
Product Heavy plate
Produit Tôle forte
(B01)

Werksauftrags-Nr. 0000100712
Works order No.
N° de commande
(A08)
Lieferschein-Nr. 0088492523
Dispatch note No. 07.10.2019
Avis d'expédition N°

Werkstoff und Lieferbedingung S355J2+N
Steel grade and terms of delivery DIN EN 10025-2 04/05
Nuance et conditions de livraison AD 2000 W1 05/2018
(B02–B03) DIN EN 10029 A 02/11
DIN EN 10163-2 Kl. B UG3 03/05

Abnahme WS
Inspection
Reception
(A05)

Zugversuch / Tensile test / Essai de traction (C10–C29)

Proben-Nr. Specimen No. N° éprouvette (C00)	Schmelzen-Nr. Heat No. N° Coulée (B07)	Ort Location Lieu (C01) 1) 2) 3)	Richt. Direct. Orient. (C02) 4)	Zustand Cond. Cond. (B05) 5)	Form Type Type (C10) 6)	Streckgrenze Yield point Limite d'élasticité (C11) ReH N/mm2	Zugfestigkeit Tensile strength Résistance (C12) Rm N/mm2 470 – 630	ReH/Rm ReH/Rm ReH/Rm	Bruchdehnung Elongation Allongement (C13) A5 % ≥ 20 7)	
150650 *)	732241	K4G	Q	N	P	402	541	0,74	32	
150830	00275	K4G	Q	N	P	408	557	0,73	28	

1) K: Kopf / Top / Tête
2) 4: 1/4 Breite / 1/4 Width / 1/4 Largeur
3) G: Erzeugnisdicke / Thickness of product / Epaisseur du produit
4) Q: quer / transversal / transversal
5) N: normalisiert / normalized / normalisé
6) P: prismatisch / prismatic / prismatique
7) A5: Lo=5,65 √So
*) Das Probestück ist nicht Bestandteil der Lieferung / The sample product is not part of the delivery / Le produit-échantillon ne fait pas partie de la livraison

Kerbschlagbiegeversuch / Impact test / Essai de résilience (C40–C49)

Proben-Nr. Specimen No. N° éprouvette (C00)	Schmelzen-Nr. Heat No. N° Coulée (B07)	Ort Location Lieu (C01) 1) 2) 3)	Richt. Direct. Orient. (C02) 4)	Zustand Cond. Cond. (B05) 5)	Probenform Type of specimen Type d'éprouvette (C40–C41)	Temperatur Temperature Température (C03) °C	Schlagarbeit Impact energy Energie de rupture (C42–C43) 1 J ≥ 19	2	3	MW 6) J ≥ 27
150650 *)	732241	K4O	L	N	KV450	-020	181	179	170	177
150830	00275	K4O	L	N	KV600	-020	157	170	162	163

1) K: Kopf / Top / Tête
2) 4: 1/4 Breite / 1/4 Width / 1/4 Largeur
3) O: oberflächennah / near surface / près de la peau
4) L: längs / longitudinal / longitudinal
5) N: normalisiert / normalized / normalisé
6) MW: Mittelwert / Average / Moyenne
*) Das Probestück ist nicht Bestandteil der Lieferung / The sample product is not part of the delivery / Le produit-échantillon ne fait pas partie de la livraison

Es wird bestätigt, daß die Lieferung den Anforderungen der Lieferbedingung entspricht.
We hereby certify that the delivered material complies with the terms of the order.
Nous certifions que la fourniture répond aux conditions de livraison.
(Z01)
QM-System: Certification as per ISO 9001 since 28 February 1990

Herstellerzeichen
Trademark
Sigle du producteur
(A04)

Ilsenburger Grobblech GmbH
Veckenstedter Weg 10
D-38871 Ilsenburg
(A01)

Abnahmestempel
Inspection Stamp
Poinçon de l'expert
(Z03)

CE

Abnahmebeauftragter
Inspection Representative
Représentant autorisé
(Z02)

Cyron

Diese durch ein geeignetes Datenverarbeitungssystem erstellte Bescheinigung ist gemäß EN 10 204, Abschnitt 5, ohne Unterschrift gültig.
This certificate was prepared by a suitable data processing system and is valid without signature according to EN 10 204, section 5.
Ce certificat a été établi par un système adéquat de traitement de données, il est valable sans signature selon EN 10 204, section 5.

SALZGITTER: 118342 33297286 2020051101 - Giulio Zanelli 06.05.2020 Z1361623.003 S. 3

C.5 Welding procedure specifications

ZM CONSTRUCTIONS MÉTALLIQUES	CAHIER DE SOUDAGE ATELIER PR	Date Révision : 05.03.2020 Indice : 0 Page 2/9

2 GÉNÉRALITÉS

L'objectif de ce cahier de soudage est de décrire les paramètres essentiels et les conditions nécessaires à l'exécution des travaux de soudure en atelier.

Cage d'essai est un ouvrage de classe d'exécution EXC2 selon la classification de l'EN1090 -2.

Les documents de référence liés à l'établissement de ce cahier de soudage sont les suivants :

Document de référence	Domaine d'application / Titre	**Applicable au projet**
Normes SIA 263 & 263/1 (éd. 2013)	Constructions en acier – Spécifications complémentaires	X
NF EN 1090-2	Assemblages soudés/Qualification modes opératoires/contrôles non destructifs	EX C 2
ISO 15614-1	Qualification des modes opératoires de soudage	X
EN 287-1 ou ISO 9606-1	Certification des soudeurs	X
EN 1418 ou 14732	Certification des opérateurs en soudure	X
NF EN ISO 3834-2	Certification soudage	X
NF EN ISO 14555	Q MOS connecteurs	X

QUALITÉ DES SOUDURES

La qualité de soudage applicable à l'ouvrage selon CPS § 780.310 est la suivante :

- Tableau explicatif des qualités :

Qualité des soudures	Zone / partie de l'ouvrage
B+	Classe B avec des exigences supplémentaires selon l'EN1090 -2, seulement pour des cas exceptionnels
B	La soudure est équivalente à la matière des pièces assemblées, convient aux sollicitations importantes (si entailles éliminées, convient également aux sollicitations à la fatigue)
C	Pour sollicitations moyennes (qualité standard des cordons d'angle)
D	Pour sollicitations faibles (par ex. soudures constructives)

MATÉRIAUX D'APPORTS

1. Entreposage des matériaux d'apports :

Les matériaux d'apports sont à entreposer dans un local sous clé, sec et abrité

2. 2. Entretien des matériaux d'apport :

a. Filarc PZ6102 Ø 1,2
pas d'étuvage nécessaire, mais toujours tenir au sec.

Les certificats des matériaux d'apport sont annexés dans un document séparé intitulé « Recueils des certificats matière».

3 SUIVI DU SOUDAGE

Pour les soudures QB, les soudeurs identifient par poinçon les soudures effectuées. Cette identification doit être reportée sur le document de contrôle non-destructif des soudures. Des fiches de suivi de soudage sont établies pour les soudures QB. Elles sont reportées sur les « fiches de suivi de soudage »

Contrôle des soudures

L'étendue desc ontrôles des soudures est la suivante :

	QC	QB	QB+
1) Contrôle visuel (VT) et dimensionnel	100%	**	**
		**	**
2) Contrôle magnétoscopique (MT)			**
	**	**	
Soudures partiellement pénétrées	20%	**	
Autres	20%	**	

3) Contrôle par ultrason (UT)	
Soudures en pp	50%
Autres soudures entièrement pénétrées	50%

Les soudures complètement pénétrées sont contrôlées à l'ultrason (UT), conformément aux dispositions des normes ISO 11666, ISO 17640 et ISO 23279.

Les cordons d'angle sont contrôlés par magnétoscopie (MT), conformément aux normes ISO 17638 et ISO 23278.

L'étendue détaillée des contrôles de soudure figure sur le tableau annexé « listing des soudures ».

4 PLANS DE REPERAGE TYPE DES SOUDURES

.

Les plans suivant définissent visuellement l'étendue des CND par type d'élément.

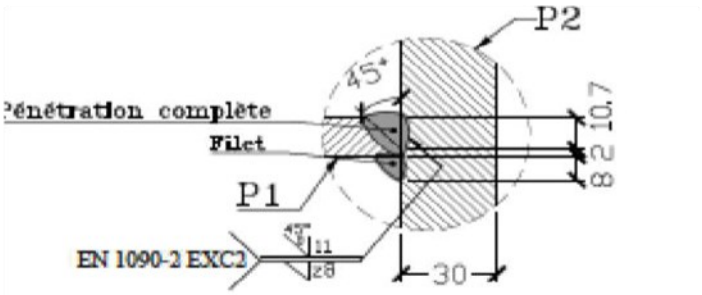

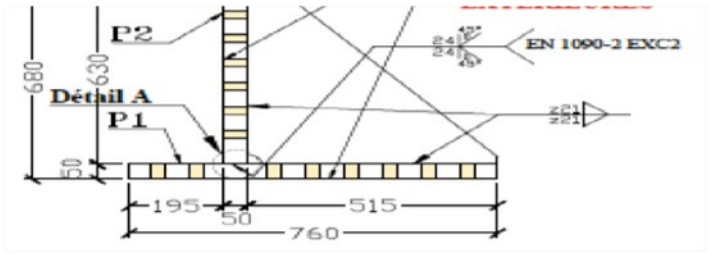

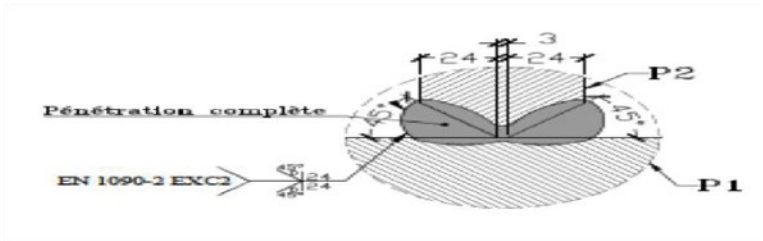

ZM CONSTRUCTIONS MÉTALLIQUES	CAHIER DE SOUDAGE ATELIER PR	Date Révision : 05.03.2020 Indice : 0 Page 10/9

6 ANNEXE DMOS.

Spécification 1.1.N		Symbole du joint	
Description :	Cordon d'angle mono et multipasse		
Matériau de base :	S355J2	Ep. t1-t2 :	10 - 40mm
Procédé :	MAG 138	QMOS No :	43419 - 39T

Préparation et séquences de soudage

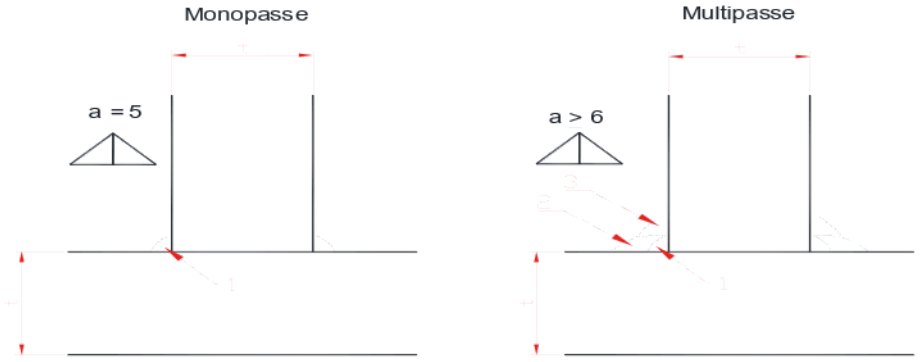

Procédé de soudage Passe n°		Racine MAG 138 1		Remplissage MAG 138 2 à n	
Fournisseur / type matière d'apport		Filarc / PZ 6102		Filarc / PZ 6102	
Désignation		EN ISO 17632 A : T46 4 M M 2 H5		EN ISO 17632 A: T46 4 M M 2 H5	
Diamètre		1.2mm		1.2mm	
Type gaz / poudre		Argon / Co2 (M 21)		Argon / Co2 (M 21)	
Débit gaz		16 / 20 litres /minutes		16 / 20 litres /minutes	
Position de soudage		PB		PB	
Polarité		DC+		DC+	
Mode de transfert		pulvérisation axiale		pulvérisation axiale	
Ampères	(±10%)	250	*A*	255	*A*
Volts	(±10%)	30	*V*	30	*V*
Vitesse fil	(±10%)	10	*m/min*	10	*m/min*
Vitesse d'avance	(±10%)	30	*cm/min*	34	*cm/min*
Apport de chaleur	(±25%)	12.0	*kJ/cm*	10.8	*kJ/cm*
Apport de chaleur min		9.0	*kJ/cm*	8.0	*kJ/cm*
Apport de chaleur max		15.0	*kJ/cm*	13.4	*kJ/cm*
Pré - chauffage		100 °C			
Temp. entre passes				< 250 °C	
Remarques :					

Version N°1	Revision:2	Validation	
Établi par :NMO	JPO	Contrôle par:	IWE/EWE Guiseppe D'Agostino
Date :02.09.2014	08.01.2018	Date et signature:	08.01.2018

ZM CONSTRUCTIONS MÉTALLIQUES

CAHIER DE SOUDAGE ATELIER
PR

Date Révision : 05.03.2020
Indice : 0
Page 11/9

Spécification 1.2.C		Symbole du joint	
Description :	Soudure à pénétration partielle en K ou demi-K		
Matériau de base :	S355 J2	épaisseurs :	40 à 160 mm
Procédé :	MAG 138	QMOS N° :	42641 - 34D

Préparation et séquences de soudage

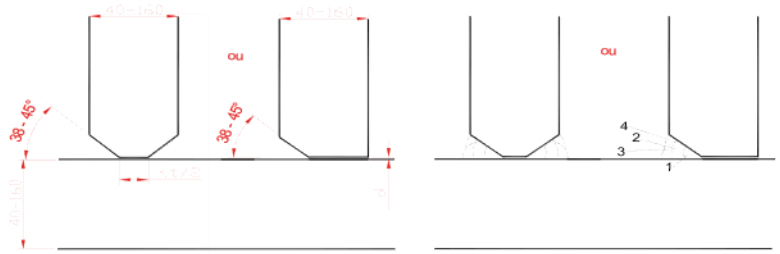

talon bloqué: d=0
EXE 3: d<2mm
EXE 4: d<1mm

Procédé de soudage Passe n°		Racine MAG première			Remplissage MAG remplissage		
Fournisseur / type matière d'apport		Filarc / PZ 6102			Filarc / PZ 6102		
Désignation		EN ISO 17632 A : T46 4 M M 2 H5			EN ISO 17632 A : T46 4 M M 2 H5		
Diamètre		1.2mm			1.2mm		
Type et débit gaz		Ar-CO_2 (M21) // 18 l/min			Ar-CO2 (M21) // 18 l/min		
Diamètre buse et stick out		21mm // 15mm			21mm // 15mm		
Position de soudage		PB			PB		
Polarité		DC+			DC+		
Mode de transfert		pulvérisation axiale			pulvérisation axiale		
Passe	**n°**	**1**	**2**		**3**	**4+**	
Ampères	(±10%)	260	270	A	280	280	A
Volts	(±10%)	32	32	V	32	32	V
Vitesse fil	(±10%)	10	10	m/min	10	10	m/min
Vitesse d'avance	(±10%)	21	23	cm/min	30	30	cm/min
Apport de chaleur	(±15%)	19.0	18.0	kJ/cm	14.3	14.3	kJ/cm
Apport de chaleur min		13.9	13.4	kJ/cm	17.7	9.9	kJ/cm
Apport de chaleur max		23.2	22.3	kJ/cm	17.8	16.6	kJ/cm
Pré - chauffage		120 °C			--		
Temp. entre passes		< 250 °C			< 250 °C		

Remarques :

Version N°1	Revision:2	Validation	
Établi par :NMO	JPO	Contrôle par:	IWE/EWE Guiseppe D'Agostino
Date :13.07.2012	20.02.2018	Date et signature:	

ZM CONSTRUCTIONS MÉTALLIQUES	CAHIER DE SOUDAGE ATELIER PR	Date Révision : 05.03.2020 Indice : 0 Page 12/9

Spécification 1.4.H		Symbole du joint	
Description :	Soudure à pénétration total en V en X ou K		
Matériau de base :	S355J2	épaisseurs :	10 à 40mm
Procédé :	MAG 138	QMOS N° :	43303 - 38L

Préparation et séquences de soudage

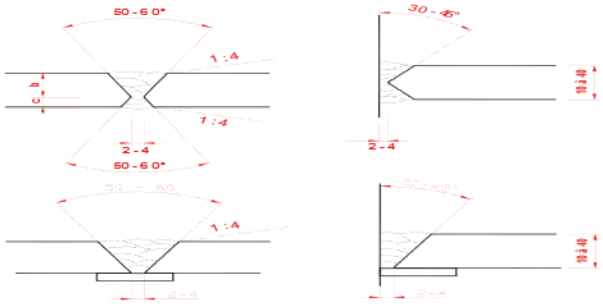

Procédé de soudage Passe n°		Racine MAG première			Remplissage MAG remplissage		
Fournisseur / type matière d'apport		Filarc / PZ 6102			Filarc / PZ 6102		
Désignation		EN ISO 17632 A : T46 4 M M 2 H5			EN ISO 17632 A : T46 4 M M 2 H5		
Diamètre		1.2mm			1.2mm		
Type et débit gaz		Ar-CO_2 (M21) // 18 l/min			Ar-CO2 (M21) // 18 l/min		
Diamètre buse et stick out		21mm // 15mm			21mm // 15mm		
Position de soudage		PA / PB			PA / PB		
Polarité		DC +			DC +		
Mode de transfert		CC	pulv. axiale		pulvérisation axiale		
Passe	**n°**	**1**	**2**		**3+**	**4+**	
Ampères	(±10 %)	142	270	*A*	280	280	*A*
Volts	(±10 %)	21	30	*V*	31	31	*V*
Vitesse fil	(±10 %)	3.7	10	*m/min*	10	10	*m/min*
Vitesse d'avance	(±10 %)	16	25	*cm/min*	40	40	*cm/min*
Apport de chaleur	(±25 %)	8.9	15.6	*kJ/cm*	10.4	10.4	*kJ/cm*
Apport de chaleur min		6.7	12.6	*kJ/cm*	7.8	7.6	*kJ/cm*
Apport de chaleur max		11.1	21.1	*kJ/cm*	13.0	12.6	*kJ/cm*
Pré - chauffage		60 °C			--		
Temp. entre passes		< 250 °C			< 250 °C		

Remarques :

Version N°	1	Révision: 2	Validation :	
Établi par	NMO	JPO	Contrôlé par	IWE/EWE Giuseppe D'Agostino
Date	11.02.2016.	05.02.2018	Date et signature:	

ZM CONSTRUCTIONS MÉTALLIQUES	CAHIER DE SOUDAGE ATELIER PR	Date Révision : 05.03.2020 Indice : 0 Page 13/9

Spécification 5.1	Symbole	

Description :	Soudure de goujons en atelier		
Matériau de base :	S355K2N	Diamètres	13 à 22 mm
Procédé :	783	QMOS N° :	41661-26P

Préparation et séquences de soudage

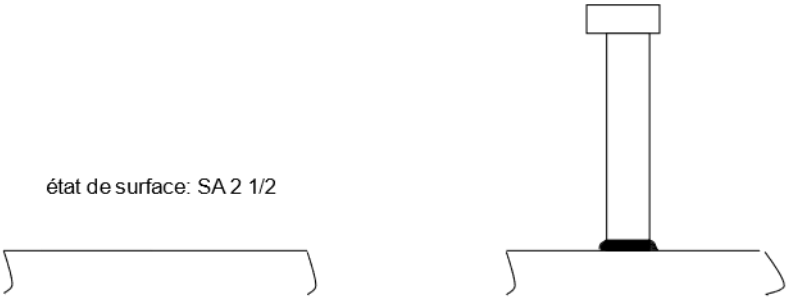

Procédé de soudage 783	□ □□	□ □□	□ □□	□ □□	Préchauffage Epaisseur	Temp.
Désignation goujons	Köco // Nelson				≤ 30mm	dégourdiss
Désignation bagueréfractaire	P 10				31 - 50mm	70°C
Nature du courant	Triphasé 50 Hz				51 - 100mm	100°C
Polarité goujon	négative				> 100mm	120°C
Position de soudage	PA					
Intensité en ampères [A] ±10%	1000	1200	1580	1980		
Tension d'arc en volts [V] ±10%	30	30	30	30		
Temps d'arc en seconde [ms] ±10%	500	600	800	1000		

Remarques :	
Générateur:	Köcö 2600E
Pistolet:	K 24

Version N° O	Revision:1	Validation	
Établi par : NMO	JPO	Contrôle par:	IWE/EWE Guiseppe D'Agostino
Date 15.10.2008	05.04.2018	Date et signature:	

C.6 Welding procedure qualification records

AC Contrôle Sàrl
NDT Laboratoire d'essai des matériaux
CND-NDT / Technique de soudage
Av. de la Gare 41, 1870 Monthey 1
Succ. Rte des Courtraits 13, 1880 Bex
LEM

Prüf-Nr.: VP *Inspetion No.:* **N° d'inspection: 38L**	Auftrags-Nr.: **43303-ZM** *Reference No.:* **N° de référence:**	SVTI-Lauf-Nr. TÜV-Lauf-Nr.	Seite 1 von 6 *Page of* **Page de**		

CERTIFICAT DE QUALIFICATION D´UN MODE OPÉRATOIRE DE SOUDAGE

WELDING PROCEDURE APPROVAL TEST CERTIFICATE / ZERTIFIKAT - ANERKENNUNG VON SCHWEISSVERFAHREN (WPAR)

Zertifizierstelle: *Certification Body:* **Organisme de certification:**	**AC Contrôle Sàrl** **CH-1870 Monthey**	Zeichen: *Sign:* **Timbre:**	38L
Hersteller / Anschrift: *Manufacturer / Address:* **Constructeur / Adresse:**	**Zwahlen & Mayr** **1860 Aigle**	Beleg-Nr. des Herstellers: *Manufacturer's Reference No.:* **N° de référence du constructeur**	**DMOS** / WPS No. 1.4.H
Vorschrift/Prüfnorm: *Code/Testing Standard:* **Code / Norme d´essai:**	EN ISO 15614-1 EN 1090-2	Datum der Schweißung: *Date of Welding:* **Date du soudage:**	13.06.2014

DOMAINE DE VALIDITÉ - GELTUNGSBEREICH - *RANGE OF APPROVAL*

Prüfgegenstand: *Test object:* **Objet de l'examen:**	Plaque	Nahtart: *Joint Type:* **Type de joint:** s. EN 15614-1 / EN 288-4 Tab. 7/9	BW, ss nb
Schweißprozeß: *Welding Process:* **Procédé de soudage:**	138	Dicke [mm]: *Parent Metal Thickness [mm]:* **Épaisseur du matériau [mm]:**	10-40
Werkstoffgruppe: *Parent Metal Group:* **Groupe de matériaux de base::**	Selon CR ISO 15608 1.2	Außendurchmesser [mm]: *Pipe Outside Diameter [mm]:* **Diamètre extérieur [mm]:**	--
Zusatzwerkstoff/Bezeichn.: *Filler Metal Type/Designation* **Métal d´apport, type et désignation:**	Filarc PZ 6102 EN ISO 17632A : T 46 M M 2 H5	Stromart: *Type of Welding Current:* **Nature du courant de soudage:**	DC+
Schutzgas / Wurzelschutz: *Shielding Gas / Backing Gas:* **Gaz de protection / Purge:**	M21	Pulver: *Flux:* **Flux:**	--
Schweißpositionen: *Welding Positions:* **Positions de soudage:**	PA		
Betriebstemperatur: *Working Temperature:* **Température de service:**	Wie Grundwerkstoff bzw. Zusatzwerkstoff, jedoch nicht tiefer als : *As base material and filler metal respectively, however not lower than :* **Comme métal de base et métal d´apport respectivement, mais pas inférieure à :**		-20°C
Vorwärmung: *Preheat:* **Préchauffage:**	Dégourdissage		
Wärmenachbehandlung: *Post Weld Heat Treatment:* **Traitement thermique après soudage:**	Aucun		

AUTRES PARAMÈTRES - SONSTIGE ANGABEN - *OTHER INFORMATION* -

Hiermit wird bestätigt, daß die Prüfungsschweißungen in Übereinstimmung mit den Anforderungen der vorbezeichneten Vorschriften bzw. Prüfnormen zufriedenstellend vorbereitet, geschweißt und geprüft wurden. */ Certified that test welds were pepared, welded and tested satisfactorily in accordance with the requirements of the code or the testing standard indicated above. /* **Nous certifions que les essais de soudage ont été préparés, soudés et contrôlés avec succès, conformément aux exigences du code ou de la norme d´essai ci-dessus mentionné(e).**

Ort: *Location:* **Lieu:**	Bex	Datum der Ausstellung: *Date of issue:* **Date d´émission:**	3.7.2014	Name und Unterschrift des Zertifizierers: *Name and Signature:* **Nom et signature:**	P. Athanasiadès IWE
Anlagen: *Annexes:* **Annexes:**	N° 1 **DMOS** / WPS n° 2 **Certificat de matière** - Werkstoffzeugniss			Zertifizierstelle: *Certification Body:* **Organisme de certification:**	AC Contrôle Sàrl 1880 BEX

AC Contrôle Sàrl
NDT **Laboratoire d'essai des matériaux**
CND-NDT / Technique de soudage
Av. de la Gare 41, 1870 Monthey 1
Succ. Rte des Courtraits 13, 1880 Bex
LEM

Prüf-Nr.: VP *Inspetion No.:* **N° d'inspection: 38L**	Auftrags-Nr.: **43303-ZM** *Reference No.:* **N° de référence:**	SVTI-Lauf-Nr. TÜV-Lauf-Nr.	Seite **2** von **6** *Page* *of* **Page** **de**

DÉFINITION DU TÉMOIN SOUDÉ (1)

EINZELHEITEN ZUR PRÜFSTÜCKSCHWEISSUNG (1) / *DETAILS OF WELD TEST (1)*

Hersteller: *Manufacturer:* **Constructeur:**	**Zwahlen & Mayr** **1860 Aigle**	Ort / Datum der Schweißung: *Location / Date of Welding:* **Lieu / Date du soudage:**	Aigle 13.6.2014
Name des Schweißers: *Welder's Name:* **Nom du soudeur:**	Milosevic Zlatko Bastos Alcides	Art der Vorbereitung und Reinigung: *Method of Preparation and Cleaning:* **Méthode de préparation et nettoyage:**	Oxycoupage, meulage

COUPONS - PRÜFSTÜCKE - TEST PIECES

Nr. *No.* **N°**	Schweißprozeß *Welding Process* **Procédé de soudage**	Dicke *Thickness* **Épaisseur** **[mm]**	Durchmesser *Outside Diameter* **Diamètre extérieur** **[mm]**	Schweißposition *Welding Position* **Pos. du soudage**	Nahtart *Joint Type* **Type de joint**	Grundwerkstoff (Spezifikation) *Parent Metal (Specification)* **Matériau de base (spécification)** Zeugnis liegt vor/*Certific. submitted/Certific. presenté**)
38L	138	20	--	PA	BW ss nb	S355K2+N, DK87

PRÉPARATION DE L´ASSEMBLAGE (croquis)* - NAHTVORBEREITUNG (Zeichnung)* - *WELD PREPARATION (Sketch)**

Gestaltung der Verbindung / *Joint Design* / **Réalisation de l´assemblage**	Schweißfolge / *Welding Sequence* / **Répartition des passes**
côtes selon DMOS 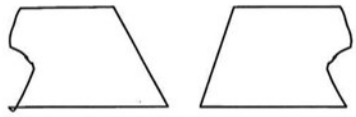	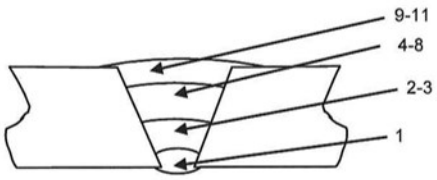

PARAMÈTRES DE SOUDAGE - EINZELHEITEN FÜR DAS SCHWEISSEN - *WELDING DETAILS*

Prüfstück/Lage *Test Piece/Run* **Coupon/Passe** **Nr.-*No.-N°* / ++**	Prozeß *Process* **Procédé**	Schweißzusatz *Filler Metal* **Métal d´apport** **Ø [mm]**	Stromstärke *Current* **Ampérage** **[A]**	Spannung *Voltage* **Tension** **[V]**	Stromart/ Polung *Type of current/ Polarity* **Type de courant/**	Drahtvorschub/ Schweißgeschwindigkeit *Wire Feed/Travel Speed* **Vitesse de déroulement du fil / Vitesse d´avance** **[cm/min] *)**	Wärme-einbringung *Heat Input* **Énergie de soudage** **[kJ/cm] *)**
1 W	138 acc	1.2	142	21	DC +	3.7 / 16	8.9
2-3 F	138 apa	1.2	277	30.8	DC +	10.2 / 24.3	16.9
5-8 F	138 apa	1.2	277	30.8	DC +	10.2 / 39.5	10.4
9-11 D	138 apa	1.2	280	31	DC +	10.2 / 41.2	10.1

acc= arc court circuit
apa= arc pulvérisation axiale

++ W = Wurzellage - *Root Pass Weld* - **Passe de fond**
F = Füllage - *Filler Pass Run* - **Passe de remplissage**
D = Decklage - *Cover Pass* - **Passe de finition**
K = Gegenlage - *Capping Pass* - **Passe de reprise a l´envers**
P = Plattierung - *Cladding* - **Placage**
oder Nr. gem. Zeichnung - *or No. according sketch* - **ou N° suivant croquis**

*) falls erforderlich / *if required* / **si nécessaire**

AC Contrôle Sàrl
NDT Laboratoire d'essai des matériaux
CND-NDT / Technique de soudage
Av. de la Gare 41, 1870 Monthey 1
Succ. Rte des Courtraits 13, 1880 Bex
LEM

Prüf-Nr.: VP | Auftrags-Nr.: 43303-ZM | SVTI-Lauf-Nr. | Seite 3 von 6
Inspetion No.: | *Reference No.:* | TÜV-Lauf-Nr. | *Page of*
N° d'inspection: 38L | **N° de référence:** | | **Page de**

DÉFINITION DU TÉMOIN SOUDÉ (2)

EINZELHEITEN ZUR PRÜFSTÜCKSCHWEISSUNG / (2)*DETAILS OF WELD TEST (2)*

Zusatzwerkstoff - *Filler Metal* - **Métal d´apport**

Type, Bezeichnung, Handelsbezeichnung: *Type, Designation, Trade name:* **Type, Désignation, Marque de fabrique:** Filarc PZ 6102, lot PV3230541 EN ISO 17632A : T 46 M M 2 H5

Sondervorschriften für Trocknung oder Lagerung: *Any Special Drying or Baking:* **Précautions de séchage ou d´étuvage:** Selon indications du fabricant

Schutzgas: *Shielding Gas:* **Gaz de protection:** M21 — Gasdurchflußmenge [l/min]: *Gas Flow Rate [l/min]:* **Débit gazeux [l/min]:** 18

Wurzelschutz: *Backing Gas:* **Purge:** -- — Gasdurchflußmenge [l/min]: *Gas Flow Rate [l/min]:* **Débit gazeux [l/min]:** --

Pulver: *Flux:* ***Flux:*** --

Wolframelektrode, *Tungsten Electrode,* **Électrode de tungstène,** Art /Durchmesser: *Type / Size:* **Type / Dimension:** --

Einzelheiten über Ausfugen / Badsicherung: *Details of Back Gouging / Backing:* **Détails sur la reprise à l´envers:** --

Vorwärmtemperatur [°C]: *Preheat Temperature [°C]:* **Température de préchauffage [°C]:** 60°C — Zwischenlagentemperatur [°C]: *Interpass Temperature [°C]:* **Température entre passes [°C]:** <250

Weitere Informationen *): *Other Information *):* **Autres paramètres *):** --

TRAITEMENT THERMIQUE APRÈS SOUDAGE - WÄRMENACHBEHANDLUNG - *POST WELD HEAT TREATMENT*

Verfahren / Bemerkungen *Method / Remarks* **Méthode / Remarques**	Aufheizrate [°C/h] *) *Heating Rate* **Vitesse de chauffage**	Haltedauer [min] *Holding Time* **Temps de maintien**	Haltetemperatur [°C] *Hold Temperature* **Temp. de maintien**	Abkühlrate [°C/h] *) *Cooling Rate* **Vit. de**
aucun				

Das vorbezeichnete Prüfstück wurde geschweißt in Anwesenheit von:
The above test piece was welded in the presence of:
Le coupon témoin ci-dessus a été soudé en présence de:
N. Moussaoui , EWE

Name und Unterschrift des Zertifizierers: *Name and Signature:* **Nom et signature:**

Zertifizierstelle: *Certification Body:* **Organisme de certification:** AC Contrôle Sàrl 1880 BEX

*) falls erforderlich / *if required* / **si nécessaire**

AC Contrôle Sàrl
NDT Laboratoire d'essai des matériaux
CND-NDT / Technique de soudage
Av. de la Gare 41, 1870 Monthey 1
Succ. Rte des Courtraits 13, 1880 Bex
LEM

Prüf-Nr.: VP / *Inspetion No.:* / **N° d'inspection: 38L**
Auftrags-Nr.: **43303-ZM** / *Reference No.:* / **N° de référence:**
SVTI-Lauf-Nr. / TÜV-Lauf-Nr.
Seite 4 von 6 / *Page of* / **Page de**

RÉSULTATS DES ESSAIS (1)

PRÜFERGEBNISSE (1) / *TEST RESULTS (1)*

Sichtprüfung: / *Visual Examination:* / **Examen visuel:**	erfüllt / *satisfactory* / **satisfaisant**	Durchstrahlungsprüfung *): / *Radiography *):* / **Radiographie *):**	na
Farbeindring- / Magnetpulverprüfung *): / *Penetrant / Magnetic Particle Test *):* / **Ressuage / Magnétoscopie *):**	erfüllt / *satisfactory* / **satisfaisant**	Ultraschallprüfung *): / *Ultrasonic Examination *):* / **Ultrasons *):**	erfüllt / *satisfactory* / **satisfaisant**

ESSAIS DE TRACTION - ZUGPRÜFUNG - TENSILE TESTS

Temperatur [°C]: / Temperature:/**Température:** RT

Nr. *No.* **N°**	Pos. *Loc.* **Pos.**	Art **) *Sort* **) **Nature** **)	Abmessungen *Dimensions* **Dimensions** [mm x mm]	Re [MPa]	Rp 0,2/1,0 [MPa]	Rm [MPa]	A [%] an / *on* / **sur** L_0 [mm]: __	Z [%]	Bruchlage ***) *Fracture Locat.* **Posit. rupture**	Bemerkungen *Remarks* **Remarques**
Anforderungen Requirements /				345		470-630	20		--	--
38L-1	PA	TW	7x20	481		509	-		PM-GWL	
38L-2	PA	TW	7x20	494		509	-		PM-GWL	

) TW = Quer zur Naht - *Transv. to the Weld* - **Travers soudure
AW = Schweißgutprobe - *All-weld Metal* - **Métal déposé**

***) PM = Grundwerkstoff - *Base Material* - **Métal de base**
H = WEZ -*HAZ* - **ZAT**
W = Schweißgut - *Weld Metal* - **Métal déposé**
GWL = Bruch außerh. L_0 - *Fracture outside L_0* - **Cassure hors de L_0**

ESSAI DE PLIAGE - BIEGEPRÜFUNG - BEND TEST

Biegedorn-Durchmesser : / Former Diameter:/**Diamètre du mandrin:** 4 x t

Nr. *No.* **N°**	Pos. *Loc.* **Pos.**	Art **) *sort***)* **nature** **)	Dicke *thickn.* **épaiss.** [mm]	Biegewinkel/-dehnung *bend. angle /elongation* **angle-allong. de pliage** ∢	L_0 [mm]	%	Bemerkung *Remark* **Remarque**	Nr. *No.* **N°**	Pos. *Loc.* **Pos.**	Art **) *sort***)* **nature** **)	Dicke *thickn.* **épaiss**	Biegewinkel/-dehnung *bend. angle /elongation* **angle-allong. de pliage** ∢	L_0 [mm]	%	Bemerkung *Remark* **Remarque**
38L-1	PA	S	10	180			Aucune rupture	38L-3	PA	S	10	180			Aucune rupture
38L-2	PA	S	10	180			Aucune rupture	38L-4	PA	S	10	180			Aucune rupture

) **F = Decklage in Zugzone - Face - **Endroit** **R** = Wurzel/Gegenseite in Zugzone - Root/Back side - **Envers** **S** = Seitenbiegeprobe - Side - **Côté**

ESSAIS DE RESILIENCE

KERBSCHLAGBIEGEPRÜFUNG - *IMPACT TESTS*

Art: / *Sort:* / **Nature:** Charpy-V

Anforderung [J]: / *Requirements [J]:* / **Exigences [J]:** ≥ 40

Nr. *No.* **N°**	Position *Location* **Position**	Kerblage *Notch Location* Sens de l'entaille	Größe *Size*/**Dimens.** [mm x mm]	Temp. *Temp.*/**Temp.** [°C]	Werte - *Values* - **Valeurs** [J] 1	2	3	Σn/n [J]	Bemerkungen *Remarks* **Remarques**
38L-1	PA	VWT	10x8	-20	70	68	69	69	
38L-2	PA	VHT	10x8	-20	68	72	68	69	

- bei Untermaßproben sind die Kerbschlagwerte hochzurechnen — Arbeitsvermögen des Pendelschlagwerks: 300 J

*) falls erforderlich / *if required* / **si nécessaire**

AC Contrôle Sàrl
NDT Laboratoire d'essai des matériaux
CND-NDT / Technique de soudage
Av. de la Gare 41, 1870 Monthey 1
Succ. Rte des Courtrails 13, 1880 Bex
LEM

Prüf-Nr.: VP *Inspection No.:* **N° d'inspection: 38L** | Auftrags-Nr.: 43303-ZM *Reference No.:* **N° de référence:** | SVTI-Lauf-Nr. TÜV-Lauf-Nr. | Seite 5 von 6 *Page of* **Page de**

RÉSULTATS DES ESSAIS (2)

PRÜFERGEBNISSE (2) / *TEST RESULTS (2)*

ANALYSE CHIMIQUE [%]

CHEMISCHE ANALYSE - [%]*CHEMICAL COMPOSITION [%]* *)

PM =Grundwerkstoff - *Base Material* - **Métal de base**
WM =Schweißgut - *Weld Metal* - **Métal déposé**

Nr. *No.* N°	Art *Sort* Nature	C	Si	Mn	P	S						

*ESSAI DE DURETE *)*

HÄRTEPRÜFUNG *) - *HARDNESS TEST **

Lage der Messungen (Skizze) *)
*Location of Measurements (Sketch) *)*
Localisation des mesures (croquis) *)

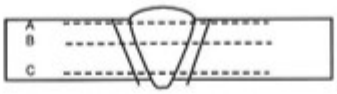

Art /Last: - *Type / Load:* - **Type / Charge:** **Vickers 10kp**

Nr. *No.* N°	Meßreihe *Measuring Line* Ligne de mesure	Grundwerkstoff *Base Material* Métal de base			WEZ *HAZ* ZAT			Schweißgut *Weld Metal* Métal déposé			WEZ *HAZ* ZAT			Grundwerkstoff *Base Material* Métal de base		
38L	A	147	156	165	228	221	213	225	228	235	245	254	264	193	191	193
	B	147	156	181	187	193	199	199	206	213	236	206	206	206	181	185
	C	143	156	193	187	187	193	199	193	206	213	206	193	181	181	181

EXAMEN DE LA STRUCTURE - GEFÜGEUNTERSUCHUNG - *TEXTURE EXAMINATION*

Fotos / **photos :** Seite **Page 6**

Nr. *No.* N°	Position *Location* Position	Gefüge *Texture/* Structure Makro Macro	Gefüge *Texture/* Structure Mikro Micro	Gefügebeurteilung *Texture Assessment*/Analyse de la structure
38L		X		Succession des passes convenable et fusion parfaite
38l			X	Sans fissures ni défauts de structure
				fehlerfreier Nahtaufbau und einwandfreie Durchschweißung
				frei von Rissen und Gefügefehlern

AUTRES ESSAIS - SONSTIGE PRÜFUNGEN - *OTHER TESTS**) / REMARQUES - BEMERKUNGEN - *REMARKS*

Die Prüfungen wurden ausgeführt in Anwesenheit von:
Test carried out in the presence of:
Les essais ont été effectués en présence de:

Laboratoire d'essai des matériaux
CH–1880 BEX

Die Prüfungen wurden entsprechend den Prüfgrundlagen durchgeführt.
The tests have been performed in accordance with the specifications.
Les essais ont été réalisés selon les spécifications.

Die Prüfergebnisse sind:
Test Results were:/
Les résultats des essais sont:

X zufriedenstellend *acceptable /* **acceptables**

nicht zufriedenstellend *not acceptable /* **non acceptables**

Name und Unterschrift des Zertifizierers:
Name and Signature:
Nom et signature:

Zertifizierstelle:
Certification Body:
Organisme de certification:

AC Contrôle Sàrl
1880 BEX

*) falls erforderlich / *if required* / **si nécessaire**

AC Contrôle Sàrl
NDT Laboratoire d'essai des matériaux
CND-NDT / Technique de soudage
Av. de la Gare 41, 1870 Monthey 1
Succ. Rte des Courtraits 13, 1880 Bex
LEM

Prüf-Nr.: VP *Inspetion No.:* **N° d'inspection: 38L**	Auftrags-Nr.: *Reference No.:* **N° de référence:**	**43303-ZM**	SVTI-Lauf-Nr. TÜV-Lauf-Nr.	Seite *Page* **Page**	6	von *of* **de**	6

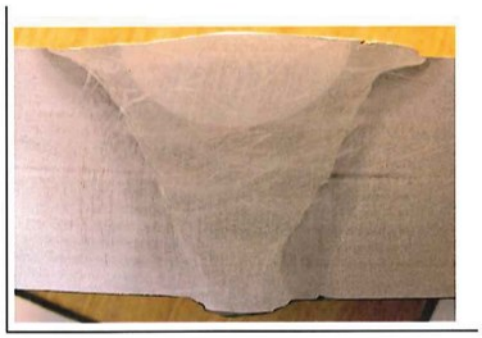

Photo. 38L M. 2 : 1

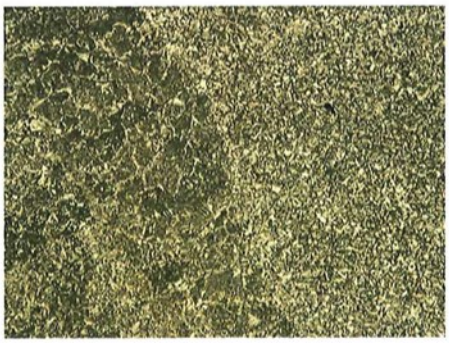

Photo. 38l M. 200 : 1

ZM CONSTRUCTIONS MÉTALLIQUES

DMOS-P

Spécification 1.4.H		Symbole du joint 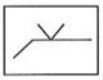	
Description :	Soudure à pénétration totale en V sans support et sans reprise envers		
Matériau de base :	S355 K2+N	épaisseurs :	20mm
Procédé :	MAG 138	QMOS N° :	

Préparation et séquences de soudage

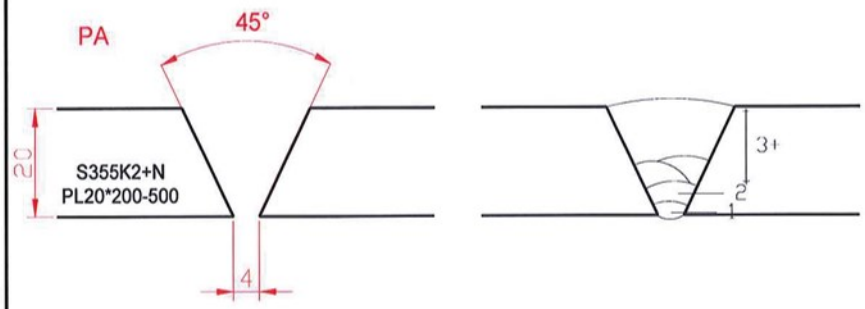

Procédé de soudage		Racine MAG 138			Remplissage MAG 138		
Passe n°		première			remplissage		
Fournisseur / type matière d'apport		Filarc / PZ 6102			Filarc / PZ 6102		
Désignation		EN 758 : T 46 4 M M 2 H5			EN 758 : T 46 4 M M 2 H5		
Diamètre		1.2mm			1.2mm		
Type et débit gaz		Argon / Co2 (M 21)			Argon / Co2 (M 21)		
Diamètre buse et stick out		16 / 20 litres /minutes			16 / 20 litres /minutes		
Position de soudage		PA			PA		
Polarité		DC +			DC +		
Mode de transfert		pulvérisation axiale			pulvérisation axiale		
Passe	**n°**	**1**	**2-3**		**3+**	**4+**	
Ampères	(±10%)	140	280	*A*	280	280	*A*
Volts	(±10%)	21	31	*V*	31	31	*V*
Vitesse fil	(±10%)	3.7	10	*m/min*	10	10	*m/min*
Vitesse d'avance	(±10%)	16	25	*cm/min*	40	40	*cm/min*
Apport de chaleur	(±25%)	8.8	16.7	*kJ/cm*	10.4	10.4	*kJ/cm*
Pré - chauffage		dégourdissage			dégourdissage		
Temp. entre passes		< 250°C			< 250°C		

Remarques :
QMOS à effectuer selon EN 15614 et EN 1090-2

Établi par :		NMO		
Date :		27.05.2014		
Version N°	0	27.05.2014		

ESAB

CERTIFICAT DE RÉCEPTION (3.1) - Analyse chimique
RELEVÉ DE CONTRÔLE (2.2) - Propriétés mécaniques/
INSPECTION CERTIFICATE (3.1) - Chemical analysis
TEST REPORT (2.2) - Mechanical properties

Date/Date: 2013-06-28

Numéro de certificat/Cert no: EC23013336 rev. 0

Notre commande/Our order:	616354	Votre commande/Your order:	FAX DU 27.05.13
Notre référence/Our ref:	Simone Schwarz Germany	Votre référence/Your ref:	
Compte client/Cust no:	CHB00017	Votre numéro de fax/Your fax:	
Date de commande client/Your date:	20130528	Votre e-mail/Your e-mail:	

Adresse de facturation/Invoice address
STUCKI SOUDURE SA

AU GRIVAZ
1607 PALEZIEUX
Switzerland

Destinataire du certificat/Cert receiver

Adresse de livraison/Delivery address
ZWAHLEN & MAYR SA
CONSTRUCTIONS METALLIQUES
ZONE INDUSTRIELLE 2
1860 AIGLE
Switzerland

LIVRAISON/DELIVERY Numéro de lot/Lot no: PV3230541 Quantité/Quantity: 313

PRODUIT/PRODUCT

Marque/Brand:	Filarc ✓
Description/Desc:	FILARC PZ6102 1.2mm 16kg
Numéro article/Item no:	**2621127730**

CLASSIFICATIONS/CLASSIFICATIONS

SFA/AWS A5.18	E70C-6M H4
EN ISO 17632-A	T 46 4 M M 2 H5

PROPRIÉTÉS MÉCANIQUES/MECHANICAL PROPS

Valeurs typiques/Typical data conforme à/acc to EN 10204 - 2.2

Standard/Standard:	EN
Autres/Auxiliary:	M21 (EN ISO 14175)
Condition/Condition:	As welded

ESSAI DE TRACTION/TENSILE

Rp0.2	Rm	A5
485 MPa	570 MPa	28.9 %

RÉSILIENCES/IMPACT

Temp	KV
-40 °C	75 J

COMPOSITION CHIMIQUE/ CHEMICAL COMPOSITION

Valeurs réelles/Actual results conforme à/acc to EN 10204 - 3.1

All weld metal

Autres/Auxiliary: M21 (EN ISO 14175)

C	0.09%
Si	0.71%
Mn	1.7%
P	0.012%
S	0.025%
Cr	0.03%
Ni	0.01%
Mo	0.01%
Nb	0.003%
Cu	0.01%
V	0.010%

COMMENTAIRES/COMMENTS

15.07.13

Produit fourni suivant programme AQ correspondant au standard EN ISO 9001.
Ce certificat est produit d'une façon électronique et valable sans signature.
Pour questions supplémentaires s.v.p. adressez-vous à:
ESAB AG, Neuhofstr. 4, CH-6340 Baar, Tel +41-44-7412525, Fax +41-44-7403055, info@esab.ch, www.esab.ch
Product supplied under a QA Programme fulfilling the EN ISO 9001 standard.
This certificate is produced electronically and is valid without signature.
Please refer any queries to: (see above)

Validation - Analyse chimique/Validation - Chemical Analysis		Validation - Autres/Validation - Others	
Milan Macek	Quality Manager	Shaun Studholme	Product Manager

AC Contrôle Sàrl
Laboratoire d'essai des matériaux
CND-NDT / Technique de soudage
Av. de la Gare 41, 1870 Monthey 1
Succ. Rte des Courtraits 13, 1880 Bex

Prüf-Nr.: VP *Inspetion No.:* **N° d'inspection: 39T**	Auftrags-Nr.: **43419-ZM** *Reference No.:* **N° de référence:**	SVTI-Lauf-Nr. TÜV-Lauf-Nr.	Seite 1 von 6 *Page of* **Page de**		

CERTIFICAT DE QUALIFICATION D´UN MODE OPÉRATOIRE DE SOUDAGE

WELDING PROCEDURE APPROVAL TEST CERTIFICATE / **ZERTIFIKAT - ANERKENNUNG VON SCHWEISSVERFAHREN (WPAR)**

Zertifizierstelle: *Certification Body:* **Organisme de certification:**	**AC Contrôle Sàrl** **CH-1870 Monthey**	Zeichen: *Sign:* **Timbre:**	39T
Hersteller / Anschrift: *Manufacturer / Address:* **Constructeur / Adresse:**	**Zwahlen & Mayr** **1860 Aigle**	Beleg-Nr. des Herstellers: *Manufacturer´s Reference No.:* **N° de référence du constructeur**	**DMOS** / WPS No. 1.1.N
Vorschrift/Prüfnorm: *Code/Testing Standard:* **Code / Norme d´essai:**	EN ISO 15614-1 EN 1090-2	Datum der Schweißung: *Date of Welding:* **Date du soudage:**	30.9.2014

DOMAINE DE VALIDITÉ - GELTUNGSBEREICH - *RANGE OF APPROVAL*

Prüfgegenstand: *Test object:* **Objet de l'examen:**	Té / double Té	Nahtart: *Joint Type:* **Type de joint:** s. EN 15614-1 / EN 288-4 Tab. 7/9	FW sl ml
Schweißprozeß: *Welding Process:* **Procédé de soudage:**	138	Dicke [mm]: *Parent Metal Thickness [mm]:* **Épaisseur du matériau [mm]:**	**10-40** gorge a : sl :3.7-7.5 gorge a : ml : tout
Werkstoffgruppe: *Parent Metal Group:* **Groupe de matériaux de base::**	Selon CR ISO 15608 1.2	Außendurchmesser [mm]: *Pipe Outside Diameter [mm]:* **Diamètre extérieur [mm]:**	≥ 500 (PA ≥ 150)
Zusatzwerkstoff/Bezeichn.: *Filler Metal Type/Designation* **Métal d´apport, type et désignation:**	Filarc PZ 6102 EN ISO 17632A : T 46 4 M M 2 H5	Stromart: *Type of Welding Current:* **Nature du courant de soudage:**	DC+
Schutzgas / Wurzelschutz: *Shielding Gas / Backing Gas:* **Gaz de protection / Purge:**	M21	Pulver: *Flux:* **Flux:**	--
Schweißpositionen: *Welding Positions:* **Positions de soudage:**	PB		
Betriebstemperatur: *Working Temperature:* **Température de service:**	Wie Grundwerkstoff bzw. Zusatzwerkstoff, jedoch nicht tiefer als : *As base material and filler metal respectively, however not lower than :* **Comme métal de base et métal d´apport respectivement, mais pas inférieure à :**		-20°C
Vorwärmung: *Preheat:* **Préchauffage:**	dégourdissage		
Wärmenachbehandlung: *Post Weld Heat Treatment:* **Traitement thermique après soudage:**	Aucun		

AUTRES PARAMÈTRES - SONSTIGE ANGABEN - *OTHER INFORMATION* -

Hiermit wird bestätigt, daß die Prüfungsschweißungen in Übereinstimmung mit den Anforderungen der vorbezeichneten Vorschriften bzw. Prüfnormen zufriedenstellend vorbereitet, geschweißt und geprüft wurden. */ Certified that test welds were pepared, welded and tested satisfactorily in accordance with the requirements of the code or the testing standard indicated above. /* **Nous certifions que les essais de soudage ont été préparés, soudés et contrôlés avec succès, conformément aux exigences du code ou de la norme d´essai ci-dessus mentionné(e).**

Ort: *Location:* **Lieu:**	Bex	Datum der Ausstellung: *Date of issue:* **Date d´émission:**	15.10.2014	Name und Unterschrift des Zertifizierers: *Name and Signature:* **Nom et signature:**	P. Attanasio IWE
Anlagen: *Annexes:* **Annexes:**	N° 1 **DMOS** / WPS n° 2 **Certificat de matière** - Werkstoffzeugniss			Zertifizierstelle: *Certification Body:* **Organisme de certification:**	AC Contrôle Sàrl 1880 BEX

AC Contrôle Sàrl
NDT **Laboratoire d'essai des matériaux**
CND-NDT / Technique de soudage
Av. de la Gare 41, 1870 Monthey 1
Succ. Rte des Courtraits 13, 1880 Bex
LEM

Prüf-Nr.: VP *Inspetion No.:* **N° d'inspection: 39T** | Auftrags-Nr.: **43419-ZM** *Reference No.:* **N° de référence:** | SVTI-Lauf-Nr. TÜV-Lauf-Nr. | Seite **2** von **6** *Page* **Page** *of* **de**

DÉFINITION DU TÉMOIN SOUDÉ (1)

EINZELHEITEN ZUR PRÜFSTÜCKSCHWEISSUNG (1) / *DETAILS OF WELD TEST (1)*

Hersteller: *Manufacturer:* **Constructeur:** **Zwahlen & Mayr 1860 Aigle**

Ort / Datum der Schweißung: *Location / Date of Welding:* **Lieu / Date du soudage:** Aigle 30.09.2014

Name des Schweißers: *Welder´s Name:* **Nom du soudeur:** Cibarro Baltazar

Art der Vorbereitung und Reinigung: *Method of Preparation and Cleaning:* **Méthode de préparation et nettoyage:** Oxycoupage, meulage

COUPONS - PRÜFSTÜCKE - TEST PIECES

Nr. *No.* **N°**	Schweißprozeß *Welding Process* **Procédé de soudage**	Dicke *Thickness* **Épaisseur [mm]**	Durchmesser *Outside Diameter* **Diamètre extérieur [mm]**	Schweißposition *Welding Position* **Pos. du soudage**	Nahtart *Joint Type* **Type de joint**	Grundwerkstoff (Spezifikation) *Parent Metal (Specification)* **Matériau de base (spécification)** Zeugnis liegt vor/*Certific. submitted/Certific. presenté**)
39T	138	20	--	PB	FW sl FW ml	S355K2+N, DG95

PRÉPARATION DE L´ASSEMBLAGE (croquis)* - NAHTVORBEREITUNG (Zeichnung)* - *WELD PREPARATION (Sketch)**

Gestaltung der Verbindung / *Joint Design* / **Réalisation de l´assemblage**

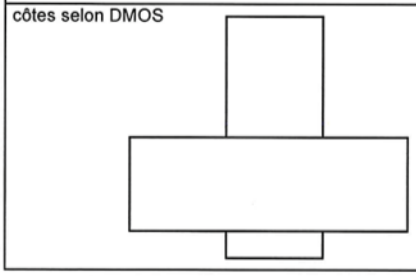

Schweißfolge / *Welding Sequence* / **Répartition des passes**

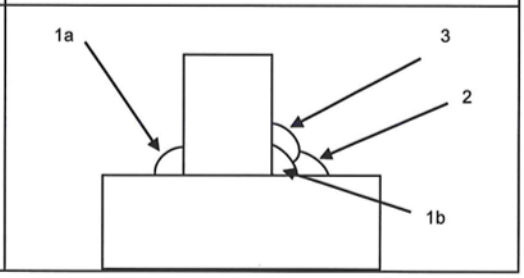

PARAMÈTRES DE SOUDAGE - EINZELHEITEN FÜR DAS SCHWEISSEN - *WELDING DETAILS*

Prüfstück/Lage *Test Piece/Run* **Coupon/Passe** **Nr.-*No.-N°* / ++**	Prozeß *Process* **Procédé**	Schweißzusatz *Filler Metal* **Métal d´apport** **Ø [mm]**	Stromstärke *Current* **Ampérage** **[A]**	Spannung *Voltage* **Tension** **[V]**	Stromart/ Polung *Type of current/ Polarity* **Type de courant/**	Drahtvorschub/ Schweißgeschwindigkeit *Wire Feed/Travel Speed* **Vitesse de déroulement du fil / Vitesse d´avance [cm/min] *)**	Wärme-einbringung *Heat Input* **Énergie de soudage [kJ/cm] *)**
1a, 1b	138	1.2	250	30.0	DC +	9.8 / 30	12.0
2	138	1.2	255	29.6	DC +	9.8 / 34	10.7
3	138	1.2	250	29.6	DC +	9.8 / 35	10.1

Arc pulvérisation axiale

Pour traction en croix selon EN ISO 9018, 4 soudures identiques sont réalisées
Soit 4 fois 1a (épr.39Ts), soit 4 fois 1b+2+3 (épr.39Tm).

++ W = Wurzellage - *Root Pass Weld* - **Passe de fond**
F = Füllage - *Filler Pass Run* - **Passe de remplissage**
D = Decklage - *Cover Pass* - **Passe de finition**
K = Gegenlage - *Capping Pass* - **Passe de reprise a l´envers**
P = Plattierung - *Cladding* - **Placage**
oder Nr. gem. Zeichnung - *or No. according sketch* - **ou N° suivant croquis**

*) falls erforderlich / *if required* / **si nécessaire**

AC Contrôle Sàrl
NDT Laboratoire d'essai des matériaux
CND-NDT / Technique de soudage
Av. de la Gare 41, 1870 Monthey 1
Succ. Rte des Courtraits 13, 1880 Bex

Prüf-Nr.: VP *Inspetion No.:* **N° d'inspection: 39T**	Auftrags-Nr.: *Reference No.:* **N° de référence:**	**43419-ZM**	SVTI-Lauf-Nr. TÜV-Lauf-Nr.	Seite *Page* **Page**	3	von *of* **de**	6

DÉFINITION DU TÉMOIN SOUDÉ (2)

EINZELHEITEN ZUR PRÜFSTÜCKSCHWEISSUNG / (2)*DETAILS OF WELD TEST (2)*

Zusatzwerkstoff - *Filler Metal* - **Métal d´apport**

Type, Bezeichnung, Handelsbezeichnung: *Type, Designation, Trade name:* **Type, Désignation, Marque de fabrique:**	Filarc PZ 6102, lot PV 4260581 EN ISO 17632A : T 46 4 M M 2 H5
Sondervorschriften für Trocknung oder Lagerung: *Any Special Drying or Baking:* **Précautions de séchage ou d´étuvage:**	Selon indications du fabricant

Schutzgas: *Shielding Gas:* **Gaz de protection:**	M21	Gasdurchflußmenge [l/min]: *Gas Flow Rate [l/min]:* **Débit gazeux [l/min]:**	18
Wurzelschutz: *Backing Gas:* **Purge:**	--	Gasdurchflußmenge [l/min]: *Gas Flow Rate [l/min]:* **Débit gazeux [l/min]:**	--
Pulver: *Flux:* ***Flux:***	--		
Wolframelektrode, *Tungsten Electrode,* **Électrode de tungstène,**	Art /Durchmesser: *Type / Size:* **Type / Dimension:**	--	
Einzelheiten über Ausfugen / Badsicherung: *Details of Back Gouging / Backing:* **Détails sur la reprise à l´envers:**		--	
Vorwärmtemperatur [°C]: *Preheat Temperature [°C]:* **Température de préchauffage [°C]:**	50°C	Zwischenlagentemperatur [°C]: *Interpass Temperature [°C]:* **Température entre passes [°C]:**	<250
Weitere Informationen *): *Other Information *):* **Autres paramètres *):**	--		

TRAITEMENT THERMIQUE APRÈS SOUDAGE - WÄRMENACHBEHANDLUNG - *POST WELD HEAT TREATMENT*

Verfahren / Bemerkungen *Method / Remarks* **Méthode / Remarques**	Aufheizrate [°C/h] *) *Heating Rate* **Vitesse de chauffage**	Haltedauer [min] *Holding Time* **Temps de maintien**	Haltetemperatur [°C] *Hold Temperature* **Temp. de maintien**	Abkühlrate [°C/h] *) *Cooling Rate* **Vit. de**
aucun				

Das vorbezeichnete Prüfstück wurde geschweißt in Anwesenheit von:
The above test piece was welded in the presence of:
Le coupon témoin ci-dessus a été soudé en présence de:
N. Moussaoui , EWE

Name und Unterschrift des Zertifizierers:
Name and Signature:
Nom et signature:
P. Athanasiadès EWE

Zertifizierstelle:
Certification Body:
Organisme de certification:
AC Contrôle Sàrl
1880 BEX

*) falls erforderlich / *if required* / **si nécessaire**

AC Contrôle Sàrl
NDT Laboratoire d'essai des matériaux
CND-NDT / Technique de soudage
Av. de la Gare 41, 1870 Monthey 1
Succ. Rte des Courtraits 13, 1880 Bex

Prüf-Nr.: VP / *Inspetion No.:* / **N° d'inspection: 39T** | Auftrags-Nr.: / *Reference No.:* / **N° de référence:** **43419-ZM** | SVTI-Lauf-Nr. / TÜV-Lauf-Nr. | Seite / *Page* / **Page** 4 von / *of* / **de** 6

RÉSULTATS DES ESSAIS (1)

PRÜFERGEBNISSE (1) / *TEST RESULTS (1)*

Sichtprüfung: / *Visual Examination:* / **Examen visuel:**	erfüllt / *satisfactory* / **satisfaisant**	Durchstrahlungsprüfung *): / *Radiography *):* / **Radiographie *):**	na
Farbeindring- / Magnetpulverprüfung *): / *Penetrant / Magnetic Particle Test *):* / **Ressuage / Magnétoscopie *):**	erfüllt / *satisfactory* / **satisfaisant**	Ultraschallprüfung *): / *Ultrasonic Examination *):* / **Ultrasons *):**	na

ESSAIS DE TRACTION - ZUGPRÜFUNG - TENSILE TESTS

Temperatur [°C]: / Temperature:/**Température:** RT

Nr. *No.* **N°**	Pos. *Loc.* **Pos.**	Art **) *Sort* **) **Nature** **)	Abmessungen *Dimensions* **Dimensions** [mm x mm]	Re [MPa]	Rp 0,2/1,0 [MPa]	Rm [MPa]	A [%] an / *on* / **sur** L_0 [mm]: 50	Z [%]	Bruchlage ***) *Fracture Locat.* **Posit. rupture**	Bemerkungen *Remarks* **Remarques**
Anforderungen / Requirements /			surf. rupture			> 376 (PM=470)			--	d'après EN ISO 9018
39Ts	PB	TW	503.42			551			W	
39Ts	PB	TW	465.66			581			W	
39Ts	PB	TW	445.23			583			W	
39Tm	PB	TW	609.01			528			W	
39Tm	PB	TW	636.34			495			W	
39Tm	PB	TW	594.00			556			PM	

) TW = Quer zur Naht - *Transv. to the Weld* - **Travers soudure
AW = Schweißgutprobe - *All-weld Metal* - **Métal déposé**

***) PM = Grundwerkstoff - *Base Material* - **Métal de base**
H = WEZ -*HAZ* - **ZAT**
W = Schweißgut - *Weld Metal* - **Métal déposé**
GWL = Bruch außerh. L_0 - *Fracture outside* L_0 - **Cassure hors de** L_0

ESSAI DE PLIAGE - BIEGEPRÜFUNG - BEND TEST

Biegedorn-Durchmesser : / Former Diameter:/**Diamètre du mandrin**: 4 x t

Nr. *No.* **N°**	Pos. *Loc.* **Pos.**	Art **) *sort***)* **nature** **)	Dicke *thickn.* **épaiss.** [mm]	Biegewinkel/-dehnung *bend. angle /elongation* **angle-allong. de pliage** ∢	L_0 [mm]	%	Bemerkung *Remark* **Remarque**	Nr. *No.* **N°**	Pos. *Loc.* **Pos.**	Art **) *sort***)* **nature** **)	Dicke *thickn.* **épaiss**	Biegewinkel/-dehnung *bend. angle /elongation* **angle-allong. de pliage** ∢	L_0 [mm]	%	Bemerkung *Remark* **Remarque**
															na

) F = Decklage in Zugzone - Face - **Endroit R = Wurzel/Gegenseite in Zugzone - Root/Back side - **Envers** S = Seitenbiegeprobe - Side - **Côté**

ESSAIS DE RESILIENCE

KERBSCHLAGBIEGEPRÜFUNG - *IMPACT TESTS*

Art: / *Sort:* / **Nature:** Charpy-V

Anforderung [J]: / *Requirements [J]:* / **Exigences [J]:** ≥ 40

Nr. *No.* **N°**	Position *Location* **Position**	Kerblage *Notch Location* Sens de l´entaille	Größe *Size*/**Dimens.** [mm x mm]	Temp. *Temp.*/**Temp.** [°C]	Werte - *Values* - **Valeurs** [J] 1 2 3	Σn/n [J]	Bemerkungen *Remarks* **Remarques**
							na

- bei Untermaßproben sind die Kerbschlagwerte hochzurechnen — Arbeitsvermögen des Pendelschlagwerks: 300 J

*) falls erforderlich / *if required* / **si nécessaire**

AC Contrôle Sàrl
NDT Laboratoire d'essai des matériaux
CND-NDT / Technique de soudage
Av. de la Gare 41, 1870 Monthey 1
Succ. Rte des Courtraits 13, 1880 Bex

Prüf-Nr.: VP *Inspetion No.:* **N° d'inspection: 39T** | Auftrags-Nr.: **43419-ZM** *Reference No.:* **N° de référence:** | SVTI-Lauf-Nr. TÜV-Lauf-Nr. | Seite 5 von 6 *Page of* **Page de**

RÉSULTATS DES ESSAIS (2)
PRÜFERGEBNISSE (2) / *TEST RESULTS (2)*

ANALYSE CHIMIQUE [%]
CHEMISCHE ANALYSE - [%]*CHEMICAL COMPOSITION [%]* *)

PM =Grundwerkstoff - *Base Material* - **Métal de base**
WM =Schweißgut - *Weld Metal* - **Métal déposé**

Nr. *No.* N°	Art *Sort* Nature	C	Si	Mn	P	S						

*ESSAI DE DURETE *)*
HÄRTEPRÜFUNG *) - *HARDNESS TEST *)*

Lage der Messungen (Skizze) *)
*Location of Meassurements (Sketch) *)*
Localisation des mesures (croquis) *)

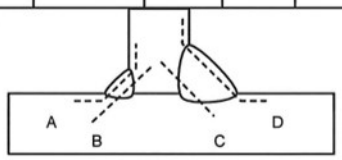

Art /Last: - *Type / Load:* - **Type / Charge:** **Vickers 10kp**

Nr. *No.* N°	Meßreihe *Measuring Line* Ligne de mesure	Grundwerkstoff *Base Material* Métal de base			WEZ *HAZ* ZAT			Schweißgut *Weld Metal* Métal déposé			WEZ *HAZ* ZAT			Grundwerkstoff *Base Material* Métal de base		
39T	A sl	175	164	181	228	274	351	274	236	228	351	322	236	193	170	160
	B sl	151	170	181	254	285	351	233	236	236	309	297	274	193	160	163
	C ml	160	176	179	206	221	285	228	228	221	297	254	236	181	181	160
	D ml	160	165	165	221	245	309	233	213	297	213	213	213	176	160	160
			base											gousset		

EXAMEN DE LA STRUCTURE - GEFÜGEUNTERSUCHUNG - *TEXTURE EXAMINATION*

Fotos / **photos** : Seite **Page 6**

Nr. *No.* N°	Position *Location* Position	Gefüge *Texture/* **Structure** Makro **Macro**	Mikro **Micro**	Gefügebeurteilung *Texture Assessment/***Analyse de la structure**
39T sl	PB	X		Succession des passes convenable et fusion parfaite
39T ml	PB	X		Sans fissures ni défauts de structure
				fehlerfreier Nahtaufbau und einwandfreie Durchschweißung
				frei von Rissen und Gefügefehlern

AUTRES ESSAIS - SONSTIGE PRÜFUNGEN - *OTHER TESTS*)* / REMARQUES - BEMERKUNGEN - *REMARKS*

Die Prüfungen wurden ausgeführt in Anwesenheit von:
Test carried out in the presence of:
Les essais ont été effectués en présence de:

Laboratoire d'essai des matériaux CH–1880 BEX

Die Prüfungen wurden entsprechend den Prüfgrundlagen durchgeführt.
The tests have been performed in accordance with the specifications.
Les essais ont été réalisés selon les spécifications.

Die Prüfergebnisse sind:
Test Results were:/
Les résultats des essais sont:

X zufriedenstellend *acceptable / acceptables*

nicht zufriedenstellend *not acceptable /* **non acceptables**

Name und Unterschrift des Zertifizierers:
Name and Signature:
Nom et signature:

P. Athanasiadès
IWE
AC Contrôle Sàrl
1880 BEX

Zertifizierstelle:
Certification Body:
Organisme de certification:

*) falls erforderlich / *if required* / **si nécessaire**

AC Contrôle Sàrl
NDT Laboratoire d'essai des matériaux
CND-NDT / Technique de soudage
Av. de la Gare 41, 1870 Monthey 1
Succ. Rte des Courtraits 13, 1880 Bex
LEM

Prüf-Nr.: VP *Inspetion No.:* **N° d'inspection: 39T**	Auftrags-Nr.: *Reference No.:* **N° de référence:**	**43419-ZM**	SVTI-Lauf-Nr. TÜV-Lauf-Nr.	Seite *Page* **Page**	6	von *of* **de**	6

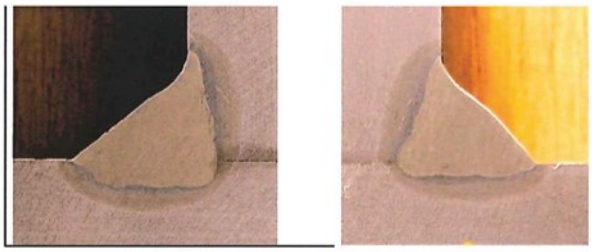

Photo. 39T sl 1+2 (a= 5) M. 3 : 1

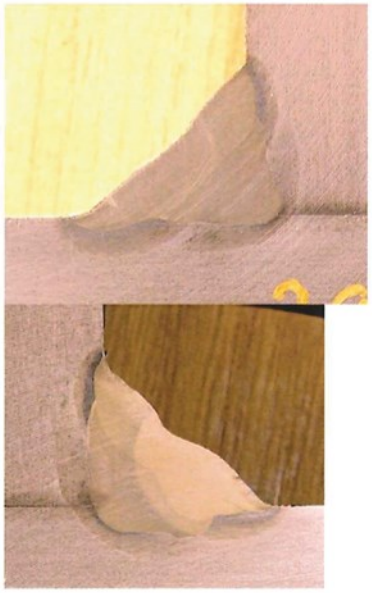

39T ml 1+2 (a = 9) M. 3 : 1

ZM CONSTRUCTIONS MÉTALLIQUES

SPECIFICATION DE SOUDAGE

Spécification 1.1.N	Symbole du joint 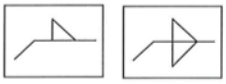		
Description :	Cordon d'angle mono et multipasse		
Matériau de base :	S355K2N / S355K2N	épaisseurs :	10 - 40 mm
Procédé :	MAG 138	QMOS No :	43419-39T

Préparation et séquences de soudage

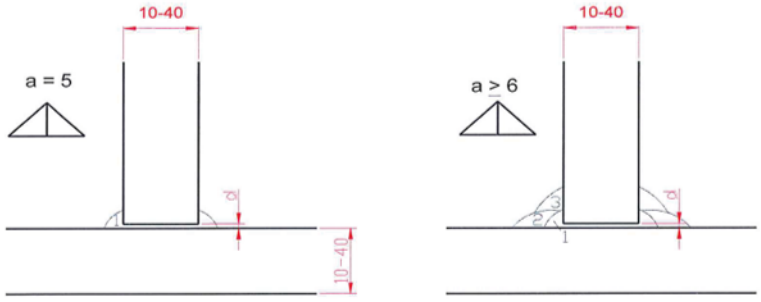

Talon bloqué : d = 0
EXC 4 : d ≤ 1 mm
EXC 3 : d ≤ 2mm

Procédé de soudage		Racine MAG 138		Remplissage MAG 138		
Passe n°		1		2 à n		
Fournisseur / type matière d'apport		Filarc / PZ 6102		Filarc / PZ 6102		
Désignation		EN 758 : T 46 4 M M 2 H5		EN 758 : T 46 4 M M 2 H5		
Diamètre		1.2mm		1.2mm		
Type gaz / poudre		Argon / Co2 (M 21)		Argon / Co2 (M 21)		
Débit gaz		16 / 20 litres /minutes		16 / 20 litres /minutes		
Position de soudage		PB		PB		
Polarité		DC+		DC+		
Mode de transfert		pulvérisation axiale		pulvérisation axiale		
Passe n°		1		2	3+	
Ampères	(±10%)	250	*A*	255	250	*A*
Volts	(±10%)	30	*V*	29.6	29.6	*V*
Vitesse fil	(±10%)	9.8	*m/min*	9.8	9.8	*m/min*
Vitesse d'avance	(±10%)	30	*cm/min*	34	35	*cm/min*
Apport de chaleur	(±15%)	12.0	*kJ/cm*	10.7	10.1	*kJ/cm*
Pré - chauffage		Dégourdissage				
Temp. entre passes				< 250°C		

Remarques :				
Établi par :		NMO	YUR	
Date :		02.09.2014	20.10.2014	
Version N°	1	02.09.2014	20.10.2014	

AC Contrôle Sàrl
Route de Clos-Donroux 1, 1870 Monthey
Tel. +41 24 472 21 51, Fax +41 24 472 21 52

Laboratoire d'essai des matériaux
CH - 1870 Monthey

Prüf-Nr.: VP Inspetion No.: **N° d'inspection: 26P**	Auftrags-Nr.: **ZM** Reference No.: **N° de référence: 26P - 41661**	SVTI-Lauf-Nr. TÜV-Lauf-Nr.	**Seite** Page Page	1	**von** of de	3

CERTIFICAT DE QUALIFICATION D´UN MODE OPÉRATOIRE DE SOUDAGE

Zertifizierstelle:
Certification Body:
Organisme de certification:
AC Contrôle Sàrl
CH-1870 Monthey

Zeichen: **26P**
Sign:
marquage

Hersteller / Anschrift:
Manufacturer / Address:
Constructeur / Adresse:
Zwahlen & Mayr
1860 Aigle

Beleg-Nr. des Herstellers: **DMOS**
Manufacturer´s Reference No.: **(WPS) No.**
N° de référence du constructeur: **5.1**

Vorschrift/Prüfnorm:
Code/Testing Standard:
Code/Norme d´essai:
SVTI 505
NF EN ISO 14555 / NF A89-020-1 / NFA 89-021-1

Datum der Schweißung: **26.8.09**
Date of Welding:
Date du soudage:

Etendue des contrôles selon NF EN ISO 14555 et NFA89-020-1 Prüfumfang nach *EN ISO 14555 und NFA89-020-1*	**goujon sur tôle** Bolzen auf Blech / *stud on sheet metal /*
Bolzenschweißverfahren: **783** *stud welding procedure/mode opératoire de soudage de goujons* Bolzenschweißen mit: **Fusion et forgeage avec bague en céramique** *stud welding with/ soudage de goujons avec*	Bolzendurchmesser (mm): **13** *diameter of stud/diamètre du goujon (mm)* Bolzendurchmesser (mm): **22** *diameter of stud/diamètre du goujon (mm)*
Bolzenwerkstoff nach ISO 13918: **S235J2G3** *materialof stud under* ISO 13918 */matériau du goujon selon* ISO 13918	Bolzenlänge (mm): **150** *length of stud/longueur du goujon (mm)*
Grundwerkstoff nach DIN EN 10 025: **S355K2** *basic material under DIN EN 10 025/matériau de base selon DIN EN 10 025*	Bolzenkennzeichnung: **Köcö // Nelson** *registration of stud/désignation du goujon*
Stähle nach EN ISO 15614-1, Tab. 3, Gruppe: **1.2** *steels under/acier selon EN ISO 15614-1, Tab. 3, group/groupe*	Bezeichnung des Keramikringes: **P 10** *marking of ceramic ring/spécification d'annau céramique*
	Rücktrocknung des Keramikringes: **non** *redrying of cermaic ring/reséchage d'annau céramique*
Dicke des Grundwerkstoffes (mm): **25** *thikness of basic material/épaisseur matériau de base (mm):*	
	Dämpfung / amortisseur: **oui**
Schweißposition (Pistolen-Position): **PA** *position of welding gun/du pistolet*	Stromquelle: **Köcö 2600 E / VDE 0542** *currency / source de courant*
Vorwärmtemperatur: (°C): **20°C** *temperature of pre-warming/de préchauffage : (°C)*	Schweißpistole/kopf: **K 24** *welding gun(head)/pistolet(tête)*
Soudeur .**Lhote, n° 3**	Steuergerät: **na** *control system/commande*

Schweißstrom ***welding current/courant de soudage*** **[A]**	**Schweißzeit** ***weld time/temps de passa courant de soudage*** **[ms]**	**Überstand** ***protrusion/dépassement*** **[mm]**	**Abhub** ***lift/levée*** **[mm]**	**Plongée[mm]**	**Bemerkungen** ***remarks/remarques***
1000 **2000**	**500** **980**	5 5	1.5 3.0	4-5 5-6	

SONSTIGE ANGABEN - *OTHER INFORMATION - AUTRES PARAMÈTRES*

BILDBEILAGEN ZUR METALLOGRAFISCHEN UNTERSUCHUNG: siehe Seite 3 / Illustration of metallographic examination see page 3 / **Illustration de l'examen metallographique voir page 3**
EINZELHEITEN ZUR PRÜFSTÜCKSCHWEISSUNG UND/ SCHWEISSANWEISUNG (WPS): siehe Seite(n) **4** / see page 4 for details of welding spec (WPS) / **voir page 4 pour détails des données de soudure (WPS)**

Hiermit wird bestätigt, daß die Prüfungsschweißungen in Übereinstimmung mit den Anforderungen der vorbezeichneten Vorschriften bzw. Prüfnormen zufriedenstellend vorbereitet, geschweißt und geprüft wurden. */ Certified that test welds were pepared, welded and tested satisfactorily in accordance with the requirements of the code or the testing standard indicated above. / Nous certifions que les essais de soudage ont été préparés, soudés et contrôlés avec succès, conformément aux exigences du code ou de la norme d´essai ci-dessus mentionné(e).*

Ort: **Monthey**
Location:
Lieu:

Datum der Ausstellung: 30.9.2009
Date of issue:
Date d´émission:

Name und Unterschrift:
Name and Signature:
Nom et signature:
P. Athanasiadès, EWE

Anlagen: Einzelheiten zur Prüftstückschweissung
Annexes: WPS
Annexes: Abnahmeprüfzeugnis 3.1
(nicht zutreffendes streichen)

Zertifizierstelle:
Certification Body:
Organisme de certification:
AC Contrôle, Monthey

FO56276D/Rev.AP /27.08.09

AC Contrôle Sàrl
Route de Cios-Donroux 1, 1870 Monthey
Tel. +41 24 472 21 51, Fax +41 24 472 21 52

Laboratoire d'essai des matériaux
CH - 1870 Monthey

Prüf-Nr.: VP / Inspetion No.: / **N° d'inspection: 26P**
Auftrags-Nr.: **ZM** / Reference No.: / **N° de référence: 26P - 41661**
SVTI-Lauf-Nr. / TÜV-Lauf-Nr.
Seite 2 **von** 3 / Page of / Page de

RÉSULTATS DES ESSAIS

PRÜFERGEBNISSE / *TEST RESULTS*

1) Sichtprüfung / visual inspection / **examen visuel suivant EN ISO 14555 (17p.) et/ou NFA89-020-1 (36p.)**

critère	**Nombre de goujons essayés**	**Acceptés**	**Rebutés**	**Résultat conforme**
Verticalité	36 + 36	36 + 36	0	oui
Nivellement	36 + 36	36 + 36	0	oui
Raccordement du bourrelet par rapport au goujon	36 + 36	35 + 34	1 + 2	oui
Raccordement du bourrelet par rapport au support	36 + 36	35 + 35	1 + 1	oui
Défaut de compacité	36 + 36	36 + 36	0	oui
Excentrement du bourrelet	36 + 36	34 + 35	2 + 1	oui
Bourrelet avec projection de métal	36 + 36	36 + 36	0	oui
Essai au marteau	36 + 36	36 + 36	0	oui
Bemerkungen: remarks/**remarques**	Ø 13 mm + Ø 22 mm	Ø 13 + Ø 22		**Examen visuel réussi**

2) Biegeprüfung gemäß, EN ISO 14555 / bend test in according to EN ISO 14555/ **essais de pliage suivant EN ISO 14555 (60°) et NFA89-020-1 (90°)**

Probe Nr. specimen no/essai no.	**Biegewinkel bend angle / angle de pliage**	**Bruchlage loc. of fracture /pos. de cassure**	**Résultat conforme**	**Probe Nr. specimen no/essai no.**	**Biegewinkel bend angle / angle de pliage**	**Bruchlage loc. of fracture /pos. de cassure**	**Résultat conforme**
26P-13-1	90°	Aucune rupture	oui	26P-22-1	90°	Aucune rupture	oui
26P-13-2	90°	Aucune rupture	oui	26P-22-2	90°	Aucune rupture	oui
26P-13-3	90°	Aucune rupture	oui	26P-22-3	90°	Aucune rupture	oui
26P-13-4	90°	Aucune rupture	oui	26P-22-4	90°	Aucune rupture	oui
26P-13-5	90°	Aucune rupture	oui	26P-22-5	90°	Aucune rupture	oui
26P-13-6	90°	Aucune rupture	oui	26P-22-6	90°	Aucune rupture	oui
26P-13-7	90°	Aucune rupture	oui	26P-22-7	90°	Aucune rupture	oui
26P-13-8	90°	Aucune rupture	oui	26P-22-8	90°	Aucune rupture	oui
26P-13-9	90°	Aucune rupture	oui	26P-22-9	90°	Aucune rupture	oui
26P-13-10	90°	Aucune rupture	oui	26P-22-10	90°	Aucune rupture	oui
Bemerkungen **remarques**	Ø 13 mm				Ø 22 mm		**Essai de pliage réussi**

3) Essais de pliage alterné suivant NFA89-020-1

Probe Nr. specimen no/essai no.	**Biegewinkel bend angle / angle de pliage**	**Bruchlage loc. of fracture /pos. de cassure**	**Résultat conforme**	**Probe Nr. specimen no/essai no.**	**Biegewinkel bend angle / angle de pliage**	**Bruchlage loc. of fracture /pos. de cassure**	**Résultat conforme**
26P-13-1	20 x 30°	Aucune rupture	oui	26P-22-1	20 x 30°	Aucune rupture	oui
26P-13-2	20 x 30°	Aucune rupture	oui	26P-22-2	20 x 30°	Aucune rupture	oui
26P-13-3	20 x 30°	Aucune rupture	oui	26P-22-3	20 x 30°	Aucune rupture	oui
26P-13-4	20 x 30°	Aucune rupture	oui	26P-22-4	20 x 30°	Aucune rupture	oui
26P-13-5	20 x 30°	Aucune rupture	oui	26P-22-5	20 x 30°	Aucune rupture	oui
26P-13-6	20 x 30°	Aucune rupture	oui	26P-22-6	20 x 30°	Aucune rupture	oui
26P-13-7	20 x 30°	Aucune rupture	oui	26P-22-7	20 x 30°	Aucune rupture	oui
26P-13-8	20 x 30°	Aucune rupture	oui	26P-22-8	20 x 30°	Aucune rupture	oui
26P-13-9	20 x 30°	Aucune rupture	oui	26P-22-9	20 x 30°	Aucune rupture	oui
26P-13-10	20 x 30°	Aucune rupture	oui	26P-22-10	20 x 30°	Aucune rupture	oui
Bemerkungen **remarques**							**Essai de pliage alterné réussi**

4) Zugprüfung gemäß, EN ISO 14555 / tensile test, in compliance with EN ISO 14555 **/ essais de traction, suivant EN ISO 14555 : na**
Remplacé par RT : 5 pièces, résultat conforme.

5) Essai d'arrasage suivant NFA89-020-1 : 6 pièces, résultat MT :conforme

6) Makroschliff / macro cut /coupe macro (voir illustration page 3) suivant EN ISO 14555 et/ou NFA89-020-1
Bewertung/assessment/**évaluation**: **conforme**

7) Coupe micrographique suivant NFA89-020-1 (voir illustration page 3) **conforme**

Abkürzungen / abbreviations/abréviations:

no = einwandfrei/**impeccable**
uc = Schweißwulst ungleichmäßig/weld bulge irregular/**bourrelet de soudage irrégulier**
ic = Schweißwulst nicht geschlossen/weld bulge not compact / **bourrelet de soudage incomplet**
201 2x3 = Beispiel/example/**exemple**: 2 Poren von 3 mm Ø/2 pores of/de 3 mm

nf = kein Bruch/no fracture/**pas de cassure**
wf = Bruch in der Schweißung/fracture in weld zone/**cassure dans la soudure**
sf = Bruch im Bolzen / fracture in the bolt / **cassure dans le goujon**
a = erfüllt / fulfilled / **conforme**
na = nicht erfüllt / not fulfilled / **non conforme**

FO56276D/Rev.AP /27.08.09

Laboratoire d'essai des matériaux
CH - 1870 Monthey

AC Contrôle Sàrl
Route de Clos-Donroux 1, 1870 Monthey
Tel. +41 24 472 21 51, Fax +41 24 472 21 52

Prüf-Nr.: VP Inspetion No.: N° d'inspection: 26P	Auftrags-Nr.: ZM Reference No.: N° de référence: 26P - 41661	SVTI-Lauf-Nr. TÜV-Lauf-Nr.	Seite Page Page	3	von of de	3

BEMERKUNGEN - *REMARKSS - REMARQUESS*

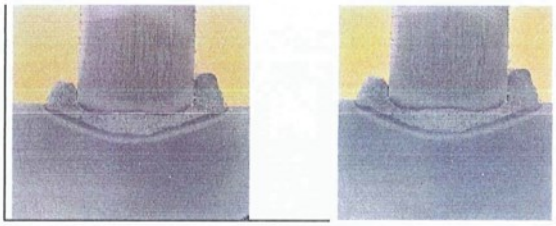

Abb. / Illustration 26P-13 3 : 1

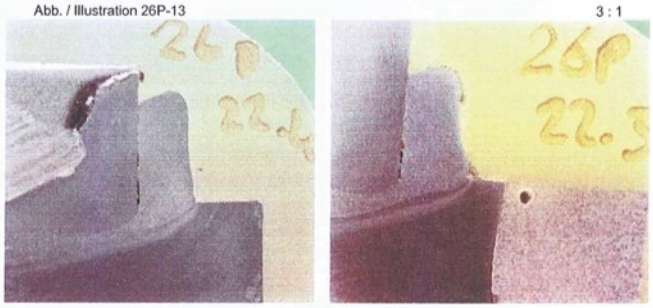

Abb. / Illustration 26P-22 3 : 1

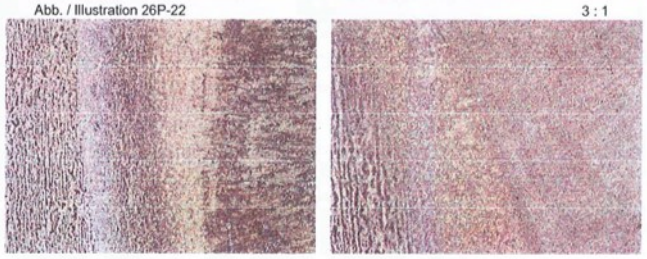

Abb. / Illustration 26p-13 26p-22 200 : 1

Die Prüfungen wurden ausgeführt in Anwesenheit von: */Test carried out in the presence of:* ***/les essais ont été effectués en présence de:***

P. Chinna, EWS

Die Prüfergebnisse sind: */ Test Results are:* ***/ les résultats des essais sont***

☒ zufriedenstellend *acceptable /* ***acceptables***

☐ nicht zufriedenstellend *not acceptable /* ***non acceptables***

Die Prüfungen wurden entsprechend den Prüfgrundlagen durchgeführt.
The tests have been performed in accordance with the specifications.
Les essais ont été effectués selon les spécifications.

Name und Unterschrift des Zertifizierers:

Name and Signature: P. Athanasiadès
Nom et signature:

Zertifizierstelle:
Certification Body: AC Contrôle, Monthey
Organisme de certification:

*) falls erforderlich / *if required / si nécessaire*

FO56276D/Rev.AP /27.08.09

ZM CONSTRUCTIONS MÉTALLIQUES

DMOS-P

Spécification 5.1.13	Symbole 

Description :	Soudure de goujons en atelie r		
Procédé :	783	QMOS N° :	

Préparation et séquences de soudage

état de surface: SA 2 1/2

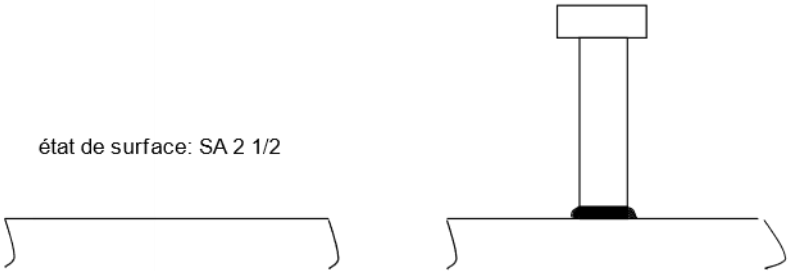

Paramètres

Matériau de base :	S355K2+N	Epaisseur :	25 mm
Type goujons :	Köco	Dimension :	13 x 150 mm
Qualité goujon :	S235J2G3		
Désignation bague :	P 10 C450	Séchage bague :	non
Position de soudage	PA		
Nature du courant	Triphasé 50 Hz	Source courant :	Köco 2600E / VDE 054 2
Pistolet / tête	LWB / K 24	Amortisseur :	oui ~~non~~
Polarité goujon :	Négative		
Intensité :	1000 A	Dépassement :	5 mm
Temps d'arc :	500 ms	Levée :	1.5 mm
Préchauffage :	ambiante (≥14°C)	Postchauffage :	non

Remarques :
QMOS à effectuer selon NF 14555 et A89-020-1 & A89-021-1

Établi par :		NMO	Contrôlé par :	
Date :		17.08.2009	Date :	
Version N°	1	17.08.2009		

ZM CONSTRUCTIONS MÉTALLIQUES

DMOS-P

Spécification 5.1.22	Symbole 

Description :	Soudure de goujons en atelie r		
Procédé :	783	QMOS N° :	

Préparation et séquences de soudage

état de surface: SA 2 1/2

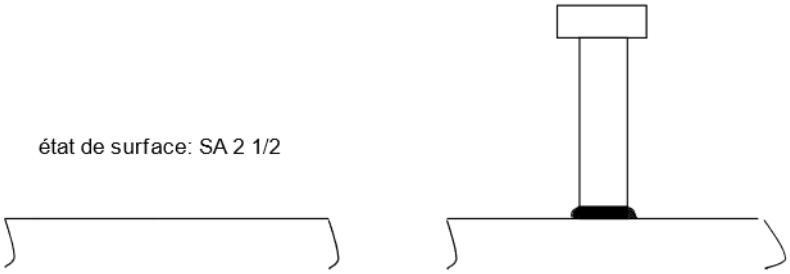

Paramètres

Matériau de base :	S355K2+N	Epaisseur :	25 mm
Type goujons :	Nelson	Dimension :	22 x 150 mm
Qualité goujon :	S235J2G3		
Désignation bague :	KSN 22 C45 0	Séchage bague :	non
Position de soudage	PA		
Nature du courant	Triphasé 50 Hz	Source courant :	Köco 2600E / VDE 054 2
Pistolet / tête	LWB / K 24	Amortisseur :	oui ~~non~~
Polarité goujon :	Négative		
Intensité :	2000 A	Dépassement :	5 mm
Temps d'arc :	980 ms	Levée :	3.0 mm
Préchauffage :	ambiante (≥14°C)	Postchauffage :	non

Remarques :
QMOS à effectuer selon NF 14555 et A89-020-1 & A89-021-1

Établi par :		NMO	Contrôlé par :	
Date :		17.08.2009	Date :	
Version N°	1	17.08.2009		

Appendix D Detailed instrumentation plan

Description

This appendix includes a detailed instrumentation plan of all the sensors that were employed in the experiment. The exact location of the sensors is shown for the test frame/setup and the slab. The appendix also includes a summary of the working sensors as well as those that were damaged during the tests. The procedure for deriving the forces/deformations in Chapters 5 and Appendix E is described.

D.1 Test frame/setup instrumentation plan

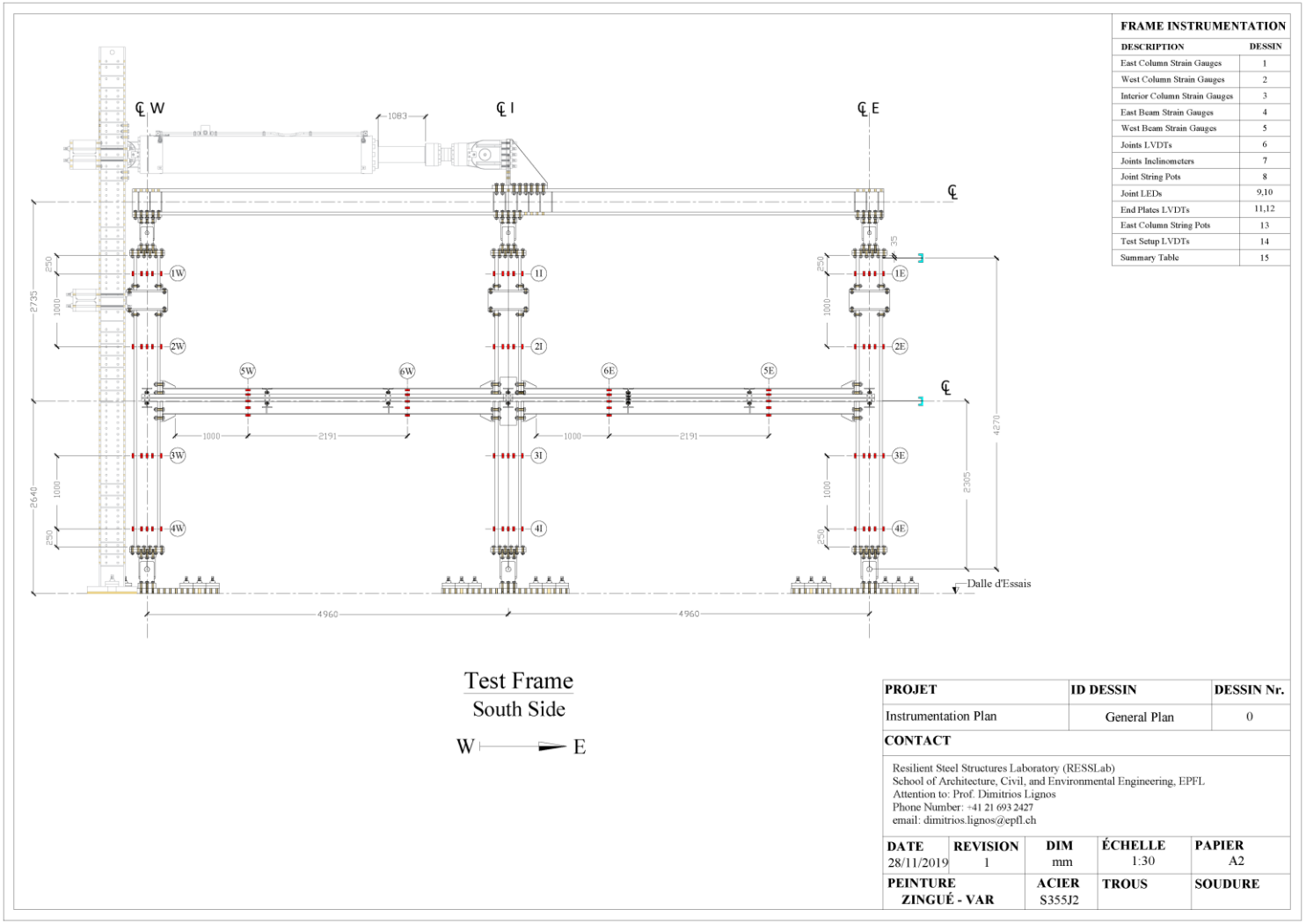

FRAME INSTRUMENTATION	
DESCRIPTION	**DESSIN**
East Column Strain Gauges	1
West Column Strain Gauges	2
Interior Column Strain Gauges	3
East Beam Strain Gauges	4
West Beam Strain Gauges	5
Joints LVDTs	6
Joints Inclinometers	7
Joint String Pots	8
Joint LEDs	9,10
End Plates LVDTs	11,12
East Column String Pots	13
Test Setup LVDTs	14
Summary Table	15

PROJET	ID DESSIN	DESSIN Nr.
Instrumentation Plan	General Plan	0

CONTACT

Resilient Steel Structures Laboratory (RESSLab)
School of Architecture, Civil, and Environmental Engineering, EPFL
Attention to: Prof. Dimitrios Lignos
Phone Number: +41 21 693 2427
email: dimitrios.lignos@epfl.ch

DATE	REVISION	DIM	ÉCHELLE	PAPIER
28/11/2019	1	mm	1:30	A2

PEINTURE	ACIER	TROUS	SOUDURE
ZINGUÉ - VAR	S355J2		

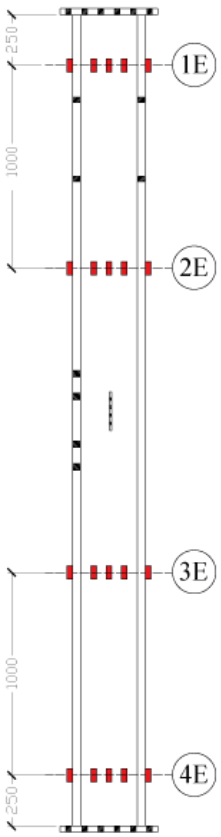

East Column
Scale (1:20)

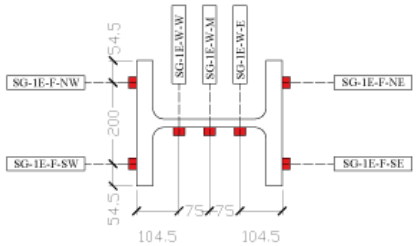

1E
Scale (1:10)

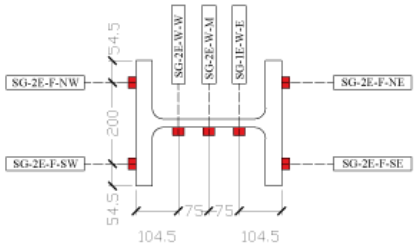

2E
Scale (1:10)

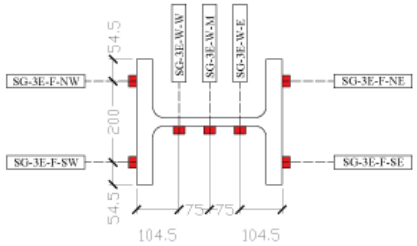

3E
Scale (1:10)

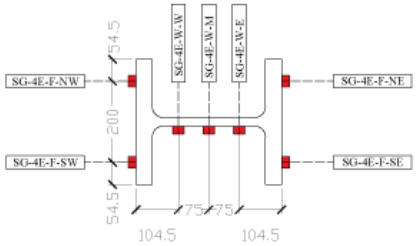

4E
Scale (1:10)

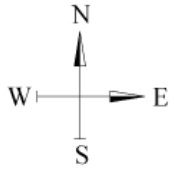

STRAIN GAUGES - EAST COLUMN
(120 ± 0.5 Ω)

#	ID	LOCATION	LENGTH [MM]
1	SG-1E-F-NE	1E - Flange North East	5
2	SG-1E-F-SE	1E - Flange South East	5
3	SG-1E-F-NW	1E - Flange North West	5
4	SG-1E-F-SW	1E - Flange South West	5
5	SG-1E-W-E	1E - Flange Web East	5
6	SG-1E-W-M	1E - Flange Web Middle	5
7	SG-1E-W-W	1E - Flange Web West	5
8	SG-2E-F-NE	2E - Flange North East	5
9	SG-2E-F-SE	2E - Flange South East	5
10	SG-2E-F-NW	2E - Flange North West	5
11	SG-2E-F-SW	2E - Flange South West	5
12	SG-2E-W-E	2E - Flange Web East	5
13	SG-2E-W-M	2E - Flange Web Middle	5
14	SG-2E-W-W	2E - Flange Web West	5
15	SG-3E-F-NE	3E - Flange North East	5
16	SG-3E-F-SE	3E - Flange South East	5
17	SG-3E-F-NW	3E - Flange North West	5
18	SG-3E-F-SW	3E - Flange South West	5
19	SG-3E-W-E	3E - Flange Web East	5
20	SG-3E-W-M	3E - Flange Web Middle	5
21	SG-3E-W-W	3E - Flange Web West	5
22	SG-4E-F-NE	4E - Flange North East	5
23	SG-4E-F-SE	4E - Flange South East	5
24	SG-4E-F-NW	4E - Flange North West	5
25	SG-4E-F-SW	4E - Flange South West	5
26	SG-4E-W-E	4E - Flange Web East	5
27	SG-4E-W-M	4E - Flange Web Middle	5
28	SG-4E-W-W	4E - Flange Web West	5

PROJET		ID DESSIN		DESSIN Nr.
Instrumentation Plan		East Column Strain Gauges		1
DATE 28/11/2019	REVISION 1	DIM mm	ÉCHELLE VAR	PAPIER A3

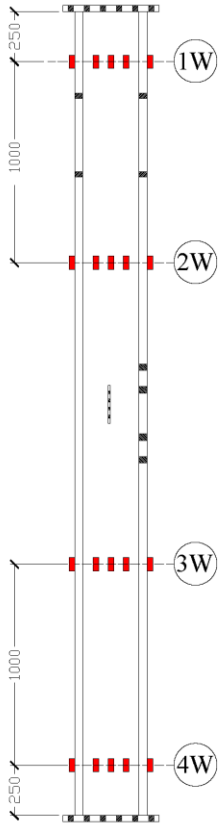

West Column
Scale (1:20)

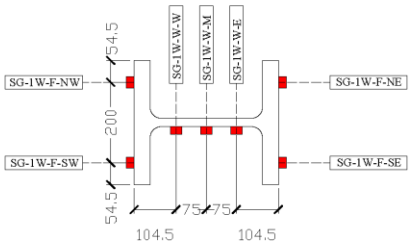

1W
Scale (1:10)

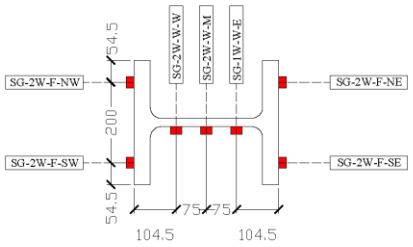

2W
Scale (1:10)

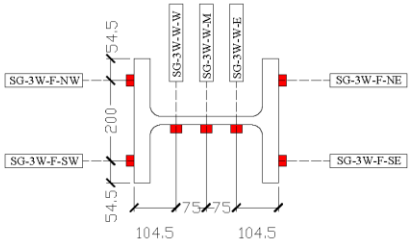

3W
Scale (1:10)

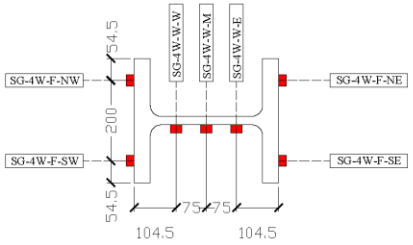

4W
Scale (1:10)

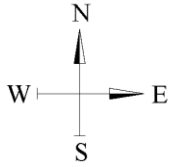

STRAIN GAUGES - WEST COLUMN
(120 ± 0.5 Ω)

#	ID	LOCATION	LENGTH [MM]
1	SG-1W-F-NE	1W - Flange North East	5
2	SG-1W-F-SE	1W - Flange South East	5
3	SG-1W-F-NW	1W - Flange North West	5
4	SG-1W-F-SW	1W - Flange South West	5
5	SG-1W-W-E	1W - Flange Web East	5
6	SG-1W-W-M	1W - Flange Web Middle	5
7	SG-1W-W-W	1W - Flange Web West	5
8	SG-2W-F-NE	2W - Flange North East	5
9	SG-2W-F-SE	2W - Flange South East	5
10	SG-2W-F-NW	2W - Flange North West	5
11	SG-2W-F-SW	2W - Flange South West	5
12	SG-2W-W-E	2W - Flange Web East	5
13	SG-2W-W-M	2W - Flange Web Middle	5
14	SG-2W-W-W	2W - Flange Web West	5
15	SG-3W-F-NE	3W - Flange North East	5
16	SG-3W-F-SE	3W - Flange South East	5
17	SG-3W-F-NW	3W - Flange North West	5
18	SG-3W-F-SW	3W - Flange South West	5
19	SG-3W-W-E	3W - Flange Web East	5
20	SG-3W-W-M	3W - Flange Web Middle	5
21	SG-3W-W-W	3W - Flange Web West	5
22	SG-4W-F-NE	4W - Flange North East	5
23	SG-4W-F-SE	4W - Flange South East	5
24	SG-4W-F-NW	4W - Flange North West	5
25	SG-4W-F-SW	4W - Flange South West	5
26	SG-4W-W-E	4W - Flange Web East	5
27	SG-4W-W-M	4W - Flange Web Middle	5
28	SG-4W-W-W	4W - Flange Web West	5

PROJET		ID DESSIN		DESSIN Nr.
Instrumentation Plan		West Column Strain Gauges		2
DATE 28/11/2019	**REVISION** 1	**DIM** mm	**ÉCHELLE** VAR	**PAPIER** A3

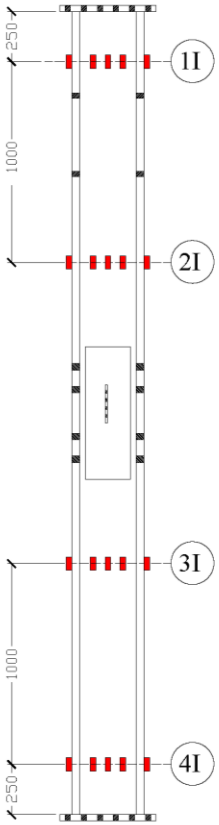

Interior Column
Scale (1:20)

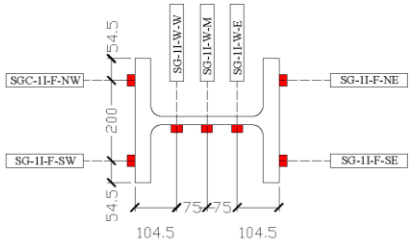

1I
Scale (1:10)

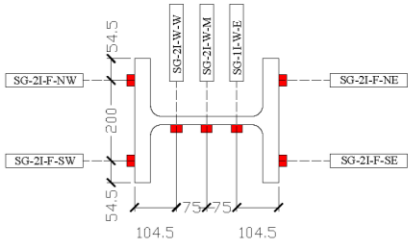

2I
Scale (1:10)

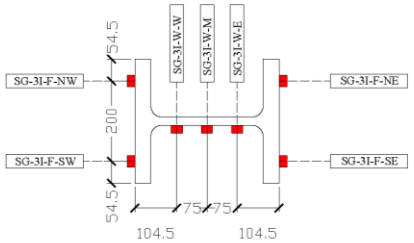

3I
Scale (1:10)

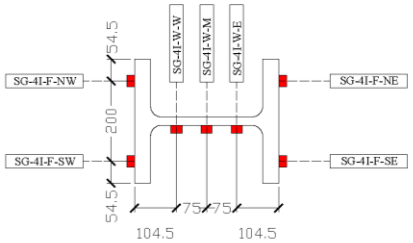

4I
Scale (1:10)

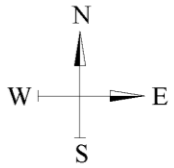

STRAIN GAUGES - INT. COLUMN
(120 ± 0.5 Ω)

#	ID	LOCATION	LENGTH [MM]
1	SG-1I-F-NE	1I - Flange North East	5
2	SG-1I-F-SE	1I - Flange South East	5
3	SG-1I-F-NW	1I - Flange North West	5
4	SG-1I-F-SW	1I - Flange South West	5
5	SG-1I-W-E	1I - Flange Web East	5
6	SG-1I-W-M	1I - Flange Web Middle	5
7	SG-1I-W-W	1I - Flange Web West	5
8	SG-2I-F-NE	2I - Flange North East	5
9	SG-2I-F-SE	2I - Flange South East	5
10	SG-2I-F-NW	2I - Flange North West	5
11	SG-2I-F-SW	2I - Flange South West	5
12	SG-2I-W-E	2I - Flange Web East	5
13	SG-2I-W-M	2I - Flange Web Middle	5
14	SG-2I-W-W	2I - Flange Web West	5
15	SG-3I-F-NE	3I - Flange North East	5
16	SG-3I-F-SE	3I - Flange South East	5
17	SG-3I-F-NW	3I - Flange North West	5
18	SG-3I-F-SW	3I - Flange South West	5
19	SG-3I-W-E	3I - Flange Web East	5
20	SG-3I-W-M	3I - Flange Web Middle	5
21	SG-3I-W-W	3I - Flange Web West	5
22	SG-4I-F-NE	4I - Flange North East	5
23	SG-4I-F-SE	4I - Flange South East	5
24	SG-4I-F-NW	4I - Flange North West	5
25	SG-4I-F-SW	4I - Flange South West	5
26	SG-4I-W-E	4I - Flange Web East	5
27	SG-4I-W-M	4I - Flange Web Middle	5
28	SG-4I-W-W	4I - Flange Web West	5

PROJET		ID DESSIN		DESSIN Nr.
Instrumentation Plan		Interior Column Strain Gauges		3
DATE 28/11/2019	**REVISION** 1	**DIM** mm	**ÉCHELLE** VAR	**PAPIER** A3

East Beam
Scale (1:20)

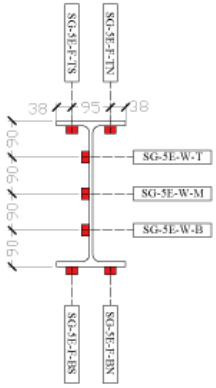

5E
Scale (1:10)

Top
S N
Bottom

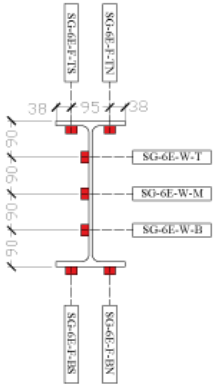

6E
Scale (1:10)

STRAIN GAUGES - EAST BEAM (120 ± 0.5 Ω)

#	ID	LOCATION	LENGTH [MM]
1	SG-5E-F-TS	5E - Flange Top South	5
2	SG-5E-F-TN	5E - Flange Top North	5
3	SG-5E-F-BS	5E - Flange Bottom South	5
4	SG-5E-F-BN	5E - Flange Bottom North	5
5	SG-5E-W-T	5E - Web Top	5
6	SG-5E-W-M	5E - Web Middle	5
7	SG-5E-W-B	5E - Web Bottom	5
8	SG-6E-F-TS	6E - Flange Top South	5
9	SG-6E-F-TN	6E - Flange Top North	5
10	SG-6E-F-BS	6E - Flange Bottom South	5
11	SG-6E-F-BN	6E - Flange Bottom North	5
12	SG-6E-W-T	6E - Web Top	5
13	SG-6E-W-M	6E - Web Middle	5
14	SG-6E-W-B	6E - Web Bottom	5

PROJET		ID DESSIN		DESSIN Nr.
Instrumentation Plan		East Beam Strain Gauges		4
DATE 28/11/2019	REVISION 1	DIM mm	ÉCHELLE VAR	PAPIER A3

West Beam
Scale (1:20)

STRAIN GAUGES - WEST BEAM (120 ± 0.5 Ω)			
#	ID	LOCATION	LENGTH [MM]
1	SG-5W-F-TS	5W - Flange Top South	3
2	SG-5W-F-TN	5W - Flange Top North	3
3	SG-5W-F-BS	5W - Flange Bottom South	3
4	SG-5W-F-BN	5W - Flange Bottom North	3
5	SG-5W-W-T	5W - Web Top	3
6	SG-5W-W-M	5W - Web Middle	3
7	SG-5W-W-B	5W - Web Bottom	3
8	SG-6W-F-TS	6W - Flange Top South	3
9	SG-6W-F-TN	6W - Flange Top North	5
10	SG-6W-F-BS	6W - Flange Bottom South	3
11	SG-6W-F-BN	6W - Flange Bottom North	3
12	SG-6W-W-T	6W - Web Top	3
13	SG-6W-W-M	6W - Web Middle	3
14	SG-6W-W-B	6W - Web Bottom	3

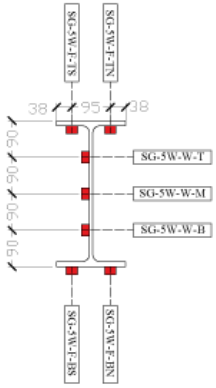

5W
Scale (1:10)

Top
S N
Bottom

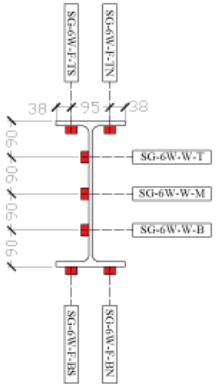

6W
Scale (1:10)

PROJET		ID DESSIN		DESSIN Nr.
Instrumentation Plan		West Beam Strain Gauges		5
DATE 28/11/2019	REVISION 1	DIM mm	ÉCHELLE VAR	PAPIER A3

LVDTS - JOINTS			
#	ID	LOCATION	RANGE [MM]
1	LVDT-E-E	East Joint - East Location	±5
2	LVDT-E-W	East Joint - West Location	±5
3	LVDT-W-E	West Joint - East Location	±5
4	LVDT-W-W	West Joint - West Location	±5
5	LVDT-I-E	Interior Joint - East Location	±5
6	LVDT-I-W	Interior Joint - West Location	±5

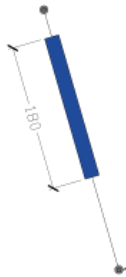

Detail A
Scale 2:1

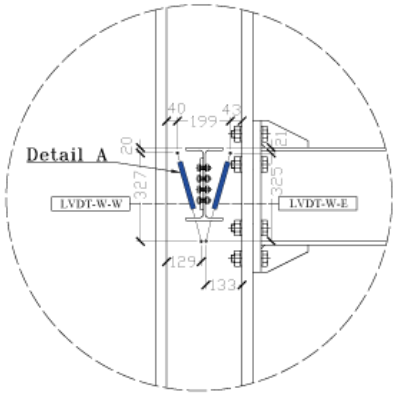

West Column Joint (North)

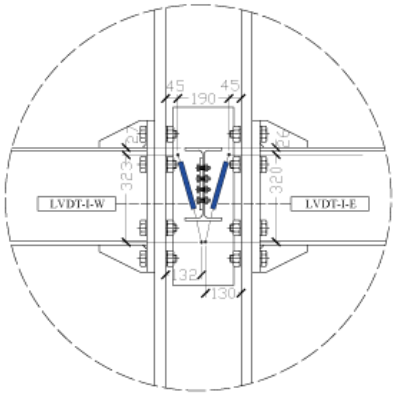

Interior Column Joint (North)

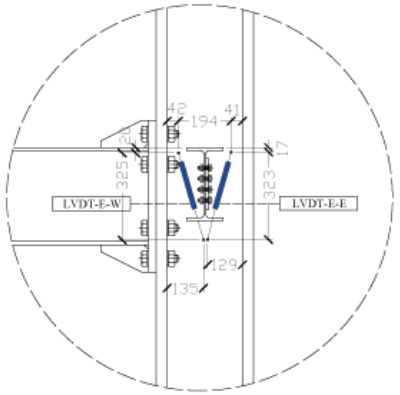

East Column Joint (North)

PROJET		ID DESSIN		DESSIN Nr.
Instrumentation Plan		Joint LVDTs		6
DATE 28/07/2021	REVISION 1	DIM mm	ÉCHELLE 1:15	PAPIER A3

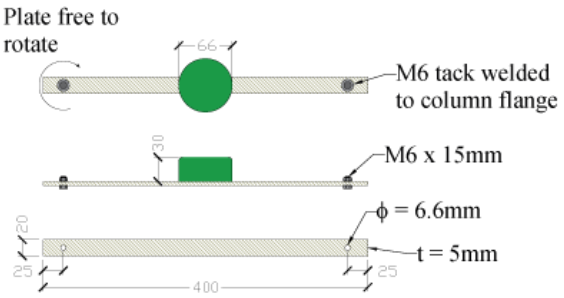

Detail A
Scale 2:1

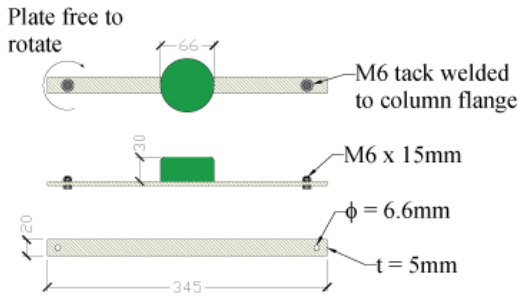

Detail B
Scale 2:1

INCLINOMETERS - JOINTS			
#	ID	LOCATION	RANGE [MM]
1	INCLE-E-F-E	East Joint - East Flange	±65°
2	INCLE-E-F-W	East Joint - West Flange	±65°
3	INCLE-E-W-B	East Joint - Bottom Web	±65°
4	INCLE-W-F-E	West Joint - East Flange	±65°
5	INCLE-W-F-W	West Joint - West Flange	±65°
6	INCLE-W-W-B	West Joint - Bottom Web	±65°
7	INCLE-I-F-E	Interior Joint - East Flange	±65°
8	INCLE-I-F-W	Interior Joint - West Flange	±65°
9	INCLE-I-W-B	Interior Joint - Bottom Web	±65°

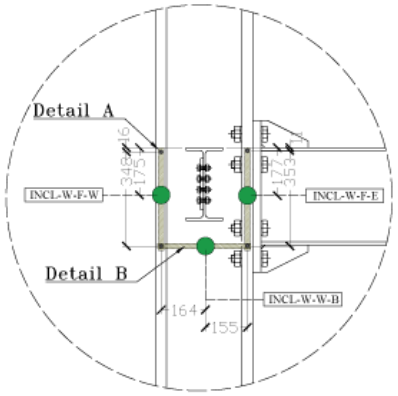

West Column Joint (South)

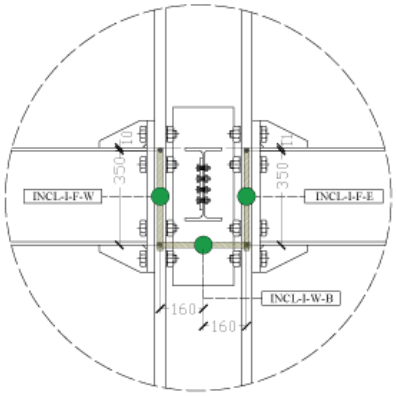

Interior Column Joint (North)

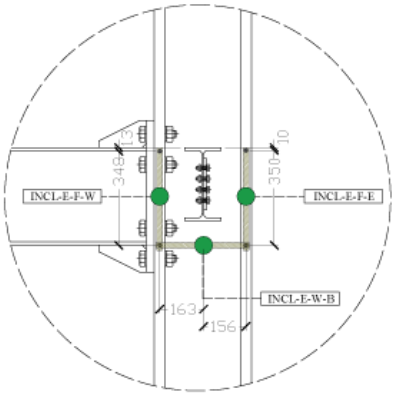

East Column Joint (South)

PROJET		ID DESSIN		DESSIN Nr.
Instrumentation Plan		Joint Inclinometers		7
DATE 28/07/2021	REVISION 1	DIM mm	ÉCHELLE 1:15	PAPIER A3

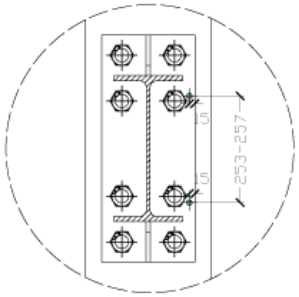

SIDE VIEW

Scale (1:10)

STRING POTS - JOINTS			
#	ID	LOCATION	RANGE [MM]
1	SP-E-TW	East Joint - Top West Location	±300
2	SP-E-BW	East Joint - Bottom West Location	±300
3	SP-W-TE	West Joint - Top East Location	±300
4	SP-W-BE	West Joint - Bottom East Location	±300
5	SP-I-TW	Interior Joint - Top West Location	±300
6	SP-I-BW	Interior Joint - Bottom West Location	±300
7	SP-I-TE	Interior Joint - Top East Location	±300
8	SP-I-BE	Interior Joint - Bottom East Location	±300

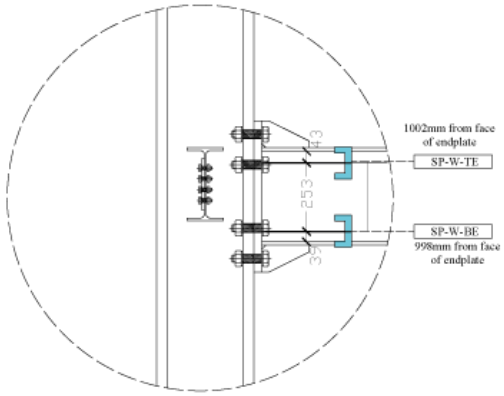

West Column Joint

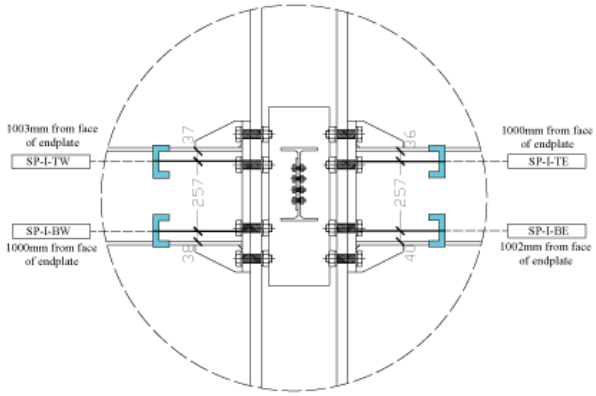

Interior Column Joint

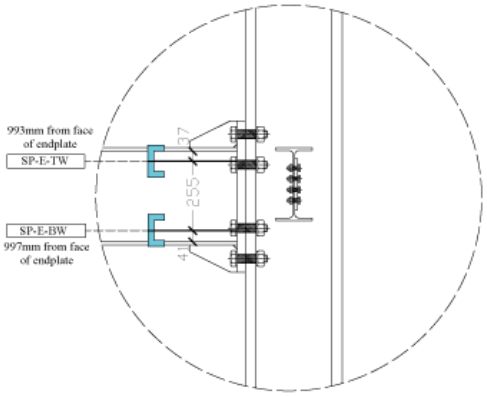

East Column Joint

PROJET		ID DESSIN		DESSIN Nr.
Instrumentation Plan		Joint String Pots		8
DATE 28/07/2021	REVISION 1	DIM mm	ÉCHELLE 1:15	PAPIER A3

LEDS - JOINTS	
LOCATION	**N°**
Interior Joint	46

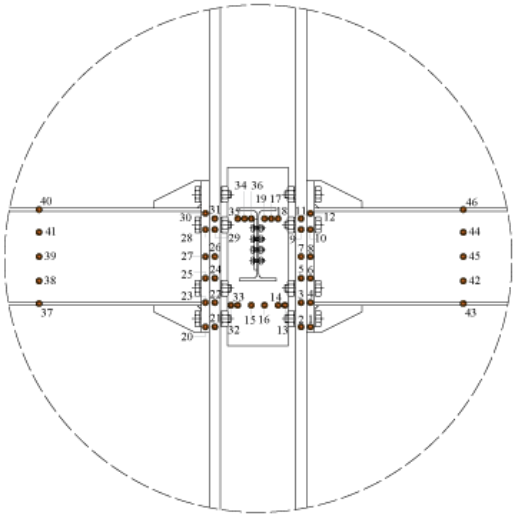

Markers

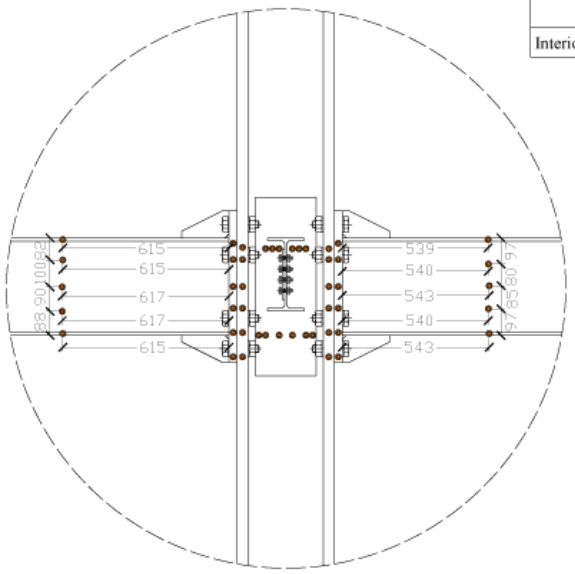

LEDs Location

W E

PROJET		ID DESSIN		DESSIN Nr.
Instrumentation Plan		Joint LEDs		9
DATE 28/07/2021	**REVISION** 1	**DIM** mm	**ÉCHELLE** 1:15	**PAPIER** A3

LEDS - JOINTS	
LOCATION	**N°**
Interior Joint	46

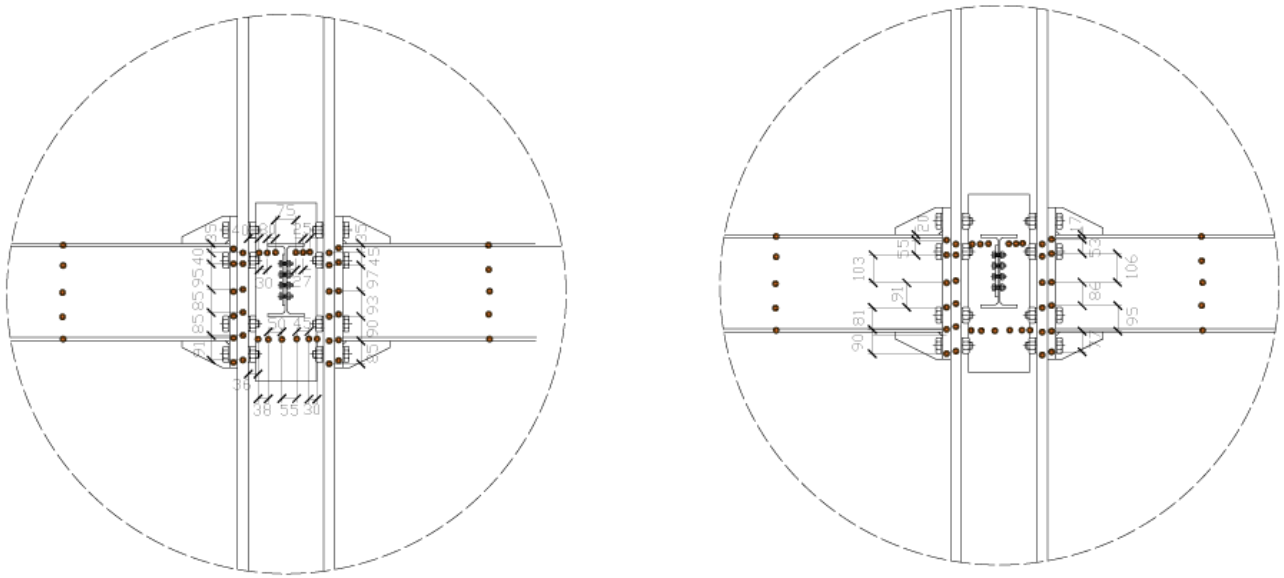

LEDs Location

W ⟶ E

PROJET		**ID DESSIN**		**DESSIN Nr.**
Instrumentation Plan		Joint LEDs		10
DATE 28/07/2021	**REVISION** 1	**DIM** mm	**ÉCHELLE** 1:15	**PAPIER** A3

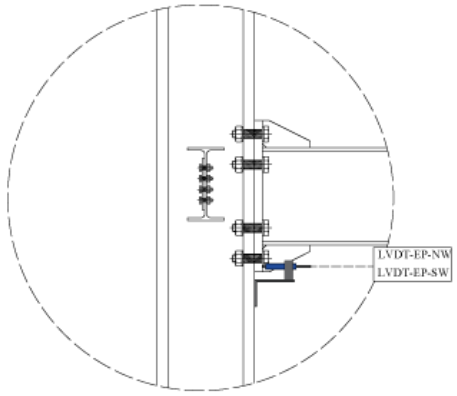

West Column Joint

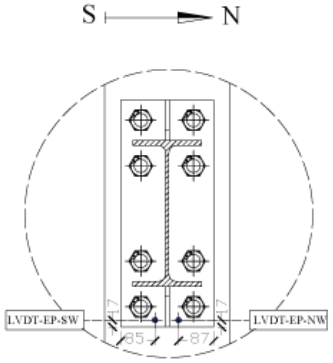

SIDE VIEW

Scale (1:10)

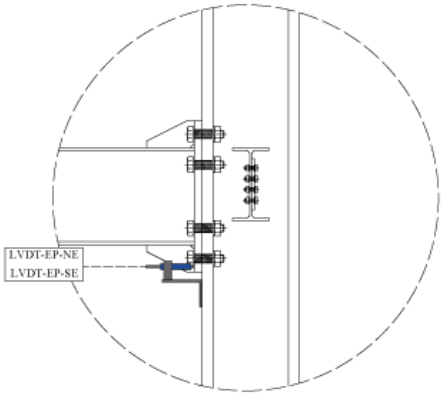

East Column Joint

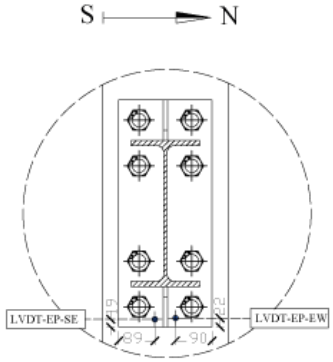

SIDE VIEW

Scale (1:10)

LVDTS - END PLATES			
#	ID	LOCATION	RANGE [MM]
1	LVDT-EP-NW	West End Plate - North	±10
2	LVDT-EP-SW	West End Plate - South	±10
3	LVDT-EP-NE	East End Plate - North	±10
4	LVDT-EP-SE	East End Plate - South	±10

PROJET		ID DESSIN		DESSIN Nr.
Instrumentation Plan		End Plate LVDTs		11
DATE 28/07/2021	REVISION 1	DIM mm	ÉCHELLE 1:15	PAPIER A3

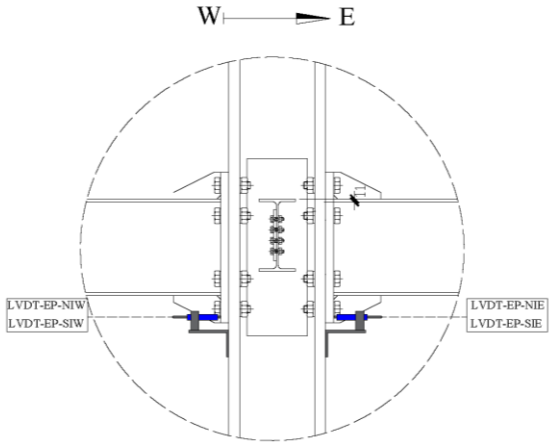

Interior Column Joint

LVDTS* - END PLATES			
#	ID	LOCATION	RANGE [MM]
1	LVDT-EP-NIW	Interior End Plate - Northwest	±10
2	LVDT-EP-SIW	Interior End Plate - Southwest	±10
3	LVDT-EP-NIE	Interior End Plate - Northwest	±10
4	LVDT-EP-SIE	Interior End Plate - Southwest	±10

** Added during the AISC symmetric cyclic loading protocol following 2% rads*

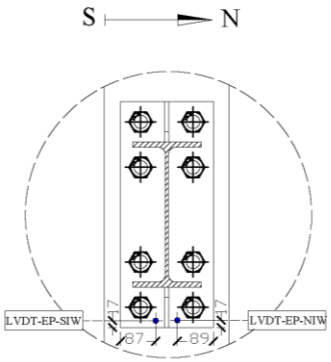

SIDE VIEW

Scale (1:10)

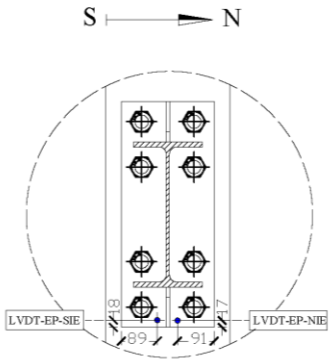

SIDE VIEW

Scale (1:10)

PROJET		ID DESSIN		DESSIN Nr.
Instrumentation Plan		End Plate LVDTs		12
DATE 28/07/2021	**REVISION** 1	**DIM** mm	**ÉCHELLE** 1:15	**PAPIER** A3

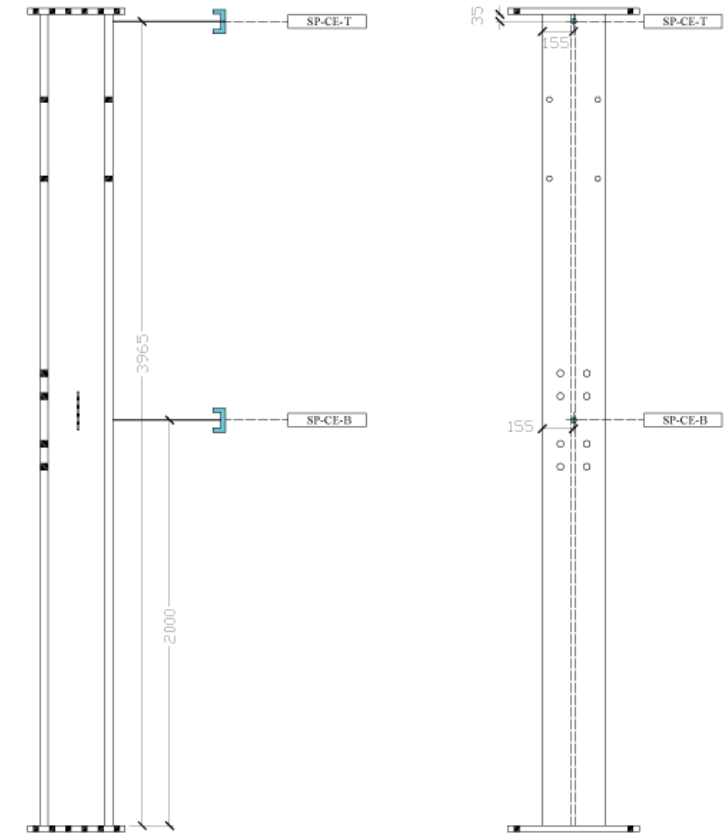

FRONT VIEW

SIDE VIEW

East Column

STRING POTS - EAST COLUMN			
#	ID	LOCATION	RANGE [MM]
1	SP-CE-T	East Column - Top Location	±1000
2	SP-CE-B	East Column - Bottom Location	± 500

PROJET		ID DESSIN		DESSIN Nr.
Instrumentation Plan		East Column String Pots		13
DATE 28/07/2021	REVISION 1	DIM mm	ÉCHELLE 1:20	PAPIER A3

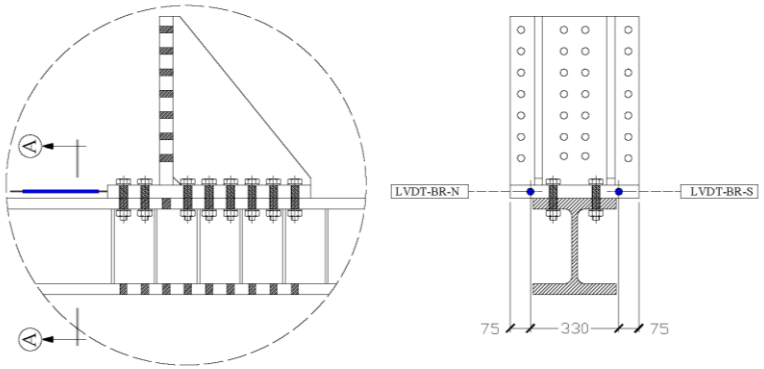

ELEVATION SEC A-A

Bracket

ELEVATION SIDE VIEW

Bottom Connection

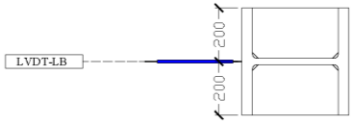

Loading Beam

LVDTS - SETUP			
#	ID	LOCATION	RANGE [MM]
1	LVDT-BR-S	Bracket - South Location	±10
2	LVDT-BR-N	Bracket - North Location	±10
3	LVDT-P-S[1]	Pin - South Location	±10
4	LVDT-P-N[1]	Pin - North Location	±10
5	LVDT-BP-S[2]	Base Plate - South Location	±10
6	LVDT-BP-N[2]	Base Plate - North Location	±10
7	LVDT-LB	Loading Beam	±20

[1] Replaced by 1 sensor LVDT-P during the AISC symmetric cyclic loading protocol following 2% rads

[2] Replaced by 1 sensor LVDT-BP during the AISC symmetric cyclic loading protocol following 2% rads

PROJET		ID DESSIN		DESSIN Nr.
Instrumentation Plan		Test Setup LVDTs		14
DATE 28/11/2019	REVISION 1	DIM mm	ÉCHELLE 1:15	PAPIER A3

FRAME INSTRUMENTATION PLAN SUMMARY				
QUAN	Sensor	Gauge Length [mm]	Resistance [Ω]	Range [mm or °]
112	Strain Gauges	VARIES	250 ± 0.5	-
6	LVDTs	-	-	±5
14	LVDTs	-	-	±10
1	LVDT	-	-	±20
9	Inclinometers	-	-	±65°
46	LEDs	-	-	-
1	String Pot	-	-	±1000
1	String Pot	-	-	±500
8	String Pot	-	-	±300

PROJET		ID DESSIN		DESSIN Nr.
Instrumentation Plan		Summary Table		15
DATE 28/11/2019	REVISION 1	DIM mm	ÉCHELLE -	PAPIER A3

D.2 Slab instrumentation plan

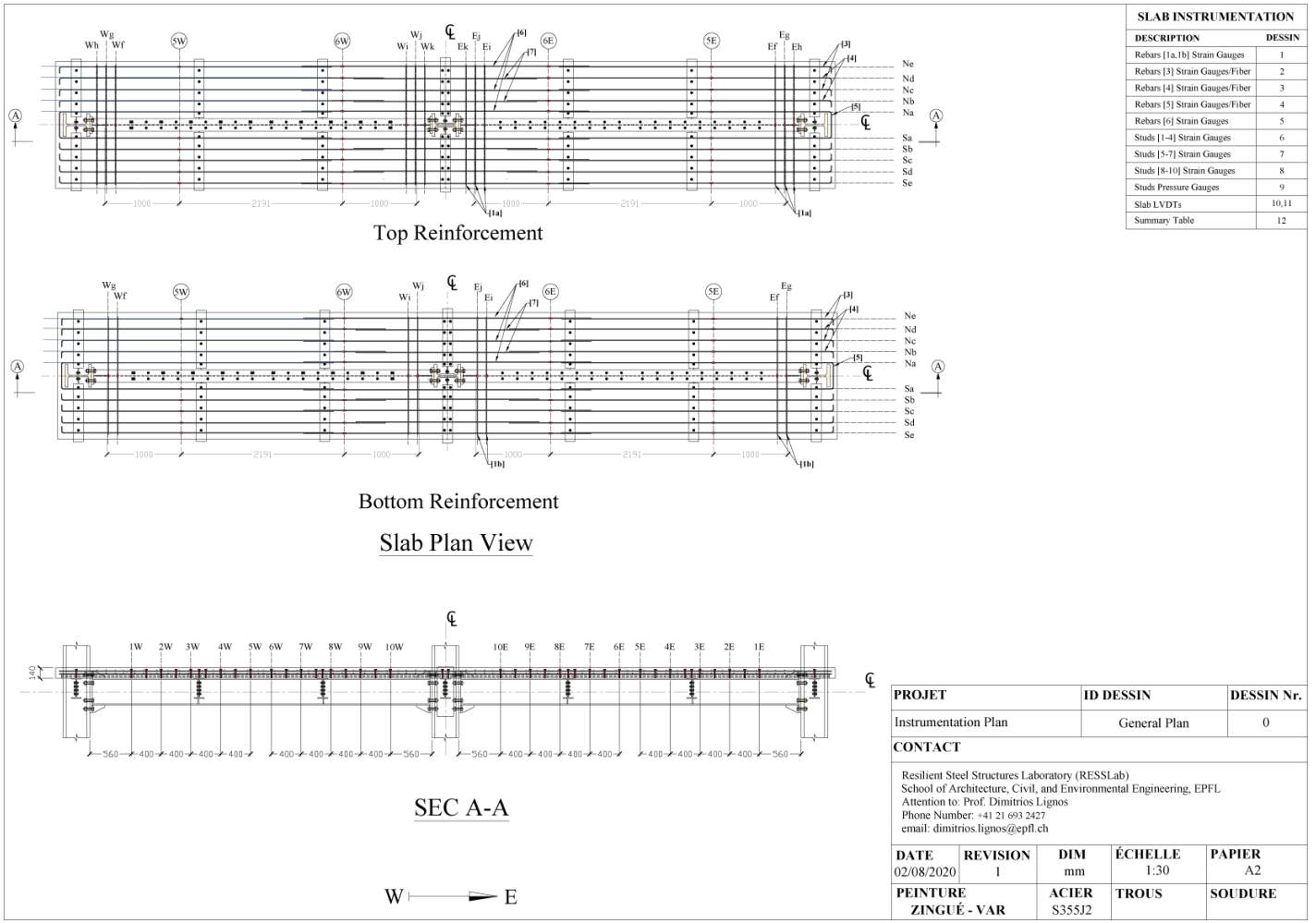

SLAB INSTRUMENTATION	
DESCRIPTION	DESSIN
Rebars [1a,1b] Strain Gauges	1
Rebars [3] Strain Gauges/Fiber	2
Rebars [4] Strain Gauges/Fiber	3
Rebars [5] Strain Gauges/Fiber	4
Rebars [6] Strain Gauges	5
Studs [1-4] Strain Gauges	6
Studs [5-7] Strain Gauges	7
Studs [8-10] Strain Gauges	8
Studs Pressure Gauges	9
Slab LVDTs	10,11
Summary Table	12

PROJET	ID DESSIN	DESSIN Nr.
Instrumentation Plan	General Plan	0

CONTACT

Resilient Steel Structures Laboratory (RESSLab)
School of Architecture, Civil, and Environmental Engineering, EPFL
Attention to: Prof. Dimitrios Lignos
Phone Number: +41 21 693 2427
email: dimitrios.lignos@epfl.ch

DATE	REVISION	DIM	ÉCHELLE	PAPIER
02/08/2020	1	mm	1:30	A2
PEINTURE		**ACIER**	**TROUS**	**SOUDURE**
ZINGUÉ - VAR		S355J2		

Strain Gauges
x12 [1a] Bars

SG-S-TEf
SG-S-TEg
SG-S-TEh
SG-S-TEi
SG-S-TEj
SG-S-TEk
SG-S-TWf
SG-S-TWg
SG-S-TWh
SG-S-TWi
SG-S-TWj
SG-S-TWk

Strain Gauges
x8 [1b] Bars

SG-S-BEf
SG-S-BEg
SG-S-BEi
SG-S-BEj
SG-S-BWf
SG-S-BWg
SG-S-BWi
SG-S-BWj

STRAIN GAUGES [1a, 1b] REBARS (120 ± 0.5 Ω)

#	ID	LOCATION	LENGTH [MM]
1	SG-S-TEf	Ef - Slab Top Rebar [1a]	3
2	SG-S-TEg	Eg - Slab Top Rebar [1a]	3
3	SG-S-TEh	Eh - Slab Top Rebar [1a]	3
4	SG-S-TEi	Ei - Slab Top Rebar [1a]	3
5	SG-S-TEj	Ej - Slab Top Rebar [1a]	3
6	SG-S-TEk	Ek - Slab Top Rebar [1a]	3
7	SG-S-TWf	Wf - Slab Top Rebar [1a]	3
8	SG-S-TWg	Wg - Slab Top Rebar [1a]	3
9	SG-S-TWh	Wh - Slab Top Rebar [1a]	3
10	SG-S-TWi	Wi - Slab Top Rebar [1a]	3
11	SG-S-TWj	Wj - Slab Top Rebar [1a]	3
12	SG-S-TWk	Wk - Slab Top Rebar [1a]	3
13	SG-S-BEf	Ef - Slab Bottom Rebar [1b]	3
14	SG-S-BEg	Eg - Slab Bottom Rebar [1b]	3
15	SG-S-BEi	Ei - Slab Bottom Rebar [1b]	3
16	SG-S-BEj	Ej - Slab Bottom Rebar [1b]	3
17	SG-S-BWf	Wf - Slab Bottom Rebar [1b]	3
18	SG-S-BWg	Wg - Slab Bottom Rebar [1b]	3
19	SG-S-BWi	Wi - Slab Bottom Rebar [1b]	3
20	SG-S-BWj	Wj - Slab Bottom Rebar [1b]	3

PROJET		ID DESSIN		DESSIN Nr.
Instrumentation Plan		Rebar [1a, 1b] Strain Gauges		1
DATE 26/02/2020	REVISION 1	DIM mm	ÉCHELLE 1:15	PAPIER A3

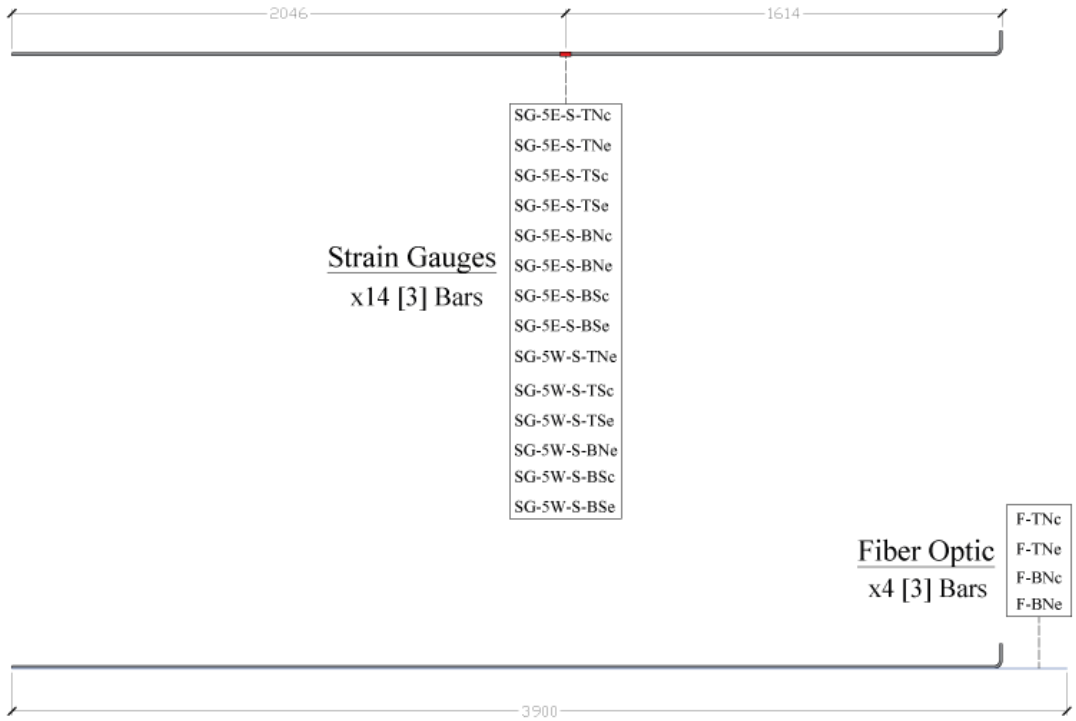

STRAIN GAUGES [3] REBARS (120 ± 0.5 Ω)

#	ID	LOCATION	LENGTH [MM]
1	SG-5E-S-TNc	5E Nc - Slab Top Rebar	3
2	SG-5E-S-TNe	5E Ne - Slab Top Rebar	3
3	SG-5E-S-TSc	5E Sc - Slab Top Rebar	3
4	SG-5E-S-TSe	5E Se - Slab Top Rebar	3
5	SG-5E-S-BNc	5E Nc - Slab Bottom Rebar	3
6	SG-5E-S-BNe	5E Ne - Slab Bottom Rebar	3
7	SG-5E-S-BSc	5E Sc - Slab Bottom Rebar	3
8	SG-5E-S-BSe	5E Se - Slab Bottom Rebar	3
9	SG-5W-S-TNe	5W Ne - Slab Top Rebar	3
10	SG-5W-S-TSc	5W Sc - Slab Top Rebar	3
11	SG-5W-S-TSe	5W Se - Slab Top Rebar	3
12	SG-5W-S-BNe	5W Ne - Slab Bottom Rebar	3
13	SG-5W-S-BSc	5W Sc - Slab Bottom Rebar	3
14	SG-5W-S-BSe	5W Se - Slab Bottom Rebar	3

FIBER OPTIC [3] REBARS

#	ID	LOCATION	LENGTH [MM]
1	F-TNc	Nc - Slab Top Rebar	3900
2	F-TNe	Ne - Slab Top Rebar	3900
3	F-BNc	Nc - Slab Bottom Rebar	3900
4	F-BNe	Ne - Slab Bottom Rebar	3900

PROJET		ID DESSIN		DESSIN Nr.
Instrumentation Plan		Rebar [3] Strain Gauges / Fiber		2
DATE 02/08/2020	REVISION 1	DIM mm	ÉCHELLE 1:15	PAPIER A3

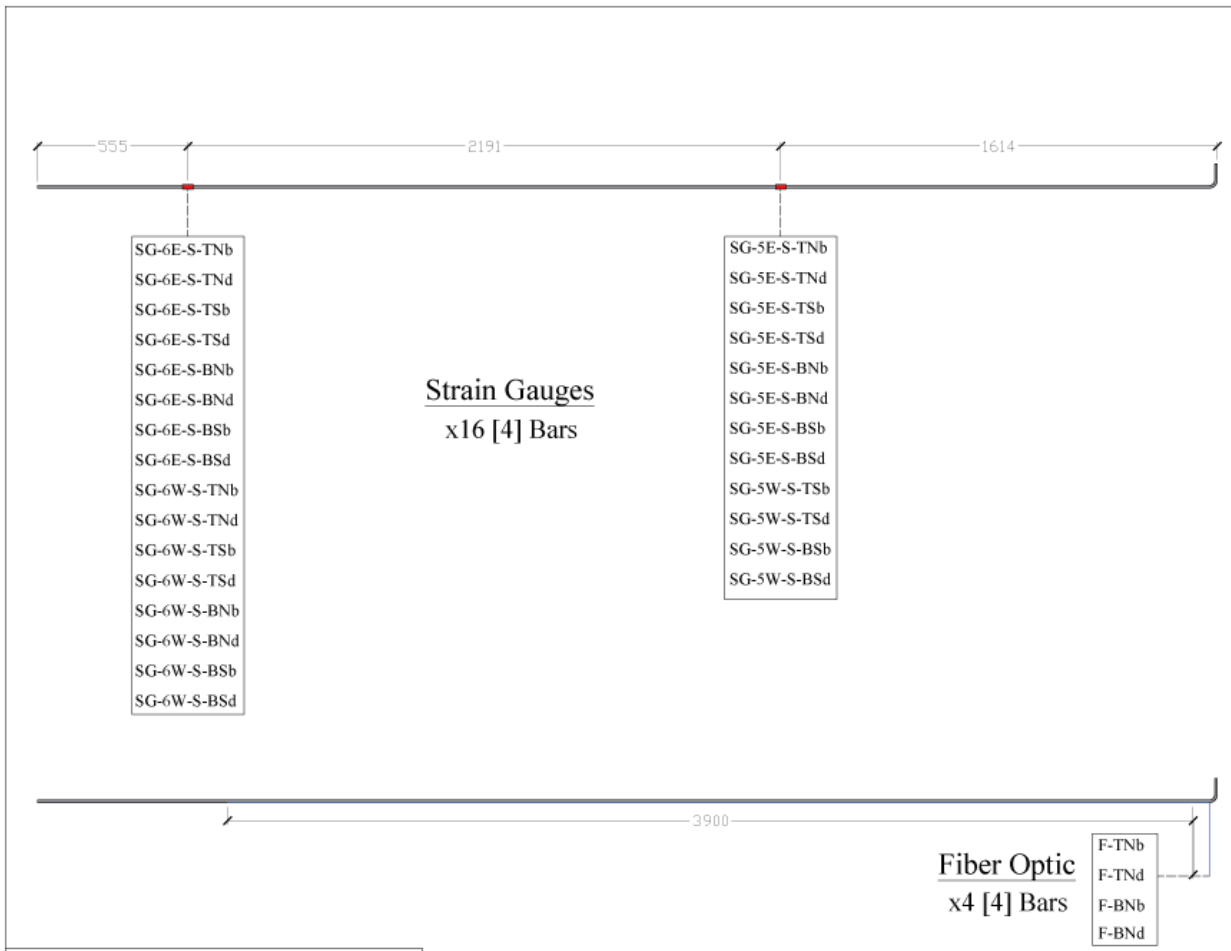

STRAIN GAUGES [4] REBARS
(120 ± 0.5 Ω)

#	ID	LOCATION	LENGTH [MM]
1	SG-5E-S-TNb	5E Nb - Slab Top Rebar	3
2	SG-5E-S-TNd	5E Nd - Slab Top Rebar	3
3	SG-5E-S-TSb	5E Sb - Slab Top Rebar	3
4	SG-5E-S-TSd	5E Sd - Slab Top Rebar	3
5	SG-5E-S-BNb	5E Nb - Slab Bottom Rebar	3
6	SG-5E-S-BNd	5E Nd - Slab Bottom Rebar	3
7	SG-5E-S-BSb	5E Sb - Slab Bottom Rebar	3
8	SG-5E-S-BSd	5E Sd - Slab Bottom Rebar	3
9	SG-5W-S-TSb	5W Sb - Slab Top Rebar	3
10	SG-5W-S-TSd	5W Sd - Slab Top Rebar	3
11	SG-5W-S-BSb	5W Sb - Slab Bottom Rebar	3
12	SG-5W-S-BSd	5W Sd - Slab Bottom Rebar	3
13	SG-6E-S-TNb	6E Nb - Slab Top Rebar	3
14	SG-6E-S-TNd	6E Nd - Slab Top Rebar	3
15	SG-6E-S-TSb	6E Sb - Slab Top Rebar	3
16	SG-6E-S-TSd	6E Sd - Slab Top Rebar	3
17	SG-6E-S-BNb	6E Nb - Slab Bottom Rebar	3
18	SG-6E-S-BNd	6E Nd - Slab Bottom Rebar	3
19	SG-6E-S-BSb	6E Sb - Slab Bottom Rebar	3
20	SG-6E-S-BSd	6E Sd - Slab Bottom Rebar	3
21	SG-6W-S-TNb	6W Nb - Slab Top Rebar	3
22	SG-6W-S-TNd	6W Nd - Slab Top Rebar	3
23	SG-6W-S-TSb	6W Sb - Slab Top Rebar	3
24	SG-6W-S-TSd	6W Sd - Slab Top Rebar	3
25	SG-6W-S-BNb	6W Nb - Slab Bottom Rebar	3
26	SG-6W-S-BNd	6W Nd - Slab Bottom Rebar	3
27	SG-6W-S-BSb	6W Sb - Slab Bottom Rebar	3
28	SG-6W-S-BSd	6W Sd - Slab Bottom Rebar	3

FIBER OPTIC [4] REBARS

#	ID	LOCATION	LENGTH [MM]
1	F-TNb	Nb- Slab Top Rebar	3900
2	F-TNd	Nd- Slab Top Rebar	3900
3	F-BNb	Nb - Slab Bottom Rebar	3900
4	F-BNd	Nd - Slab Bottom Rebar	3900

PROJET		ID DESSIN		DESSIN Nr.
Instrumentation Plan		Rebar [4] Strain Gauges / Fiber		3
DATE 26/02/2020	**REVISION** 1	**DIM** mm	**ÉCHELLE** 1:15	**PAPIER** A3

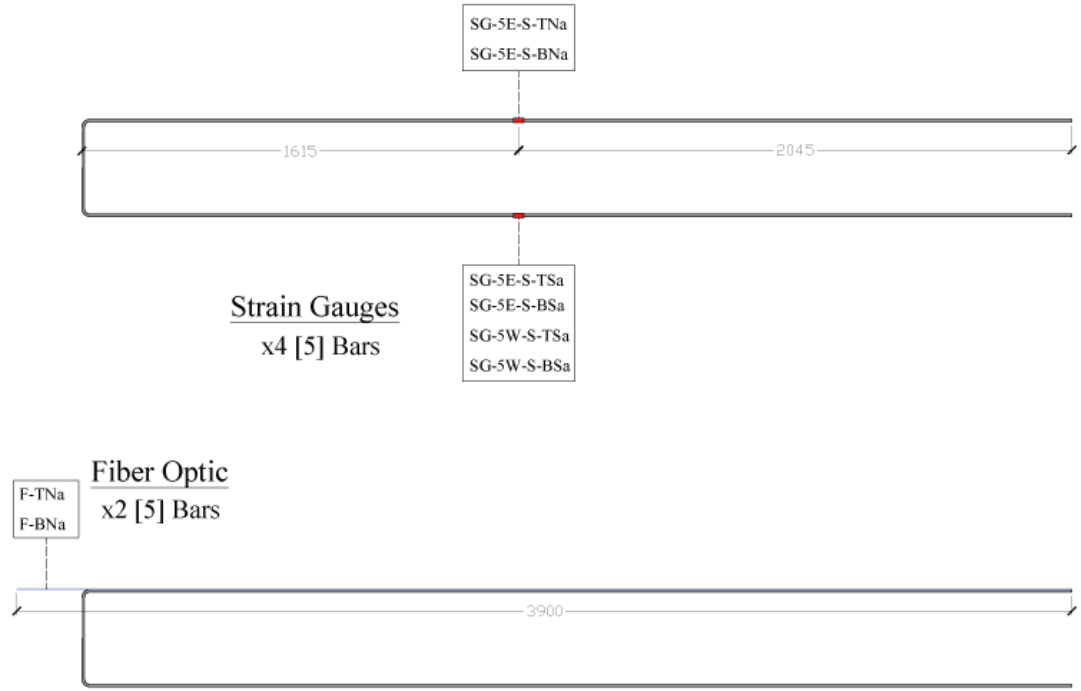

STRAIN GAUGES [5] REBARS
(120 ± 0.5 Ω)

#	ID	LOCATION	LENGTH [MM]
1	SG-5E-S-TNa	5E Na - Slab Top Rebar	3
2	SG-5E-S-TSa	5E Sa - Slab Top Rebar	3
3	SG-5E-S-BNa	5E Na - Slab Bottom Rebar	3
4	SG-5E-S-BSa	5E Sa - Slab Bottom Rebar	3
5	SG-5W-S-TSa	5W Sa - Slab Top Rebar	3
6	SG-5W-S-BSa	5W Sa - Slab Bottom Rebar	3

FIBER OPTIC [5] REBARS

#	ID	LOCATION	LENGTH [MM]
1	F-TNa	Na- Slab Top Rebar	3900
2	F-BNa	Na - Slab Bottom Rebar	3900

PROJET		ID DESSIN		DESSIN Nr.
Instrumentation Plan		Rebar [5] Strain Gauges / Fiber		4
DATE 28/11/2019	REVISION 1	DIM mm	ÉCHELLE 1:15	PAPIER A3

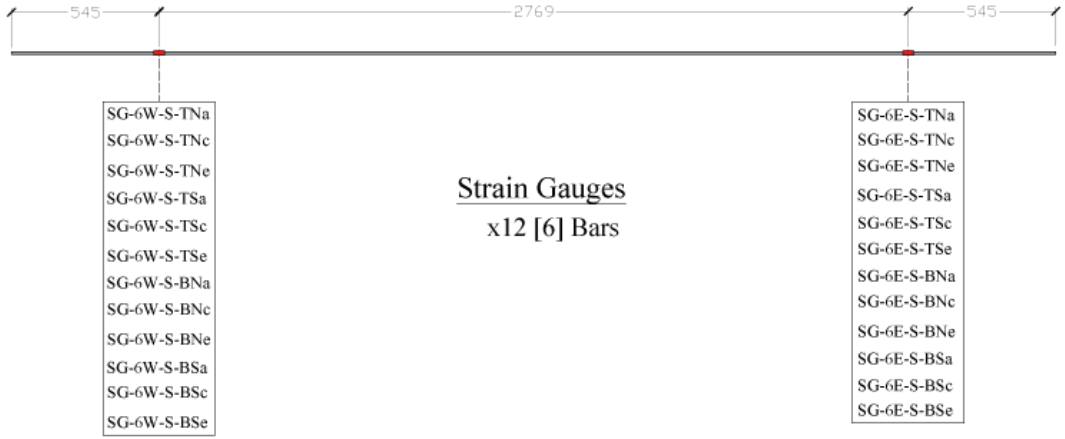

Strain Gauges
x12 [6] Bars

STRAIN GAUGES [6] REBARS
(120 ± 0.5 Ω)

#	ID	LOCATION	LENGTH [MM]
1	SG-6E-S-TNa	6E Na - Slab Top Rebar	3
2	SG-6E-S-TNc	6E Nc - Slab Top Rebar	3
3	SG-6E-S-TNe	6E Ne - Slab Top Rebar	3
4	SG-6E-S-TSa	6E Sa - Slab Top Rebar	3
5	SG-6E-S-TSc	6E Sc - Slab Top Rebar	3
6	SG-6E-S-TSe	6E Se - Slab Top Rebar	3
7	SG-6E-S-BNa	6E Na - Slab Bottom Rebar	3
8	SG-6E-S-BNc	6E Nc - Slab Bottom Rebar	3
9	SG-6E-S-BNe	6E Ne - Slab Bottom Rebar	3
10	SG-6E-S-BSa	6E Sa - Slab Bottom Rebar	3
11	SG-6E-S-BSc	6E Sc - Slab Bottom Rebar	3
12	SG-6E-S-BSe	6E Se - Slab Bottom Rebar	3
13	SG-6W-S-TNa	6W Na - Slab Top Rebar	3
14	SG-6W-S-TNc	6W Nc - Slab Top Rebar	3
15	SG-6W-S-TNe	6W Ne - Slab Top Rebar	3
16	SG-6W-S-TSa	6W Sa - Slab Top Rebar	3
17	SG-6W-S-TSc	6W Sc - Slab Top Rebar	3
18	SG-6W-S-TSe	6W Se - Slab Top Rebar	3
19	SG-6W-S-BNa	6W Na - Slab Bottom Rebar	3
20	SG-6W-S-BNc	6W Nc - Slab Bottom Rebar	3
21	SG-6W-S-BNe	6W Ne - Slab Bottom Rebar	3
22	SG-6W-S-BSa	6W Sa - Slab Bottom Rebar	3
23	SG-6W-S-BSc	6W Sc - Slab Bottom Rebar	3
24	SG-6W-S-BSe	6W Se - Slab Bottom Rebar	3

PROJET		ID DESSIN		DESSIN Nr.
Instrumentation Plan		Rebar [6] Strain Gauges		5
DATE 26/02/2020	REVISION 1	DIM mm	ÉCHELLE 1:15	PAPIER A3

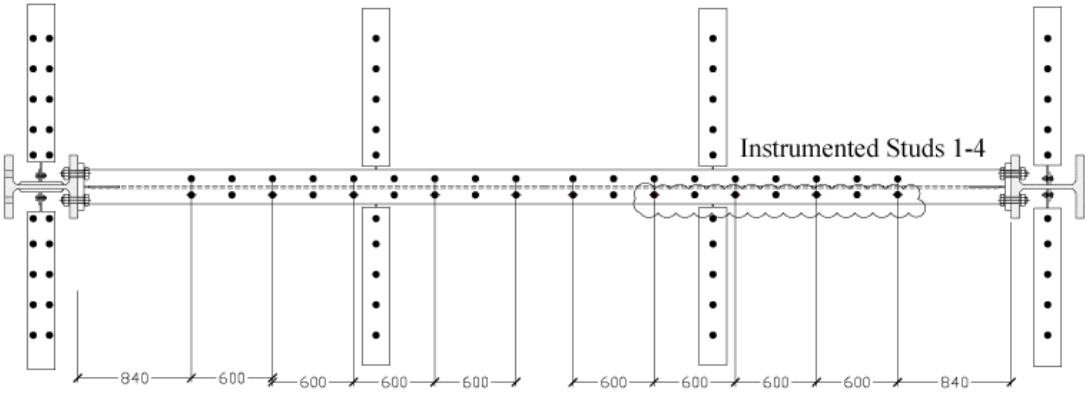

East Beam Plan View

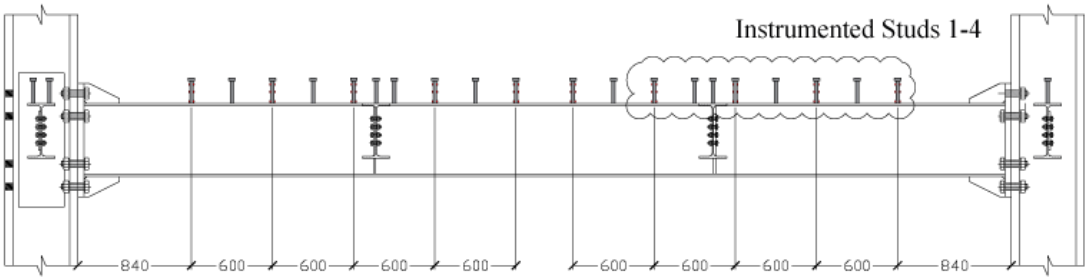

East Beam Side View

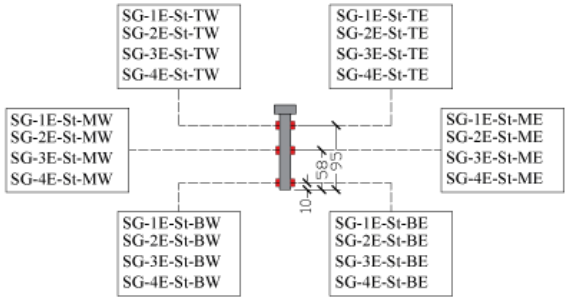

Strain Gauges
x4 Studs

Scale (1:6)

STRAIN GAUGES STUDS [1-4]
(120 Ω ± 0.5 Ω)

#	ID	LOCATION	LENGTH [MM]
1	SG-1E-St-TE	1E - Shear Stud Top East	5
2	SG-1E-St-ME	1E - Shear Stud Middle East	5
3	SG-1E-St-BE	1E - Shear Stud Bottom East	5
4	SG-1E-St-TW	1E - Shear Stud Top West	3
5	SG-1E-St-MW	1E - Shear Stud Middle West	3
6	SG-1E-St-BW	1E - Shear Stud Bottom West	3
7	SG-2E-St-TE	2E - Shear Stud Top East	5
8	SG-2E-St-ME	2E - Shear Stud Middle East	5
9	SG-2E-St-BE	2E - Shear Stud Bottom East	5
10	SG-2E-St-TW	2E - Shear Stud Top West	3
11	SG-2E-St-MW	2E - Shear Stud Middle West	3
12	SG-2E-St-BW	2E - Shear Stud Bottom West	3
13	SG-3E-St-TE	3E - Shear Stud Top East	5
14	SG-3E-St-ME	3E - Shear Stud Middle East	5
15	SG-3E-St-BE	3E - Shear Stud Bottom East	5
16	SG-3E-St-TW	3E - Shear Stud Top West	3
17	SG-3E-St-MW	3E - Shear Stud Middle West	3
18	SG-3E-St-BW	3E - Shear Stud Bottom West	3
19	SG-4E-St-TE	4E - Shear Stud Top East	5
20	SG-4E-St-ME	4E - Shear Stud Middle East	5
21	SG-4E-St-BE	4E - Shear Stud Bottom East	5
22	SG-4E-St-TW	4E - Shear Stud Top West	3*
23	SG-4E-St-MW	4E - Shear Stud Middle West	3
24	SG-4E-St-BW	4E - Shear Stud Bottom West	3

** 350 Ω ± 1.5 Ω*

PROJET		ID DESSIN		DESSIN Nr.
Instrumentation Plan		Studs [1-4] Strain Gauges		6
DATE 08/11/2020	**REVISION** 1	**DIM** mm	**ÉCHELLE** 1:20	**PAPIER** A3

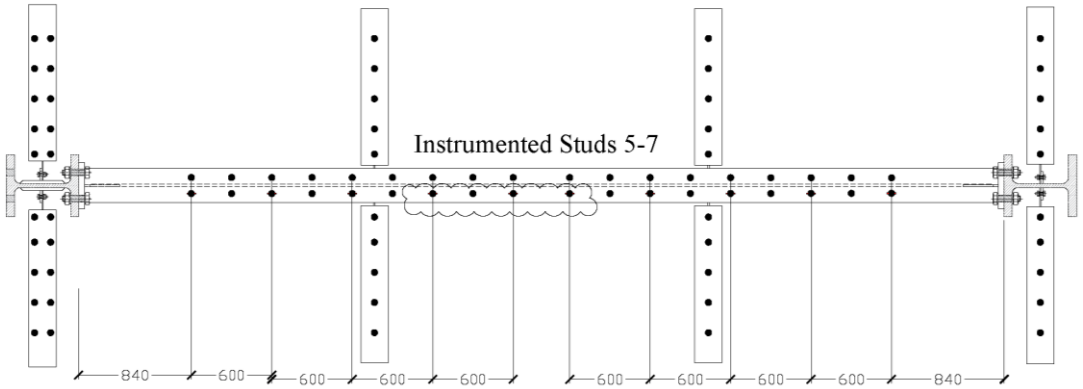

East Beam Plan View

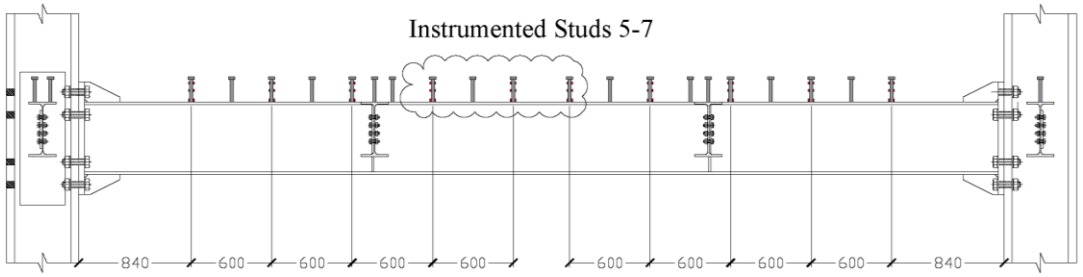

East Beam Side View

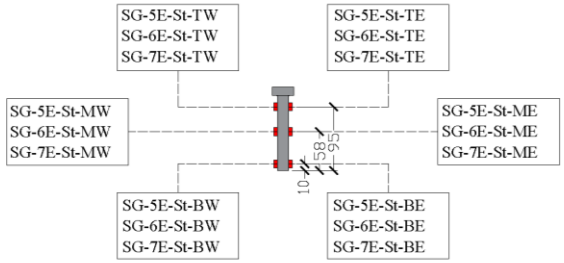

Strain Gauges
x3 Studs

Scale (1:6)

STRAIN GAUGES STUDS [5-7]
(120 Ω ± 0.5 Ω)

#	ID	LOCATION	LENGTH [MM]
1	SG-5E-St-TE	5E - Shear Stud Top East	3
2	SG-5E-St-ME	5E - Shear Stud Middle East	5
3	SG-5E-St-BE	5E - Shear Stud Bottom East	5
4	SG-5E-St-TW	5E - Shear Stud Top West	3*
5	SG-5E-St-MW	5E - Shear Stud Middle West	3*
6	SG-5E-St-BW	5E - Shear Stud Bottom West	6*
7	SG-6E-St-TE	6E - Shear Stud Top East	3*
8	SG-6E-St-ME	6E - Shear Stud Middle East	6*
9	SG-6E-St-BE	6E - Shear Stud Bottom East	6*
10	SG-6E-St-TW	6E - Shear Stud Top West	3*
11	SG-6E-St-MW	6E - Shear Stud Middle West	6*
12	SG-6E-St-BW	6E - Shear Stud Bottom West	6*
13	SG-7E-St-TE	7E - Shear Stud Top East	3*
14	SG-7E-St-ME	7E - Shear Stud Middle East	6*
15	SG-7E-St-BE	7E - Shear Stud Bottom East	6*
16	SG-7E-St-TW	7E - Shear Stud Top West	3*
17	SG-7E-St-MW	7E - Shear Stud Middle West	6*
18	SG-7E-St-BW	7E - Shear Stud Bottom West	6*

** 350 Ω ± 1.5 Ω*

PROJET		ID DESSIN		DESSIN Nr.
Instrumentation Plan		Studs [5-7] Strain Gauges		7
DATE	**REVISION**	**DIM**	**ÉCHELLE**	**PAPIER**
08/11/2020	1	mm	1:20	A3

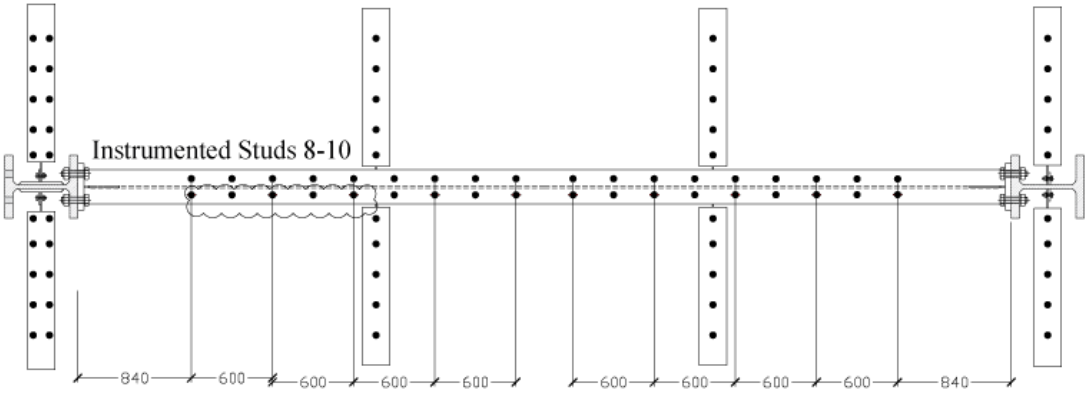

East Beam Plan View

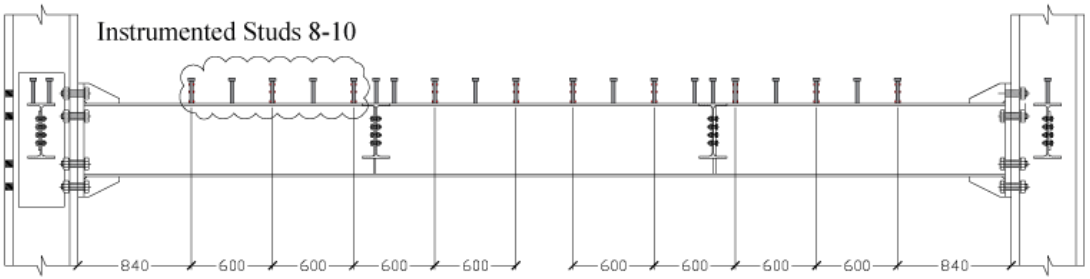

East Beam Side View

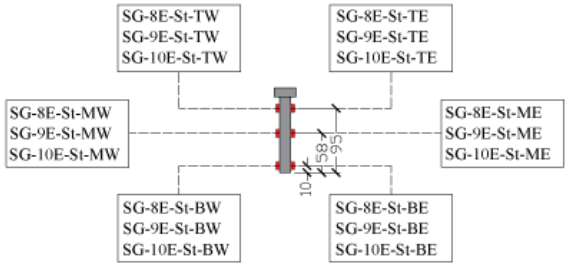

Strain Gauges

x3 Studs

Scale (1:6)

STRAIN GAUGES STUDS [8-10]
(350 Ω ± 1.5 Ω)

#	ID	LOCATION	LENGTH [MM]
1	SG-8E-St-TE	8E - Shear Stud Top East	3
2	SG-8E-St-ME	8E - Shear Stud Middle East	3
3	SG-8E-St-BE	8E - Shear Stud Bottom East	6
4	SG-8E-St-TW	8E - Shear Stud Top West	3
5	SG-8E-St-MW	8E - Shear Stud Middle West	3
6	SG-8E-St-BW	8E - Shear Stud Bottom West	6
7	SG-9E-St-TE	9E - Shear Stud Top East	3
8	SG-9E-St-ME	9E - Shear Stud Middle East	3
9	SG-9E-St-BE	9E - Shear Stud Bottom East	6
10	SG-9E-St-TW	9E - Shear Stud Top West	3
11	SG-9E-St-MW	9E - Shear Stud Middle West	3
12	SG-9E-St-BW	9E - Shear Stud Bottom West	6
13	SG-10E-St-TE	10E - Shear Stud Top East	3
14	SG-10E-St-ME	10E - Shear Stud Middle East	3
15	SG-10E-St-BE	10E - Shear Stud Bottom East	6
16	SG-10E-St-TW	10E - Shear Stud Top West	3
17	SG-10E-St-MW	10E - Shear Stud Middle West	3
18	SG-10E-St-BW	10E - Shear Stud Bottom West	6

PROJET		ID DESSIN		DESSIN Nr.
Instrumentation Plan		Studs [8-10] Strain Gauges		8
DATE 08/11/2020	REVISION 1	DIM mm	ÉCHELLE 1:20	PAPIER A3

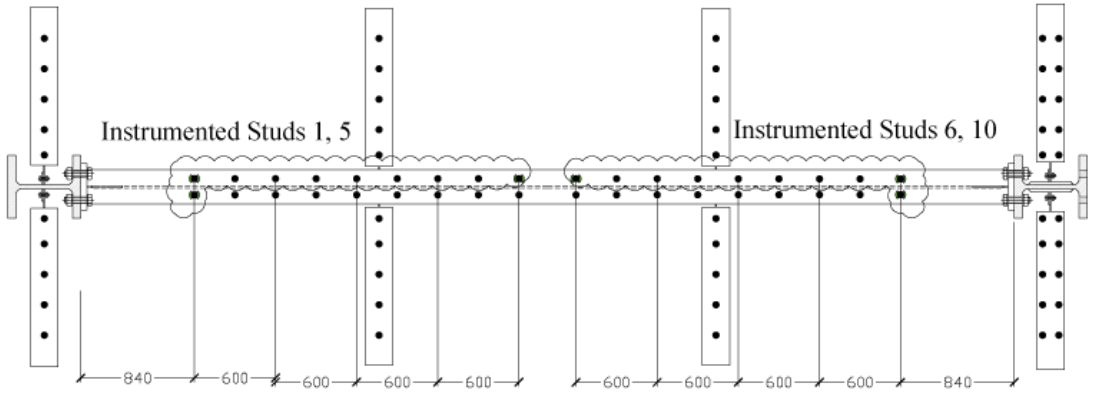

West Beam Plan View

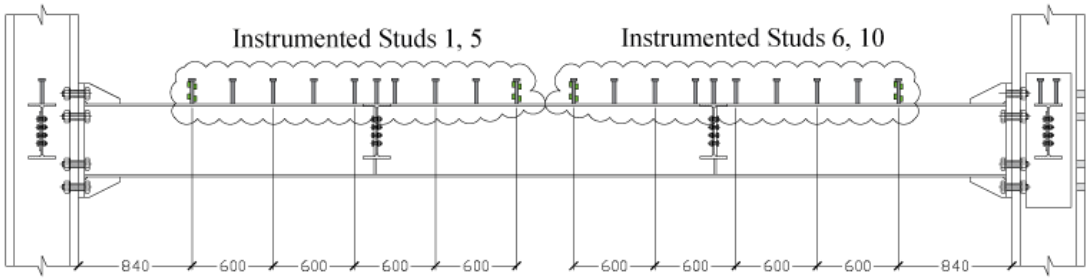

West Beam Side View

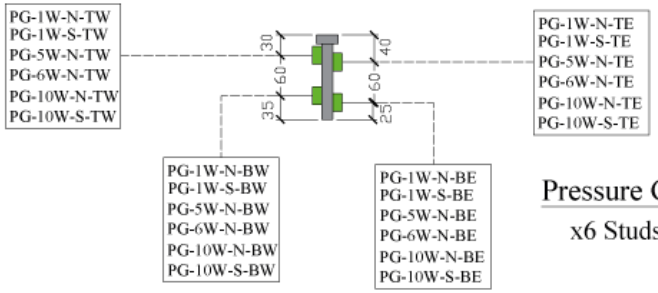

Scale (1:6)

Pressure Gauges

x6 Studs

PRESSURE GAUGES STUDS (120 Ω ± 2%)

#	ID	LOCATION	LENGTH [MM]
1	PG-1W-N-TE	1E-N - Shear Stud Top	3
2	PG-1W-N-BE	1E-N - Shear Stud Bottom	3
3	PG-1W-N-TW	1W-N - Shear Stud Top	3
4	PG-1W-N-BW	1W-N - Shear Stud Bottom	3
5	PG-1W-S-TE	1E-S - Shear Stud Top	3
6	PG-1W-S-BE	1E-S - Shear Stud Bottom	3
7	PG-1W-S-TW	1W-S - Shear Stud Top	3
8	PG-1W-S-BW	1W-S - Shear Stud Bottom	3
9	PG-5W-N-TE	5E - Shear Stud Top	3
10	PG-5W-N-BE	5E - Shear Stud Bottom	3
11	PG-5W-N-TW	5W - Shear Stud Top	3
12	PG-5W-N-BW	5W - Shear Stud Bottom	3
13	PG-6W-N-TE	6E - Shear Stud Top	3
14	PG-6W-N-BE	6E - Shear Stud Bottom	3
15	PG-6W-N-TW	6W - Shear Stud Top	3
16	PG-6W-N-BW	6W - Shear Stud Bottom	3
17	PG-10W-N-TE	10E-N - Shear Stud Top	3
18	PG-10W-N-BE	10E-N - Shear Stud Bottom	3
19	PG-10W-N-TW	10W-N - Shear Stud Top	3
20	PG-10W-N-BW	10W-N - Shear Stud Bottom	3
21	PG-10W-S-TE	10E-S - Shear Stud Top	3
22	PG-10W-S-BE	10E-S - Shear Stud Bottom	3
23	PG-10W-S-TW	10W-S - Shear Stud Top	3
24	PG-10W-S-BW	10W-S - Shear Stud Bottom	3

PROJET		ID DESSIN		DESSIN Nr.
Instrumentation Plan		Studs Pressure Gauges		9
DATE 16/11/2020	REVISION 1	DIM mm	ÉCHELLE 1:20	PAPIER A3

LVDTS SLAB			
#	ID	LOCATION	RANGE [MM]
1	LVDT-1W-S	West Beam West Joint	±10
2	LVDT-5W-S	West Beam Middle	±10
3	LVDT-10W-S	West Beam Interior Joint	±10

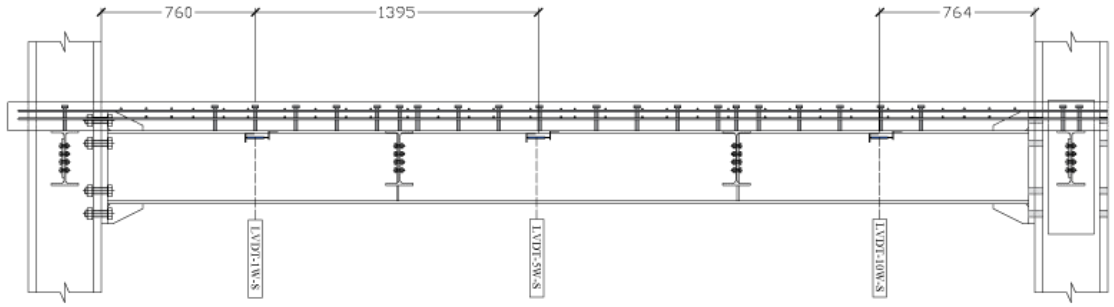

West Beam Side View

PROJET		ID DESSIN		DESSIN Nr.
Instrumentation Plan		Slab LVDTs		10
DATE 28/07/2021	REVISION 1	DIM mm	ÉCHELLE 1:20	PAPIER A3

LVDTS SLAB			
#	ID	LOCATION	RANGE [MM]
1	LVDT-1E-S	East Beam East Joint	±10
2	LVDT-6E-S	East Beam Middle	±10
3	LVDT-10E-S	East Beam Interior Joint	±10

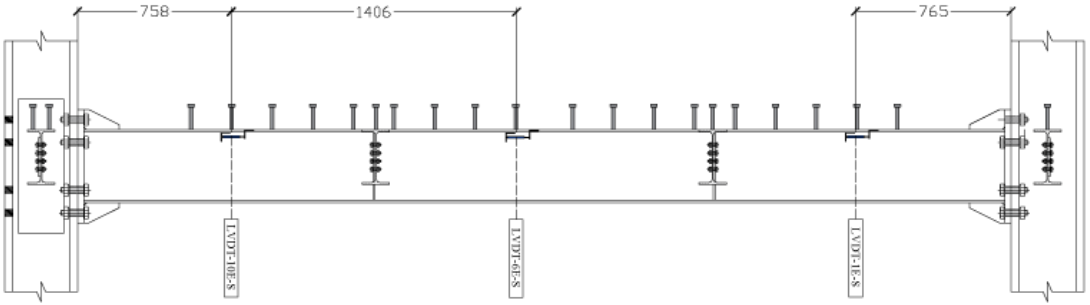

East Beam Side View

PROJET		ID DESSIN		DESSIN Nr.
Instrumentation Plan		Slab LVDTs		11
DATE 28/07/2021	REVISION 1	DIM mm	ÉCHELLE 1:20	PAPIER A3

SLAB INSTRUMENTATION PLAN SUMMARY					
QUAN	Sensor	Gauge Length [mm]	Resistance [Ω]	Length [mm]	Range [mm]
152	Strain Gauges _	VARIES	VARIES	-	-
10	Fiber-Optic Cable	-	-	3900	-
24	Pressure Gauges (PMS40)	3	250 ± 2%	-	-
6	LVDTs	-	-	-	±10

PROJET		**ID DESSIN**		**DESSIN Nr.**
Instrumentation Plan		Summary Table		12
DATE 02/08/2020	**REVISION** 1	**DIM** mm	**ÉCHELLE** -	**PAPIER** A3

D.3 Summary of working sensors

In this section, the working sensors in three data acquisition systems (DAQs) are summarized for each test: (i) DAQ1 includes strain gauges, pressure gauges, LVDTs, inclinometers, string potentiometers and load cells; (ii) DAQ2 corresponds to that of the LED Coordinate System; and (iii) DAQ3 corresponds to that of the fiber optic measurement system. Tables D.1, D.2 and D.3 summarize the number of working sensors in each test for DAQ1, DAQ2 and DAQ3, respectively. The sensors that were damaged or non-functional during a test are not included in the number of working sensors.

Tables D.4, D.5 and D.6 show the DAQ1 sensors that were damaged in each test. Sensors that were damaged during the tests are highlighted in grey.

Table D.7 shows the DAQ2 LED bulbs that were not functional during each test.

Table D.8 shows the DAQ3 fiber optic cables that were damaged in each test. The fiber optic cables that were damaged during the tests are highlighted in grey

Table D.1 Summary of working sensors in DAQ1

Loading Protocol	File Name	Test Date	# of Working Sensors	# of Lines
Elastic[1]	Elastic_Bare[1]	28.10.2020	119	6530
AISC	Elastic	06.05.2021	239	24,808
	AISC_0.375-0.5	03.06.2021	206	50,609
	AISC_0.75-1.5	09.06.2021	187	69,579
	AISC_2-4	20.07.2021	160	114,247
SAC Near-Fault	SAC_Near_Fault	22.07.2021	164	60,982
Collapse Consistent	Collapse_Consistent	22.07.2021	162	85,215

[1] Bare frame (i.e., without slab) subjected to a cyclic elastic protocol up to 0.4% rads

Table D.2 Summary of working sensors in DAQ2

Loading Protocol	File Name	Test Date	# of Working Sensors	# of Lines
AISC	Elastic_LED	06.05.2021	46	124,735
	AISC_0.375-0.5_LED	03.06.2021	46	51,362
	AISC_0.75-1.5_LED	09.06.2021	46	62,804
	AISC_2-4_LED	20.07.2021	15	232,639
SAC Near-Fault	SAC_Near_Fault_LED	22.07.2021	42	123,068
Collapse Consistent	Collapse_Consistent_LED	22.07.2021	42	171,437

Table D.3 Summary of working sensors in DAQ3

Loading Protocol	Folder Name	Test Date	# of Working Sensors
AISC	Elastic_FOM	06.05.2021	8
	AISC_0.375-0.5_FOM	03.06.2021	7
	AISC_0.75-1.5_FOM	09.06.2021	8
	AISC_2-4_FOM	20.07.2021	7
Near-Fault	SAC_Near_Fault_FOM	22.07.2021	7
Collapse Consistent	Collapse_Consistent_FOM	22.07.2021	7

Table D.4 Damaged strain gauges in all tests

Elastic	AISC 0.375-0.5%	AISC 0.75-1.5%	AISC 2-4%	SAC Near-Fault	Collapse-Consistent
SG-5E-S-BNc	SG-5E-S-BNa	SG-5E-S-BNa	SG-2E-F-NE[1,2]	SG-2I-F-SE[1]	SG-2I-F-SE
SG-5E-S-BSd	SG-5E-S-BNc	SG-5E-S-BNc	SG-2E-F-SE[1,2]	SG-2W-F-NE[1]	SG-2I-F-NE[1]
SG-5E-S-TSa	SG-5E-S-BNe	SG-5E-S-BSa	SG-2W-F-NW[1,2]	SG-5E-S-BNa	SG-2W-F-NE
SG-5E-S-TSe	SG-5E-S-BSa	SG-5E-S-BSb[1]	SG-5E-S-BNa	SG-5E-S-BNb	SG-2W-F-SW[1]
SG-5W-S-BNa	SG-5E-S-BSc	SG-5E-S-BSc	SG-5E-S-BNb	SG-5E-S-BNc	SG-5E-S-BNa
SG-5W-S-BNb	SG-5E-S-BSd	SG-5E-S-BSd	SG-5E-S-BNc	SG-5E-S-BNd	SG-5E-S-BNb
SG-5W-S-BNc	SG-5E-S-BSe	SG-5E-S-BSe[1]	SG-5E-S-BNd	SG-5E-S-BNe	SG-5E-S-BNc
SG-5W-S-BNd	SG-5E-S-TNa	SG-5E-S-TNa	SG-5E-S-BNe	SG-5E-S-BSa	SG-5E-S-BNd
SG-5W-S-BNe	SG-5E-S-TNb	SG-5E-S-TNb	SG-5E-S-BSa	SG-5E-S-BSb	SG-5E-S-BNe
SG-5W-S-BSb	SG-5E-S-TNc	SG-5E-S-TNc	SG-5E-S-BSb	SG-5E-S-BSc	SG-5E-S-BSa
SG-5W-S-BSc	SG-5E-S-TNe	SG-5E-S-TNe	SG-5E-S-BSc	SG-5E-S-BSd	SG-5E-S-BSb
SG-5W-S-BSd[1]	SG-5E-S-TSa	SG-5E-S-TSa	SG-5E-S-BSd	SG-5E-S-BSe	SG-5E-S-BSc
SG-5W-S-BSe	SG-5E-S-TSb	SG-5E-S-TSb	SG-5E-S-BSe	SG-5E-S-TNa	SG-5E-S-BSd
SG-5W-S-TNa	SG-5E-S-TSc	SG-5E-S-TSc	SG-5E-S-TNa	SG-5E-S-TNb	SG-5E-S-BSe
SG-5W-S-TNb	SG-5E-S-TSe	SG-5E-S-TSd[1]	SG-5E-S-TNb	SG-5E-S-TNc	SG-5E-S-TNa
SG-5W-S-TNc	SG-5W-S-BNe	SG-5E-S-TSe	SG-5E-S-TNc	SG-5E-S-TNd	SG-5E-S-TNb
SG-5W-S-TNd	SG-5W-S-BSa	SG-5W-S-BNe	SG-5E-S-TNd	SG-5E-S-TNe	SG-5E-S-TNc
SG-5W-S-TNe	SG-5W-S-BSb	SG-5W-S-BSa	SG-5E-S-TNe	SG-5E-S-TSa	SG-5E-S-TNd
SG-5W-S-TSa[1]	SG-5W-S-BSc	SG-5W-S-BSb	SG-5E-S-TSa	SG-5E-S-TSb	SG-5E-S-TNe
SG-5W-S-TSb[1]	SG-5W-S-BSd	SG-5W-S-BSc	SG-5E-S-TSb	SG-5E-S-TSc	SG-5E-S-TSa
SG-5W-S-TSc	SG-5W-S-BSe	SG-5W-S-BSd	SG-5E-S-TSc	SG-5E-S-TSd	SG-5E-S-TSb
SG-5W-S-TSd	SG-5W-S-TNe	SG-5W-S-BSe	SG-5E-S-TSd	SG-5E-S-TSe	SG-5E-S-TSc
SG-5W-S-TSe[1]	SG-5W-S-TSa	SG-5W-S-TNe	SG-5E-S-TSe	SG-5W-S-BNe	SG-5E-S-TSd
SG-6E-S-BNa[1]	SG-5W-S-TSb	SG-5W-S-TSa	SG-5W-S-BNe	SG-5W-S-BSa	SG-5E-S-TSe
SG-6E-S-BNb	SG-5W-S-TSc	SG-5W-S-TSb	SG-5W-S-BSa	SG-5W-S-BSb	SG-5W-S-BNe
SG-6E-S-BNc[1]	SG-5W-S-TSd	SG-5W-S-TSc	SG-5W-S-BSb	SG-5W-S-BSc	SG-5W-S-BSa
SG-6E-S-BSb[1]	SG-5W-S-TSe	SG-5W-S-TSd	SG-5W-S-BSc	SG-5W-S-BSd	SG-5W-S-BSb
SG-6E-S-BSc	SG-6E-S-BNa	SG-5W-S-TSe	SG-5W-S-BSd	SG-5W-S-BSe	SG-5W-S-BSc
SG-6E-S-BSd	SG-6E-S-BNb	SG-6E-S-BNa	SG-5W-S-BSe	SG-5W-S-TNe	SG-5W-S-BSd
SG-6E-S-BSe[1]	SG-6E-S-BNc	SG-6E-S-BNb	SG-5W-S-TNe	SG-5W-S-TSa	SG-5W-S-BSe
SG-6E-S-TNa[1]	SG-6E-S-BNe	SG-6E-S-BNc	SG-5W-S-TSa	SG-5W-S-TSb	SG-5W-S-TNe
SG-6E-S-TNb	SG-6E-S-BSa	SG-6E-S-BNd[1]	SG-5W-S-TSb	SG-5W-S-TSc	SG-5W-S-TSa
SG-6E-S-TNc[1]	SG-6E-S-BSb	SG-6E-S-BNe	SG-5W-S-TSc	SG-5W-S-TSd	SG-5W-S-TSb
SG-6E-S-TNd[1]	SG-6E-S-BSc	SG-6E-S-BSa	SG-5W-S-TSd	SG-5W-S-TSe	SG-5W-S-TSc

SG-6E-S-TNe[1]	SG-6E-S-BSd	SG-6E-S-BSb	SG-5W-S-TSe	SG-6E-S-BNa	SG-5W-S-TSd
SG-6W-S-BNa	SG-6E-S-BSe	SG-6E-S-BSc	SG-6E-S-BNa	SG-6E-S-BNb	SG-5W-S-TSe
SG-6W-S-BNc	SG-6E-S-TNa	SG-6E-S-BSd	SG-6E-S-BNb	SG-6E-S-BNc	SG-6E-S-BNa
SG-6W-S-BNd[1]	SG-6E-S-TNb	SG-6E-S-BSe	SG-6E-S-BNc	SG-6E-S-BNd	SG-6E-S-BNb
SG-6W-S-BNe	SG-6E-S-TNc	SG-6E-S-TNa	SG-6E-S-BNd	SG-6E-S-BNe	SG-6E-S-BNc
SG-6W-S-BSa	SG-6E-S-TNd	SG-6E-S-TNb	SG-6E-S-BNe	SG-6E-S-BSa	SG-6E-S-BNd
SG-6W-S-BSc	SG-6E-S-TNe	SG-6E-S-TNc	SG-6E-S-BSa	SG-6E-S-BSb	SG-6E-S-BNe
SG-6W-S-TNa[1]	SG-6E-S-TSa	SG-6E-S-TND	SG-6E-S-BSb	SG-6E-S-BSc	SG-6E-S-BSa
SG-6W-S-TNc	SG-6E-S-TSc[1]	SG-6E-S-TNe	SG-6E-S-BSc	SG-6E-S-BSd	SG-6E-S-BSb
SG-6W-S-TND	SG-6E-S-TSe	SG-6E-S-TSc	SG-6E-S-BSd	SG-6E-S-BSe	SG-6E-S-BSc
SG-6W-S-TNe	SG-6W-S-BNa	SG-6E-St-ME	SG-6E-S-BSe	SG-6E-S-TNa	SG-6E-S-BSd
SG-6W-S-TSb	SG-6W-S-BNb	SG-6E-St-TE	SG-6E-S-TNa	SG-6E-S-TNb	SG-6E-S-BSe
SG-6W-S-TSd	SG-6W-S-BNc	SG-6W-S-BNa	SG-6E-S-TNb	SG-6E-S-TNc	SG-6E-S-TNa
SG-6W-S-TSe	SG-6W-S-BND	SG-6W-S-BNb	SG-6E-S-TNc	SG-6E-S-TND	SG-6E-S-TNb
SG-S-BEi[1]	SG-6W-S-BNe	SG-6W-S-BNc	SG-6E-S-TND	SG-6E-S-TNe	SG-6E-S-TNc
SG-S-BEj[1]	SG-6W-S-BSa	SG-6W-S-BND	SG-6E-S-TNe	SG-6E-S-TSb	SG-6E-S-TND
SG-S-TEi[1]	SG-6W-S-BSc	SG-6W-S-BNe	SG-6E-S-TSb[1]	SG-6E-S-TSc	SG-6E-S-TNe
SG-S-TEj1	SG-6W-S-BSe	SG-6W-S-BSc	SG-6E-S-TSc	SG-6E-St-BE	SG-6E-S-TSb
SG-S-TWh	SG-6W-S-TNa	SG-6W-S-BSe	SG-6W-S-BNa	SG-6E-St-BW	SG-6E-S-TSc
SG-1E-St-ME	SG-6W-S-TNb	SG-6W-S-TNa	SG-6W-S-BNb	SG-6E-St-ME	SG-6W-S-BNa
SG-1E-St-MW	SG-6W-S-TNc	SG-6W-S-TNb	SG-6W-S-BNc	SG-6E-St-MW	SG-6W-S-BNb
SG-1E-St-TE	SG-6W-S-TND	SG-6W-S-TNc	SG-6W-S-BND	SG-6E-St-TE	SG-6W-S-BNc
SG-1E-St-TW	SG-6W-S-TNe	SG-6W-S-TND	SG-6W-S-BNe	SG-6W-S-BNa	SG-6W-S-BND
SG-2E-St-BE	SG-6W-S-TSa	SG-6W-S-TNe	SG-6W-S-BSa	SG-6W-S-BNb	SG-6W-S-BNe
SG-2E-St-BW	SG-6W-S-TSb	SG-6W-S-TSb	SG-6W-S-BSb	SG-6W-S-BNc	SG-6W-S-BSa
SG-2E-St-MW	SG-6W-S-TSd	SG-6W-S-TSc	SG-6W-S-BSc	SG-6W-S-BND	SG-6W-S-BSb
SG-2E-St-TE	SG-6W-S-TSe	SG-6W-S-TSd	SG-6W-S-BSd	SG-6W-S-BNe	SG-6W-S-BSc
SG-2E-St-TW	SG-S-BEf	SG-6W-S-TSe	SG-6W-S-BSe	SG-6W-S-BSa	SG-6W-S-BSd
SG-3E-St-TE	SG-S-BEg	SG-S-BEf	SG-6W-S-TNa	SG-6W-S-BSb	SG-6W-S-BSe
SG-3E-St-TW	SG-S-BEi	SG-S-BEg	SG-6W-S-TNb	SG-6W-S-BSc	SG-6W-S-TNa
SG-4E-St-BE	SG-S-BEj	SG-S-BEi	SG-6W-S-TNc	SG-6W-S-BSd	SG-6W-S-TNb
SG-4E-St-ME	SG-S-BWi	SG-S-BEj	SG-6W-S-TND	SG-6W-S-BSe	SG-6W-S-TNc
SG-4E-St-TE	SG-S-TEf	SG-S-BWi	SG-6W-S-TNe	SG-6W-S-TNa	SG-6W-S-TND
SG-5E-St-MW	SG-S-TEg	SG-S-TEf	SG-6W-S-TSb	SG-6W-S-TNb	SG-6W-S-TNe
SG-5E-St-TW	SG-S-TEi	SG-S-TEi	SG-6W-S-TSc	SG-6W-S-TNc	SG-6W-S-TSb
SG-6E-St-ME	SG-S-TEj	SG-S-TEj	SG-6W-S-TSd	SG-6W-S-TND	SG-6W-S-TSc
SG-6E-St-TE	SG-S-TEk	SG-S-TEk	SG-6W-S-TSe	SG-6W-S-TNe	SG-6W-S-TSd
SG-7E-St-TE	SG-S-TWh	SG-S-TWh	SG-S-BEf	SG-6W-S-TSb	SG-6W-S-TSe
SG-8E-St-TE	SG-S-TWi	SG-1E-St-BE[1]	SG-S-BEg[1]	SG-6W-S-TSc	SG-S-BEf
SG-9E-St-TE	SG-1E-St-ME	SG-1E-St-BW	SG-S-BEi	SG-6W-S-TSd	SG-S-BEg
SG-9E-St-TW	SG-1E-St-MW	SG-1E-St-ME	SG-S-BEj	SG-6W-S-TSe	SG-S-BEi
SG-10E-St-TW	SG-1E-St-TE	SG-1E-St-MW	SG-S-BWf	SG-S-BEf	SG-S-BEj
	SG-1E-St-TW	SG-1E-St-TE	SG-S-BWg[1]	SG-S-BEg	SG-S-BWf
	SG-2E-St-BE	SG-1E-St-TW	SG-S-BWi	SG-S-BEi	SG-S-BWg
	SG-2E-St-BW	SG-2E-St-BE	SG-S-BWj[1]	SG-S-BEj	SG-S-BWi
	SG-2E-St-MW	SG-2E-St-BW	SG-S-TEf	SG-S-BWf	SG-S-BWj

SG-2E-St-TE	SG-2E-St-ME[1]	SG-S-TEh[1]	SG-S-BWg	SG-S-TEf
SG-2E-St-TW	SG-2E-St-MW	SG-S-TEi	SG-S-BWi	SG-S-TEh
SG-3E-St-BE[1]	SG-2E-St-TE	SG-S-TEj	SG-S-BWj	SG-S-TEi
SG-3E-St-TE	SG-2E-St-TW	SG-S-TEk	SG-S-TEf	SG-S-TEj
SG-3E-St-TW	SG-3E-St-BE	SG-S-TWf	SG-S-TEh	SG-S-TEk
SG-4E-St-BE	SG-3E-St-BW[1]	SG-S-TWg[1]	SG-S-TEi	SG-S-TWf
SG-4E-St-BW[1]	SG-3E-St-ME[1]	SG-S-TWh	SG-S-TEj	SG-S-TWg[1]
SG-4E-St-ME	SG-3E-St-TE	SG-1E-St-BE	SG-S-TEk	SG-S-TWh
SG-4E-St-TE	SG-3E-St-TW	SG-1E-St-BW	SG-S-TWf	SG-1E-St-BE
SG-5E-St-MW	SG-4E-St-BE	SG-1E-St-ME	SG-S-TWg	SG-1E-St-BW
SG-5E-St-TW	SG-4E-St-BW	SG-1E-St-MW	SG-S-TWh	SG-1E-St-ME
SG-6E-St-ME	SG-4E-St-ME	SG-1E-St-TE	SG-1E-St-BE	SG-1E-St-MW
SG-6E-St-TE	SG-4E-St-MW[1]	SG-1E-St-TW	SG-1E-St-BW	SG-1E-St-TE
SG-7E-St-TE	SG-4E-St-TE	SG-2E-St-BE	SG-1E-St-ME	SG-1E-St-TW
SG-8E-St-TE	SG-4E-St-TW	SG-2E-St-BW	SG-1E-St-MW	SG-2E-St-BE
SG-9E-St-BE[1]	SG-5E-St-BE[1]	SG-2E-St-ME	SG-1E-St-TE	SG-2E-St-BW
SG-9E-St-BW	SG-5E-St-BW[1]	SG-2E-St-MW	SG-1E-St-TW	SG-2E-St-ME
SG-9E-St-MW	SG-5E-St-MW	SG-2E-St-TE	SG-2E-St-BE	SG-2E-St-MW
SG-9E-St-TE	SG-5E-St-TW	SG-2E-St-TW	SG-2E-St-BW	SG-2E-St-TE
SG-9E-St-TW	SG-6E-St-BE[1]	SG-3E-St-BE	SG-2E-St-ME	SG-2E-St-TW
SG-10E-St-BE[1]	SG-6E-St-BW[1]	SG-3E-St-BW	SG-2E-St-MW	SG-3E-St-BE
SG-10E-St-BW[1]	SG-7E-St-BE[1]	SG-3E-St-ME	SG-2E-St-TE	SG-3E-St-BW
SG-10E-St-ME[1]	SG-7E-St-BW[1]	SG-3E-St-MW	SG-2E-St-TW	SG-3E-St-ME
SG-10E-St-MW	SG-7E-St-ME[1]	SG-3E-St-TE	SG-3E-St-BE	SG-3E-St-MW
SG-10E-St-TE[1]	SG-7E-St-MW[1]	SG-3E-St-TW	SG-3E-St-BW	SG-3E-St-TE
SG-10E-St-TW	SG-7E-St-TE	SG-4E-St-BE	SG-3E-St-ME	SG-3E-St-TW
	SG-7E-St-TW[1]	SG-4E-St-BW	SG-3E-St-MW	SG-4E-St-BE
	SG-8E-St-BE[1]	SG-4E-St-ME	SG-3E-St-TE	SG-4E-St-BW
	SG-8E-St-BW[1]	SG-4E-St-MW	SG-3E-St-TW	SG-4E-St-ME
	SG-8E-St-ME[1]	SG-4E-St-TE	SG-4E-St-BE	SG-4E-St-MW
	SG-8E-St-MW[1]	SG-4E-St-TW	SG-4E-St-BW	SG-4E-St-TE
	SG-8E-St-TE	SG-5E-St-BE	SG-4E-St-ME	SG-4E-St-TW
	SG-9E-St-BE	SG-5E-St-BW	SG-4E-St-MW	SG-5E-St-BE
	SG-9E-St-BW	SG-5E-St-ME[1]	SG-4E-St-TE	SG-5E-St-BW
	SG-9E-St-ME[1]	SG-5E-St-MW	SG-4E-St-TW	SG-5E-St-ME
	SG-9E-St-MW	SG-5E-St-TE[1]	SG-5E-St-BE	SG-5E-St-MW
	SG-9E-St-TE	SG-5E-St-TW	SG-5E-St-BW	SG-5E-St-TE
	SG-9E-St-TW	SG-6E-St-BE	SG-5E-St-ME	SG-5E-St-TW
	SG-10E-St-BE	SG-6E-St-BW	SG-5E-St-MW	SG-6E-St-BE
	SG-10E-St-BW	SG-6E-St-ME	SG-5E-St-TE	SG-6E-St-BW
	SG-10E-St-ME	SG-6E-St-MW[1]	SG-5E-St-TW	SG-6E-St-ME
	SG-10E-St-MW	SG-6E-St-TE	SG-7E-St-BE	SG-6E-St-MW
	SG-10E-St-TE	SG-7E-St-BE	SG-7E-St-BW	SG-6E-St-TE
	SG-10E-St-TW	SG-7E-St-BW	SG-7E-St-ME	SG-7E-St-BE
		SG-7E-St-ME	SG-7E-St-MW	SG-7E-St-BW
		SG-7E-St-MW	SG-7E-St-TE	SG-7E-St-ME

SG-7E-St-TE	SG-7E-St-TW	SG-7E-St-MW
SG-7E-St-TW	SG-8E-St-BE	SG-7E-St-TE
SG-8E-St-BE	SG-8E-St-BW	SG-7E-St-TW
SG-8E-St-BW	SG-8E-St-ME	SG-8E-St-BE
SG-8E-St-ME	SG-8E-St-MW	SG-8E-St-BW
SG-8E-St-MW	SG-8E-St-TE	SG-8E-St-ME
SG-8E-St-TE	SG-9E-St-BE	SG-8E-St-MW
SG-9E-St-BE	SG-9E-St-BW	SG-8E-St-TE
SG-9E-St-BW	SG-9E-St-ME	SG-9E-St-BE
SG-9E-St-ME	SG-9E-St-MW	SG-9E-St-BW
SG-9E-St-MW	SG-9E-St-TE	SG-9E-St-ME
SG-9E-St-TE	SG-9E-St-TW	SG-9E-St-MW
SG-9E-St-TW	SG-10E-St-BE	SG-9E-St-TE
SG-10E-St-BE	SG-10E-St-BW	SG-9E-St-TW
SG-10E-St-BW	SG-10E-St-ME	SG-10E-St-BE
SG-10E-St-ME	SG-10E-St-MW	SG-10E-St-BW
SG-10E-St-MW	SG-10E-St-TE	SG-10E-St-ME
SG-10E-St-TE	SG-10E-St-TW	SG-10E-St-MW
SG-10E-St-TW		SG-10E-St-TE
		SG-10E-St-TW

[1] Sensors damaged during the test
[2] Sensors replaced after the test

Table D.5 Damaged pressure gauges in all tests

Elastic	AISC 0.375-0.5%	AISC 0.75-1.5%	AISC 2-4%	SAC Near-Fault	Collapse-Consistent
PG-1W-N-TW	PG-1W-N-BE	PG-1W-N-BE	PG-1W-N-BE	PG-1W-N-BE	PG-1W-N-BE
PG-1W-N-TE	PG-1W-N-BW	PG-1W-N-BW	PG-1W-N-BW	PG-1W-N-BW	PG-1W-N-BW
PG-1W-N-BW	PG-1W-N-TE	PG-1W-N-TE	PG-1W-N-TE	PG-1W-N-TE	PG-1W-N-TE
PG-1W-N-BE	PG-1W-N-TW	PG-1W-N-TW	PG-1W-N-TW	PG-1W-N-TW	PG-1W-N-TW
PG-1W-S-BW	PG-1W-S-BE	PG-1W-S-BE	PG-1W-S-BE	PG-1W-S-BE	PG-1W-S-BE
PG-1W-S-BE	PG-1W-S-BW	PG-1W-S-BW	PG-1W-S-BW	PG-1W-S-BW	PG-1W-S-BW
PG-5W-N-BW	PG-5W-N-BE	PG-5W-N-BE	PG-1W-S-TE	PG-1W-S-TE	PG-1W-S-TE
PG-5W-N-BE	PG-5W-N-BW	PG-5W-N-BW	PG-1W-S-TW[1]	PG-1W-S-TW	PG-1W-S-TW
PG-6W-N-TW	PG-5W-N-TE	PG-5W-N-TE	PG-5W-N-BE	PG-5W-N-BE	PG-5W-N-BE
PG-6W-N-TE	PG-6W-N-BE[1]	PG-6W-N-BE	PG-5W-N-BW	PG-5W-N-BW	PG-5W-N-BW
PG-10W-N-TW	PG-6W-N-TE	PG-6W-N-BW[1]	PG-5W-N-TE	PG-5W-N-TE	PG-5W-N-TE
PG-10W-N-BW	PG-6W-N-TW	PG-6W-N-TE	PG-5W-N-TW	PG-5W-N-TW	PG-5W-N-TW
PG-10W-N-BE	PG-6W-S-BE	PG-6W-N-TW	PG-6W-N-BE	PG-6W-N-BE	PG-6W-N-BE
PG-10W-S-TW	PG-10W-N-TW	PG-10W-N-TE[1]	PG-6W-N-BW	PG-6W-N-BW	PG-6W-N-BW
PG-10W-S-TE	PG-10W-N-BW	PG-10W-N-BE	PG-6W-N-TE	PG-6W-N-TE	PG-6W-N-TE
	PG-10W-N-BE	PG-10W-N-BW	PG-6W-N-TW	PG-6W-N-TW	PG-6W-N-TW
	PG-10W-S-TW	PG-10W-N-TW	PG-10W-N-BE	PG-10W-N-BE	PG-10W-N-BE
	PG-10W-S-TE	PG-10W-S-TE	PG-10W-N-BW	PG-10W-N-BW	PG-10W-N-BW
		PG-10W-S-TW	PG-10W-N-TE	PG-10W-N-TE	PG-10W-N-TE
			PG-10W-N-TW	PG-10W-N-TW	PG-10W-N-TW
			PG-10W-S-BE[1]	PG-10W-S-BE	PG-10W-S-BE
			PG-10W-S-BW[1]	PG-10W-S-BW	PG-10W-S-BW
			PG-10W-S-TE	PG-10W-S-TE	PG-10W-S-TE
			PG-10W-S-TW	PG-10W-S-TW	PG-10W-S-TW

[1] Sensors damaged during the test

Table D.6 Damaged/detached LVDTs and inclinometers in all tests

Elastic	AISC 0.375-0.5%	AISC 0.75-1.5%	AISC 2-4%	SAC Near-Fault	Collapse-Consistent
LVDT-BP[1]	LVDT-BP[1]	LVDT-BP[1]	LVDT-BP-S[1]	LVDT-BP-S[1]	LVDT-BP-S[1]
LVDT-EP-NIW[2]	LVDT-EP-NIW[2]	LVDT-EP-NIW[2]	LVDT-BP-N[1]	LVDT-BP-N[1]	LVDT-BP-N[1]
LVDT-EP-SIW[2]	LVDT-EP-SIW[2]	LVDT-EP-SIW[2]	LVDT-P-S[1]	LVDT-P-S[1]	LVDT-P-S[1]
LVDT-EP-NIE[2]	LVDT-EP-NIE[2]	LVDT-EP-NIE[2]	LVDT-P-N[1]	LVDT-P-N[1]	LVDT-P-N[1]
LVDT-EP-SIE[2]	LVDT-EP-SIE[2]	LVDT-EP-SIE[2]	INCL-I-F-W[3,4]		
LVDT-P[1]	LVDT-P[1]	LVDT-P[1]	LVDT-EP-NIW[3,4]		
			LVDT-EP-SIW[3,4]		

[1] Sensors LVDT-BP-S and LVDT-BP-N were replaced with one sensor, LVDT-BP during the AISC 2-4% test
Sensors LVDT-P-S and LVDT-P-N were replaced with one sensor, LVDT-P during the AISC 2-4% test
[2] Sensors added during the AISC 2-4% test
[3] Sensors damaged during the test
[4] Sensors replaced after the test

Table D.7 Non-functional (hidden) LED bulbs in all tests

AISC 2-4%	SAC Near-Fault	Collapse-Consistent
1	1	1
2	10	10
3	12	12
4	32	32
5		
6		
7		
8		
9		
10		
11		
13		
14		
15		
16		
19		
20		
21		
22		
23		
24		
25		
26		
27		
28		
29		
30		
31		
32		
33		
36		

Table D.8 Damaged fiber optic cables in all tests

Elastic	AISC 0.375-0.5%	AISC 0.75-1.5%	AISC 2-4%	SAC Near-Fault	Collapse-Consistent
F-BNc	F-BNc	F-BNc	F-BNc	F-BNc	F-BNc
F-TNb	F-TNb	F-TNb	F-TNb	F-TNb	F-TNb
	F-TNa[2]		F-TNa[1]	F-TNa	F-TNa

[1] Sensor damaged during the test
[2] Sensor repaired after the test

D.4 Derivation of the forces/deformations

This section provides the methodological steps for deducing forces/deformations in Chapters 5 and Appendix E. A notation list can be found in section D.4.14.

D.4.1 Cross-sectional forces

The bending moment and axial forces were obtained at cross sections instrumented with strain gauges (see Appendix D1, Drawings Nr. 0 to 5). Referring to Figure D.1, each cross section was instrumented with seven strain gauges (three on the web and two on each flange), unless otherwise specified in the instrumentation list. The flange and web of the profile were discretized, and the forces were deduced by integrating the stresses along the area of the cross section as follows,

$$M_o = \sum_i E\varepsilon_i z_i(\delta A_i) \tag{D.1}$$

$$N_o = \sum_i E\varepsilon_i(\delta A_i) \tag{D.2}$$

For instance, at cross section 2E in the East column (see Appendix D1, Drawing Nr. 1), the uniaxial strains gauge identifications (IDs) are as follows:

− ε_1: SG-2E-F-NW

− ε_2: SG-2E-F-SW

− ε_3: SG-2E-W-W

− ε_4: SG-2E-W-M

− ε_5: SG-2E-W-E

− ε_6: SG-2E-F-NE

− ε_7: SG-2E-F-SE

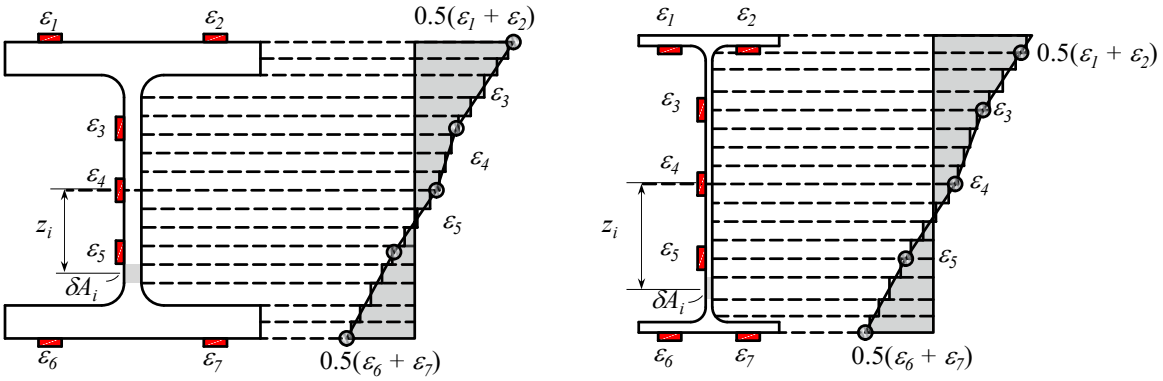

Figure D.1 Derivation of the cross-sectional forces, (a) HEM320 column cross section; (b) IPE360 beam cross section

The cross-sectional forces were calculated using the average measured dimensions of the column and beam cross sections. The measured dimensions are illustrated in Tables D.9 and D.10 at four equally spaced locations in the columns and five equally spaced locations in the beams. Note that the calculation of the axial force in the column cross sections through stress integration was not found to be reliable. The error in the strain gauge measurement near cross-sectional discontinuities resulted in an error in the axial force when the stresses were integrated across the thick column flanges. The column axial forces were observed to drift throughout loading (see discussion section D.4.5). Accordingly, the axial forces in the columns were not derived using the strain gauge data but through force equilibrium as described in section D.4.5.

Table D.9 Measured dimensions of the column cross sections

	Location	h_c [mm]	b_{fc} [mm]	t_{fc} [mm]
West Column	#1	359.0	308.8	39.9
	#2	359.3	309.0	39.9
	#3	360.5	308.5	40.0
	#4	359.3	309.0	39.8
Average		359.5	308.8	39.9
Interior Column	#1	359.9	308.5	40.1
	#2	359.0	308.5	40.0
	#3	359.5	308.9	40.2
	#4	359.7	308.7	40.1
Average		359.5	308.7	40.1
East Column	#1	359.9	308.7	40
	#2	359.1	308.5	39.9
	#3	360.5	308.9	40
	#4	359.5	308.7	40
Average		359.8	308.7	40.0
Average - All Columns		359.6	308.7	40.0

Table D.10 Measured dimensions of the beam cross sections

	Location	h_b [mm]	b_{fb} [mm]	t_{fb} [mm]
West Beam	#1	359.8	170.5	12.0
	#2	359.0	170.7	11.2
	#3	359.4	170.8	12.0
	#4	359.4	170.2	11.9
	#5	359.4	170.4	12.2
Average		359.4	170.5	11.8
East Beam	#1	358.9	170.2	12.1
	#2	358.7	170.0	12.2
	#3	359.3	171.0	12.5
	#4	359.5	170.2	12.5
	#5	360.0	170.1	12.4
Average		359.3	170.3	12.3
Average - All Beams		359.3	170.4	12.1

Damaged strain gauge readings were disregarded from the integration during a loading stage. The cross-sectional forces were not computed if the two strain gauges on either flange of the columns were damaged. In that case, the moment diagram was constructed as described in section D.4.3. The damaged strain gauges are shown in Table D.11 along with the corresponding loading protocol during which damage occurred. Between loading sequences, damaged strain gauges were replaced with new ones.

Table D.11 Damaged strain gauges

ID	Loading Protocol	Location
SG-4E-F-NE	AISC 0-0.5% rads	Cross section 4E
SG-2E-F-SE	AISC 2-4% rads	Cross section 2E
SG-2E-F-NE	AISC 2-4% rads	Cross section 2E
SG-2I-F-SE	Collapse Consistent	Cross section 2I
SG-2I-F-NE	Collapse Consistent	Cross section 2I

D.4.2 Story drift ratio

Referring to Figure D.2, the story drift ratio (SDR) was calculated at the column top level using the string potentiometer (SP-CE-T) mounted on the East column (see Appendix D1, Drawing Nr. 13) as follows,

$$\text{SDR} = \frac{\delta_{SP,E}}{h_{SP}} \tag{D.3}$$

$-\ \delta_{SP,E}$, sensor ID: SP-CE-T

$-\ h_{SP} = 4270$ mm (distance from center of bottom structural pin to the location where the string potentiometer was mounted, as shown in Figure D.2)

Note that during the last unloading excursion of the collapse consistent protocol (beyond -2% rads), the string potentiometer was removed because the displacement exceeded the allowable range of the sensor. The SDR was derived from the actuator displacement in this case as follows,

$$\text{SDR} = \frac{\delta_A - s_{Br} - \frac{F_A}{K_R}}{H} \tag{D.4}$$

$-\ K_R = 67.4$ kN/mm

$-\ H = 4615$ mm (centerline distance between the two structural pins as shown in Figure D.2)

The sensor IDs are,

$-\ \delta_A$: D-ACT

$-\ F_A$: F-ACT

$-s_{Br}$: LVDT-BR-S and LVDT-BR-N

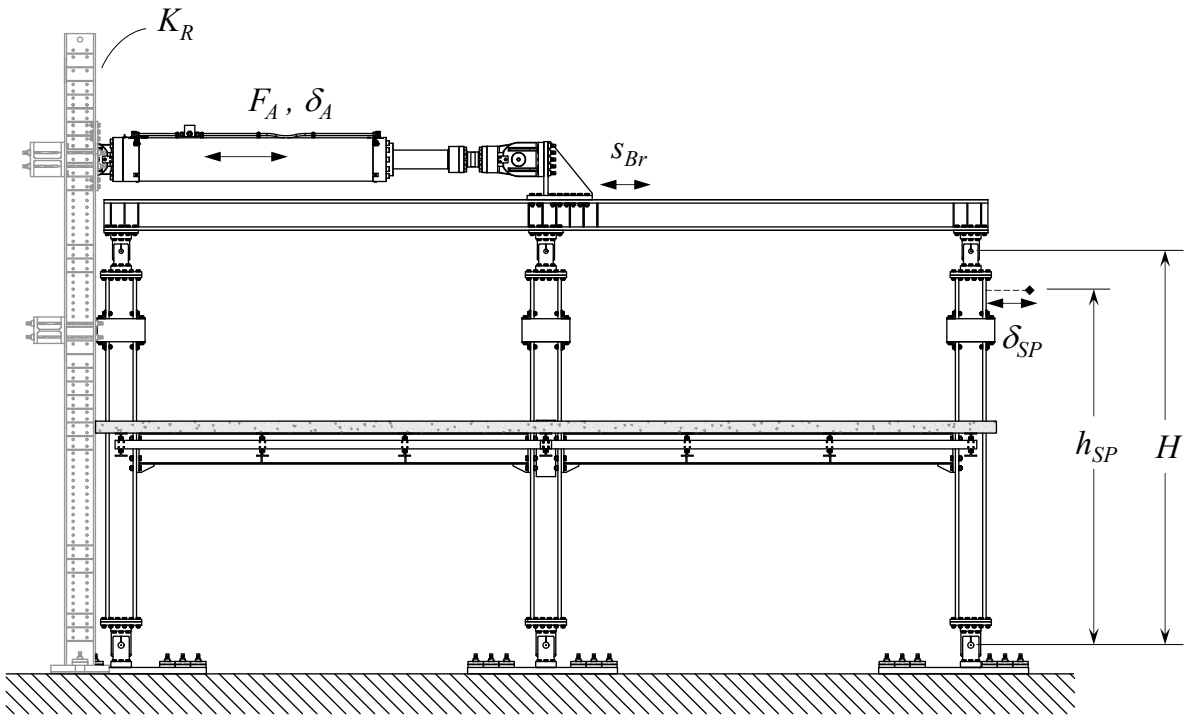

Figure D.2 String pot and actuator displacements for the derivation of the story drift ratio

D.4.3 Column shear forces / base shear

The shear forces in the columns were obtained from the slope of the moment diagram (see Figure D.3). The inflection points are located at the center of the top and bottom structural pins. Since the moment diagram is linear, it can be constructed from only one derived cross-sectional moment, if needed. This was done if the moments at both instrumented cross sections could not be derived due to damage in the strain gauges during loading (see Table D.1). Shown in Figure D.3 is the moment diagram in the East column. The shear forces in the top and bottom portion of the East column were calculated from the slope of the moment diagram as follows,

$$V_{cE,top} = \frac{M_{c,2E} - M_{c,1E}}{h_{2E} - h_{1E}} \tag{D.5}$$

$$V_{cE,bot} = \frac{M_{c,3E} - M_{c,4E}}{h_{3E} - h_{4E}} \tag{D.6}$$

$-\ h_{1E} = 560$ mm

$-\ h_{2E} = 1560$ mm

$-\ h_{3E} = 1555$ mm

– h_{4E} = 555 mm

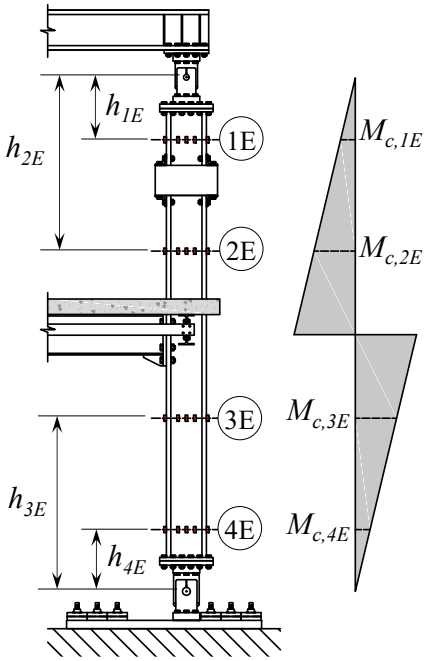

Figure D.3 Moment diagram in the East column of the test frame

The shear forces in the West and Interior columns were derived in a similar manner. The base shear was calculated as the sum of the shear forces in the bottom region of the columns. Global equilibrium was checked in order to verify the top and bottom column shear forces. Figure D.4 shows the free-body diagram for the axial and shear forces in the beams and columns. Referring to Figure D.4,

$$V_{Base} = \sum_i V_{ci,bot} = -\sum_i V_{ci,top} = -F_{A,h} \tag{D.7}$$

$$F_{A,h} = F_A \cdot \cos\left(\frac{H \cdot [1 - \cos(\mathrm{SDR})]}{L_A}\right) \tag{D.8}$$

– H = 4615 mm (see Figure D.4

– L_A = 5100 mm (see Figure D.4)

– F_A, sensor ID: F-ACT (see Figure D.4)

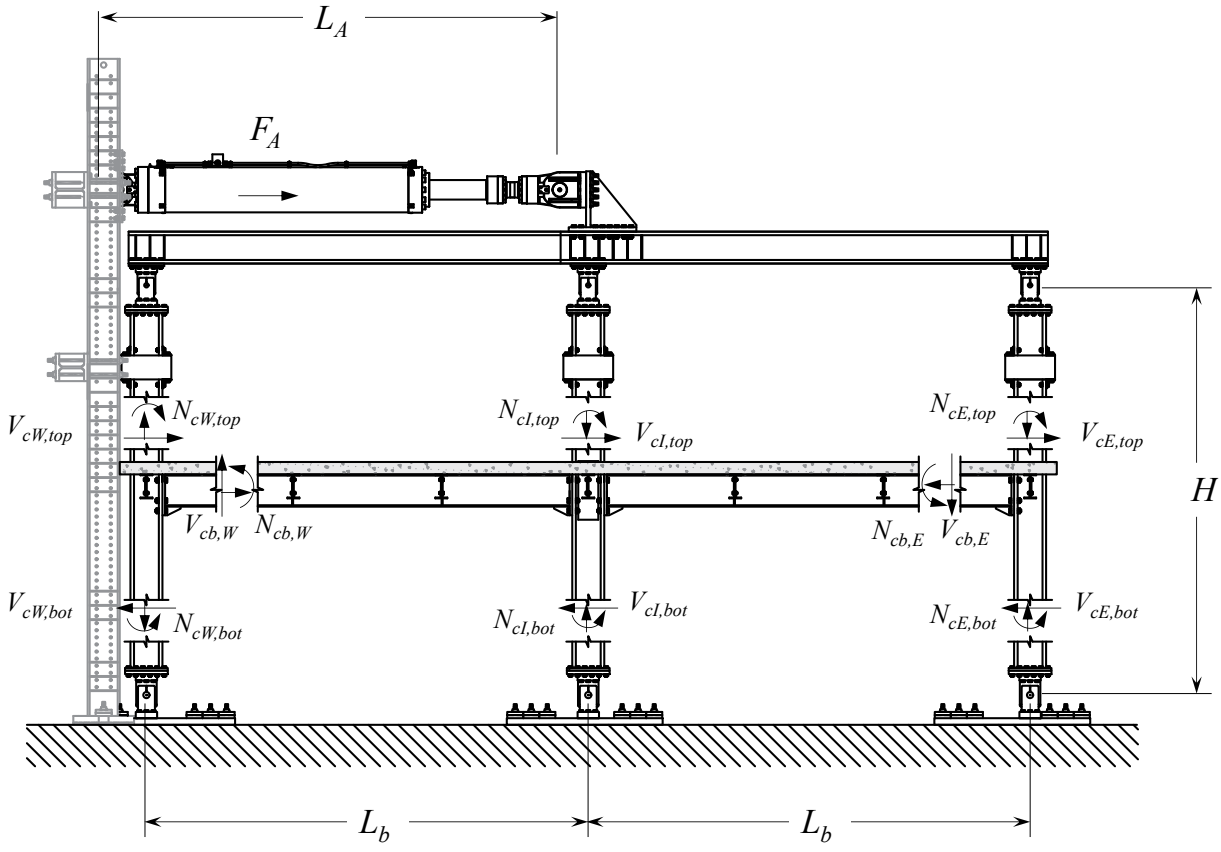

Figure D.4 Free body diagram of the test frame showing the moment, shear and axial forces in the beams and columns. For clarity, the forces are only shown on one side of the cross section (nearest to the main girder and exterior columns)

Figure D.5 shows that the total shear force throughout the whole loading history (i.e., AISC symmetric cyclic, SAC near-fault and collapse-consistent protocols) in the top and bottom regions of the columns matches the horizontal force applied by the actuator within an accuracy of 5%.

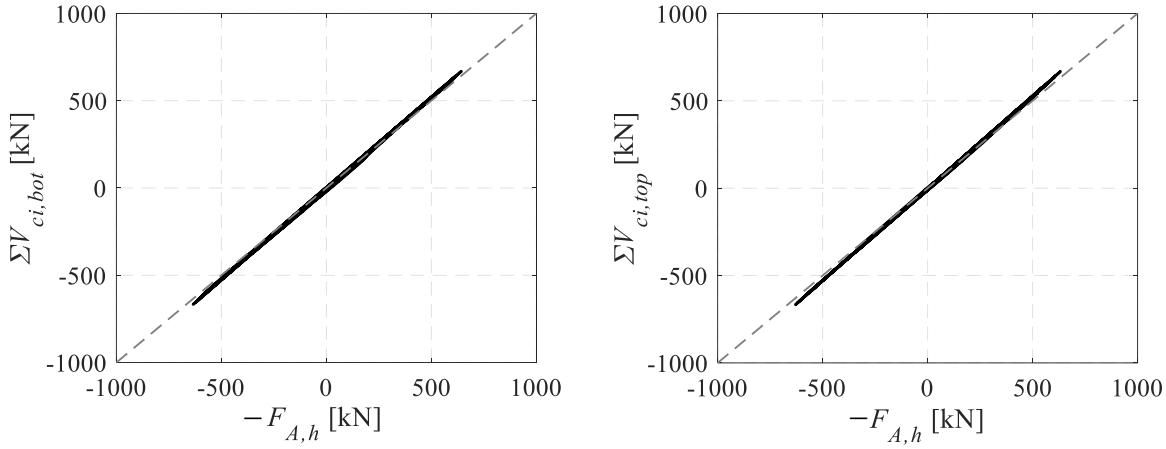

(a) (b)

Figure D.5 Check for global equilibrium throughout the whole loading history, (a) total shear force in the bottom regions of the columns; (b) total shear force in the top regions of the columns

D.4.4 Composite steel beam shear forces

The strain gauge measurements did not accurately reproduce the axial forces in the column cross sections as mentioned in section D.4.1. Therefore, the shear force in the beams could not be obtained by equilibrium of the axial forces in the exterior columns. Instead, the shear forces in the beams were obtained by assuming the flexural stiffness of the West and East beams are equal during the AISC symmetric cyclic loading protocol. Accordingly, the shear forces were derived by global equilibrium as follows (see Figure D.4),

$$V_{cb,E} = V_{cb,W} = F_{A,h} \cdot \frac{H}{2L_b} \tag{D.9}$$

$- H = 4615$ mm

$- L_b = 4960$ mm

Note that this assumption is not valid in the near-fault and collapse-consistent protocols in which the loading is asymmetric. For these two protocols, the shear force in the beam was obtained by computing the moment gradient between the instrumented beam cross sections. For the East beam (see Figure D.6a),

$$V_{cb,E} = \frac{M_{cb,5E} - M_{cb,6E}}{L_{56E}} \tag{D.10}$$

$-\ L_{56E} = 2191$ mm (see Figure D.6a)

The moment at each cross section was computed by assuming that the axial force in the slab acts at the center of the concrete above the steel deck as shown in Figure D.6b.

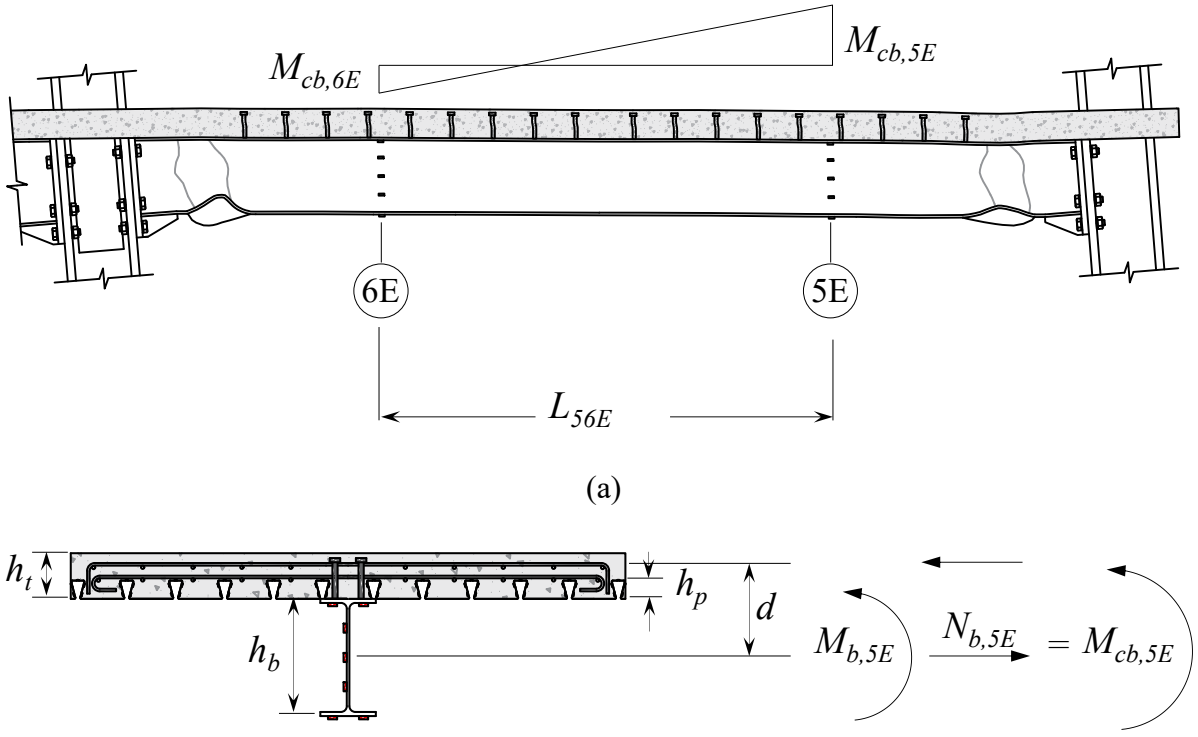

Figure D.6 Derivation of the shear force in the East composite steel beam, (a) moment gradient between the instrumented cross sections; (b) calculation of the composite steel beam moment at the instrumented cross section 5E

In order to verify the above assumptions, moment equilibrium was checked and verified at the interior beam-to-column joint as shown in Figure D.7 and Figure D.8. The derivation of the moments given the shear forces in the composite steel beams is described in section D.4.6.

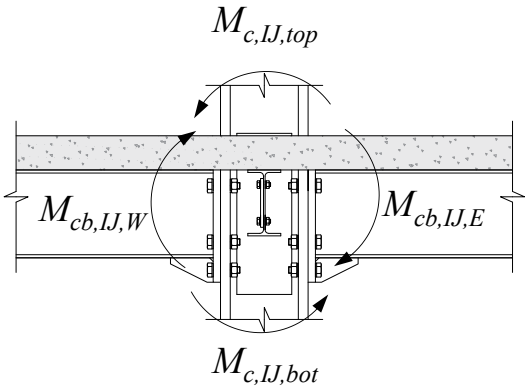

Figure D.7 Moment equilibrium at the interior joint

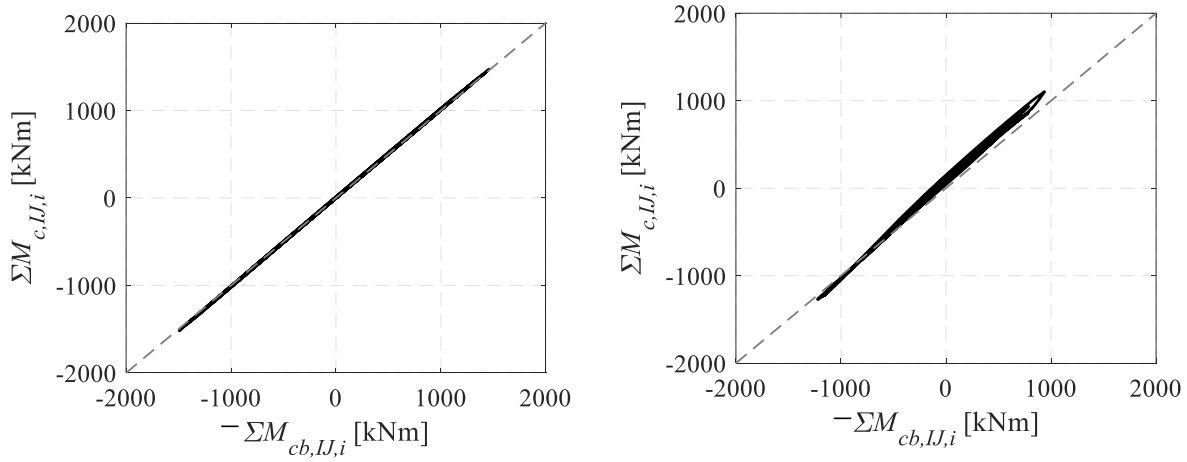

Figure D.8 Check for moment equilibrium at the interior joint, (a) AISC symmetric cyclic loading protocol; (b) SAC near-fault protocol

The shear force in the West composite steel beam was calculated in a similar manner.

D.4.5 Axial forces in the columns

Referring to Figure D.4, the axial force equilibrium in the top and bottom regions of the columns is checked as follows,

$$\sum_i N_{ci,bot} = \sum_i N_{ci,top} = -F_{A,v} \tag{D.11}$$

$$F_{A,v} = F_A \cdot \sin\left(\frac{H \cdot [1 - \cos(\mathrm{SDR})]}{L_A}\right) \tag{D.12}$$

$-$ H = 4615 mm (see Figure D.4)

$-$ L_A = 5100 mm (see Figure D.4)

$-$ F_A, sensor ID: F-ACT (see Figure D.4)

Figure D.9 shows that equilibrium was not satisfied when the axial forces were obtained from the strain gauge measurements.

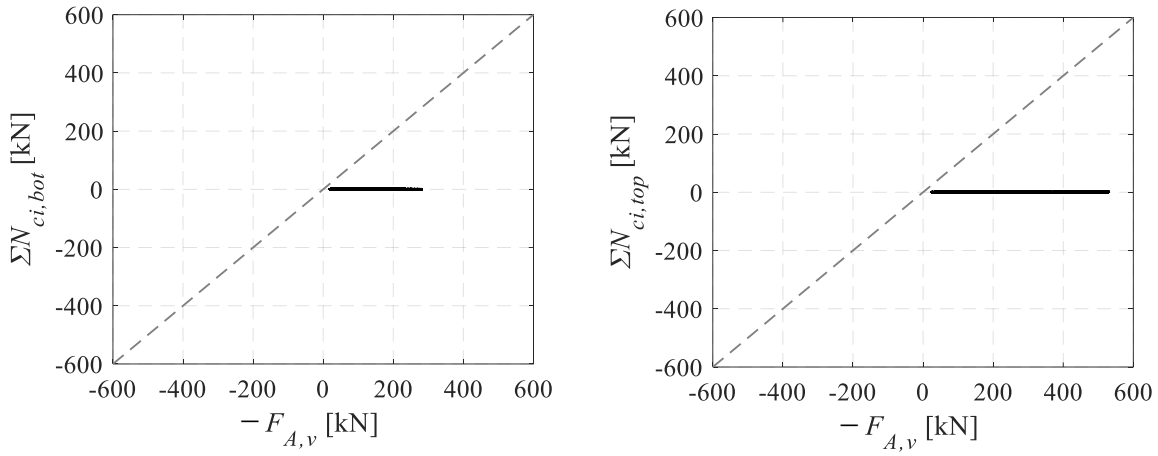

(a) (b)

Figure D.9 Check for global equilibrium throughout the entire loading history, (a) total axial force in the bottom regions of the columns; (b) total axial force in the top regions of the columns

The axial force in the top regions of the East column, $N_{cE,top}$ was calculated through equilibrium in the loading beam (see Figure D.10),

$$M_{LB,Br} = F_A \cdot h_{LB-Br} \tag{D.13}$$

$$M_{LB,I} = V_{cI,top} \cdot h_{LB-pin} \tag{D.14}$$

$$M_{LB,E} = V_{cE,top} \cdot h_{LB-pin} \tag{D.15}$$

$$N_{cE,top} = V_{LB,E} = \frac{0.5 \cdot \left(M_{LB,Br} + M_{LB,I}\right) - M_{LB,E}}{L_b} \tag{D.16}$$

$-$ h_{LB-Br} = 651 mm (see Figure D.10)

$-$ h_{LB-Pin} = 425 mm (see Figure D.10)

$-\ L_b$ = 4960 mm (see Figure D.10

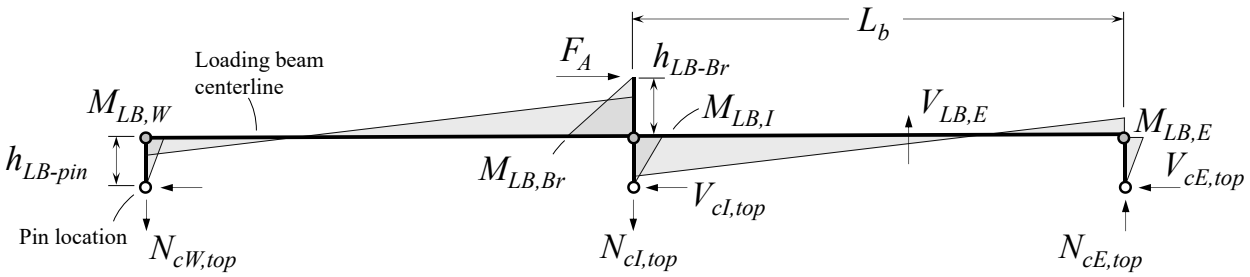

Figure D.10 Free body diagram at the location of the top pins

The axial force in the top region of the West column, $N_{cW,top}$ was calculated in a similar manner.

Figure D.11 shows a comparison between the calculated axial forces in the top regions of the West and East columns ($N_{cW,top}$ and $N_{cE,top}$) and those obtained through the strain gauge measurements ($N_{cW,top}{}'$ and $N_{cE,top}{}'$). As discussed earlier, there is a considerable error in obtaining the column forces using the strain gauge measurements. The axial force in the top regions of the columns drifts throughout loading. This agrees with the findings from Figure D.9b.

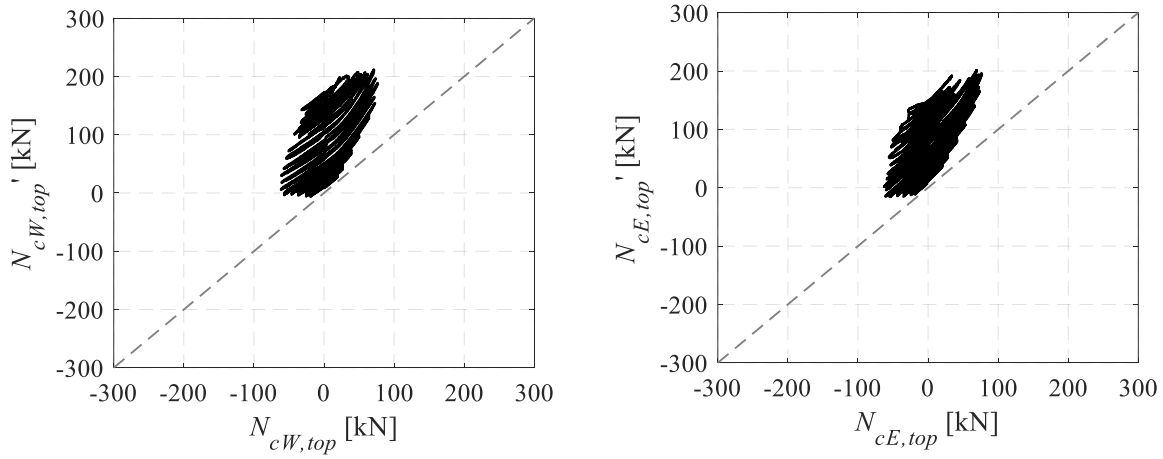

Figure D.11. Comparison between the calculated and measured axial forces in the top regions of the (a) West column; and (b) East column

Based on the above, the axial force in the bottom region of the East column was derived by equilibrium at the exterior joints as follows (see Figure D.4),

$$N_{cE,bot} = V_{cb,E} + N_{cE,top} \tag{D.17}$$

The axial force in the bottom region of the West column, $N_{cW,bot}$ was calculated in a similar manner.

D.4.6 Composite steel beam moments

The composite steel beam moments were obtained by equilibrium. Shown in Figure D.12 is the moment equilibrium at the East exterior joint,

$$M_{cb,EJ} = M_{c,EJ,bot} + M_{c,EJ,top} \tag{D.18}$$

The moment in the East composite steel beam at distance *x* from the center of the exterior joints was derived as follow,

$$M_{cb,E,x} = M_{cb,EJ} - V_{cb,E} \cdot x \tag{D.19}$$

Where x is the distance as shown in Figure D.12.

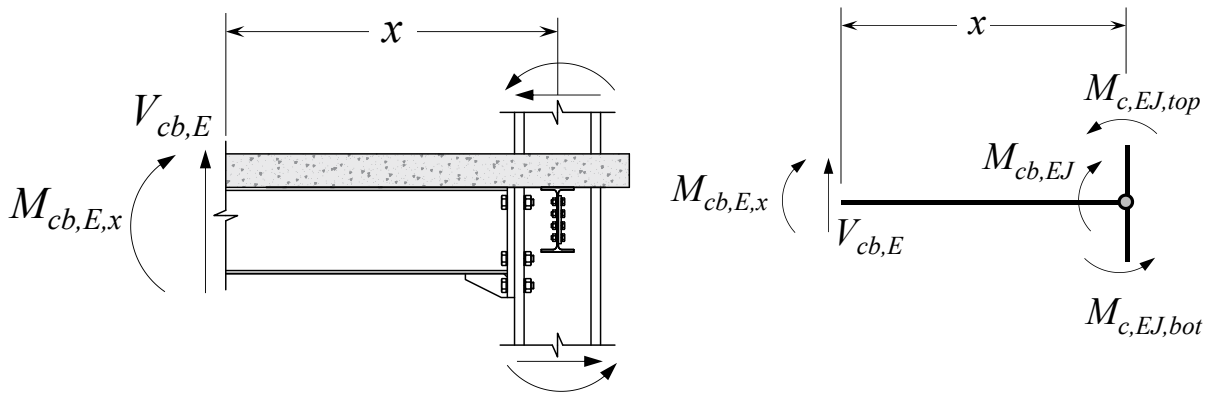

(a) (b)

Figure D.12 (a) Moment in the East composite steel beam; (b) moment equilibrium at the East exterior joint

The moments in the West composite steel beam were calculated in a similar manner. Note that the axial force in the composite steel beam was assumed to act at the center of the joint; hence, the moment due to the eccentricity of the axial force in the composite steel beam was not considered. The rationale is that prior to framing action, the axial force in the composite steel beam was negligible. For instance, at 3% rads, the maximum axial force in the West composite steel beam was 116 kN.

Assuming that the concrete remains fully elastic throughout the width of the slab, the eccentricity of the axial force was conservatively calculated to be 107 mm. The moment due to this eccentricity was 12.4 kNm or 1.3% of the maximum moment at the West exterior joint. Moreover, at high lateral drift demands where framing action becomes substantial (> 4% rads), the eccentricity of the axial force is expected to decrease as the column face concrete crushes.

D.4.7 Axial force, shear force and moment diagrams at selected drift amplitudes

For illustration purpose, the axial force (see Figure D.13), shear force (see Figure D.*14*) and moment diagrams (see Figure D.*15*) are shown at two different drift amplitudes. The one corresponds to the first loading excursion of the +1% rads drift amplitude of the AISC symmetric cyclic loading protocol. The second drift level corresponds to the first +6% excursion of the SAC near-fault protocol.

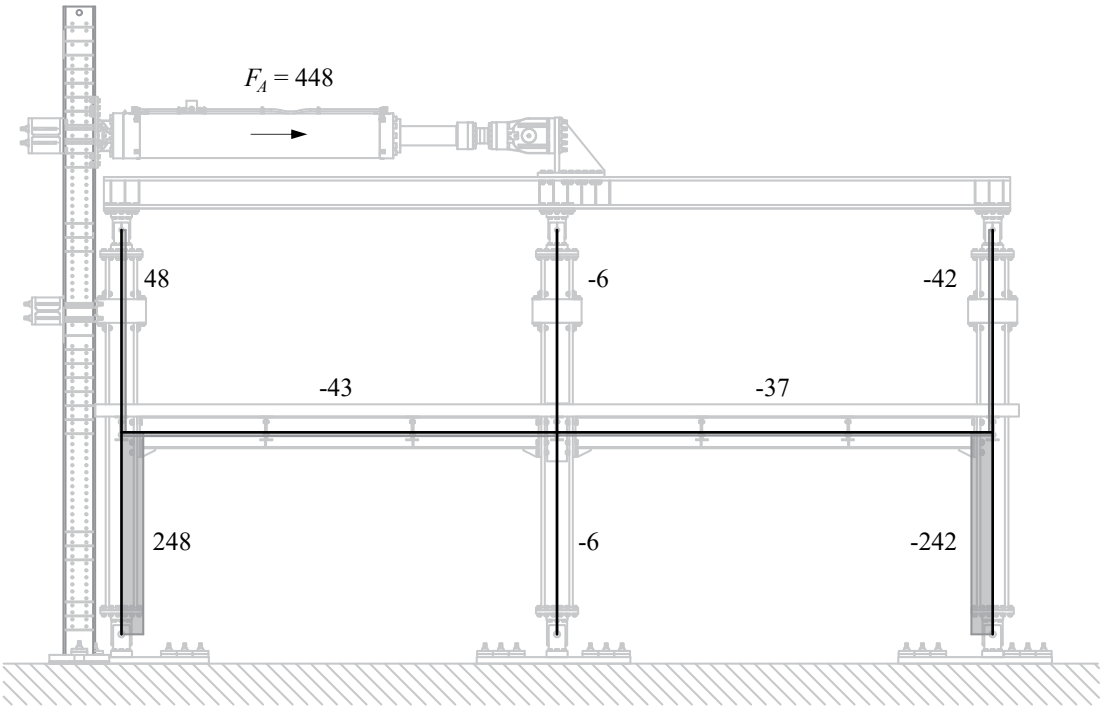

(a)

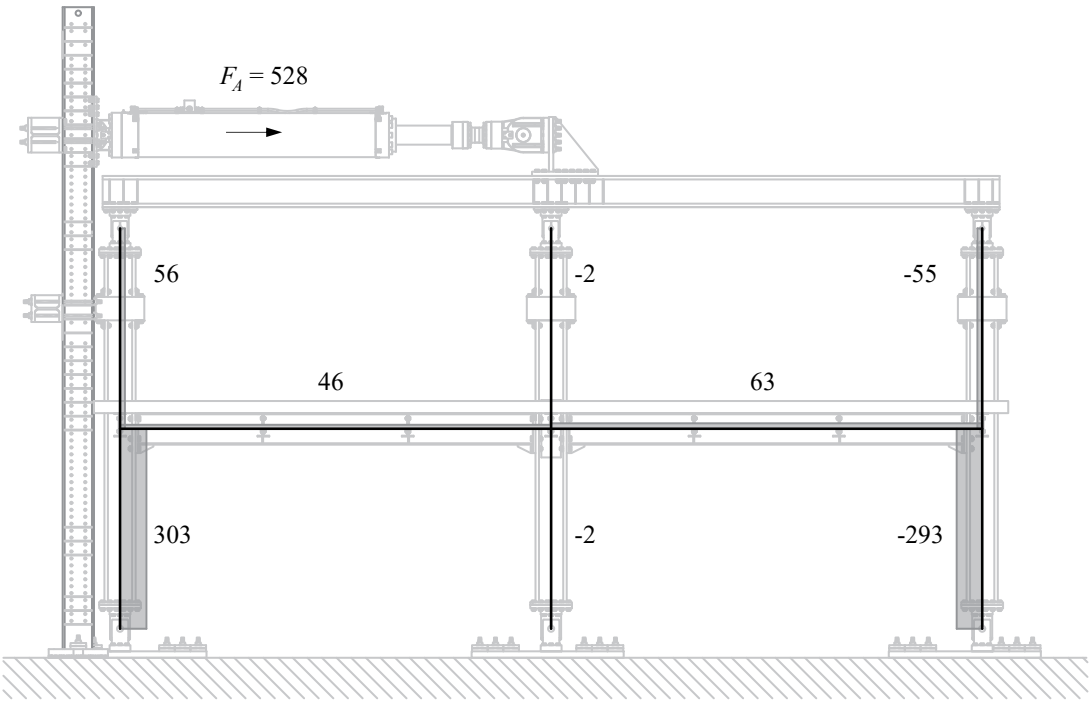

(b)

Figure D.13 Axial force diagram in the test frame (in kN), (a) +1% rads (AISC symmetric cyclic protocol); (b) +6% rads (SAC near-fault protocol – negative sign denotes compressive load)

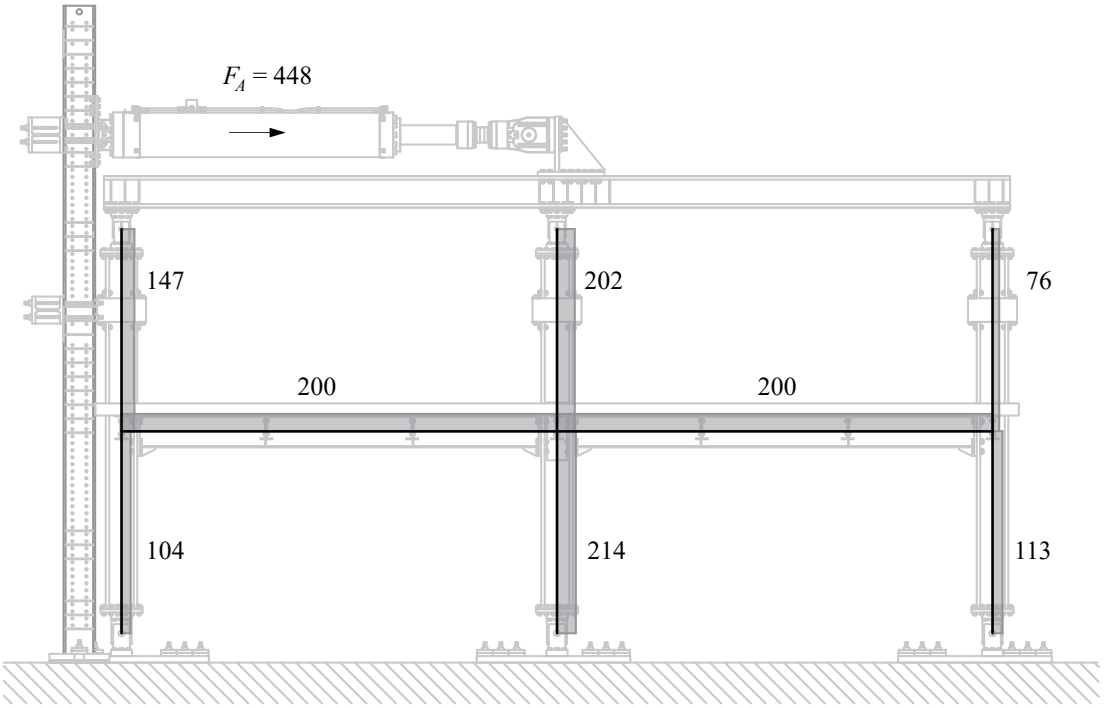

(a)

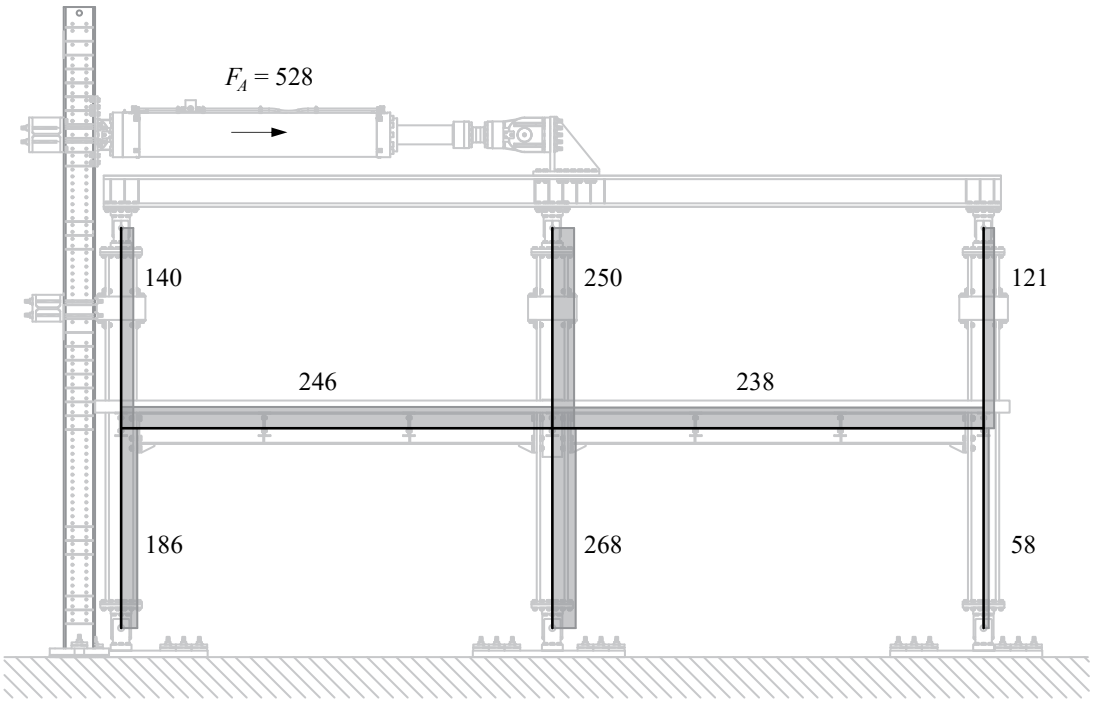

(b)

Figure D.14 Shear force diagram in the test frame (in kN), (a) +1% rads (AISC symmetric cyclic protocol); (b) +6% rads (SAC near-fault protocol)

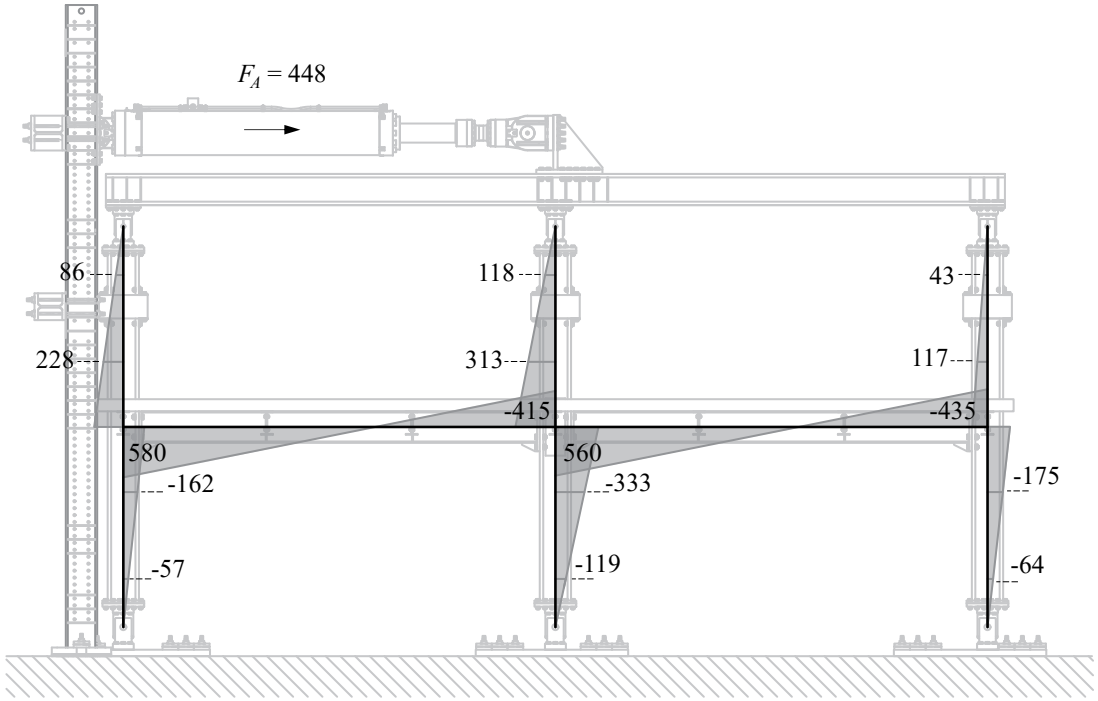

(a)

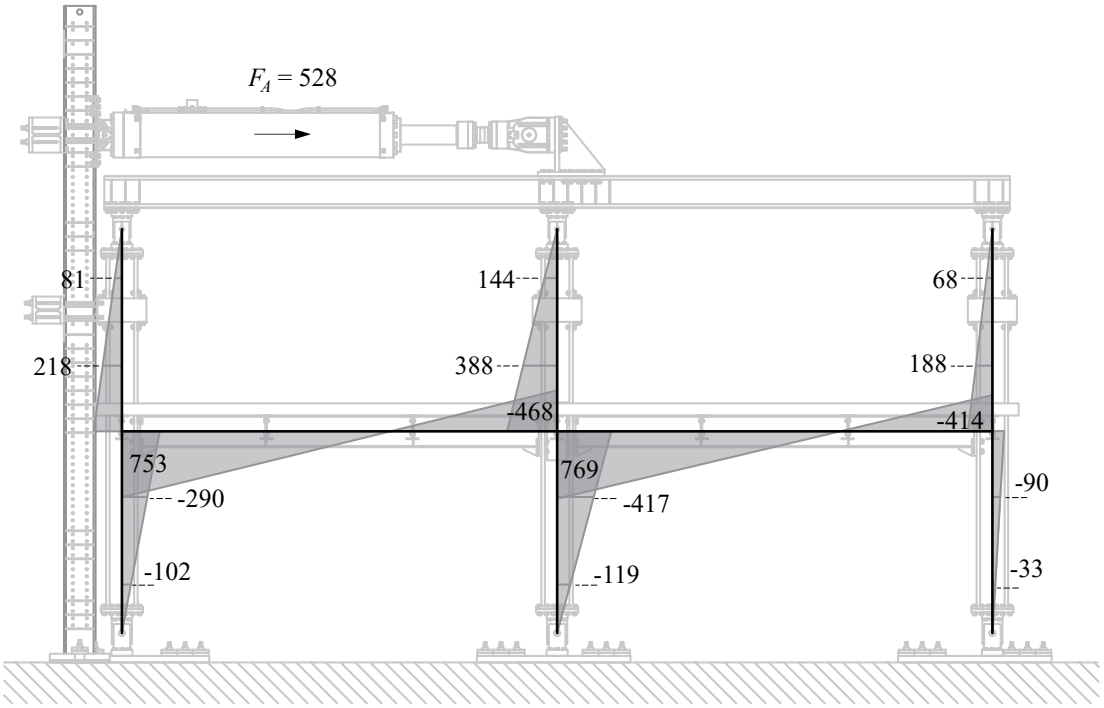

(b)

Figure D.15 Moment diagram in the test frame (in kNm), (a) +1% rads (AISC symmetric cyclic protocol); (b) +6% rads (SAC near-fault protocol)

D.4.8 Computation of chord rotations

The composite steel beam and column chord rotations were obtained from the inclinometer readings (see Appendix D1, Drawing Nr. 7) as per the equations proposed by Rahiminia and Namba (2013). These were modified to account for the test frame configuration and the angle due to the gap opening between the end plate and the column flange, θ_{EP}. Figure D.16 shows the derivation of the East composite steel beam and column chord rotations at the interior joint,

$$\theta_b = \frac{\theta_{INCL,l} + \theta_{INCL,r}}{2} + \theta_{INCL,b} \cdot \frac{h_c}{L_b - h_c} - \theta_{EP} \tag{D.20}$$

$$\theta_{EP} = \frac{\delta_{EP}}{0.5h_b} \tag{D.21}$$

$$\theta_c = \text{SDR} \cdot \frac{H}{H - h_b} - \frac{\theta_{INCL,l} + \theta_{INCL,r}}{2} \cdot \frac{h_b}{H - h_b} - \theta_{INCL,b} \tag{D.22}$$

e.g., At the interior joint, the sensor IDs are,

$-\ \theta_{INCL,l}$: INCL-I-F-W (see Figure D.16)

$-\ \theta_{INCL,r}$: INCL-I-F-E (see Figure D.16)

$-\ \theta_{INCL,b}$: INCL-I-W-B (see Figure D.16)

$-\delta_{EP}$: LVDT-EP-NIE and LVDT-EP-SIE

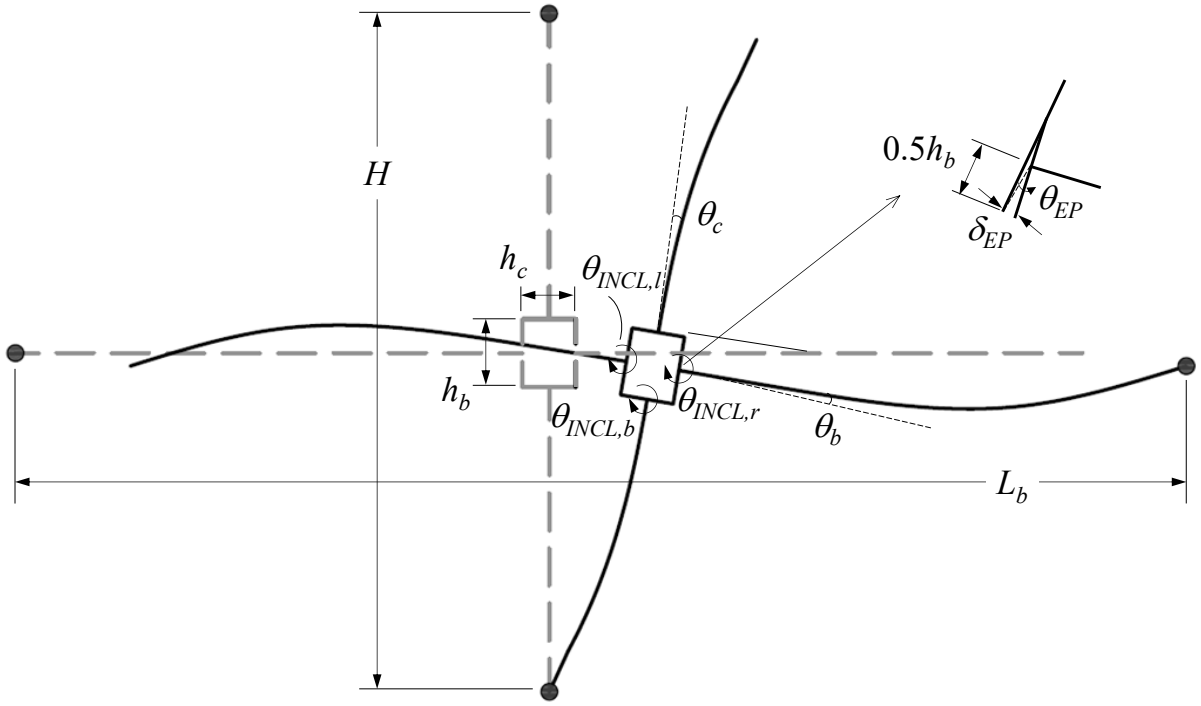

Figure D.16 Derivation of the composite steel beam and column chord rotations at the interior joint

Note that during the AISC protocol (2% to 4% rads) the inclinometer on the west flange of the interior column (sensor ID: INCL-I-F-W) experienced drifting. Accordingly, the measurement was not included in the calculation of the chord rotation. Only the inclinometer on the east flange was considered in this case.

D.4.9 Column web panel zone shear demands and distortions

For each column, the web panel zone demand was calculated according to Kim and Engelhardt (2002). Under sagging bending, the effective depth was assumed to act at the center of the concrete above the steel deck. Under hogging bending, the effective depth is assumed to act between the beam flanges (see Figure D.17a).

For the interior joint (see Figure D.17a),

$$V_{PZ,I} = \frac{M^{+}_{IW,cf}}{d^{+}_{eff}} + \frac{M^{-}_{IE,cf}}{d^{-}_{eff}} - \frac{V_{c,I,top} + V_{c,I,bot}}{2} \tag{D.23}$$

For the East exterior joint under sagging bending,

$$V_{PZ,E} = \frac{M^{+}_{E,cf}}{d^{+}_{eff}} - \frac{V_{c,E,top} + V_{c,E,bot}}{2} \tag{D.24}$$

For the East exterior joint under hogging bending,

$$V_{PZ,E} = \frac{M^{-}_{E,cf}}{d^{-}_{eff}} - \frac{V_{c,E,top} + V_{c,E,bot}}{2} \tag{D.25}$$

The panel zone demand in the West exterior joint was calculated in a similar manner to that in the East exterior joint.

The distortion of the column web panel zone was obtained from the LVDTs (see Appendix D1, Drawing Nr. 6) on the column web (see Figure D.17b) The sensor IDs shown herein correspond to the sensors on the interior joint column web panel zone.

$$\gamma = (\Delta_1 - \Delta_2).\frac{\sqrt{a^2_{PZ,I} + b^2_{PZ,I}}}{2a_{PZ,I} \cdot b_{PZ,I}} \tag{D.26}$$

e.g., At the interior joint, the sensor IDs are,

$-\ \Delta_1$: LVDT-I-W

$-\ \Delta_2$: LVDT-I-E

The exterior West and East column web panel zone distortions were calculated in a similar manner.

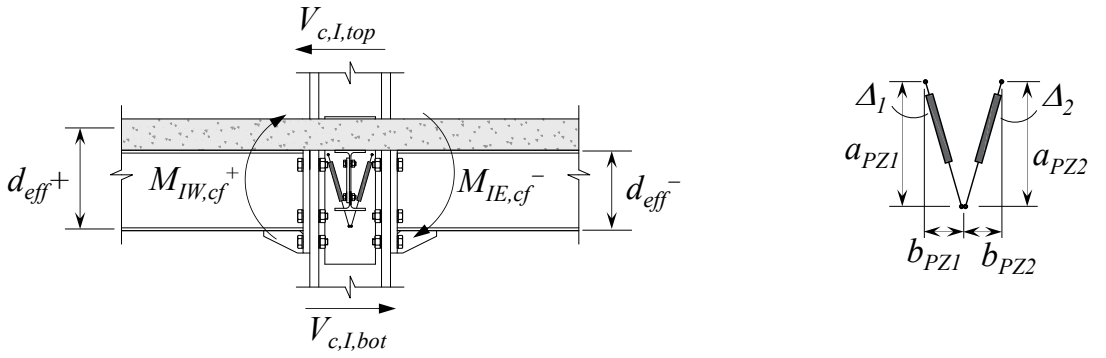

(a) (b)

Figure D.17 (a) Forces acting on the column web panel zone at the interior joint; (b) column web panel zone LVDTs dimensions/deformations distortion calculation

D.4.10 Composite steel beam and slab axial forces

The composite steel beam axial force was obtained by equilibrium at the exterior joints. Shown in Figure D.18 is the force equilibrium at the East exterior joint at cross section 5E,

$$N_{cb,E} = -(V_{c,E,bot} + V_{c,E,top}) \tag{D.27}$$

The axial force in the West composite steel beam was calculated in a similar manner.

The slab axial force was derived at the instrumented cross sections in the beams (see Appendix D1, Drawings Nr. 4 and 5) through force equilibrium at the exterior joint. At cross section 5E,

$$N_{s,5E} = N_{cb,E} - N_{b,5E} \tag{D.28}$$

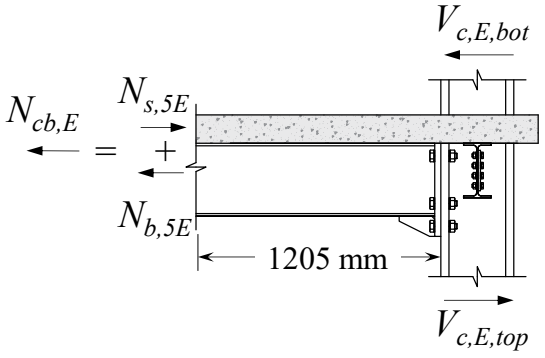

Figure D.18 Force equilibrium at the East exterior joint

The axial forces in the slab at all instrumented cross sections were calculated in a similar manner.

D.4.11 Beam axial shortening

Axial shortening in the beam was derived from the string pot measurements (see Appendix D1, Drawing Nr. 8) at the beam centerline by assuming that it mostly occurs in the dissipative zones of the beams. For the West beam (Figure D.19), beam axial shortening was calculated as follows,

$$\delta_{b,W} = 0.5 \cdot \left(\delta_{W,top} + \delta_{W,bot} + \delta_{I,bot} + \delta_{I,top}\right) \tag{D.29}$$

e.g., In the West composite steel beam the sensor IDs are,

$-\delta_{W,top}$: SP-W-TE (see Figure D.19)

$-\delta_{I,top}$: SP-I-TW (see Figure D.19

$-\delta_{W,bot}$: SP-W-BE (see Figure D.19)

$-\delta_{I,bot}$: SP-I-BW (see Figure D.19

The axial shortening in the East beam was calculated in a similar manner.

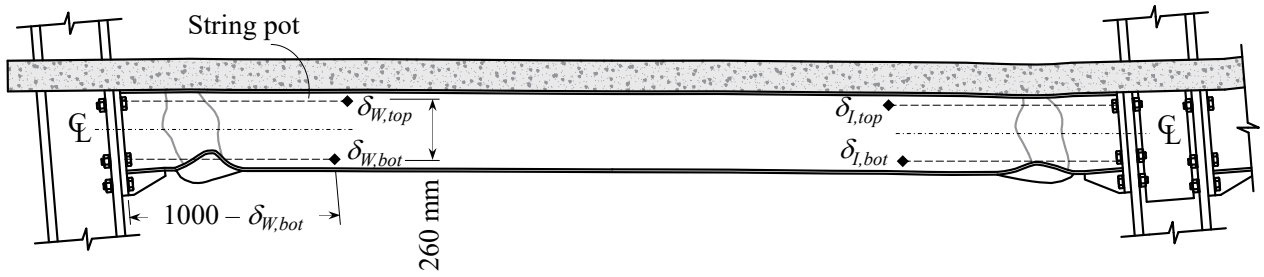

Figure D.19 Derivation of the West beam axial shortening from the string pots at the beam ends

D.4.12 Rebar strain measurements

The ODiSI 6108 fiber optic measurement (FOM) system by *LUNA Innovations* (LUNA 2013) was used to obtain the continuous strain data on the longitudinal rebars at the West exterior joint. This system performs measurements by means of an Optical Frequency Domain Reflectometry (OFDR) to obtain the strain profile in the rebars at a refined spatial resolution. In the test program, a 0.65 mm

spatial resolution was employed. Strain measurements were sampled at a frequency of 0.39 Hz. The noise level was up to 10 microstrains.

The procedure for processing the strain measurements is documented below:

1- The strain data in each fiber was stored in an $m \times n$ matrix as shown in Figure D.20b. The first column corresponds to the time which was synchronized with the data from the other sensors on the test frame. The first row corresponds to the location along the fiber at which the strain was measured (see Figure D.20a).

2- The matrix was trimmed such that the start point x_s corresponded to the point at which the fiber enters the slab edge (see Figure D.20a). These start location values had been obtained prior to the test and are included in the shared folder along with the fiber optic strain measurements.

3- After each test, the residual strain values were added to the first step of the next test.

Two functions were coded to obtain the strain data at any instance: The first function, 'FiberStrain-Profile.m', produces the continuous strain values between any two locations on the rebars. The second function, 'SlabStrainProfile.m', produces the strain values in the rebars at any location along the width of the slab. The two functions are available with FOM data.

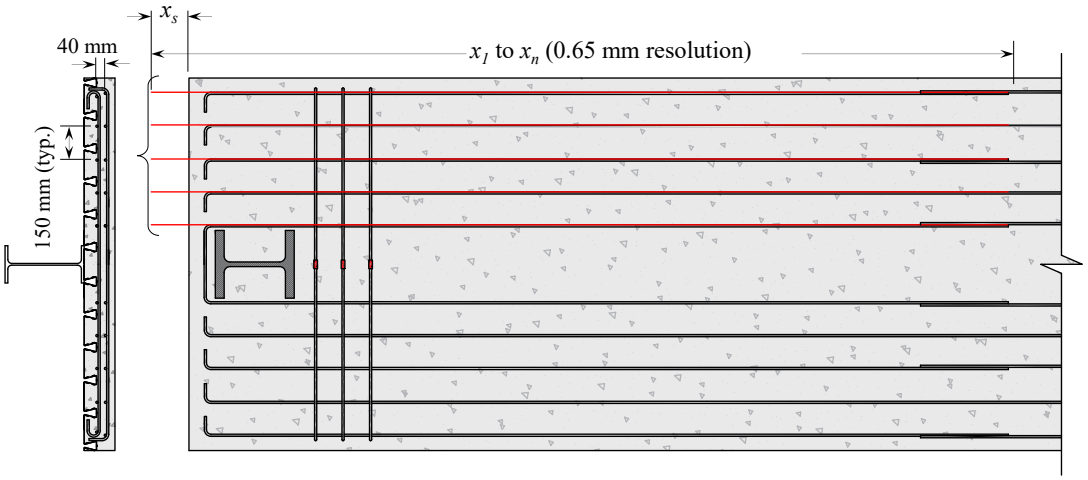

(a)

Location

Time	x_1	x_2	...	x_s	...	x_n
t_1	ε_{11}	ε_{12}	...	ε_{1s}	...	ε_{1n}
t_2	ε_{21}	ε_{22}	...	ε_{2s}	...	ε_{2n}
⋮	⋮	⋮	⋮	⋮	⋮	⋮
t_m	ε_{m1}	ε_{m2}	...	ε_{ms}	...	ε_{mn}

Start point in the slab

(b)

Figure D.20 (a) FOM system strain measurement locations and gauge pitch (i.e., resolution); (b) $m \times n$ matrix of strain measurements for a typical fiber

D.4.13 Digital Image Correlation (DIC) measurements

Digital Image Correlation (DIC) photos were acquired with a frequency of 0.2 Hz. The size of the random speckle pattern on the slab was 2 to 3 mm as discussed in Chapter 5. Displacement analysis was then performed with Vic-3D software (Vic-3D 2010) using a subset size that ranged between 25 × 25 and 35 × 35 pixels. The subset size was selected such that the displacement error was below 1/50 times the pixel size. DIC measurements from subsequent tests were stitched together by processing the images with reference images taken in the initial test. Figures D.21 and D.22 show that the noise level for strain measurement at the surface of the slab was within 300 microstrains in the longitudinal and transverse directions.

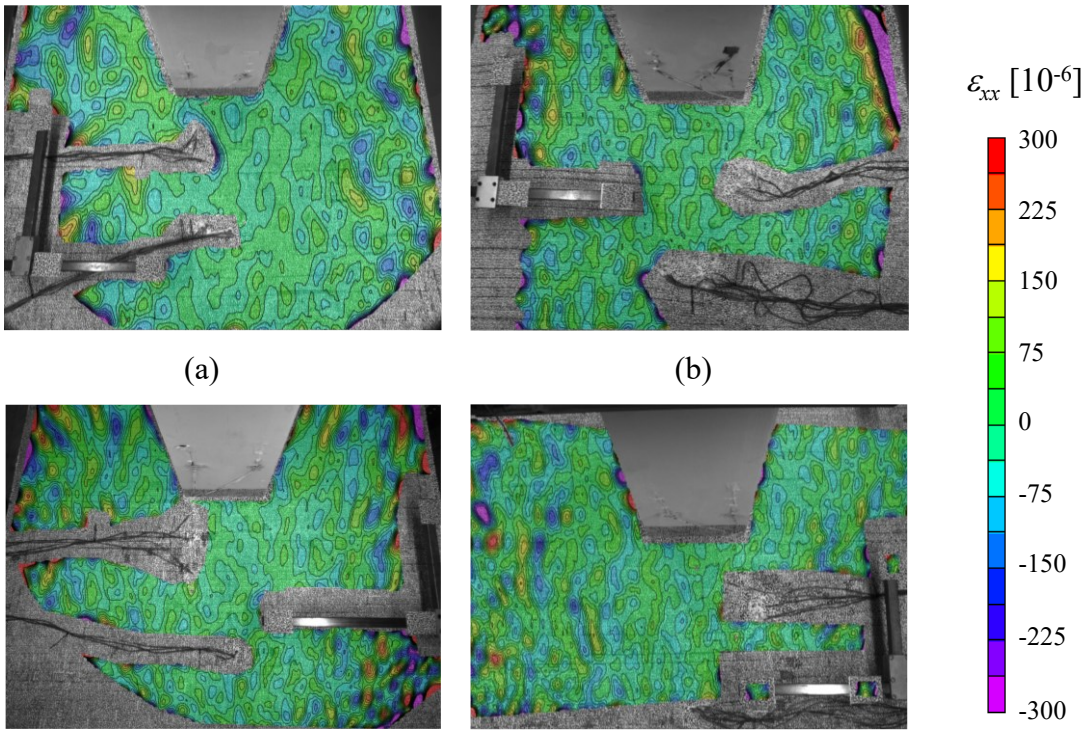

Figure D.21 Transverse strain noise levels at the surface of the slab at (a) West interior joint; (b) West exterior joint; (c) East exterior joint; (d) East interior joint

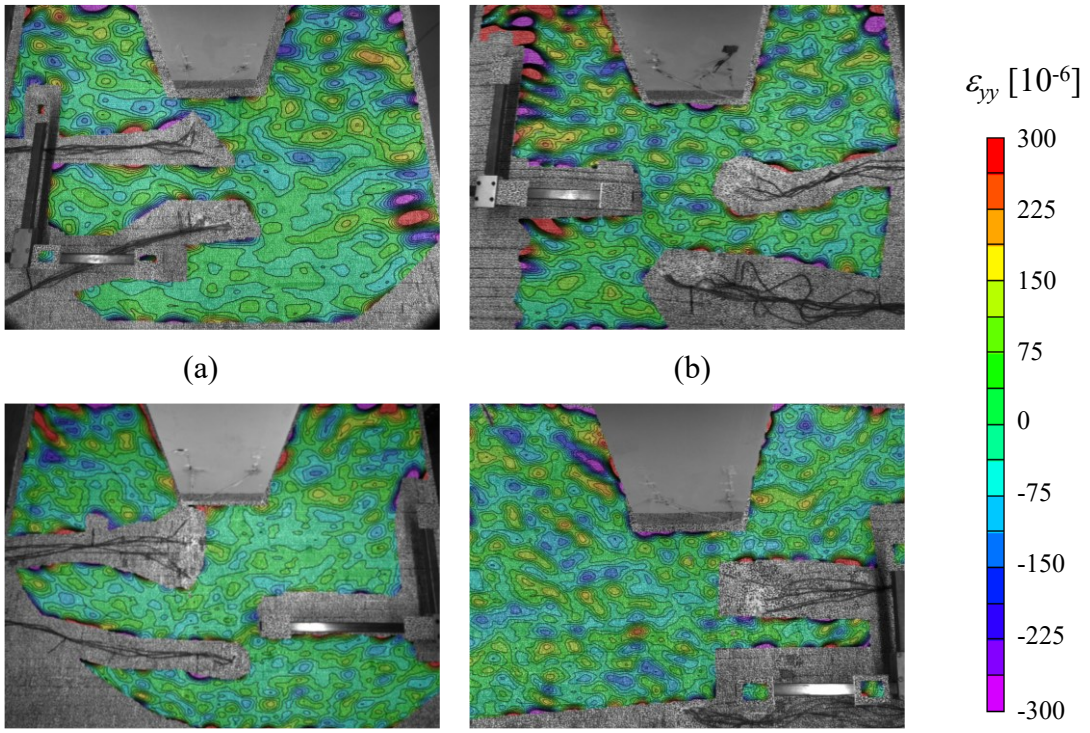

Figure D.22 Longitudinal strain noise levels at the surface of the slab at (a) West interior joint; (b) West exterior joint; (c) East exterior joint; (d) East interior joint

D.4.14 Notation

$a_{PZ,I}$ = vertical distance between the fixed points of the LVDTs on the interior column web panel zone taken as the average of a_{PZ1} and a_{PZ2} (see Figure D.17b)

b_{fb} = IPE360 beam flange width

b_{fc} = HEM320 beam flange width

$b_{PZ,I}$ = horizontal distance between the fixed points of the LVDTs on the interior column web panel zone taken as the average of b_{PZ1} and b_{PZ2} (see Figure D.17b)

d_{eff}^{+} = column web panel zone effective depth under sagging bending (see Figure D.17a)

d_{eff}^{-} = column web panel zone effective depth under hogging bending (see Figure D.17a)

h_{1E} = distance between cross section 1E and the top inflection point (i.e., center of the top pin), (see Figure D.3)

h_{2E} = distance between cross section 2E and the top inflection point (i.e., center of the top pin), (see Figure D.3)

h_{3E} = distance between cross section 3E and the bottom inflection point (i.e., center of the top pin), (see Figure D.3)

h_{4E} = distance between cross section 4E and the bottom inflection point (i.e., center of the top pin), (see Figure D.3)

h_b = HEM320 beam depth (see Figure D.16)

h_c = HEM320 column depth (see Figure D.16)

h_{LB-pin} = distance between the top pin clevises and the centerline of the loading beam (see Figure D.10)

h_{LB-Br} = distance between the applied actuator force and the centerline of the loading beam (see Figure D.10)

h_{SP} = distance from the top string pot on the East column to the bottom inflection point (i.e. center of the bottom clevis) (see Figure D.2)

s_{Br} = average slip of the bracket (see Figure D.2)

t_{fb} = IPE360 beam flange thickness

t_{fc} = HEM320 beam flange thickness

x = distance from the center of the East exterior joint (column centerline) to the location at which the moment is calculated (see Figure D.12)

x_s = location on the optic fiber at which it enters the edge of the slab (see Figure D.20a)

z_i = distance from the centroid of the discretized area to the centroid of the cross section instrumented with strain gauges (see Figure D.1)

E = modulus of elasticity of steel

F_A = force applied by the actuator (see Figure D.4)

$F_{A,h}$ = horizontal component of the force applied by the actuator

$F_{A,v}$ = vertical component of the force applied by the actuator

H = distance between the top and bottom inflection points (i.e. distance between the center of the clevises), (see Figure D.2 andFigure D.*16*)

K_R = lateral stiffness of the reaction frame

L_{56E} = distance between the instrumented cross sections in the East beam (see Figure D.6)

L_b = beam length measured from the column centerlines (see Figure D.4 andFigure D.*16*)

L_A = distance between the clevises of the actuator (see Figure D.4)

M_o = calculated moment at the cross section instrumented with strain gauges

$M_{cb,IJ,i}$ = composite steel beam moment at the center of the interior joint: West and East beams (see Figure D.8)

$M_{c,1E}$ = moment in the East column at cross section 1E (see Figure D.3)

$M_{c,2E}$ = moment in the East column at cross section 2E (see Figure D.3)

$M_{c,3E}$ = moment in the East column at cross section 3E (see Figure D.3)

$M_{c,4E}$ = moment in the East column at cross section 4E (see Figure D.3)

$M_{c,EJ,bot}$ = column bottom moment at the center of the East exterior joint (see Figure D.12)

$M_{c,EJ,top}$ = column top moment at the center of the East exterior joint (see Figure D.12)

$M_{c,IJ,bot}$ = column bottom moment at the center of the interior joint (see Figure D.7)

$M_{c,IJ,top}$ = column top moment at the center of the interior joint (see Figure D.7)

$M_{cb,5E}$ = moment in the East composite steel beam at cross section 5E (see Figure D.6)

$M_{cb,6E}$ = moment in the East composite steel beam at cross section 6E (see Figure D.6)

$M_{cb,EJ}$ = composite steel beam moment at the center of the East exterior joint (see Figure D.12)

$M_{cb,E,x}$ = moment in the East composite steel beam moment at a distance x from the East exterior joint (see Figure D.12)

$M_{cb,IJ,E}$ = moment in the East composite steel beam at the center of the interior joint (see Figure D.7)

$M_{cb,IJ,W}$ = moment in the West composite steel beam at the center of the interior joint (see Figure D.7)

$M_{c,IJ,i}$ = column moment at the center of the interior joint: top and bottom (see Figure D.8)

$M_{E,cf}^{+}$ = sagging bending moment at the face of the East column

$M_{E,cf}^{-}$ = hogging bending moment at the face of the East column

$M_{IE,cf}^{+}$ = hogging bending moment at the East face of the interior column (see Figure D.17a)

$M_{IW,cf}^{+}$ = sagging bending moment at the West face of the interior column (see Figure D.17a)

$M_{LB,Br}$ = moment in the bracket at the centerline of the loading beam (see Figure D.10)

$M_{LB,E}$ = moment in the top East pin at the centerline of the loading beam (see Figure D.10)

$M_{LB,I}$ = moment in the top interior pin at the centerline of the loading beam (see Figure D.10)

$M_{LB,W}$ = moment in the top West pin at the centerline of the loading beam (see Figure D.10)

N_o = calculated axial force at the cross section instrumented with strain gauges

$N_{cb,E}$ = axial force in the East composite steel beam (see Figure D.18)

$N_{ci,bot}$ = axial force in the bottom region of each column: West, Interior and East (see Figure D.4)

$N_{ci,top}$ = axial force in the top region of each column: West, Interior and East (see Figure D.4)

$N_{cE,bot}$ = axial force in the bottom region of the East exterior column (see Figure D.4)

$N_{cE,top}$ = axial force in the top region of the East exterior column (see Figure D.4)

$N_{cE,bot}{}'$ = axial force in the bottom region of the East exterior column obtained from strain gauge measurements (see Figure D.11)

$N_{cE,top}{}'$ = axial force in the top region of the East exterior column obtained from strain gauge measurements (see Figure D.11)

$N_{cI,bot}$ = axial force in the bottom region of the interior column (see Figure D.4)

$N_{cI,top}$ = axial force in the top region of the interior column (see Figure D.4)

$N_{cW,bot}$ = axial force in the bottom region of the West exterior column (see Figure D.4)

$N_{cW,top}$ = axial force in the top region of the West exterior column (see Figure D.4)

$N_{s,5E}$ = axial force in the slab at cross section 5E (see Figure D.18)

$N_{b,5E}$ = axial force in the steel beam at cross section 5E (see Figure D.18)

SDR = story drift ratio (see section D.4.2)

$V_{cb,E}$ = shear force in the East composite steel beam (see Figure D.4)

$V_{cb,W}$ = shear force in the East composite steel beam (see Figure D.4)

$V_{ci,bot}$ = shear force in the bottom region of each column: West, Interior and East (see Figure D.4)

$V_{ci,top}$ = shear force in the top region of each column: West, Interior and East (see Figure D.4)

$V_{cE,bot}$ = shear force in the bottom region of the East exterior column (see Figure D.18)

$V_{cE,top}$ = shear force in the top region of the East exterior column (see Figure D.18)

$V_{cI,bot}$ = shear force in the bottom region of the interior column (see Figure D.17a)

$V_{cI,top}$ = shear force in the top region of the interior column (see Figure D.17a)

V_{Base} = total base shear of the test frame

$V_{LB,E}$ = shear force in the East span of the loading beam (see Figure D.10)

$V_{PZ,E}$ = East column web panel zone demand

$V_{PZ,I}$ = interior column web panel zone demand

γ = column web panel zone distortion (see Figure D.17b)

$\delta_{b,W}$ = average axial shortening along the centerline of the West beam (see Figure D.19)

δ_A = applied actuator displacement (see Figure D.2)

δ_{EP} = gap opening between the end plate and the column flange (see Figure D.16)

$\delta_{I,bot}$ = measurement of the bottom string pot located in the West beam at the interior joint (see Figure D.19)

$\delta_{I,top}$ = measurement of the top string pot located in the West beam at the interior joint (see Figure D.19)

$\delta_{SP,E}$ = measurement of the top string pot on the East column (see Figure D.2)

$\delta_{W,bot}$ = measurement of the bottom string pot located in the West beam at the exterior joint (see Figure D.19)

$\delta_{W,top}$ = measurement of the top string pot located in the West beam at the exterior joint (see Figure D.19)

δA_i = area of each discretized region in the cross section instrumented with strain gauges (see Figure D.1)

ε_i = measured uniaxial strains at the cross section instrumented with strain gauges (see Figure D.1)

θ_b = composite steel beam chord rotation (see Figure D.16)

θ_c = column chord rotation (see Figure D.16)

θ_{EP} = angle due to the gap opening between the end plate and the column flange (see Figure D.16)

$\theta_{INCL,l}$ = measurement of the inclinometer on the left side of the joint (see Figure D.16)

$\theta_{INCL,r}$ = measurement of the inclinometer on the right side of the joint (see Figure D.16)

$\theta_{INCL,b}$ = measurement of the inclinometer at the bottom of the joint (see Figure D.16)

Δ_1 = measurement of the LVDT on the left side of the column web (see Figure D.17b)

Δ_2 = measurement of the LVDT on the right side of the column web (see Figure D.17b)

Appendix E Supplementary results from the experimental program

Description

This appendix provides supplementary results, from the 2-bay composite steel moment-resisting frame experimental program, that were not included in Chapter 5.

E.1 Main sequence of events at each joint throughout the loading history

Table E.1 Performance summary of the composite steel beam at the West exterior joint

	Sagging Bending			Hogging Bending		
	M_b [kNm]	SDR [% rad]	θ_b [% rad]	M_b [kNm]	SDR [% rad]	θ_b [% rad]
Effective Yield[1]	772	1.4	1	-523	-1.3	-1.1
Peak	855	3.5	2.8	-552	-1.9	-1.8
80% Peak	684	8.1	7.6	-441	-3.9	-4.1
50% Peak	427	10.4	10.1	NA	NA	NA
End of the Test	105	15	15.4	NA	NA	NA

(1) Derived according to El Jisr et al. (2019)
NA: Not available

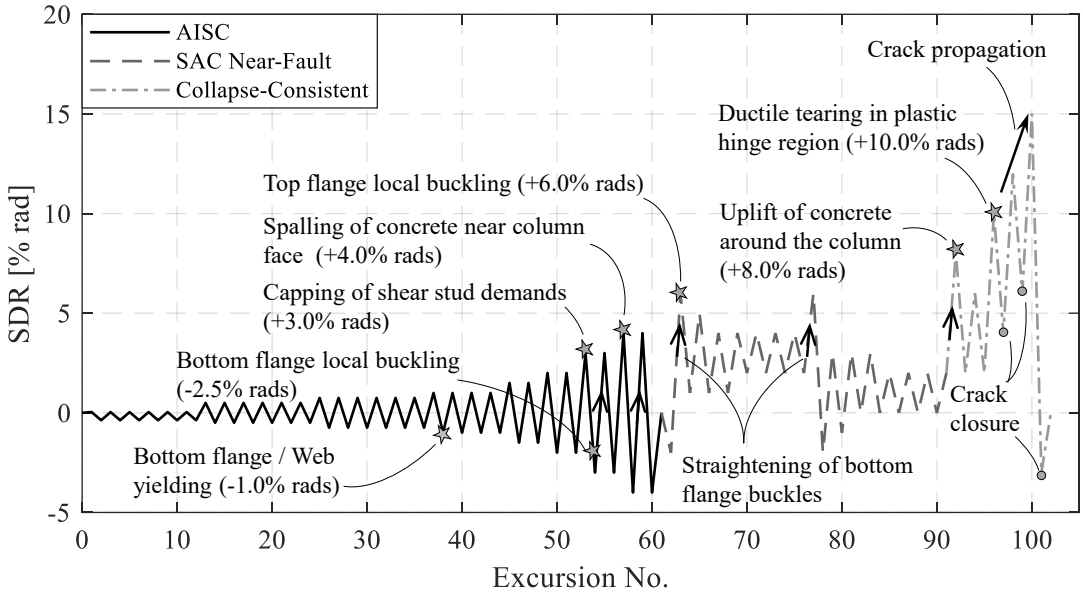

Figure E.1 West exterior joint main events throughout the loading history

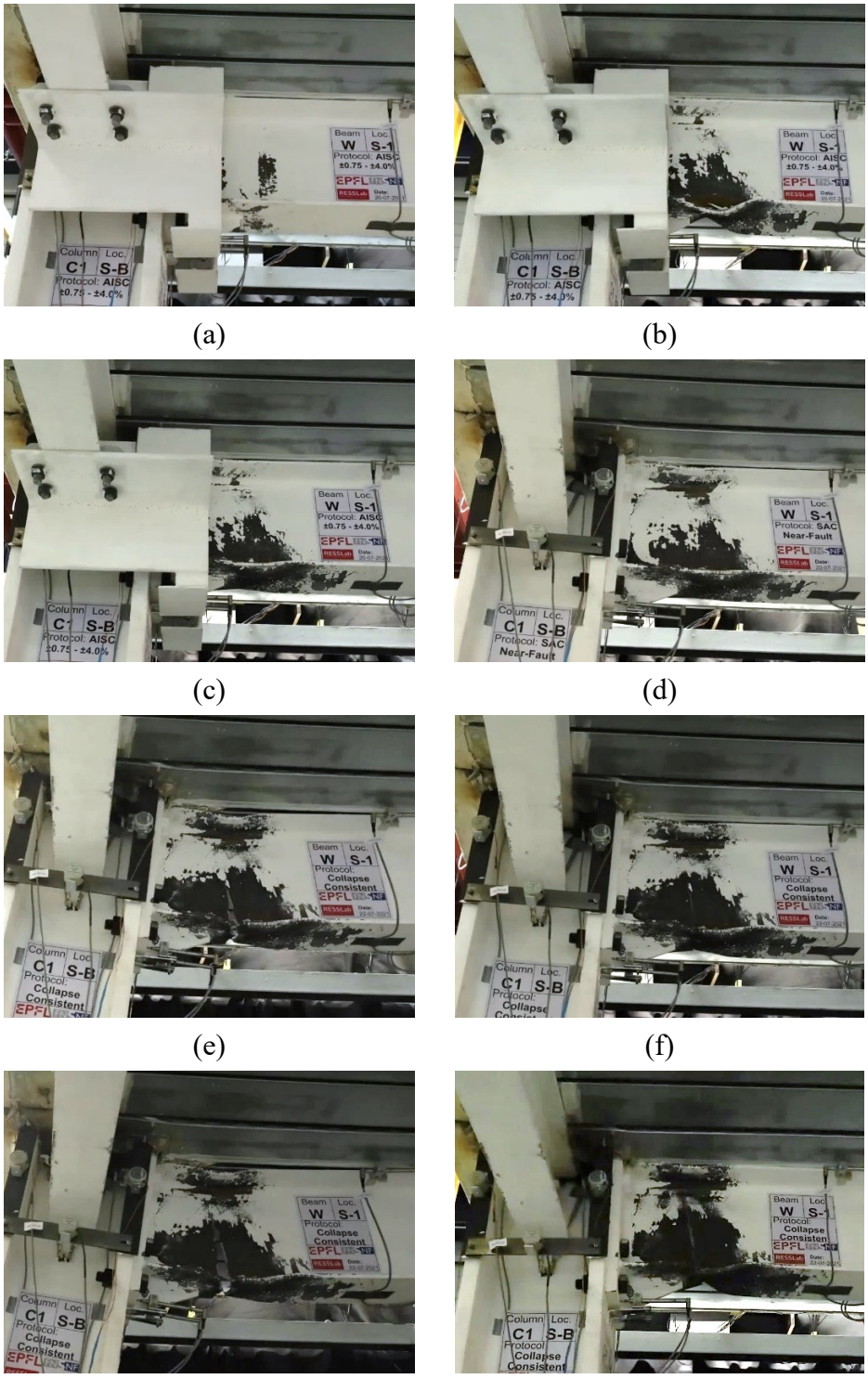

Figure E.2 West exterior joint at selected lateral drift demands: (a) bottom flange and web yielding (-2% rads, AISC symmetric loading protocol); (b) local buckling (-4% rads, AISC symmetric loading protocol); (c) straightening of the bottom flange local buckles at load reversal (+4% rads, AISC symmetric loading protocol); (d) top flange local buckling and straightening of the bottom flange local buckles (+6% rads, SAC near-fault protocol); (e) crack initiation and propagation (+10% rads, collapse-consistent protocol; (f) crack closure at load reversal (+6% rads, collapse-consistent protocol); (g) crack propagation (+15% rads, collapse-consistent protocol); (h) crack closure at load reversal (-3% rads, collapse-consistent protocol)

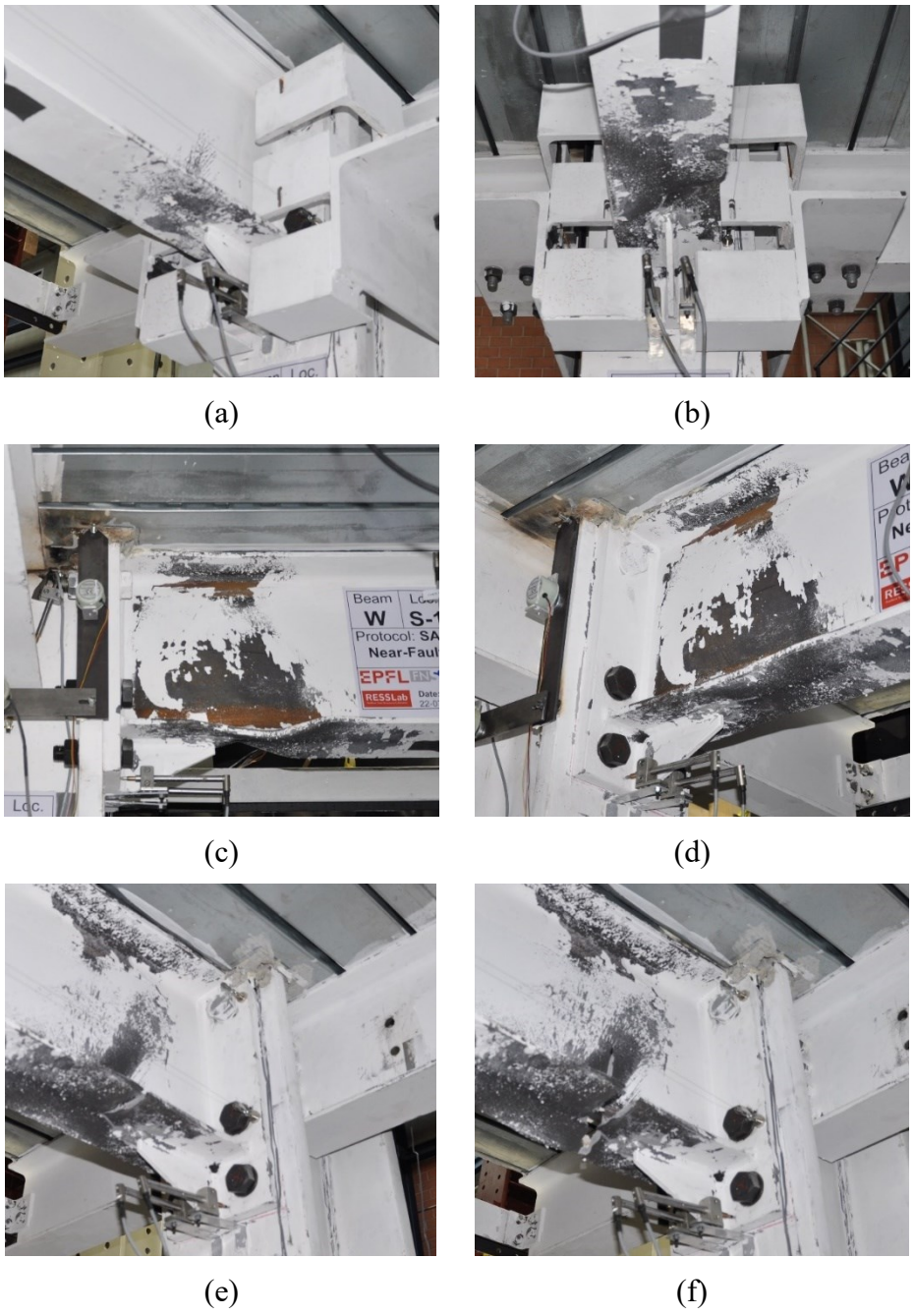

Figure E.3 Damage progression in the West exterior joint: (a) bottom flange and web yielding (-2% rads, AISC symmetric loading protocol); (b) bottom flange local buckling (-4% rads, AISC symmetric loading protocol); (c) bottom flange local buckling (-2% rads, SAC near-fault protocol); (d) straightening of the bottom flange local buckles (+6% rads, SAC near-fault protocol); (e) crack initiation due to ultra-low cycle fatigue (+10% rads, collapse-consistent protocol); (f) crack propagation (+12% rads, collapse-consistent protocol)

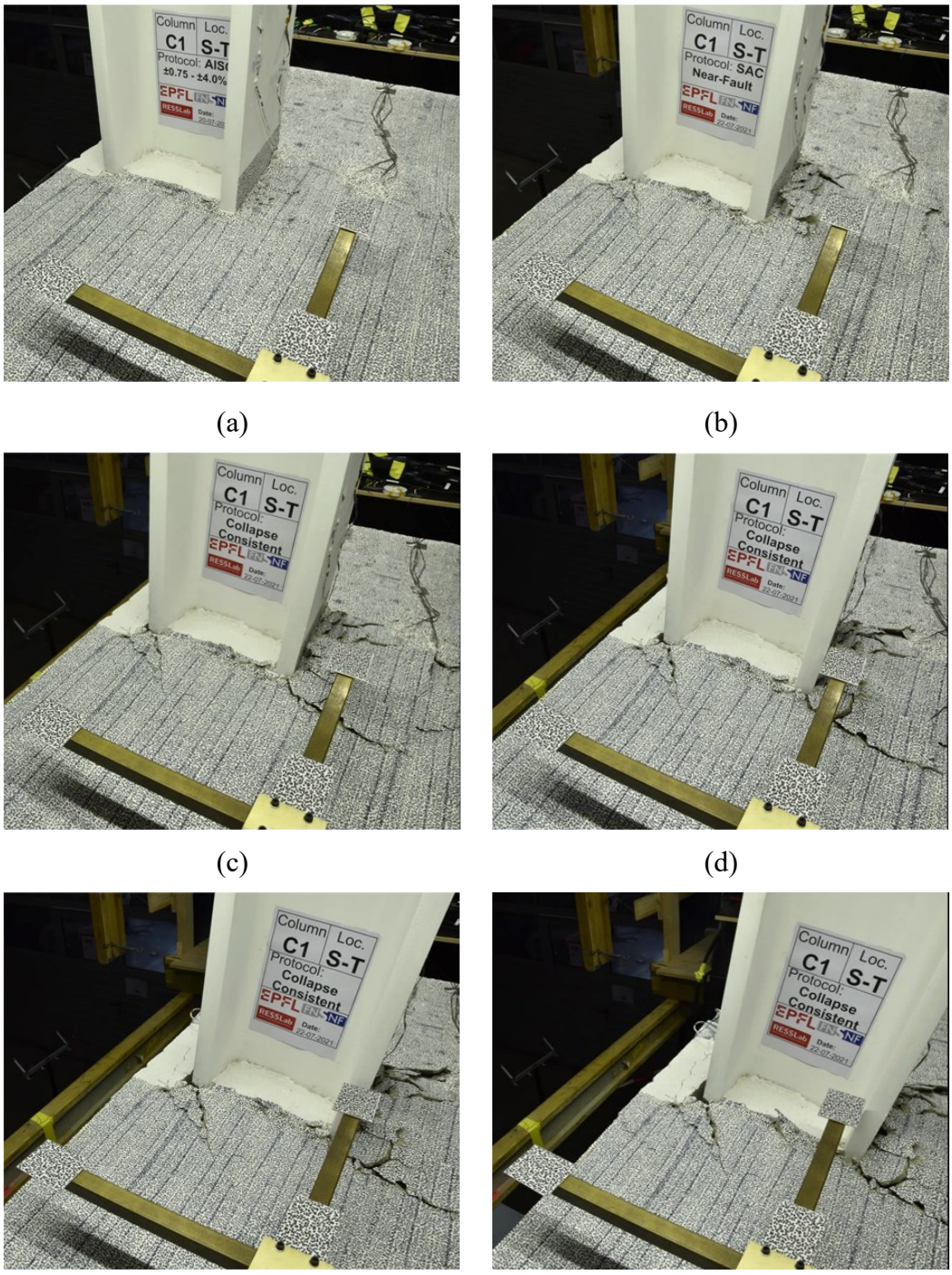

(a) (b)

(c) (d)

(e) (f)

Figure E.4 Slab state at the West exterior joint at selected lateral drift demands (a) concrete crushing at the column face (+4% rads, AISC symmetric loading protocol); (b) concrete spalling at the column face (+6% rads, SAC near-fault protocol); (c to f) uplift of the concrete around the column (+8% rads, +10%, +12% and +15% rads respectively, collapse-consistent protocol)

Table E.2 Performance summary of the composite steel beam at the West interior joint

	Sagging Bending			Hogging Bending		
	M_b [kNm]	SDR [% rad]	θ_b [% rad]	M_b [kNm]	SDR [% rad]	θ_b [% rad]
Effective Yield[1]	703	-1.3	0.8	-508	1.3	-0.7
Peak	824	-3	2.5	-516	2.5	-1.6
80% Peak	NA	NA	NA	-413	5.1	-3.3
End of the Test	NA	NA	NA	-278	15	-15.9

(1) Derived according to El Jisr et al. (2019)
NA: Not available

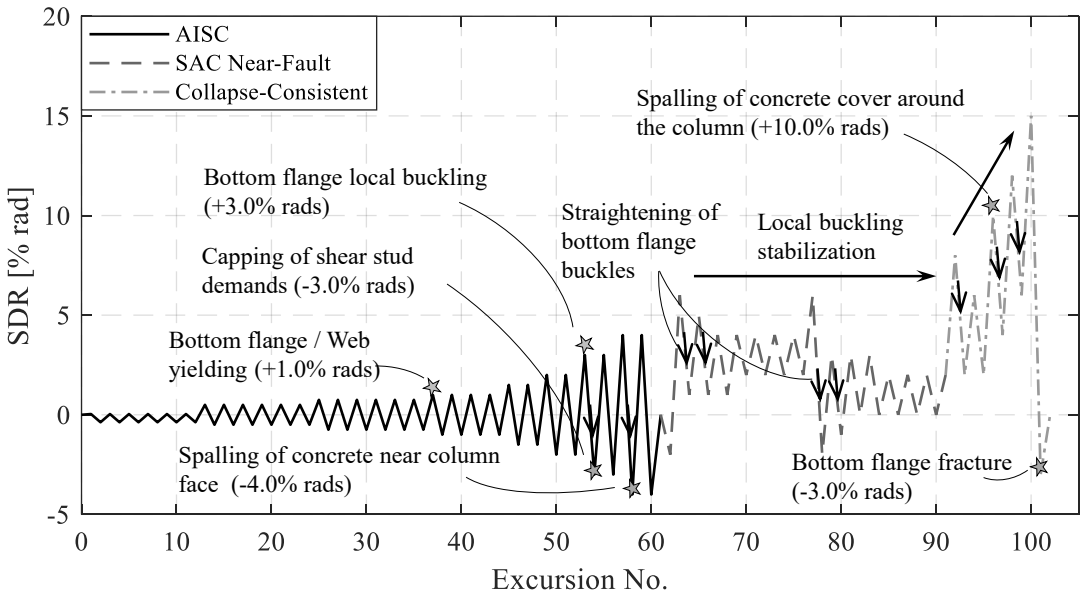

Figure E.5 West interior joint: main events throughout the loading history

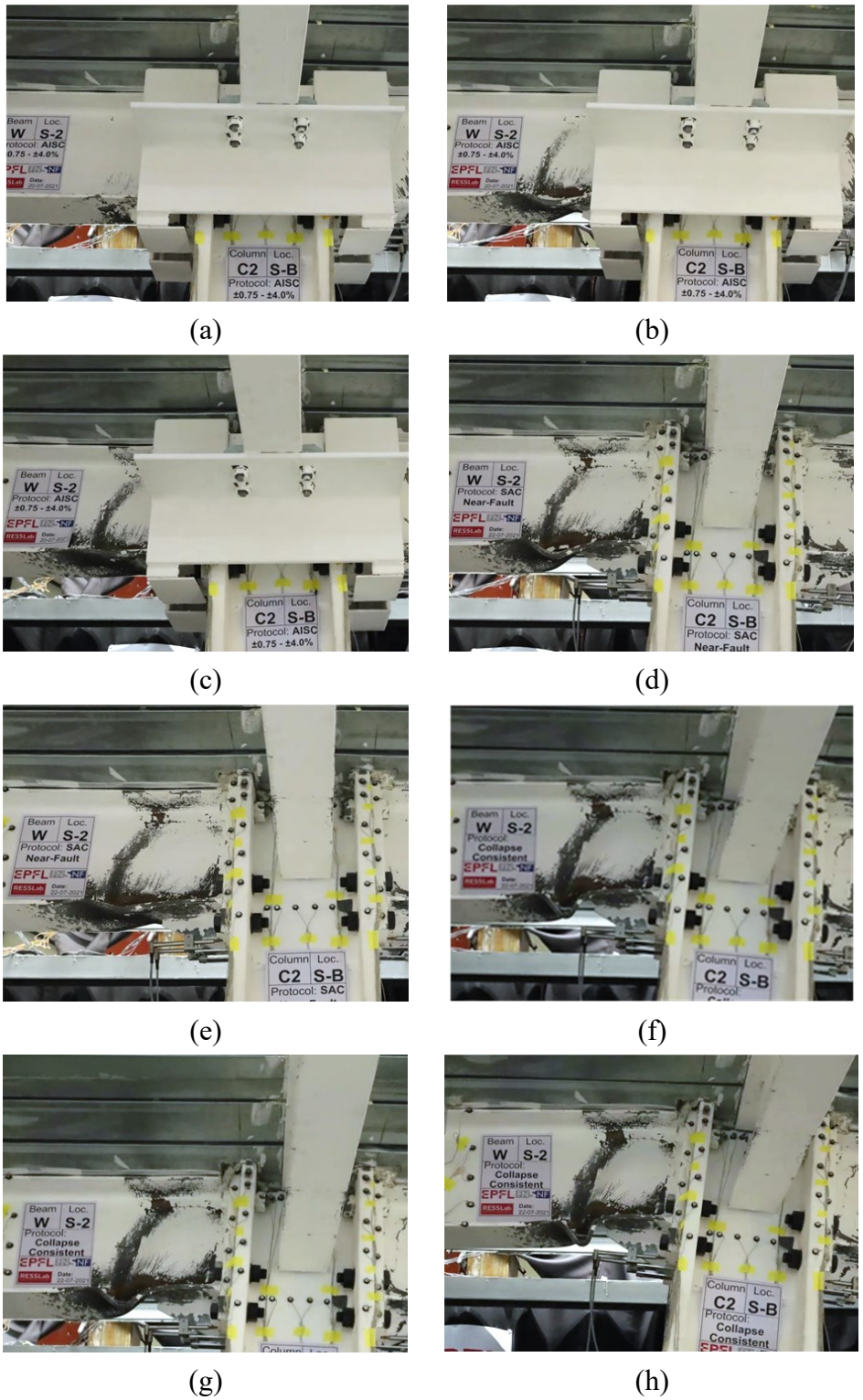

Figure E.6 West interior joint at selected lateral drift demands: (a) bottom flange and web yielding (+2% rads, AISC symmetric loading protocol); (b) bottom flange local buckling (+4% rads, AISC symmetric loading protocol); (c) straightening of the bottom flange local buckles at load reversal (-4% rads, AISC symmetric loading protocol); (d) bottom flange local buckling (+6% rads, SAC near-fault protocol); (e) partial straightening of the bottom flange local buckles at load reversal (-2% rads, SAC near-fault protocol); (f) bottom flange local buckling (+12% rads, collapse-consistent protocol; (g) partial straightening of bottom flange local buckles at load reversal (+6% rads, collapse-consistent protocol); (h) bottom flange local buckling (+15% rads, collapse-consistent protocol)

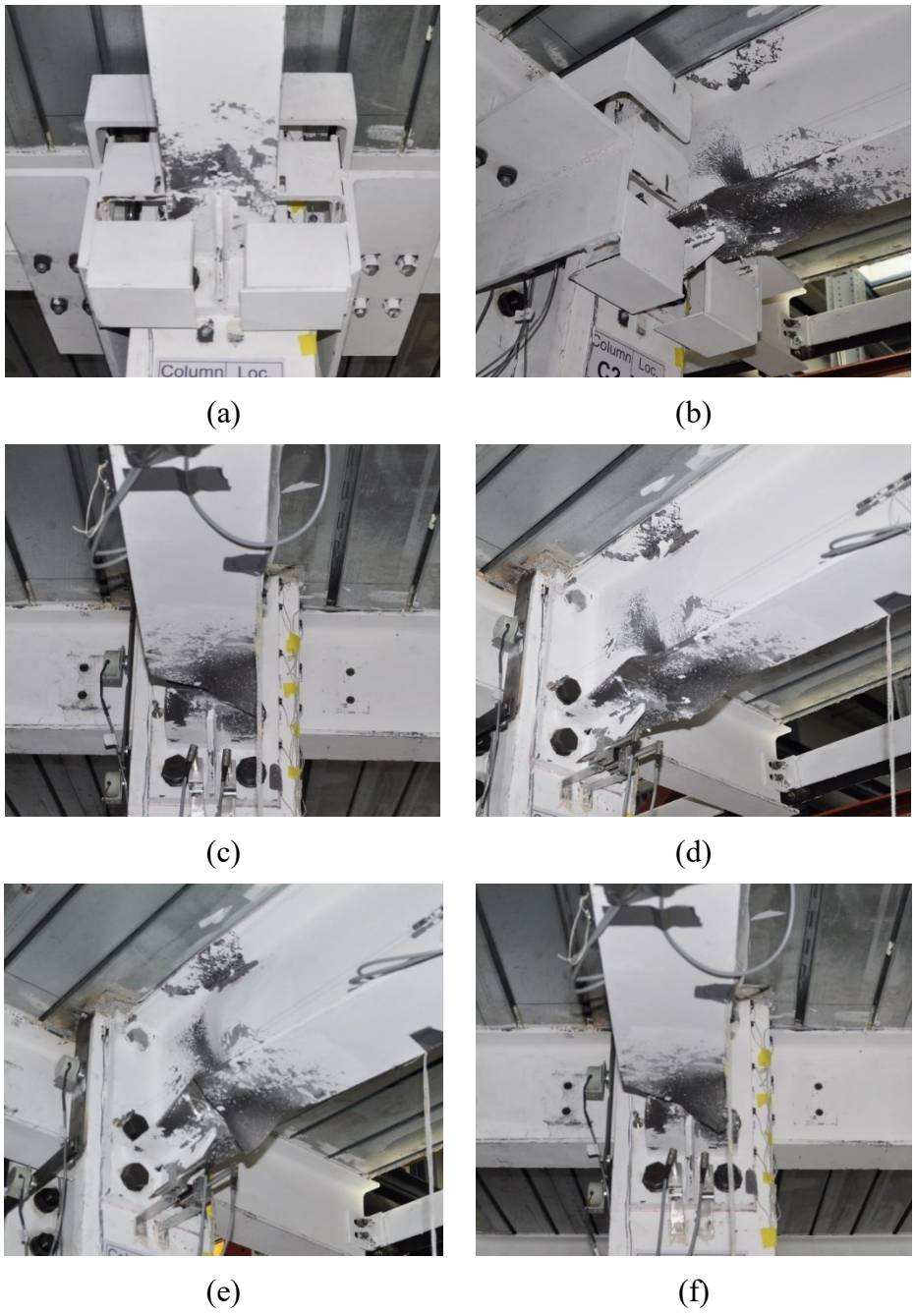

Figure E.7 Damage progression in the West interior joint: (a) bottom flange and web yielding (+2% rads, AISC symmetric loading protocol); (b) straightening of the bottom flange local buckles (-4% rads, AISC symmetric loading protocol); (c) bottom flange local buckling (+6% rads, SAC near-fault protocol); (d) partial straightening of the bottom flange local buckles (-2% rads, SAC near-fault protocol); (e) bottom flange local buckling (+15% rads, collapse-consistent protocol); (f) out-of-plane movement of the bottom flange due to local buckling (+15% rads, collapse-consistent protocol)

Table E.3 Performance summary of the composite steel beam at the East interior joint

	Sagging Bending			Hogging Bending		
	M_b [kNm]	SDR [% rad]	θ_b [% rad]	M_b [kNm]	SDR [% rad]	θ_b [% rad]
Effective Yield[1]	758	1.4	0.8	-548	-1.3	-0.8
Peak	883	2.9	2	-559	-2	-1.4
80% Peak	707	6	5.5	447	-3.8	-3.4
50% Peak	442	8.4	8.5	NA	NA	NA
End of the Test	105	15	15.9	NA	NA	NA

(1) Derived according to El Jisr et al. (2019)
NA: Not available

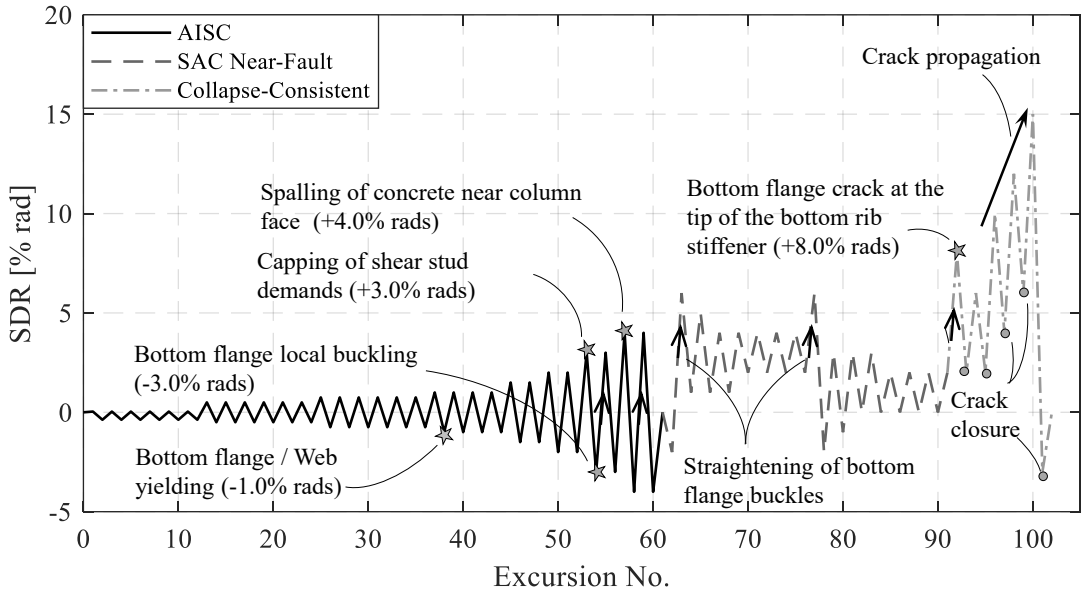

Figure E.8 East interior joint main events throughout the loading history

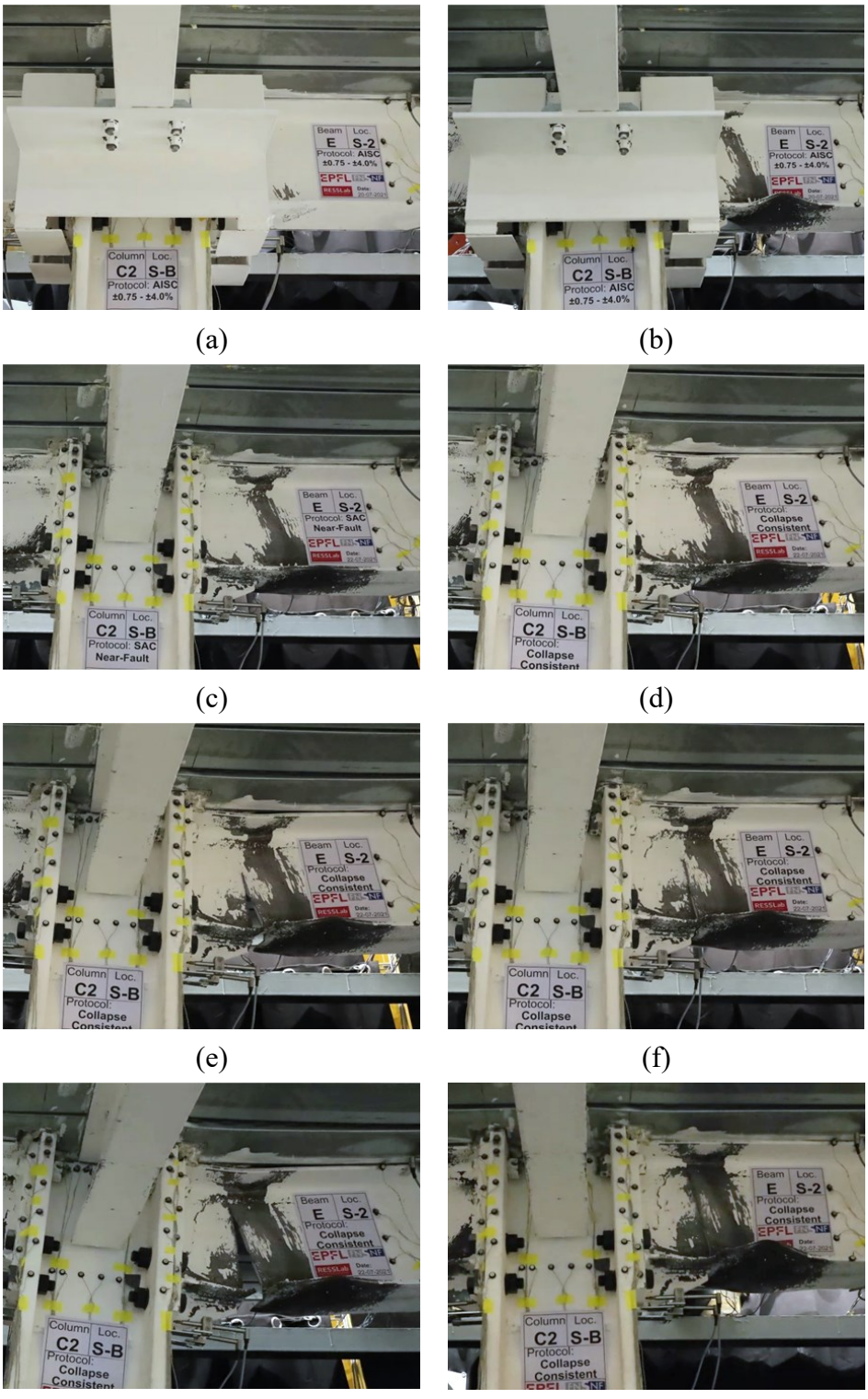

Figure E.9 East interior joint at selected lateral drift demands: (a) bottom flange and web yielding (-2% rads, AISC symmetric loading protocol); (b) bottom flange local buckling (-4% rads, AISC symmetric loading protocol); (c) straightening of the bottom flange local buckles (+6% rads, SAC near-fault protocol); (d) crack initiation at the tip of the bottom rib stiffener (+8% rads, collapse-consistent protocol; (e) crack propagation (+10% rads, collapse-consistent protocol); (f) crack closure at load reversal (+4% rads, collapse-consistent protocol); (g) crack propagation (+15% rads, collapse-consistent protocol); (h) crack closure at load reversal (-3% rads, collapse-consistent protocol)

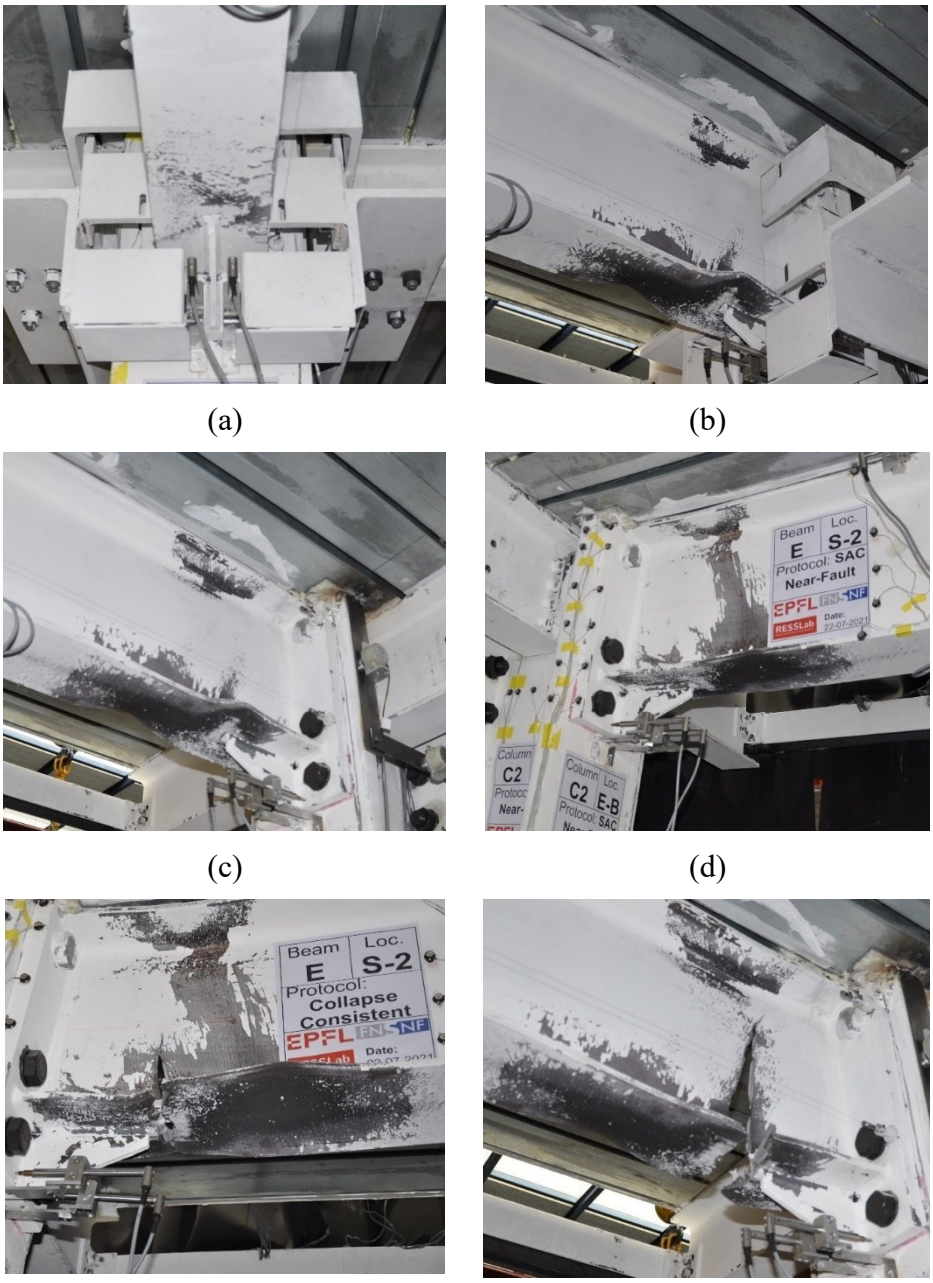

Figure E.10 Damage progression in the East interior joint: (a) bottom flange yielding (-2% rads, AISC symmetric loading protocol); (b) bottom flange local buckling (-4% rads, AISC symmetric loading protocol); (c) bottom flange local buckling (-2% rads, SAC near-fault protocol); (d) straightening of the bottom flange local buckles (+6% rads, SAC near-fault protocol); (e) crack initiation at the tip of the bottom stiffener (+8% rads, collapse-consistent protocol); (f) crack propagation (+15% rads, collapse-consistent protocol)

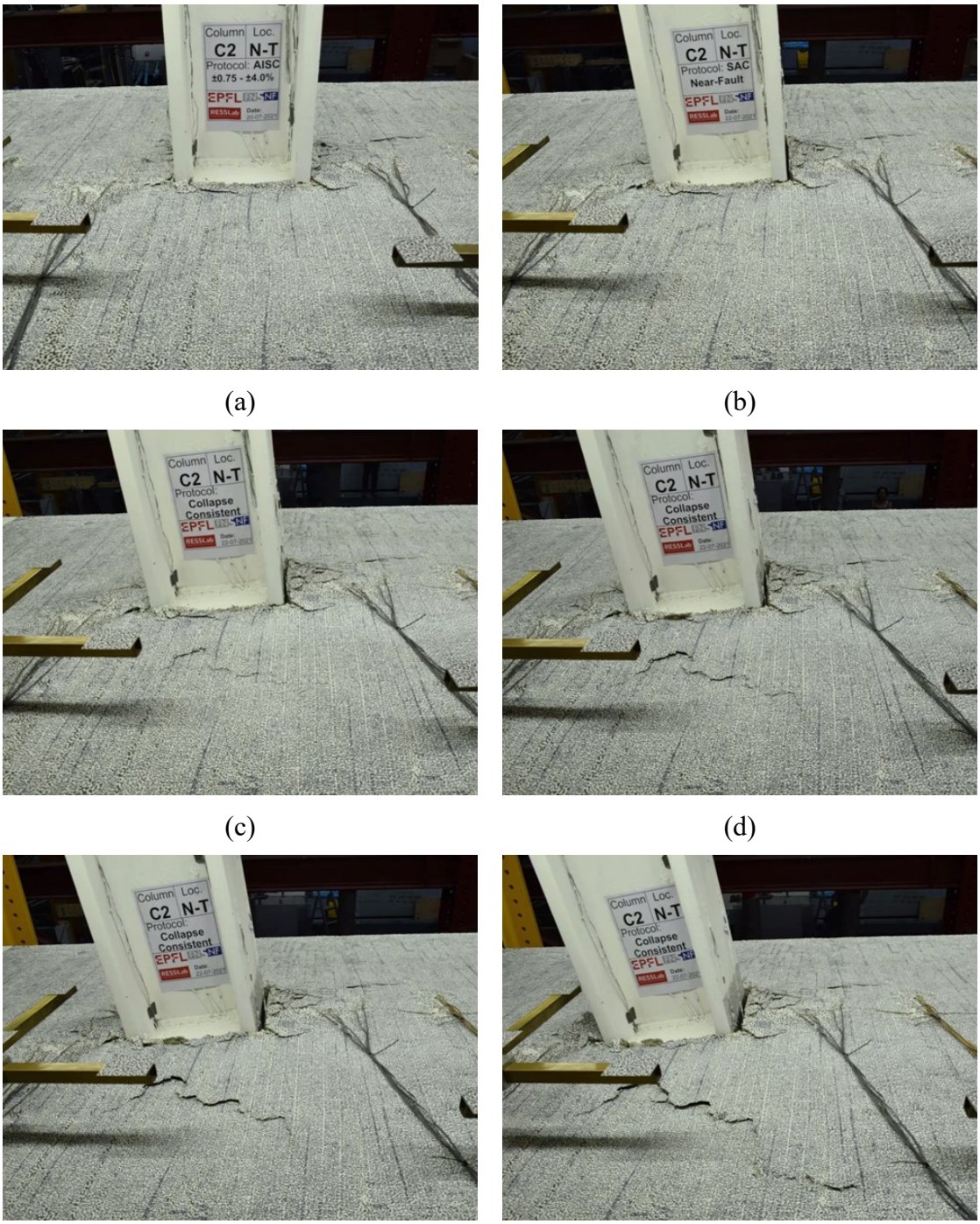

(a) (b)

(c) (d)

(e) (f)

Figure E.11 Slab state at the interior joint at selected lateral drift demands: (a) concrete crushing at the column face (+4% rads, AISC symmetric loading protocol); (b) concrete spalling at the column face (+6% rads, SAC near-fault protocol); (c to f) uplift of the concrete around the column (+8% rads, +10%, +12% and +15% rads respectively, collapse-consistent protocol)

Table E.4 Performance summary of the composite steel beam at the East exterior joint

	Sagging Bending			Hogging Bending		
	M_b [kNm]	SDR [% rad]	θ_b [% rad]	M_b [kNm]	SDR [% rad]	θ_b [% rad]
Effective Yield	694	-1.3	0.9	-461	1.2	-0.9
Peak	823	-3[a]	2.5	-513	2[b]	-1.8
80% Peak	NA	NA	NA	-410	4.3	-4.4
End of the Test	NA	NA	NA	-270	15	-16.2

(1) Derived according to El Jisr et al. (2019)
NA: Not available

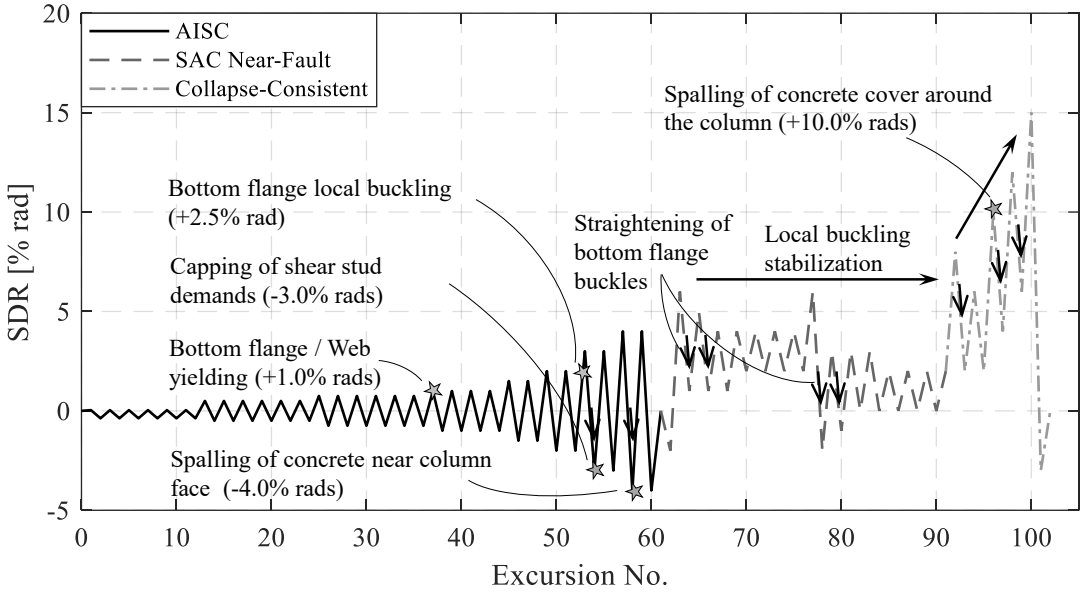

Figure E.12 East exterior joint main events throughout the loading history

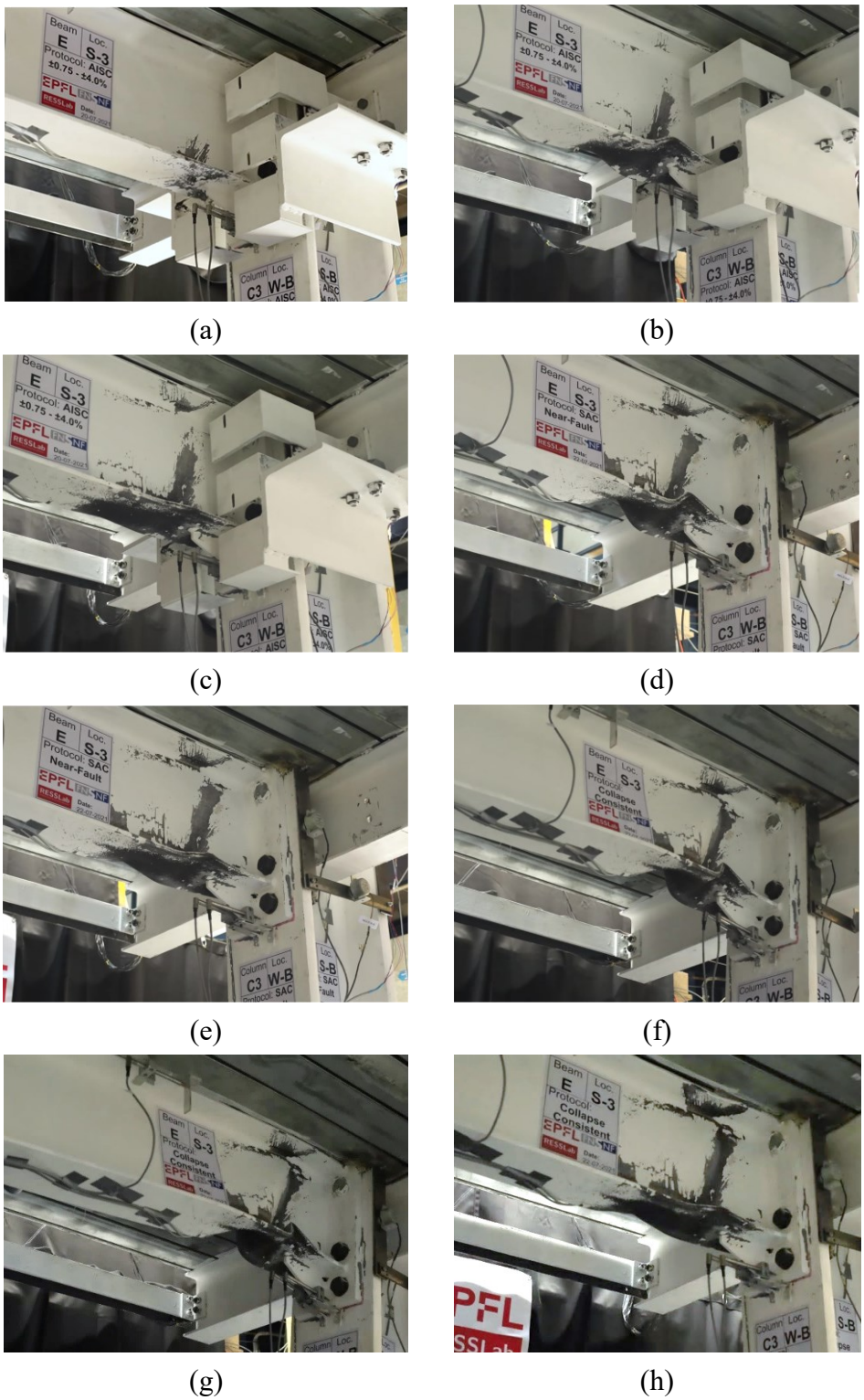

Figure E.13 East exterior joint at selected lateral drift demands: (a) bottom flange and web yielding (+2% rads, AISC symmetric loading protocol); (b) bottom flange local buckling (+4% rads, AISC symmetric loading protocol); (c) straightening of the bottom flange local buckles at load reversal (-4% rads, AISC symmetric loading protocol); (d) bottom flange local buckling (+6% rads, SAC near-fault protocol); (e) straightening of bottom flange local buckles at load reversal (-2% rads, SAC near-fault protocol); (f) bottom flange local buckling (+12% rads, collapse-consistent protocol; (g) bottom flange local buckling (+15% rads, collapse-consistent protocol); (h) straightening of the bottom flange local buckles at load reversal (-3% rads, collapse-consistent protocol)

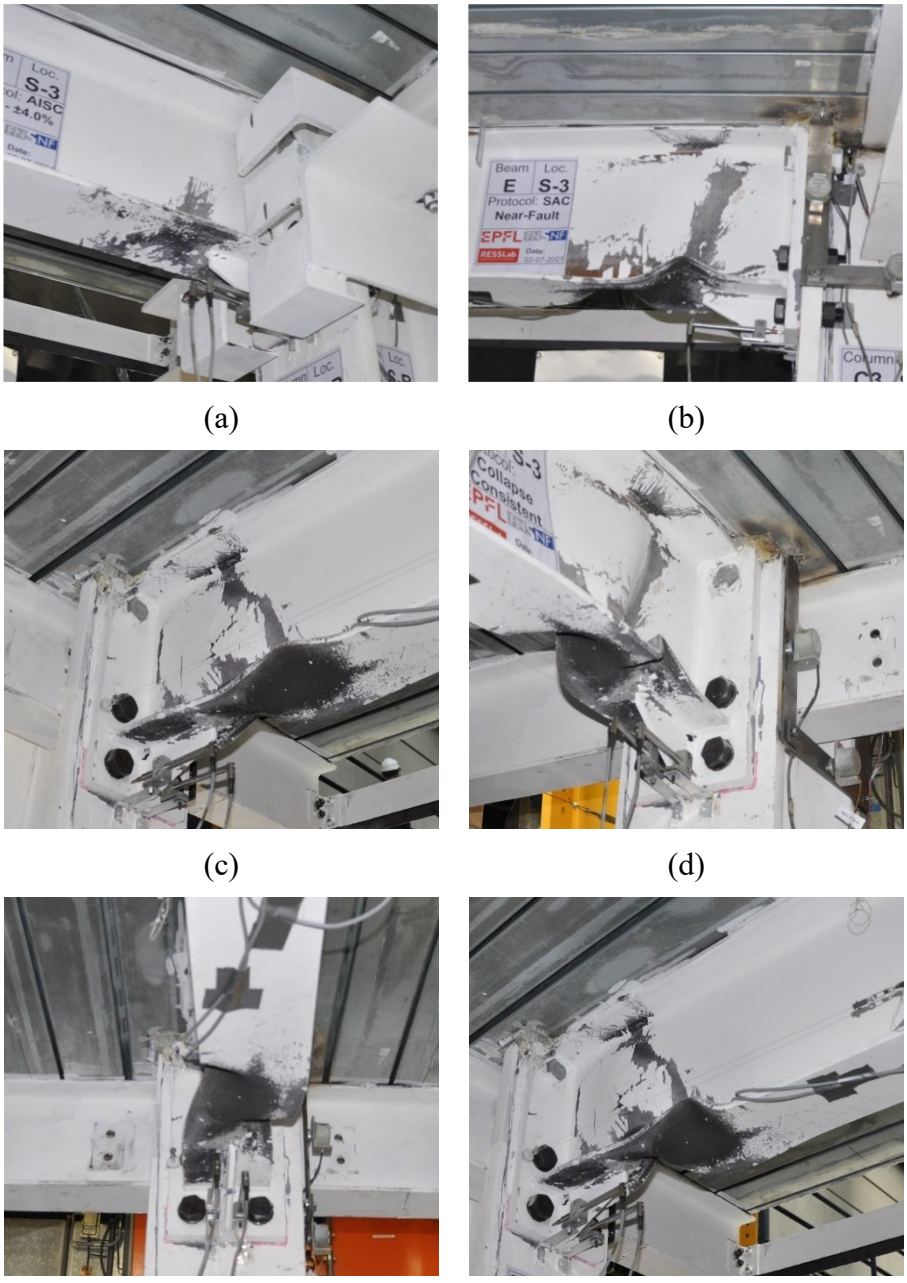

(a) (b)

(c) (d)

(e) (f)

Figure E.14 Damage progression in the East exterior joint: (a) bottom flange yielding (+2% rads, AISC symmetric loading protocol); (b) bottom flange local buckling (+6% rads, SAC near-fault protocol); (c) partial straightening of the bottom flange local buckles (-2% rads, SAC near-fault protocol); (d) bottom flange local buckling (+12% rads, collapse-consistent protocol); (e) out-of-plane movement of the bottom flange due to local buckling (+15% rads, collapse-consistent protocol); (f) straightening of the bottom flange local buckles (-3% rads, collapse-consistent protocol)

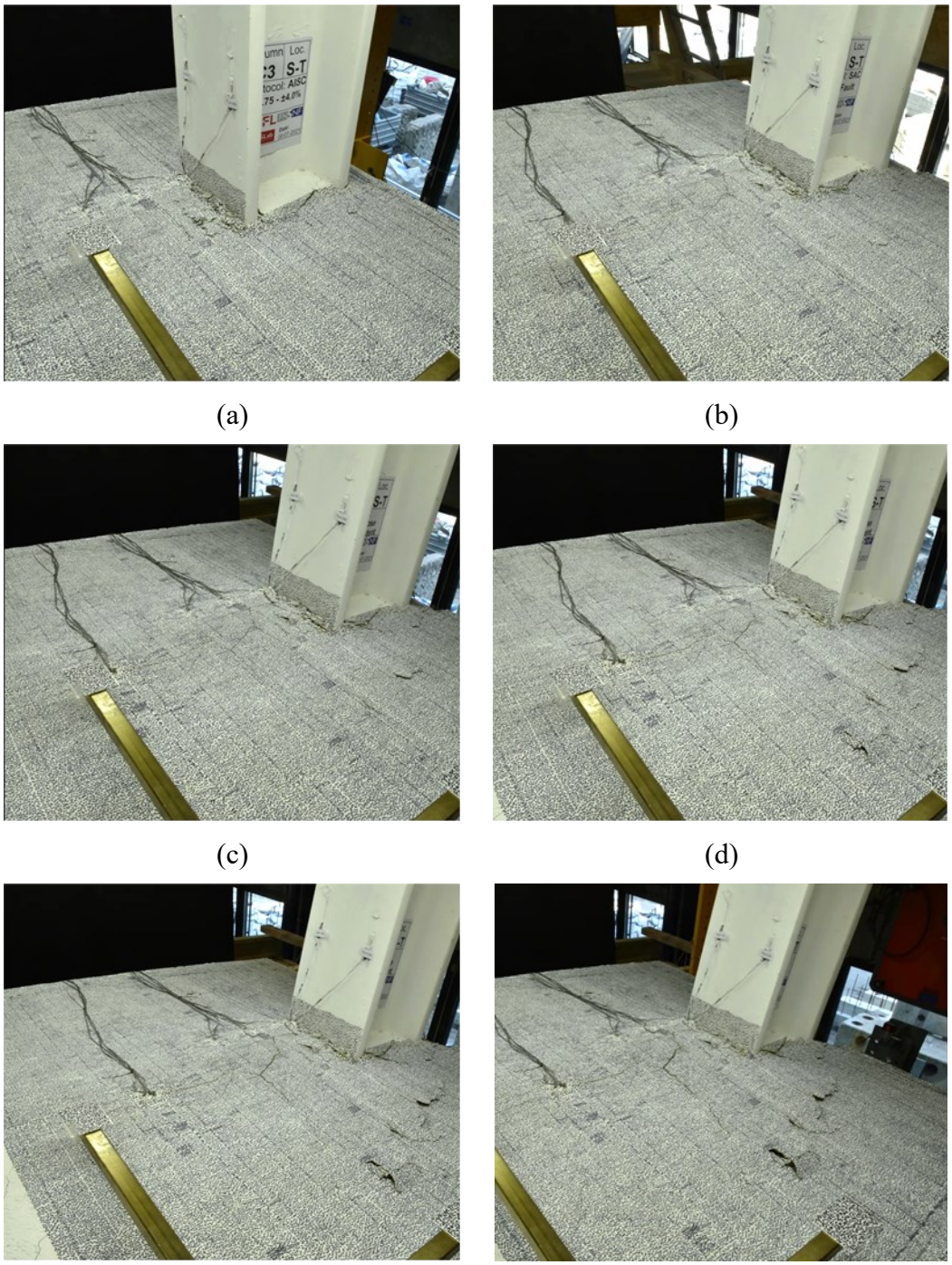

(a) (b)

(c) (d)

(e) (f)

Figure E.15 Slab state at the East exterior joint at selected lateral drift demands: (a) concrete crushing at the column face (-4% rads, AISC symmetric loading protocol); (b) concrete spalling at the column face (+6% rads, SAC near-fault protocol); (c to f) uplift of the concrete around the column (+8% rads, +10%, +12% and +15% rads respectively, collapse-consistent protocol)

E.2 Hysteretic behavior of the columns and column web panel zones

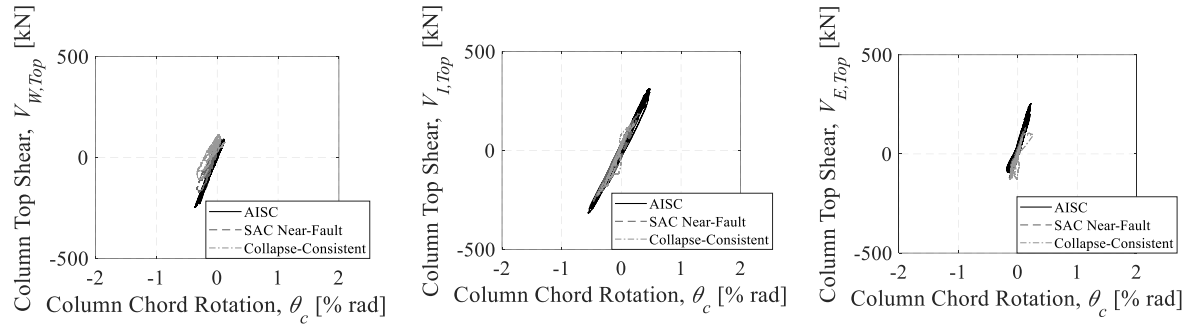

(a) (b) (c)

Figure E.16 Hysteretic behavior of the columns throughout the loading history: (a) West column; (b) Interior column; (c) East column

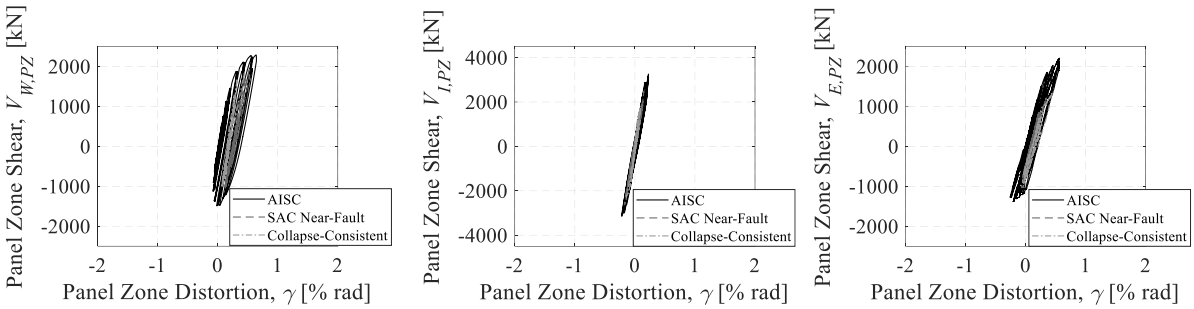

(a) (b) (c)

Figure E.17 Hysteretic behavior of the column web panel zones throughout the loading history: (a) West column; (b) Interior column; (c) East column

E.3 Hysteretic behavior of the beam-slab connections at the instrumented cross sections

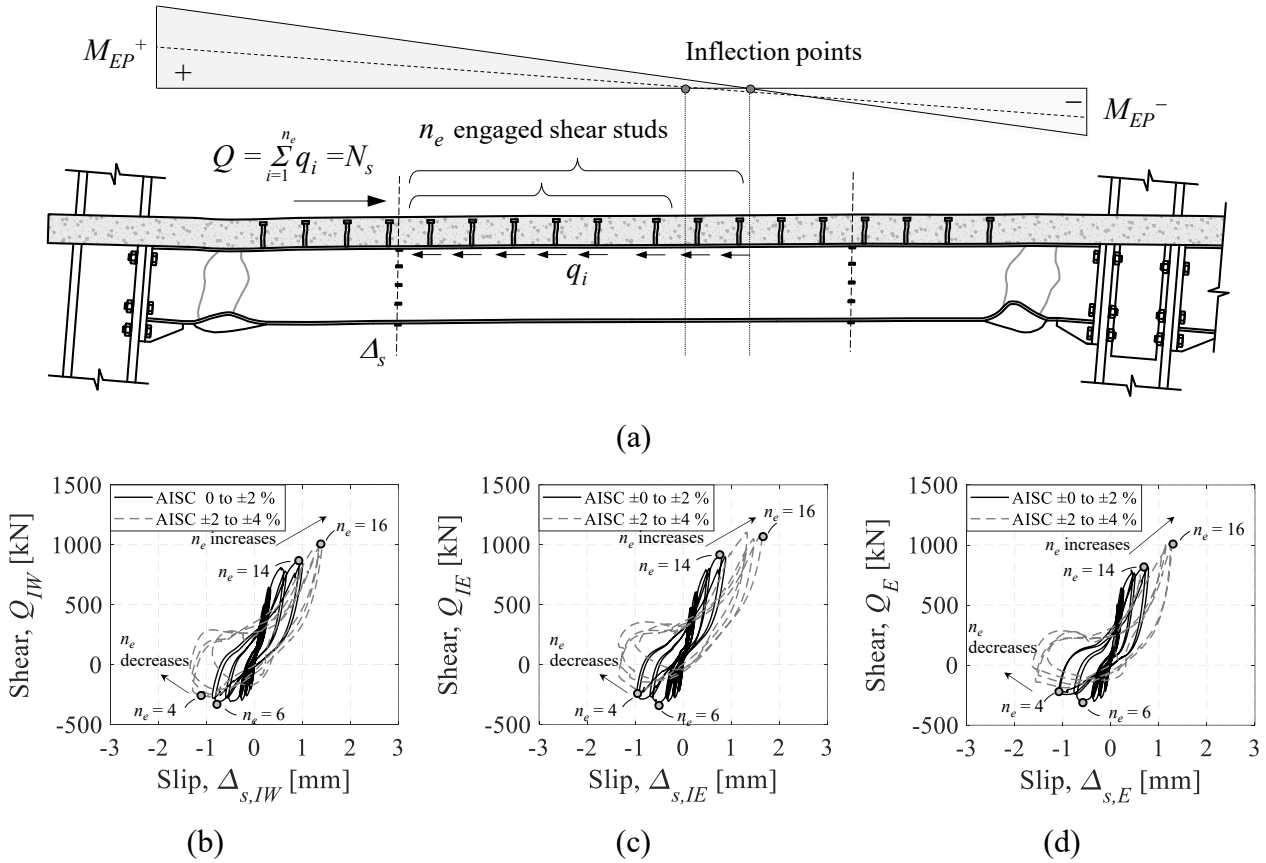

Figure E.18 Beam-slab connection response: (a) derivation of shear demand on beam-slab connection at the instrumented cross sections; hysteretic behavior of the beam-slab connection at the instrumented (b) West interior cross section; (c) East interior cross section; and (d) East exterior cross section under the AISC protocol

E.4 Longitudinal strain profiles at the instrumented cross sections in the beams and position of neutral axes throughout the loading history

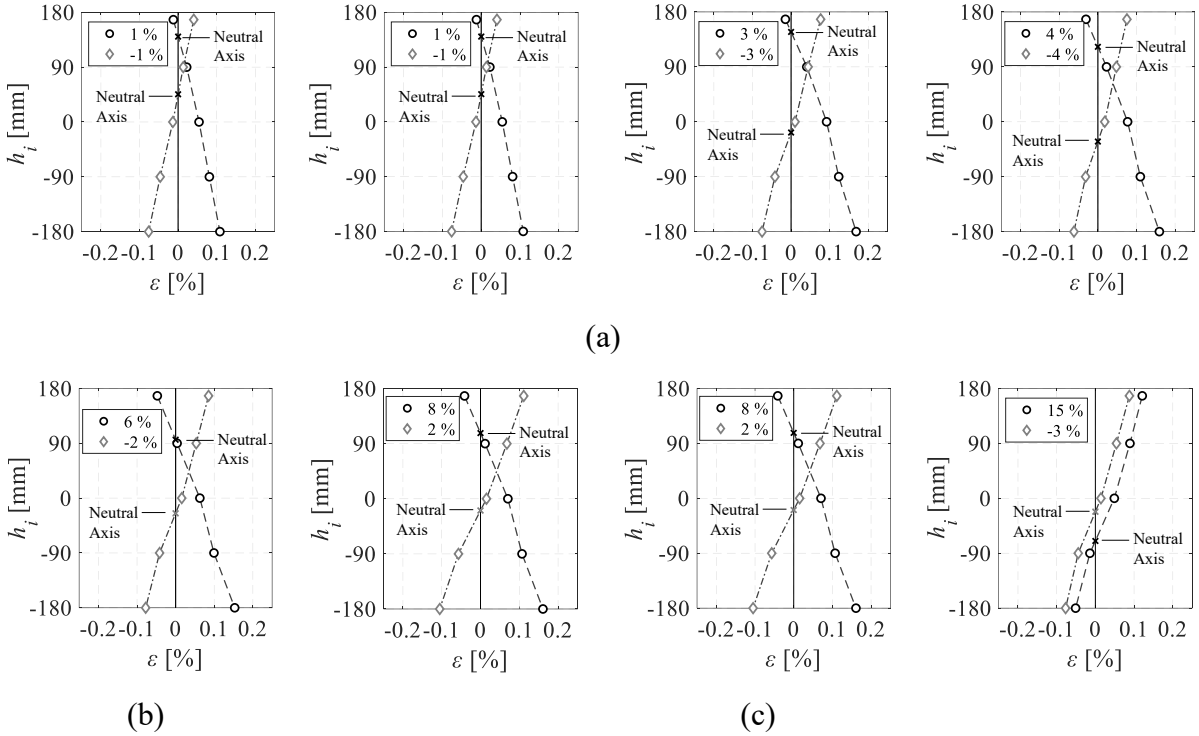

(a)

(b) (c)

Figure E.19 Longitudinal strain profile at 1205 mm from the column face of the West beam at the exterior joint, (a) AISC symmetric loading protocol; (b) SAC near-fault protocol; (c) collapse-consistent protocol

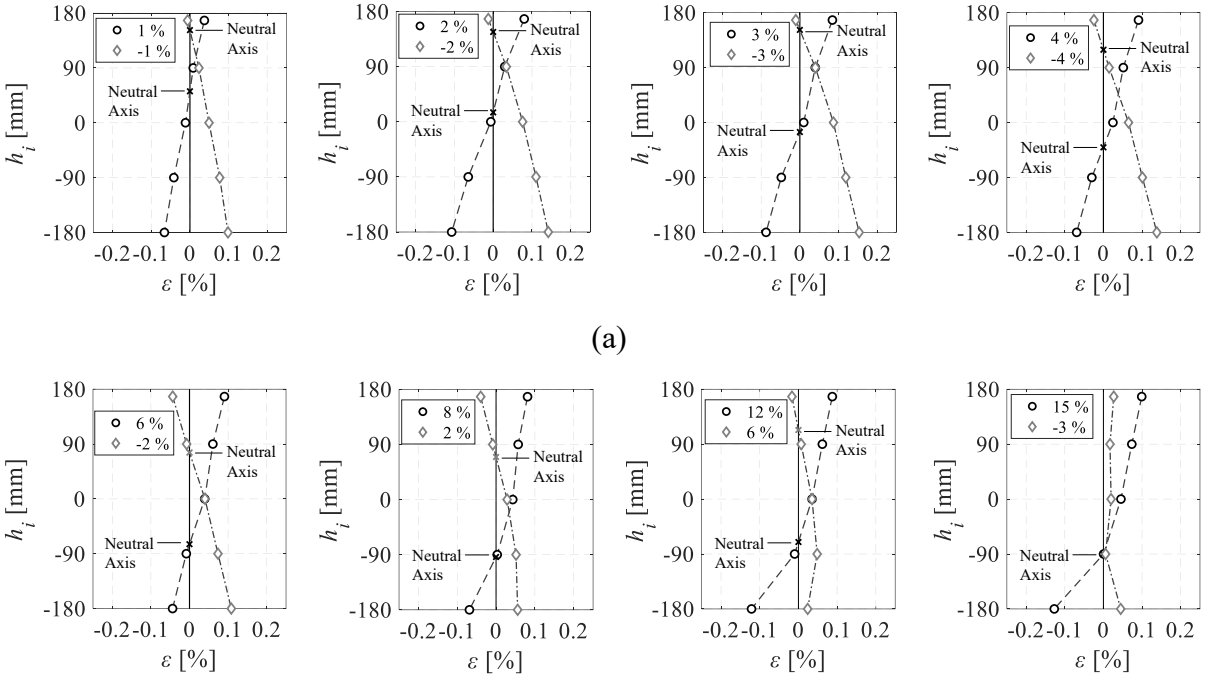

Figure E.20 Longitudinal strain profile at 1205 mm from the column face of the West beam at the interior joint, (a) AISC symmetric loading protocol; (b) SAC near-fault protocol; (c) collapse-consistent protocol

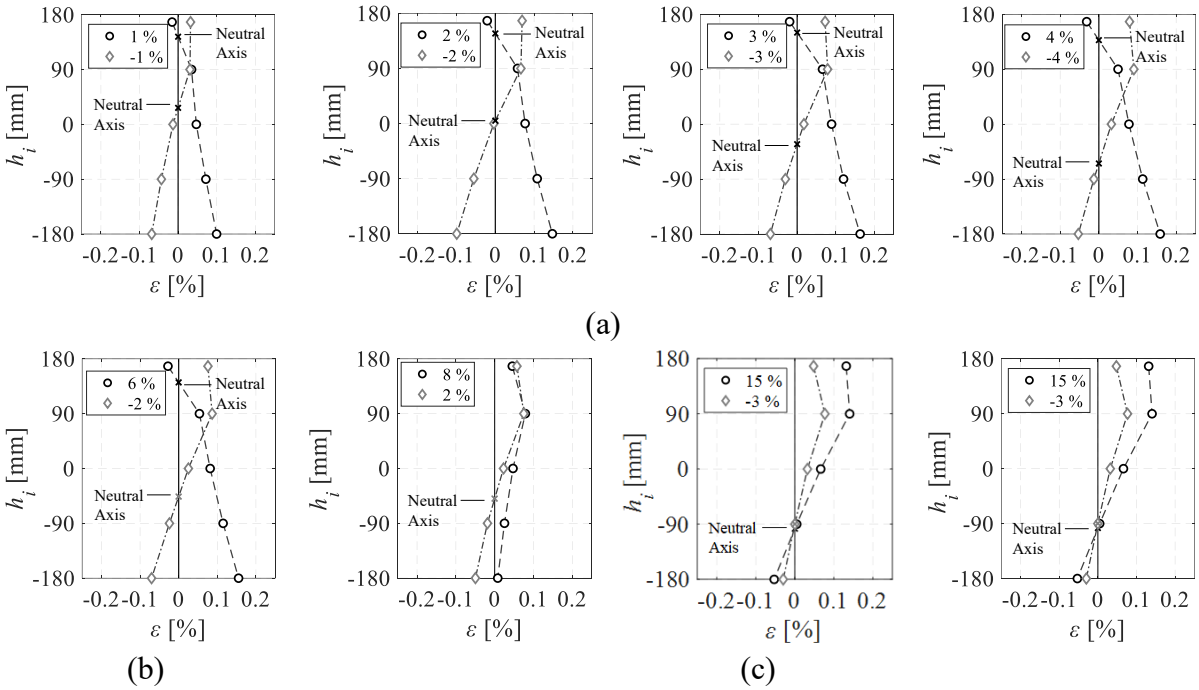

Figure E.21 Longitudinal strain profile at 1205 mm from the column face of the East beam at the interior joint, (a) AISC symmetric loading protocol; (b) SAC near-fault protocol; (c) collapse-consistent protocol

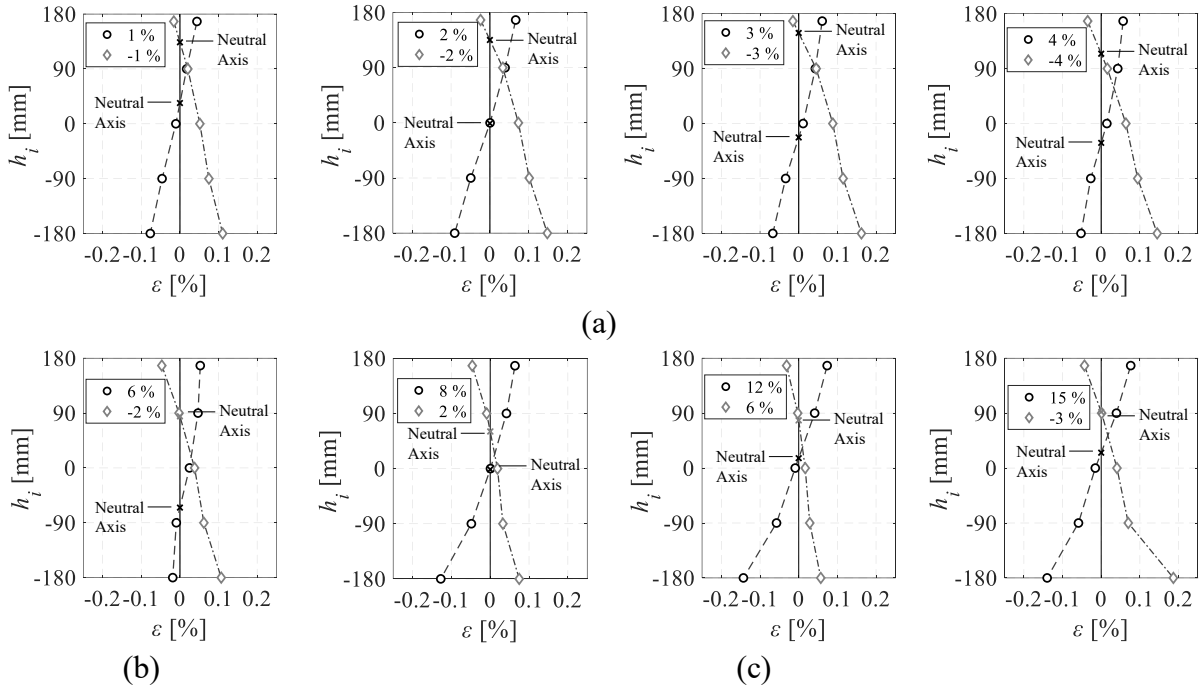

Figure E.22 Longitudinal strain profile at 1205 mm from the column face of the East beam at the exterior joint, (a) AISC symmetric loading protocol; (b) SAC near-fault protocol; (c) collapse-consistent protocol

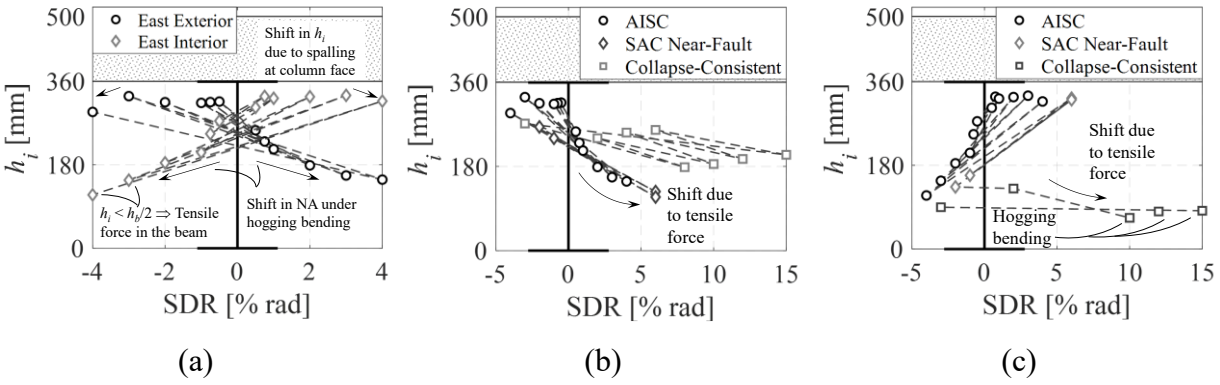

Figure E.23 Neutral axis positions of the East beam at exterior and interior joints; (a) AISC loading protocol; (b) East beam at exterior joint; (c) East beam at interior joint

E.5 Axial force in the East composite steel beam throughout the loading history

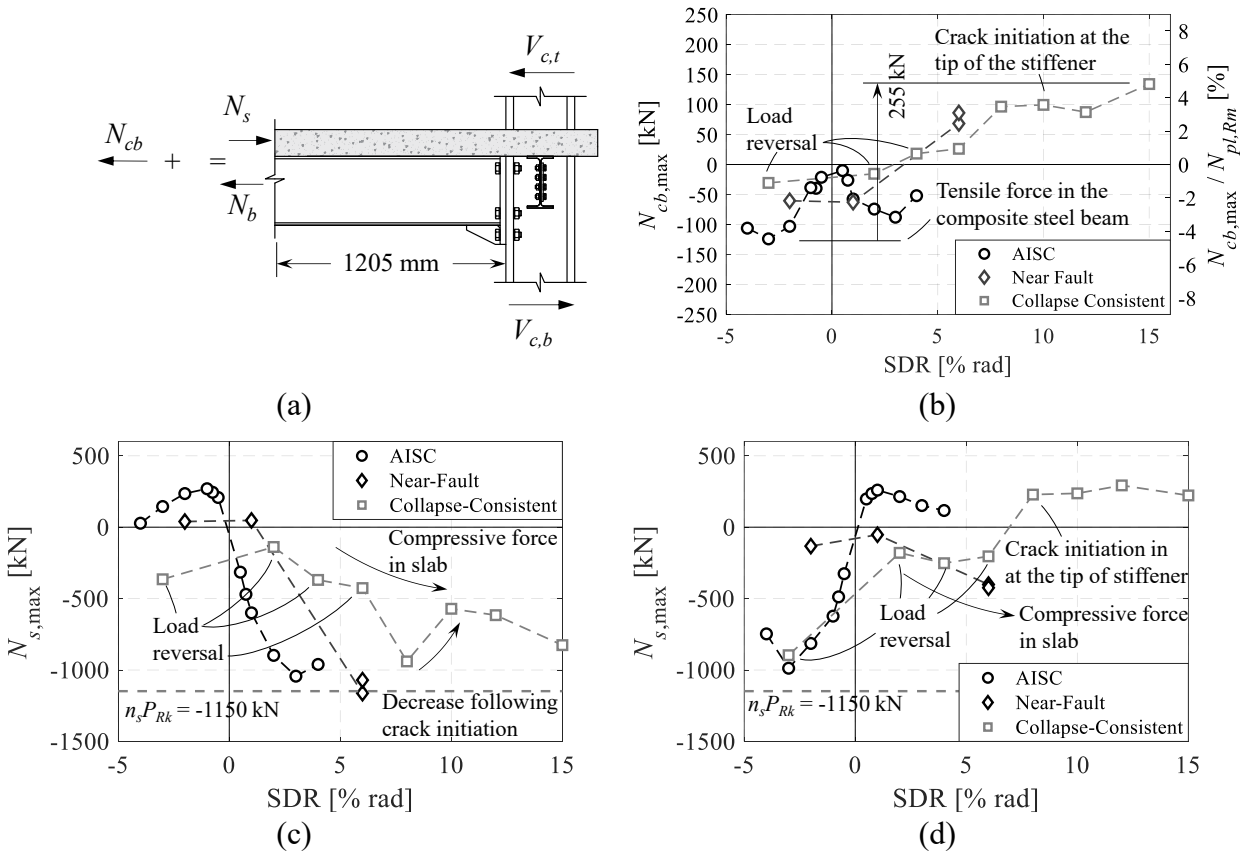

Figure E.24 Axial force in the East composite steel beam (N_{cb}) and slab (N_s), 1205 mm from the face of the exterior and interior columns (i.e., at the instrumented cross sections) at peak lateral drift demands: (a) derivation; (b) maximum axial force in the composite steel beam; (c) maximum axial force in the slab at the exterior cross section; (d) maximum axial force in the slab at the interior cross section

E.6 Transverse and longitudinal strains at the surface of the slab at the East exterior and West interior joints

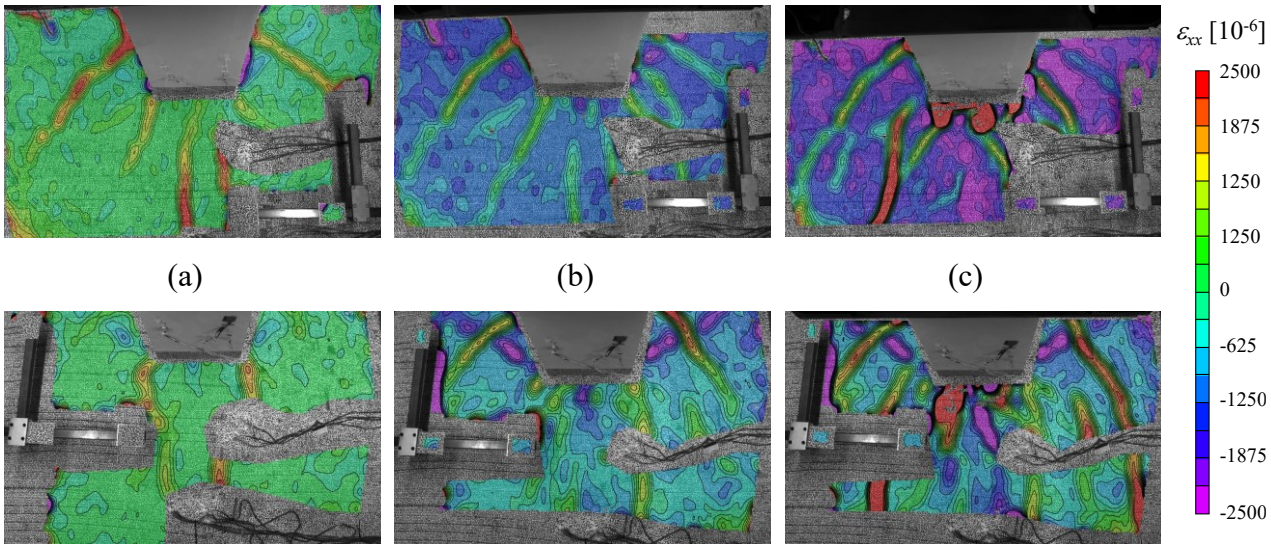

Figure E.25 Transverse strains at the surface of the slab at peak lateral drift demands up to 3% rads under sagging bending; Top: East interior joint at (a) -1% rads; (b) -2% rads; (c) -3% rads; Bottom: West exterior joint at (d) -1% rads; (e) -2% rads; (f) -3% rads

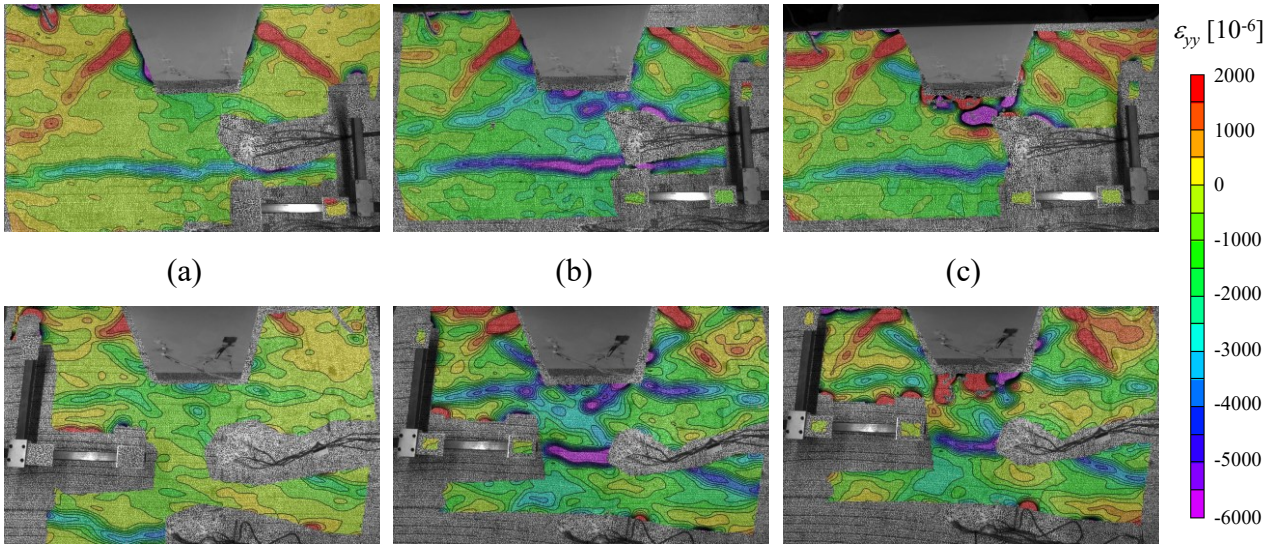

Figure E.26 Longitudinal strains at the surface of the slab at peak lateral drift ratios up to 3% rads under sagging bending; Top: East interior joint at (a) -1% rads; (b) -2% rads; (c) -3% rads; Bottom: West exterior joint at (d) -1% rads; (e) -2% rads; (f) -3% rads

E.7 Crack pattern in the slab and longitudinal rebars uniaxial strain distribution

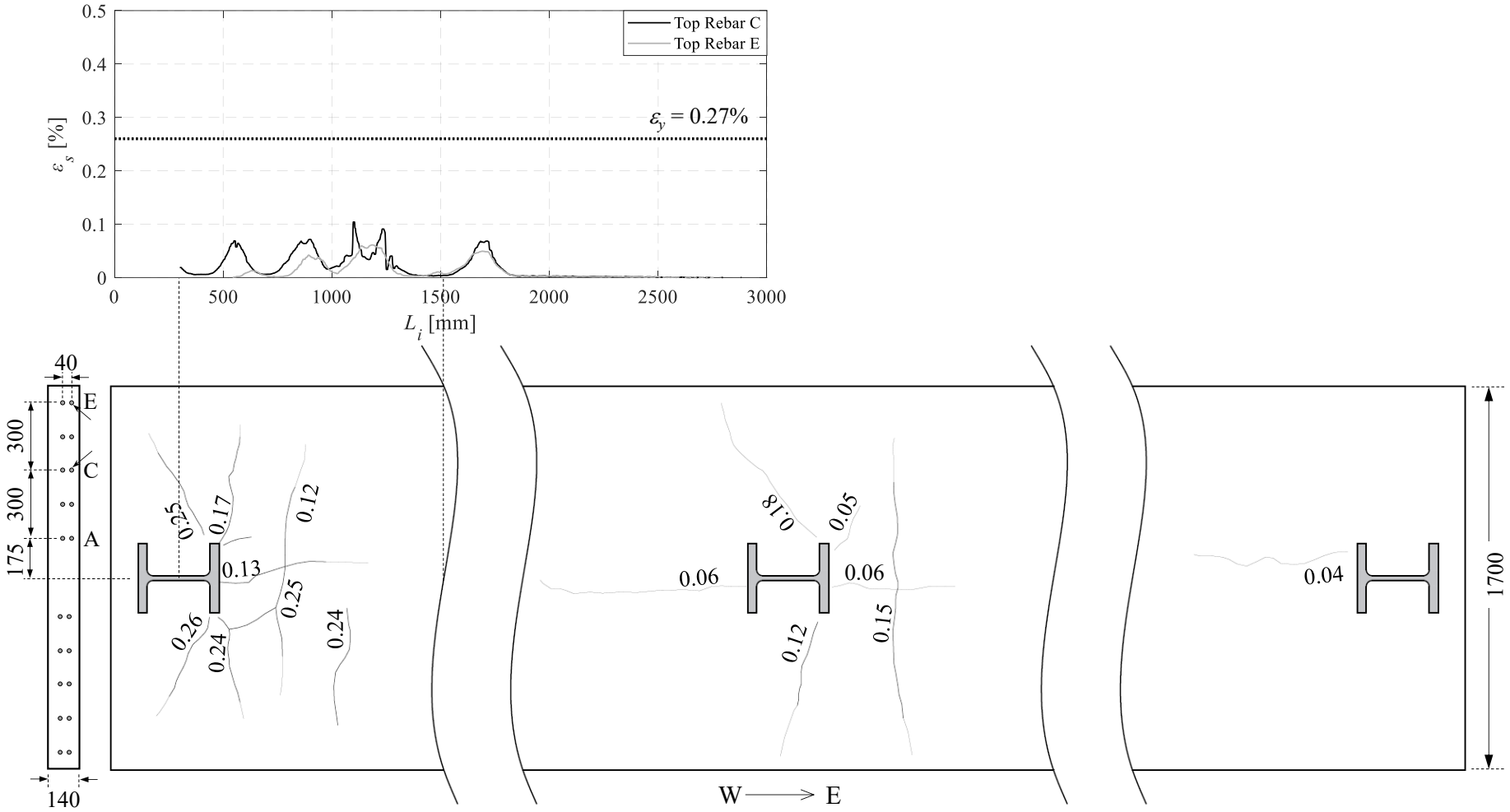

Figure E.27 Top: uniaxial longitudinal strains in selected slab rebars at the West exterior joint at a lateral drift demand of -0.5% rads; Bottom: crack pattern/crack width (mm) in the slab around each column at a lateral drift demand of -0.5% rads

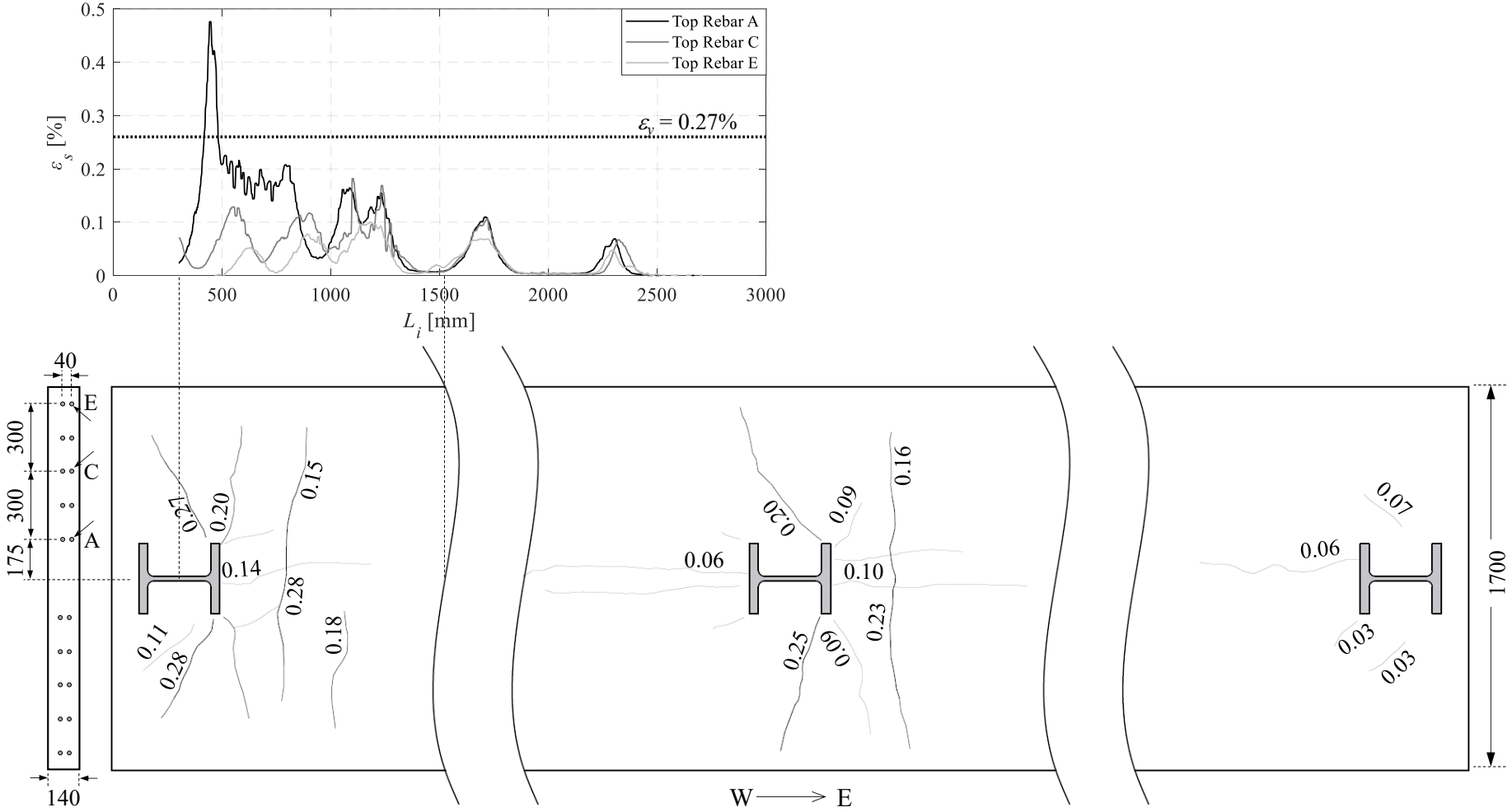

Figure E.28 Top: uniaxial longitudinal strains in selected slab rebars at the West exterior joint at a lateral drift demand of -1% rads; Bottom: crack pattern/crack width (mm) in the slab around each column at a lateral drift demand of -1% rads

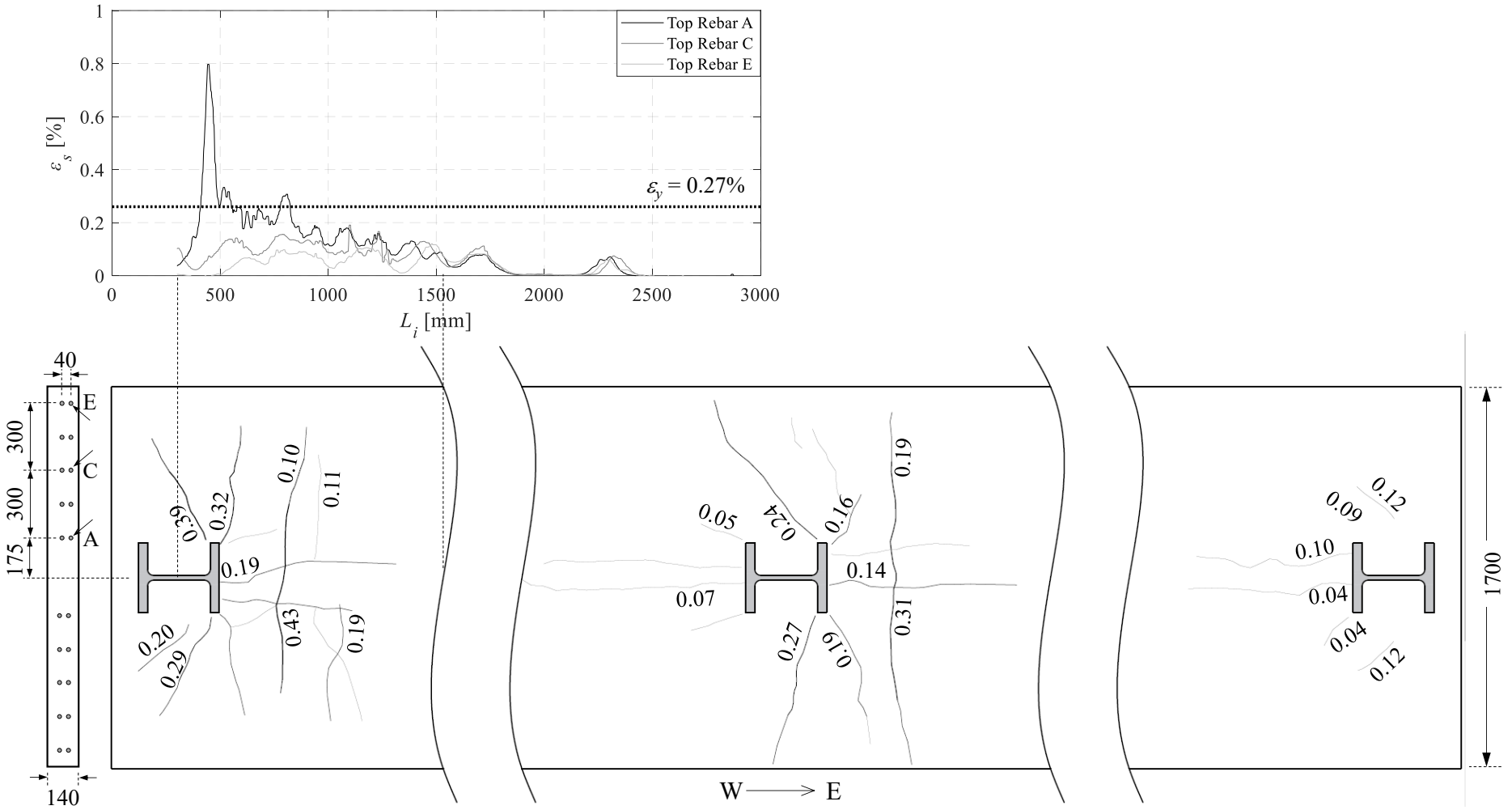

Figure E.29 Top: uniaxial longitudinal strains in selected slab rebars at the West exterior joint at a lateral drift demand of -1.5% rads; Bottom: crack pattern/crack width (mm) in the slab around each column at a lateral drift demand of -1.5% rads

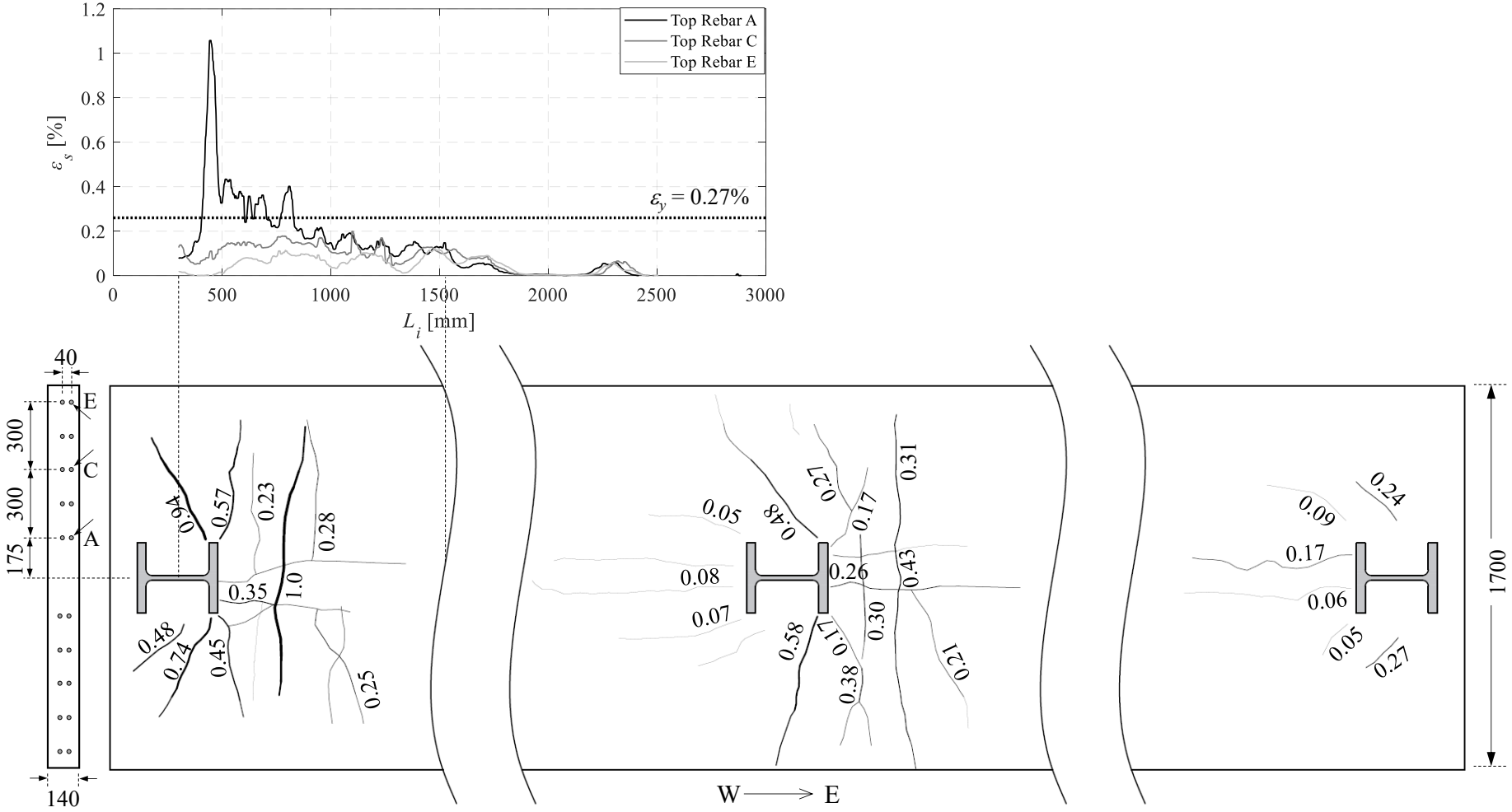

Figure E.30 Top: uniaxial longitudinal strains in selected slab rebars at the West exterior joint at a lateral drift demand of -2% rads; Bottom: crack pattern/crack width (mm) in the slab around each column at a lateral drift demand of -2% rads

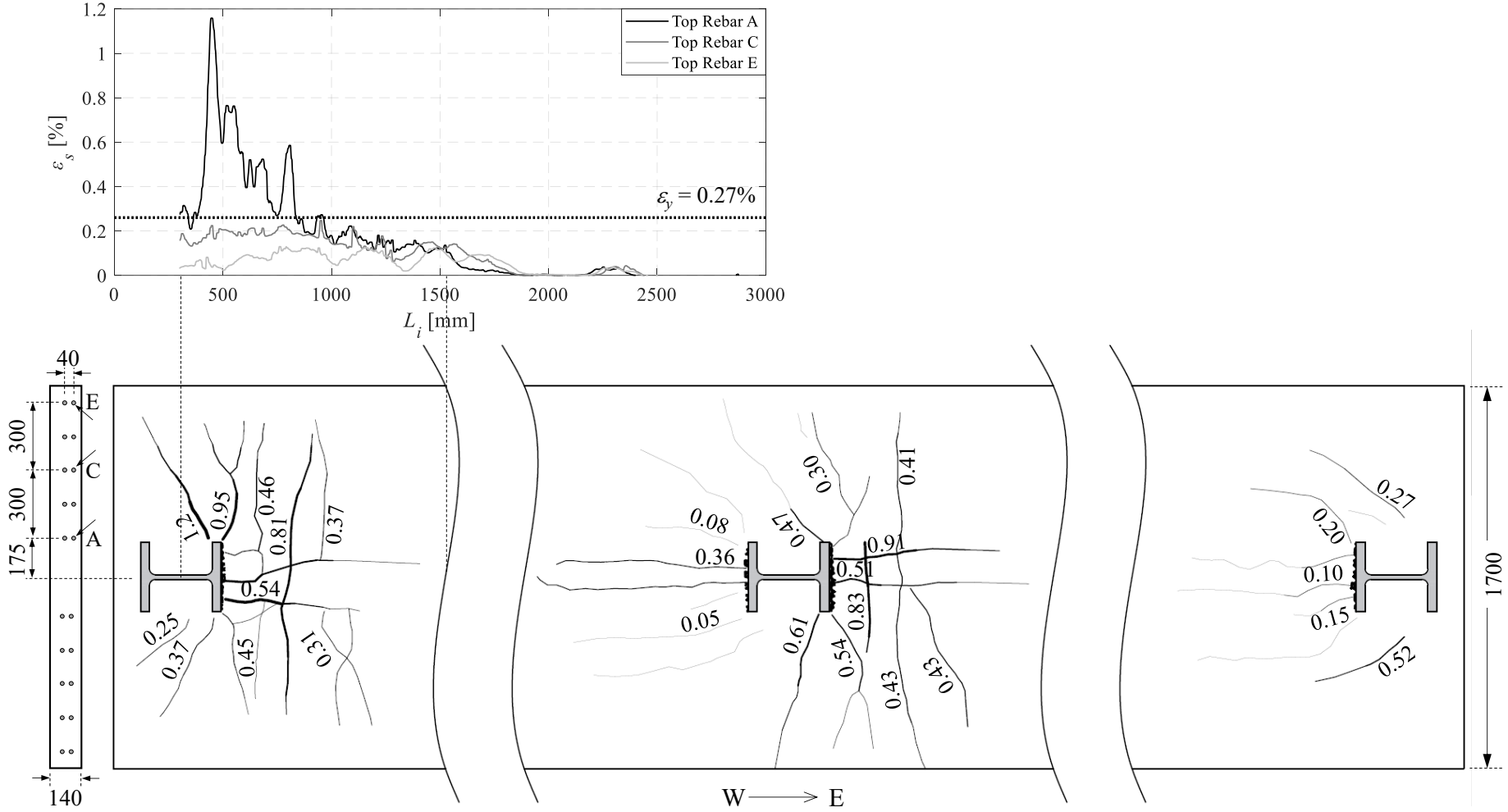

Figure E.31 Top: uniaxial longitudinal strains in selected slab rebars at the West exterior joint at a lateral drift demand of -3% rads; Bottom: crack pattern/crack width (mm) in the slab around each column at a lateral drift demand of -3% rads

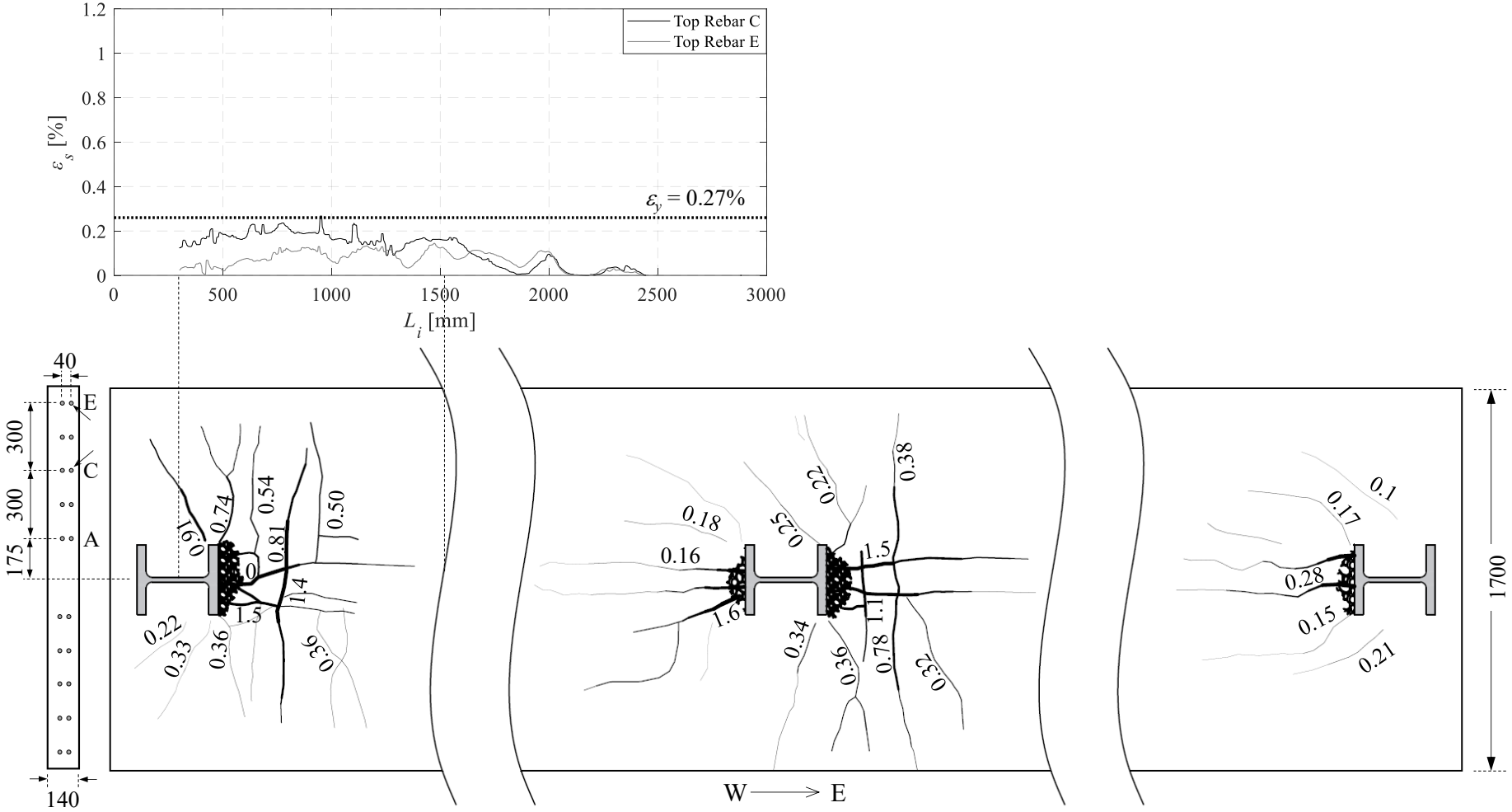

Figure E.32 Top: uniaxial longitudinal strains in selected slab rebars at the West exterior joint at a lateral drift demand of -4% rads; Bottom: crack pattern/crack width (mm) in the slab around each column at a lateral drift demand of -4% rads

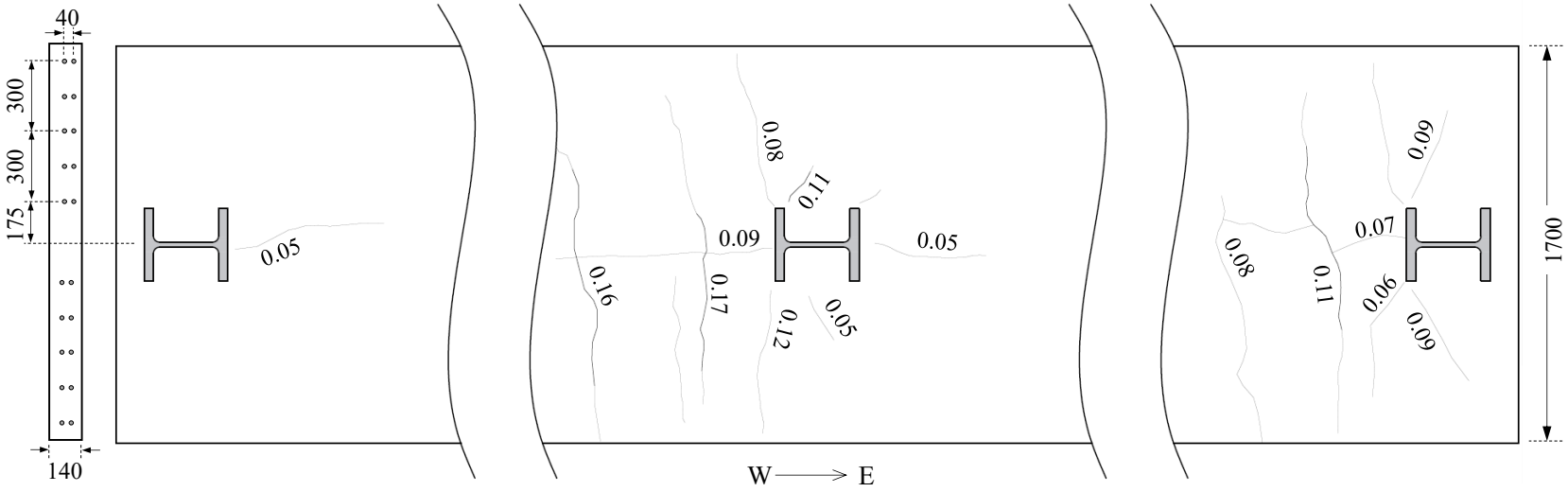

(a)

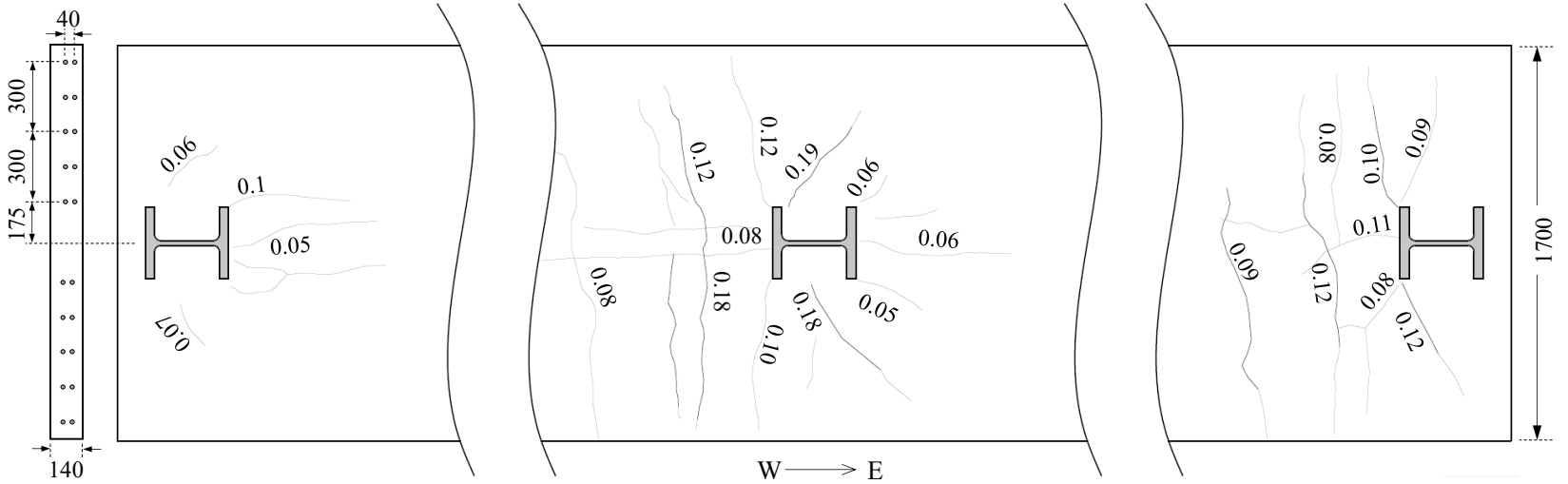

(b)

Figure E.33 Crack pattern/crack width (mm) in the slab around each column at (a) +0.5% rads and (b) +1% rads lateral drift demands

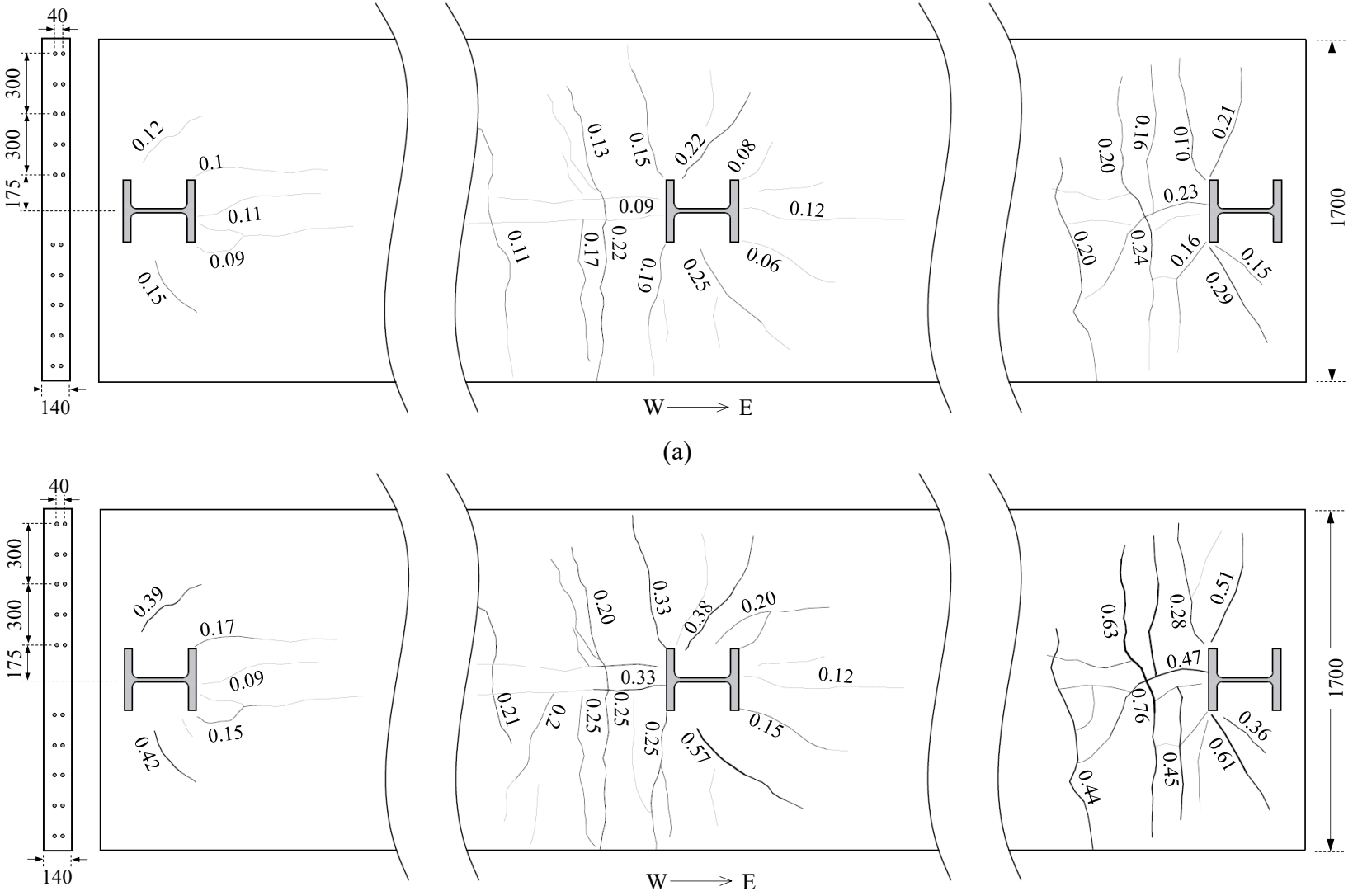

Figure E.34 Crack pattern/crack width (mm) in the slab around each column at (a) +1.5% rads and (b) +2% lateral drift demand

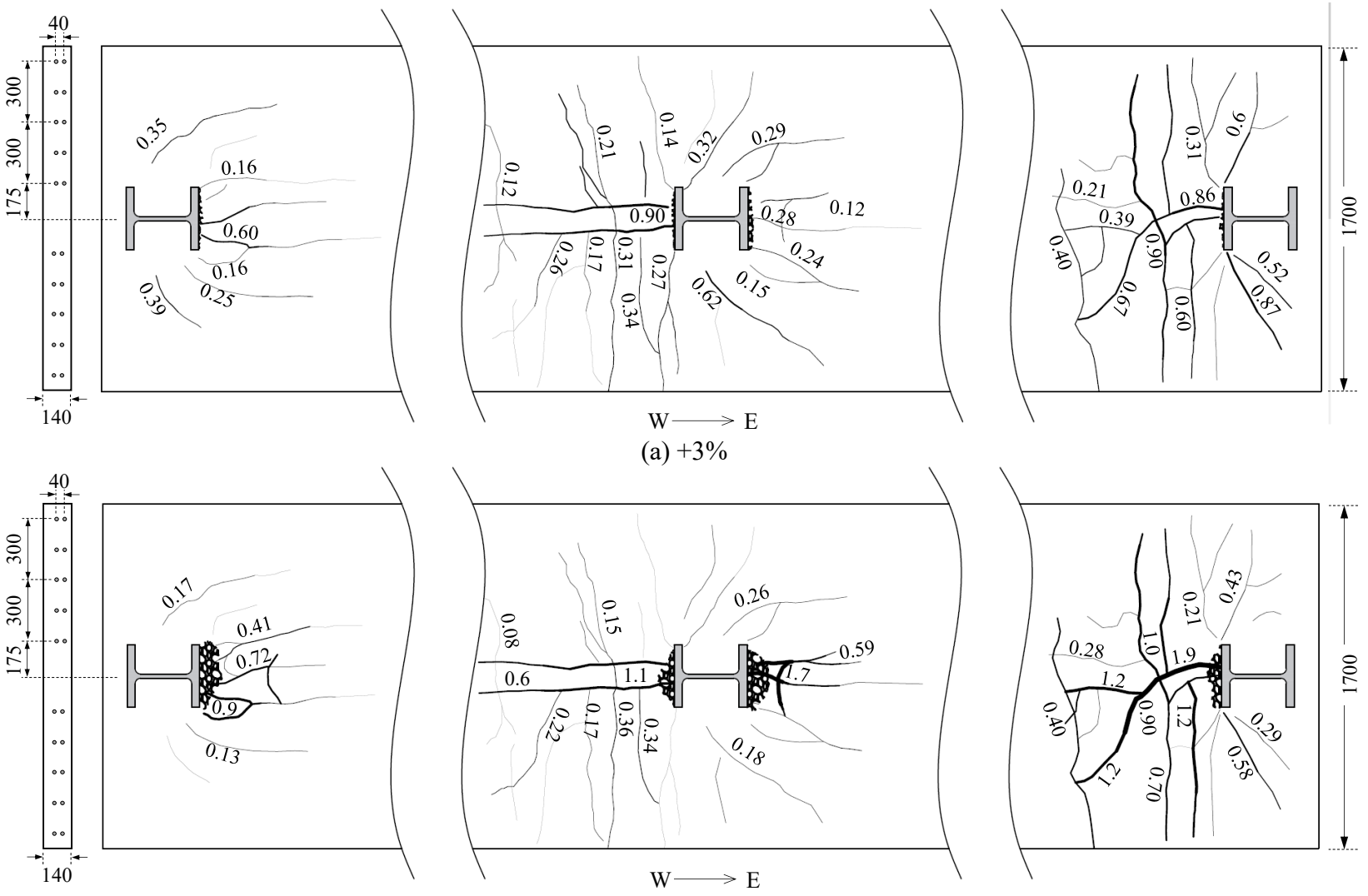

Figure E.35 Crack pattern/crack width (mm) in the slab around each column at (a) +3% rads and (b) +4% rads lateral drift demand

References

Abaqus. (2014). *ABAQUS - FEA/CAE*. Dassault Systems Simulia Corp., RI, USA.

AIJ. (2006). *Report of seismic performance improvement of civil, architectural structures subjected to long-period ground motions generated by subduction zone*. Architectural Institute of Japan, Tokyo, Japan.

AIJ. (2010a). *Recommendation for limit state design of steel structures*. 3rd edn, Architectural Institute of Japan, Tokyo.

AIJ. (2010b). *Design recommendations for composite construction*. 2nd edn, Architectural Institute of Japan, Tokyo.

AISC. (2016a). *Seismic provisions for structural steel buildings, ANSI/AISC 341-16*. American Institute of Steel Construction, Chicago, IL, USA.

AISC. (2016b). *Specification for structural steel buildings, ANSI/AISC 360-16*. American Institute of Steel Construction, Chicago, IL, USA.

AISC. (2016c). *Prequalified connections for special and intermediate steel moment frames for seismic applications, ANSI/AISC 358-16*. American Institute for Steel Construction, Chicago, IL, USA.

AISC. (2022). *Seismic provisions for evaluation and retrofit of existing structural steel buildings, AISC 342-22*. (In development), American Institute of Steel Construction, Chicago, IL, USA.

Alashker, Y., El-Tawil, S., and Sadek, F. (2010). "Progressive collapse resistance of steel-concrete composite floors." *Journal of Structural Engineering*, American Society of Civil Engineers, 136(10), 1187–1196.

Amadio, C., Clemente, I., Macorini, L., and Fragiacomo, M. (2008). "Seismic behaviour of hybrid systems made of PR composite frames coupled with dissipative bracings." *Earthquake Engineering & Structural Dynamics*, Wiley, 37(6), 861–879.

Amadio, C., and Fragiacomo, M. (1993). "A finite element model for the study of creep and shrinkage effects in composite beams with deformable shear connections." *Costruzioni Metalliche*, 4, 213–228.

Ammerman, D. J. (1988). "Behavior and design of frames with semi-rigid composite connections." PhD Thesis, University of Minnesota, Minneapolis, MN, USA.

An, L., and Cederwall, K. (1996). "Push-out tests on studs in high strength and normal strength concrete." *Journal of Constructional Steel Research*, Elsevier, 36(1), 15–29.

Aoki, H., and Masuda, M. (1985). "Statistical investigation on mechanical properties of structural steel based on coupon tests." *Journal of Structural and Construction Engineering AIJ*, Architectural Institute of Japan, 358, 94–105.

Araújo, M., Macedo, L., and Castro, J. M. (2017). "Evaluation of the rotation capacity limits of steel members defined in EC8-3." *Journal of Constructional Steel Research*, Elsevier, 135, 11–29.

Aribert, J. M., and Lachal, A. (2000). "Cyclic behaviour of the shear connection component in composite joints." *Proceedings of 3rd International Conference on the Behavior of Steel Structures in Seismic Areas (STESSA)*, Balkema, Montreal, Canada, 105–112.

Asada, H., Matoba, H., Tanaka, T., and Yamada, S. (2015). "Retrofit effects for composite beam: Study on seismic retrofit of beam-to-column connection using supplemental H-section haunches - Part 2." *Journal of Structural and Construction Engineering AIJ*, Architectural Institute of Japan, 80(715), 1479–1487.

ASCE. (2016). *Minimum design loads and associated criteria for buildings and other structures, ASCE/SEI 7-16*. American Society of Civil Engineers, Reston, VA, USA.

ASCE. (2017). *Seismic evaluation and retrofit of existing buildings, ASCE/SEI 41-17*. American Society of Civil Engineers, Reston, VA, USA.

Aslani, H., and Miranda, E. (2005). "Fragility assessment of slab-column connections in existing non-ductile reinforced concrete buildings." *Journal of Earthquake Engineering*, World Scientific, 9(06), 777–804.

ASTM. (2014). *A standard test method for static modulus of elasticity and poisson's ratio of concrete in compression, ASTM C469/C469M*. American Society for Testing and Materials, West Conshohocken, PA, USA.

ASTM. (2015). *Standard specification for structural steel shapes, ASTM A992/A992M-11*. American Society for Testing and Materials, West Conshohocken, PA, USA.

ASTM. (2016). *Standard test methods for tension testing of metallic materials, ASTM E8 / E8M-16a*. American Society for Testing and Materials, West Conshohocken, PA, USA.

Ayoub, A. (2005). "A force-based model for composite steel–concrete beams with partial interaction." *Journal of Constructional Steel Research*, Elsevier, 61(3), 387–414.

Ayoub, A., and Filippou, F. C. (2000). "Mixed formulation of nonlinear steel-concrete composite beam element." *Journal of Structural Engineering*, American Society of Civil Engineers, 126(3), 371–381.

Baker, J. W. (2011). "Conditional mean spectrum: tool for ground-motion selection." *Journal of Structural Engineering*, American Society of Civil Engineers, 137(3), 322–331.

Bärtschi, R. (2005). *Load bearing behaviour of composite beams in low degrees of partial shear connection*. Report No. 290, Swiss Federal Institute of Technology in Zürich (ETH), Zürich, Switzerland.

Baskar, K., Shanmugam, N. E., and Thevendran, V. (2002). "Finite-element analysis of steel–concrete composite plate girder." *Journal of Structural Engineering*, American Society of Civil Engineers, 128(9), 1158–1168.

Benjamin, J. R., and Cornell, C. A. (1970). *Probability, statistics, and decision for civil engineers*. McGraw-Hill, New York, USA.

Boore, D. M., and Atkinson, G. M. (2008). “Ground-motion prediction equations for the average horizontal component of PGA, PGV, and 5%-damped PSA at spectral periods between 0.01 s and 10.0 s.” *Earthquake Spectra*, SAGE Publications, 24(1), 99–138.

Bouwkamp, J. G., Parung, H., and Plumier, A. (1998). “Bi-directional cyclic study of a three-dimensional composite frame.” *Proceedings of the 11th European Conference on Earthquake Engineering (ECEE)*, Balkema, Rotterdam, Netherlands.

Braconi, A., Finetto, M., and Degee, H. (2013). *Optimising the seismic performance of steel and steel-concrete structures by standardising material quality control (OPUS)*. European Commission, Luxembourg.

Braconi, A., Salvatore, W., Tremblay, R., and Bursi, O. S. (2007). “Behaviour and modelling of partial-strength beam-to-column composite joints for seismic applications.” *Earthquake Engineering & Structural Dynamics*, Wiley, 36(1), 142–161.

Bursi, O. S., and Ballerini, M. (1996). “Behavior of a steel-concrete composite substructure with full and partial shear connection.” *Proceedings of the 11th World Conference on Earthquake Engineering (WCEE)*, Pergamon, Oxford, UK.

Bursi, O. S., and Gramola, G. (1999). “Behaviour of headed stud shear connectors under lowcycle high amplitude displacements.” *Materials and Structures*, Springer, 32(4), 290–297.

Bursi, O. S., and Gramola, G. (2000). “Behaviour of composite substructures with full and partial shear connection under quasi-static cyclic and pseudo-dynamic displacements.” *Materials and Structures*, Springer, 33(3), 154–163.

Bursi, O. S., Haller, M., Lennon, T., Bianco, L., Mallardo, R., Demonceau, J. F., Franssen, J. M., Jaspart, J. P., Hanus, F., Plumier, A., Bayo, E., Garcia, J., Alderighi, E., Braconi, A., and Salvatore, W. (2009). *Prefabricated composite beam-to-column filled tube or partially reinforced-concrete encased column connections for severe seismic and fire loadings*. European Commission, Luxembourg.

Bursi, O. S., and Jaspart, J.-P. (1998). “Basic issues in the finite element simulation of extended end plate connections.” *Computers & Structures*, Elsevier, 69(3), 361–382.

Bursi, O. S., Sun, F.-F., and Postal, S. (2005). “Non-linear analysis of steel–concrete composite frames with full and partial shear connection subjected to seismic loads.” *Journal of Constructional Steel Research*, Elsevier, 61(1), 67–92.

Cardone, D., and Perrone, G. (2015). “Developing fragility curves and loss functions for masonry infill walls.” *Earthquakes and Structures*, Techno-Press, 9(1), 257–279.

Carreira, D. J., and Chu, K.-H. (1985). “Stress-strain relationship for plain concrete in compression.” *ACI Journal Proceedings*, American Concrete Institute, 797–804.

de Castro e Sousa, A. de, Hartloper, A. R., and Lignos, D. G. (2021). “Cyclic metal plasticity model parameters with limited information: constrained optimization approach.” *Journal of Engineering Mechanics*, American Society of Civil Engineers, 147(7), 04021035.

de Castro e Sousa, A., and Lignos, D. G. (2018). *On the inverse problem of classic nonlinear plasticity models*. Report No. 231968, École Polytechnique Fédérale de Lausanne (EPFL), Lausanne, Switzerland.

de Castro e Sousa, A., Suzuki, Y., and Lignos, D. (2020). “Consistency in solving the inverse problem of the Voce-Chaboche constitutive model for plastic straining.” *Journal of Engineering Mechanics*, American Society of Civil Engineers, 146(9), 04020097.

Castro, J. M., Dávila-Arbona, F. J., and Elghazouli, A. Y. (2008). “Seismic design approaches for panel zones in steel moment frames.” *Journal of Earthquake Engineering*, Taylor & Francis, 12(1), 34–51.

Castro, J. M., Elghazouli, A. Y., and Izzuddin, B. A. (2007). “Assessment of effective slab widths in composite beams.” *Journal of Constructional Steel Research*, Elsevier, 63(10), 1317–1327.

CEN. (2002a). *EN 1990: Eurocode: Basis of structural design*. European Committee for Standardization, Brussels, Belgium.

CEN. (2002b). *EN 1991-1-1: Eurocode 1: Action on structures*. European Committee for Standardization, Brussels, Belgium.

CEN. (2003). *EN 1991-1-3: Eurocode 1: Action on structures - Part 1-3: General actions- Snow loads*. European Committee for Standardization, Brussels, Belgium.

CEN. (2004a). *EN 1998-1: Eurocode 8: Design of structures for earthquake resistance – Part 1: General rules, seismic actions and rules for buildings*. European Committee for Standardization, Brussels, Belgium.

CEN. (2004b). *EN 1994-1-1: Eurocode 4: Design of composite steel and concrete structures – Part 1-1: General rules and rules for buildings*. European Committee for Standardization, Brussels, Belgium.

CEN. (2004c). *EN 1992-1-1: Eurocode 2: Design of concrete structures - Part 1-1: General rules and rules for buildings*. European Committee for Standardization, Brussels, Belgium.

CEN. (2005a). *EN 1998-3: Eurocode 8: Design of structures for earthquake resistance – Part 3: Assessment and retrofitting of buildings*. European Committee for Standardization, Brussels, Belgium.

CEN. (2005b). *EN 1993-1-1: Eurocode 3: Design of steel structures – Part 1-1: General rules and rules for buildings*. European Committee for Standardization, Brussels, Belgium.

CEN. (2005c). *EN 1993-1-8: Eurocode 3: Design of steel structures - Part 1-8: Design of joints*. European Committee for Standardization, Brussels, Belgium.

CEN. (2010). *EN 1991-1-4: Eurocode 1: Action on structures - Part 1-4: General actions- Wind actions*. European Committee for Standardization, Brussels, Belgium.

CEN. (2018). *EN 1090-2: Execution of steel structures and aluminium structures - Part 2 : Technical requirements for steel*. European Committee for Standardization, Brussels, Belgium.

CEN. (2019). *Eurocode 8: Design of structures for earthquake resistance - Part 1-2: Rules for new buildings (100% draft)*. European Committee for Standardization, Brussels, Belgium.

Charney, F. A., Iyer, H., and Spears, P. W. (2005). “Computation of major axis shear deformations in wide flange steel girders and columns.” *Journal of Constructional Steel Research*, Elsevier, 61(11), 1525–1558.

Chatterjee, S., and Hadi, A. S. (2015). *Regression analysis by example*. Wiley, Hoboken, NJ, USA.

Chen, S.-J., and Chao, Y. C. (2001). “Effect of composite action on seismic performance of steel moment connections with reduced beam sections.” *Journal of Constructional Steel Research*, Elsevier, 57(4), 417–434.

Cheng, C.-T., Chan, C.-F., and Chung, L.-L. (2007). “Seismic behavior of steel beams and CFT column moment-resisting connections with floor slabs.” *Journal of Constructional Steel Research*, Elsevier, 63(11), 1479–1493.

Cheng, C.-T., and Chen, C.-C. (2005). “Seismic behavior of steel beam and reinforced concrete column connections.” *Journal of Constructional Steel Research*, Elsevier, 61(5), 587–606.

Chi, B., and Uang, C.-M. (2002). “Cyclic response and design recommendations of reduced beam section moment connections with deep columns.” *Journal of Structural Engineering*, American Society of Civil Engineers, 128(4), 464–473.

Chung, W. J., Cho, J. W., and Belytschko, T. (1998). “On the dynamic effects of explicit FEM in sheet metal forming analysis.” *Engineering Computations*, Emerald, 15(6), 750–776.

Ciutina, A. L., and Dubina, D. (2003). “Influence of column web stiffening on the seismic behaviour of beam-to- column joints.” *Proceedings of the Conference on Behaviour of Steel Structures in Seismic Areas (STESSA)*, Naples, Italy, 269–275.

Ciutina, A. L., and Stratan, A. (2008). “Cyclic performances of shear connectors.” *Proceedings of the International Conference on Composite Construction in Steel and Concrete VI*, American Society of Civil Engineers, Reston, VA, USA, 52–64.

Civjan, S. A., Engelhardt, M. D., and Gross, J. L. (2001). “Slab effects in SMRF retrofit connection tests.” *Journal of Structural Engineering*, American Society of Civil Engineers, 127(3), 230–237.

Civjan, S. A., and Singh, P. (2003). “Behavior of shear studs subjected to fully reversed cyclic loading.” *Journal of Structural Engineering*, American Society of Civil Engineers, 129(11), 1466–1474.

Clifton, C., Bruneau, M., MacRae, G., Leon, R., and Fussell, A. (2011). “Steel structures damage from the Christchurch earthquake series of 2010 and 2011.” *Bulletin of the New Zealand Society for Earthquake Engineering*, New Zealand Society for Earthquake Engineering, 44(4), 297–318.

Cordova, P. P., and Deierlein, G. G. (2005). *Validation of the seismic performance of composite RCS frames: Full-scale testing, analytical modeling, and seismic design*. Report No. 155, The John A. Blume Earthquake Engineering Center, Stanford University, Stanford, CA, USA.

Cornell, C. A., and Krawinkler, H. (2000). *Progress and challenges in seismic performance assessment*. Pacific Earthquake Engineering Research Center Newsletter, Pacific Earthquake Engineering Research Center, Berkeley, CA, USA.

Cowper, G. R. (1966). “The shear coefficient in Timoshenko’s beam theory.” *Journal of Applied Mechanics*, American Society of Mechanical Engineers, 33(2), 335–340.

Crow, E. L., Davis, F. A., Maxfield, M. W., and Davis, F. R. (1960). *Statistics manual with examples taken from ordnance development*. Courier Corporation, Dover, New York, USA.

CSI. (2019). *SAP2000 v.20.1 Integrated finite element analysis and design of structures*. CSI (Computers and Structures Inc.), Berkeley, CA, USA.

D'Aniello, M., Tartaglia, R., Costanzo, S., Campanella, G., Landolfo, R., and De Martino, A. (2018). "Experimental tests on extended stiffened end-plate joints within equal joints project." *Key Engineering Materials*, Trans Tech, 763, 406–413.

Deierlein, G. G., Reinhorn, A. M., and Willford, M. R. (2010). *Nonlinear structural analysis for seismic design*. NEHRP Seismic Design Technical Brief No. 4, National Institute of Standards and Technology, Gaithersburg, MD, USA.

Del Carpio, M., Mosqueda, G., and Lignos, D. G. (2014). *Hybrid simulation of the seismic response of a steel moment frame building structure through collapse*. Report No. MCEER-14-0003, University of Buffalo, State University of New York, Buffalo, NY, USA.

Del Carpio, R., Mosqueda, G., and Lignos, D. G. (2018). "Seismic performance of a steel moment frame subassembly tested from the onset of damage through collapse." *Earthquake Engineering & Structural Dynamics*, Wiley, 45(10), 1563–1580.

Denavit, M. D., Hajjar, J. F., Perea, T., and Leon, R. T. (2016). "Seismic performance factors for moment frames with steel-concrete composite columns and steel beams." *Earthquake Engineering & Structural Dynamics*, Wiley, 45(10), 1685–1703.

Donahue, S., Engelhardt, M., Clayton, P., Williamson, E., and Helwig, T. (2017). "Role of the floor system in the cyclic response of composite steel gravity framing." *Proceeding of the 8th International Conference on Composite Construction in Steel and Concrete (CCVIII)*, Jackson, WY, USA.

Donahue, S. M. (2019). "The role of the floor system in the seismic response of steel gravity framing." PhD Thesis, The University of Texas at Austin, Austin, TX, USA.

Doneux, C. (2002). "Study of transfer mechanisms of bending moments at beam-to-column joints in composite structures loaded by a seismic action." PhD Thesis, University of Liège, Liège, Belgium.

Dooley, K. L., and Bracci, J. M. (2001). "Seismic evaluation of column-to-beam strength ratios in reinforced concrete frames." *Structural Journal*, American Concrete Institute, 98(6), 843–851.

Du Plessis, D. P., and Daniels, J. H. (1972). *Strength of composite beam to column connections*. Report No. 374.3, Fritz Engineering Laboratory, Lehigh University, Bethlehem, PA, USA.

Eads, L., Miranda, E., Krawinkler, H., and Lignos, D. G. (2013). "An efficient method for estimating the collapse risk of structures in seismic regions." *Earthquake Engineering & Structural Dynamics*, Wiley, 42(1), 25–41.

Eads, L., Miranda, E., and Lignos, D. G. (2015). "Average spectral acceleration as an intensity measure for collapse risk assessment." *Earthquake Engineering & Structural Dynamics*, Wiley, 44(12), 2057–2073.

EECS. (1986). *Recommended testing procedures for assessing the behaviour of structural steel elements under cyclic loads*. European Convention for Constructional Steelwork, Brussels, Belgium.

El Jisr, H., Elkady, A., and Lignos, D. G. (2019). "Composite steel beam database for seismic design and performance assessment of composite-steel moment-resisting frame systems." *Bulletin of Earthquake Engineering*, Springer, 17(6), 3015–3039.

El Jisr, H., Elkady, A., and Lignos, D. G. (2020). "Hysteretic behavior of moment-resisting frames considering slab restraint and framing action." *Journal of Structural Engineering*, American Society of Civil Engineers, 146(8), 04020145.

El Jisr, H., Kempter, N., and Lignos, D. G. (2021a). “Full-scale testing of a 2-bay composite moment resisting frame under lateral cyclic loading - design and setup description.” *Proceedings of the 9th International Conference on Composite Construction in Steel and Concrete (CCIX)*, RUHR-Universität Bochum, Stromberg, Germany.

El Jisr, H., Kohrangi, M., and Lignos, D. G. (2021b). “Proposed nonlinear macro-model for seismic risk assessment of composite-steel moment resisting frame.” *Earthquake Engineering & Structural Dynamics*, Wiley, (Under review).

El Jisr, H., and Lignos, D. (2021). “Fragility assessment of beam-slab connections for informing earthquake-induced repairs in composite-steel moment resisting frames.” *Frontiers in Built Environment*, 7(1).

Elghazouli, A. Y. (2010). “Assessment of European seismic design procedures for steel framed structures.” *Bulletin of Earthquake Engineering*, Springer, 8(1), 65–89.

Elghazouli, A. Y., Castro, J. M., and Izzuddin, B. A. (2008). “Seismic performance of composite moment-resisting frames.” *Engineering Structures*, Elsevier, 30(7), 1802–1819.

Elkady, A., Ghimire, S., and Lignos, D. G. (2018). “Fragility curves for wide-flange steel solumns and implications for building-specific earthquake-induced loss assessment.” *Earthquake Spectra*, SAGE Publications, 34(3), 1405–1429.

Elkady, A., Güell, G., and Lignos, D. G. (2020). “Proposed methodology for building-specific earthquake loss assessment including column residual axial shortening.” *Earthquake Engineering & Structural Dynamics*, Wiley, 49(4), 339–355.

Elkady, A., and Lignos, D. G. (2014). “Modeling of the composite action in fully restrained beam-to-column connections: implications in the seismic design and collapse capacity of steel special moment frames.” *Earthquake Engineering & Structural Dynamics*, Wiley, 43(13), 1935–1954.

Elkady, A., and Lignos, D. G. (2015a). “Analytical investigation of the cyclic behavior and plastic hinge formation in deep wide-flange steel beam-columns.” *Bulletin of Earthquake Engineering*, Springer, 13(4), 1097–1118.

Elkady, A., and Lignos, D. G. (2015b). “Effect of gravity framing on the overstrength and collapse capacity of steel frame buildings with perimeter special moment frames.” *Earthquake Engineering & Structural Dynamics*, Wiley, 44(8), 1289–1307.

Elkady, A., and Lignos, D. G. (2018a). “Improved seismic design and nonlinear modeling recommendations for wide-flange steel columns.” *Journal of Structural Engineering*, American Society of Civil Engineers, 144(9), 04018162.

Elkady, A., and Lignos, D. G. (2018b). “Full-scale testing of deep wide-flange steel columns under multiaxis cyclic loading: Loading sequence, boundary effects, and lateral stability bracing force demands.” *Journal of Structural Engineering*, American Society of Civil Engineers, 144(2), 04017189.

El-Tawil, S., and Deierlein, G. G. (2001). “Nonlinear analysis of mixed steel-concrete frames. I: Element formulation.” *Journal of Structural Egineering*, American Society of Civil Engineers, 127(6), 647–655.

Engelhardt, M. D., Venti, M. J., Fry, G. T., Jones, S. L., and Holliday, S. D. (2000). *Behavior and design of radius cut reduced beam section connections*. Report No. SAC/BD-00/17, SAC Joint Venture, Sacramento, CA, USA.

Fan, J. S., and Liu, W. (2014). “Tests on shear studs using profiled steel sheeting subjected to cyclic loading.” *Applied Mechanics and Materials*, Trans Tech, 578–579, 196–200.

Fardis, M. N. (2018). “Capacity design: Early history.” *Earthquake Engineering & Structural Dynamics*, Wiley, 47(14), 2887–2896.

FEMA. (2000a). *State of the art report on connection performance (FEMA-355D)*. Federal Emergency Management Agency, Washington, D.C., USA.

FEMA. (2000b). *Recommended seismic design criteria for new steel moment-frame buildings (FEMA-350)*. Federal Emergency Management Agency, Washington, D.C., USA.

FEMA. (2009). *Quantification of building seismic performance factors (FEMA-P695)*. Federal Emergency Management Agency, Washington, D.C., USA.

FEMA. (2012). *Seismic performance assessment of buildings (FEMA-P58-1)*. Federal Emergency Management Agency, Washington, D.C., USA.

Fenwick, R. C., and Megget, L. M. (1993). “Elongation and load deflection characteristics of reinforced concrete members containing plastic hinges.” *Bulletin of the New Zealand Society for Earthquake Engineering*, New Zealand Society for Earthquake Engineering, 26(1), 28–41.

Fujisawa, K., Ichinohe, Y., Sugimoto, M., and Sonoda, M. (2013). “Statistical study on mechanical properties and chemical compositions of SN Steels.” *Summary of Technical Papers of Annual Meeting*, Architectural Institute of Japan, Tokyo, Japan, 699–700.

Galanis, P. H., and Moehle, J. P. (2015). “Development of collapse indicators for risk assessment of older-type reinforced concrete buildings.” *Earthquake Spectra*, SAGE Publications, 31(4), 1991–2006.

Gardoni, P., Der Kiureghian, A., and Mosalam, K. M. (2002). “Probabilistic capacity models and fragility estimates for reinforced concrete columns based on experimental observations.” *Journal of Engineering Mechanics*, American Society of Civil Engineers, 128(10), 1024–1038.

Gattesco, N. (1999). “Analytical modeling of nonlinear behavior of composite beams with deformable connection.” *Journal of Constructional Steel Research*, Elsevier, 52(2), 195–218.

Genikomsou, A. S., and Polak, M. A. (2015). “Finite element analysis of punching shear of concrete slabs using damaged plasticity model in ABAQUS.” *Engineering Structures*, Elsevier, 98, 38–48.

Giardini, D., Woessner, J., Danciu, L., Crowley, H., Cotton, F., Grünthal, G., Pinho, R., Valensise, G., Akkar, S., and Arvidsson, R. (2013). *Seismic hazard harmonization in Europe (SHARE): Online Data Resource*.

Goto, Y., Kumar, G. P., and Kawanishi, N. (2010). “Nonlinear finite-element analysis for hysteretic behavior of thin-walled circular steel columns with in-filled concrete.” *Journal of Structural Engineering*, American Society of Civil Engineers, 136(11), 1413–1422.

Gulec, C. K., Gibbons, B., Chen, A., and Whittaker, A. S. (2011). “Damage states and fragility functions for link beams in eccentrically braced frames.” *Journal of Constructional Steel Research*, Elsevier, 67(9), 1299–1309.

Gupta, A., and Krawinkler, H. (1999). *Seismic demands for performance evaluation of steel moment resisting frame structures*. Report No. 132, The John A. Blume Earthquake Engineering Research Center, Stanford University, Stanford, CA, USA.

Hartloper, A., and Lignos, D. G. (2017). "11.29: Updates to the ASCE-41-13 provisions for the nonlinear modeling of steel wide-flange columns for performance-based earthquake engineering." *Proceedings of the 8th European Conference on Steel and Composite Structures*, Wiley, Copenhagen, Denmark, 3072–3081.

Haselton, C. B., Liel, A. B., Deierlein, G. G., Dean, B. S., and Chou, J. H. (2011). "Seismic collapse safety of reinforced concrete buildings. I: Assessment of ductile moment frames." *Journal of Structural Engineering*, American Society of Civil Engineers, 137(4), 481–491.

Hawkins, N. M., and Mitchell, D. (1984). "Seismic response of composite shear connections." *Journal of Structural Engineering*, American Society of Civil Engineers, 110(9), 2120–2136.

Henry, R. S., Dizhur, D., Elwood, K. J., Hare, J., and Brunsdon, D. (2017). "Damage to concrete buildings with precast floors during the 2016 Kaikoura earthquake." *Bulletin of the New Zealand Society for Earthquake Engineering*, New Zealand Society for Earthquake Engineering, 50(2), 174–186.

Herrera, R. A. (2005). "Seismic behavior of concrete filled tube column wide flange beam frames." PhD Thesis, Lehigh University, Bethlehem, PA, USA.

Herrera, R. A., Ricles, J. M., and Sause, R. (2008). "Seismic performance evaluation of a large-scale composite MRF using pseudodynamic testing." *Journal of Structural Engineering*, American Society of Civil Engineers, 134(2), 279–288.

Ibarra, L. F., and Krawinkler, H. (2005). *Global collapse of frame structures under seismic excitations*. Report No. 152, The John A. Blume Earthquake Engineering Center, Stanford University, Stanford, CA, USA.

Ibarra, L. F., Medina, R. A., and Krawinkler, H. (2005). "Hysteretic models that incorporate strength and stiffness deterioration." *Earthquake Engineering & Structural Dynamics*, Wiley, 34(12), 1489–1511.

Joglekar, M., Murry, P., Jirsa, J., and Klingner, R. (1984). "Full scale tests of beam-column joints." *Structural Journal*, American Concrete Institute, 84, 271–304.

Joglekar, M. R. (1984). "Behavior of reinforced concrete floor systems under lateral loads." PhD Thesis, The University of Texas at Austin, Austin, TX, USA.

Johansson, M., and Gylltoft, K. (2002). "Mechanical behavior of circular steel–concrete composite stub columns." *Journal of Structural Engineering*, American Society of Civil Engineers, 128(8), 1073–1081.

Jones, S. L., Fry Gary T., and Engelhardt Michael D. (2002). "Experimental evaluation of cyclically loaded reduced beam section moment connections." *Journal of Structural Engineering*, American Society of Civil Engineers, 128(4), 441–451.

Kanno, R. (2016). "Advances in steel materials for innovative and elegant steel structures in Japan–A review." *Structural Engineering International*, Taylor & Francis, 26(3), 242–253.

Kim, K. D., and Engelhardt, M. D. (2002). “Monotonic and cyclic loading models for panel zones in steel moment frames.” *Journal of Constructional Steel Research*, Elsevier, 58(5–8), 605–635.

Kim, S.-Y., and Lee, C.-H. (2017). “Seismic retrofit of welded steel moment connections with highly composite floor slabs.” *Journal of Constructional Steel Research*, Elsevier, 139, 62–68.

Kim, Y.-J., Oh, S.-H., and Moon, T.-S. (2004). “Seismic behavior and retrofit of steel moment connections considering slab effects.” *Engineering Structures*, Elsevier, 26(13), 1993–2005.

Kishiki, S., Kadono, D., Satsukawa, K., and Yamada, S. (2010). “Consideration of composite effects on elasto-plastic behavior of panel-zone.” *Journal of Structural and Construction Engineering AIJ*, Architectural Institute of Japan, 75(654), 1527–1536.

Kohrangi, M., Bazzurro, P., Vamvatsikos, D., and Spillatura, A. (2017). “Conditional spectrum-based ground motion record selection using average spectral acceleration.” *Earthquake Engineering & Structural Dynamics*, Wiley, 46(10), 1667–1685.

Kolwankar, S., Kanvinde, A., Kenawy, M., Lignos, D., and Kunnath, S. (2018). “Simulating local buckling-induced softening in steel members using an equivalent nonlocal material model in displacement-based fiber elements.” *Journal of Structural Engineering*, American Society of Civil Engineers, 144(10), 04018192.

Krawinkler, H. (1978). “Shear in beam-column joints in seismic design of steel frames.” *Engineering Journal*, American Institute of Steel Construction, 15(3), 82–91.

Krawinkler, H. (2009). “Loading histories for cyclic tests in support of performance assessment of structural components.” *Proceedings of the 3rd International Conference on Advances in Experimental Structural Engineering*, San Francisco, CA, USA.

Krawinkler, H., Akshay, G., Medina, R., and Luco, M. (2000). *Development of loading histories for testing of steel beam-to-column assemblies*. Report No. SAC BD-00/10, Department of Civil and Environmental Engineering, Stanford University, Stanford, CA, USA.

Krawinkler, H., and Miranda, E. (2004). “Performance-based earthquake engineering.” *Earthquake Engineering: From Engineering Seismology to Performance-Based Engineering*, Bozorgnia and VV Bertero, CRC Press, Boca Ration, FL, USA.

Krawinkler, H., and Seneviratna, G. (1998). “Pros and cons of a pushover analysis of seismic performance evaluation.” *Engineering Structures*, Elsevier, 20(4–6), 452–464.

Krawinkler, H., Zohrei, M., Lashkari-Irvani, B., Cofie, N. G., and Hadidi-Tamjed, H. (1983). *Recommendations for experimental studies on the seismic behavior of steel components and materials*. Report No. 61, The John A. Blume Earthquake Engineering Center, Stanford University, Stanford, CA, USA.

Kwasniewski, L., Stojadinović, B., and Goel, S. C. (2002). *Local and lateral-torsional buckling of wide-flange beams*. Report 7.15-1, SAC Joint Venture, Richmond, CA, USA.

Lam, D., and El-Lobody, E. (2005). “Behavior of headed stud shear connectors in composite beam.” *Journal of Structural Engineering*, American Society of Civil Engineers, 131(1), 96–107.

Landolfo, R., D’Aniello, M., Costanzo, S., Tartaglia, R., Stratan, A., Dubina, D., Vulcu, C., Maris, C., Zub, C., Da Silva, L., Rebelo, C., Augusto, H., Shahbazian, A., Gentili, F., Jaspart, J.-P., Demonceau, J.-F., Van Hoang, L., Elghazouli, A., Tsitos, A., Vassart, O., Nunez, E. M., Dehan, V., and

Hamreza, C. (2018). *European pre-qualiified steel joints (EQUALJOINTS)*. European Commission, Brussels, Belgium.

Lee, C. H., Jeon, S. W., Kim, J. H., and Uang, C. M. (2005). "Effects of panel zone strength and beam web connection method on seismic performance of reduced beam section steel moment connections." *Journal of Structural Engineering*, American Society of Civil Engineers, 131(12), 1854–1865.

Lee, C. H., Jung, J. H., Kim, S. Y., and Kim, J. J. (2016). "Investigation of composite slab effect on seismic performance of steel moment connections." *Journal of Constructional Steel Research*, Elsevier, 117, 91–100.

Lee, J., and Fenves, G. L. (1998). "Plastic-damage model for cyclic loading of concrete structures." *Journal of Engineering Mechanics*, American Society of Civil Engineers, 124(8), 892–900.

Lemaitre, J., and Chaboche, J. L. (1990). *Mechanics of solid materials*. Cambridge University Press, Cambridge, UK.

Leon, R. T. (1983). "The influence of floor members on the behavior of reinforced concrete beam column joints subjected to severe cyclic loading." PhD Thesis, University of Texas at Austin.

Leon, R. T., and Alsamsam, I. (1993). "Performance and serviceability of composite floors." *Proceedings of Structural Engineering in Natural Hazards Mitigation*, University of Minnesota, Minneapolis, MN, USA, 1479–1484.

Leon, R., T. and Jirsa, J. O. (1986). "Bidirectional loading of RC beam-column joints." *Earthquake Spectra*, SAGE Publications, 2(3), 537–564.

Leon, R. T. (1990a). "Shear strength and hysteretic behavior of interior beam-column joints." *Structural Journal*, American Concrete Institute, 87(1), 3–11.

Leon, R. T. (1990b). "Semi-rigid composite construction." *Journal of Constructional Steel Research*, Elsevier, 15(1–2), 99–120.

Leon, R. T., and Deierlein, G. G. (1996). "Considerations for the use of quasi-static testing." *Earthquake Spectra*, SAGE Publications, 12(1), 87–109.

Leon, R. T., Hajjar, J. F., and Gustafson, M. A. (1998). "Seismic response of composite moment-resisting connections. I: Performance." *Journal of Structural Engineering*, American Society of Civil Engineers, 124(8), 868–876.

Liang, Q. Q., Uy, B., Bradford, M. A., and Ronagh, H. R. (2005). "Strength analysis of steel–concrete composite beams in combined bending and shear." *Journal of Structural Engineering*, American Society of Civil Engineers, 131(10), 1593–1600.

Lignos, D. G., Hartloper, A. R., Elkady, A., Deierlein, G. G., and Hamburger, R. (2019). "Proposed updates to the ASCE 41 nonlinear modeling parameters for wide-flange steel columns in support of performance-based seismic engineering." *Journal of Structural Engineering*, American Society of Civil Engineers, 145(9), 04019083.

Lignos, D. G., Hikino, T., Matsuoka, Y., and Nakashima, M. (2013). "Collapse assessment of steel moment frames based on E-Defense full-scale shake table collapse tests." *Journal of Structural Engineering*, American Society of Civil Engineers, 139(1), 120–132.

Lignos, D. G., and Karamanci, E. (2013). “Drift-based and dual-parameter fragility curves for concentrically braced frames in seismic regions.” *Journal of Constructional Steel Research*, Elsevier, 90, 209–220.

Lignos, D. G., Kolios, D., and Miranda, E. (2010). “Fragility assessment of reduced beam section moment connections.” *Journal of Structural engineering*, American Society of Civil Engineers, 136(9), 1140–1150.

Lignos, D. G., and Krawinkler, H. (2011). “Deterioration modeling of steel components in support of collapse prediction of steel moment frames under earthquake loading.” *Journal of Structural Engineering*, American Society of Civil Engineers, 137(11), 1291–1302.

Lignos, D. G., and Krawinkler, H. (2013). “Development and utilization of structural component databases for performance-based earthquake engineering.” *Journal of Structural Engineering*, American Society of Civil Engineers, 139(8), 1382–1394.

Lignos, D. G., Krawinkler, H., and Whittaker, A. S. (2011). “Prediction and validation of sidesway collapse of two scale models of a 4-story steel moment frame.” *Earthquake Engineering & Structural Dynamics*, Wiley, 40(7), 807–825.

Lin, T., Harmsen, S. C., Baker, J. W., and Luco, N. (2013). “Conditional spectrum computation incorporating multiple causal earthquakes and ground-motion prediction models.” *Bulletin of the Seismological Society of America*, Seismological Society of America, 103(2A), 1103–1116.

Liu, J., and Astaneh-Asl, A. (2004). “Moment–rotation parameters for composite shear tab connections.” *Journal of Structural Engineering*, American Society of Civil Engineers, 130(9), 1371–1380.

Lu, L., Xu, Y., and Zheng, H. (2017). “Investigation of composite action on seismic performance of weak-axis column bending connections.” *Journal of Constructional Steel Research*, Elsevier, 129, 286–300.

Lubliner, J., Oliver, J., Oller, S., and Onate, Ejij. (1989). “A plastic-damage model for concrete.” *International Journal of Solids and Structures*, Elsevier, 25(3), 299–326.

LUNA. (2013). *Optical backscatter reflectometer 6100*. User Guide, LUNA Technologies Inc., Blacksburg, HI, USA.

Macedo, L., Silva, A., and Castro, J. M. (2019). “A more rational selection of the behaviour factor for seismic design according to Eurocode 8.” *Engineering Structures*, Elsevier, 188, 69–86.

MacRae, G. A., and Clifton, G. C. (2015). “Research on seismic performance of steel structures.” *Proceedings of Steel Innovations Conference*, Auckland, New Zealand..

MacRae, G., Hobbs, M., Bull, D., Chaudhari, T., Leon, R., Clifton, C., and Chase, G. (2013). “Slab effects on beam-column subassemblies—Beam strength and elongation issues.” *Proceedings of the International Conference on Composite Construction in Steel and Concrete*, American Society of Civil Engineers, Reston, VA, USA, 77–92.

Mahin, S. A. (1998). “Lessons from damage to steel buildings during the Northridge earthquake.” *Engineering Structures*, Elsevier, 20(4–6), 261–270.

Mahin, S. A., and Bertero, V. V. (1975). *An evaluation of some methods for predicting seismic behavior of reinforced concrete buildings*. Report No. EERC 75-5, Pacific Earthquake Engineering Research Center, University of California, Berkeley, CA, USA.

Maison, B. F., and Speicher, M. S. (2016). "Loading protocols for ASCE 41 backbone curves." *Earthquake Spectra*, SAGE Publications, 32(4), 2513–2532.

Malley, J., Carter, C., Hajjar, J., Lignos, D.G., Roeder, C., and Saunders, M. (2011). *Research plan for the study of seismic behavior and design of deep, slender wide flange structural steel beam-column members*. Report No. 11-917-13, National Institute of Standards and Technology, Gaithersburg, MD, USA.

Matsumura, T., and Mizuno, E. (2007). "3-D FEM analyses on internal state inside the concrete filled steel tubular columns subjected to flexural deformation under axial loading." *Journal of Applied Mechanics*, Japan Society of Civil Engineers, 11, 307–318.

McKenna, F. (1997). "Object oriented finite element programming frameworks for analysis, algorithms and parallel computing." PhD Thesis, University of California, Berkeley, Berkeley, CA,USA.

Mehanny, S. S., and Deierlein, G. G. (2000). *Modeling and assessment of seismic performance of composite frames with reinforced concrete columns and steel beams*. Report No. 155, John A. Blume Earthquake Engineering Center, Stanford University, Stanford, CA, USA.

Mele, E. (2002). "Moment resisting welded connections: an extensive review of design practice and experimental research in USA, Japan and Europe." *Journal of Earthquake Engineering*, World Scientific, 6(01), 111–145.

Menapace, R. (1997). "Modellazione in campo ciclico di giunti travecolonna per structure composte in acciaio e calcestruzzo." PhD Thesis, University of Trento, Trento, Italy.

Monelli, D., Pagani, M., Weatherill, G., Silva, V., and Crowley, H. (2012). "The hazard component of OpenQuake: The calculation engine of the Global Earthquake Model." *Proceedings of the 15th World Conference on Earthquake Engineering (WCEE)*, Citeseer, Lisbon, Portugal, 24–28.

Motallebi, M., Lignos, D. G., and Rogers, C. A. (2019). "Full-scale testing of stiffened extended shear tab connections under combined axial and shear forces." *Engineering Structures*, Elsevier, 185, 90–105.

Nakajima, A., Saiki, I., Kokai, M., Doi, K., Takabayashi, Y., and Ooe, H. (2003). "Cyclic shear force–slip behavior of studs under alternating and pulsating load condition." *Engineering structures*, Elsevier, 25(5), 537–545.

Nakashima, M., Matsumiya, T., Suita, K., and Liu, D. (2006). "Test on full-scale three-storey steel moment frame and assessment of ability of numerical simulation to trace cyclic inelastic behaviour." *Earthquake Engineering & Structural Dynamics*, Wiley, 35(1), 3–19.

Nakashima, M., Matsumiya, T., Suita, K., and Zhou, F. (2007). "Full-scale test of composite frame under large cyclic loading." *Journal of Structural Engineering*, American Society of Civil Engineers, 133(2), 297–304.

Nakashima, M., Roeder, C. W., and Maruoka, Y. (2000). "Steel moment frames for earthquakes in United States and Japan." *Journal of Structural Engineering*, American Society of Civil Engineers, 126(8), 861–868.

Nam, T. T., and Kasai, K. (2012). "Study on shake table experimental results regarding composite action of a full-scale steel building tested to collapse." *Proceedings of the 9th International Conference on Urban Earthquake Engineering/4th Asia Conference on Earthquake Engineering*, Tokyo Institute of Technology, Tokyo, Japan, 1111–1116.

NIST. (2010). *Applicability of nonlinear multiple-degree-of-freedom modeling for design*. Report No. 10-917-9, National Institute of Standards and Technology, Gaithersburg, MD, USA.

Okazaki, T., Lignos, D. G., Midorikawa, M., Ricles, J. M., and Love, J. (2013). "Damage to steel buildings observed after the 2011 Tohoku-Oki earthquake." *Earthquake Spectra*, SAGE Publications, 29(S1), S219–S243.

Ollgaard, J., Roger, R., and Fisher, J. (1971). *Shear strength of stud connectors in lightweight and normal-weight concrete*. Report No. 71-10, Lehigh University, Bethlehem, PA, USA.

Osteraas, J., and Krawinkler, H. (1989). "Behavior of steel buildings, the Mexico earthquake of September 19, 1985." *Earthquake Spectra*, SAGE Publications, 5(1), 51–88.

Panagiotakos, T. B., and Fardis, M. N. (2001). "Deformations of reinforced concrete members at yielding and ultimate." *Structural Journal*, American Concrete Institute, 98(2), 135–148.

PEER/ATC. (2010). *Modeling and acceptance criteria for seismic design and analysis of tall buildings (PEER/ATC 72–1)*. Applied Technology Council (ATC), Redwood City, CA, USA.

Plumier, A., and Doneux, C. (2001). *Seismic behaviour and design of composite steel concrete structures*. Report No. 4, European Commission, Brussels, Belgium.

Plumier, A., Doneux, C., Bouwkamp, J. G., and Plumier, 1 C. (1998). "Slab design in connection zone of composite frames." *Proceedings of the 11th European Conference on Earthquake Engineering (ECEE)*, Balkema, Rotterdam, Netherlands.

Porter, K., Kennedy, R., and Bachman, R. (2007). "Creating fragility functions for performance-based earthquake engineering." *Earthquake Spectra*, SAGE Publications, 23(2), 471–489.

Prior, A. M. (1994). "Applications of implicit and explicit finite element techniques to metal forming." *Journal of Materials Processing Technology*, Elsevier, 45(1–4), 649–656.

Qi, L., Paquette, J., Eatherton, M., Leon, R., Bogdan, T., Popa, N., and Nunez, E. (2018). "Analysis of fracture behavior of large steel beam-column connections." *Proceedings of the 12th International Conference on Advances in Steel-Concrete Composite Structures (ASCCS)*, Universitat Politècnica València, València, Spain.

Ramirez, C. M., Lignos, D. G., Miranda, E., and Kolios, D. (2012). "Fragility functions for pre-Northridge welded steel moment-resisting beam-to-column connections." *Engineering Structures*, Elsevier, 45, 574–584.

Rassati, G. A., Leon, R. T., and Noè, S. (2004). "Component modeling of partially restrained composite joints under cyclic and dynamic loading." *Journal of Structural Engineering*, American Society of Civil Engineers, 130(2), 343–351.

Retamales, R., Davies, R., Mosqueda, G., and Filiatrault, A. (2013). "Experimental seismic fragility of cold-formed steel framed gypsum partition walls." *Journal of Structural Engineering*, American Society of Civil Engineers, 139(8), 1285–1293.

Rex, C. O., and Easterling, W. S. (2000). "Behavior and modeling of reinforced composite slab in tension." *Journal of Structural Engineering*, American Society of Civil Engineers, 126(7), 764–771.

Ricles, J. M., Fisher, J. W., Lu, L.-W., and Kaufmann, E. J. (2002). "Development of improved welded moment connections for earthquake-resistant design." *Journal of Constructional Steel Research*, Elsevier, 58(5–8), 565–604.

Ricles, J. M., Zhang, X., Lu, L.-W., and Fisher, J. W. (2004). *Development of seismic guidelines for deep-column steel moment connections*. Report No. 04-13, ATLSS, Lehigh University, Bethlehem, PA, USA.

Roeder, C. W. (2002). "General issues influencing connection performance." *Journal of Structural Engineering*, American Society of Civil Engineers, 128(4), 420–428.

Roeder, C. W., Lumpkin, E. J., and Lehman, D. E. (2012). "Seismic performance assessment of concentrically braced steel frames." *Earthquake Spectra*, SAGE Publications, 28(2), 709–727.

Ruiz-García, J., and Negrete, M. (2009). "Drift-based fragility assessment of confined masonry walls in seismic zones." *Engineering Structures*, Elsevier, 31(1), 170–181.

Saari, W. K., Hajjar, J. F., Schultz, A. E., and Shield, C. K. (2004). "Behavior of shear studs in steel frames with reinforced concrete infill walls." *Journal of Constructional Steel Research*, Elsevier, 60(10), 1453–1480.

Saari, W. K., Schultz, A. E., Hajjar, J. F., and Shield, C. K. (1999). *Behavior of shear connectors in steel frames with reinforced concrete infill walls*. Report No. ST-99-1, University of Minnesota, Minneapolis, MN, USA.

SAC Joint Venture. (1997). *Protocol for fabrication, inspection, testing, and documentation of beam-column connection tests and other experimental specimens*. Rep. No. SAC/BD-97 2, SAC Joint Venture, Richmond, CA, USA.

Salari, M. R., and Spacone, E. (2001). "Finite element formulations of one-dimensional elements with bond-slip." *Engineering Structures*, Elsevier, 23(7), 815–826.

Sanchez-Ricart, L., and Plumier, A. (2008). "Parametric study of ductile moment-resisting steel frames: A first step towards Eurocode 8 calibration." *Earthquake Engineering & Structural Dynamics*, Wiley, 37(7), 1135–1155.

Schafer, B., Easterling, W. S., Sabelli, R., Eatherton, M. R., and Hajjar, J. F. (2019). *Steel diaphragm innovation initiative workshop report*. Cold-Formed Steel Research Consortium (CFSRC), Baltimore, MD, USA.

Selamet, S., and Garlock, M. (2010). "Guidelines for modeling three dimensional structural connection models using finite element methods." *Proceedings of the International Symposium: Steel Structures, Culture & Sustainability*, Turkish Constructional Steelwork Association, Istanbul, Turkey.

Shin, S., and Engelhardt, M. D. (2013). "Cyclic performance of deep column moment frames with weak panel zones." *Proceedings of Advances in Structural Engineering and Mechanics (ASEM13)*, Advanced Institute of Science and Technology, Jeju, Korea.

SIA. (2011). *SIA 269/3: Existing structures – Steel structures*. Schweizerischer Ingenieur- und Architektenverein, Postfach, Zurich, Switzerland.

Sjaarda, M., Walbridge, S., and West, J. S. (2018). "Assessment of shear connection through composite beam modeling." *Transportation Research Record*, SAGE Publications, 2672(41), 177–185.

Skiadopoulos, A., Elkady, A., and Lignos, D. G. (2021). "Proposed panel zone model for seismic design of steel moment-resisting frames." *Journal of Structural Engineering*, American Society of Civil Engineers, 147(4), 04021006.

Suita, K., Yamada, S., Tada, M., Kasai, K., Matsuoka, Y., and Shimada, Y. (2008). "Collapse experiment on 4-story steel moment frame: Part 2 - Detail of collapse behavior." *Proceedings of the 14th World Conference on Earthquake Engineering (WCEE)*, Beijing, China.

Sumner, E. A., and Murray, T. M. (2002). "Behavior of extended end-plate moment connections subject to cyclic loading." *Journal of Structural Engineering*, American Society of Civil Engineers, 128(4), 501–508.

Sun, Q., Nie, X., Denavit, M. D., Fan, J., and Liu, W. (2019). "Monotonic and cyclic behavior of headed steel stud anchors welded through profiled steel deck." *Journal of Constructional Steel Research*, Elsevier, 157, 121–131.

Suzuki, A., and Kimura, Y. (2019). "Cyclic behavior of component model of composite beam subjected to fully reversed cyclic loading." *Journal of Structural Engineering*, American Society of Civil Engineers, 145(4), 04019015.

Suzuki, Y., and Lignos, D. (2018). "Fiber-based model for earthquake-induced collapse simulation of steel frame buildings." *Proceedings of the 11th US national conference on earthquake engineering*, Earthquake Engineering Research Institute, Oakland, CA, USA.

Suzuki, Y., and Lignos, D. G. (2015). "Large scale collapse experiments of wide-flange steel beam-columns." *Proceedings of the 8th International Conference on Behavior of Steel Structures in Seismic Areas (STESSA)*, Tongji University, Shanghai, China.

Suzuki, Y., and Lignos, D. G. (2019). "Development of collapse-consistent loading protocols for experimental testing of steel columns." *Earthquake Engineering & Structural Dynamics*, Wiley, 49(2), 114–131.

Suzuki, Y., and Lignos, D. G. (2021). "Experimental evaluation of steel columns under seismic hazard-consistent collapse loading protocols." *Journal of Structural Engineering*, American Society of Civil Engineers, 147(4), 04021020.

Tagawa, Y., Kato, B., and Aoki, H. (1989). "Behavior of composite beams in steel frame under hysteretic loading." *Journal of Structural Engineering*, American Society of Civil Engineers, 115(8), 2029–2045.

Taghavi, S., and Miranda, E. (2003). *Response assessment of nonstructural building elements*. Report No. 2003/05, Pacific Earthquake Engineering Research Center, Berkeley, CA, USA.

Tarbali, K., and Bradley, B. A. (2016). "The effect of causal parameter bounds in PSHA-based ground motion selection." *Earthquake Engineering & Structural Dynamics*, Wiley, 45(9), 1515–1535.

Tartaglia, R., D'Aniello, M., Rassati, G. A., Swanson, J. A., and Landolfo, R. (2018). "Full strength extended stiffened end-plate joints: AISC vs recent European design criteria." *Engineering Structures*, Elsevier, 159, 155–171.

Taylor, J. R. (1997). *An introduction to error analysis*. University Science Books, Sausalito, CA, USA.

Tremblay, R., Tchebotarev, N., and Filiatrault, A. (1997). "Seismic performance of RBS connections for steel moment resisting frames: influence of loading rate and floor slab." *Proceedings of 2nd International Conference on the Behavior of Steel Structures in Seismic Areas (STESSA)*, Kyoto, Japan.

Tschemmernegg, F., and Queiroz, G. (1995). “Mechanical modeling of semi-rigid joints for the analysis of framed steel and composite structures.” *Proceedings of the 3rd International Workshop on Connections in Steel Structures*, Elsevier, Trento, Italy, 237–247.

Tsitos, A., Bravo-Haro, M. A., and Elghazouli, A. Y. (2018). “Influence of deterioration modelling on the seismic response of steel moment frames designed to Eurocode 8.” *Earthquake Engineering & Structural Dynamics*, Wiley, 47(2), 356–376.

Uang, C.-M., Yu, Q.-S. “Kent,” Noel, S., and Gross, J. (2000). “Cyclic testing of steel moment connections rehabilitated with RBS or welded haunch.” *Journal of Structural Engineering*, American Society of Civil Engineers, 126(1), 57–68.

Vamvatsikos, D., and Cornell, C. A. (2002). “Incremental dynamic analysis.” *Earthquake Engineering & Structural Dynamics*, Wiley, 31(3), 491–514.

Venables, W. N., and Ripley, B. D. (2013). *Modern applied statistics with S-PLUS*. Springer Science & Business Media, New York, USA.

Vic-3D. (2010). *Vic-3D*. Correlated Solutions, Irmo, SC, USA.

Voce, E. (1948). “The relationship between stress and strain for homogeneous deformation.” *Journal of the Institute of Metals*, 74, 537–562.

Yamada, S., Satsukawa, K., and Kishiki, S. (2009). “Elasto-plastic behavior of panel zone in beam to external column connection with concrete slab.” *Journal of Structural and Construction Engineering AIJ*, Architectural Institute of Japan, 74(644), 1841–1849.

Young, B. (1972). *Residual stresses in hot-rolled members*. Report No. CUED/C-Struct/TR.8, Department of Engineering, University of Cambridge, Cambridge, UK.

Zandonini, R., and Bursi, O. S. (2000). “Cyclic behavior of headed stud shear connectors.” *Proceedings of Composite Construction in Steel and Concrete IV*, American Society of Civil Engineers, Reston, VA, USA, 470–482.

Zareian, F., and Kanvinde, A. (2013). “Effect of column-base flexibility on the seismic response and safety of steel moment-resisting frames.” *Earthquake Spectra*, SAGE Publications, 29(4), 1537–1559.

Zareian, F., and Medina, R. A. (2010). “A practical method for proper modeling of structural damping in inelastic plane structural systems.” *Computers & Structures*, Elsevier, 88(1), 45–53.

Zerbe, H., and Durrani, A. (1989). “Seismic response of connections in two-bay R/C frame subassemblies.” *Journal of Structural Engineering*, American Society of Civil Engineers, 115(11), 2829–2844.

Zhai, C., Lu, B., Wen, W., Ji, D., and Xie, L. (2018). “Experimental study on shear behavior of studs under monotonic and cyclic loadings.” *Journal of Constructional Steel Research*, Elsevier, 151, 1–11.

Zhou, F., Mosalam, K. M., and Nakashima, M. (2007). “Finite-element analysis of a composite frame under large lateral cyclic loading.” *Journal of Structural Engineering*, American Society of Civil Engineers, 133(7), 1018–1026.

Zona, A., Barbato, M., and Conte, J. P. (2008). “Nonlinear seismic response analysis of steel–concrete composite frames.” *Journal of Structural Engineering*, American Society of Civil Engineers, 134(6), 986–997.

Curriculum Vitae

Hammad El Jisr
Avenue du Silo 5
1020 Renens
Switzerland

Phone : +41 078 653 71 57
jisrhammad@gmail.com

PERSONAL STATEMENT

A highly motivated structural engineer seeking a challenging career in a forward-thinking company

EDUCATION

2017 – Present

École Polytechnique Fédérale de Lausanne (EPFL), Switzerland
Doctor of Philosophy (PhD) in Civil Engineering (December 2021)

PhD Dissertation Topic: "The Role of the Composite Floor System and Framing Action in the Seismic Performance of Composite Steel Moment-Resisting Frames"
Supervisor: Professor Dimitrios G. Lignos

Description: The project investigates the seismic stability and collapse behaviour of composite steel concrete moment frames by means of numerical modelling and a full-scale experimental program. Multi-fidelity modelling techniques are used to comprehend the role of the composite slab on the strength and stiffness deteriorating mechanisms under seismic loads. System-level analyses of composite moment frames are conducted through novel macro-modelling techniques in order to quantify the seismic risk and develop risk-based metrics that contribute to the advancement of current seismic provisions.

Doctoral Courses: Performance-based earthquake engineering, Seismic engineering, Advanced steel design, Scientific programming for engineers

2013 – 2014

Imperial College London, UK (Top in civil engineering in the UK)
MSc & DIC in General Structural Engineering (Top of the class, Distinction: 85.6%)

Thesis Topic: *"Local Buckling of Class 4 Elliptical Hollow Sections under Pure Axial Compression and Pure Uni-axial Bending"*
Supervisor: Professor Leroy Gardner

Specialist Subjects: Concrete and steel buildings, bridges, plated structures, concrete materials, stability, dynamics, finite element analysis, and non-linear structural analysis

Design Projects:
- Conceptual design of an arch bridge
- Preliminary design of a 7-story steel building with a steel transfer truss

2009 – 2013

American University of Beirut, Lebanon
Bachelor's in civil and Environmental Engineering (GPA: 4.0/4.0)

1996 – 2009

International School of Choueifat Koura, Lebanon
Baccalaureate/ General Sciences (2nd in North Lebanon out of 1883; Ave. 88.4%)

WORK EXPERIENCE

2017 – Present

École Polytechnique Fédérale de Lausanne (EPFL)
Teaching Assistant

Semester Projects:
- CIVIL-490 - Construction Project: Design of Composite-Steel Structures
- CIVIL-492 – Laboratory GC: Dynamic Stability of Steel Structures under Seismic Excitations Using a New Way to Learn about Structural Behaviour

2015 – 2017

Dar Al Handasah (Shair and Partners), Lebanon
Junior Structural Engineer

- Worked with the bridges team to model and design post-tensioned continuous beam bridges in Doha. Frame as well as grillage models were produced and the deck and substructure were designed according to BS 5400.
- Worked on a proposal for a series of bridges in Obhur Creek, Jeddah. Conceptual designs for 2 different alternatives were

proposed: Precast segmental post-tensioned deck and cast in-situ post-tensioned deck
- Worked on modelling a grid of prestressed transfer beams that supports the steel dome of Abraj Kudai in Makkah

2012 **UC Berkeley Pacific Earthquake Engineering Research Center, USA**
Intern (3 months)

- Testing of small-scale highly-resilient bridge columns
- Exposed to new column technologies for improving the performance of bridges

PUBLICATIONS

Journal Articles:
J1. El Jisr, H., Elkady, A., and Lignos, D. G. (2019). "Composite steel beam database for seismic design and performance assessment of composite-steel moment-resisting frame systems." *Bulletin of Earthquake Engineering*, Springer, 17(6), 3015–3039.
J2. El Jisr, H., Lignos, D. G., and Elkady, A. (2020). "Hysteretic Behavior of Moment-Resisting Frames Considering Slab Restraint and Framing Action." *Journal of Structural Engineering*, American Society of Civil Engineers, 146(8), 04020145.
J3. El Jisr, H., and Lignos, D. (2021). "Fragility Assessment of Beam-Slab Connections for Informing Earthquake-Induced Repairs in Composite-Steel Moment Resisting Frames." *Frontiers in Built Environment*, 7(1).

Conference Papers:
C1. El Jisr, H., and Lignos, D. (2018). "Composite Beam Effects and Implications to Seismic Design Provisions." *Proceedings of the 16th European Conference on Earthquake Engineering*. Thessaloniki, Greece.
C2. El Jisr, H., Kempter, N., and Lignos, D. G. (2021). "Full-scale Testing of a 2-Bay Composite Moment Resisting Frame under Lateral Cyclic Loading - Design and Setup Description." *Proceedings of the 9th International Conference on Composite Construction in Steel and Concrete*, RUHR-Universität Bochum, Stromberg, Germany
C3. El Jisr, H., and Lignos, D. G. (2021). "Hysteretic Behaviour of Shear Stud Connectors in Composite Steel Moment-Resisting Frames." *Eurosteel Proceedings*, Ernst & Sohn, Sheffield, UK

SKILLS

Languages
- English: Fluent (C2)
- French: Intermediate (B1)
- Arabic: Native

Computing Skills

Proficient in:

- Engineering Software Package: SAP, ETABS, SAFE, CSiBridge, OpenSEES, SCIA Engineer
- Finite Element Software Package: Abaqus, Ansys
- CAD Software Packages: AutoCAD, Autodesk Fusion 360, Autodesk Civil 3D
- Programming Languages: MATLAB, C++, Python, Fortran
- Microsoft Office

Work Ethics

Hardworking, strive for high achievement, perfectionist, conscientious, uses initiatives for individual and teamwork with excellent communication skills

AWARDS

- *Gyebi Kufuor Memorial Prize:* Annual award to a student of the Department of Civil and Environmental Engineering for excellence in Concrete Structures and Technology (Imperial College London)

- Placed on the Dean's honour list for top students for all the academic semesters (American University of Beirut)

REFERENCES

Available upon request